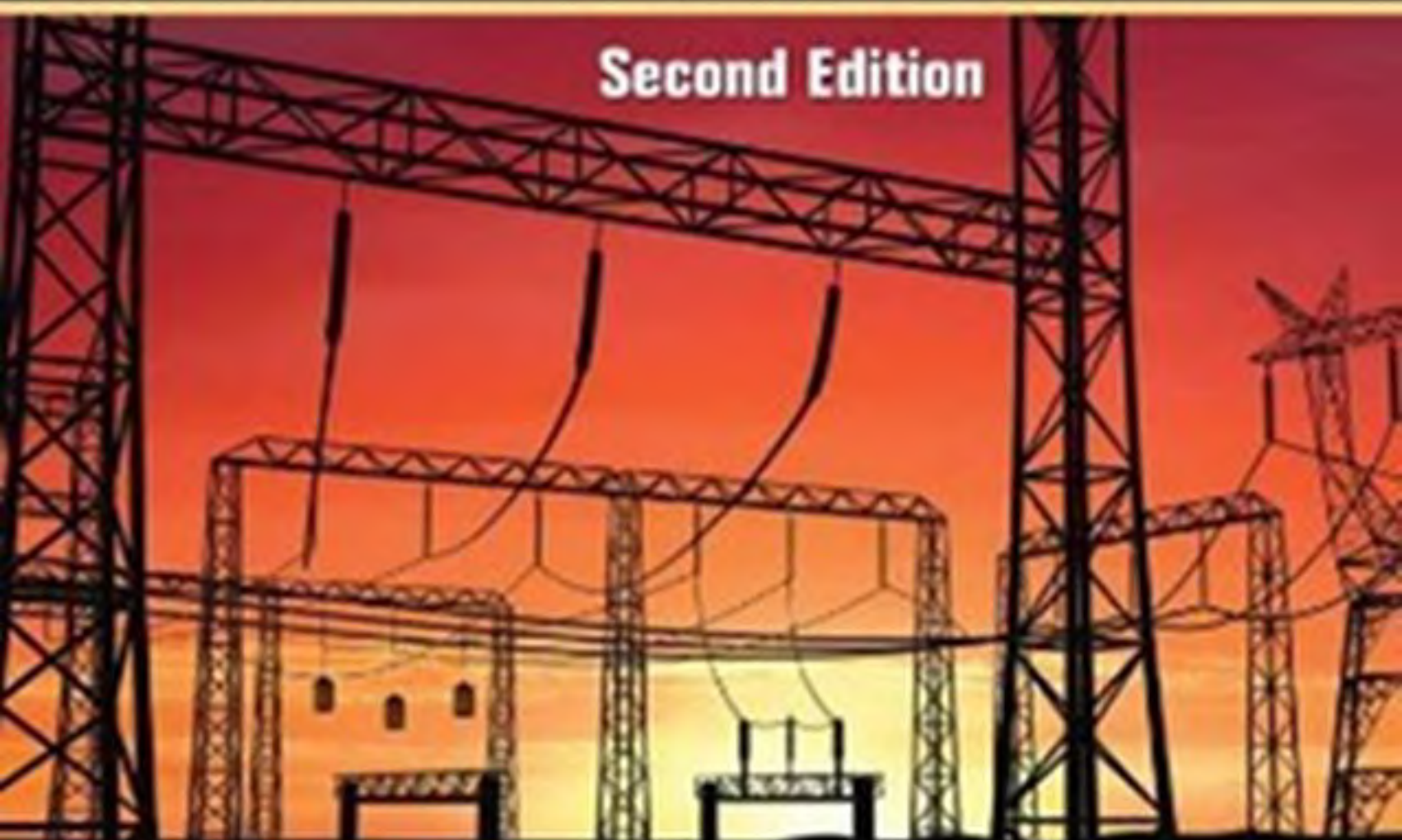


Transformer Design Principles



With Applications to Core-Form Power Transformers

Second Edition



Robert M. Del Vecchio • Bertrand Poulin
Pierre T. Feghali • Dilipkumar M. Shah
Rajendra Ahuja



CRC Press
Taylor & Francis Group

Transformer Design Principles

**With Applications to
Core-Form Power Transformers**

Second Edition

Transformer Design Principles

**With Applications to
Core-Form Power Transformers
Second Edition**

**Robert M. Del Vecchio • Bertrand Poulin
Pierre T. Feghali • Dilipkumar M. Shah
Rajendra Ahuja**



CRC Press

Taylor & Francis Group
Boca Raton London New York

CRC Press is an imprint of the
Taylor & Francis Group, an **informa** business

MATLAB® is a trademark of The MathWorks, Inc. and is used with permission. The MathWorks does not warrant the accuracy of the text or exercises in this book. This book's use or discussion of MATLAB® software or related products does not constitute endorsement or sponsorship by The MathWorks of a particular pedagogical approach or particular use of the MATLAB® software.

CRC Press
Taylor & Francis Group
6000 Broken Sound Parkway NW, Suite 300
Boca Raton, FL 33487-2742

© 2010 by Taylor and Francis Group, LLC
CRC Press is an imprint of Taylor & Francis Group, an Informa business

No claim to original U.S. Government works

Printed in the United States of America on acid-free paper
10 9 8 7 6 5 4 3 2 1

International Standard Book Number: 978-1-4398-0582-4 (Hardback)

This book contains information obtained from authentic and highly regarded sources. Reasonable efforts have been made to publish reliable data and information, but the author and publisher cannot assume responsibility for the validity of all materials or the consequences of their use. The authors and publishers have attempted to trace the copyright holders of all material reproduced in this publication and apologize to copyright holders if permission to publish in this form has not been obtained. If any copyright material has not been acknowledged please write and let us know so we may rectify in any future reprint.

Except as permitted under U.S. Copyright Law, no part of this book may be reprinted, reproduced, transmitted, or utilized in any form by any electronic, mechanical, or other means, now known or hereafter invented, including photocopying, microfilming, and recording, or in any information storage or retrieval system, without written permission from the publishers.

For permission to photocopy or use material electronically from this work, please access www.copyright.com (<http://www.copyright.com/>) or contact the Copyright Clearance Center, Inc. (CCC), 222 Rosewood Drive, Danvers, MA 01923, 978-750-8400. CCC is a not-for-profit organization that provides licenses and registration for a variety of users. For organizations that have been granted a photocopy license by the CCC, a separate system of payment has been arranged.

Trademark Notice: Product or corporate names may be trademarks or registered trademarks, and are used only for identification and explanation without intent to infringe.

Library of Congress Cataloging-in-Publication Data

Transformer design principles : with applications to core-form power transformers /
authors, Robert M. Del Vecchio ... [et al.]. -- 2nd ed.
p. cm.
"A CRC title."
Includes bibliographical references and index.
ISBN 978-1-4398-0582-4 (alk. paper)
1. Electric transformers--Design and construction. I. Del Vecchio, Robert M. II. Title.

TK2551.T765 2010
621.31'4--dc22

2009050603

Visit the Taylor & Francis Web site at
<http://www.taylorandfrancis.com>

and the CRC Press Web site at
<http://www.crcpress.com>

Contents

Preface.....	xiii
1. Introduction	1
1.1 Historical Background	1
1.2 Uses in Power Systems	2
1.3 Core-Form and Shell-Form Transformers	8
1.4 Stacked and Wound Core Construction	9
1.5 Transformer Cooling	10
1.6 Winding Types	12
1.7 Insulation Structures	14
1.8 Structural Elements	18
1.9 Modern Trends	21
2. Magnetism and Related Core Issues	23
2.1 Introduction	23
2.2 Basic Magnetism	25
2.3 Hysteresis	28
2.4 Magnetic Circuits.....	30
2.5 Inrush Current.....	35
2.6 Distinguishing Inrush from Fault Current	38
2.7 Optimal Core Stacking.....	46
3. Circuit Model of a Two-Winding Transformer with Core	49
3.1 Introduction	49
3.2 Circuit Model of the Core	49
3.3 Two-Winding Transformer Circuit Model with Core.....	53
3.4 Approximate Two-Winding Transformer Circuit Model without Core.....	56
3.5 Vector Diagram of a Loaded Transformer with Core	61
3.6 Per-Unit System	62
3.7 Voltage Regulation	64
4. Reactance and Leakage Reactance Calculations	69
4.1 Introduction	69
4.2 General Method for Determining Inductances and Mutual Inductances	70
4.2.1 Energy by Magnetic Field Methods	71
4.2.2 Energy from Electric Circuit Methods.....	73
4.3 Two-Winding Leakage Reactance Formula	76

- 4.4 Ideal Two-, Three-, and Multiwinding Transformers80
 - 4.4.1 Ideal Autotransformers83
- 4.5 Leakage Reactance for Two-Winding Transformers Based on Circuit Parameters.....84
 - 4.5.1 Leakage Reactance for a Two-Winding Autotransformer88
- 4.6 Leakage Reactances for Three-Winding Transformers88
 - 4.6.1 Leakage Reactance for an Autotransformer with a Tertiary Winding92
 - 4.6.2 Leakage Reactance between Two Windings Connected in Series and a Third Winding97
 - 4.6.3 Leakage Reactance of a Two-Winding Autotransformer with X-Line Taps98
 - 4.6.4 More General Leakage Reactance Calculations101
- 5. Phasors, Three-Phase Connections, and Symmetrical Components103
 - 5.1 Phasors.....103
 - 5.2 Wye and Delta Three-Phase Connections107
 - 5.3 Zig-Zag Connection112
 - 5.4 Scott Connection114
 - 5.5 Symmetrical Components117
- 6. Fault Current Analysis123
 - 6.1 Introduction123
 - 6.2 Fault Current Analysis on Three-Phase Systems124
 - 6.2.1 Three-Phase Line-to-Ground Fault127
 - 6.2.2 Single-Phase Line-to-Ground Fault.....127
 - 6.2.3 Line-to-Line Fault128
 - 6.2.4 Double Line-to-Ground Fault129
 - 6.3 Fault Currents for Transformers with Two Terminals per Phase130
 - 6.3.1 Three-Phase Line-to-Ground Fault133
 - 6.3.2 Single-Phase Line-to-Ground Fault.....133
 - 6.3.3 Line-to-Line Fault134
 - 6.3.4 Double Line-to-Ground Fault135
 - 6.3.5 Zero-Sequence Circuits.....136
 - 6.3.6 Numerical Example for a Single Line-to-Ground Fault138
 - 6.4 Fault Currents for Transformers with Three Terminals per Phase139
 - 6.4.1 Three-Phase Line-to-Ground Fault142
 - 6.4.2 Single-Phase Line-to-Ground Fault.....143
 - 6.4.3 Line-to-Line Fault145
 - 6.4.4 Double Line-to-Ground Fault147

- 6.4.5 Zero-Sequence Circuits 149
 - 6.4.6 Numerical Examples 149
 - 6.5 Asymmetry Factor 153
- 7. Phase-Shifting and Zig-Zag Transformers 155**
 - 7.1 Introduction 155
 - 7.2 Basic Principles 157
 - 7.3 Squashed Delta Phase-Shifting Transformer 159
 - 7.3.1 Zero-Sequence Circuit Model 163
 - 7.4 Standard Delta Phase-Shifting Transformer 165
 - 7.4.1 Zero-Sequence Circuit Model 169
 - 7.5 Two-Core Phase-Shifting Transformer 170
 - 7.5.1 Zero-Sequence Circuit Model 174
 - 7.6 Regulation Effects 175
 - 7.7 Fault Current Analysis 177
 - 7.7.1 Squashed Delta Fault Currents 179
 - 7.7.2 Standard Delta Fault Currents 181
 - 7.7.3 Two-Core Phase-Shifting Transformer Fault
Currents..... 182
 - 7.8 Zig-Zag Transformer 184
 - 7.8.1 Calculation of Electrical Characteristics 185
 - 7.8.2 Per-Unit Formulas 189
 - 7.8.3 Zero-Sequence Impedance 190
 - 7.8.4 Fault Current Analysis 192
- 8. Multiterminal Three-Phase Transformer Model 195**
 - 8.1 Introduction 195
 - 8.2 Theory 196
 - 8.2.1 Two-Winding Leakage Inductance..... 196
 - 8.2.2 Multiwinding Transformers 197
 - 8.2.3 Transformer Loading..... 201
 - 8.3 Transformers with Winding Connections within a Phase 202
 - 8.3.1 Two Secondary Windings in Series 202
 - 8.3.2 Primary Winding in Series with a Secondary
Winding..... 203
 - 8.3.3 Autotransformer 204
 - 8.4 Multiphase Transformers 205
 - 8.4.1 Delta Connection..... 207
 - 8.4.2 Zig-Zag Connection..... 209
 - 8.5 Generalizing the Model..... 211
 - 8.6 Regulation and Terminal Impedances 213
 - 8.7 Multiterminal Transformer Model for Balanced and
Unbalanced Load Conditions..... 215
 - 8.7.1 Theory..... 216
 - 8.7.2 Admittance Representation..... 218

8.7.2.1	Delta Winding Connection	220
8.7.3	Impedance Representation	222
8.7.3.1	Ungrounded Y Connection.....	223
8.7.3.2	Series-Connected Windings from the Same Phase.....	225
8.7.3.3	Zig-Zag Winding Connection.....	227
8.7.3.4	Autoconnection	228
8.7.3.5	Three Windings Joined	228
8.7.4	Terminal Loading	229
8.7.5	Solution Process	230
8.7.5.1	Terminal Currents and Voltages	230
8.7.5.2	Winding Currents and Voltages.....	230
8.7.6	Unbalanced Loading Examples	231
8.7.6.1	Autotransformer with Buried Delta Tertiary and Fault on Low-Voltage Terminal	231
8.7.6.2	Power Transformer with Fault on Delta Tertiary.....	232
8.7.6.3	Power Transformer with Fault on Ungrounded Y Secondary	233
8.7.7	Balanced Loading Example.....	234
8.7.7.1	Standard Delta Phase-Shifting Transformer....	234
8.7.8	Discussion.....	236
9.	Rabins' Method for Calculating Leakage Fields, Leakage Inductances, and Forces in Transformers	239
9.1	Introduction	239
9.2	Theory.....	240
9.3	Rabins' Formula for Leakage Reactance.....	253
9.3.1	Rabins' Method Applied to Calculate the Leakage Reactance between Two Windings That Occupy Different Radial Positions.....	253
9.3.2	Rabins' Method Applied to Calculate the Leakage Reactance between Two Axially Stacked Windings.....	257
9.3.3	Rabins' Method Applied to Calculate the Leakage Reactance for a Collection of Windings.....	259
9.4	Application of Rabins' Method to Calculate the Self-Inductance of and Mutual Inductance between Coil Sections.....	260
9.5	Determining the B-Field	263
9.6	Determination of Winding Forces.....	264
9.7	Numerical Considerations	267
10.	Mechanical Design.....	269
10.1	Introduction	269
10.2	Force Calculations.....	271

- 10.3 Stress Analysis.....273
 - 10.3.1 Compressive Stress in the Key Spacers275
 - 10.3.2 Axial Bending Stress per Strand276
 - 10.3.3 Tilting Strength279
 - 10.3.4 Stress in the Tie Bars283
 - 10.3.5 Stress in the Pressure Ring.....289
 - 10.3.6 Hoop Stress.....290
 - 10.3.7 Radial Bending Stress291
- 10.4 Radial Buckling Strength298
 - 10.4.1 Free Unsupported Buckling299
 - 10.4.2 Constrained Buckling.....302
 - 10.4.3 Experiment to Determine Buckling Strength.....303
- 10.5 Stress Distribution in a Composite Wire–Paper Winding Section307
- 10.6 Additional Mechanical Considerations312
- 11. Electric Field Calculations.....315**
 - 11.1 Simple Geometries.....315
 - 11.1.1 Planar Geometry315
 - 11.1.2 Cylindrical Geometry.....318
 - 11.1.3 Spherical Geometry321
 - 11.1.4 Cylinder–Plane Geometry322
 - 11.2 Electric Field Calculations Using Conformal Mapping.....327
 - 11.2.1 Physical Basis.....327
 - 11.2.2 Conformal Mapping.....328
 - 11.2.3 Schwarz–Christoffel Transformation332
 - 11.2.4 Conformal Map for the Electrostatic Field Problem334
 - 11.2.4.1 Electric Potential and Field Values338
 - 11.2.4.2 Calculations and Comparison with a Finite Element Solution346
 - 11.2.4.3 Estimating Enhancement Factors.....350
 - 11.3 Finite Element Electric Field Calculations.....352
- 12. Capacitance Calculations357**
 - 12.1 Introduction357
 - 12.2 Distributive Capacitance along a Winding or Disk358
 - 12.3 Stein’s Disk Capacitance Formula363
 - 12.4 General Disk Capacitance Formula.....371
 - 12.5 Coil Grounded at One End with Grounded Cylinders on Either Side372
 - 12.6 Static Ring on One Side of a Disk374
 - 12.7 Terminal Disk without a Static Ring.....375
 - 12.8 Capacitance Matrix376
 - 12.9 Two Static Rings378

12.10	Static Ring between the First Two Disks.....	382
12.11	Winding Disk Capacitances with Wound-in Shields.....	382
12.11.1	Analytic Formula.....	383
12.11.2	Circuit Model.....	386
12.11.3	Experimental Methods.....	391
12.11.4	Results	392
12.12	Multistart Winding Capacitance.....	396
13.	Voltage Breakdown and High-Voltage Design.....	399
13.1	Introduction	399
13.2	Principles of Voltage Breakdown.....	400
13.2.1	Breakdown in Solid Insulation	405
13.2.2	Breakdown in Transformer Oil	407
13.3	Geometric Dependence of Transformer-Oil Breakdown	410
13.3.1	Theory.....	412
13.3.2	Planar Geometry	412
13.3.3	Cylindrical Geometry.....	415
13.3.4	Spherical Geometry	416
13.3.5	Comparison with Experiment.....	418
13.3.6	Generalization	419
13.3.6.1	Breakdown for the Cylinder–Plane Geometry	421
13.3.6.2	Breakdown for the Disk–Disk-to-Ground Plane Geometry	421
13.3.7	Discussion	424
13.4	Insulation Coordination.....	425
13.5	Continuum Model of Winding Used to Obtain the Impulse–Voltage Distribution	429
13.5.1	Uniform Capacitance Model	430
13.5.2	Traveling Wave Theory	434
13.6	Lumped-Parameter Model for Transient Voltage Distribution.....	435
13.6.1	Circuit Description.....	435
13.6.2	Mutual and Self-Inductance Calculations.....	438
13.6.3	Capacitance Calculations.....	438
13.6.4	Impulse–Voltage Calculations and Experimental Comparisons.....	439
13.6.5	Sensitivity Studies.....	444
14.	Losses	447
14.1	Introduction	447
14.2	No-Load or Core Losses.....	448
14.2.1	Building Factor.....	452
14.2.2	Interlaminar Losses	452

- 14.3 Load Losses.....455
 - 14.3.1 I^2R Losses.....455
 - 14.3.2 Stray Losses456
 - 14.3.2.1 Eddy Current Losses in the Coils457
 - 14.3.2.2 Tieplate Losses.....461
 - 14.3.2.3 Tieplate and Core Losses Due to
Unbalanced Currents.....469
 - 14.3.2.4 Tank and Clamp Losses475
 - 14.3.3 Stray Losses Obtained from 3D Finite Element
Analyses482
 - 14.3.3.1 Shunts on the Clamps.....483
 - 14.3.3.2 Shunts on the Tank Wall.....486
 - 14.3.3.3 Effects of Three-Phase Currents on Losses.....487
 - 14.3.3.4 Stray Losses from the 3D Analysis versus
Analytical and Test Losses489
- 14.4 Tank and Shield Losses Due to Nearby Busbars490
 - 14.4.1 Losses Obtained with 2D Finite Element Study.....491
 - 14.4.2 Losses Obtained Analytically.....491
 - 14.4.2.1 Current Sheet492
 - 14.4.2.2 Delta Function Current.....493
 - 14.4.2.3 Collection of Delta Function Currents495
 - 14.4.2.4 Model Studies498
- 14.5 Tank Losses Associated with the Bushings500
 - 14.5.1 Comparison with a 3D Finite Element Calculation505
- 15. Thermal Design.....507**
 - 15.1 Introduction507
 - 15.2 Thermal Model of a Disk Coil with Directed Oil Flow508
 - 15.2.1 Oil Pressures and Velocities.....510
 - 15.2.2 Oil Nodal Temperatures and Path Temperature
Rises514
 - 15.2.3 Disk Temperatures.....516
 - 15.3 Thermal Model for Coils without Directed Oil Flow517
 - 15.4 Radiator Thermal Model.....518
 - 15.5 Tank Cooling.....522
 - 15.6 Oil Mixing in the Tank.....523
 - 15.7 Time Dependence.....526
 - 15.8 Pumped Flow.....527
 - 15.9 Comparison with Test Results.....528
 - 15.10 Determining m and n Exponents533
 - 15.11 Loss of Life Calculation.....535
 - 15.12 Cable and Lead Temperature Calculation538
 - 15.13 Tank Wall Temperature Calculation.....542
 - 15.14 Tieplate Temperature.....544
 - 15.15 Core Steel Temperature Calculation.....547

- 16. Load Tap Changers..... 549
 - 16.1 Introduction 549
 - 16.2 General Description of Load Tap Changers 549
 - 16.3 Types of Regulation 550
 - 16.4 Principles of Operation 552
 - 16.4.1 Resistive Switching 552
 - 16.4.2 Reactive Switching with Preventive Autotransformers..... 553
 - 16.5 Connection Schemes 555
 - 16.5.1 Power Transformers 555
 - 16.5.2 Autotransformers..... 556
 - 16.5.3 Use of Auxiliary Transformers..... 561
 - 16.5.4 Phase-Shifting Transformers 562
 - 16.5.5 Reduced versus Full-Rated Taps 562
 - 16.6 General Maintenance..... 562
- 17. Miscellaneous Topics 565
 - 17.1 Setting the Impulse Test Generator to Achieve Close to Ideal Waveshapes..... 565
 - 17.1.1 Impulse Generator Circuit Model 567
 - 17.1.2 Transformer Circuit Model 569
 - 17.1.3 Determining the Generator Settings for Approximating the Ideal Waveform 572
 - 17.1.4 Practical Implementation..... 576
 - 17.2 Impulse or Lightning Strike on a Transformer through a Length of Cable 579
 - 17.2.1 Lumped Parameter Model 579
 - 17.2.1.1 Numerical Example 581
 - 17.2.2 Traveling Wave Theory 582
 - 17.3 Air Core Inductance..... 584
 - 17.4 Electrical Contacts..... 587
 - 17.4.1 Contact Resistance 588
 - 17.4.2 Thermal Considerations..... 589
 - 17.4.3 Practical Considerations 592
- References 593

Preface

Like the original edition, the second edition of our book focuses on the physical principles behind transformer design and operation. This edition includes some, but not all, material from the first edition, with corrections as needed. It also includes a lot of new material, in particular, a chapter on multiterminal transformers, a section on a relatively new oil breakdown methodology, and a section on zig-zag transformers. The material has also been reorganized into what we hope is a more logical development. This edition uses the metric (international, or SI) system exclusively.

Transformers function in an environment where electrical, mechanical, and thermal requirements must be satisfied. Concepts from each of these disciplines must therefore be brought to bear on the design process. Starting from basic principles and providing a lot of background material, we derive design formulas and methods. Stressing the fundamentals will enable the design engineer and the transformer user, such as a utility engineer, to have a better understanding of the rationale behind design practices.

Because many of the design procedures are mathematically complicated, computer methods will most likely be employed in their implementation; personal computers can be used for this, and a good mathematical library would also be helpful. Since the first edition, electromagnetic 3D finite element programs have also become more generally available and useful. We will present some calculations using this tool, especially in conjunction with the impedance boundary method for dealing with eddy current losses in high-permeability materials such as tank walls. As in the first edition, important results can also be obtained with a 2D version.

Although this book primarily deals with power transformers, the physical principles we discuss and the mathematical modeling techniques we present apply equally well to other types of transformers. We keep the presentation as general as possible, with minimal use of jargon, so that designers or users of other transformer types will have little difficulty applying the results to their own designs. The emphasis on fundamentals will allow us to see where better approximations or different assumptions can be made in order to improve the accuracy or broaden the applicability of the results.

References are listed alphabetically at the end of the book and are referred to generally by the first three letters of the first author's last name followed by the last two digits of the publication date, for example, [Abc98]; where this format cannot be followed, an appropriate substitute is made.

1

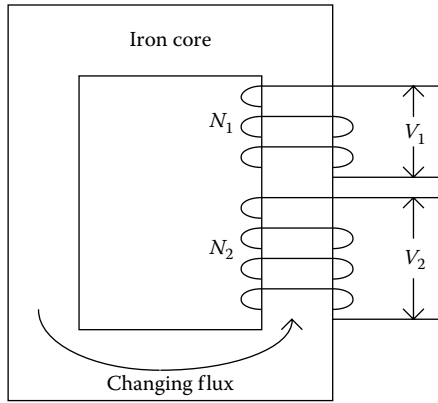
Introduction

1.1 Historical Background

Transformers are electrical devices that change or transform voltage levels between two circuits. In the process, current values are also transformed; however, the power transferred between the circuits is unchanged, except for a typically small loss that occurs in the process. This power transfer occurs only in alternating current (AC) or transient electrical conditions. Transformer operation is based on the *principle of induction* discovered by Faraday in 1831. He found that when a changing magnetic flux links a circuit, a voltage or electromotive force (emf) is induced in the circuit. The induced voltage is proportional to the number of turns linked by the changing flux. Thus, when two circuits are linked by a common flux and have different linked turns, different voltages will be induced; this is shown in [Figure 1.1](#), in which an iron core carries the common flux. The induced voltages V_1 and V_2 will differ, since the linked turns N_1 and N_2 differ.

Devices such as inductors, which are based on Faraday's discovery, were little more than laboratory curiosities until the advent of AC electrical systems for power distribution toward the end of the nineteenth century. The development of AC power systems and transformers occurred almost simultaneously because they are closely linked. The first practical transformer was invented by the Hungarian engineers Karoly Zipernowsky, Otto Blathy, and Miksa Deri in 1885 [Jes96], who worked for the Hungarian Ganz factory. Their device had a closed toroidal core made of iron wire. Its primary voltage was a few kilovolts, and the secondary voltage was about 100 volts. It was first used to supply electric lighting.

Although modern transformers differ considerably from these early models, the operating principle is still the same. In addition to the transformers used in power systems, which range in size from small units that are attached to the tops of telephone poles to units as large as a small house and weighing hundreds of tons, there are a myriad of transformers that are used in the electronics industry. These range in size from larger units weighing a few pounds, which are used to convert electrical outlet voltage to lower values required by transistorized circuitry, to the smaller

**FIGURE 1.1**

Transformer principle illustrated for two circuits linked by a common changing flux.

microtransformers, which are deposited directly onto silicon substrates via lithographic techniques.

We will not cover all of these transformer types in detail, but will instead focus on larger power transformers. However, many of the issues and principles discussed in this chapter are applicable to all transformers.

1.2 Uses in Power Systems

The transfer of electrical power over long distances becomes more efficient as the voltage level rises. This can be shown by considering a simplified example: Power P needs to be transferred over a long distance, in terms of the voltage V and line current I , power P can be expressed as

$$P = VI \quad (1.1)$$

For the purpose of discussion, let us assume that the line and load at the other end are purely resistive so that V and I are in phase (i.e., real quantities). For a line of length L and cross-sectional area A , its resistance is given by

$$R = \rho \frac{L}{A} \quad (1.2)$$

where ρ is the electrical resistivity of the line conductor. The line or transmission loss is

$$\text{Loss} = I^2 R \quad (1.3)$$

and the voltage drop in the line is

$$\text{Voltage drop} = IR \quad (1.4)$$

Substituting for I from Equation 1.1, the loss divided by the input power and the voltage drop divided by the input voltage are as follows:

$$\frac{\text{Loss}}{P} = \frac{PR}{V^2}, \quad \frac{\text{Voltage drop}}{V} = \frac{PR}{V^2} \quad (1.5)$$

Assuming that P is given, the fractional loss and voltage drop for a given line resistance greatly reduce as the voltage increases. However, there are limits to increasing the voltage, such as the availability of adequate and safe insulation structures and the increase of corona losses.

As we can see from Equation 1.5, for a given input power and fractional loss or voltage drop in the line, the line resistance increases as the voltage squared. Equation 1.2 shows that since L and ρ are fixed, with an increase in R with V the wire area A decreases, so that the wire weight per unit length also decreases. This implies that power at higher voltages can be transmitted by a line conductor of less weight at the same line efficiency as measured by line loss divided by power transmitted.

In practice, long-distance power transmission is carried out with voltages of 100–500 kV, and more recently, even up to 765 kV. These high voltages are, however, not safe for usage in households or factories. Therefore, transformers are necessary to convert these high voltages to lower levels at the receiving end. In addition, generators are designed to produce electrical power at voltage levels of ~10–40 kV for practical reasons such as cost and efficiency. Thus, transformers are also necessary at the sending end of the line to boost the generator voltage up to the required transmission levels. Figure 1.2 shows a simplified version of a power system, with actual voltages indicated.

Modern power systems usually have more than one voltage step-down from transmission to final distribution, with each step-down requiring a

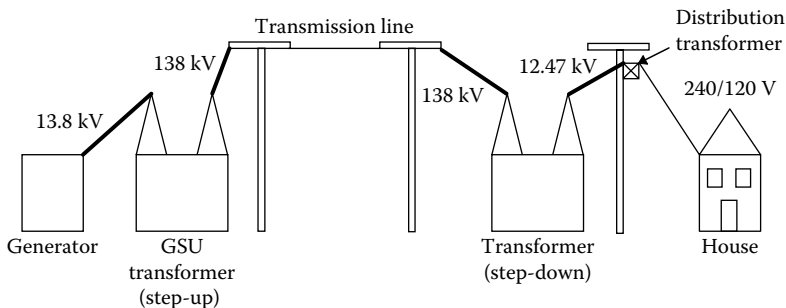


FIGURE 1.2

Schematic drawing of a power system. GSU stands for generator step-up transformer.

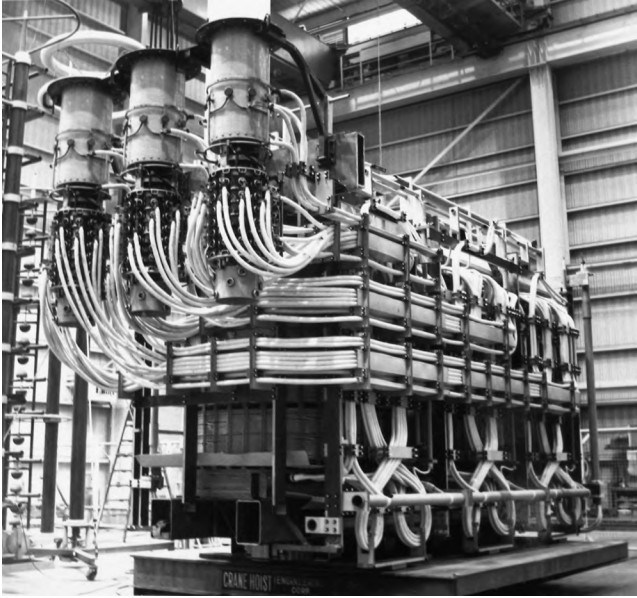
**FIGURE 1.3**

(See color insert following page 338.) Transformer located in a switching station and surrounded by auxiliary equipment. (Courtesy of Waukesha Electric Systems.)

transformer. Figure 1.3 shows a transformer situated in a switchyard. The transformer takes input power from a high-voltage line and converts it to lower-voltage power for local use. The voltage of the secondary power can be further stepped down before reaching the final consumer. This transformer can also supply power to a large number of smaller step-down transformers. A transformer of the size shown in Figure 1.3 can support a large factory or a small town.

Fine voltage adjustments are often necessary to compensate for voltage drops in the lines and other equipment. Since these voltage drops depend on the load current, they vary throughout the day. Transformer voltages can be adjusted by equipping transformers with tap changers, which are devices that add or subtract turns from a winding, thus altering its voltage. These devices can be used under load conditions or when the power is disconnected from the transformer and are called load or deenergized tap changers, respectively.

Load tap changers are sophisticated mechanical devices that can be controlled remotely. Tap changing can be made to occur automatically when the voltage levels drop below or rise above certain predetermined values. Maintaining nominal or expected voltage levels is highly desirable because much electrical equipment is designed to operate efficiently only within a certain voltage range. This is particularly true for solid-state equipment. Deenergized

**FIGURE 1.4**

Three-load tap changers attached to three windings of a power transformer. These tap changers were made by the Maschinenfabrik Reinhausen Co. in Germany.

tap changing is usually performed manually, which can be useful if a utility changes its operating voltage level at one location or if a transformer is moved to a different location where the operating voltage is slightly different. It is used less frequently than load tap changing. Figure 1.4 shows three load tap changers and their connections to three windings of a power transformer. The same transformer can be equipped with both types of tap changers.

Most power systems today are three-phase systems, that is, they produce sinusoidal voltages and currents in three separate lines or circuits with the sinusoids displaced in time relative to each other by one-third of a cycle or 120 electrical degrees, as shown in [Figure 1.5](#). At any point in time, the three voltages sum to zero. Such a system enables the use of generators and motors without commutators, which are cheaper and safer to operate. Thus, transformers that transform all three phase voltages are necessary. This can be accomplished by using three separate transformers, one for each phase, or more commonly by combining all three phases within a single unit, permitting some economies, particularly in the core structure ([Figure 1.6](#)). Like the voltages and currents, the three fluxes produced by the different phases are displaced in time by one-third of a cycle relative to each other, that is, when they overlap in the top or bottom yokes of the core, they cancel each other out. Thus, the yoke steel does not have to be designed to carry more flux than is produced by a single phase.

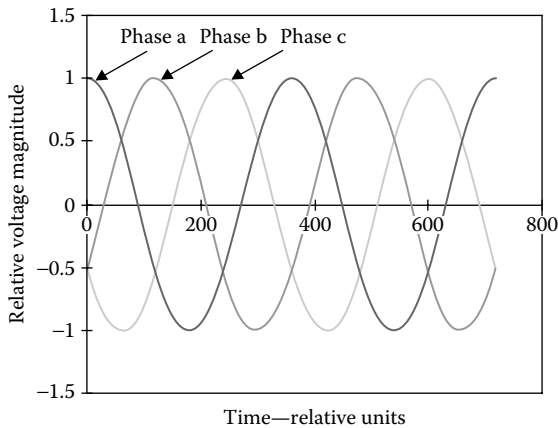


FIGURE 1.5
Three-phase voltages versus time.

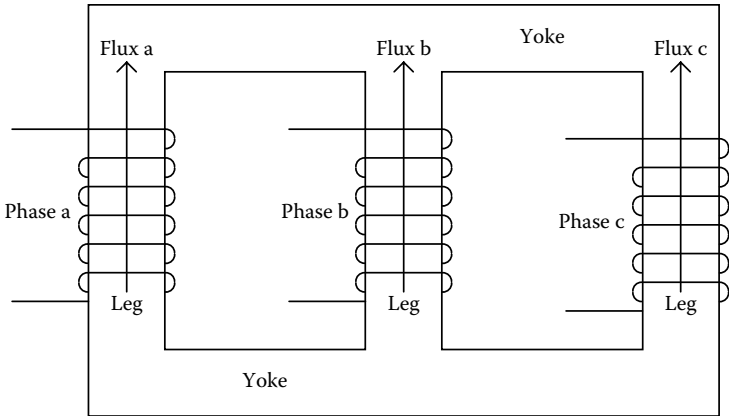


FIGURE 1.6
Three-phase transformer using a three-phase core.

Single-phase power is desirable at some stages in the power distribution system; for example, it is the common form of household power. Only one of the output circuits of a three-phase unit is used to feed power to a household or a group of households, and the other circuits feed similar groups of households. Because of the large numbers of households involved, on average, each phase will be equally loaded.

Because modern power systems are interconnected to share power between systems, sometimes voltages do not match at the interconnection points. Although tap-changing transformers can adjust the voltage magnitudes, they do not alter the phase angle. A phase angle mismatch can be corrected with a phase-shifting transformer, which inserts an adjustable phase shift between

the input and output voltages and currents. Large power phase shifters generally require two three-phase cores housed in separate tanks. A fixed phase shift, usually of 30° , can be introduced by suitably interconnecting the phases of standard three-phase transformers, but this is not adjustable.

Transformers are fairly passive devices containing very few moving parts, which include the tap changers and cooling fans used in most units and pumps used in oil-filled transformers to improve cooling. Because of their passive nature, transformers are expected to last a long time, commonly 25–50 years, with very little maintenance. Often, these units are replaced before their lifetime ends because of improvements in losses, efficiency, and other aspects. A certain amount of routine maintenance is naturally required. In oil-filled transformers, the oil quality must be checked periodically and filtered or replaced if necessary because good oil quality ensures sufficient dielectric strength to protect against electrical breakdown. In many power systems, the key parameters of the transformers such as oil and winding temperatures, voltages, currents, and oil quality as reflected in gas evolution are monitored continuously. These parameters can then be used to trigger logic devices to take corrective action should they fall outside the acceptable operating limits. This strategy can help prolong the useful operating life of a transformer. Figure 1.7 shows the end of a transformer tank where a control cabinet containing the



FIGURE 1.7

(See color insert following page 338.) End view of a transformer tank showing the control cabinet at the bottom left, which houses the electronics. The radiators are shown at the far left. (Courtesy of Waukesha Electric Systems.)

monitoring circuitry is located. Radiator banks equipped with fans projecting from the sides of the transformer tank are also shown. This transformer is fully assembled and is being moved to the testing location in the plant.

1.3 Core-Form and Shell-Form Transformers

Although transformers are primarily classified according to their function in a power system, they also have subsidiary classifications based on their construction. Examples of the former type of classification include generator step-up transformers, which are connected directly to the generator and raise the voltage up to the line transmission level, and distribution transformers, which are the final step in a power system, transferring single-phase power directly to the household or customer. Examples of the latter type of classification include core-form and shell-form transformers.

The basic difference between core-form and shell-form transformers is illustrated in [Figure 1.8](#). In a core-form transformer, the coils are wrapped or stacked around the core and form cylindrical-shaped coils. In general, high-voltage and low-voltage coils are wound concentrically, with the low-voltage coil inside the high-voltage one. In the shell-form design, the core is wrapped or stacked around the coils, which are generally flat or oval shaped and are called pancake coils, with the high- and low-voltage windings stacked side by side, generally in more than one layer in an alternating fashion.

Each of these construction types has advantages and disadvantages. Perhaps the ultimate distinction between the two is the cost. In distribution transformers, the shell-form design is very popular because the core can be economically wrapped around the coils. For moderate to large power transformers, the core-form design is more common, because the short circuit forces can be better managed with the cylindrical-shaped windings.

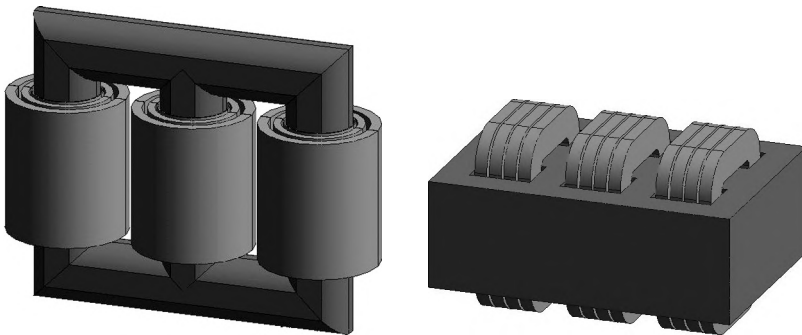


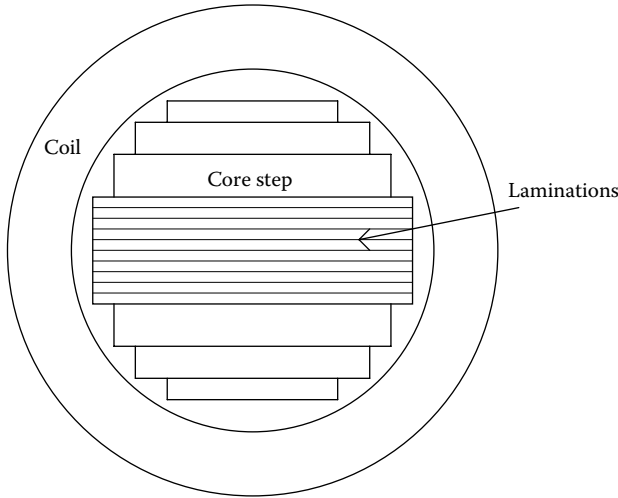
FIGURE 1.8
Three-phase core-form and shell-form transformers contrasted.

1.4 Stacked and Wound Core Construction

In both core-form and shell-form construction types, the core is made of thin layers or laminations of electrical steel, which is developed for its magnetic properties. These magnetic properties, however, are best along a particular direction, called the rolling direction, because the hot steel slabs move in this direction through the rolling mill, which squeezes them down to thin sheets. Thus in a good core design, this is the direction the flux naturally wants to take. The laminations can be wrapped around the coils or stacked. Wrapped or wound cores have few, if any, joints, so they carry flux nearly uninterrupted by gaps. Stacked cores have gaps at the corners where the core steel changes direction, resulting in poorer magnetic characteristics when compared with wound cores. In larger power transformers, stacked cores are more common, whereas in small distribution transformers, wound cores predominate. The laminations for both types of cores are coated with an insulating coating to prevent the development of large eddy current paths, which would lead to high losses.

In one type of wound core construction, the core is wound into a continuous coil, and is cut so that it can be inserted around the coils. The cut laminations are then shifted relative to each other and reassembled to form a staggered or stepped-type joint. This type of joint allows the flux to make a smoother transition over the cut region than would be possible with a butt-type joint where the laminations are not staggered. Very often in addition to cutting, the core is reshaped into a rectangular shape to provide a tighter fit around the coils. Because the reshaping and cutting operations introduce stress into the steel, which is generally bad for the magnetic properties, these cores need to be reannealed before use to help restore the magnetic properties. A wound core without a joint would need to be wound around the coils, or the coils would need to be wound around the core. Techniques for doing this are available but are somewhat costly.

In the stacked cores used for core-form transformers, the coils are circular cylinders that surround the core legs. In smaller transformers, up to a 10 MVA three-phase rating or a 5 MVA single-phase rating, the cross section of the core legs may be circular or rectangular, based on either economical reasons or the manufacturer's preference and technology. In larger ranges, the preferred cross section of the core is circular, as this will maximize the flux-carrying area. In practice, the core is stacked in steps, which approximates a circular cross section as shown in [Figure 1.9](#). Note that the laminations come out of the paper and carry flux in the sheet rolling direction. The space between the core and the innermost coil is needed to provide insulation clearance for the voltage difference between the winding and the core, which is at ground potential. The space is also used to accommodate the cooling medium, such as oil, to cool the core and the inner coil. Structural elements to prevent the coil from collapsing under short circuit forces may also be placed in this region.

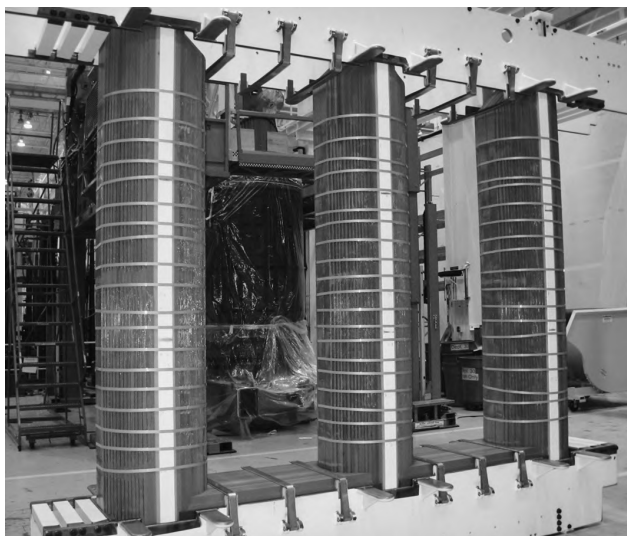
**FIGURE 1.9**

Stepped core used in core-form transformers to approximate a circular cross section.

In practice, because only a limited number of standard sheet widths are kept in inventory and because stack heights are also discretized, at least by the thickness of an individual sheet, ideal circular coverage cannot be achieved. [Figure 1.10](#) shows a three-phase stepped core for a core-form transformer without the top yoke, which is added after the coils are inserted over the legs. The bands around the legs are used to facilitate the handling of the core and can also be used to hold the laminations together more tightly and prevent them from vibrating during service. Such vibrations are a source of noise.

1.5 Transformer Cooling

Because the efficiency of power transformers is usually greater than 99%, the input and output powers are nearly the same. However, because of the small amount of inefficiency, losses occur inside the transformer. These losses are I^2R losses in the conductors, losses in the electrical steel due to the changing magnetic flux, and losses in metallic tank walls and other metallic structures caused by the stray time varying flux, which induces eddy currents. These losses lead to temperature increases, which must be controlled by cooling. The primary cooling media for transformers are oil and air. In oil-cooled transformers, the coils and core are immersed in an oil-filled tank. The oil is then circulated through radiators or other types of heat exchangers so that the ultimate cooling medium is the surrounding air, or possibly water for

**FIGURE 1.10**

(See color insert following page 338.) Three-phase stepped core for a core-form transformer without the top yoke.

some types of heat exchangers. In small distribution transformers, the tank surface in contact with the air provides enough cooling surface so that radiators are not needed. Sometimes, in these units, the tank surface area is augmented by means of fins or corrugations.

The cooling medium in contact with the coils and core must provide adequate dielectric strength to prevent electrical breakdown or discharge between components at different voltage levels. For this reason, oil immersion is common in higher-voltage transformers because oil has a higher breakdown strength than air. Often the natural convection of oil through the windings, driven by buoyancy effects, provides adequate cooling so that pumping is not necessary. Air is a more efficient cooling medium when it is blown by fans through the windings for air-cooled units.

In some applications, the choice of oil or air as the coolant is dictated by safety considerations such as the possibility of fires. For units inside buildings, air cooling is common because of the reduced fire hazard. Although transformer oil is combustible, there is usually little danger of fire because the transformer tank is often sealed from the outside air or the oil surface is blanketed with an inert gas such as nitrogen. Although the flash point of oil is quite high, if excessive heating or sparking occurs inside an oil-filled tank, combustible gasses could be released.

Environment also plays a role in the choice of coolants. Mineral oil used in transformers is known to be detrimental to the environment if there is an accident. For transformers such as those used on planes or trains or units

designed to be transportable for emergency use, air cooling is preferred. For other units that are not so restricted, oil cooling is preferred. Oil-cooled transformers are used in everyday units, from large generator or substation units to distribution units on telephone poles.

Other cooling media find limited use in certain applications, such as sulfur hexafluoride gas, which is usually pressurized. This is a relatively inert gas that has a higher breakdown strength than air and is used in high-voltage units where oil cannot be used and where air does not provide enough dielectric strength. Usually, the standard transformer oil is used in oil-cooled transformers. However, for specialized usage, other types of oils are also used. For example, silicone oil can be used at a higher temperature than the standard transformer oil and is less of a fire hazard. Natural ester-based oils are also used increasingly for environmental reasons. These are made from edible seeds and are biodegradable. They also have a low flammability and are nontoxic.

1.6 Winding Types

The two main methods of winding the coils for core-form power transformers are shown in Figure 1.11. Both types are cylindrical coils that have an overall rectangular cross section. In a disk coil, the turns are arranged in horizontal

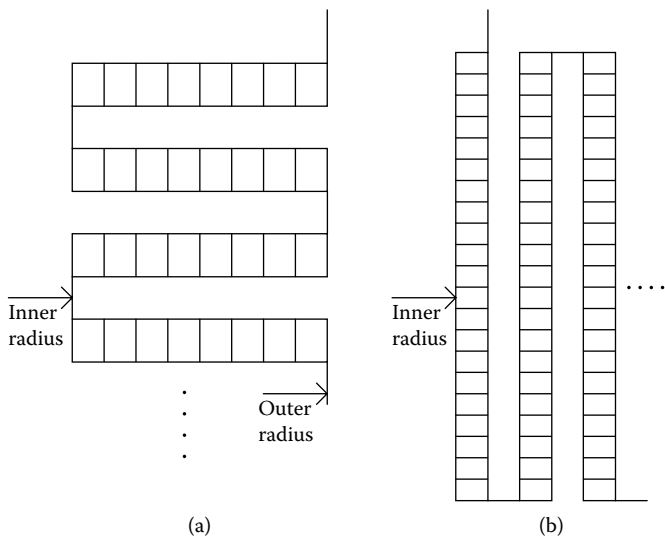


FIGURE 1.11
Two major types of coil construction for core-form power transformers. (a) Disk coil, (b) layer coil.

layers called disks, which are wound alternately out-in, in-out, and so on. The winding is usually continuous so that the last inner or outer turn gradually transitions between the adjacent layers. When the disks have only one turn, the winding is called a helical winding. The total number of turns will usually determine whether the winding will be a disk or helical winding. The turns within a disk are usually touching so that a double layer of insulation separates the metallic conductors. The space between the disks is left open, except for structural separators called radial spacers or key spacers. This allows room for cooling fluid to flow between the disks, in addition to providing clearance for withstanding the voltage difference between them.

In a layer coil, the coils are wound in vertical layers, top-bottom, bottom-top, and so on. The turns are typically wound in contact with each other in the layers, but the layers are separated by spacers so that the cooling fluid can flow between them. These coils are also usually continuous, with the last bottom or top turn transitioning between the layers.

Both types of winding are used in practice, and each type has proponents. In certain applications, one or the other type may be more efficient. However, in general, they both can be designed to function well in terms of ease of cooling, ability to withstand high voltage surges, and mechanical strength under short circuit conditions.

If these coils are wound with more than one wire or cable in parallel, then crossovers or transpositions, which interchange the positions of the parallel cables at various points along the winding, must be inserted. This will cancel the loop voltages induced by the stray flux. Otherwise, such voltages will drive currents around the loops formed when the parallel turns are joined at both ends of the winding, creating extra losses.

The stray flux also causes localized eddy currents in the conducting wire. Their magnitude depends on the cross-sectional dimensions of the wire. These eddy currents and their associated losses can be reduced by subdividing the wire into strands of smaller cross-sectional dimensions. However, these strands are then parallel and must therefore be transposed to reduce the loop voltages and currents. This can be done during the winding process, when the parallel strands are wound individually. Wire of this type, consisting of individual strands covered with an insulating paper wrap, is called magnet wire. The transpositions can also be built into a cable called continuously transposed cable, which generally consists of a bundle of 5–83 strands or more, each covered with a thin enamel coating. One strand at a time is transposed along the cable so that all the strands are eventually transposed at every turn around the core. The overall bundle is then sheathed in a paper wrap.

Figure 1.12 shows a disk winding situated over inner windings and core and clamped at both ends via the insulating blocks and steel structure. Short horizontal gaps are visible between the disks. Vertical columns of radial or key spacer projections are also visible. This outer high-voltage winding is center fed so that the top and bottom halves are connected in parallel. The leads feeding this winding are on the left.

**FIGURE 1.12**

(See color insert following page 338.) Disk winding shown in position over inner windings and core. Clamping structures and leads are also shown. (Courtesy of Waukesha Electric Systems.)

1.7 Insulation Structures

Transformer windings and leads must operate at high voltages relative to the core, tank, and structural elements. In addition, different windings and even parts of the same winding operate at different voltages. Therefore, some form of insulation should be provided between these various parts to prevent voltage breakdown or corona discharges. The surrounding oil or air, which provides cooling, also has some insulating value. The oil is of a special composition and must be purified to remove small particles and moisture. The type of oil most commonly used is called transformer oil. Further insulation is provided by paper that covers the wire or cables. When saturated with oil, this paper has a high insulation value. Besides paper, other types of

wire covering are sometimes used, mainly for specialty applications such as operation at a higher temperature. Other insulating structures are made of pressboard and are generally made in the form of a sheet and often wrapped in a cylindrical shape. Pressboard is a material made of cellulose fibers that are compacted together into a fairly dense and rigid matrix. Key spacers, blocking material, and lead support structures are commonly made of pressboard or wood.

Although normal operating voltages are quite high (10–500 kV), the transformer must be designed to withstand even higher voltages that can occur when lightning strikes the electrical system or when power is suddenly switched on or off in some part of the system. Such voltages occur rarely and can permanently damage the insulation and disable the unit unless the insulation is designed to withstand them. Events causing these voltages are usually of a short duration. The insulation breakdown depends on time. A short-duration high-voltage pulse is no more likely to cause breakdown than a long-duration low-voltage pulse. That is, the same insulation that can withstand continuously-present normal operating voltages can also withstand the brief high voltages arising from lightning strikes or switching operations. To ensure that the abnormal voltages do not exceed the breakdown limits determined by their expected durations, lightning or surge arrestors are often used to limit the voltages to a certain value so that breakdown will not occur, assuming their durations remain within the expected range.

Because of the different dielectric constants of oil or air and paper, the electric stresses are unequally divided between them. Since the dielectric constant of oil is about half that of paper, and that of air is an even smaller fraction than that of paper, the electric stresses are generally higher in oil or air than in the paper insulation. Unfortunately, oil or air has a lower breakdown stress than paper. Subdividing the oil gaps using thin insulating barriers, usually made of pressboard, can increase the breakdown stress in the oil. Thus, large oil gaps between the windings are usually subdivided by multiple pressboard barriers, as shown schematically in [Figure 1.13](#). This is referred to as the major insulation structure. The oil gap thicknesses are maintained by long vertical narrow sticks glued around the circumference of the cylindrical pressboard barriers. The barriers are often extended by end collars, which curve around the ends of the windings to provide subdivided oil gaps at both ends of the windings to strengthen these end oil gaps against voltage breakdown.

The minor insulation structure consists of the smaller oil gaps that separate the disks and are maintained by the key spacers—narrow insulators, usually made of pressboard, spaced radially around the disk's circumference, as shown in [Figure 1.13b](#). In general, these oil gaps are small enough that subdivision is not required. In addition, the turn-to-turn insulation, usually made of paper, can be considered a part of the minor insulation structure. [Figure 1.14](#) shows a winding during construction with key spacers and vertical sticks visible.

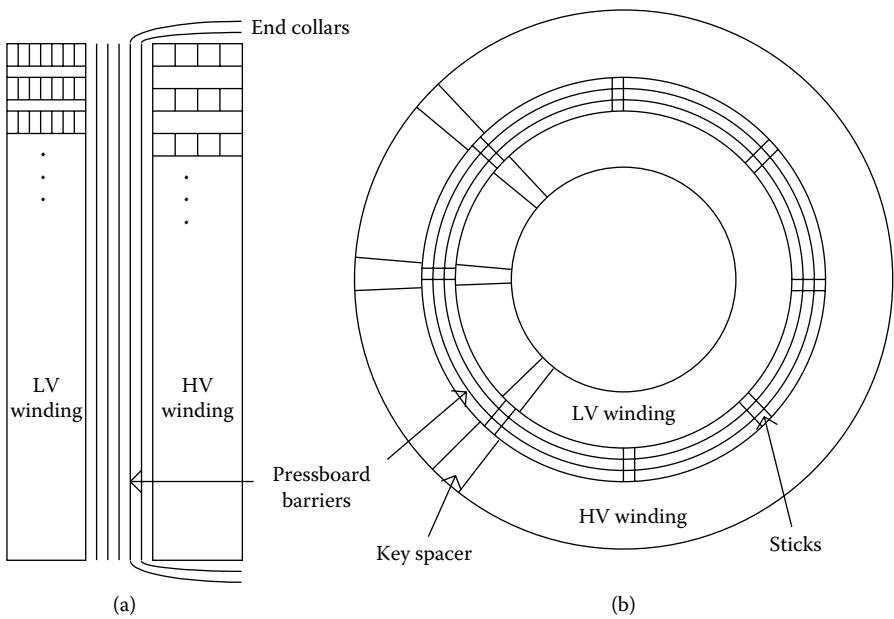


FIGURE 1.13 Major insulation structure consisting of multiple barriers between windings. Not all the key spacers or sticks are shown. (a) Side view, (b) top view.

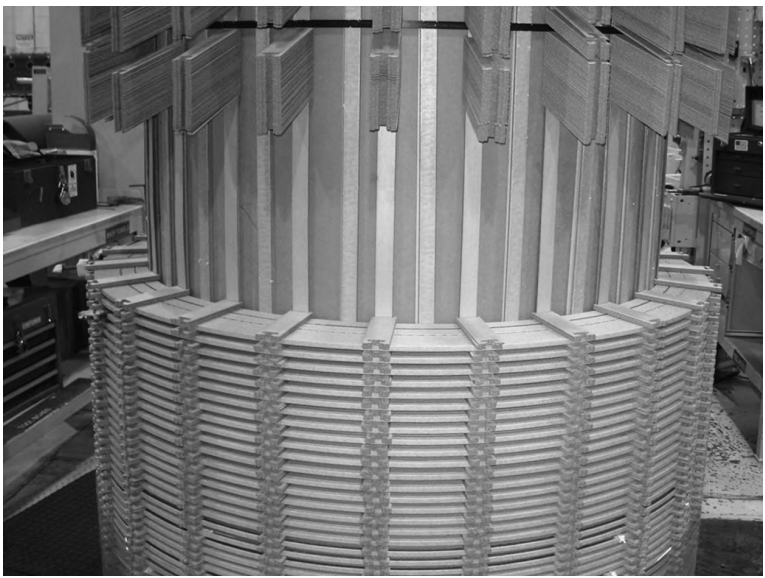
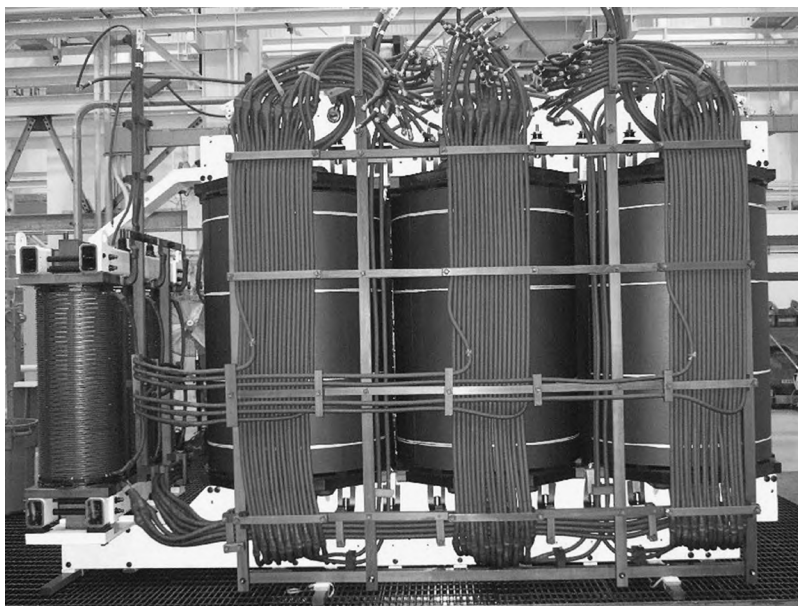


FIGURE 1.14 (See color insert following page 338.) A partially wound winding showing the key spacers and vertical sticks.

**FIGURE 1.15**

(See color insert following page 338.) Leads and their supporting structure emerging from the coils on one side of a three-phase transformer. (Courtesy of Waukesha Electric Systems.)

The leads that connect the windings to the bushings or tap changers or to other windings must also be properly insulated because they are high voltage and pass close to tank walls or structural supports, which are grounded. They can also pass close to other leads at different voltages. High stresses can be developed at bends in the leads, particularly if they are sharp, so that additional insulation may be required in these areas. Figure 1.15 shows an extensive set of leads along with structural supports made of pressboard or wood. The leads pass close to the metallic clamps at the top and bottom and will also be near the tank wall when the core and coil assembly is inserted into the tank.

Although voltage breakdown levels in oil can be increased by means of barrier subdivisions, there is another breakdown process that occurs along the surfaces of the insulation due to creep, which must also be guarded against. Creep breakdown requires that sufficiently high electric stresses are directed along the surface as well as the presence of sufficiently long uninterrupted paths over which the high stresses are present. Thus, the barriers themselves, sticks, key spacers, and lead supports can be a source of breakdown due to creep. Ideally, one should position these insulation structures so that their surfaces conform to the voltage equipotential surfaces to which the electric field is perpendicular, and thus, no electric fields will be directed along the surface. This is not always possible in practice, and sometimes a compromise must be reached.

The major and minor insulation designs, including overall winding-to-winding separation, number of barriers, disk-to-disk separation, and paper covering thickness, are often determined by design rules based on extensive experience. However, in newer or unusual designs, a field calculation using a finite-element program or other numerical procedure is often desirable, especially when there is potential for creep breakdown. Although these methods can provide accurate calculations of electric stresses, the breakdown process is not as well understood, so there is usually some judgment involved in determining the acceptable level of electrical stress.

1.8 Structural Elements

Under normal operating conditions, the electromagnetic forces acting on the transformer windings are quite modest. However, if a short-circuit fault occurs, the winding currents can increase between 10- and 30-fold, resulting in forces 100–900 times the normal because the forces increase as the square of the current. The windings and supporting structure must be designed to withstand these fault current forces without permanent distortion of the windings or supports. Because current protection devices are usually installed, the fault currents are interrupted after a few cycles, however, that is still long enough to do some damage if the supporting structure is inadequate.

Faults can be caused by falling trees that hit power lines, providing a direct current path to the ground or by animals or birds bridging across two lines belonging to different phases, causing a line-to-line short. These rarely occur, but their probability increases over the 20–50-year lifetime of a transformer so that sufficient mechanical strength to withstand such events is required.

The coils are generally supported with pressure rings at the ends. These are thick rings made of pressboard or another material that cover the winding ends. The center opening allows the core to pass through. The size of the rings is between 30 and 180 mm for large power transformers. Since all the windings are not necessarily of the same height, some pressboard or wood blocking is required between the tops of the windings and the rings. Additional blocking is usually placed between the ring and the top yoke and clamping structure to provide clearance between the high winding voltages and the grounded core and metallic clamp ([Figure 1.12](#)).

The top and bottom clamps are joined by vertical tie plates, sometimes called flitch plates, which pass along the sides of the core. The tie plates are solidly attached at both ends so that they pull the top and bottom clamps together by means of tightening bolts, thus compressing the windings. The compressive forces are transmitted along the windings via the key spacers, which must be strong enough to accommodate these forces. The clamps and tie plates are usually made of structural steel. Axial forces, which tend to

**FIGURE 1.16**

(See color insert following page 338.) Top view of a clamping structure for a three-phase transformer.

elongate the windings when a fault occurs, will put the tie plates in tension. The tie plates must also be strong enough to carry the gravitational load when the core and coils are lifted as a unit because the lifting hooks are attached to the clamps. The tie plates are about 10 mm thick and are of varying widths depending on the expected short-circuit forces and transformer weight. The width is often subdivided to reduce eddy current losses. Figure 1.16 shows a top view of the clamping structure.

The radial fault forces are countered inwardly by the sticks separating the oil barriers and by additional support next to the core. The windings themselves, particularly the innermost winding, are often made of hardened copper or bonded cable to provide additional resistance to the inward radial forces. The outermost winding is usually subjected to an outer radial force, putting the wires or cables in tension. The material must be strong enough to resist these tensile forces, as there is no supporting structure on the outside to counter these forces. A measure of the material's strength is its proof stress—the stress required to produce a permanent elongation of 0.2% (sometimes 0.1% is used). Copper of a specified proof stress can be ordered from the wire or cable supplier.

The leads are also acted on by extra forces during a fault. These forces are produced by the stray flux from the coils or from nearby leads, interacting with the lead's current. The leads are therefore braced by wood or pressboard supports that extend from the clamps. This lead support structure can be

quite complicated, especially if there are many leads and interconnections, so it is usually custom-made for each unit. An example of such a structure is shown in [Figure 1.15](#).

The assembled coil, core, clamps, and lead structure are placed in a transformer tank. The tank serves many functions: It contains the oil for an oil-filled unit and protects not only the coils and other transformer components but also personnel from the high voltages present inside the grounded tank. If it is made of soft (magnetic) steel, it keeps stray flux from reaching outside the tank. The tank is usually airtight so that air cannot enter and oxidize the oil.

Besides being a containment vessel, the tank also has numerous attachments such as bushings for getting the electrical power into and out of the unit, an electronic control and monitoring cabinet for recording and transferring sensor information to remote processors or receiving remote control signals, and radiators with or without fans to provide cooling. On certain units, there is a separate tank compartment for tap-changing equipment. Some units have a conservator attached to the tank cover or to the top of the radiators. This is a large, usually cylindrical structure that contains oil that is contiguous with the main tank oil. The conservator also has an air space, which is separated from the oil by a sealed diaphragm. Thus, as the tank oil expands and contracts due to temperature changes, the flexible diaphragm accommodates these volume changes while maintaining a sealed oil environment. Figure 1.17 shows a large power transformer with a cylindrical

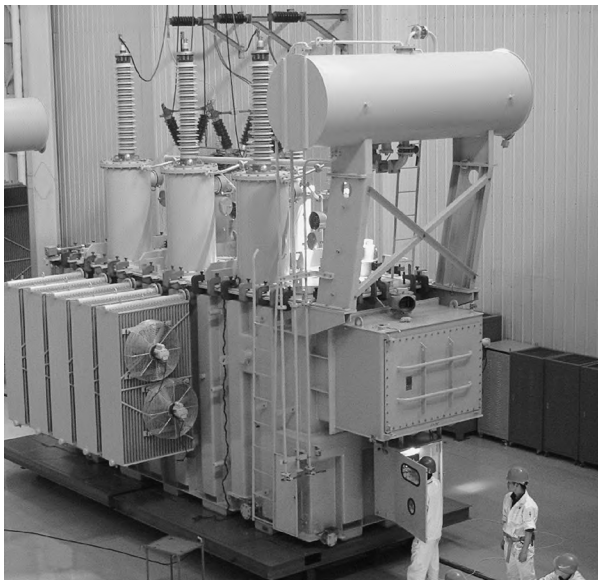


FIGURE 1.17

(See color insert following page 338.) Large power transformer showing tank and attachments.

conservator visible on top. Bushings mounted on top of the tank are visible and the radiators with fans are also shown. Technicians are working on the control box.

1.9 Modern Trends

Changes in power transformers tend to occur very slowly. The issues of reliability over long periods of time and compatibility with existing systems must be addressed by any new technology. One major change that has been ongoing since the earliest transformers is the improvement in the core steel. The magnetic properties, including losses, have improved dramatically over the years. Better stacking methods, such as stepped lapped construction, have resulted in lower losses at the joints. The use of laser or mechanical scribing has also helped to lower the losses in these steels. Further incremental improvements in all of these areas can be expected.

The development of amorphous metals as a core material is relatively new. Although these materials have very low losses, even lower than the best-rolled electrical steels, they also have a rather low saturation induction (~1.5 T vs. 2 T for rolled steels). They are also rather brittle and difficult to stack. This material is more expensive than rolled electrical steel, and since expense is always an issue, this has limited its use. However, this could change with the cost of no-load losses. Amorphous metals are used as wound cores in distribution transformers; however their use as stacked cores in large power transformers is not common.

The development of improved wire types, such as transposed cable with epoxy bonding, is an ongoing process. Newer types of wire insulation coverings, such as Nomex, are now used. Nomex is a synthetic material that can be used at higher temperatures than paper. It has a lower dielectric constant than paper, so it produces a more favorable stress level in the adjacent oil than does paper. Although it is more expensive than paper, it has found a niche in air-cooled transformers and in the rewinding of older transformers. Its thermal characteristics would be underutilized in transformers filled with transformer oil because of the limitations on the oil temperatures.

Pressboard insulation has undergone various improvements over time, such as precompressing to produce higher density material. This results in greater dimensional stability in transformer applications and is especially helpful in the case of the key spacers that bear the compressional forces acting on the winding. Also, preformed parts made of pressboard, such as collars at the winding ends and high-voltage lead insulation assemblies, are becoming more common and are facilitating the development of higher-voltage transformers.

Perhaps the biggest scientific breakthrough that could revolutionize future transformers is the discovery of high-temperature superconductors, which are still in the early stages of development. They can operate at liquid nitrogen temperatures, a big improvement over the older superconductors that operate at liquid helium temperatures. However, making these new superconductors into wires of the lengths required in transformers is very difficult. Nevertheless, prototype units are being built and technological improvements can be expected [Meh97].

One change occurring in newer transformers is the increasing use of online monitoring devices. Fiber optic temperature sensors are inserted directly into the windings to monitor the hottest winding temperature. This can be used to keep the transformer's loading or overloading within the appropriate bounds so that the acceptable insulation and adjacent oil temperatures are not exceeded and the thermal life is not negatively impacted. Gas analysis devices are being developed to continuously record the amounts and composition of gasses in the cover gas or dissolved in the oil. This can provide an early indication of overheating or arcing so corrective action can be taken before the situation deteriorates further. Newer fiber optic current sensors are being developed based on the Faraday effect. These weigh considerably less than present current sensors and are much less bulky. Newer miniaturized voltage sensors are also being developed. Sensor data can be sent in digitized form from the transformer to a remote computer for further processing. New software analysis tools should also help to more accurately analyze fault conditions or operational irregularities.

Although tap changers are mechanical marvels that operate very reliably over hundreds of thousands of tap changing operations, as with any mechanical device, they are subject to wear and must be replaced or refurbished from time to time. Electronic tap changers that use solid state components have been developed. Aside from essentially eliminating the wear problem, they also have a much faster response time than mechanical tap changers, which is very useful in some applications. Their expense compared to that of mechanical tap changers has been one factor limiting their use. Further developments, perhaps resulting in a lower cost, can be expected in this area.

As mentioned in [Section 1.2](#), there are incentives to transmit power at higher voltages. Some of the newer high-voltage transmission lines operate in a DC mode. In these cases, the conversion equipment at the ends of the lines that change AC to DC and vice versa requires a transformer, but this transformer does not need to operate at the line voltage. For high-voltage AC lines, however, the transformer must operate at these higher voltages. Transformers operating in the range of 750–800 kV have been built, and even higher voltage units have been developed. A better understanding of high-voltage breakdown mechanisms, especially in oil, is needed to spur growth in this area.

2

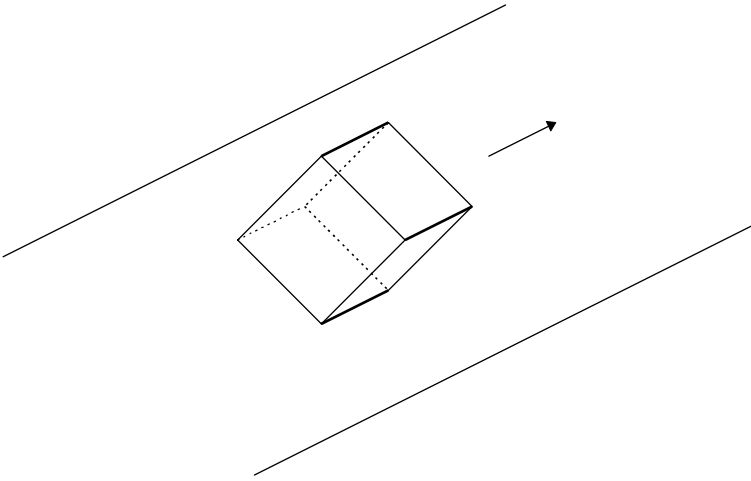
Magnetism and Related Core Issues

2.1 Introduction

Transformer cores are constructed predominantly from ferromagnetic material. The most commonly used material is iron, with the addition of small amounts of silicon and other elements that help improve the magnetic properties and/or lower losses. Other materials, such as the nickel-iron alloys (permalloys) and the iron oxides (ferrites), are used in electronic transformers. The amorphous metals, generally consisting of iron, boron, and other additions, are also used as cores for distribution transformers. All these materials are broadly classified as ferromagnetic and, as such, share many common properties, such as saturation magnetization or induction, hysteresis, and a Curie temperature above which they cease to be ferromagnetic.

Cores made of silicon (Si) steel (~3% Si) are constructed using multiple layers of the material in sheet form. The material is fabricated in rolling mills from hot slabs or ingots into thin sheets of 0.18–0.3 mm thickness and up to 1 m wide through a complex process of multiple rolling, annealing, and coating stages. Silicon steel has its best magnetic properties along the rolling direction, and a well-constructed core will take advantage of this. These good rolling-direction magnetic properties are due to the underlying crystalline orientation, which forms a Goss or cube-on-edge texture, as shown in [Figure 2.1](#). The cubic crystals have the highest permeability along the cube edges. The visible edges pointing along the rolling direction are highlighted in [Figure 2.1](#). Modern practices can achieve crystal alignments of >95%. The permeability is much lower along the cube diagonals or cube face diagonals, the latter of which point in the sheet width direction.

In addition to aiding crystal alignment, silicon also helps increase the resistivity of steel from about $25 \mu\Omega \cdot \text{cm}$ for low-carbon magnetic steel to about $50 \mu\Omega \cdot \text{cm}$ for 3% Si-Fe. This higher resistivity leads to lower eddy current losses. Silicon also lowers the saturation induction from about 2.1 T for low-carbon steel to about 2.0 T for 3% Si-Fe. Silicon confers some brittleness on the material, which is an obstacle to rolling to even thinner sheets. At higher silicon levels, the brittleness increases to the point where rolling

**FIGURE 2.1**

Goss or cube-on-edge crystalline texture of silicon steel.

becomes difficult. This is unfortunate because the magnetostriction of the steel disappears at 6% silicon content. Magnetostriction is a length change or strain produced by the induction in the material. At AC frequencies, this contributes to the noise level in a transformer.

Nickel-iron alloys or permalloys are also produced in sheet form. Because of their malleability, they can be rolled extremely thin, resulting in very low eddy current losses so that they can be used in high-frequency applications. Their saturation induction is lower than that of silicon steel.

Ferrite cores are made of sintered powder and generally have isotropic magnetic properties. They can be cast directly into the desired shape or machined after casting. They have extremely high resistivities that permit their use in high-frequency applications. However, they have rather low saturation inductions.

Amorphous metals are produced by directly casting the liquid melt onto a rotating, internally cooled drum. The liquid solidifies very rapidly, resulting in the amorphous (noncrystalline) texture of the final product. The material comes off the drum in the form of a thin ribbon of a given width, which can be up to 250 mm. The material has a magnetic anisotropy determined by the casting direction and subsequent magnetic anneals so that the best magnetic properties are along the casting direction. Its saturation induction is about 1.5 T. Because of its thinness and composition, it has extremely low losses. Amorphous materials are very brittle, which has limited their use in wound cores. Their low losses make them attractive for use in distribution transformers, especially when no-load loss evaluations are high.

Ideally, a transformer core would carry the flux along the direction of highest permeability and in a closed path. Path interruptions caused by joints, which are occupied by low permeability air or oil, lead to poorer overall magnetic properties. In addition, cutting or slitting can introduce localized stresses that degrade the magnetic properties. In stacked cores, joints are often formed by overlapping the laminations in steps to facilitate flux transfer. However, the corners result in higher loss. The higher loss can be accounted for in the design by multiplying the ideal magnetic circuit losses, usually provided by the manufacturer on a per-unit weight basis, by a building factor of > 1 . Another, possibly better, way to account for the extra loss is to apply a loss multiplying factor to the steel occupying the corner or joint region only. More fundamental methods to account for these extra losses have been proposed, but these tend to be too calculationally intensive for routine use. Joints also give rise to a higher exciting current, that is, the current in the coils necessary to drive the required flux around the core.

2.2 Basic Magnetism

The discovery by Hans Christian Oersted that currents give rise to magnetic fields led physicist André-Marie Ampere to propose that material magnetism results from localized currents. Ampere proposed that large numbers of small current loops, appropriately oriented, could create the magnetic fields associated with magnetic materials and permanent magnets. At the time, the atomic nature of matter was not understood. With the Bohr model of the atom, in which electrons are in orbit around a small massive nucleus, the localized currents could be associated with the moving electron. This gives rise to an orbital magnetic moment. Today the orbital magnetic moment arises naturally from a quantum description of the atom, which has replaced the Bohr model. In addition to the orbital magnetism, the electron itself was found to possess a magnetic moment that could not be understood simply from the circulating current point of view. Atomic magnetism results from a combination of both orbital and electron moments.

In some materials, the atomic magnetic moments either cancel each other or are very small so that little material magnetism results. These are known as paramagnetic or diamagnetic materials, depending on whether an applied field increases or decreases the magnetization. Their permeabilities relative to vacuum are nearly equal to 1. In other materials, the atomic moments are large, and there is an innate tendency for them to align due to quantum mechanical forces. These are called ferromagnetic materials. The alignment forces are of a very short range, operating only over atomic distances. Nevertheless, they create regions of aligned magnetic moments, called domains, within a magnetic material. Although each domain has a common

orientation, the orientation differs from domain to domain. The narrow separations between domains are regions where the magnetic moments are transitioning from one orientation to another. These transition zones are known as domain walls.

In nonoriented magnetic materials, the domains are typically very small and randomly oriented. With the application of a magnetic field, the domain orientation tends to align with the field direction. In addition, favorably oriented domains tend to grow at the expense of unfavorably oriented ones. As the magnetic field increases, all the domains eventually point in the direction of the magnetic field, resulting in a state of magnetic saturation. Further increases in the magnetic field cannot orient more domains, so the magnetization does not increase but is said to *saturate*. From this point, further increases in induction are due to increases in the field only.

The relation between induction **B**, magnetization **M**, and field **H** (boldface symbols are used to denote vectors) is:

$$\mathbf{B} = \mu_0 (\mathbf{H} + \mathbf{M}) \quad (2.1)$$

where $\mu_0 = 4\pi \times 10^{-7}$ henry/meter in SI units. For many materials, **M** is proportional to **H**:

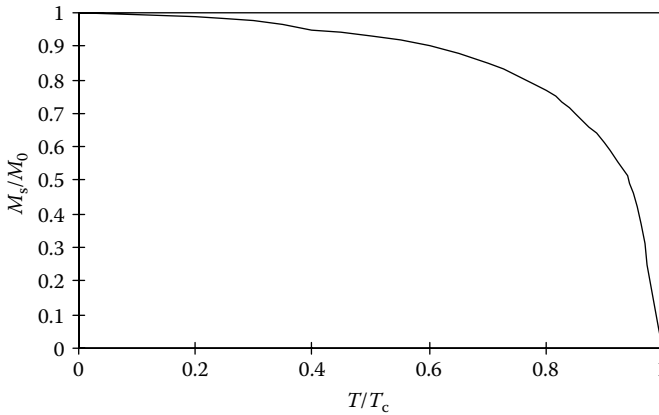
$$\mathbf{M} = \chi \mathbf{H} \quad (2.2)$$

where χ is the susceptibility, which need not be a constant. Substituting into Equation 2.1:

$$\mathbf{B} = \mu_0 (1 + \chi) \mathbf{H} = \mu_0 \mu_r \mathbf{H} \quad (2.3)$$

where $\mu_r = 1 + \chi$ is the relative permeability. We see in Equation 2.1 that, as **M** saturates because all the domains are similarly oriented, **B** can only increase due to increases in **H**. This occurs at fairly high **H** or exciting current values, since **H** is proportional to the exciting current. At saturation, because all the domains have the same orientation, there are no domain walls. Because **H** is generally small compared to **M** for high-permeability ferromagnetic materials up to saturation, the saturation magnetization and saturation induction are nearly the same and will be used interchangeably.

As the temperature increases, the thermal energy begins to compete with the alignment energy and the saturation magnetization decreases until the Curie point is reached, where ferromagnetism completely disappears. For 3% Si-Fe, the saturation magnetization or induction at 20°C is 2.0 T (Tesla) and the Curie temperature is 746°C. This should be compared with pure iron, in which the saturation induction at 20°C is 2.1 T and the Curie temperature is 770°C. The decrease in the temperature closely follows a theoretical relationship of the ratios of saturation induction at absolute temperature T to saturation induction at $T = 0^\circ\text{K}$ to the ratio of absolute temperature T to the

**FIGURE 2.2**

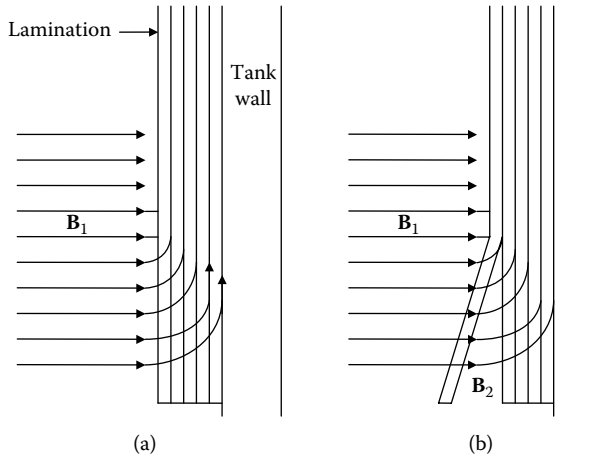
Relationship between saturation magnetization and absolute temperature, expressed in relative terms for pure iron. This also applies reasonably well to other ferromagnetic materials containing predominately iron, nickel, or cobalt. M_s is the saturation magnetization at absolute temperature T , M_0 is the saturation magnetization at $T = 0^\circ\text{K}$, and T_c is the Curie temperature in $^\circ\text{K}$.

Curie temperature expressed in $^\circ\text{K}$. This relationship is shown as a graph in Figure 2.2 [Ame57] for pure iron. This same graph also applies rather closely to other iron-containing magnetic materials such as silicon-iron (Si-Fe) and to nickel- and cobalt-based magnetic materials.

Thus, to find the saturation magnetization of 3% Si-Fe at a temperature of 200°C (i.e., 473°K), take the ratio $T/T_c = 473/1019 = 0.464$. From the graph, we know this corresponds to $M_s/M_0 = 0.94$. On the other hand, we know that at 20°C , where $T/T_c = 0.287$, $M_s/M_0 = 0.98$. Thus, $M_0 = 2.0/0.98 = 2.04$ and $M_s (T = 200^\circ\text{C}) = 0.94 \times 2.04 = 1.92$ T. This is only a 4% drop in saturation magnetization from its 20°C value. As core temperatures are unlikely to reach 200°C , temperature effects on magnetization should not be a problem in transformers under normal operating conditions.

Ferromagnetic materials typically exhibit the phenomenon of magnetostriction, that is, a length change or strain resulting from the induction or flux density that they carry. Since this length change is independent of the sign of the induction, for an AC induction at frequency f , the length oscillations occur at frequency $2f$. These length vibrations contribute to the noise level in transformers. Magnetostriction is actually a fairly complex phenomenon and can exhibit hysteresis as well as anisotropy.

Another, often overlooked, source of noise in transformers is the transverse vibrations of the laminations at unsupported free ends. These vibrations occur at the outer surfaces of the core and shunts if they are not constrained and can be shown qualitatively by considering the situation shown in Figure 2.3. In Figure 2.3a, a leakage flux density vector \mathbf{B}_1 is impinging on a packet of tank shunt laminations that are flat against the tank wall and rigidly constrained.

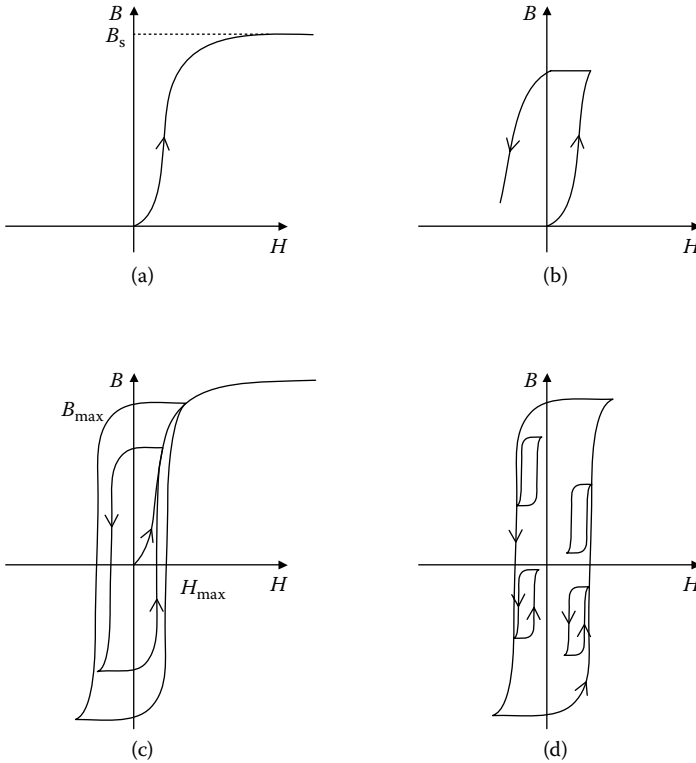
**FIGURE 2.3**

Geometry for obtaining a qualitative understanding of the force on (a) no loose laminations and (b) loose end lamination.

After striking the lamination packet, the flux is diverted into the packet and transported upward, since we are looking at the bottom end. In Figure 2.3b, the outer lamination is constrained only up to a certain distance from the end, beyond which it is free to move. Part of the flux density B_1 is diverted along this outer packet, and a reduced flux density B_2 impinges on the remaining packets. The magnetic energy associated with Figure 2.3b is lower than that of the energy associated with Figure 2.3a. A force is associated with this change in magnetic energy. This force acts to pull the outer lamination outward and is independent of the sign of B , so that if B is sinusoidal of frequency f , the force will have a frequency of $2f$. Thus, this type of vibration also contributes to the transformer noise at the same frequency as magnetostriction.

2.3 Hysteresis

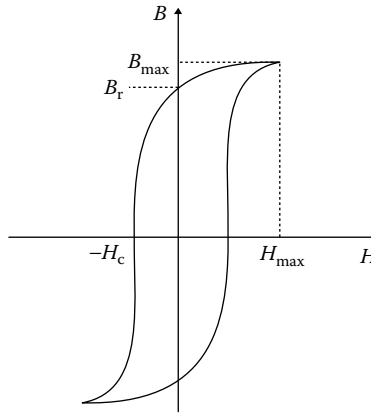
Hysteresis, as the name implies, means that the present state of a ferromagnetic material depends on its past magnetic history. This is usually illustrated by means of a B - H diagram. Changes in the magnetic field are assumed to occur slowly enough that eddy current effects can be ignored. We assume the B and H fields are collinear although, in general, they need not be. Thus, we can drop the vector notation. If we start with a completely demagnetized specimen (this state requires careful preparation) and increase the magnetic field from 0, the material will follow the initial curve as shown in Figure 2.4a. This curve can be continued to saturation B_s . If the field is

**FIGURE 2.4**

Hysteresis processes. (a) Initial curve; (b) following a normal hysteresis loop after reversal from the initial curve; (c) family of normal hysteresis loops; and (d) minor or incremental hysteresis loops.

reversed and decreased at some point along the initial curve, the material will follow a normal hysteresis loop, as shown in Figure 2.4b. If the magnetic field is cycled repeatedly between $\pm H_{\max}$, the material will stay on a normal hysteresis loop determined by H_{\max} . There is a whole family of such loops, as shown in Figure 2.4c. The largest loop occurs when B_{\max} reaches B_s and is called the major loop. These normal loops are symmetrical about the origin. If at some point along a normal loop, other than the extreme points, the field is reversed and cycled through a smaller cycle back to its original value before the reversal, a minor or incremental loop is traced, as shown in Figure 2.4d. Considering the many other possibilities for field reversals, the resulting hysteresis paths can become quite complicated.

Perhaps the most important magnetic path is a normal hysteresis loop, as this is traced in a sinusoidal cyclic magnetization process. Several key points along such a path are shown in Figure 2.5. As the field is lowered from H_{\max} to zero, the remaining induction is called the remanence, B_r . As

**FIGURE 2.5**

Key points along a normal hysteresis loop.

the field is further lowered into negative territory, the absolute value of the field at which the induction drops to zero is called the coercivity H_c . Because the loop is symmetrical about the origin, it has corresponding points on the negative branch. At any point on a magnetization path, the ratio of B to H is called the permeability, while the slope of the B - H curve at the given point is called the differential permeability. Other types of permeability can be defined. The area of the hysteresis loop is the magnetic energy per unit volume and per cycle dissipated in hysteresis processes.

In oriented Si-Fe, the relative permeability for inductions reasonably below saturation is so high that the initial curve is close to the B axis if B and H are measured in the same units as they are in the Gaussian system or if B versus $\mu_0 H$ is plotted in the SI system. In addition, the hysteresis loops are very narrow and closely hug the initial curve. Thus, for all practical purposes, we can assume a single-valued B - H characteristic for these high-permeability materials coinciding with the initial curve. Because inductions in transformer cores are kept well below saturation in normal operations to avoid high exciting currents, the effects of saturation are hardly noticeable, and the core, for many purposes, can be assumed to have a constant permeability.

2.4 Magnetic Circuits

In stacked cores, especially cores containing butt joints, as well as in gapped reactor cores, the magnetic path for the flux is not through a homogeneous magnetic material; rather, it is through gaps occupied by air or oil or other

nonmagnetic materials of relative permeability equal to 1. In such cases, effective permeabilities can be derived by using a magnetic circuit approximation. This approximation derives from the mathematical similarity of magnetic and electrical laws. In resistive electrical circuits, the conductivities of the wires and circuit elements are usually much higher than the surrounding medium (usually air), so that little current leaks away from the circuit. However, in magnetic circuits in which the flux corresponds to the electric current, the circuit permeability, which is the analog of conductivity, is not many orders of magnitude higher than that of the surrounding medium, and flux leakage does occur. Thus, although the circuit approach is nearly exact for electric circuits, it is only approximate for magnetic circuits [Del94].

Corresponding to Kirchoff's current law at a node,

$$\sum_i I_i = 0 \quad (2.4)$$

where I_i is the current into a node along a circuit branch i (positive if entering the node, negative if leaving), we have the approximate magnetic counterpart

$$\sum_i \Phi_i = 0 \quad (2.5)$$

where Φ_i is the flux into a node. Whereas Equation 2.4 is based on conservation of current and ultimately charge, Equation 2.5 is based on conservation of flux. Kirchoff's voltage law can be expressed as:

$$\sum_i V_i = \oint \mathbf{E} \cdot d\boldsymbol{\ell} = \text{emf} \quad (2.6)$$

where \mathbf{E} is the electric field and the voltage drops V_i are taken around the loop in which an electromotive force (emf) is induced. The integrals in Equation 2.6 are path integrals. With \mathbf{E} corresponding to \mathbf{H} , the magnetic analogy is

$$\sum_i (NI)_i = \oint \mathbf{H} \cdot d\boldsymbol{\ell} = \text{mmf} \quad (2.7)$$

where $(NI)_i$ are the amp-turns and mmf is the magnetomotive force.

In terms of current density \mathbf{J} and flux density \mathbf{B} , we have:

$$I = \int \mathbf{J} \cdot d\mathbf{A}, \quad \Phi = \int \mathbf{B} \cdot d\mathbf{A} \quad (2.8)$$

so that \mathbf{J} and \mathbf{B} are corresponding quantities in the two systems. In Equation 2.8, the integrals are surface integrals. Ohm's law in its basic form can be written as

$$\mathbf{J} = \sigma \mathbf{E} \quad (2.9)$$

where σ is the conductivity. In the magnetic system, this corresponds to

$$\mathbf{B} = \mu \mathbf{H} \quad (2.10)$$

where μ is the permeability.

To obtain the resistance and corresponding reluctance expressions for simple geometries, consider a resistive or reluctive element of length L and uniform cross-sectional area A as shown in Figure 2.6. Let a uniform current density J flow through the resistive element and a uniform flux density B flow through the magnetic element normal to the surface area A . Then,

$$I = JA, \quad \Phi = BA \quad (2.11)$$

Let a uniform electric field E drive the current and a uniform magnetic field H drive the flux. Then,

$$V = EL, \quad NI = HL \quad (2.12)$$

Using Equation 2.9, we have

$$\frac{I}{A} = \sigma \frac{V}{L} \Rightarrow V = \left(\frac{L}{\sigma A} \right) I \quad (2.13)$$

where the quantity in parentheses is called the resistance. Similarly, from Equation 2.10,

$$\frac{\Phi}{A} = \mu \frac{NI}{L} \Rightarrow NI = \left(\frac{L}{\mu A} \right) \Phi \quad (2.14)$$

where the quantity in parenthesis is called the reluctance. A similar analysis could be carried out for other geometries using the basic field correspondences.

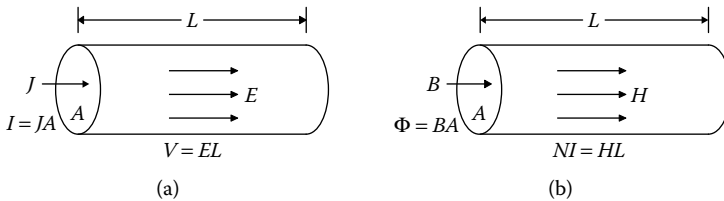
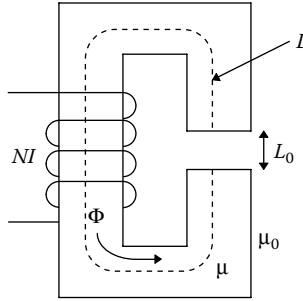


FIGURE 2.6

Geometries for simple resistance and reluctance calculation. (a) Simple resistive electrical element; and (b) simple reluctive magnetic element.

**FIGURE 2.7**

Air gap magnet driven by $\text{mmf} = NI$.

As an application of the circuit approach, consider a simple magnetic core with an air gap as shown in Figure 2.7. A flux Φ is driven around the circuit by a coil generating an mmf of NI . The path through the magnetic core of permeability $\mu = \mu_0\mu_r$ has a mean length L and the path in the air gap of permeability μ_0 has a length L_0 . The reluctances in the magnetic material and air gap are

$$R_{\text{mag}} = \frac{L}{\mu_0\mu_r A}, \quad R_{\text{air}} = \frac{L_0}{\mu_0 A} \quad (2.15)$$

Since these reluctances are in series, we have:

$$NI = \Phi \left(\frac{L}{\mu_0\mu_r A} + \frac{L_0}{\mu_0 A} \right) = \Phi \frac{L}{\mu_0\mu_r A} \left(1 + \mu_r \frac{L_0}{L} \right) \quad (2.16)$$

Thus, since μ_r can be quite large, the reluctance with the air gap can be much larger than that without the air gap, so that more mmf is required to drive a given flux. Note that we have ignored fringing in the air gap. This could be approximately accounted for by letting the area A be larger in the air gap than in the core material.

In general, for two reluctances in a series having the same cross-sectional area A but lengths L_1, L_2 and permeabilities μ_1, μ_2 , the total reluctance is

$$R_{\text{tot}} = \frac{L_1}{\mu_1 A} + \frac{L_2}{\mu_2 A} = \frac{L}{A} \left(\frac{f_1}{\mu_1} + \frac{f_2}{\mu_2} \right) \quad (2.17)$$

where $L = L_1 + L_2$, $f_1 = L_1/L$, $f_2 = L_2/L$. Thus, the effective permeability of the combination is given by

$$\frac{1}{\mu_{\text{eff}}} = \frac{f_1}{\mu_1} + \frac{f_2}{\mu_2} \quad (2.18)$$

In Equation 2.18, the μ 's can be taken as relative permeabilities since μ_0 factors out. This could be extended to more elements in series. An identical relationship holds for the effective conductivity of a series of equal cross-sectional area resistive elements. As a numerical example, suppose material 1 is magnetic steel with a relative permeability of 10,000 and material 2 is air with a relative permeability of 1. For a small air or oil joint, let $f_2 = 0.001$ and therefore $f_1 = 0.999$. From Equation 2.18, we see that $1/\mu_{\text{eff}} = 0.0000999 + 0.001 = 0.0010999$, so that $\mu_{\text{eff}} = 909$. Thus, this small air gap results in a fairly large decrease in the circuit relative permeability from that of a circuit consisting of only magnetic steel. According to Equation 2.18, if μ_1 is very large and $\mu_2 = 1$, μ_{eff} approaches $1/f_2$, and the overall relative permeability is determined by the relative size of the gap in the magnetic circuit.

Thus, in a transformer core with joints, the effective permeability is reduced relative to that of an ideal core without joints. This requires a higher exciting current to drive a given flux through the core. The core losses will also increase, mainly due to flux distortion near the joint region. For linear materials, the slope of the B - H curve will decrease for a jointed core when compared with an unjointed ideal core. For materials that follow a hysteresis loop, the joints will skew or tilt the effective hysteresis loop of a jointed core away from the B axis towards the positive H axis when compared with the unjointed ideal core. This can be shown by writing Equation 2.7 as

$$NI = H_1 \ell_1 + H_2 \ell_2 = H_{\text{eff}} \ell \quad (2.19)$$

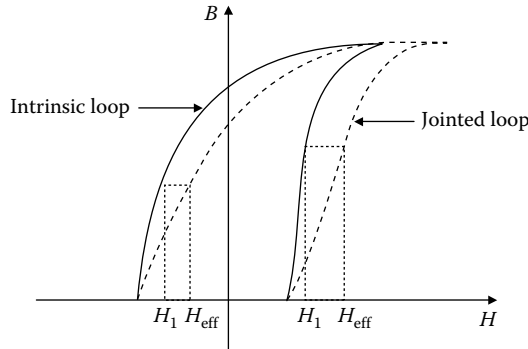
where H_1 is the field in the core steel and H_2 is the field in the gap. ℓ_1 and ℓ_2 are core and gap lengths, ℓ is the total length, and H_{eff} is an effective applied field. Assuming that the gap is linear with permeability μ_0 (relative permeability = 1), we have:

$$B_2 = \mu_2 H_2 \quad (2.20)$$

Also assume that there is no leakage, the core and gap have the same cross-sectional area, and the flux is uniformly distributed across it. Then, $B_1 = B_2 = B$ from flux continuity. Thus, for the H -field in the core material, we get:

$$H_1 = H_{\text{eff}} \frac{\ell}{\ell_1} - \frac{B \ell_2}{\mu_0 \ell_1} \quad (2.21)$$

Because $\ell \approx \ell_1$, H_1 is more negative than H_{eff} when B is positive. The effect of this on the hysteresis loop of the jointed core is shown in [Figure 2.8](#). Remember that H_{eff} is proportional to the mmf by Equation 2.19, and H_1 is the field in the core that traces the intrinsic hysteresis loop. On the top part of the loop, $B > 0$, so $H_1 < H_{\text{eff}}$. This means that the intrinsic hysteresis loop shifts to the left of the loop associated with the jointed core. Since the shift is proportional to B , it is greater at the top of the loop and vanishes when $B = 0$.

**FIGURE 2.8**

Effect of air or oil gaps on the hysteresis loop.

This tilts the jointed core loop to the right. On the lower half of the loop, where B is negative, $H_1 > H_{\text{eff}}$. This means that the intrinsic loop shifts to the right of the jointed core loop, and the shift is again proportional to B . Thus the jointed core tilts to the left at the bottom, as expected by symmetry. Notice that the remanence decreases for the jointed loop because according to Equation 2.21, when $H_{\text{eff}} = 0$, $H_1 < 0$ and the associated B value is lower down on the jointed loop.

2.5 Inrush Current

When a transformer is disconnected from its power source, the current is interrupted and the magnetic field or mmf driving flux through the core is reduced to zero. As we have seen in [Section 2.4](#), the core retains a residual induction, called the remanence, when the hysteresis path is on the positive descending (negative ascending) branch of a normal loop. A residual induction also can occur in other cases, but it will not have as high a magnitude. To drive the core to the zero-magnetization state, the peak induction should be lowered gradually while cycling the field. Because the intrinsic normal hysteresis loops for oriented Si-Fe have fairly flat tops or bottoms, the remanence is close to the peak induction; however, the presence of gaps in the core reduces this somewhat. When the unit is reenergized by a voltage source, the flux change must match the voltage change according to Faraday's law:

$$V = -N \frac{d\Phi}{dt} \quad (2.22)$$

For a sinusoidal voltage source, the flux is also sinusoidal:

$$\Phi = \Phi_p \sin(\omega t + \varphi) \quad (2.23)$$

where Φ_p is the peak flux. Substituting this into Equation 2.22, we get

$$V = -N\omega\Phi_p \cos(\omega t + \varphi) \quad (2.24)$$

Hence, the peak voltage, using $\omega = 2\pi f$, where f is the frequency in hertz, is

$$V_p = 2\pi f N \Phi_p \quad (2.25)$$

Thus to follow the voltage change, the flux must change by $\pm\Phi_p$ over a cycle. If, in a worst case scenario, the voltage source is turned on when the voltage is at a value that requires a negative Φ_p value and the remanent induction has a positive value of B_r so that the associated core flux is $B_r A_c$, where A_c is the core area, then the flux will increase to $2\Phi_p + B_r A_c$ when the voltage reaches a value corresponding to $+\Phi_p$. If we assume the flux change occurs in the core, as it normally does, so that $\Phi_p = B_p A_c$, then the core induction will increase to $2B_p + B_r$. Since B_p is usually ~10–20% below saturation in typical power transformers, the core will be driven strongly into saturation, which requires a very high exciting current. This exciting current is called the inrush current and can be many times the normal load current in a transformer.

As saturation is approached, the flux will no longer remain confined to the core, but will spill into the air or oil space inside the coil that supplies the exciting current. Thus, beyond saturation, the entire area inside the exciting coil, including the core, must be considered the flux-carrying area with an incremental relative permeability of 1. Let B_r be the residual induction in the core, which, without loss of generality, we can assume to be positive. We will assume that this is the remanence. Thus, the residual flux is $\Phi_r = B_r A_c$. Let $\Delta\Phi$ be the flux change required to bring the voltage from its turn-on point up to its maximum value, in the same sense as the residual flux. $\Delta\Phi$ could be positive, negative, or zero, depending on the turn-on point. We assume it is positive here.

Part of the increase in $\Delta\Phi$ will simply bring the induction up to the saturation level, expending little exciting power or current. This part is approximately given by $(B_s - B_r)A_c$, where B_s is the saturation induction. Beyond this point, further increases in $\Delta\Phi$ occur with the expenditure of high exciting current since the incremental relative permeability is 1. Beyond saturation, the core and air or oil have the same permeability, so the incremental flux density will be the same throughout the interior of the coil, ignoring end effects. Letting the interior coil area up to the mean radius R_m be A ($A = \pi R_m^2$), the incremental flux density is

$$B_{inc} = \frac{\Delta\Phi - (B_s - B_r)A_c}{A} \quad (2.26)$$

The incremental magnetic field inside the coil, ignoring end effects, is $H_{\text{inc}} = NI/h$, where NI are the exciting amp-turns and h is the coil height. We ignore the exciting amp-turns required to reach saturation, as these are comparatively small. Because the permeability for this flux change is μ_0 , we have $B_{\text{inc}} = \mu_0 H_{\text{inc}} = \mu_0 NI/h$, which implies, using Equation 2.26:

$$NI = \frac{h}{\mu_0 A} [\Delta\Phi - (B_s - B_r) A_c] \quad (2.27)$$

Assuming, in the worst case, that the voltage is turned on at a corresponding flux density that is at the most negative point in the cycle, we have, using Equation 2.25:

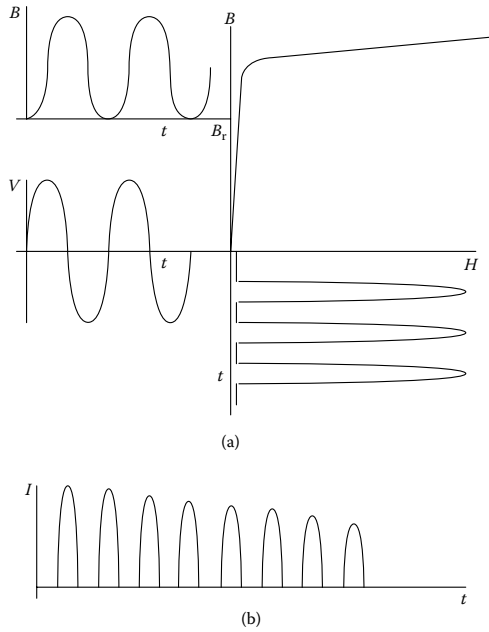
$$\Delta\Phi_{\text{max}} = 2\Delta\Phi_p = \frac{2V_p}{2\pi f N} = 2B_p A_c \quad (2.28)$$

In the third equality in Equation 2.28, we compute this flux change mathematically as if it all occurred in the core (as it would under normal conditions) even though we know this is not physically true. Thus, substituting the maximum flux change $\Delta\Phi_{\text{max}}$ for $\Delta\Phi$ for a worst case situation, Equation 2.27 becomes

$$NI_{\text{max}} = \frac{h A_c}{\mu_0 A} (2B_p + B_r - B_s) \quad (2.29)$$

As a numerical example, consider transformers with stacked cores and step-lapped joints where $B_r \approx 0.9 B_p$. Taking $h = 2$ m, $A_c/A = 0.5$, $B_p = 1.7$ T, $B_r = 0.9$, $B_p = 1.53$ T, and $B_s = 2$ T, we obtain $NI_{\text{max}} = 2.33 \times 10^6$ A • T. For $N = 500$, $I_{\text{max}} = 4660$ A. This is very high for an exciting current.

Although the voltage is constrained to be sinusoidal, the exciting current will be distorted mainly due to saturation effects. Even below saturation, there is some distortion due to nonlinearity in the B - H curve. [Figure 2.9a](#) illustrates the situation on inrush. The sinusoidal voltage is proportional to the incremental induction, which is displaced by the remanent induction. It requires high H values near its peak and comparatively small to zero H values near its trough. This is reflected in the exciting current, which is proportional to H . This current appears as a series of positive pulses separated by broad regions of near zero value as shown in [Figure 2.9a](#). The positive current pulses appear undistorted because they are associated with the saturated portion of the B - H curve, where the relative permeability is close to 1. The high exciting inrush current will decrease with time due to resistive effects, as shown in [Figure 2.9b](#).

**FIGURE 2.9**

Distortion of exciting current due to saturation. (a) B - H curve indirectly relating voltage to exciting current; and (b) exciting current proportional to H versus time.

2.6 Distinguishing Inrush from Fault Current

Because the inrush current can be as large as a fault current, it must be distinguished in some way so that false alarms are not set off when the unit is turned on. The type of current can be determined by determining the second harmonic content of each current. To this end, we will examine the time dependence of the two types of current. Using Equation 2.23, we can write

$$\Delta\Phi = \Phi_p \sin(\omega t + \phi) - \Phi_p \sin\phi = B_p A_c [\sin(\omega t + \phi) - \sin\phi] \quad (2.30)$$

where the flux change is measured from $t = 0$, and we are using $B_p A_c$ as a substitute for Φ_p . Thus, using Equation 2.27 and ignoring the resistive damping since we are only interested in examining the first few cycles,

$$I(t) = \frac{h A_c B_p}{\mu_0 N A} \left[\sin(\omega t + \phi) - \frac{(B_s + B_p \sin\phi - B_r)}{B_p} \right] \quad (2.31)$$

This last equation holds as long as $I(t)$ is positive. $I(t)$ is nearly zero for negative values of the expression on the right-hand side since the core is not

then saturated. Equation 2.31 remains positive over a cycle for values of ωt between

$$\omega t_1 = \sin^{-1} X - \phi \quad \text{and} \quad \omega t_2 = \pi - \sin^{-1} X - \phi \quad (2.32)$$

where

$$X = \frac{B_s + B_p \sin \phi - B_r}{B_p}$$

Thus, the interval per cycle over which Equation 2.31 is positive is

$$\omega t_2 - \omega t_1 = \pi - 2 \sin^{-1} X \quad (2.33)$$

We assume that ϕ can vary between $-\pi/2$ and $+\pi/2$. Shifting the time origin to t_1 , Equation 2.31 becomes

$$I(t) = \begin{cases} I_p [\sin(\omega t + \sin^{-1} X) - X], & 0 \leq \omega t \leq \pi - 2 \sin^{-1} X \\ 0, & \pi - 2 \sin^{-1} X \leq \omega t \leq 2\pi \end{cases} \quad (2.34)$$

where

$$I_p = \frac{hA_c B_p}{\mu_0 N A}$$

Extreme values of X are determined by $\sin \phi = \pm 1$:

$$X_{\min} = -1 + \frac{B_s - B_r}{B_p}, \quad X_{\max} = 1 + \frac{B_s - B_r}{B_p} \quad (2.35)$$

Thus, X cannot be < -1 . If $X > 1$, this simply means that there is no noticeable inrush current. Equation 2.34 is graphed in [Figure 2.10](#) for $X = -0.5$.

We will find the harmonic content of Equation 2.34 by performing a Fourier analysis. To facilitate this, we rewrite Equation 2.34 as

$$I(t) = \begin{cases} I_p [\sqrt{1 - X^2} \sin \omega t + X \cos \omega t - X], & 0 \leq \omega t \leq \pi - 2 \sin^{-1} X \\ 0, & \pi - 2 \sin^{-1} X \leq \omega t \leq 2\pi \end{cases} \quad (2.36)$$

We use the expansion

$$I(t) = a_0 + \sum_{k=1}^{\infty} (a_k \cos k\omega t + b_k \sin k\omega t) \quad (2.37)$$

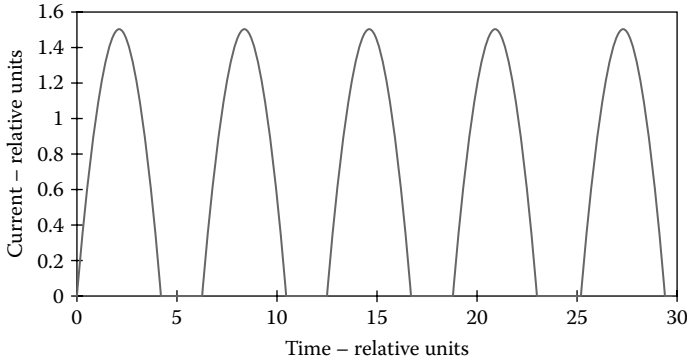


FIGURE 2.10
Inrush current (normalized) for $X = -0.5$.

where

$$a_0 = \frac{1}{2\pi} \int_0^{2\pi} I(\omega t) d(\omega t)$$

$$a_k = \frac{1}{\pi} \int_0^{2\pi} I(\omega t) \cos(k\omega t) d(\omega t)$$

$$b_k = \frac{1}{\pi} \int_0^{2\pi} I(\omega t) \sin(k\omega t) d(\omega t)$$

Evaluating the first few harmonics and letting $\alpha = \pi - 2 \sin^{-1} X$, we get

$$\begin{aligned} \frac{a_0}{I_p} &= \frac{1}{2\pi} \left\{ \sqrt{1-X^2} (1 - \cos \alpha) + X (\sin \alpha - \alpha) \right\} \\ \frac{a_1}{I_p} &= \frac{1}{\pi} \left\{ \sqrt{1-X^2} \frac{\sin^2 \alpha}{2} + X \left(\frac{\alpha}{2} + \frac{\sin 2\alpha}{4} - \sin \alpha \right) \right\} \\ \frac{a_2}{I_p} &= \frac{1}{\pi} \left\{ \sqrt{1-X^2} \left[\frac{2}{3} (1 - \cos^3 \alpha) + \cos \alpha - 1 \right] \right. \\ &\quad \left. + X \left(\sin \alpha - \frac{2 \sin^3 \alpha}{3} - \frac{\sin 2\alpha}{2} \right) \right\} \\ \frac{b_1}{I_p} &= \frac{1}{\pi} \left\{ \sqrt{1-X^2} \left(\frac{\alpha}{2} - \frac{\sin 2\alpha}{4} \right) + X \left(\frac{\sin^2 \alpha}{2} + \cos \alpha - 1 \right) \right\} \\ \frac{b_2}{I_p} &= \frac{1}{\pi} \left\{ 2\sqrt{1-X^2} \frac{\sin^3 \alpha}{3} + X \left[\frac{2}{3} (1 - \cos^3 \alpha) - \frac{(1 - \cos 2\alpha)}{2} \right] \right\} \end{aligned} \quad (2.38)$$

The ratio of second harmonic amplitude to fundamental amplitude is given by

$$\frac{2^{\text{nd}}}{1^{\text{st}}} = \frac{\sqrt{a_2^2 + b_2^2}}{\sqrt{a_1^2 + b_1^2}} \tag{2.39}$$

This is tabulated in Table 2.1 for a range of X values.

Thus, we see that the second harmonic amplitude is a significant fraction of the fundamental for most X values. In fact, the lowest practical X value can be determined from Equation 2.35 by setting $B_s = 2$ T, $B_p \approx 1.75$ T, $B_r = 0.9$, and $B_p = 1.57$ T. We then obtain $X = -0.75$. At this value, the ratio of second to first harmonic amplitude is $>8\%$, which can be considered a lower limit for this ratio.

As a comparison, we will now examine the time dependence of the fault current. We will ignore the load current at the time of the fault and assume that the transformer is suddenly grounded at $t = 0$. The equivalent circuit is shown in Figure 2.11. Here, R and L are the resistance and leakage reactance of the transformer, respectively, including any contributions from the system. The voltage is given by

$$V = V_p \sin(\omega t + \varphi) \tag{2.40}$$

TABLE 2.1

Ratio of Second to First Harmonic Amplitudes for Inrush Current as a Function of Parameter X

X	Second/First Harmonic Amplitude	X	Second/First Harmonic Amplitude
-0.9	0.0195	0.1	0.4773
-0.8	0.0569	0.2	0.5157
-0.7	0.1023	0.3	0.5137
-0.6	0.1478	0.4	0.4607
-0.5	0.1915	0.5	0.3815
-0.4	0.2342	0.6	0.3057
-0.3	0.2775	0.7	0.2443
-0.2	0.3228	0.8	0.1974
-0.1	0.3717	0.9	0.1618
0	0.4244		

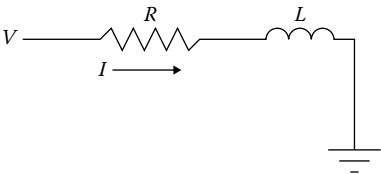


FIGURE 2.11
Circuit for fault current analysis.

where ϕ is the phase angle, which can generally have any value because the fault can occur at any time during the voltage cycle. The circuit equation is

$$V_p \sin(\omega t + \phi) = \begin{cases} RI + L \frac{dI}{dt}, & t \geq 0 \\ 0, & t < 0 \end{cases} \quad (2.41)$$

Using Laplace transforms [Hue72], the current transform is given by

$$I(s) = \frac{V_p (s \sin \phi + \omega \cos \phi)}{(R + Ls)(s^2 + \omega^2)} \quad (2.42)$$

Taking the inverse transform, we obtain

$$I(t) = \frac{V_p}{R \sqrt{1 + \left(\frac{\omega L}{R}\right)^2}} \left[\sin(\beta - \phi) e^{-\frac{R}{L}t} + \sin(\omega t + \phi - \beta) \right] \quad (2.43)$$

where

$$\beta = \tan^{-1} \left(\frac{\omega L}{R} \right)$$

The steady-state peak current amplitude is given by

$$I_{p,ss} = \frac{V_p}{R \sqrt{1 + \left(\frac{\omega L}{R}\right)^2}} \quad (2.44)$$

Using this equation and letting $\tau = \omega t$, $v = \omega L/R$, we can rewrite Equation 2.43 as

$$\begin{aligned} I(\tau) &= I_{p,ss} \left[\sin(\beta - \phi) e^{-\frac{\tau}{v}} + \sin(\tau + \phi - \beta) \right] \\ &= I_{p,ss} \left[\sin(\beta - \phi) \left(e^{-\frac{\tau}{v}} - \cos \tau \right) + \cos(\beta - \phi) \sin \tau \right] \end{aligned} \quad (2.45)$$

where

$$\beta = \tan^{-1} v$$

To find the maximum amplitude for a given ϕ , we need to solve the following equation:

$$\frac{\partial I}{\partial \tau} = \sin(\beta - \phi) \left(\frac{e^{-\frac{\tau}{v}}}{v} - \sin \tau \right) - \cos(\beta - \phi) \cos \tau = 0 \quad (2.46)$$

In addition, to determine the value of ϕ that produces the largest fault current, we need to solve the following equation:

$$\frac{\partial I}{\partial \phi} = \cos(\beta - \phi) \left(e^{-\frac{\tau}{v}} - \cos \tau \right) - \sin(\beta - \phi) \sin \tau = 0 \quad (2.47)$$

Solving Equations 2.46 and 2.47 simultaneously, we find

$$\tan(\beta - \phi) = v = \tan \beta \quad (2.48)$$

$$e^{-\frac{\tau}{v}} - v \sin \tau - \cos \tau = 0 \quad (2.49)$$

Equation 2.48 shows that $\phi = 0$ produces the maximum amplitude, and the time at which this maximum amplitude occurs is given by solving Equation 2.49 for $\tau > 0$. Substituting this into Equation 2.45, we obtain

$$\frac{I_{\max}}{I_{p,ss}} = \sqrt{1 + v^2} \sin \tau \quad (2.50)$$

This is the asymmetry factor over the steady steady-state peak amplitude with τ obtained by solving Equation 2.49.

The asymmetry factor is generally considered to be with respect to the steady-state rms current value. This new ratio is called K in the literature and is given by substituting $I_{p,ss} = \sqrt{2}I_{rms,ss}$ in Equation 2.50:

$$K = \frac{I_{\max}}{I_{rms,ss}} = \sqrt{2(1 + v^2)} \sin \tau, \quad v = \frac{\omega L}{R} = \frac{x}{r} \quad (2.51)$$

We have expressed the ratio of leakage impedance to resistance as x/r . x and r are normalized quantities, that is, the leakage reactance and resistance divided by a base impedance value, which cancels out in the ratio. Equation 2.51 has been parametrized as [IEE93]

$$K = \sqrt{2} \left\{ 1 + e^{-\frac{r}{x} \left(\phi + \frac{\pi}{2} \right)} \sin \phi \right\}, \quad \phi = \tan^{-1} \left(\frac{x}{r} \right) = \beta \quad \text{and} \quad \frac{x}{r} = v \quad (2.52)$$

This parametrization agrees with Equation 2.51 to within 0.7%. Table 2.2 shows some of the *K* values obtained by the two methods.

At $\phi = 0$, where the asymmetry is greatest, Equation 2.45 becomes

$$I(\tau) = \frac{\sqrt{2}I_{rms,ss}}{\sqrt{1 + v^2}} \left[v \left(e^{-\frac{\tau}{v}} - \cos \tau \right) + \sin \tau \right] \tag{2.53}$$

This is graphed in Figure 2.12 for $v = 10$.

TABLE 2.2
Comparison of Exact with Parameterized *K* Values

$v = x/r$	<i>K</i> (Exact)	<i>K</i> (Parameterized)
1	1.512	1.509
2	1.756	1.746
5	2.192	2.184
10	2.456	2.452
50	2.743	2.743
1000	2.828	2.824

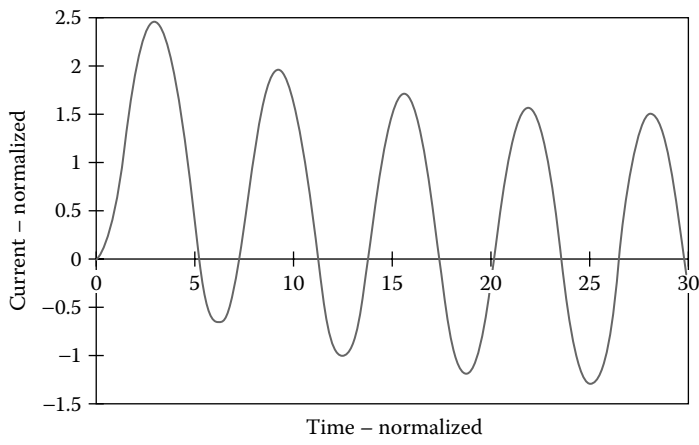


FIGURE 2.12
Fault current versus time for the case of maximum offset and $v = x/r = 10$.

The lowest Fourier coefficients of Equation 2.45 are

$$\begin{aligned}
 \frac{a_o}{I_{p,ss}} &= \sin(\beta - \varphi) \frac{v}{2\pi} \left(1 - e^{-\frac{2\pi}{v}} \right) \\
 \frac{a_1}{I_{p,ss}} &= \sin(\beta - \varphi) \left[\frac{v}{\pi(1 + v^2)} \left(1 - e^{-\frac{2\pi}{v}} \right) - 1 \right] \\
 \frac{a_2}{I_{p,ss}} &= \sin(\beta - \varphi) \frac{v}{\pi(1 + 4v^2)} \left(1 - e^{-\frac{2\pi}{v}} \right) \\
 \frac{b_1}{I_{p,ss}} &= \sin(\beta - \varphi) \frac{v^2}{\pi(1 + v^2)} \left(1 - e^{-\frac{2\pi}{v}} \right) + \cos(\beta - \varphi) \\
 \frac{b_2}{I_{p,ss}} &= \sin(\beta - \varphi) \frac{2v^2}{\pi(1 + 4v^2)} \left(1 - e^{-\frac{2\pi}{v}} \right)
 \end{aligned} \tag{2.54}$$

The ratio of second harmonic amplitude to fundamental amplitude (Equation 2.39) is tabulated in Table 2.3 for a range of φ and v values.

TABLE 2.3

Ratio of Second Harmonic to Fundamental Amplitude of Fault Current for Various Values of the Reactance to Resistance Ratio and Voltage Phase Angle

$v = x/r$	$\varphi = 0^\circ$	$\varphi = 30^\circ$	$\varphi = 45^\circ$	$\varphi = 90^\circ$	$\varphi = 120^\circ$	$\varphi = 135^\circ$
1	0.0992	0.0357	0	0.119	0.168	0.166
2	0.128	0.0752	0.0440	0.0752	0.152	0.167
3	0.127	0.0831	0.0566	0.0475	0.123	0.145
4	0.118	0.0819	0.0589	0.0323	0.101	0.124
5	0.109	0.0778	0.0576	0.0232	0.0543	0.107
6	0.0996	0.0731	0.0550	0.0175	0.0735	0.0941
7	0.0916	0.0684	0.0521	0.0137	0.0644	0.0835
8	0.0845	0.0641	0.0493	0.0110	0.0572	0.0750
9	0.0784	0.0601	0.0465	0.0090	0.0515	0.0680
10	0.0730	0.0565	0.0440	0.0075	0.0467	0.0622
15	0.0540	0.0432	0.0341	0.0036	0.0320	0.0434
20	0.0427	0.0347	0.0276	0.0022	0.0242	0.0333
25	0.0352	0.0290	0.0232	0.0014	0.0195	0.0270
50	0.0188	0.0158	0.0128	0.0004	0.0099	0.0138
100	0.0097	0.0083	0.0067	0.0001	0.0050	0.0070
500	0.0020	0.0017	0.0014	0	0.0010	0.0014
1000	0.0010	0.0008	0.0007	0	0.0005	0.0007

For power transformers, x/r is usually >20 . From Table 2.3, we see that the second harmonic content relative to the fundamental is $<4.3\%$ for $x/r > 20$. On the other hand, we found in Table 2.1 that the second-to-first harmonic ratio is $>8\%$ under virtually all conditions for the inrush current for power transformers. Thus, determining this ratio can distinguish inrush from fault currents. In fact, x/r should fall below 10 before this method breaks down.

2.7 Optimal Core Stacking

As discussed in Section 1.4, cores for power transformers are normally constructed of stacks of thin laminations often arranged to approximate a circular shape. Because of the limited number of lamination widths available, the circular shape consists of a finite number of stacks or steps, with all the laminations in a given step having the same width. Thus, the circular shape is not completely filled with flux carrying steel. The stacking pattern must be optimized for a given number of steps in order to fill the circular area with as much core steel as possible. In addition, because of the insulating, nonferromagnetic coating applied to the laminations, the area of the lamination stacks must be corrected for this coating thickness in order to arrive at the true flux carrying area of the core. This correction or stacking factor is normally about 96%; that is, the actual core carrying area is about 96% of the geometric stack area.

For a given number of steps, we can maximize the core area to obtain an optimal stacking pattern. Figure 2.13 shows the geometric parameters that

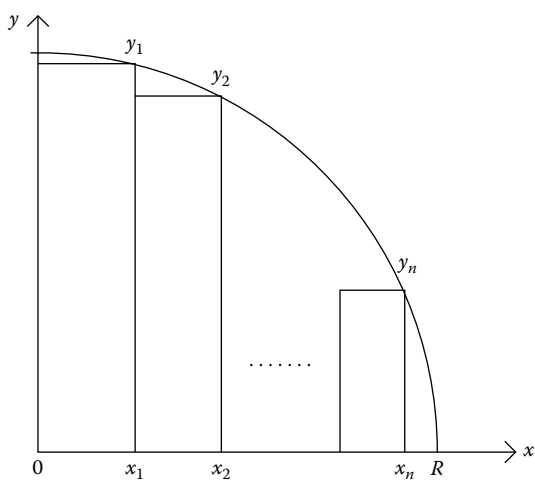


FIGURE 2.13 Geometric parameters for finding the optimum step pattern.

can be used in such an optimization, namely the x and y coordinates of the stack corners, which touch the circle of radius R . Only one-fourth of the geometry is modeled, due to symmetry considerations.

The corner coordinates must satisfy

$$x_i^2 + y_i^2 = R^2 \quad (2.55)$$

For a core with n steps, where n refers to the number of stacks in half the core cross section, the core area, A_n , is given by

$$A_n = 4 \sum_{i=1}^n (x_i - x_{i-1}) y_i = 4 \sum_{i=1}^n (x_i - x_{i-1}) \sqrt{R^2 - x_i^2} \quad (2.56)$$

where $x_0 = 0$. Thus, the independent variables are the x_i , because the y_i can be determined from them using Equation 2.55. To maximize A_n , we need to solve the n equations:

$$\frac{\partial A_n}{\partial x_i} = 0 \quad (2.57)$$

We can show that

$$\frac{\partial^2 A_n}{\partial^2 x_i} < 0 \quad (2.58)$$

so that the solution to Equation 2.57 does represent a maximum. Applying Equation 2.57 to 2.56, after some algebraic manipulation, we get:

$$(R^2 - x_i^2) [x_{i+1}^2 - x_i (3x_i - 2x_{i-1})] + x_i^2 (x_i - x_{i-1})^2 = 0 \quad \text{for } i = 1 \cdots n \quad (2.59)$$

In the first and last equations ($i = 1$ and $i = n$), we need to use $x_0 = 0$ and $x_{n+1} = R$.

Equation 2.59 represents a set of nonlinear equations, and an approximate solution scheme such as a Newton–Raphson iteration can be used to solve these types of equations. These equations can be normalized by dividing by R^4 so that the normalized solution coordinates x_i/R are independent of R . [Table 2.4](#) gives the normalized solution for various numbers of steps.

In practice, because only a limited number of standard sheet widths are kept in inventory and because stack heights are also discretized, at least by the thickness of an individual sheet, the ideal coverage given in the table cannot be achieved. A practical method of handling this is to optimize, assuming continuous variables as was done here, and then to readjust the stack dimensions to correspond to the nearest discretized choices available, in such a way that the stacks do not fall outside the core circle. In addition, there must often be room for the tie or flitch plates on the outside of the core stack.

TABLE 2.4
Normalized x Coordinates Which Maximize the Core Area for
a Given Number of Steps

Number of Steps, n	Fraction of Circle Occupied, $A_n/\pi R^2$	Normalized x Coordinates, x_i/R
1	0.6366	0.7071
2	0.7869	0.5257, 0.8506
3	0.8510	0.4240, 0.7070, 0.9056
4	0.8860	0.3591, 0.6064, 0.7951, 0.9332
5	0.9079	0.3138, 0.5336, 0.7071, 0.8457, 0.9494
6	0.9228	0.2802, 0.4785, 0.6379, 0.7700, 0.8780, 0.9599
7	0.9337	0.2543, 0.4353, 0.5826, 0.7071, 0.8127, 0.9002, 0.9671
8	0.9419	0.2335, 0.4005, 0.5375, 0.6546, 0.7560, 0.8432, 0.9163, 0.9723
9	0.9483	0.2164, 0.3718, 0.4998, 0.6103, 0.7071, 0.7921, 0.8661, 0.9283, 0.9763
10	0.9534	0.2021, 0.3476, 0.4680, 0.5724, 0.6648, 0.7469, 0.8199, 0.8836, 0.9376, 0.9793

Room can be allocated by fixing the value of x_n in the aforementioned equations. Simply set x_n equal to a value necessary to accommodate the tie plates and drop the n th equation in Equation 2.59. Core cooling ducts can also be accommodated by reducing the thickness of one of the neighboring stacks where the cooling ducts are to be located by the thickness of the cooling duct. These adjustments will lower the core area from the maximized area, but are necessary in practice.

3

Circuit Model of a Two-Winding Transformer with Core

3.1 Introduction

Circuit models are often used when a transformer is part of a larger circuit such as a utility network, in which case only the terminal characteristics of the transformer are usually of interest. In this chapter, we will primarily be concerned with transformers operating at steady-state power frequencies, generally 50 or 60 hertz (Hz). In these cases, capacitive effects can usually be ignored. When the core is operating sufficiently below saturation, core non-linearity effects can also be ignored. For transient processes such as those occurring during switching or lightning strikes, a more detailed transformer model is needed. We will first develop a circuit model of the core and then consider the effects of adding windings.

3.2 Circuit Model of the Core

Here we will consider a single-phase core and transformer. Usually, three-phase cores and transformers can be analyzed as three separate single-phase units, and interconnections among the phases can be added later. For simplicity, only a two-winding transformer having a primary and secondary winding will be considered here. The primary winding is normally attached to the input power source, while the secondary winding feeds a load or loads.

If the secondary winding is open circuited, the transformer will behave like an inductor with a high-permeability closed iron core and will therefore have a high inductance so that little exciting current is required to generate the primary voltage or back electromotive force (emf). Some I^2R loss will be generated by the exciting current in the primary winding; however, this will be small when compared with the load current losses. There will be losses in the core, however, due to the changing flux. These losses are, to a

good approximation, proportional to the square of the induction (B^2) and hence, they are also proportional to the square of the voltage across the core. Thus, these losses can be accounted for by placing an equivalent resistor across the transformer voltage and ground, where the resistor has the following value:

$$R_c = \frac{V_{\text{rms}}^2}{W_c} \quad (3.1)$$

where V_{rms} is the rms phase voltage and W_c is the core loss. Here, we assume that the primary voltage is sinusoidal, which is usually the case. The open-circuited inductance can be obtained from the following equation:

$$V = L_c \frac{dI_{\text{ex}}}{dt} \Rightarrow L_c = \frac{V_{\text{rms}}}{\omega I_{\text{ex,rms}}} \quad (3.2)$$

where I_{ex} is the inductive component of the exciting current. This current can be sinusoidal or nonsinusoidal, depending on whether the core is operating linearly or nonlinearly. Because the voltage V is generally sinusoidal, the first expression in Equation 3.2 would require L_c to be a nonlinear function of I_{ex} when the core is operating nonlinearly. The second expression in Equation 3.2 is valid when I_{ex} is sinusoidal with angular frequency $\omega = 2\pi f$, with f the frequency in hertz. As long as the core is operating reasonably far from saturation, we can assume that I_{ex} is sinusoidal and L_c is a constant inductance. Thus, the circuit so far will look like that shown in Figure 3.1. The resistance R_p is the resistance of the primary (or excited) winding. Note that as saturation is approached, the inductance L_c and the resistance R_c will become nonlinear. If necessary, capacitive effects can be included by placing an equivalent capacitance in parallel with the core inductance and resistance. Since the core losses are supplied by the input power source, a component of

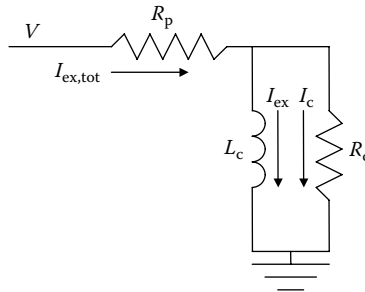


FIGURE 3.1

Transformer core circuit model with open-circuited secondary winding.

the total excitation current, $I_{\text{ex,tot}}$ generates the core loss. We labeled it I_c in the figure, which is in quadrature, that is, at a 90° phase angle, with I_{ex} .

A useful circuit model for the core when the excitation is sinusoidal and nonlinearities are ignored is shown in Figure 3.2. R_c is the core resistance, accounting for the core loss, and $X_c = \omega L_c$ is the magnitude of the core reactance, accounting for the magnetization of the core. j is the unit imaginary, which mathematically produces the 90° phase relation between resistance and reactance.

Now we will show how the parameters of this circuit model can be extracted from test data and then we will use them to obtain the core power factor, that is, the fraction of the core power that is dissipated as loss. The resistance can be obtained from the calculated or tested core losses as given by Equation 3.1. This, in turn, allows the calculation of the current I_R from the formula

$$I_R = \frac{V}{R_c} \quad (3.3)$$

Here, V and I are assumed to be rms quantities.

Letting Z_c equal the parallel combination of X_c and R_c , we have

$$\frac{1}{Z_c} = -\frac{j}{X_c} + \frac{1}{R_c} \quad (3.4)$$

Hence

$$\frac{1}{|Z_c|^2} = \frac{1}{X_c^2} + \frac{1}{R_c^2} \quad (3.5)$$

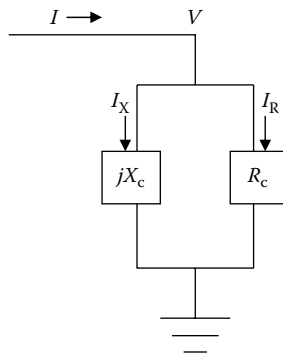


FIGURE 3.2

Transformer core circuit model with sinusoidal excitation.

Rewriting and taking square roots, we have

$$\frac{1}{X_c} = \sqrt{\frac{1}{|Z_c|^2} - \frac{1}{R_c^2}} \quad (3.6)$$

If V , taken as the reference phasor (a real quantity), and the magnitude of I , the input current available from test data are known, we have

$$Z_c = \frac{V}{|I|} \quad (3.7)$$

Thus, the magnitude of Z_c can be obtained by inputting the required test data into the last formula. This allows us to calculate X_c from the previous formula. Knowing X_c , we can get the current I_x from the formula:

$$I_x = \frac{V}{jX_c} \quad (3.8)$$

The magnitude of the power into the core is given by $V|I|$, where $|I|$ is the magnitude of the input current. The power dissipated in losses is given by VI_R . Thus, the ratio of the power loss to the input power is the power factor:

$$\text{Power factor} = \frac{I_R}{|I|} \quad (3.9)$$

This is usually denoted by $\cos \theta$, where θ is the angle between the total current I and the real current I_R in the complex plane.

As a numerical example, assuming a single-phase core, let $V = 40,000$ V, $W = 2000$ W, and $I = 0.25$ A. Then, we get

$$R_c = V^2/W = 800,000 \Omega$$

$$I_R = V/R_c = 0.05 \text{ A}$$

$$Z_c = V/|I| = 160,000 \Omega$$

$$X_c = 163,300 \Omega$$

$$I_x = -jV/X_c = -j0.245 \text{ A}$$

$$\text{Power factor} = \cos \theta = I_R/|I| = 0.200$$

3.3 Two-Winding Transformer Circuit Model with Core

When the secondary circuit is connected to a load, the emf generated in the secondary winding by the changing core flux will drive a current through the secondary circuit. This additional current (amp-turns) alters the core flux unless equal and opposite amp-turns flow in the primary winding. Since the core flux is determined by the impressed primary voltage, the net amp-turns must equal the small exciting amp-turns. Hence, the primary and secondary amp-turns due to load current, excluding the exciting current, must cancel out.

Figure 3.3 shows a schematic of the flux pattern in a two-winding transformer under load. The currents are taken as positive when they flow into a winding, and the dots on the terminals indicate that, when positive exciting current flows into the transformer, the winding sense is such that the induced voltage is positive at that terminal relative to the terminal at the other end of the winding. Notice that the bulk of the flux flows through the core and links both windings. However, some of the flux links only one winding. When referring to flux linkages, we assume partial linkages are included. Some of these can be seen in the Figure 3.3.

Faraday's law for the voltage induced in a coil is based on the concept of flux linkages. We have assumed that a flux Φ passing through a coil of N turns links all N turns so that the flux linkage is $N\Phi$. As seen in Figure 3.3, except for the core flux, the flux linking a coil only links some of the turns or sometimes only a fraction of a turn. For further development, we assume that Φ is the flux linkage per turn so that $N\Phi$ does equal the flux linkage, λ .

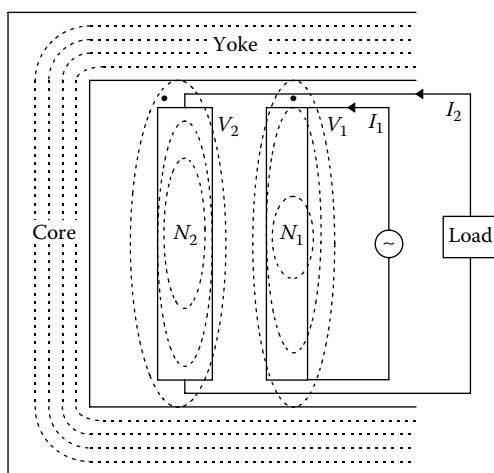


FIGURE 3.3

Schematic of a two-winding single-phase transformer with leakage flux.

Therefore, we have $\Phi = \lambda/N$. If the flux linked 100% of every turn of the coil, then Φ would be the total flux passing through the coil.

Some of the flux linking one of the coils is created by a current in the second coil (see Figure 3.3). We can further define Φ_{ij} as the flux per coil i turn linking coil j due to a current in coil j with a corresponding interpretation of λ_{ij} . Thus, Φ_{11} is the flux per coil 1 turn linking coil 1 due to its own current, and Φ_{12} is the flux per coil 1 turn linking coil 1 due to a current in coil 2. The corresponding flux linkages are λ_{11} and λ_{12} . We use λ_i with a single subscript to refer to the total flux linkage of coil i . Thus, we have

$$\begin{aligned}\lambda_1 &= \lambda_{11} + \lambda_{12} = N_1 (\Phi_{11} + \Phi_{12}) \\ \lambda_2 &= \lambda_{22} + \lambda_{21} = N_2 (\Phi_{22} + \Phi_{21})\end{aligned}\tag{3.10}$$

It is further useful to define the leakage flux per turn as

$$\begin{aligned}\Phi_{\ell 1} &= \Phi_{11} - \Phi_{21} \\ \Phi_{\ell 2} &= \Phi_{22} - \Phi_{12}\end{aligned}\tag{3.11}$$

In the following discussion, we usually refer to Φ with or without subscripts as a flux, but it should be understood that it is a flux per turn. Thus, the leakage flux for coil 1 is the self-flux for coil 1 minus the flux linking coil 2 due to the current in coil 1. Since the core flux links both coils, this flux is excluded from the leakage flux. The same applies to the leakage flux for coil 2. The word *leakage flux* gives the impression that this is flux that has leaked out of the core, but in reality it is simply flux that does not link both coils. Most of this flux is in the medium surrounding the core, usually oil or air. Both oil and air are linear materials with relative permeabilities close to 1. Thus, the inductances associated with this flux given by

$$L_{\ell 1} = \frac{N_1 \Phi_{\ell 1}}{I_1}, \quad L_{\ell 2} = \frac{N_2 \Phi_{\ell 2}}{I_2}\tag{3.12}$$

are nearly unaffected by core nonlinearities. These are called single-winding leakage inductances and are essentially constant.

Combining Equations 3.10 and 3.11, we have

$$\lambda_1 = N_1 (\Phi_{\ell 1} + \Phi_{21} + \Phi_{12}), \quad \lambda_2 = N_2 (\Phi_{\ell 2} + \Phi_{12} + \Phi_{21})\tag{3.13}$$

Let $\Phi_c = \Phi_{12} + \Phi_{21}$. As we can see from Equation 3.13, this is a common flux linking both coils and is therefore predominately core flux. From Equations 3.12 and 3.13, we can see that

$$\lambda_1 = L_{\ell 1} I_1 + N_1 \Phi_c, \quad \lambda_2 = L_{\ell 2} I_2 + N_2 \Phi_c\tag{3.14}$$

The voltage equations for the two windings are

$$V_1 = R_1 I_1 + \frac{d\lambda_1}{dt}, \quad V_2 = R_2 I_2 + \frac{d\lambda_2}{dt} \quad (3.15)$$

where λ_1 and λ_2 are the total flux linkages for windings 1 and 2, and R_1, R_2 are their resistances. Substituting from Equation 3.14, the voltage equations become

$$\begin{aligned} V_1 &= R_1 I_1 + L_{\ell 1} \frac{dI_1}{dt} + N_1 \frac{d\Phi_c}{dt} \\ V_2 &= R_2 I_2 + L_{\ell 2} \frac{dI_2}{dt} + N_2 \frac{d\Phi_c}{dt} \end{aligned} \quad (3.16)$$

Although we obtained Φ_c by adding fluxes produced by each coil acting separately, in reality, this common flux is produced by the simultaneous actions of both coils. When the resultant flux is nonlinear, it can no longer be regarded as a simple addition of separate fluxes. Thus, when nonlinear effects are important, Φ_c requires a broader interpretation.

Figure 3.4 shows a circuit diagram for Equation 3.16. The circuit contains an ideal transformer with a turns ratio of N_1/N_2 . This is the same as the voltage ratio between the primary and secondary sides as seen in the figure and given by

$$\frac{E_1}{E_2} = \frac{N_1}{N_2} \quad (3.17)$$

E_1 and E_2 are voltages induced in the primary or secondary windings by the changing common flux, as is required by Faraday's law. Separating out this common flux provides the physical basis for the ideal transformer.

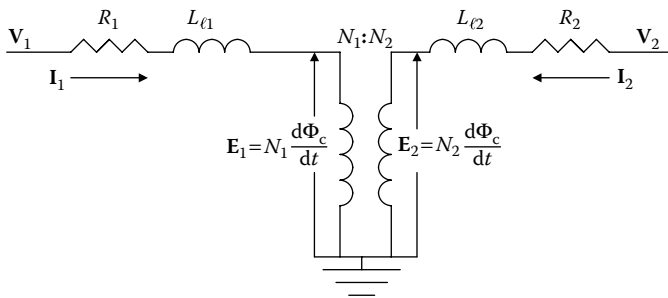
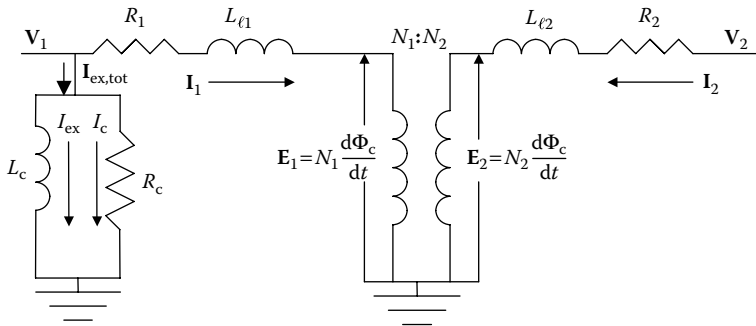


FIGURE 3.4

Circuit model of a loaded two-winding transformer, including a possibly nonlinear ideal transformer.

**FIGURE 3.5**

Circuit model of a loaded two-winding transformer, including a possibly nonlinear core and an ideal transformer.

The two-winding circuit model so far has ignored details of the core excitation. This excitation must come from the difference between the amp-turns of windings 1 and 2 and is typically small. To account for this, it is customary to siphon off this amp-turn difference from one of the windings and let it flow into the core circuit model shown in Figure 3.1. We can consider the core circuit to be a shunt branch of one of the windings in Figure 3.4, usually the primary winding, labeled 1 in the figure. For physical reasons, this core shunt branch should be placed after the primary winding resistance and leakage reactance, since the exciting current flows in the primary winding. The core shunt branch will then directly determine the core voltage E_1 , rather than getting its value from the common flux. However, the common flux is known from the design or a test, and we assume that there is an inevitable voltage drop in going from the primary terminal to the core itself.

Because this exciting current is small, an approximation is often made to place the core shunt branch at the terminal itself. This is expedient for later developments, where it will be desirable to have amp-turn balance in the main transformer circuit. This approximation can be improved by adding the winding resistance and leakage reactance to the core's resistance and reactance. This circuit model with core is shown in Figure 3.5. In this figure, the current into terminal 1 would be $I_{ex,tot} + I_1$. If desired, capacitive effects can be included by placing a capacitor in parallel with the core circuit.

3.4 Approximate Two-Winding Transformer Circuit Model without Core

Our main concern now will be the transformer circuit beyond the core shunt branch, so we will not further discuss this branch. We recognize that, while V_1 is still the voltage at the primary terminal, I_1 is not the primary terminal

current, although it is very close to it. Provided V_1 is sinusoidal, I_1 will also be sinusoidal, as long as the exciting current is small.

Amp-turn balance in the ideal transformer requires that

$$N_1 \mathbf{I}_1 + N_2 \mathbf{I}_2 = 0 \quad (3.18)$$

Our current convention that positive current flows into the positive terminals requires that I_1 or I_2 must be negative in order for Equation 3.18 to hold. Since current is assumed to flow into the primary winding because this current comes from the power source, the current I_2 must be negative. A negative current into a terminal is the same as a positive current out of the terminal.

Rewriting Equation 3.16, we have

$$\begin{aligned} V_1 &= R_1 I_1 + L_{\ell 1} \frac{dI_1}{dt} + E_1 \\ V_2 &= R_2 I_2 + L_{\ell 2} \frac{dI_2}{dt} + E_2 \end{aligned} \quad (3.19)$$

Using Equations 3.17 and 3.18, we can transform Equation 3.19 into the following equation:

$$V_1 = \frac{N_1}{N_2} V_2 + \left[R_1 + \left(\frac{N_1}{N_2} \right)^2 R_2 \right] I_1 + \left[L_{\ell 1} + \left(\frac{N_1}{N_2} \right)^2 L_{\ell 2} \right] \frac{dI_1}{dt} \quad (3.20)$$

The circuit model for Equation 3.20 is shown in Figure 3.6. Note that the ideal transformer is a device for transforming the secondary voltage V_2 to the primary side, which accounts for the first term on the right-hand side of Equation 3.20.

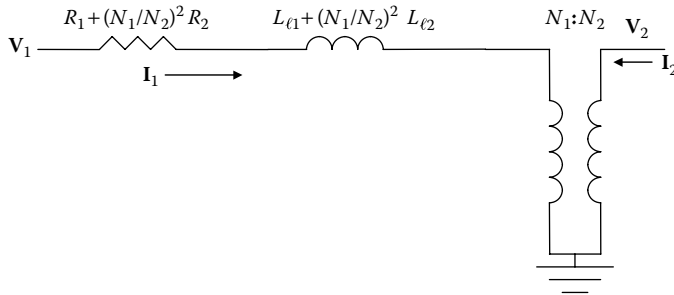


FIGURE 3.6

Circuit model of a two-winding transformer under a load referred to the primary side.

We can combine the resistances and inductances to give equivalent quantities:

$$R_{1,\text{eq}} = R_1 + \left(\frac{N_1}{N_2}\right)^2 R_2, \quad L_{1,\text{eq}} = L_{\ell 1} + \left(\frac{N_1}{N_2}\right)^2 L_{\ell 2} \quad (3.21)$$

These are the two-winding resistance and the leakage inductance referred to the primary side. Although the equivalent resistance accounts for I^2R losses in the windings, it can also be modified to account for losses caused by the stray flux because these are proportional to the square of the current to a good approximation.

Transformers, and especially power transformers, generally operate with currents and voltages that are sinusoidal in time. These are often treated as complex quantities called phasors, which will be discussed in more detail in Chapter 5. For now, we will note that the time derivative of a phasor of angular frequency ω is given by

$$\frac{d\mathbf{I}}{dt} = j\omega\mathbf{I} \quad (3.22)$$

where boldfaced quantities are used to denote phasors. Applying this to the time derivative in Equation 3.20 and using Equation 3.21, we get

$$\mathbf{V}_1 = \frac{N_1}{N_2} \mathbf{V}_2 + R_{1,\text{eq}} \mathbf{I}_1 + j\omega L_{1,\text{eq}} \mathbf{I}_1 \quad (3.23)$$

We can now define an equivalent impedance (two-winding impedance) by

$$Z_{1,\text{eq}} = R_{1,\text{eq}} + j\omega L_{1,\text{eq}} \quad (3.24)$$

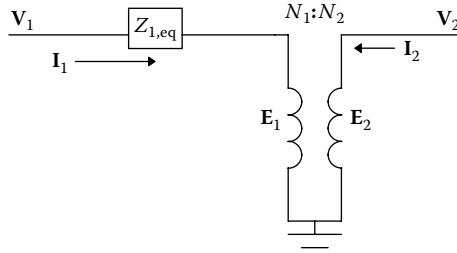
Using this, Equation 3.23 simplifies to

$$\mathbf{V}_1 = \mathbf{I}_1 Z_{1,\text{eq}} + \mathbf{E}_1, \quad \mathbf{V}_2 = \mathbf{E}_2 \quad (3.25)$$

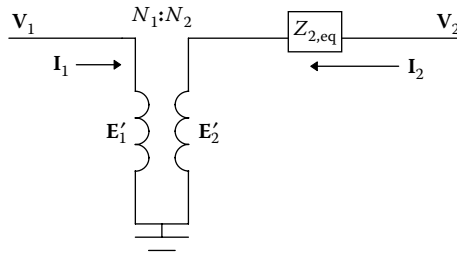
Here \mathbf{E}_1 and \mathbf{E}_2 denote voltages across the ideal transformer, with $\mathbf{E}_2 = \mathbf{V}_2$ and $\mathbf{E}_1 = (N_1/N_2)\mathbf{E}_2$. These are not the same voltages across the ideal transformer as those in Figure 3.4, although the same symbol is used. They obey the voltage ratio Equation 3.17. Of course, the amp-turn balance (Equation 3.18) also holds for this ideal transformer. The equivalent circuit for Equation 3.25 is shown in Figure 3.7.

Using Equations 3.17 and 3.18, we can transform Equation 3.25 into

$$\mathbf{V}_2 = \frac{N_2}{N_1} \mathbf{V}_1 + \left(\frac{N_2}{N_1}\right)^2 Z_{1,\text{eq}} \mathbf{I}_2 \quad (3.26)$$

**FIGURE 3.7**

Simplified circuit model of a two-winding transformer under a load referred to the primary side.

**FIGURE 3.8**

Simplified circuit model of a two-winding transformer under a load referred to the secondary side.

Letting $\mathbf{E}'_1 = V_1$ and $\mathbf{E}'_2 = (N_2/N_1)\mathbf{E}'_1$ and defining

$$Z_{2,\text{eq}} = \left(\frac{N_2}{N_1} \right)^2 Z_{1,\text{eq}} = R_{2,\text{eq}} + j\omega L_{2,\text{eq}} \quad (3.27)$$

where

$$R_{2,\text{eq}} = R_2 + \left(\frac{N_2}{N_1} \right)^2 R_1, \quad L_{2,\text{eq}} = L_{\ell 2} + \left(\frac{N_2}{N_1} \right)^2 L_{\ell 1} \quad (3.28)$$

We can express Equation 3.26 as

$$\mathbf{V}_2 = Z_{2,\text{eq}} \mathbf{I}_2 + \mathbf{E}'_2, \quad \mathbf{V}_1 = \mathbf{E}'_1 \quad (3.29)$$

The \mathbf{E} s are primed to emphasize that these are different from the \mathbf{E} s in Equation 3.26; however, they still obey the voltage ratio Equation 3.17 for an ideal transformer. The circuit model for Equation 3.29 is shown in Figure 3.8.

Note the symmetry between [Figures 3.7](#) and [3.8](#). This is especially clear from a comparison of Equations 3.21 and 3.28. We could have initially transferred impedances to the secondary side and arrived at Equation 3.28 directly. From both of these equations, as well as from Equation 3.27, we can see that impedances are transferred across an ideal transformer by the square of the turns ratio or its reciprocal, depending on which way the transfer occurs.

The exciting current may be shared by both windings rather than being restricted to the primary winding when load current flows. This can lead to legitimate circuit models with shunt branches on either side. All of these are mathematically equivalent because impedances can be transferred across the ideal transformer present in the circuit. We have demonstrated this for a series impedance, and it is shown for a shunt impedance in [Figure 3.9](#).

In [Figure 3.9a](#), we have the relationships

$$E_1 = I_{1s}Z_1, \quad \frac{E_1}{E_2} = \frac{N_1}{N_2}, \quad \frac{I_1}{I_2} = -\frac{N_2}{N_1}, \quad I'_1 = I_1 + I_{1s} \quad (3.30)$$

Manipulating these equations, we obtain

$$E_2 = \left(\frac{N_2}{N_1} \right) \left[I'_1 + \left(\frac{N_2}{N_1} \right) I_2 \right] Z_1 \quad (3.31)$$

From [Figure 3.9b](#), we have $I_2 = I'_2 + I_{2s}$ and $I'_1/I'_2 = -N_2/N_1$. Equation 3.31 becomes

$$E_2 = \left(\frac{N_2}{N_1} \right)^2 Z_1 I_{2s} = Z_2 I_{2s} \quad (3.32)$$

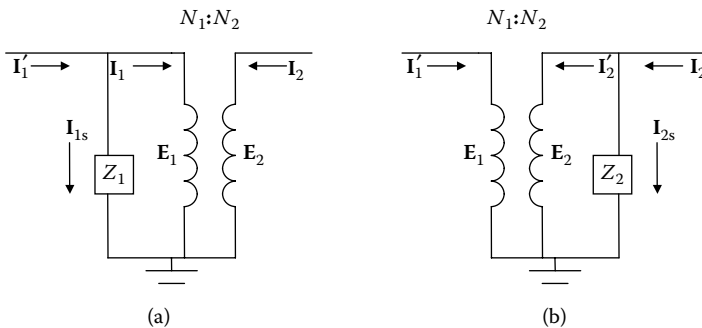


FIGURE 3.9

Transfer of shunt impedances across the ideal transformer: (a) shunt impedance on the primary side; and (b) shunt impedance on the secondary side.

where

$$Z_2 = \left(\frac{N_2}{N_1} \right)^2 Z_1 \quad (3.33)$$

Equation 3.33 shows that shunt impedances are also transferred across an ideal transformer by the square of the turns ratio (in this case, the reciprocal). In deriving Equation 3.32, we have kept the terminal currents the same in Figures 3.9a and b. The currents in the ideal transformer, however, are different. The voltages across the ideal transformers, E_1 and E_2 , are the same in Figures 3.9a and b. This situation differs from that of the transfer of a series impedance across an ideal transformer, where we found that the currents in the two ideal transformers remained the same but the voltages differed.

3.5 Vector Diagram of a Loaded Transformer with Core

For increased accuracy, the core excitation circuit can be added to the circuit model developed in Section 3.4, where the leakage impedances were transferred to one side of the ideal transformer. This is a good approximation because the core excitation current is small when compared with the load currents. In Figure 3.5, we placed the core excitation circuit at terminal 1. However, as we saw in Section 3.4, the core excitation can also be transferred across the ideal transformer. Since we want to explore the relationship between the load current and voltage and the excitation current and voltage, the core excitation impedance branch, along with the 2-winding leakage impedance, will be placed at terminal 2. This will lead to the circuit diagram shown in Figure 3.10.

For the vector (complex plane) diagram, we assume that the positive sense of the secondary current is out of terminal 2, as it normally is. Since we are only looking at the secondary side, this assumption will not conflict with our normal sign conventions. We also assume that the secondary ideal

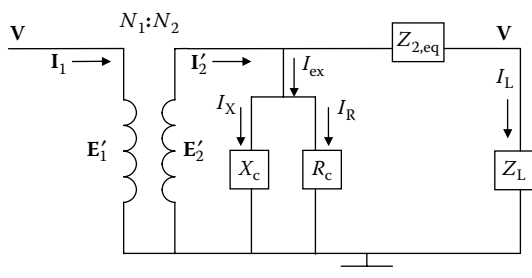
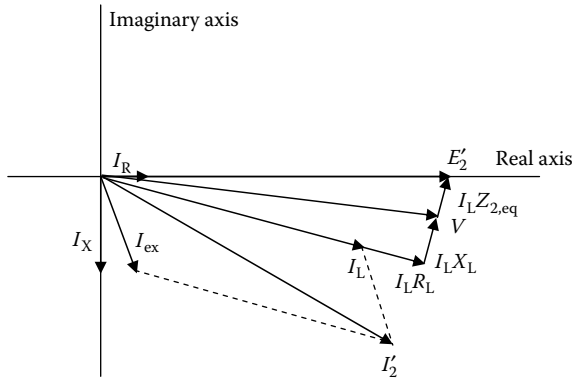


FIGURE 3.10

Circuit diagram of a loaded transformer with a core excitation circuit on the secondary side.

**FIGURE 3.11**

Vector diagram showing the relationships between the voltages and currents in a loaded two-winding transformer with a core.

transformer voltage E'_2 is the reference voltage and that all currents and voltages are sinusoidal. Note that the voltage drop V , across a reactance X , and current I through the reactance are related by $V = jXI$. Because multiplication by j in the complex plane corresponds to a counterclockwise rotation of 90° , the voltage drop across a reactance is in a perpendicular direction to the current direction. On the other hand, for a resistor R , the voltage drop is $V = IR$, so this voltage drop is in the direction of the current. For an impedance with resistive and reactive components, the voltage drop direction is determined by the relative magnitudes of the resistive and reactive components.

We will assume that the load impedance in Figure 3.10 is mostly resistive and is given by $Z_L = R_L + jX_L$, whereas the leakage impedance is entirely reactive. The vector diagram corresponding to Figure 3.10 is shown in Figure 3.11.

This diagram is not to scale. The exciting current is usually a much smaller vector relative to the load current. Note that the core flux is in the direction of the exciting current I_X , whereas the leakage flux is in the direction of the load current I_L . These flux densities can overlap near the center of the core legs. For predominantly resistive load currents, their vector addition does not increase the magnitude of the resultant flux density very much, whereas for reactive load currents, the flux densities associated with these currents add directly. When reactive load currents are high, the possibility of saturating the center of the core legs due to this phenomenon must be considered.

3.6 Per-Unit System

Transformer impedances, along with other quantities such as voltages and currents, are often expressed in the per-unit (pu) system, that is, as a ratio

with respect to the transformer's nominal or rated phase quantities. Thus, if the rated or base phase voltages are V_{b1} , V_{b2} and the base currents are I_{b1} , I_{b2} , where 1 and 2 refer to the primary and secondary sides, then the base impedances are

$$Z_{b1} = \frac{V_{b1}}{I_{b1}}, \quad Z_{b2} = \frac{V_{b2}}{I_{b2}} \quad (3.34)$$

We assume that the rated or base voltages, currents, and impedances transfer from one side to the other by means of the ideal transformer relationships among voltages, currents, and impedances. These base quantities are all taken to be positive, so the minus sign is not used in the base current transfer across sides. Thus, the base power P_b is the same on both sides of an ideal two-winding transformer:

$$P_b = V_{b1}I_{b1} = V_{b2}I_{b2} \quad (3.35)$$

In an actual transformer, the real power into the transformer is nearly the same as that leaving on the secondary side because the transformer losses are a small fraction of the power transferred.

The per-unit base quantities of interest are current, voltage, and power. From Equation 3.35, we see that these quantities are interdependent. Only two independent base quantities are needed in most applications. Of the three, the base power P_b is usually specified, which is the same on both sides of an ideal two-winding transformer. It normally refers to the rated power per phase into a transformer and remains fixed regardless of the number of secondary windings, whether loaded or not. The other base quantity is the base voltage, and this will differ from winding to winding or terminal to terminal. This usually means the rated or no-load voltage of the winding or terminal, whichever is being considered.

Assuming power and voltage as base quantities, the primary-side voltage V_1 , current I_1 , and impedance Z_1 are expressed in the per-unit system by

$$V_{1,\text{pu}} = v_1 = \frac{V_1}{V_{b1}}, \quad I_{1,\text{pu}} = i_1 = I_1 \frac{V_{b1}}{P_b}, \quad Z_{1,\text{pu}} = z_1 = Z_1 \frac{P_b}{V_{b1}^2} \quad (3.36)$$

and the secondary quantities are also expressed similarly. As indicated in Equation 3.36, we use lowercase letters to denote per-unit quantities.

Often, the per-unit values are multiplied by 100 and expressed as a percentage, but care must be taken, since this can lead to errors.

Because the base voltages, currents, and impedances transfer across the ideal transformer in the same manner as their corresponding circuit quantities, the per-unit values of the circuit quantities are the same on both the primary and secondary sides. Although voltages, currents, and impedances for

transformers of greatly different power ratings can differ considerably, their per-unit values tend to be similar, which facilitates calculations of per-unit quantities such as resistances or reactances for any-size transformer. Thus, the two-winding leakage reactances are generally in the range of 5–15% for all power transformers when expressed in the per-unit system. The exciting currents of modern power transformers are typically ~0.1% in the per-unit system. This is also the percentage of their rated load current because this has a value of 100% in the per-unit system. The two-winding resistances, which account for the transformers' losses, can be estimated in the per-unit system by noting that modern power transformers are typically >99.5% efficient. This means that <0.5% of the rated input power goes into losses. Thus, we have

$$\frac{\text{Losses}}{\text{Rated power}} = \frac{R_1 I_{b1}^2}{P_b} = \frac{R_1 P_b}{V_{b1}^2} = \frac{R_1}{Z_{b1}} = r < 0.5\% \quad (3.37)$$

We will use X for reactance magnitudes, where $X = \omega L$, with L the inductance. Thus, x will be a per-unit reactance. Using Equation 3.37 and the above estimate of the leakage reactance in the per-unit system for power transformers, we can estimate the x/r ratio:

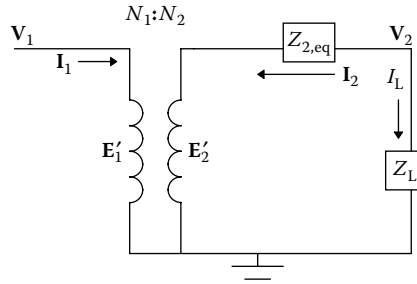
$$\frac{x}{r} = \frac{0.05 - 0.15}{< 0.005} > 10 - 30 \quad (3.38)$$

Thus, 10 is probably a lower limit and is high enough to allow discriminating inrush from fault current on the basis of second-harmonic analysis.

3.7 Voltage Regulation

We will now discuss voltage regulation as an application of the transformer circuit model we just developed and the per-unit system. In this context, the core characteristics do not play a significant role, so we will use the simplified circuit model of Figure 3.8. *Voltage regulation* is defined as the change in the magnitude of the secondary voltage between its open-circuited value and its value when loaded divided by the value when loaded with the primary voltage held constant. We can represent the load by an impedance Z_L . The relevant circuit is shown in Figure 3.12, in which a load current I_L is shown where $I_L = -I_2$.

It is convenient to perform this calculation in the per-unit system, using lowercase letters to represent per-unit quantities. Since base quantities transfer across the ideal transformer, as do their corresponding physical quantities, we have

**FIGURE 3.12**

Circuit model of a two-winding transformer with a load on the secondary side.

$$\begin{aligned} \mathbf{e}'_1 &= \frac{\mathbf{E}'_1}{V_{b1}} = \frac{(N_1/N_2)\mathbf{E}'_2}{(N_1/N_2)V_{b2}} = \frac{\mathbf{E}'_2}{V_{b2}} = \mathbf{e}'_2 = \mathbf{e} \\ \mathbf{i}_1 &= \frac{\mathbf{I}_1}{I_{b1}} = -\frac{(N_2/N_1)\mathbf{I}_2}{(N_2/N_1)I_{b2}} = -\frac{\mathbf{I}_2}{I_{b2}} = -\mathbf{i}_2 = \mathbf{i}_L \end{aligned} \quad (3.39)$$

Therefore, the ideal transformer can be eliminated from the circuit in the per-unit system because the voltages and currents in this system are the same on both sides of the ideal transformer. Also, since $z_{2,\text{eq}} = z_{1,\text{eq}}$, we can drop the numerical subscript and denote the equivalent transformer per-unit impedance by

$$z = r + jx \quad (3.40)$$

where r is the per-unit two-winding resistance and x is the per-unit two-winding leakage reactance. Similarly, we write

$$z_L = \frac{Z_L}{Z_{b2}} = r_L + jx_L \quad (3.41)$$

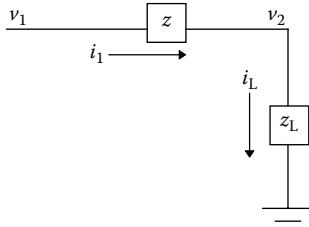
The per-unit circuit is shown in [Figure 3.13](#).

Thus, when the secondary terminal is open-circuited so that z_L and its ground connection are missing ([Figure 3.13](#)), the open-circuited value of v_2 is

$$v_{2,\text{oc}} = v_1 \quad (3.42)$$

We assume that \mathbf{v}_1 is a reference phasor (zero phase angle) and v_1 is therefore its magnitude. When the load is present, we have

$$\mathbf{v}_2 = \mathbf{i}_L z_L, \quad \mathbf{v}_1 = \mathbf{i}_L (z + z_L) \quad (3.43)$$

**FIGURE 3.13**

The circuit in [Figure 3.12](#) shown in the per-unit system.

From Equation 3.43, we have

$$\mathbf{v}_2 = \frac{z_L \mathbf{v}_1}{(z + z_L)} = \frac{\mathbf{v}_1}{(1 + z/z_L)} \Rightarrow |\mathbf{v}_2| = \frac{v_1}{|1 + z/z_L|} \quad (3.44)$$

Hence, the voltage regulation is given by

$$\frac{v_{2,oc} - |\mathbf{v}_2|}{|\mathbf{v}_2|} = \left| 1 + \frac{z}{z_L} \right| - 1 \quad (3.45)$$

At this point, it is customary to express the complex number z_L in its polar form:

$$z_L = |z_L| e^{j\theta}, \quad |z_L| = \sqrt{r_L^2 + x_L^2}, \quad \theta = \tan^{-1} \left(\frac{x_L}{r_L} \right) \quad (3.46)$$

From Equation 3.43, we note that the magnitude of z_L is also given by

$$|z_L| = \left| \frac{\mathbf{v}_2}{\mathbf{i}_L} \right| = \frac{v_2}{i_L}$$

where the magnitudes of v_2 and i_L are represented by the symbols in ordinary type. Keeping the Cartesian representation of a complex number for z , we have for the ratio:

$$\begin{aligned} \frac{z}{z_L} &= (r + jx) \left(\frac{i_L}{v_2} \right) e^{-j\theta} = \left(\frac{i_L}{v_2} \right) (r + jx)(\cos \theta - j \sin \theta) \\ &= \left(\frac{i_L}{v_2} \right) (r \cos \theta + x \sin \theta) + j(x \cos \theta - r \sin \theta) \end{aligned} \quad (3.47)$$

Substituting Equation 3.47 into Equation 3.45, we get:

$$\begin{aligned} \text{Regulation} &= \sqrt{\left[1 + \left(\frac{i_L}{v_2}\right)(r \cos \theta + x \sin \theta)\right]^2 + \left[\left(\frac{i_L}{v_2}\right)(x \cos \theta - r \sin \theta)\right]^2} - 1 \\ &= \sqrt{1 + 2\left(\frac{i_L}{v_2}\right)(r \cos \theta + x \sin \theta) + \left(\frac{i_L}{v_2}\right)^2 (r^2 + x^2)} - 1 \end{aligned} \quad (3.48)$$

Since z is generally small compared with z_L , the terms other than unity in Equation 3.48 are small when compared to unity. Using the approximation for small ϵ :

$$\sqrt{1 + \epsilon} = 1 + \frac{1}{2}\epsilon - \frac{1}{8}\epsilon^2 \quad (3.49)$$

the regulation is given to second order in z/z_L by

$$\text{Regulation} = \left(\frac{i_L}{v_2}\right)(r \cos \theta + x \sin \theta) + \frac{1}{2}\left(\frac{i_L}{v_2}\right)^2 (x \cos \theta - r \sin \theta)^2 \quad (3.50)$$

4

Reactance and Leakage Reactance Calculations

4.1 Introduction

The leakage reactance calculations performed here apply to a single-phase unit or to one phase of a three-phase transformer. The phase can have multiple windings, interconnected in such a way that only two or three terminals (external or buried) result. Thus, autotransformers, with or without tertiary windings, as well as transformers with separate tap windings are included. The calculations for windings that are interconnected are based on two-winding leakage reactances. These reactances can be obtained from a simple analytical formula, which will be presented in this chapter, from finite element calculations, or from more complicated analytical methods, such as Rabins' method, which will be presented in Chapter 9. We will also be giving the per-unit expressions for these reactances.

It is usually desirable to design some reactance into a transformer in order to limit any fault current. These currents flow in the transformer windings when, for example, a terminal is shorted to the ground. When this happens, the internal impedance of a transformer, which is mainly reactive, is primarily responsible for limiting this current. In addition, these reactances determine the voltage regulation of the unit. Hence, it is desirable at the design stage to be able to calculate these reactances based on the geometry of the coils and core and the nature of the (single-phase) winding interconnections.

Although impedances have a resistive component, winding resistances are usually not too difficult to calculate, especially direct current (DC) resistances. Complications arise from the eddy current contributions, which are usually generated by the time-varying flux from neighboring windings. Eddy currents produced by the current within the winding itself are usually kept small by subdividing the cross-sectional area of the winding into multiple parallel strands and then transposing these. For power transformers, the resistances are usually small when compared with leakage reactances, but should be taken into account when greater accuracy is desired.

We will begin by discussing the general theory of inductance calculations. Reactances are obtained from the inductances by multiplying the inductances by the angular frequency under sinusoidal conditions, which are assumed here. The following references are used in this chapter: [Del94], [MIT43], [Lyo37], [Blu51], [Wes64].

4.2 General Method for Determining Inductances and Mutual Inductances

Self- and mutual inductances are usually defined in terms of flux linkages between circuits. However, they can be calculated more conveniently in terms of magnetic energy. In this section, we will show the equivalence of these methods and develop useful formulas for determining these inductances in terms of the magnetic field values.

Consider a set of stationary circuits as shown in Figure 4.1a. We assume that we slowly increase their currents by means of batteries with variable control. While calculating the work done by the batteries, we ignore any I^2R

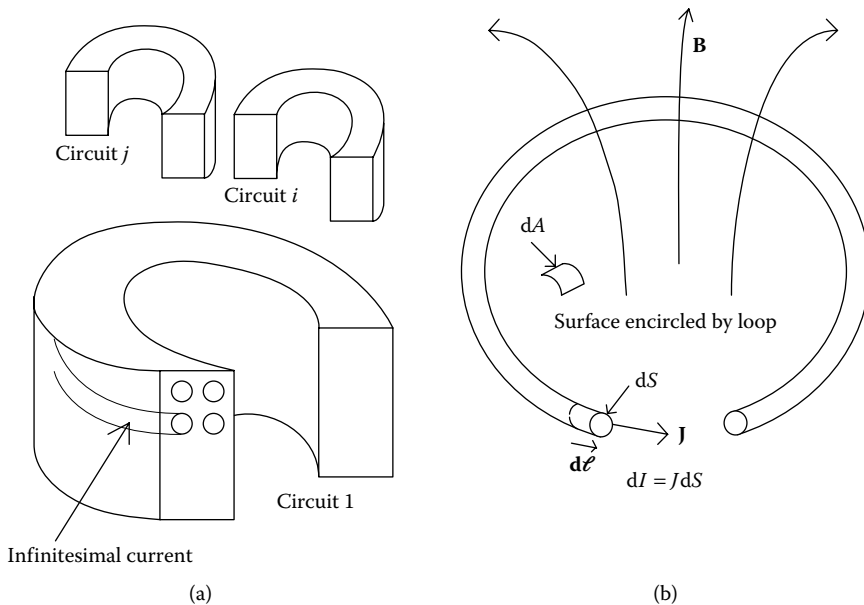


FIGURE 4.1

Method of circuit subdivision used to calculate self- and mutual inductances. (a) Collection of circuits subdivided into infinitesimal current loops and (b) infinitesimal current loop, which is part of a system of circuits.

or dissipative losses or, more realistically, we can treat these separately. Thus, we are only interested in the work necessary to establish the magnetic field. Since we assume losses to be zero, this work will equal the magnetic energy stored in the final field. Because of the changing flux linking the different circuits, electromotive forces (emfs) will be induced in them by Faraday's law. We assume that the battery controllers are adjusted so that the battery voltages just balance the induced voltages throughout the process. Because the circuits can have finite cross-sectional areas as shown in the figure, we imagine subdividing them into infinitesimal circuits or tubes carrying an incremental part of the total current, dI , as in [Figure 4.1b](#).

4.2.1 Energy by Magnetic Field Methods

The incremental energy dW , which the batteries supply during a time interval dt , is

$$dW = dt \int V dI = dt \int \underset{\substack{\text{cross-sectional} \\ \text{area of circuits}}}{V} dS \quad (4.1)$$

Here, the integrand is the infinitesimal power flowing through the infinitesimal circuit or loop carrying current dI and along which a voltage V is induced. The integral simply represents the sum of these powers. We have also substituted the current density J and the infinitesimal cross-sectional area dS for the incremental current in the loop so that the last integral is over the cross-sectional area of the circuits. From Faraday's law for a single-turn circuit we get:

$$V = \frac{d\Phi}{dt} \quad (4.2)$$

where Φ is the flux linked by the circuit. Substituting V from Equation 4.2 into Equation 4.1, we get:

$$dW = \int \underset{\substack{\text{cross-sectional} \\ \text{area of circuits}}}{d\Phi} dS \quad (4.3)$$

By definition

$$\Phi = \int \underset{\text{area of loop}}{\mathbf{B} \cdot \mathbf{n}} dA = \int \underset{\text{area of loop}}{(\nabla \times \mathbf{A}) \cdot \mathbf{n}} dA = \oint \underset{\text{along loop}}{\mathbf{A} \cdot d\boldsymbol{\ell}} \quad (4.4)$$

In Equation 4.4, we have introduced the vector potential, \mathbf{A} , where

$$\mathbf{B} = \nabla \times \mathbf{A} \quad (4.5)$$

We have also used Stoke's theorem [Pug62]. We are denoting vectors by bold faced quantities here. Since we will not be using phasors in this chapter, no confusion should arise.

In Equation 4.4, the surface integral is over the surface encircled by the wire loop and the line integral is along the loop as shown in Figure 4.1b. \mathbf{n} is the unit normal to the surface encircled by the loop, and $d\ell$ is the infinitesimal distance vector along the loop. Note that $d\ell$ points in the same direction as \mathbf{J} considered a vector. Since the current loops are fixed, we obtain the following equation by taking the differential of Equation 4.4

$$d\Phi = \oint_{\text{along loop}} d\mathbf{A} \cdot d\ell \quad (4.6)$$

Substituting this into Equation 4.3, we get

$$dW = \int_{\substack{\text{cross-sectional} \\ \text{area of circuits}}} \left(\oint_{\text{along loop}} d\mathbf{A} \cdot d\ell \right) \mathbf{J} dS \quad (4.7)$$

Since \mathbf{J} points along $d\ell$ and since the volume element $dV = d\ell dS$, we can rewrite Equation 4.7 as

$$dW = \int_{\substack{\text{cross-sectional} \\ \text{area of circuits}}} \left(\oint_{\text{along loop}} d\mathbf{A} \cdot \mathbf{J} d\ell dS \right) = \int_{\text{volume of circuits}} d\mathbf{A} \cdot \mathbf{J} dV \quad (4.8)$$

By changing to a volume integral, we are simply recognizing the fact that the integral over the cross-sectional area of the circuits, combined with an integral along the lengths of the infinitesimal circuits, amounts to an integration over the volume of the circuits. Recognizing that the circuit remains stationary during this process, the total work done to establish the final field values is

$$W = \int_0^A dW = \int_{\substack{\text{volume} \\ \text{of circuits}}} dV \int_0^A \mathbf{J} \cdot d\mathbf{A} = \frac{1}{2} \int_{\substack{\text{volume} \\ \text{of circuits}}} \mathbf{A} \cdot \mathbf{J} dV \quad (4.9)$$

where the last equality follows if \mathbf{A} increases proportionally with \mathbf{J} as we build up the fields.

For calculation purposes, it is sometimes more convenient to express Equations 4.8 and 4.9 in terms of the field values directly. The volume integration in both equations could be taken over all space because the current density is zero everywhere except within the circuits. (By all space, we

mean the solution space of the problem of interest, ignoring the rest of the universe.) For this, we use one of Maxwell's equations in SI units, ignoring displacement currents:

$$\nabla \times \mathbf{H} = \mathbf{J} \quad (4.10)$$

where \mathbf{H} is the magnetic field. Substituting into Equation 4.8, we get

$$dW = \int_{\text{all space}} d\mathbf{A} \cdot (\nabla \times \mathbf{H}) dV \quad (4.11)$$

Using the vector identity for general vector fields \mathbf{P}, \mathbf{Q} [Pug62], we get

$$\nabla \cdot (\mathbf{P} \times \mathbf{Q}) = \mathbf{Q} \cdot (\nabla \times \mathbf{P}) - \mathbf{P} \cdot (\nabla \times \mathbf{Q}) \quad (4.12)$$

We have, upon substitution into Equation 4.11 with the identification $\mathbf{P} \rightarrow \mathbf{H}$, $\mathbf{Q} \rightarrow d\mathbf{A}$,

$$\begin{aligned} dW &= \int_{\text{all space}} \mathbf{H} \cdot (\nabla \times d\mathbf{A}) dV + \int_{\text{all space}} \nabla \cdot (\mathbf{H} \times d\mathbf{A}) dV \\ &= \int_{\text{all space}} \mathbf{H} \cdot d\mathbf{B} dV + \int_{\text{boundary surface}} (\mathbf{H} \times d\mathbf{A}) \cdot \mathbf{n} dS \end{aligned} \quad (4.13)$$

In Equation 4.13, we have used the definition of \mathbf{A} given in Equation 4.5 and the divergence theorem to convert the last volume integral into a surface integral. The surface integral generally vanishes since the boundary surface is usually at infinity where the fields drop to zero. Thus, we can drop it to get

$$dW = \int_{\text{all space}} \mathbf{H} \cdot d\mathbf{B} dV \quad (4.14)$$

The total work done to establish the final field values is

$$W = \int_0^{\mathbf{B}} dW = \int_{\text{all space}} dV \int_0^{\mathbf{B}} \mathbf{H} \cdot d\mathbf{B} = \frac{1}{2} \int_{\text{all space}} \mathbf{H} \cdot \mathbf{B} dV \quad (4.15)$$

where the last equality follows for the situation where \mathbf{B} increases proportionally with \mathbf{H} . Either Equation 4.9 or Equation 4.15 can be used to calculate the magnetic energy.

4.2.2 Energy from Electric Circuit Methods

We will now show how the magnetic energy can be related to inductances or leakage inductances from circuit considerations. The voltages induced in

the circuits of Figure 4.1a can be written in terms of inductances and mutual inductances as

$$V_i = \sum_j M_{ij} \frac{dI_j}{dt} \quad (4.16)$$

where M_{ij} is the mutual inductance between circuits i and j . When $j = i$, $M_{ii} = L_i$, where L_i is the self-inductance of circuit i . The incremental energy for the circuits of Figure 4.1a can be expressed, making use of Equation 4.16, as

$$dW = \sum_i V_i I_i dt = \sum_{i,j} M_{ij} I_i dI_j = \sum_i L_i I_i dI_i + \sum_{i \neq j} M_{ij} I_i dI_j \quad (4.17)$$

For linear systems, it can be shown that $M_{ij} = M_{ji}$. Thus, the second sum in Equation 4.17 can be written as

$$\begin{aligned} \sum_{j \neq i} M_{ij} I_i dI_j &= \frac{1}{2} \left(\sum_{i \neq j} M_{ij} I_i dI_j + \sum_{i \neq j} M_{ji} I_j dI_i \right) \\ &= \frac{1}{2} \sum_{i \neq j} M_{ij} (I_i dI_j + I_j dI_i) = \sum_{i < j} M_{ij} d(I_i I_j) \end{aligned} \quad (4.18)$$

The first equality in this equation is a matter of changing the index labels in the sum and the second equality results from the symmetric nature of M_{ij} for linear systems. The third equality results from double counting, which happens when i and j are summed independently. Substituting Equation 4.18 into Equation 4.17, we get

$$dW = \frac{1}{2} \sum_i L_i d(I_i^2) + \sum_{i < j} M_{ij} d(I_i I_j) \quad (4.19)$$

Integrating this last equation, we get

$$W = \frac{1}{2} \sum_i L_i I_i^2 + \sum_{i < j} M_{ij} I_i I_j \quad (4.20)$$

Thus, Equation 4.20 is another way to express the magnetic energy in terms of inductances and mutual inductances. As an example, consider a single circuit for which we want to know the self-inductance. From Equation 4.20, we have

$$L_1 = \frac{2W}{I_1^2} \quad (4.21)$$

where W can be calculated from Equation 4.9 or 4.15 with only the single circuit in the geometry. W is usually obtainable from finite element codes. If we have two circuits, then Equation 4.20 becomes

$$L_1 I_1^2 + L_2 I_2^2 + 2M_{12} I_1 I_2 = 2W \quad (4.22)$$

If these two circuits are the high- (label 1) and low- (label 2) voltage coils of a two-winding ideal transformer with N_1 and N_2 turns, respectively, then we have $I_2/I_1 = -N_1/N_2$, so that Equation 4.22 becomes

$$L_1 + \left(\frac{N_1}{N_2} \right)^2 L_2 - 2 \left(\frac{N_1}{N_2} \right) M_{12} = \frac{2W}{I_1^2} \quad (4.23)$$

The expression on the left is the two-winding leakage inductance as referred to the high-voltage side [MIT43]. The magnetic energy on the right side can be calculated from Equations 4.9 or 4.15 with the two windings in the geometry and with the ampere-turns (amp-turns) balanced. Multiplying by $\omega = 2\pi f$ produces the leakage reactance.

The mutual inductance between two circuits is needed in detailed circuit models of transformers in which the circuits of interest are sections of the same or different coils. We can obtain this quantity in terms of the vector potential. By definition, the mutual inductance between circuits 1 and 2 M_{12} , is the flux produced by circuit 2, which links circuit 1, divided by the current in circuit 2. Circuits 1 and 2 can be interchanged in this definition without changing the value of the mutual inductance for linear systems. We use the infinitesimal loop approach, as illustrated in [Figure 4.1](#), to obtain this quantity. Each infinitesimal loop represents an infinitesimal fraction of a turn. For circuit 1, an infinitesimal loop carrying current dI_1 represents a fractional turn dI_1/I_1 . Therefore, the flux linkage between this infinitesimal turn due to the flux produced by circuit 2, $d\lambda_{12}$, is

$$\begin{aligned} d\lambda_{12} &= \frac{dI_1}{I_1} \int_{\text{surface enclosed by}} \mathbf{B}_2 \cdot \mathbf{ndS}_1 = \frac{dI_1}{I_1} \int_{\text{surface enclosed by}} (\nabla \times \mathbf{A}_2) \cdot \mathbf{ndS}_1 \\ &= \frac{dI_1}{I_1} \oint_{\text{along infinitesimal}} \mathbf{A}_2 \cdot \mathbf{d\ell}_1 \end{aligned} \quad (4.24)$$

where Stokes' theorem has been used. Integrating this expression over the cross-sectional area of circuit 1, and using the fact that $dI_1 = J_1 dS_1$ and that \mathbf{J}_1 as a vector points along $\mathbf{d\ell}_1$, we can write

$$\lambda_{12} = \frac{1}{I_1} \int_{\text{cross-sectional}} J_1 dS_1 \left(\oint_{\text{along infinitesimal}} \mathbf{A}_2 \cdot \mathbf{d\ell}_1 \right) = \frac{1}{I_1} \int_{\text{volume of circuit 1}} \mathbf{A}_2 \cdot \mathbf{J}_1 dV_1 \quad (4.25)$$

where we have used the same integration devices as we used previously. Thus, the mutual inductance between these circuits is given by

$$M_{12} = \frac{\lambda_{12}}{I_2} = \frac{1}{I_1 I_2} \int_{\text{volume of circuit 1}} \mathbf{A}_2 \cdot \mathbf{J}_1 dV_1 \quad (4.26)$$

This formula reduces to the formula for self-inductance when 1 and 2 are the same circuit and $M_{11} = L_1$.

The mutual inductance calculation (Equation 4.26), together with the self-inductance calculation (Equation 4.21), can be used to determine the leakage inductance from Equation 4.23. However, when an iron core is involved, L_1 , L_2 , and M_{12} tend to be large quantities, so that the subtractions in Equation 4.23 can lead to large errors unless the inductances are determined with high accuracy.

4.3 Two-Winding Leakage Reactance Formula

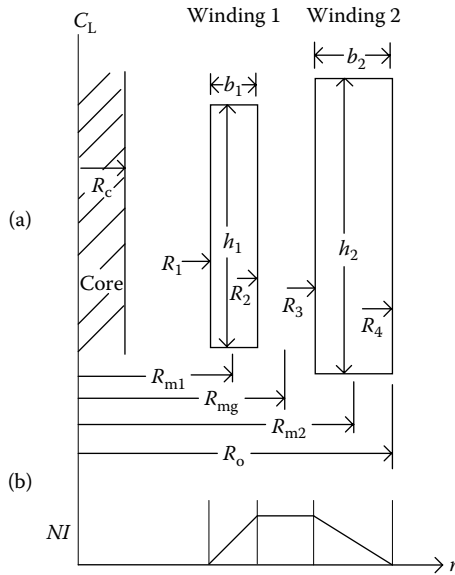
Although the two-winding leakage reactance is needed to model a two-winding transformer, the two-winding leakage reactances between pairs of windings in a multiwinding transformer are useful for modeling these transformers as well, and therefore this is an important quantity to determine. It can be calculated by advanced analytical techniques such as Rabins' method [Rab56] or finite element methods, which solve Maxwell's equations directly. These methods are especially useful if the distribution of amp-turns along the winding is nonuniform, for example due to tapped out sections or thinning in sections of windings adjacent to taps in neighboring windings. However, more simple idealized calculations have proven adequate in practice, particularly at the early design stage, and such a calculation will be discussed here.

The simple reactance calculation assumes that the amp-turns are uniformly distributed along the windings. It also treats the windings as if they were infinitely long solenoids insofar as the magnetic field is concerned, although a correction for fringing at the ends is included in the final formula.

The magnetic field inside an infinitely long solenoid can be found from symmetry considerations, using Maxwell's equation (Equation 4.10) expressed in integral form as

$$\oint \mathbf{H} \cdot d\boldsymbol{\ell} = I \quad (4.27)$$

where the integral is around a closed loop enclosing a current I through the surface of the loop. For an ideal, infinitely tall solenoid with N turns per


FIGURE 4.2

(a) Geometric and (b) electrical parameters used in two-winding leakage reactance calculation.

height h uniformly distributed, the application of this formula, together with symmetry considerations, tells us that there is a uniform axially directed field inside the solenoid with a magnitude $H = NI/h$ and a zero field outside the solenoid.

We can apply this formula to the two-winding transformer considered here. The parameters of interest are shown in Figure 4.2. The windings have a finite thickness, so the amp-turns are a function of the radius parameter r . The total amp-turns are assumed to sum to zero for the two windings, as is necessary for a leakage reactance calculation. Then the magnetic field as a function of radius can be found by applying Equation 4.27 to a rectangular loop in a plane that passes through the center line of the solenoid, which encloses both windings, with the vertical side of the rectangle outside the windings kept fixed, while the inner vertical side is gradually shifted toward the outer side. This results in a magnetic field distribution proportional to the amp-turn distribution shown in Figure 4.2b, that is in the SI system

$$H(r) = \frac{NI(r)}{h} \quad (4.28)$$

where $NI(r)$ is the function of r shown in the figure, linearly increasing from 0 through winding 1, remaining constant in the gap, and decreasing to 0

through winding 2. H is independent of the z -coordinate in this model and points vectorially in the z -direction. The flux density is therefore

$$B(r) = \mu_0 H(r) = \mu_0 \frac{NI(r)}{h} \quad (4.29)$$

Since the permeabilities of the materials in or between the winding are essentially that of vacuum, $\mu_0 = 4\pi \times 10^{-7}$ in the SI system. B also points in the z direction. We can take $h = (h_1 + h_2)/2$ as an approximation.

For purposes of calculation, we need to express B as a function of r analytically. Since the total amp-turns is zero, ignoring the signs of the currents, we have $N_1 I_1 = N_2 I_2 = NI$. Therefore, referring to [Figure 4.2](#) for an explanation of the symbols, we get for $B(r)$:

$$B(r) = \mu_0 \frac{NI}{h} \begin{cases} \frac{(r - R_1)}{(R_2 - R_1)}, & R_1 < r < R_2 \\ 1, & R_2 < r < R_3 \\ \frac{(R_4 - r)}{(R_4 - R_3)}, & R_3 < r < R_4 \end{cases} \quad (4.30)$$

The two-winding leakage inductance of winding 1 with respect to winding 2 $L_{\ell 12}$ can be obtained from the magnetic energy in the leakage field by means of the expression

$$\frac{1}{2} L_{\ell 12} I_1^2 = \frac{1}{2\mu_0} \int_{\text{space}} B^2 dV \quad (4.31)$$

Here, the order of the subscripts is important. Substituting Equation 4.30 into the integral, we get

$$\begin{aligned} \frac{1}{2\mu_0} \int_{\text{space}} B^2 dV &= \frac{(\mu_0 NI)^2}{2\mu_0 h^2} \times 2\pi h \left[\int_{R_1}^{R_2} \left(\frac{r - R_1}{R_2 - R_1} \right)^2 r dr + \int_{R_2}^{R_3} r dr + \int_{R_3}^{R_4} \left(\frac{R_4 - r}{R_4 - R_3} \right)^2 r dr \right] \\ &= \frac{\pi \mu_0 (NI)^2}{h} \times \left[\frac{(R_2^2 - R_1^2)}{6} + \frac{(R_2 - R_1)^2}{12} + \frac{(R_3^2 - R_2^2)}{2} \right. \\ &\quad \left. + \frac{(R_4^2 - R_3^2)}{6} - \frac{(R_4 - R_3)^2}{12} \right] \end{aligned} \quad (4.32)$$

In terms of mean radii R_m , thicknesses b , and gap g shown in [Figure 4.2](#), Equation 4.32 can be written as

$$\frac{1}{2\mu_0} \int_{\text{space}} B^2 dV = \frac{\pi \mu_0 (NI)^2}{h} \left[\frac{R_{m1} b_1}{3} + \frac{b_1^2}{12} + R_{mg} g + \frac{R_{m2} b_2}{3} - \frac{b_2^2}{12} \right] \quad (4.33)$$

Thus, using Equation 4.31, we find for the leakage inductance that

$$L_{\ell 12} = \frac{2\pi\mu_0 N_1^2}{h} \left[\frac{R_{m1}b_1}{3} + \frac{R_{m2}b_2}{3} + R_{mg}\mathcal{G} + \frac{b_1^2}{12} - \frac{b_2^2}{12} \right] \quad (4.34)$$

The last two terms in Equation 4.34 are often dropped because they approximately cancel. The leakage reactance magnitude is $X_{\ell 12} = 2\pi f L_{\ell 12}$, so we get

$$X_{\ell 12} = \frac{(2\pi)^2 \mu_0 f N_1^2}{h} \left[\frac{R_{m1}b_1}{3} + \frac{R_{m2}b_2}{3} + R_{mg}\mathcal{G} + \frac{b_1^2}{12} - \frac{b_2^2}{12} \right] \quad (4.35)$$

The per-unit impedance of winding 1 is

$$Z_{b1} = \frac{V_{b1}^2}{(VI)_{b1}} = \frac{N_1^2 (V_{b1}/N_1)^2}{(VI)_{b1}} \quad (4.36)$$

where $(VI)_{b1}$ is the base volt-amperes per phase and V_{b1}/N_1 is the base volts/turn for winding 1. Letting x denote the per-unit reactance, where $x = X_{\ell 12}/Z_{b1}$, we get

$$x = \frac{(2\pi)^2 \mu_0 f (VI)_{b1}}{(V_{b1}/N_1)^2 h} \left[\frac{R_{m1}b_1}{3} + \frac{R_{m2}b_2}{3} + R_{mg}\mathcal{G} + \frac{b_1^2}{12} - \frac{b_2^2}{12} \right] \quad (4.37)$$

We leave the subscripts off x because the per-unit reactance does not depend on the order of the windings. This is because the base power rating $(VI)_b$ and the base volts per turn (V_b/N) are the same for both windings. In contrast, the leakage reactance is proportional to the square of the winding turns as seen in Equation 4.35.

To correct for flux fringing at the winding ends, a good approximation is to increase h by the amount

$$s = 0.32(R_0 - R_c) \quad (4.38)$$

where R_0 is the outer radius of the outermost coil and R_c is the core radius. Thus, we obtain

$$x = \frac{(2\pi)^2 \mu_0 f (VI)_b}{(V_b/N)^2 (h+s)} \left[\frac{R_{m1}b_1}{3} + \frac{R_{m2}b_2}{3} + R_{mg}\mathcal{G} + \frac{b_1^2}{12} - \frac{b_2^2}{12} \right] \quad (4.39)$$

for the per-unit two-winding reactance.

4.4 Ideal Two-, Three-, and Multiwinding Transformers

Since leakage reactances are part of a circuit that includes an ideal transformer, it is useful to discuss the ideal transformer first, particularly one which can have more than two associated windings. Here we will consider a single-phase ideal transformer with two or more windings per phase. The phase can be one phase of a three-phase transformer provided the phases can be treated independently. Although much of the discussion concerns two- or three-winding transformers, extending it to multiwinding ideal transformers is straightforward. We will also look at the ideal autotransformer, in which the voltages of two windings are combined to produce a high voltage at one terminal and a low voltage at the other terminal.

For a two-winding transformer, the ideal conditions are

$$\frac{E_1}{E_2} = \frac{N_1}{N_2}, \quad N_1 I_1 + N_2 I_2 = 0 \quad (4.40)$$

where the E s are the voltages across the two windings with turns N_1 and N_2 , and the I s are the rated currents through the windings. We use the convention that the currents are positive into the winding. From Equation 4.40, we can show that

$$E_1 I_1 + E_2 I_2 = 0 \quad (4.41)$$

Since EI is the power, this equation says that the net power into the ideal transformer is zero, that is, the power into winding 1 equals the power out of winding 2. Thus, an ideal transformer is lossless.

For a three-winding transformer, Equation 4.40 generalizes to

$$\frac{E_1}{N_1} = \frac{E_2}{N_2} = \frac{E_3}{N_3}, \quad N_1 I_1 + N_2 I_2 + N_3 I_3 = 0 \quad (4.42)$$

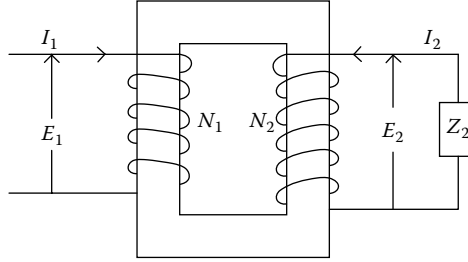
From Equation 4.42, it follows that

$$E_1 I_1 + E_2 I_2 + E_3 I_3 = 0 \quad (4.43)$$

That is, the net power into a three-winding ideal transformer is zero. These latter equations extend readily to multiwinding transformers.

Impedances transfer across an ideal transformer by the equation

$$Z_1 = \left(\frac{N_1}{N_2} \right)^2 Z_2 \quad (4.44)$$

**FIGURE 4.3**

Ideal two-winding transformer with a load on its secondary terminals.

An ideal two-winding transformer is depicted in Figure 4.3.

It is often convenient to work with per-unit quantities. That is, we choose base values for voltages, currents, and so forth and express the actual voltages, currents, and so forth as ratios with respect to these base values. Only two independent base values need to be chosen, and these are usually taken as power or VI and voltage V . The base power is normally taken as the VI rating of the unit per phase and therefore has a fixed value for a given transformer. The base voltage is taken as the open circuit rated phase voltage of each terminal. Thus, we have $(VI)_b = (VI)_{b1} = (VI)_{b2}$ and V_{b1}, V_{b2}, \dots where b denotes the base value. From these, we derive base currents of

$$I_{b1} = \frac{(VI)_b}{V_{b1}}, \dots \quad (4.45)$$

and base impedances of

$$Z_{b1} = \frac{V_{b1}^2}{(VI)_{b1}}, \dots \quad (4.46)$$

Letting small letters denote per-unit quantities, we have

$$v_1 = \frac{V_1}{V_{b1}}, \dots \quad i_1 = \frac{I_1}{I_{b1}}, \dots \quad z_1 = \frac{Z_1}{Z_{b1}}, \dots \quad (4.47)$$

The base voltages are the actual voltages under rated conditions for the ideal transformer and therefore satisfy the voltage equations in Equations 4.40 and 4.42, so that we have

$$\frac{V_{b1}}{V_{b2}} = \frac{N_1}{N_2}, \dots \quad \frac{I_{b1}}{I_{b2}} = \frac{V_{b2}}{V_{b1}} = \frac{N_2}{N_1}, \dots \quad \frac{Z_{b1}}{Z_{b2}} = \left(\frac{V_{b1}}{V_{b2}} \right)^2 = \left(\frac{N_1}{N_2} \right)^2, \dots \quad (4.48)$$

since everything is on a common VI base. Note that the base quantities are always positive. The signs in the per-unit quantities are determined by the signs of the underlying quantity. Since all the windings are put on the same power base, Equations 4.41 and 4.43 are not applicable to base quantities.

In terms of per-unit quantities, for an ideal transformer, we have

$$e_1 = \frac{E_1}{V_{b1}} = 1, \quad e_2 = \frac{E_2}{V_{b2}} = 1, \dots \quad (4.49)$$

and, from Equations 4.42 and 4.48

$$\begin{aligned} N_1 \frac{I_1}{I_{b1}} + N_2 \frac{I_2}{I_{b1}} + N_3 \frac{I_3}{I_{b1}} &= N_1 \frac{I_1}{I_{b1}} + N_2 \frac{I_2}{I_{b2}} \left(\frac{I_{b2}}{I_{b1}} \right) + N_3 \frac{I_3}{I_{b3}} \left(\frac{I_{b3}}{I_{b1}} \right) \\ &= N_1 (i_1 + i_2 + i_3) = 0 \end{aligned} \quad (4.50)$$

Therefore,

$$i_1 + i_2 + i_3 = 0 \quad (4.51)$$

Thus, an ideal three-circuit transformer can be represented by a one-circuit description as shown in Figure 4.4, if per-unit values are used. Equation 4.51 can also be extended to more than three windings.

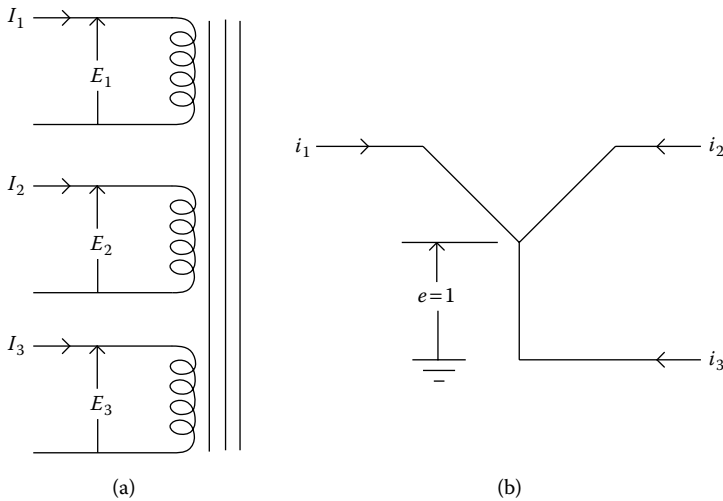


FIGURE 4.4

Ideal three-circuit transformer schematic: (a) standard quantities and (b) per-unit quantities.

4.4.1 Ideal Autotransformers

An ideal two-terminal autotransformer is shown in Figure 4.5. The two coils (labeled s for series and c for common) are connected together so that their voltages combine to produce the high terminal voltage E_1 . Thus, $E_1 = E_s + E_c$. The secondary or low terminal voltage is $E_2 = E_c$. Similarly, we can see from the figure that $I_1 = I_s$ and $I_2 = I_c - I_s = I_c - I_1$. Using the expressions for a two-winding unit, which are true regardless of the interconnections involved:

$$\frac{E_s}{N_s} = \frac{E_c}{N_c}, \quad I_s N_s + I_c N_c = 0 \quad (4.52)$$

we then find

$$E_1 = E_c \left(1 + \frac{N_s}{N_c} \right) = E_2 \left(\frac{N_c + N_s}{N_c} \right) \quad (4.53)$$

$$I_s N_s + I_c N_c = I_1 N_s + (I_1 + I_2) N_c = I_1 (N_c + N_s) + I_2 N_c = 0$$

Thus,

$$\frac{E_1}{E_2} = \left(\frac{N_c + N_s}{N_c} \right), \quad \frac{I_1}{I_2} = - \left(\frac{N_c}{N_c + N_s} \right) \quad (4.54)$$

so that the effective turns ratio as seen by the terminals is $n = (N_c + N_s)/N_c$. Any impedances on the low-voltage terminal could be transferred to the high-voltage circuit by the square of this turns ratio.

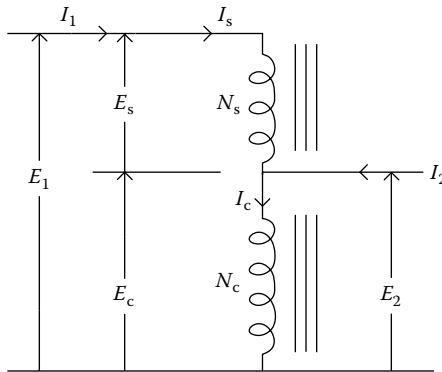


FIGURE 4.5
Ideal autotransformer.

The co-ratio is defined as

$$r = \frac{E_1 - E_2}{E_1} = 1 - \frac{E_2}{E_1} = 1 - \frac{1}{n} = \frac{n-1}{n} \quad (4.55)$$

where $r \leq 1$. The terminal power rating of an autotransformer is $E_1 I_1 (= E_2 I_2)$, but the power rating of each coil is $E_s I_s (= E_c I_c)$. The ratio of these power ratings is

$$\frac{E_s I_s}{E_1 I_1} = \frac{E_1 - E_2}{E_1} = r \quad (4.56)$$

Thus, since $r \leq 1$, the terminal rating is always greater than or equal to the single-coil rating. Since the single-coil rating is the same as the terminal rating of a conventional two-winding transformer, this shows an important advantage to using the autoconnection with $r < 1$.

4.5 Leakage Reactance for Two-Winding Transformers Based on Circuit Parameters

Although a two-winding circuit model was developed previously from magnetic flux considerations, here we will consider a model based on circuit parameters such as inductances and mutual inductances. This will allow us to extend the two-winding model to three- and eventually to multiwinding models. We will start with the terminal equations developed previously in Chapter 3:

$$V_1 = I_1 R_1 - \frac{d\lambda_1}{dt}, \quad V_2 = I_2 R_2 - \frac{d\lambda_2}{dt} \quad (4.57)$$

where λ_1 and λ_2 are the total flux linkages of coils 1 and 2 and R_1 and R_2 are the resistances of coils 1 and 2, respectively. If we let ϕ_c equal the common flux linking all turns of both coils, which is mainly the core flux, we can write

$$\lambda_1 = (\lambda_1 - N_1 \Phi_c) + N_1 \Phi_c, \quad \lambda_2 = (\lambda_2 - N_2 \Phi_c) + N_2 \Phi_c \quad (4.58)$$

The quantity $(\lambda_i - N_{i\phi c})$ is the leakage flux of coil i , which exists mainly in the oil or air and conductor material but not in the core to any great extent.

It exists in nonmagnetic (or linear) materials and therefore should depend linearly on the currents. Thus, we can write, very generally:

$$-\frac{d(\lambda_1 - N_1 \Phi_c)}{dt} = L_1 \frac{dI_1}{dt} + M_{12} \frac{dI_2}{dt} \quad (4.59)$$

or, assuming sinusoidal quantities:

$$-\frac{d(\lambda_1 - N_1 \Phi_c)}{dt} = jI_1 X_{11} + jI_2 X_{12} \quad (4.60)$$

where I_1 and I_2 are phasors, $X_{11} = 2\pi f L_1$ and $X_{12} = 2\pi f M_{12}$, where f is the frequency, and j is the imaginary unit. We do not distinguish phasors by bold-faced type here, since they all have the same phase. Using similar expressions for λ_2 , Equation 4.57 becomes

$$\begin{aligned} V_1 &= I_1 R_1 + jI_1 X_{11} + jI_2 X_{12} + E_1 \\ V_2 &= I_2 R_2 + jI_2 X_{22} + jI_1 X_{12} + E_2 \end{aligned} \quad (4.61)$$

where $E_1 = -N_1 d\Phi_c/dt$ is the no-load terminal voltage of terminal 1, and so forth for E_2 so that $E_1/E_2 = N_1/N_2$. We also use the fact that $X_{12} = X_{21}$ for linear systems.

We will ignore the exciting current of the core since it is normally much smaller than the load currents. Thus, using the amp-turn balance condition in Equation 4.40, we can rewrite Equation 4.61 as

$$\begin{aligned} V_1 &= I_1 \left[R_1 + j \left(X_{11} - \frac{N_1}{N_2} X_{12} \right) \right] + E_1 \\ V_2 &= I_2 \left[R_2 + j \left(X_{22} - \frac{N_2}{N_1} X_{12} \right) \right] + E_2 \end{aligned} \quad (4.62)$$

or, more succinctly,

$$\begin{aligned} V_1 &= I_1 Z_1 + E_1 \\ V_2 &= I_2 Z_2 + E_2 \end{aligned} \quad (4.63)$$

where Z_1 and Z_2 are single-winding leakage impedances. These last equations (4.63) correspond to those encountered in the last chapter. We have two impedances on either side of an ideal transformer. We can transform one of the impedances across the transformer by means of Equation 4.40. In particular, we let $V_2 = E'_2 = I_2 Z_2 + E_2$. Then, since $E_1/E_2 = N_1/N_2$ and $I_1/I_2 = -N_2/N_1$, $E'_2 = -(N_1/N_2)I_1 Z_2 + (N_2/N_1)E_1$ so that solving for E_1 :

$$E_1 = \frac{N_1}{N_2} E'_2 + \left(\frac{N_1}{N_2} \right)^2 I_1 Z_2 \quad (4.64)$$

Substituting the first equation in Equation 4.63, we get

$$V_1 = I_1 \left[Z_1 + \left(\frac{N_1}{N_2} \right)^2 Z_2 \right] + \frac{N_1}{N_2} E'_2, \quad V_2 = E'_2 \quad (4.65)$$

The impedances in Equation 4.63 have been transformed into a single impedance, called the two-winding leakage impedance Z_{12} . This depends on which of the single-winding impedances are transferred across the ideal transformer so that $Z_{12} \neq Z_{21}$. Simplifying the notation in Equation 4.65, we have

$$V_1 = I_1 Z_{12} + E'_1, \quad V_2 = E'_2 \quad (4.66)$$

We can convert this equation to a per-unit basis by the following process:

$$\begin{aligned} \frac{V_1}{V_{b1}} &= \frac{I_1 Z_{12}}{V_{b1}} + \frac{E'_1}{V_{b1}} = \frac{I_1}{V_{b1}} \left[\frac{V_{b1}^2}{(VI)_{b1}} \right] \left[\frac{(VI)_{b1}}{V_{b1}^2} \right] Z_{12} + \frac{E'_1}{V_{b1}} = \frac{I_1}{I_{b1}} \frac{Z_{12}}{Z_{b1}} + \frac{E'_1}{V_{b1}} \\ \frac{V_2}{V_{b1}} &= \frac{E'_2}{V_{b1}} \end{aligned} \quad (4.67)$$

or

$$v_1 = i_1 z_{12} + 1, \quad v_2 = 1$$

The equivalent circuit for Equation 4.66 is shown in Figure 4.6 along with the per-unit version.

$E'_1/E'_2 = N_1/N_2$, but $E'_1 \neq E_1$ and $E'_2 \neq E_2$ except at no load.

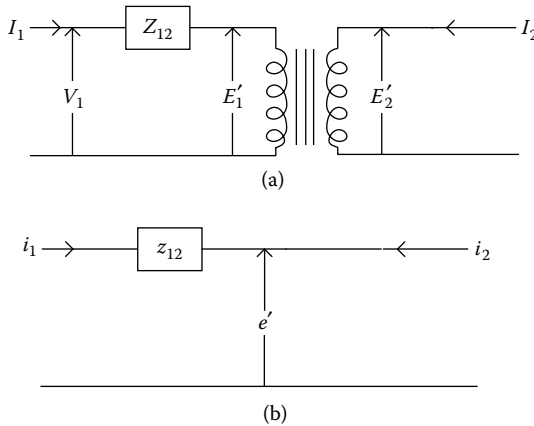


FIGURE 4.6

Circuit models of a two-winding transformer with leakage impedance: (a) circuit with a single effective 2-winding leakage impedance and (b) single circuit using per-unit quantities.

Thus, a two-winding transformer is characterized by a single value of leakage impedance Z_{12} , which has both resistive and reactive components:

$$Z_{12} = R_{12} + X_{\ell 12}$$

where

$$R_{12} = R_1 + \left(\frac{N_1}{N_2} \right)^2 R_2 \quad (4.68)$$

and

$$X_{\ell 12} = X_1 + \left(\frac{N_1}{N_2} \right)^2 X_2$$

which are referred to as the primary winding. We can obtain expressions for referring quantities to the secondary winding by interchanging 1 and 2 in Equation 4.68. In large power transformers, $X_{12} \gg R_{12}$, so we are usually concerned with obtaining leakage reactances.

In terms of the previously defined quantities from Equations 4.62 and 4.63

$$X_{\ell 12} = X_{11} + \left(\frac{N_1}{N_2} \right)^2 X_{22} - 2 \left(\frac{N_1}{N_2} \right) X_{12} \quad (4.69)$$

The leakage reactance of Equation 4.69 corresponds to the leakage inductance of Equation 4.23 by multiplying by ω . We usually will use the symbol Z_{12} when referring to leakage reactance and ignore the resistive component. The leakage reactance is often calculated by finite element energy methods, using Equation 4.23 and multiplying by ω .

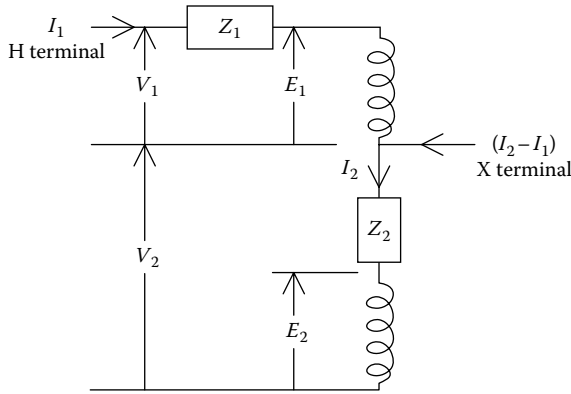
Another method of obtaining the two-winding leakage impedance, which corresponds with how it is measured, is to short circuit terminal 2 and perform an impedance measurement at terminal 1. Thus,

$$Z_{12} = \left. \frac{V_1}{I_1} \right|_{V_2=0} \quad (4.70)$$

Setting $V_2 = 0$ in Equation 4.63, we get $E_2 = -I_2 Z_2$. Substituting into the V_1 equation in Equation 4.63 and using Equation 4.40, we find

$$V_1 = I_1 \left[Z_1 + \left(\frac{N_1}{N_2} \right)^2 Z_2 \right] \quad (4.71)$$

so that, from Equation 4.70, we get $Z_{12} = Z_1 + (N_1/N_2)^2 Z_2$ as before.

**FIGURE 4.7**

Circuit model of a two-winding auto transformer with leakage impedance, based on a separate windings circuit model.

4.5.1 Leakage Reactance for a Two-Winding Autotransformer

The circuit model for a two-winding autotransformer can be constructed from separate windings as shown in Figure 4.7. From the method of obtaining leakage impedance given in Equation 4.70, we can measure the impedance at the H terminal with the X terminal shorted. However, this will yield the same leakage impedance as that of an ordinary two-winding transformer, so that $Z_{HX} = Z_{12}$ —that is, the terminal leakage impedance of a two-winding autotransformer is the same as that of a transformer with the same windings but not autoconnected.

On a per-unit basis, however, the terminal leakage impedance of an autotransformer differs from that of a regular two-winding transformer. We can see from Equation 4.46 that the base impedance is equal to the voltage squared divided by the rated power. Keeping the power base the same (since this is usually determined by the external circuit) the base impedance is proportional to the terminal voltage squared. The terminal voltage for an autotransformer is the terminal voltage of a nonautoconnected high-voltage winding divided by the co-ratio, r . Thus, the base impedance of an autotransformer is $1/r^2$ times that of a regular transformer. Since the per-unit impedance is the impedance in Ohms divided by the base impedance, this equals r^2 times the per-impedance of a regular two-winding transformer on the same power base.

4.6 Leakage Reactances for Three-Winding Transformers

We can make the same arguments for a three-winding transformer, isolating the flux common to all coils, ϕ_c , and expressing the leakage flux for each coil, which exists in nonmagnetic materials, in terms of self- and mutual inductances, which are constants. We obtain

$$\begin{aligned}
V_1 &= I_1 R_1 + j(I_1 X_{11} + I_2 X_{12} + I_3 X_{13}) + E_1 \\
V_2 &= I_2 R_2 + j(I_2 X_{22} + I_3 X_{23} + I_1 X_{12}) + E_2 \\
V_3 &= I_3 R_3 + j(I_3 X_{33} + I_1 X_{13} + I_2 X_{23}) + E_3
\end{aligned} \tag{4.72}$$

where the order of the suffixes does not matter for linear materials (constant permeability) because $X_{ij} = X_{ji}$.

Using the same assumptions as before concerning the neglect of core excitation (Equation 4.42) we substitute $I_3 = -(N_1/N_3)I_1 - (N_2/N_3)I_2$ in the first two equations and $I_2 = -(N_1/N_2)I_1 - (N_3/N_2)I_3$ in the third equation of Equation 4.72 to obtain

$$\begin{aligned}
V_1 &= I_1 \left[R_1 + j \left(X_{11} - \frac{N_1}{N_3} X_{13} \right) \right] + jI_2 \left(X_{12} - \frac{N_2}{N_3} X_{13} \right) + E_1 \\
V_2 &= I_2 \left[R_2 + j \left(X_{22} - \frac{N_2}{N_3} X_{23} \right) \right] + jI_1 \left(X_{12} - \frac{N_1}{N_3} X_{23} \right) + E_2 \\
V_3 &= I_3 \left[R_3 + j \left(X_{33} - \frac{N_3}{N_2} X_{23} \right) \right] + jI_1 \left(X_{13} - \frac{N_1}{N_2} X_{23} \right) + E_3
\end{aligned} \tag{4.73}$$

Now add and subtract $jI_1 \frac{N_1}{N_2} \left(X_{12} - \frac{N_1}{N_3} X_{23} \right)$ from the first equation, add and subtract $jI_2 \frac{N_2}{N_1} \left(X_{12} - \frac{N_2}{N_3} X_{13} \right)$ from the second, and add and subtract $jI_3 \frac{N_3}{N_1} \left(X_{13} - \frac{N_3}{N_2} X_{12} \right)$ from the third equation of Equation 4.73 to obtain

$$\begin{aligned}
V_1 &= I_1 \left[R_1 + j \left(X_{11} - \frac{N_1}{N_3} X_{13} - \frac{N_1}{N_2} X_{12} + \frac{N_1^2}{N_2 N_3} X_{23} \right) \right] + \left\{ jI_1 \frac{N_1}{N_2} \left(X_{12} - \frac{N_1}{N_3} X_{23} \right) \right. \\
&\quad \left. + jI_2 \left(X_{12} - \frac{N_2}{N_3} X_{13} \right) + E_1 \right\} \\
V_2 &= I_2 \left[R_2 + j \left(X_{22} - \frac{N_2}{N_3} X_{23} - \frac{N_2}{N_1} X_{12} + \frac{N_2^2}{N_1 N_3} X_{13} \right) \right] + \left\{ jI_1 \left(X_{12} - \frac{N_1}{N_3} X_{23} \right) \right. \\
&\quad \left. + jI_2 \frac{N_2}{N_1} \left(X_{12} - \frac{N_2}{N_3} X_{13} \right) + E_2 \right\} \\
V_3 &= I_3 \left[R_3 + j \left(X_{33} - \frac{N_3}{N_2} X_{23} - \frac{N_3}{N_1} X_{13} + \frac{N_3^2}{N_1 N_2} X_{12} \right) \right] + \left\{ jI_1 \left(X_{13} - \frac{N_1}{N_2} X_{23} \right) \right. \\
&\quad \left. + jI_3 \frac{N_3}{N_1} \left(X_{13} - \frac{N_3}{N_2} X_{12} \right) + E_3 \right\}
\end{aligned} \tag{4.74}$$

Substituting for $I_3 = -(N_1/N_3)I_1 - (N_2/N_3)I_2$ in the term in braces in the last equation, we get

$$V_3 = I_3 \left[R_3 + j \left(X_{33} - \frac{N_3}{N_2} X_{23} - \frac{N_3}{N_1} X_{13} + \frac{N_3^2}{N_1 N_2} X_{12} \right) \right] + \left\{ j I_1 \left(\frac{N_3}{N_2} X_{12} - \frac{N_1}{N_2} X_{23} \right) + j I_2 \left(\frac{N_3}{N_1} X_{12} - \frac{N_2}{N_1} X_{13} \right) + E_3 \right\} \quad (4.75)$$

Comparing the terms in braces of the resulting V_1 , V_2 , and V_3 equations, we find, using Equation 4.42,

$$\frac{\{ \} _1}{N_1} = \frac{\{ \} _2}{N_2} = \frac{\{ \} _3}{N_3} \quad (4.76)$$

Therefore, labeling the terms in brackets E'_1 , E'_2 , and E'_3 , we obtain

$$V_1 = I_1 Z_1 + E'_1, \quad V_2 = I_2 Z_2 + E'_2, \quad V_3 = I_3 Z_3 + E'_3 \quad (4.77)$$

where

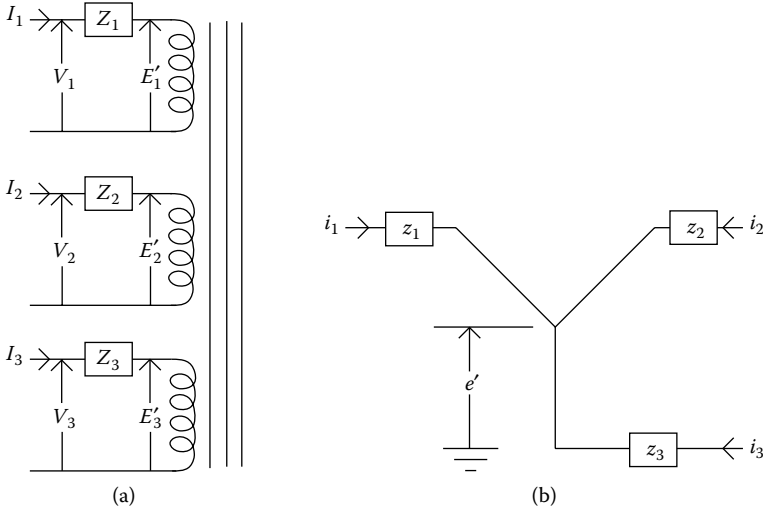
$$\begin{aligned} Z_1 &= R_1 + j \left(X_{11} - \frac{N_1}{N_3} X_{13} - \frac{N_1}{N_2} X_{12} + \frac{N_1^2}{N_2 N_3} X_{23} \right) \\ Z_2 &= R_1 + j \left(X_{22} - \frac{N_2}{N_3} X_{23} - \frac{N_2}{N_1} X_{12} + \frac{N_2^2}{N_1 N_3} X_{13} \right) \\ Z_3 &= R_3 + j \left(X_{33} - \frac{N_3}{N_2} X_{23} - \frac{N_3}{N_1} X_{13} + \frac{N_3^2}{N_1 N_2} X_{12} \right) \end{aligned} \quad (4.78)$$

and

$$\frac{E'_1}{N_1} = \frac{E'_2}{N_2} = \frac{E'_3}{N_3} \quad (4.79)$$

Here, Z_1 , Z_2 , and Z_3 are the single-winding leakage impedances. The applicable multicircuit model is shown in [Figure 4.8a](#) and the per-unit circuit is shown in [Figure 4.8b](#). This is possible because Equation 4.79 implies that $e'_1 = e'_2 = e'_3 = e'$ by the relation among the currents given in Equation 4.51. This figure should be compared with [Figure 4.4](#).

Since the single-winding leakage impedances are not directly measured or easily calculated, it is desirable to express these in terms of two-winding leakage impedances. We will refer to these two-winding leakage impedances as Z_{12} , Z_{13} , and Z_{23} , which correspond to the notation Z_{12} used previously for the two-winding case. Thus, to measure the two-winding leakage


FIGURE 4.8

Circuit models of a three-winding transformer with leakage impedance: (a) separate circuit description and (b) single circuit description in terms of per-unit values.

impedance between windings 1 and 2, we short circuit 2, open circuit 3, and measure the impedance at terminal 1:

$$Z_{12} = \frac{V_1}{I_1} \bigg|_{\substack{V_2=0 \\ I_3=0}} \quad (4.80)$$

From Equation 4.77, we see that this implies $I_2 Z_2 + E'_2 = 0$. Using the voltage and current equations in Equation 4.42, we find for Z_{12} and similarly for Z_{13} and Z_{23}

$$\begin{aligned} Z_{12} &= Z_1 + \left(\frac{N_1}{N_2} \right)^2 Z_2 \\ Z_{13} &= Z_1 + \left(\frac{N_1}{N_3} \right)^2 Z_3 \\ Z_{23} &= Z_2 + \left(\frac{N_2}{N_3} \right)^2 Z_3 \end{aligned} \quad (4.81)$$

By substituting corresponding subscripts, the resistive and reactive components of Equation 4.81 are the same as the corresponding components of the two-winding resistance and leakage reactance formulas in Equations 4.68

and 4.69. The subscript ordering is chosen so that the second subscript refers to the shorted winding. The expression changes if we reverse subscripts according to

$$Z_{21} = \left(\frac{N_2}{N_1} \right)^2 Z_{12} \quad (4.82)$$

Solving Equation 4.81 for the Z_i 's, we get

$$\begin{aligned} Z_1 &= \frac{1}{2} \left[Z_{12} + Z_{13} - \left(\frac{N_1}{N_2} \right)^2 Z_{23} \right] \\ Z_2 &= \frac{1}{2} \left(\frac{N_2}{N_1} \right)^2 \left[Z_{12} + \left(\frac{N_1}{N_2} \right)^2 Z_{23} - Z_{13} \right] \\ Z_3 &= \frac{1}{2} \left(\frac{N_3}{N_1} \right)^2 \left[Z_{13} + \left(\frac{N_1}{N_2} \right)^2 Z_{23} - Z_{12} \right] \end{aligned} \quad (4.83)$$

These equations are very useful for determining the single-winding leakage impedances from the two-winding leakage impedances for a three-winding transformer, since the two-winding impedances are fairly easily obtainable. This is not possible for a two-winding transformer because there are two single-winding leakage impedances but only one two-winding leakage impedance.

Using Equation 4.48 and the per-unit values, where Z_{b1} is the base impedance of circuit 1 so that $z_{12} = Z_{12}/Z_{b1}$ and so forth and $z_1 = Z_1/Z_{b1}$ and so forth, we find that Equation 4.83 can be expressed as

$$\begin{aligned} z_1 &= (z_{12} + z_{13} - z_{23})/2 \\ z_2 &= (z_{12} + z_{23} - z_{13})/2 \\ z_3 &= (z_{13} + z_{23} - z_{12})/2 \end{aligned} \quad (4.84)$$

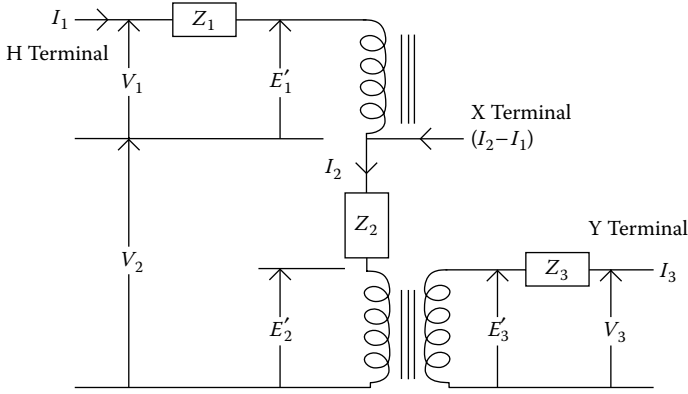
Similarly Equation 4.81 becomes, in per-unit terms,

$$z_{12} = z_1 + z_2, \quad z_{13} = z_1 + z_3, \quad z_{23} = z_2 + z_3 \quad (4.85)$$

In the case of per-unit two-winding leakage impedances, the order of the subscripts does not matter. Again, small letters are used for per-unit values.

4.6.1 Leakage Reactance for an Autotransformer with a Tertiary Winding

The autotransformer with a tertiary winding circuit model can be obtained by interconnecting elements of the three-winding transformer circuit model

**FIGURE 4.9**

Three-winding autotransformer circuit model, derived from the three separate winding circuit model.

as shown in Figure 4.9. Here, the notation corresponds to that of Figure 4.8a. The problem is to reexpress this in terms of terminal quantities. Thus, the appropriate terminal H voltage is $V_1 + V_2$, and the appropriate terminal X current is $I_2 - I_1$. Using Equation 4.77:

$$V_H = V_1 + V_2 = I_1 Z_1 + I_2 Z_2 + E'_1 + E'_2 \quad (4.86)$$

Substituting for I_2 from the amp-turn balance equation in Equation 4.42, we obtain

$$V_H = I_1 \left(Z_1 - \frac{N_1}{N_2} Z_2 \right) + \left[-\frac{N_3}{N_2} I_3 Z_2 + E'_1 + E'_2 \right] \quad (4.87)$$

Similarly, using the amp-turn balance equation in Equation 4.42, we can express $I_2 - I_1$ as $I_2 - I_1 = I_2 \left(1 + \frac{N_2}{N_1} \right) + \frac{N_3}{N_1} I_3$. Solving this for I_2 on the right-hand side and substituting V_2 in Equation 4.77, we obtain

$$V_X = V_2 = (I_2 - I_1) \frac{N_1 Z_2}{(N_1 + N_2)} + \left[-\frac{N_3}{N_1 + N_2} I_3 Z_2 + E'_2 \right] \quad (4.88)$$

By adding and subtracting $\frac{N_3^2 I_3 Z_2}{N_2(N_1 + N_2)}$ from the V_3 in Equation 4.77, we get

$$V_Y = V_3 = I_3 \left(Z_3 + \frac{N_3^2 Z_2}{N_2(N_1 + N_2)} \right) + \left[-\frac{N_3^2}{N_2(N_1 + N_2)} I_3 Z_2 + E'_3 \right] \quad (4.89)$$

We see that the terms in brackets in Equations 4.87 through 4.89 satisfy

$$\frac{[]_H}{N_1 + N_2} = \frac{[]_X}{N_2} = \frac{[]_Y}{N_3} \quad (4.90)$$

Labeling these terms in brackets E_H , E_X , and E_Y , we can rewrite Equations 4.87 through 4.89 as

$$V_H = I_H Z_H + E_H, \quad V_X = I_X Z_X + E_X, \quad V_Y = I_Y Z_Y + E_Y \quad (4.91)$$

where $V_H = V_1 + V_2$, $V_X = V_2$, $V_Y = V_3$, $I_H = I_1$, $I_X = I_2 - I_1$, $I_Y = I_3$ are terminal quantities and

$$\begin{aligned} Z_H &= Z_1 - \frac{N_1}{N_2} Z_2 \\ Z_X &= \frac{N_1}{(N_1 + N_2)} Z_2 \\ Z_Y &= Z_3 + \frac{N_3^2}{N_2(N_1 + N_2)} Z_2 \end{aligned} \quad (4.92)$$

Thus, the circuit model shown in Figure 4.10a is similar to that of Figure 4.8a with H, X, and Y substituted for 1, 2, and 3.

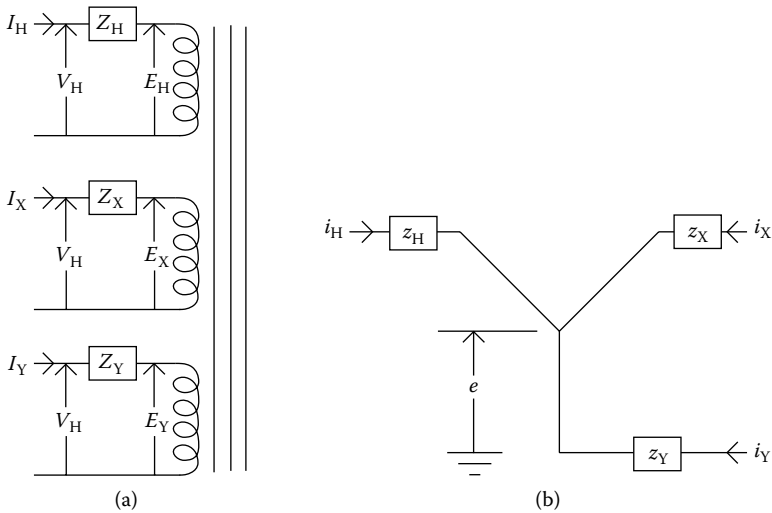


FIGURE 4.10

Circuit models of a three-winding autotransformer based on terminal parameters: (a) separate circuit description and (b) single circuit description in terms of per-unit values.

In terms of the measured two terminal impedances, we have as before

$$Z_{HX} = \left. \frac{V_H}{I_H} \right|_{V_X=0, I_Y=0} \quad (4.93)$$

Rewriting the amp-turn balance equation in Equation 4.42, we obtain

$$N_1 I_1 + N_2 (I_2 - I_1) + N_2 I_1 + N_3 I_3 = (N_1 + N_2) I_H + N_2 I_X + N_3 I_Y \quad (4.94)$$

From Equation 4.93, together with Equations 4.90, 4.91, and 4.94, we obtain

$$\begin{aligned} Z_{HX} &= Z_H + \left(\frac{N_1 + N_2}{N_2} \right)^2 Z_X \\ Z_{HY} &= Z_H + \left(\frac{N_1 + N_2}{N_3} \right)^2 Z_Y \\ Z_{XY} &= Z_X + \left(\frac{N_2}{N_3} \right)^2 Z_Y \end{aligned} \quad (4.95)$$

At this point, it is worthwhile to revert to per-unit terminal quantities. Because we have an autoconnection, by again choosing as base quantities the VI per-phase rating of the unit and the rated (no-load) terminal voltages per phase, $(VI)_b$, V_{bH} , V_{bX} , and V_{bY} , we get

$$\begin{aligned} \frac{V_{bH}}{V_{bX}} &= \frac{N_1 + N_2}{N_2}, & \frac{V_{bH}}{V_{bY}} &= \frac{N_1 + N_2}{N_3}, & \frac{V_{bX}}{V_{bY}} &= \frac{N_2}{N_3} \\ \frac{I_{bH}}{I_{bX}} &= \frac{N_2}{N_1 + N_2}, & \frac{I_{bH}}{I_{bY}} &= \frac{N_3}{N_1 + N_2}, & \frac{I_{bX}}{I_{bY}} &= \frac{N_3}{N_2} \\ \frac{Z_{bH}}{Z_{bX}} &= \left(\frac{N_1 + N_2}{N_2} \right)^2, & \frac{Z_{bH}}{Z_{bY}} &= \left(\frac{N_1 + N_2}{N_3} \right)^2, & \frac{Z_{bX}}{Z_{bY}} &= \left(\frac{N_2}{N_3} \right)^2 \end{aligned} \quad (4.96)$$

since $(VI)_b$ is the same for each terminal. From Equation 4.94, we have on a per-unit basis

$$i_H + i_X + i_Y = 0 \quad (4.97)$$

Similarly from Equation 4.90, we have on a per-unit basis

$$e_H = e_X = e_Y = e \quad (4.98)$$

On a per-unit basis, Equation 4.95 becomes, using Equation 4.96

$$z_{HX} = z_H + z_X, \quad z_{HY} = z_H + z_Y, \quad z_{XY} = z_X + z_Y \quad (4.99)$$

where the same VI base is used for all the terminals and small letters denote per-unit values. Note that the order of the subscripts for the two-winding per-unit terminal impedances does not matter. Solving these for z_H , z_X , and z_Y , we obtain a set of equations similar to Equation 4.84:

$$\begin{aligned} z_H &= (z_{HX} + z_{HY} - z_{XY})/2 \\ z_X &= (z_{HX} + z_{XY} - z_{HY})/2 \\ z_Y &= (z_{HY} + z_{XY} - z_{HX})/2 \end{aligned} \quad (4.100)$$

The per-unit circuit model is depicted in [Figure 4.10b](#).

Equation 4.92 contains terminal impedances and single-coil impedances, for which the bases are different. It is sometimes convenient to express the per-unit terminal impedances in terms of the per-unit winding impedances. We can rewrite Equation 4.92:

$$\begin{aligned} \frac{Z_H}{Z_{bH}} &= \frac{Z_1}{Z_{b1}} \left(\frac{Z_{b1}}{Z_{bH}} \right) - \frac{N_1}{N_2} \frac{Z_2}{Z_{b2}} \left(\frac{Z_{b2}}{Z_{bH}} \right) \\ \frac{Z_X}{Z_{bX}} &= \left(\frac{N_1}{N_1 + N_2} \right) \frac{Z_2}{Z_{b2}} \left(\frac{Z_{b2}}{Z_{bX}} \right) \\ \frac{Z_Y}{Z_{bY}} &= \frac{Z_3}{Z_{b3}} \left(\frac{Z_{b3}}{Z_{bY}} \right) + \frac{N_3^2}{N_2(N_1 + N_2)} \frac{Z_2}{Z_{b2}} \left(\frac{Z_{b2}}{Z_{bY}} \right) \end{aligned} \quad (4.101)$$

Keeping $(VI)_b$ the same for both per-unit values, we have

$$\begin{aligned} \frac{Z_{b1}}{Z_{bH}} &= \left(\frac{N_1}{N_1 + N_2} \right)^2, \quad \frac{Z_{b2}}{Z_{bH}} = \left(\frac{N_2}{N_1 + N_2} \right)^2 \\ \frac{Z_{b2}}{Z_{bX}} &= 1, \quad \frac{Z_{b3}}{Z_{bY}} = 1, \quad \frac{Z_{b2}}{Z_{bY}} = \left(\frac{N_2}{N_3} \right)^2 \end{aligned} \quad (4.102)$$

Substituting Equation 4.102 into Equation 4.101, we get

$$\begin{aligned} z_H &= \left(\frac{N_1}{N_1 + N_2} \right)^2 z_1 - \frac{N_1}{N_2} \left(\frac{N_2}{N_1 + N_2} \right)^2 z_2 \\ z_X &= \frac{N_1}{(N_1 + N_2)} z_2 \\ z_Y &= z_3 + \left(\frac{N_2}{N_1 + N_2} \right) z_2 \end{aligned} \quad (4.103)$$

This equation expresses the per-unit terminal impedances in terms of the per-unit single-winding impedances for a three-winding autotransformer. In terms of the terminal turns ratio defined previously, $n = (N_1 + N_2)/N_2$, this last equation can be written as

$$\begin{aligned} z_H &= \left(\frac{n-1}{n} \right)^2 z_1 - \frac{(n-1)}{n^2} z_2 \\ z_X &= \left(\frac{n-1}{n} \right) z_2 \\ z_Y &= z_3 + \frac{z_2}{n} \end{aligned} \quad (4.104)$$

The per-unit circuit model is depicted in [Figure 4.10b](#). Using Equation 4.83 or 4.84, the autotransformer circuit parameters can be derived from two-winding leakage impedance values, which can be obtained from finite element methods or analytic formulas.

Using Equation 4.99 and the expressions for z_1 , z_2 , and z_3 in terms of per-unit two-winding leakage reactances, we can obtain the terminal-to-terminal per-unit leakage reactances for the autotransformer in terms of the two-winding per-unit leakage reactances. We find that

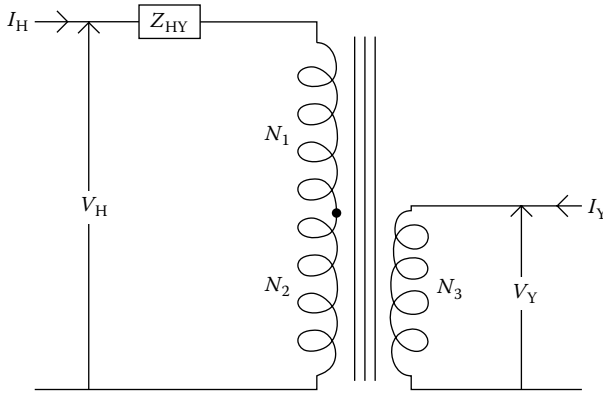
$$\begin{aligned} z_{HX} &= \left(\frac{n-1}{n} \right)^2 z_{12} \\ z_{HY} &= \frac{(1-n)}{n^2} z_{12} + \left(\frac{n-1}{n} \right) z_{13} + \frac{z_{23}}{n} \\ z_{XY} &= z_{23} \end{aligned} \quad (4.105)$$

The first equation in Equation 4.105 is the same as that found for the per-unit terminal impedance of a two-terminal autotransformer in [Section 4.5.1](#), since $(n-1)/n$ is the co-ratio. The last equation in Equation 4.105 expresses the fact that the terminal impedance between the X and Y windings is independent of the autoconnection.

4.6.2 Leakage Reactance between Two Windings Connected in Series and a Third Winding

It is useful to calculate the impedance between a pair of windings connected in series and a third winding in terms of two-winding leakage impedances, as shown in [Figure 4.11](#). This can be regarded as a special case of an autotransformer with the X-terminal open, but this leakage impedance is just Z_{HY} . From Equations 4.95 and 4.92, we obtain

$$Z_{HY} = Z_1 + Z_2 + \left(\frac{N_1 + N_2}{N_3} \right)^2 Z_3 \quad (4.106)$$

**FIGURE 4.11**

Leakage impedance between two series-connected windings and a third.

or, in per-unit terms, using Equation 4.102 together with $Z_{b3}/Z_{bH} = [N_3/(N_1 + N_2)]^2$

$$z_{HY} = \left(\frac{N_1}{N_1 + N_2} \right)^2 z_1 + \left(\frac{N_2}{N_1 + N_2} \right)^2 z_2 + z_3 \quad (4.107)$$

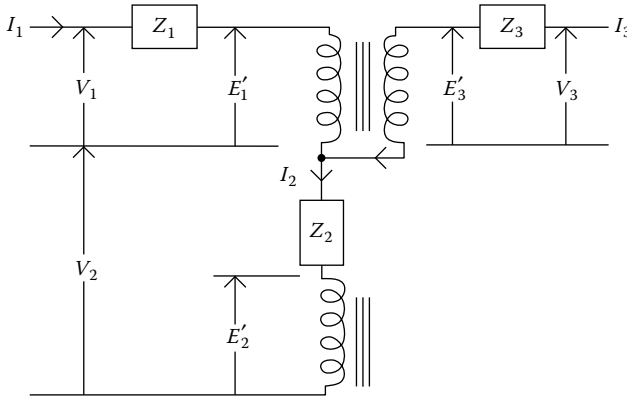
These can be expressed in terms of two-winding leakage impedances using Equation 4.83 or 4.84.

4.6.3 Leakage Reactance of a Two-Winding Autotransformer with X-Line Taps

X-line taps are taps connected to the X terminal of an autotransformer. They are used to regulate the low voltage without affecting the volts per turn of the autotransformer. Taps connected to the neutral or ground end of the LV winding affect the number of turns in both the high- and low-voltage windings. Since the high-voltage input level is assumed to be fixed by the external circuit, the volts per turn will change with the neutral tap setting, and this changes the induction level of the autotransformer. According to Faraday's law, assuming sinusoidal voltage and flux density at frequency f :

$$V_{\text{rms}} = \sqrt{2}\pi f N B_p A_c \Rightarrow \frac{V_{\text{rms}}}{N} = \sqrt{2}\pi f B_p A_c \quad (4.108)$$

where V_{rms} is the rms voltage, N is the number of turns, B_p is the peak flux density, and A_c is the core area. Since f and A_c are fixed, the flux density is determined by the volts per turn. If neutral taps are used, this characteristic must be considered in their design.

**FIGURE 4.12**

Circuit model of a two-winding autotransformer with X-line taps, derived from the three separate winding circuits.

A circuit model of a two-winding autotransformer with X-line taps constructed from the three separate winding circuit model is shown in Figure 4.12. The derivation of its two-terminal leakage impedance uses Equation 4.77 together with Equation 4.42. In terms of terminal parameters, we have $V_H = V_1 + V_2$, $V_X = V_2 + V_3$, $I_H = I_1$, $I_X = I_3$. We also require that $I_2 = I_1 + I_3$.

Thus

$$\begin{aligned}
 V_H &= V_1 + V_2 = I_1 Z_1 + (I_1 + I_3) Z_2 + E'_1 + E'_2 \\
 &= I_1 (Z_1 + Z_2) + I_3 Z_2 + E'_1 + E'_2 \\
 V_X &= V_2 + V_3 = (I_1 + I_3) Z_2 + I_3 Z_3 + E'_2 + E'_3 \\
 &= I_3 (Z_2 + Z_3) + I_1 Z_2 + E'_2 + E'_3
 \end{aligned} \tag{4.109}$$

Substitute $I_3 = -(N_1/N_3)I_1 - (N_2/N_3)I_2$ into the V_H equation and $I_1 = -(N_2/N_1)I_2 - (N_3/N_1)I_3$ into the V_X equation to obtain

$$\begin{aligned}
 V_H &= I_1 \left[Z_1 + \left(\frac{N_3 - N_1}{N_3} \right) Z_2 \right] - \frac{N_2}{N_3} I_2 Z_2 + E'_1 + E'_2 \\
 V_X &= I_3 \left[Z_3 + \left(\frac{N_1 - N_3}{N_1} \right) Z_2 \right] - \frac{N_2}{N_1} I_2 Z_2 + E'_2 + E'_3
 \end{aligned} \tag{4.110}$$

Add and subtract $\left(\frac{N_2}{N_2 + N_3} \right) I_1 Z_2$ from the V_H equation and add and subtract $\left(\frac{N_2}{N_1 + N_2} \right) I_3 Z_2$ from the V_X equation to obtain, after some algebraic manipulations,

$$\begin{aligned}
V_H &= I_1 \left[Z_1 + \left(\frac{N_3 - N_1}{N_2 + N_3} \right) Z_2 \right] + \left\{ \frac{N_2}{N_3} Z_2 \left[\left(\frac{N_3 - N_1}{N_2 + N_3} \right) I_1 - I_2 \right] + E'_1 + E'_2 \right\} \\
V_X &= I_3 \left[Z_3 + \left(\frac{N_1 - N_3}{N_1 + N_2} \right) Z_2 \right] + \left\{ \frac{N_2}{N_3} Z_2 \left[\left(\frac{N_3 - N_1}{N_1 + N_2} \right) I_1 - \left(\frac{N_2 + N_3}{N_1 + N_2} \right) I_2 \right] + E'_2 + E'_3 \right\}
\end{aligned} \tag{4.111}$$

Note that the terms in brackets satisfy the equation

$$\frac{\left\{ \right\}_H}{N_1 + N_2} = \frac{\left\{ \right\}_X}{N_2 + N_3} \tag{4.112}$$

so that Equation 4.111 can be rewritten as

$$V_H = I_H Z_H + E_H, \quad V_X = I_X Z_X + E_X \tag{4.113}$$

where

$$Z_H = Z_1 + \left(\frac{N_3 - N_1}{N_2 + N_3} \right) Z_2, \quad Z_X = Z_3 + \left(\frac{N_1 - N_3}{N_1 + N_2} \right) Z_2 \tag{4.114}$$

and

$$\frac{E_H}{N_1 + N_2} = \frac{E_X}{N_2 + N_3} \tag{4.115}$$

To obtain the two-terminal leakage impedance, we use the definition

$$Z_{HX} = \left. \frac{V_H}{I_H} \right|_{V_X=0} \tag{4.116}$$

From the amp-turn balance equation in Equation 4.42, we get

$$\begin{aligned}
N_1 I_1 + N_2 (I_1 + I_3) + N_3 I_3 &= (N_1 + N_2) I_1 + (N_2 + N_3) I_3 \\
&= (N_1 + N_2) I_H + (N_2 + N_3) I_X \\
&= 0
\end{aligned} \tag{4.117}$$

Thus, from Equations 4.113, 4.115, and 4.117, we can solve Equation 4.116 to get

$$Z_{HX} = Z_H + \left(\frac{N_1 + N_2}{N_2 + N_3} \right)^2 Z_X \tag{4.118}$$

Substituting from Equation 4.114, this becomes

$$Z_{HX} = Z_1 + \left(\frac{N_1 - N_3}{N_2 + N_3} \right)^2 Z_2 + \left(\frac{N_1 + N_2}{N_2 + N_3} \right)^2 Z_3 \quad (4.119)$$

On a per-unit basis, using a fixed $(VI)_b$ and, noting that

$$\frac{Z_{b1}}{Z_{bH}} = \left(\frac{N_1}{N_1 + N_2} \right)^2, \quad \frac{Z_{b2}}{Z_{bH}} = \left(\frac{N_2}{N_1 + N_2} \right)^2, \quad \frac{Z_{b3}}{Z_{bH}} = \left(\frac{N_3}{N_1 + N_2} \right)^2$$

we find that

$$z_{HX} = \left(\frac{N_1}{N_1 + N_2} \right)^2 z_1 + \left(\frac{N_2}{N_1 + N_2} \right)^2 \left(\frac{N_1 - N_3}{N_2 + N_3} \right)^2 z_2 + \left(\frac{N_3}{N_2 + N_3} \right)^2 z_3 \quad (4.120)$$

This is the two-terminal leakage impedance of a two-winding autotransformer with X-line taps. It can be expressed in terms of the two-winding leakage impedances using Equation 4.83 or 4.84.

4.6.4 More General Leakage Reactance Calculations

The cases considered so far cover most of the configurations encountered in practice. However, we can cover other situations by using these results as building blocks. For example, to obtain the leakage impedance between three windings connected in series and a fourth winding, we can apply Equation 4.106 or 4.107 to obtain the leakage impedances between the first two windings connected in series and the third winding. We can apply the same formula to obtain the leakage impedance between the fourth winding and the first two windings connected in series. Then we can calculate the leakage impedance between the third and fourth windings. The four windings are then reduced to a three-winding system, considering the two series-connected windings to be a single winding. Then, we can reapply Equation 4.106 or 4.107 to this three-winding system by considering the third winding connected to the two series-connected windings.

Another example is an autotransformer with tertiary and X-line taps. The circuit model can be derived from the two-winding autotransformer with X-line taps by adding a tertiary winding. Then, the two-terminal leakage reactance (Equation 4.119 or 4.120) between the series + common and X-line tap + common, together with the two-terminal leakage reactances between the tertiary and the series + common and between the tertiary and the X-line tap + common, which can be obtained via Equation 4.106 or 4.107, can be used to construct a three-terminal impedance model.

5

Phasors, Three-Phase Connections, and Symmetrical Components

5.1 Phasors

Phasors are essentially complex numbers with built-in sinusoidal time dependences. They are usually written as a complex number in polar form, for example, $C = C_{\text{Re}} + jC_{\text{Im}}$ can be expressed in polar form as

$$C = C_{\text{Re}} + jC_{\text{Im}} = |C|e^{j\theta} = |C|(\cos\theta + j\sin\theta) \quad (5.1)$$

where

$$|C| = \sqrt{C_{\text{Re}}^2 + C_{\text{Im}}^2}, \quad \theta = \tan^{-1}\left(\frac{C_{\text{Im}}}{C_{\text{Re}}}\right)$$

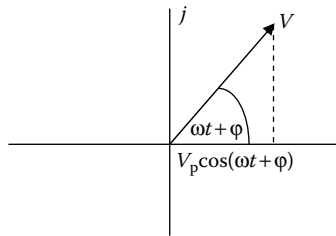
Here, $|C|$ is the magnitude of the complex number, with real and imaginary components C_{Re} and C_{Im} , and j is the unit imaginary.

A sinusoidal voltage has the form $V = V_p \cos(\omega t + \phi)$, where $\omega = 2\pi f$ is the angular frequency, f is the frequency in hertz, ϕ is the phase angle, and V_p is the peak value of the voltage, which can be written as

$$V = \text{Re}\left[V_p e^{j(\omega t + \phi)}\right] \quad (5.2)$$

where $\text{Re}[\]$ means to take the real part of the expression in brackets. In the complex plane, Equation 5.2 is the projection on the real axis of the complex number given in the brackets, as illustrated in [Figure 5.1](#).

As time increases, the complex voltage rotates counterclockwise around the origin, with the real projection varying in time as a cosine function. Currents and other voltages in a linear system, considered complex numbers, also rotate around the origin with time at the same rate because ω is the same for these. Since all of these numbers rotate together, at any snapshot in time, they all will have the same relative position with respect to each other. Therefore, we can factor out the common time dependence and consider only

**FIGURE 5.1**

Voltage as the real projection of a complex number.

the phase relationships between the numbers. This is possible because the circuit equations are linear and

$$\mathbf{V} = V_p e^{j(\omega t + \phi)} = V_p e^{j\omega t} e^{j\phi} \quad (5.3)$$

The complex number with time dependence is called a phasor and is written in boldface. However, the time dependence is usually understood or factored out, and the quantity without the time exponential factor is also called a phasor. Here we will mainly discuss phasors without explicitly including the time exponential. If time dependences are required, the quantity can be multiplied by the complex time factor $e^{j\omega t}$ and, if required, the real projection taken. This usually is not necessary because most calculations with phasors can be done without the common time-dependent factor. However, the time-dependent factor is important when performing time differentiation or integration. Note that $d\mathbf{V}/dt = j\omega\mathbf{V}$; this implicitly makes use of the built-in time dependence of the voltage phasor \mathbf{V} . We also sometimes refer to phasors as vectors because complex numbers behave like vectors in many respects in the complex plane and are usually depicted as directed arrows much like vectors, as in Figure 5.1. It is usually clear from the context whether a complex number or a mathematical vector is meant.

The voltage phasor in Equation 5.3 was written in terms of its peak magnitude V_p . However, root mean square (rms) voltages and currents are often used in power system discussions. The rms value of the voltage is given by

$$V_{\text{rms}}^2 = \frac{V_p^2}{T} \int_0^T \cos^2(\omega t + \phi) dt \quad (5.4)$$

where T is the period of the sinusoidal waveform and $T = 1/f = 2\pi/\omega$. Letting $\theta = \omega t$ in Equation 5.4, it becomes

$$V_{\text{rms}}^2 = \frac{V_p^2}{2\pi} \int_0^{2\pi} \cos^2(\theta + \phi) d\theta = \frac{V_p^2}{2} \Rightarrow V_{\text{rms}} = \frac{V_p}{\sqrt{2}} \quad (5.5)$$

This quantity can be obtained from the phasor by the formula

$$V_{\text{rms}} = \sqrt{\frac{\mathbf{V}\mathbf{V}^*}{2}} \quad (5.6)$$

where \mathbf{V}^* denotes the complex conjugate.

Another important quantity is the electrical power, which is the product of the voltage and the current. This gives the instantaneous power at any instant in time, however, we are usually interested in the average power. Since the relative phase between the voltage and current does not change with time, we can select the time origin so that the voltage has a maximum value at $t = 0$, $\phi_V = 0$, and the current phase leads the voltage by $\phi_I = \phi$. Then, the average power is

$$P_{\text{ave}} = \frac{1}{T} \int_0^T V(t)I(t)dt = \frac{V_P I_P \omega}{2\pi} \int_0^{2\pi/\omega} \cos(\omega t) \cos(\omega t + \phi) dt \quad (5.7)$$

Letting $\theta = \omega t$, this can be written

$$P_{\text{ave}} = \frac{V_P I_P}{2\pi} \int_0^{2\pi} \cos\theta \cos(\theta + \phi) d\theta = \frac{V_P I_P}{2} \cos\phi \quad (5.8)$$

In terms of rms voltage and current, $P_{\text{ave}} = V_{\text{rms}} I_{\text{rms}} \cos\phi$, and in terms of phasors, $P_{\text{ave}} = \text{Re}[\mathbf{V}\mathbf{I}^*]/2$. This leads to the definition of complex power:

$$P = \frac{\mathbf{V}\mathbf{I}^*}{2} = V_{\text{rms}} I_{\text{rms}} (\cos\phi - j \sin\phi) \quad (5.9)$$

The imaginary power is associated with reactors and capacitors in the circuit. If the imaginary power is negative, it is called capacitive power because the current leads the voltage in a capacitor, and if positive, it is called inductive power because the current lags the voltage in an inductor. Here, leading and lagging refer to the time-dependent phasors as they rotate counterclockwise with time in the complex plane. As time increases, the voltage vector passes a given point before the current vector for an inductor, and vice versa for a capacitor. For a single capacitor or inductor, $\phi = \pm\pi/2$ so that the average power vanishes according to Equation 5.8. Capacitors and inductors store power and then return it at various times during a cycle, but they do not consume power on average. For a resistor, $\phi = 0$ so that the imaginary power vanishes and the average power consumption assumes its maximum value.

Voltages and currents are often written as phasors having their rms magnitude because these are usually the quantities of interest in a power system. This is also advantageous because the power expression in Equation 5.9 can be written more simply as $P = \mathbf{V}\mathbf{I}^*$ for rms voltage and current phasors. Flux

densities (inductions), however, are usually expressed as phasors having their peak value as magnitude. Equation 5.5 can be used to convert between these different expressions.

Power systems are three-phase systems, in which the voltages and currents come in triples. The voltages and currents in the three phases are shifted in time relative to each other by one-third of a cycle. For a cycle of period T , the voltages are time-shifted by 0, $T/3$, and $2T/3$. Since $T = 1/f$, where f is the frequency in hertz, we have $\omega T/3 = 2\pi/3 = 120^\circ$ and $2\omega T/3 = 4\pi/3 = 240^\circ = -120^\circ$. Thus, the three voltages can be written (in standard order) as

$$\begin{aligned} V_a(t) &= V_a \cos(\omega t) \\ V_b(t) &= V_a \cos\left[\omega\left(t + \frac{2T}{3}\right)\right] = V_a \cos\left[\omega t + \frac{2\omega T}{3}\right] = V_a \cos(\omega t - 120^\circ) \\ V_c(t) &= V_a \cos\left[\omega\left(t + \frac{T}{3}\right)\right] = V_a \cos\left[\omega t + \frac{\omega T}{3}\right] = V_a \cos(\omega t + 120^\circ) \end{aligned} \quad (5.10)$$

Here, an arbitrary phase angle can be added to each. We have selected this arbitrary phase so that the a-voltage is maximum at time 0. These three voltages all have the same magnitude, and this is taken as the magnitude of the a-voltage. Expressed as phasors, these become

$$\mathbf{V}_a = V_a e^{j\omega t}, \quad \mathbf{V}_b = V_a e^{j(\omega t - 120^\circ)}, \quad \mathbf{V}_c = V_a e^{j(\omega t + 120^\circ)} \quad (5.11)$$

The phasors are written in boldface with the magnitudes in regular type. At time 0, these phasors can be represented in the complex plane as shown in Figure 5.2.

The phasors in Figure 5.2 are said to be balanced because $\mathbf{V}_a + \mathbf{V}_b + \mathbf{V}_c = 0$. This equation holds for every instant of time. These phasors are usually written with the time dependence factored out. This ordering of the phasors is called positive-sequence ordering. As the phasors rotate in time, the a-phasor

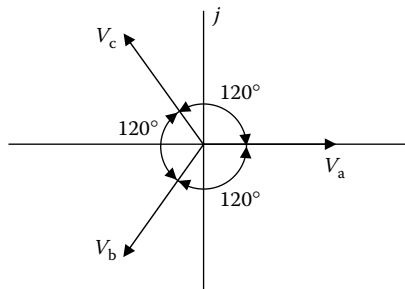


FIGURE 5.2

Phasor representation of a three-phase voltage system.

crosses the real axis first (it is already there), followed by the b-phasor, and then the c-phasor. The Cartesian form for these phasors, normalized to have unit magnitude, are given by

$$1, \quad -\frac{1}{2} - j\frac{\sqrt{3}}{2}, \quad -\frac{1}{2} + j\frac{\sqrt{3}}{2} \quad (5.12)$$

In this form, it can be seen immediately that they sum to zero.

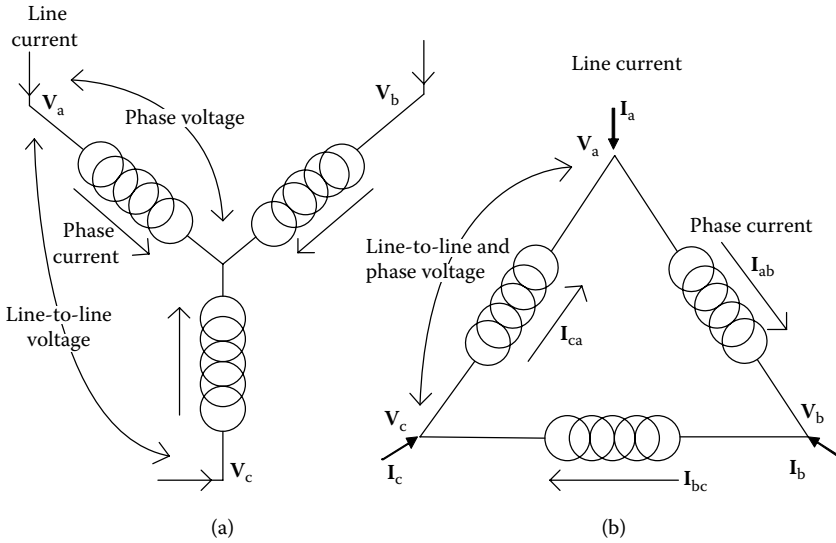
The three-phase system is convenient for the smooth operation of generators and motors, which require rotating flux; this can be established using three-phase currents. Although two independent phasors can also be used, three phasors work better. Also, two independent phasors cannot sum to zero, and summing to zero has useful implications for grounding.

5.2 Wye and Delta Three-Phase Connections

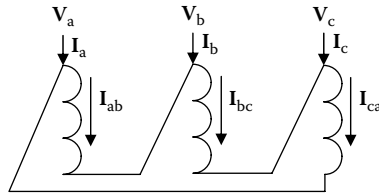
There are two basic types of three-phase connections in common use, the wye (Y) and delta (Δ) connections, as illustrated schematically in [Figure 5.3](#). In the Y connection, all three phases are connected to a common point, which may or may not be grounded. In the Δ connection, the phases are connected end to end with each other. In the Y connection, the line current flows directly into the winding, where it is called the winding or phase current. In a balanced three-phase system, the currents sum to zero at the common node, as shown in [Figure 5.3a](#). Therefore, under balanced conditions, even if this point were grounded, no current would flow to the ground. In the Δ connection, the line and phase currents are different. The line-to-line voltages in the Y connection differ from the voltages across the windings or phase voltages, whereas they are the same in the Δ connection. In [Figure 5.3a](#), the coils are shown at angles to each other in order to emphasize the phasor relationships, whereas in practice they are usually side by side and vertically oriented, as shown in [Figure 5.4](#) for the Δ connection.

The line-to-line voltages are usually specified when a power company orders a transformer. For a Δ connection, these are the same as the winding voltages. For a Y connection, these can be determined from the winding voltages and vice versa using phasor algebra. For the following calculation, we consider rated voltages and ignore impedance drops. Let \mathbf{V}_a , \mathbf{V}_b , and \mathbf{V}_c be the phase or winding voltages in a Y-connected set of transformer windings, and let \mathbf{V}_{ab} denote the line-to-line voltage between phases a and b, and so forth for the other line-to-line voltages. Then, these line-to-line voltages are given by

$$\mathbf{V}_{ab} = \mathbf{V}_a - \mathbf{V}_b, \quad \mathbf{V}_{bc} = \mathbf{V}_b - \mathbf{V}_c, \quad \mathbf{V}_{ca} = \mathbf{V}_c - \mathbf{V}_a \quad (5.13)$$

**FIGURE 5.3**

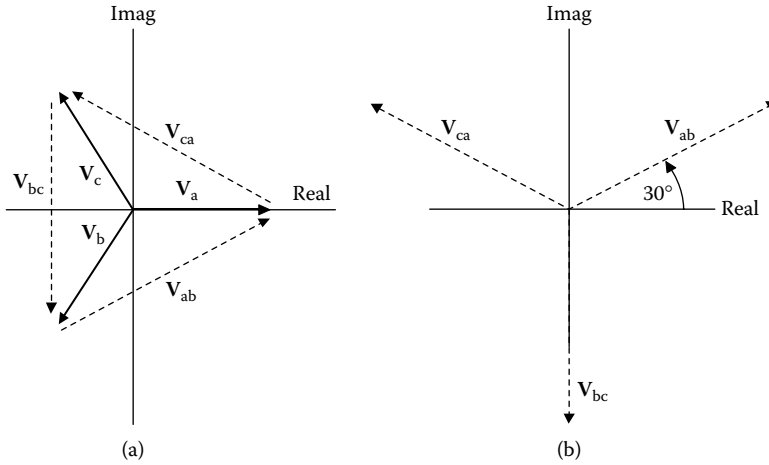
Basic three-phase connections: (a) Y connection and (b) Δ connection.

**FIGURE 5.4**

Delta interconnections as they would appear for windings on a three-phase core.

These can be readily calculated using a phasor description. The line-to-line phasors are shown graphically in Figure 5.5. Figure 5.5a shows the vector subtraction process explicitly, and Figure 5.5b shows the set of three line-to-line voltage phasors. Note that these form a positive-sequence set that is rotated 30° relative to the phase voltages. The line-to-line voltage magnitude can be found geometrically as the diagonal of the parallelogram formed by equal length sides making an angle of 120° with each other. As the different phase voltages have the same magnitude, we have

$$\begin{aligned}
 |\mathbf{V}_{ab}| &= |\mathbf{V}_a - \mathbf{V}_b| = \sqrt{|\mathbf{V}_a|^2 + |\mathbf{V}_b|^2 - 2|\mathbf{V}_a||\mathbf{V}_b|\cos 120^\circ} \\
 &= \sqrt{|\mathbf{V}_a|^2 + |\mathbf{V}_b|^2 + |\mathbf{V}_a||\mathbf{V}_b|} = \sqrt{3}|\mathbf{V}_a|
 \end{aligned}
 \tag{5.14}$$

**FIGURE 5.5**

Phasor representation of line-to-line voltages and their relation to the phase voltages in a Y-connected set of three-phase windings: (a) vector subtraction and (b) line-to-line voltages.

The graphical description of this process is useful for visualization purposes, but the math is simpler if the unit phasors of Equation 5.12 are used. In this case, we have

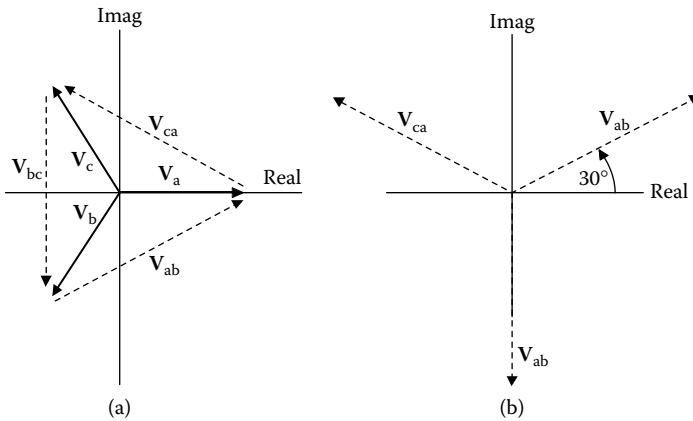
$$\begin{aligned} \mathbf{V}_{ab} &= V_a \left[1 - \left(-\frac{1}{2} - j\frac{\sqrt{3}}{2} \right) \right] = V_a \left(\frac{3}{2} + j\frac{\sqrt{3}}{2} \right) \\ &= \sqrt{3}V_a e^{j \tan^{-1} \left(\frac{1}{\sqrt{3}} \right)} = \sqrt{3}V_a e^{j30^\circ} \end{aligned} \quad (5.15)$$

Thus, the magnitude of the line-to-line voltage is $\sqrt{3}$ times the phase voltage magnitude in the Y-connected transformer coils, and the coils are rotated $+30^\circ$ relative to the phase voltages. Since the phase voltages are internal to the transformer and therefore impact the winding insulation structure, a more economical design is possible if these can be decreased. Hence, a Y connection is often used for the high-voltage coils of a three-phase transformer.

The relationship between the phase and line currents of a Δ -connected set of windings can similarly be found. From Figure 5.3, we see that the line currents are given in terms of the phase currents by

$$\mathbf{I}_a = \mathbf{I}_{ab} - \mathbf{I}_{ca}, \quad \mathbf{I}_b = \mathbf{I}_{bc} - \mathbf{I}_{ab}, \quad \mathbf{I}_c = \mathbf{I}_{ca} - \mathbf{I}_{bc} \quad (5.16)$$

These are illustrated graphically in Figure 5.6. As shown in Figure 5.6b, the line currents form a positive-sequence set rotated -30° relative to the phase currents. The magnitude relationship between the phase and line currents

**FIGURE 5.6**

Phasor representation of line currents and their relation to the phase currents in a delta-connected set of three-phase windings: (a) vector subtraction and (b) line-to-line voltages.

is similar to that of the voltages in a Y connection. To show this, we will use phasor subtraction directly in Equation 5.16. We have

$$\begin{aligned}
 I_a &= I_{ab} \left[1 - \left(-\frac{1}{2} + j\frac{\sqrt{3}}{2} \right) \right] = I_{ab} \left(\frac{3}{2} - j\frac{\sqrt{3}}{2} \right) \\
 &= \sqrt{3} I_{ab} e^{-j \tan^{-1} \left(\frac{1}{\sqrt{3}} \right)} = \sqrt{3} I_{ab} e^{-30^\circ}
 \end{aligned} \tag{5.17}$$

where we have used $I_{ab} = I_{ca}$. Nonboldfaced quantities are magnitudes.

Thus, the magnitudes of the line currents into or out of a Δ -connected set of windings are $\sqrt{3}$ times the winding or phase current magnitudes. Since low-voltage terminal currents are typically higher than high-voltage terminal currents, the low-voltage windings are often connected in Δ because decreasing the phase currents can produce a more economical design, although other considerations are often the deciding factor.

The rated power of a transformer is generally taken to be the three-phase power and is expressed in terms of terminal voltages and currents. The terminal voltage is the voltage to ground, or virtual ground in the case of a Δ connection, and the terminal current is the current into the terminal. The voltage ignores any impedance drops in the transformer, and the current assumes a rated load at unity power factor. Therefore, the voltages and currents are in phase, and we need to deal only with magnitudes. For a Y-connected set of windings, the terminal voltage to ground equals the voltage across the winding and the line current equals the phase current. Hence, the total rated power into all three phases is $3 \times$ the phase voltage \times the phase current. From Equation 5.14, the total rated power is $\sqrt{3} \times$ the line-to-line voltage \times the line current. This can be expressed mathematically as

$$\text{Power} = 3V_{\text{phase}}I_{\text{phase}} = \sqrt{3}V_{\text{line-line}}I_{\text{line}}$$

For a Δ -connected set of windings, a virtual ground is considered to be at the center of the Δ . From a geometric perspective, the center of an equilateral triangle is at a distance from a given vertex of $1/\sqrt{3} \times$ the length of a side. The Δ triangle in Figure 5.3 can be interpreted as an equilateral triangle formed from line-to-line voltage phasors. Therefore, the terminal voltage to virtual ground is the line-to-line voltage divided by $\sqrt{3}$. Thus, the total rated power is $3 \times$ the line voltage to ground \times the line current $= \sqrt{3} \times$ line-to-line voltage \times the line current. Since the phase voltage equals the line-to-line voltage and the line current $= \sqrt{3} \times$ the phase current according to Equation 5.17, the total rated power can also be expressed as $3 \times$ the phase voltage \times the phase current or the total winding power. Thus, the total rated power, whether expressed in terms of line quantities or phase quantities, is the same for Y- and Δ -connected windings and is given mathematically by the above equation.

Also note that the rated input power is the same as the power flowing through the windings. This may be obvious here, but it is not in some connections, in particular the autotransformer connection.

An interesting three-phase connection is the open Δ connection. In this connection, one of the windings of the Δ is missing although the terminal connections remain the same (Figure 5.7). This especially can be used if the three phases consist of separate units and if one of the phases is missing either because it is intended for future expansion or it has been disabled for some reason. Thus, instead of Equation 5.16 for the relationship between line and phase currents, we have

$$\mathbf{I}_a = \mathbf{I}_{ab} - \mathbf{I}_{ca}, \quad \mathbf{I}_b = -\mathbf{I}_{ab}, \quad \mathbf{I}_c = \mathbf{I}_{ca} \quad (5.18)$$

This still implies

$$\mathbf{I}_a + \mathbf{I}_b + \mathbf{I}_c = 0 \quad (5.19)$$

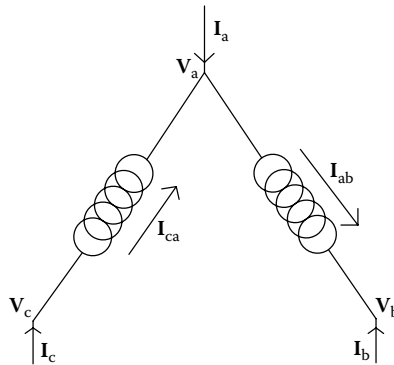


FIGURE 5.7
Open delta connection.

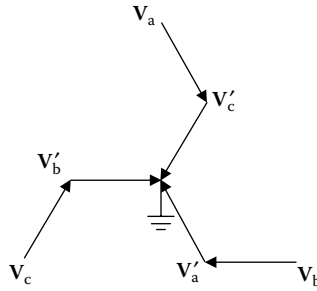
so that the terminal currents form a balanced three-phase system. Likewise, the terminal voltages form a balanced three-phase system. However, only two phases are present in the windings. In an external electrical system, the three phases are balanced. As before, the total rated input or output power is $3 \times \text{line voltage to ground} \times \text{line current} = \sqrt{3} \times \text{line-to-line voltage} \times \text{line current}$. However, as Equations 5.18 and 5.19 show, the line currents have the same magnitude as the phase or winding currents. Since the windings are designed to carry a certain maximum current under rated conditions without overheating, this winding or phase current will be the same for a full or open Δ . For a full Δ , the line current is $\sqrt{3}$ times the winding current. This means that, for an open delta, the line currents must be reduced by $1/\sqrt{3}$ times that of a full delta in order that the same phase currents flow in the windings. Therefore, since the line-to-line voltages are the same, the rated power for an open Δ is $1/\sqrt{3}$ times that of a full Δ .

For a full Δ connection, we have found that the winding power was $3 \times \text{phase voltage} \times \text{phase current}$. For an open Δ , the winding power is only $1/\sqrt{3}$ times that of a full Δ connection—the same as the terminal power. In the full Δ connection, two windings carry $2/3 \times 3 \times \text{phase voltage} \times \text{phase current} = 2 \times \text{phase voltage} \times \text{phase current}$. The same two windings in the open Δ connection carry the total rated power of $\sqrt{3} \times \text{phase voltage} \times \text{phase current}$. Thus, the utilization of the winding power in the open Δ connection is $\sqrt{3}/2$ (0.866) times that of a full Δ connection. Thus, this connection is not as efficient as a full Δ connection.

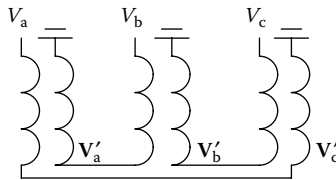
5.3 Zig-Zag Connection

The zig-zag connection is often used as a grounding connection for unbalanced faults. In normal operation, it does not allow balanced three-phase current to flow through the windings and therefore is an open circuit to this type of current. However, when an unbalanced fault occurs, this provides a path for currents that are in phase with each other and have the same magnitude. The connection is shown in [Figure 5.8](#).

The lines are oriented to indicate the direction of the voltage phasor on a phasor diagram, with the arrows indicating the direction of current flow. Only the relative orientation matters. The voltages increase from the ground point to the terminals, opposite to the direction of current flow. The lines are all of equal length, so their voltage magnitudes are all the same. A zig-zag connection requires two windings per phase for a total of six interconnected windings. The unprimed voltages in [Figure 5.8](#) are the zig windings with the label a, b, or c, corresponding to the phase to which they belong. The primed voltages are the zag windings with a label associated with their phase. Note that the zag windings have the opposite voltage orientation to the zig windings in

**FIGURE 5.8**

Zig-zag connection. The arrows indicate the direction of current flow.

**FIGURE 5.9**

Zig-zag interconnected windings on a three-phase core.

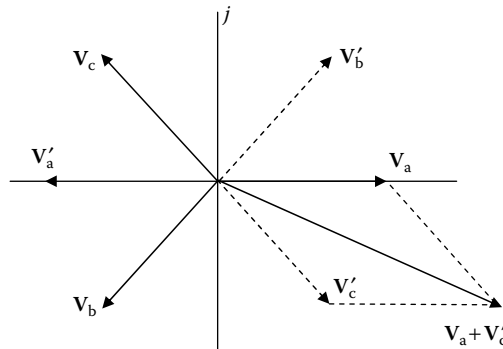
their phase. This winding interconnection, as it would appear for the set of six windings on a three-phase core, is shown in Figure 5.9.

A phasor diagram of these voltages, using the V_a phasor as the reference phasor, is given in Figure 5.10. The voltage between the a-terminal and ground is shown graphically in this figure. Using the unit phasors of Equation 5.12 and the fact that all the phasors have the same magnitude, the phasor addition can be performed algebraically

$$\begin{aligned} \mathbf{V}_{a \text{ to ground}} &= \mathbf{V}_a + \mathbf{V}'_c = V_a \left[1 - \left(-\frac{1}{2} + j\frac{\sqrt{3}}{2} \right) \right] = V_a \left(\frac{3}{2} - j\frac{\sqrt{3}}{2} \right) \\ &= \sqrt{3}V_a e^{-j30^\circ} \end{aligned} \quad (5.20)$$

Thus, the terminal voltage to ground is $\sqrt{3} \times$ the winding voltage and is shifted -30° .

We can see from Figure 5.8 that, if a-phase current flows into the a-terminal and the a-zig winding, it would also have to flow into the zag winding of the c phase. This cannot occur because we cannot achieve amp-turn balance with the c-phase current flowing into the c-zig winding. Therefore, no balanced phase currents can flow into the terminals. However, currents that are all of the same phase can flow into the terminals. In fact, we can see from the

**FIGURE 5.10**

Phasor diagram of the zig and zag voltages.

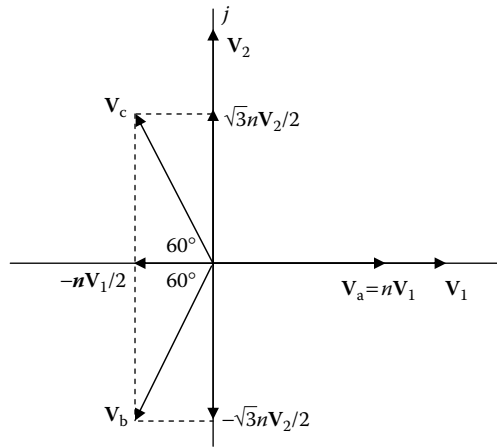
current directions in [Figure 5.8](#) and the fact that the windings all have the same number of turns (i.e., the same voltage magnitudes), that we will have amp-turn balance in all the phases in this case.

5.4 Scott Connection

The Scott connection is used to convert voltages from a two-phase system to a three-phase balanced system or vice versa. The two-phase voltage phasors are assumed to be 90° apart on a phasor diagram and of equal magnitude. They are therefore independent phasors, and any phasor can be constructed from them by a suitable vectorial combination. Before discussing the physical realization of this connection in terms of windings, we will examine the phasor relationships directly, as shown in [Figure 5.11](#). The two-phase voltages are labeled \mathbf{V}_1 and \mathbf{V}_2 and the three-phase voltages are labeled \mathbf{V}_a , \mathbf{V}_b , and \mathbf{V}_c . The three-phase voltages are constructed from components of the two-phase voltages as shown in the figure.

Here, the voltage (turns) ratio between V_a and V_1 is n , where $n = V_a/V_1$. This allows us to step the voltage up or down when going from two to three phases. The three-phase voltages have components along the two-phase voltages as shown in [Figure 5.11](#). We assume that the magnitudes of \mathbf{V}_1 and \mathbf{V}_2 are the same and that $\mathbf{V}_2 = j\mathbf{V}_1$. This is expressed mathematically as

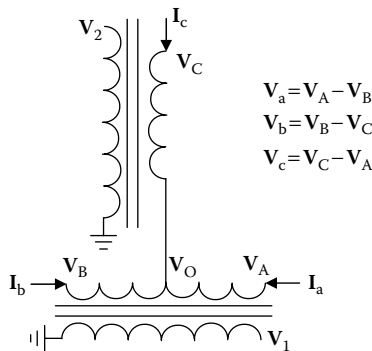
$$\begin{aligned} \mathbf{V}_a &= n\mathbf{V}_1 \\ \mathbf{V}_b &= -\frac{1}{2}n\mathbf{V}_1 - \frac{\sqrt{3}}{2}n\mathbf{V}_2 \\ \mathbf{V}_c &= -\frac{1}{2}n\mathbf{V}_1 + \frac{\sqrt{3}}{2}n\mathbf{V}_2 \end{aligned} \tag{5.21}$$

**FIGURE 5.11**

Scott connection from a two-phase system of voltages, labeled 1 and 2, to a three-phase voltage system, labeled a, b, and c.

To realize this with windings, we need two windings in the two-phase system with voltages V_1 and V_2 . These would probably have to be on separate cores since they do not form a balanced system. This means that, for conventional core designs with legs and yokes, fluxes from the two phases will not cancel out in the core yokes as they do for a three-phase balanced system of currents. However, there are times when a single core can be used [Kra88]. We will use the two-core realization given in [MIT43]. First, we note that the b and c phases each have a voltage component that is half the magnitude of the a-phase voltage. Therefore, the a phase can be constructed of two separate windings, each having the same number of turns. These windings will be on the phase 1 core. Each of the separate a-phase windings can then contribute half the a-phase voltage component to the b- and c-phase voltages. The b and c phases also have a component along phase 2 of the same magnitude but opposite sign. Both of these can come from a single winding having a voltage magnitude of $\sqrt{3}/2 \times$ the a-phase voltage magnitude. This is shown in Figure 5.12.

As shown in Figure 5.12, the three-phase voltages are line-to-line voltages. The terminal voltages are labeled V_A and so on. The subscript will also be used to label the winding ends, and a pair of these will label the winding. The three-phase system has no real ground, as is the case for a Δ connection. The A-B winding on phase 1 is center tapped, with the C-O winding on phase 2 connected to the center tap position. The C-O winding must have $\sqrt{3}/2$ times the turns in the full A-B winding. Assume the winding voltages for the a, b, and c system increase from B to A on the core 1 winding and from O to C on the core 2 winding. This is consistent with the V_1 and V_2 voltage directions for the 1 and 2 system, respectively.

**FIGURE 5.12**

Scott connection for two-phase to three-phase transformation, using windings on two separate cores.

The a-phase voltage starts at the B end of the winding and increases along both half windings to the A position, so its voltage is the sum of the voltages from each half of the A-B winding. The b-phase voltage starts at position C and decreases along the C-O winding and then decreases from O to B along half the A-B winding. Its voltage is therefore minus the C-O winding voltage minus half the A-B winding voltage as required by vector addition on the phasor diagram. The c-phase voltage starts at the A position and decreases along half the A-B winding and then increases along the C-O winding. Its voltage is therefore minus half the A-B winding voltage plus the C-O winding voltage as required by the phasor diagram vector addition.

It is interesting to consider the winding currents in the a, b, and c system. The terminal currents are shown in Figure 5.12. These should also form a balanced system and will therefore cancel at the center tap position O. Starting with the C-O winding, the c-phase current needs to balance the winding 2 current. The voltage turns ratio between these two windings is given by $V_{C-O}/V_2 = \sqrt{3}n/2$, where n was defined earlier as the turns ratio between the full A-B winding and winding 1. Therefore, for amp-turn balance, we have

$$I_c = -\frac{2}{\sqrt{3}n} I_2 = -j \frac{2}{\sqrt{3}n} I_1$$

The currents as well as the voltages for the two-phase system are at 90° with respect to each other on a phasor diagram. At the center node, we have

$$I_a + I_b = -I_c = j \frac{2}{\sqrt{3}n} I_1$$

For amp-turn balance on the phase 1 core, we require

$$I_a - I_b = -\frac{2}{n} I_1$$

Solving the above set of equations, we get

$$\mathbf{I}_a = \frac{\mathbf{I}_1}{n} \left(-1 + \frac{j}{\sqrt{3}} \right), \quad \mathbf{I}_b = \frac{\mathbf{I}_1}{n} \left(1 + \frac{j}{\sqrt{3}} \right), \quad \mathbf{I}_c = -j \frac{2}{\sqrt{3}n} \mathbf{I}_1$$

We see that these sum to zero and have amp-turn balance with the 1, 2 phase windings.

5.5 Symmetrical Components

The balanced three-phase system of voltages and currents we have discussed so far is called a positive-sequence system. The phase ordering has been a, b, and c in terms of which phasor crosses the real axis first as time increases. There is another three-phase balanced system, called a negative-sequence system with the phase ordering a, c, and b. In addition, there is a zero-sequence system that consists of three phasors of equal phase and magnitude. The zero-sequence system is not balanced in the sense that the phasors in this system do not sum to zero, but it is symmetric. The significance of these systems of phasors is that any three-phase collection of phasors can be written as a sum of phasors, one from each of these systems. The components of such a sum are called symmetrical components. This makes it possible to analyze an unbalanced three-phase system by separately analyzing the symmetric sequence systems and then adding the results. This will require a systematic treatment that we will discuss next.

In a balanced three-phase electrical system, the voltage or current phasors are of equal magnitude and are separated by 120° as discussed in [Section 5.1](#). They are shown again in Figure 5.13a, in order to contrast them

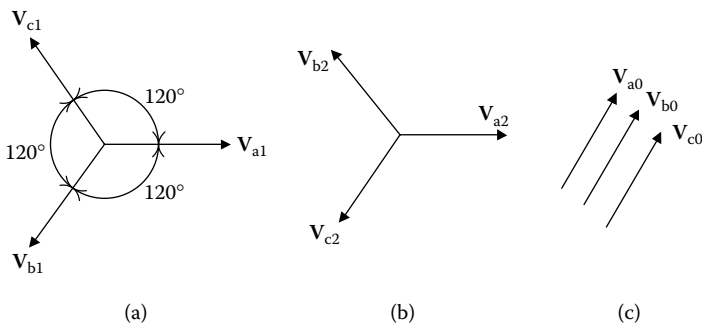


FIGURE 5.13

Symmetric systems of three-phase phasors: (a) positive sequence, (b) negative sequence, and (c) zero sequence.

with the other sequence sets, and are labeled V_{a1} , V_{b1} , and V_{c1} , where 1 denotes a positive-sequence set by convention. The unit vectors for this set were given in Equation 5.12. We will use a special notation for this set of unit vectors—the unit vector 1 stays the same, but the other two are denoted as follows:

$$\begin{aligned}\alpha &= e^{j120^\circ} = -\frac{1}{2} + j\frac{\sqrt{3}}{2} \\ \alpha^2 &= e^{j240^\circ} = e^{-j120^\circ} = -\frac{1}{2} - j\frac{\sqrt{3}}{2}\end{aligned}\tag{5.22}$$

We see from this that

$$\begin{aligned}1 + \alpha + \alpha^2 &= 0 \\ \alpha^3 &= 1 \\ \alpha^4 &= \alpha\end{aligned}\tag{5.23}$$

Thus, for a balanced three-phase positive-sequence system, we have

$$\mathbf{V}_{a1} = \mathbf{V}_{a1}, \quad \mathbf{V}_{b1} = \alpha^2 \mathbf{V}_{a1}, \quad \mathbf{V}_{c1} = \alpha \mathbf{V}_{a1}\tag{5.24}$$

Notice that \mathbf{V}_{a1} need not be along the positive real axis. α^2 and α can be thought of as rotation operators that rotate the phasor they multiply by 240° and 120° , respectively. This guarantees that \mathbf{V}_{b1} and \mathbf{V}_{c1} are 240° and 120° from \mathbf{V}_{a1} regardless of its position in the complex plane. Also, these phasors are of equal magnitude because α and its powers are of unit magnitude.

A negative-sequence set of balanced phasors is one with the phase ordering a, c, and b, as shown in [Figure 5.13b](#), which shows that

$$\mathbf{V}_{a2} = \mathbf{V}_{a2}, \quad \mathbf{V}_{b2} = \alpha \mathbf{V}_{a2}, \quad \mathbf{V}_{c2} = \alpha^2 \mathbf{V}_{a2}\tag{5.25}$$

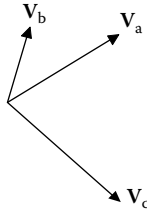
where 2 refers to negative-sequence quantities by convention. These are separated by 120° and have the same magnitude, which can differ from the positive-sequence magnitude.

A zero-sequence set of phasors is shown in [Figure 5.13c](#). These are all in phase and have equal magnitudes, which can differ from the positive- or negative-sequence magnitudes. Thus,

$$\mathbf{V}_{a0} = \mathbf{V}_{b0} = \mathbf{V}_{c0}\tag{5.26}$$

with 0 used to label zero-sequence quantities. In addition, the relative phase between the a-phasor of each set can differ from zero.

We will now show that it is possible to represent any unbalanced or unsymmetrical set of three phasors by means of these symmetric sequence sets. Let \mathbf{V}_a , \mathbf{V}_b , and \mathbf{V}_c be such an unbalanced set as shown in [Figure 5.14](#). Since the positive-, negative-, and zero-sequence symmetric sets are determined once \mathbf{V}_{a1} , \mathbf{V}_{a2} , and \mathbf{V}_{a0} are specified, we need to find only these a phase

**FIGURE 5.14**

Unsymmetrical set of three phasors.

components of the symmetric sets in terms of the original phasors to prove that this representation is possible. We write

$$\begin{aligned} \mathbf{V}_a &= \mathbf{V}_{a0} + \mathbf{V}_{a1} + \mathbf{V}_{a2} \\ \mathbf{V}_b &= \mathbf{V}_{b0} + \mathbf{V}_{b1} + \mathbf{V}_{b2} \\ \mathbf{V}_c &= \mathbf{V}_{c0} + \mathbf{V}_{c1} + \mathbf{V}_{c2} \end{aligned} \quad (5.27)$$

Using Equations 5.24 through 5.26, this can be written

$$\begin{aligned} \mathbf{V}_a &= \mathbf{V}_{a0} + \mathbf{V}_{a1} + \mathbf{V}_{a2} \\ \mathbf{V}_b &= \mathbf{V}_{a0} + \alpha^2 \mathbf{V}_{a1} + \alpha \mathbf{V}_{a2} \\ \mathbf{V}_c &= \mathbf{V}_{a0} + \alpha \mathbf{V}_{a1} + \alpha^2 \mathbf{V}_{a2} \end{aligned} \quad (5.28)$$

In matrix notation, we have

$$\begin{pmatrix} \mathbf{V}_a \\ \mathbf{V}_b \\ \mathbf{V}_c \end{pmatrix} = \begin{pmatrix} 1 & 1 & 1 \\ 1 & \alpha^2 & \alpha \\ 1 & \alpha & \alpha^2 \end{pmatrix} \begin{pmatrix} \mathbf{V}_{a0} \\ \mathbf{V}_{a1} \\ \mathbf{V}_{a2} \end{pmatrix} \quad (5.29)$$

which is often abbreviated

$$\mathbf{V}_{abc} = A \mathbf{V}_{012} \quad (5.30)$$

where \mathbf{V}_{abc} and \mathbf{V}_{012} are column vectors and A is the matrix in Equation 5.29.

\mathbf{V}_{a0} , \mathbf{V}_{a1} , and \mathbf{V}_{a2} can be found uniquely if A has an inverse. This is the case, and the result is

$$\begin{pmatrix} \mathbf{V}_{a0} \\ \mathbf{V}_{a1} \\ \mathbf{V}_{a2} \end{pmatrix} = \frac{1}{3} \begin{pmatrix} 1 & 1 & 1 \\ 1 & \alpha & \alpha^2 \\ 1 & \alpha^2 & \alpha \end{pmatrix} \begin{pmatrix} \mathbf{V}_a \\ \mathbf{V}_b \\ \mathbf{V}_c \end{pmatrix} \quad (5.31)$$

as can be verified by direct computation, using the identities in Equation 5.23. Equation 5.31 can be abbreviated to

$$\mathbf{V}_{012} = A^{-1} \mathbf{V}_{abc} \quad (5.32)$$

where A^{-1} is the matrix in Equation 5.31 including the factor $1/3$. It is the inverse of the matrix A .

Thus, given any unsymmetrical set of phasors, the symmetric positive-, negative-, and zero-sequence sets can be found. Conversely, the unsymmetrical set can be obtained given the symmetric sets or just one phasor from each symmetric set chosen customarily to be the a-phasor.

Equations 5.29 through 5.32 apply equally well to currents. We can use them to compute the power in the two systems. The three-phase power is given by

$$\begin{aligned} P &= \mathbf{V}_a \mathbf{I}_a^* + \mathbf{V}_b \mathbf{I}_b^* + \mathbf{V}_c \mathbf{I}_c^* = \mathbf{V}_{abc}^T \mathbf{I}_{abc}^* \\ &= (\mathbf{A} \mathbf{V}_{012})^T (\mathbf{A} \mathbf{I}_{012})^* = \mathbf{V}_{012}^T \mathbf{A}^T \mathbf{A}^* \mathbf{I}_{012}^* \\ &= 3 \mathbf{V}_{012}^T \mathbf{I}_{012}^* = 3(\mathbf{V}_{a0} \mathbf{I}_{a0}^* + \mathbf{V}_{a1} \mathbf{I}_{a1}^* + \mathbf{V}_{a2} \mathbf{I}_{a2}^*) \end{aligned} \quad (5.33)$$

Here, T denotes transpose, which converts a column vector to a row vector or vice versa. It also transforms a matrix so that its rows become columns. This is needed because \mathbf{V}_{abc} and \mathbf{I}_{abc} are column vectors and the dot product is a matrix product between a row and column vector. We have also used $\alpha^* = \alpha^2$ and $\alpha^{2*} = \alpha$ in Equations 5.29 and 5.31 to show that $A^T A^* = 3I$, where I is the unit matrix. Thus, the three-phase power is also equal to the sum of the powers in the three sequence networks. The factor of three occurs because the last expression in Equation 5.33 only contains the representative a-component of the sequence networks.

The advantage of using symmetrical components is that an unsymmetrical three-phase set of phasors can be analyzed in terms of three symmetrical systems of phasors. Since the component systems are symmetrical, only one phase from each symmetrical system need be analyzed, in the same manner that we need only consider one phase of a conventional balanced three-phase system. However, the circuit model that applies to each sequence may differ from the normal three-balanced phase circuit model. This latter circuit model generally applies only to the positive-sequence circuit. The negative-sequence circuit may differ from the positive, particularly if the system has generators or motors. Because generated voltages are usually of a positive sequence, voltage sources are absent from the negative-sequence circuit. For transformers, the impedances are independent of phase order so that the positive- and negative-sequence circuit impedances are identical.

The zero-sequence circuit model can differ considerably from the positive or negative one. For example, a balanced set of currents can flow into the terminals of a three-phase system, even without a path to ground, because the currents add to zero. Thus, an effective ground point can be assumed. Since zero-sequence currents are of equal magnitude and phase, they do not sum to zero and therefore cannot flow into the terminals of a three-phase system unless there is a path to ground. Thus, for zero-sequence currents to flow in a Y-connected set of windings for example, a path to ground is necessary.

In the zero-sequence circuit model for a Y connection without ground, an infinite impedance to ground must be placed in the circuit. Similarly, zero-sequence currents cannot flow into the terminals of a Δ connection because there is no path to ground; however, such currents can circulate within the Δ if they are induced there for amp-turn balance with another set of windings.

Since we alluded to the fact that the sequence impedances may differ in the three sequence networks, we must consider the conditions under which these networks are uncoupled so that they can be analyzed separately. We will start with the assumption that the three-phase balanced networks for transformers are uncoupled and are the same for all three phases. Even for a three-phase core, the mutual reactances between windings are significant only for windings on the same leg of the core and tend to be small between windings on different legs. We also generally assume that the self-inductances are the same for windings on different legs, even though there are slight differences because the magnetic environment of the center leg differs from that of the outer legs. This similarity also applies to leakage reactances. Consider the voltages across a circuit element that has impedances of Z_a , Z_b , and Z_c in the three phases. The three-phase voltages across these elements are given by

$$\begin{pmatrix} \mathbf{V}_a \\ \mathbf{V}_b \\ \mathbf{V}_c \end{pmatrix} = \begin{pmatrix} Z_a & 0 & 0 \\ 0 & Z_b & 0 \\ 0 & 0 & Z_c \end{pmatrix} \begin{pmatrix} \mathbf{I}_a \\ \mathbf{I}_b \\ \mathbf{I}_c \end{pmatrix} \quad (5.34)$$

Let Z denote the impedance matrix in Equation 5.34. Using Equations 5.30 and 5.32, we can convert the \mathbf{V} and \mathbf{I} vectors in the abc system to the 012 system to obtain

$$A^{-1}\mathbf{V}_{abc} = \mathbf{V}_{012} = A^{-1}Z\mathbf{A}\mathbf{I}_{012} \quad (5.35)$$

If the impedances Z_a and so on are unequal then the matrix $A^{-1}ZA$ contains off-diagonal terms that couple the sequence networks. However, if the impedances are equal, then we obtain a diagonal matrix and the sequences are uncoupled as shown in Equation 5.36:

$$\begin{pmatrix} \mathbf{V}_{a0} \\ \mathbf{V}_{a1} \\ \mathbf{V}_{a2} \end{pmatrix} = \begin{pmatrix} Z_a & 0 & 0 \\ 0 & Z_a & 0 \\ 0 & 0 & Z_a \end{pmatrix} \begin{pmatrix} \mathbf{I}_{a0} \\ \mathbf{I}_{a1} \\ \mathbf{I}_{a2} \end{pmatrix} \quad (5.36)$$

We see here that all the sequence impedances are the same. Therefore, this situation does not allow for the possibility that the zero-sequence impedances can differ from the positive- or negative-sequence impedances. We will examine this situation from the point of view of uncoupled-sequence

circuits, each having their own impedance. The sequence voltages across a given element are now given by

$$\begin{pmatrix} \mathbf{V}_{a0} \\ \mathbf{V}_{a1} \\ \mathbf{V}_{a2} \end{pmatrix} = \begin{pmatrix} Z_0 & 0 & 0 \\ 0 & Z_1 & 0 \\ 0 & 0 & Z_2 \end{pmatrix} \begin{pmatrix} \mathbf{I}_{a0} \\ \mathbf{I}_{a1} \\ \mathbf{I}_{a2} \end{pmatrix} \quad (5.37)$$

Letting Z represent the matrix in Equation 5.37 and applying Equations 5.30 and 5.32 to convert Equation 5.37 to the abc system, we get

$$A\mathbf{V}_{012} = \mathbf{V}_{abc} = AZA^{-1}\mathbf{I}_{abc} \quad (5.38)$$

For transformers, we have noted that $Z_1 = Z_2$. For this situation, the matrix in Equation 5.38 is given in Equation 5.39.

$$\begin{pmatrix} \mathbf{V}_a \\ \mathbf{V}_b \\ \mathbf{V}_c \end{pmatrix} = \frac{1}{3} \begin{pmatrix} (Z_0 + 2Z_1) & (Z_0 - Z_1) & (Z_0 - Z_1) \\ (Z_0 - Z_1) & (Z_0 + 2Z_1) & (Z_0 - Z_1) \\ (Z_0 - Z_1) & (Z_0 - Z_1) & (Z_0 + 2Z_1) \end{pmatrix} \begin{pmatrix} \mathbf{I}_a \\ \mathbf{I}_b \\ \mathbf{I}_c \end{pmatrix} \quad (5.39)$$

We note that when $Z_0 = Z_1$ this becomes a diagonal matrix with all diagonal elements equal to Z_1 .

Thus, when analyzing an unbalanced fault condition in transformers with zero-sequence impedances that differ from the positive- and negative-sequence impedances, we can analyze the separate sequence circuit models using Equation 5.37. We can then use the A matrix to convert the sequence quantities to the abc system. On the other hand, if we wish to analyze an unbalanced fault condition from an abc circuit system approach, then we need to use the coupled set of impedances given in Equation 5.39 when the zero and positive sequences differ [Bra82]. This will also apply to cases in which all the sequence impedances are different, except that, when converting to the abc system, the impedance matrix will be more complicated than that in Equation 5.30 unless some special conditions are placed on the sequence impedances.

6

Fault Current Analysis

6.1 Introduction

Transformers should be designed to withstand various possible faults, such as a short to ground of one or more phases. The high currents accompanying these faults, approximately 10–30 times normal, produce high forces and stresses in the windings and support structure. Also, depending on the fault duration, significant amounts of heat may be generated inside the unit. The design must accommodate the worst-case fault, which can occur from either a mechanical or thermal standpoint.

The first step when designing transformers to withstand faults is to determine the fault currents in all the windings. Since this is an electrical problem, a circuit model that includes leakage impedances of the transformer and relevant system impedances is necessary. The systems are typically represented by a voltage source in series with an impedance or by just an impedance, since we are not interested in detailed fault currents within the system, external to the transformer. The transformer circuit model considered in this chapter is that of a two- or three-terminal per-phase unit with all pairs of terminal leakage reactances given from either calculations or measurement. We ignore the core excitation because its effects on the fault currents of modern power transformers are negligible.

In this chapter we consider three-phase units and the following fault types: three-phase line to ground, single-phase line to ground, line-to-line, and double line to ground. These are the standard fault types and are important because they are the most likely to occur on actual systems. The transformer, or rather each coil, must be designed to withstand the worst (i.e., the highest current) fault it can experience. Each fault type refers to a fault on any of the single-phase terminals. For example, a three-phase fault can occur on all the high-voltage (HV) terminals (H_1 , H_2 , and H_3), all the low-voltage (LV) terminals (X_1 , X_2 , and X_3), or all the tertiary-voltage terminals (Y_1 , Y_2 , and Y_3), and so forth for the other fault types. Faults on a single-phase system can be considered three-phase faults on a three-phase system so that these are automatically included in the analysis of faults on three-phase systems.

Since the fault types considered can produce unbalanced conditions in a three-phase system, they can be treated most efficiently by using symmetrical components. In this method, an unbalanced set of voltages or currents can be represented mathematically by sets of balanced voltages or currents, called sequence voltages or currents. These can then be analyzed using sequence circuit models. The final results are obtained by transforming the voltages and currents from the sequence analysis into the voltages and currents of the real system. This method was introduced in Chapter 5, and we will use those results here. For easy reference, we will repeat the transformation equations between the normal phase abc system and the symmetrical component 012 system:

$$\begin{pmatrix} \mathbf{V}_a \\ \mathbf{V}_b \\ \mathbf{V}_c \end{pmatrix} = \begin{pmatrix} 1 & 1 & 1 \\ 1 & \alpha^2 & \alpha \\ 1 & \alpha & \alpha^2 \end{pmatrix} \begin{pmatrix} \mathbf{V}_{a0} \\ \mathbf{V}_{a1} \\ \mathbf{V}_{a2} \end{pmatrix} \quad (6.1)$$

$$\begin{pmatrix} \mathbf{V}_{a0} \\ \mathbf{V}_{a1} \\ \mathbf{V}_{a2} \end{pmatrix} = \frac{1}{3} \begin{pmatrix} 1 & 1 & 1 \\ 1 & \alpha & \alpha^2 \\ 1 & \alpha^2 & \alpha \end{pmatrix} \begin{pmatrix} \mathbf{V}_a \\ \mathbf{V}_b \\ \mathbf{V}_c \end{pmatrix} \quad (6.2)$$

The circuit model calculations to be discussed are for steady-state conditions, whereas actual faults would have a transient phase in which the currents can exceed their steady-state values for short periods of time. These enhancement effects are included using an asymmetry factor, which takes into account the resistance and reactance present at the faulted terminal and is considered to be conservative from a design point of view. This enhancement factor was calculated in Chapter 2. The following references are used in this chapter: [Ste62a], [Lyo37], [Blu51].

6.2 Fault Current Analysis on Three-Phase Systems

We assume that the system is balanced before the fault occurs, that is, any prefault (pf) voltages and currents are positive-sequence sets. Here, we consider a general electrical system as shown on the left side of [Figure 6.1](#). The fault occurs at some location on the system where fault phase currents \mathbf{I}_a , \mathbf{I}_b , and \mathbf{I}_c flow, which are shown in [Figure 6.1](#) as leaving the system. The voltages to ground at the fault point are labeled \mathbf{V}_a , \mathbf{V}_b , and \mathbf{V}_c . The system, as viewed from the fault point or terminal, is modeled using Thevenin's theorem. First, however, we resolve the voltages and currents into symmetrical components, so that we need only analyze one phase of the positive-, negative-, and

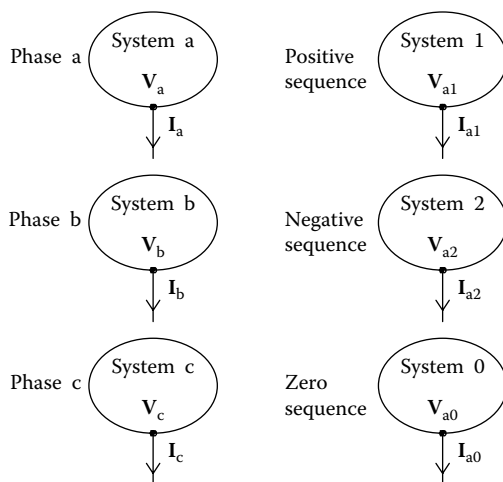


FIGURE 6.1
Fault at a point on a general electrical system.

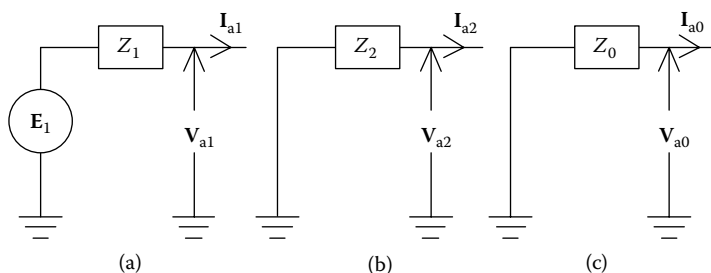


FIGURE 6.2
Thevenin equivalent sequence circuit models: (a) positive sequence, (b) negative sequence, and (c) zero sequence.

zero-sequence sets. This is indicated on the right side of [Figure 6.1](#), where the a-phase sequence set has been singled out.

In Thevenin's theorem, each of the sequence systems can be modeled as a voltage source in series with an impedance, where the voltage source is the open-circuit voltage at the fault point and the impedance is found by shorting all voltage sources and measuring or calculating the impedance to ground at the fault terminal. When applying Thevenin's theorem, note that the fault point together with the ground point is the terminal that is associated with the open-circuit voltage before the fault. When the fault occurs, the load is typically set to zero but may include a fault impedance. The resulting model is shown in [Figure 6.2](#). No voltage source is included in the negative- and zero-sequence circuits because the standard voltage sources in power systems are positive-sequence sources.

The circuit equations for Figure 6.2 are as follows:

$$\mathbf{V}_{a1} = \mathbf{E}_1 - \mathbf{I}_{a1}Z_1, \quad \mathbf{V}_{a2} = -\mathbf{I}_{a2}Z_2, \quad \mathbf{V}_{a0} = -\mathbf{I}_{a0}Z_0 \quad (6.3)$$

Since \mathbf{E}_1 is the open-circuit voltage at the fault terminal, it is the voltage at the fault point before the fault occurs and is labeled V_{pf} . We omit the label 1 because it is understood to be a positive-sequence voltage. We will also consider this a reference phasor and use ordinary type for it. Thus

$$\mathbf{V}_{a1} = V_{pf} - \mathbf{I}_{a1}Z_1, \quad \mathbf{V}_{a2} = -\mathbf{I}_{a2}Z_2, \quad \mathbf{V}_{a0} = -\mathbf{I}_{a0}Z_0 \quad (6.4)$$

If there is some impedance in the fault, it can be included in the circuit model. However, because we are interested in the worst-case faults (highest fault currents), we assume that the fault resistance is zero. If there is an impedance to ground at a neutral point in the transformer, such as, for example, at the junction of a Y-connected set of windings, then $3 \times$ its value should be included in the single-phase zero-sequence network at that point because all three zero-sequence currents flow into the neutral resistor but only one of them is represented in the zero-sequence circuit.

The types of faults considered and their voltage and current constraints are shown in Figure 6.3.

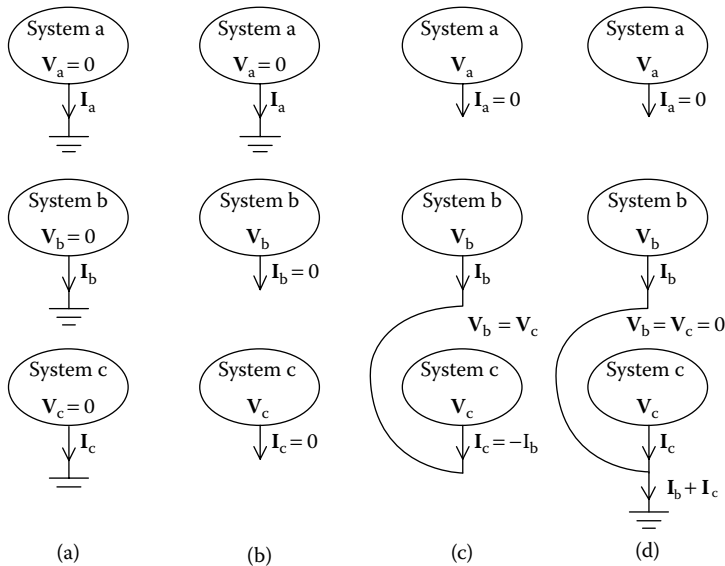


FIGURE 6.3

Standard fault types on three-phase systems: (a) three-phase line-to-ground fault, (b) single-phase line-to-ground fault, (c) line-to-line fault, and (d) double line-to-ground fault.

6.2.1 Three-Phase Line-to-Ground Fault

Three-phase faults to ground are characterized by

$$\mathbf{V}_a = \mathbf{V}_b = \mathbf{V}_c = 0 \quad (6.5)$$

as shown in [Figure 6.3a](#). From Equations 6.5 and 6.2, we find

$$\mathbf{V}_{a0} = \mathbf{V}_{a1} = \mathbf{V}_{a2} = 0 \quad (6.6)$$

Therefore, from Equation 6.4, we get

$$\mathbf{I}_{a1} = \frac{V_{pf}}{Z_1}, \quad \mathbf{I}_{a2} = \mathbf{I}_{a0} = 0 \quad (6.7)$$

Using Equations 6.7 and 6.1 applied to currents, we find

$$\mathbf{I}_a = \mathbf{I}_{a1}, \quad \mathbf{I}_b = \alpha^2 \mathbf{I}_{a1}, \quad \mathbf{I}_c = \alpha \mathbf{I}_{a1} \quad (6.8)$$

Thus, as expected, the fault currents form a balanced positive-sequence set of magnitude V_{pf}/Z_1 . This example can be carried out without the use of symmetrical components because the fault does not unbalance the system.

We can add the pf-balanced currents to the fault currents in the abc system. Although this can be done generally for all the faults, we will not explicitly do this for simplicity.

6.2.2 Single-Phase Line-to-Ground Fault

For a single-phase line-to-ground fault, we assume, without loss of generality, that the a-phase is faulted. Thus

$$\mathbf{V}_a = 0, \quad \mathbf{I}_b = \mathbf{I}_c = 0 \quad (6.9)$$

as indicated in [Figure 6.3b](#). From Equation 6.2 applied to currents, we get

$$\mathbf{I}_{a0} = \mathbf{I}_{a1} = \mathbf{I}_{a2} = \frac{\mathbf{I}_a}{3} \quad (6.10)$$

From Equations 6.9, 6.10, and 6.4, we find

$$\mathbf{V}_a = \mathbf{V}_{a0} + \mathbf{V}_{a1} + \mathbf{V}_{a2} = V_{pf} - \mathbf{I}_{a1}(Z_0 + Z_1 + Z_2) = 0$$

or

$$\mathbf{I}_{a1} = \frac{V_{pf}}{(Z_0 + Z_1 + Z_2)} = \mathbf{I}_{a2} = \mathbf{I}_{a0} \quad (6.11)$$

Using Equations 6.9 and 6.10, we get

$$\mathbf{I}_a = \frac{3V_{pf}}{(Z_0 + Z_1 + Z_2)}, \quad \mathbf{I}_b = \mathbf{I}_c = 0 \quad (6.12)$$

We will keep both Z_1 and Z_2 in our formulas when convenient even though for transformers $Z_1 = Z_2$.

Using Equations 6.1, 6.4, and 6.9 through 6.11, we can also find the short-circuited phase voltages:

$$\begin{aligned} \mathbf{V}_a &= 0, \quad \mathbf{V}_b = -\frac{V_{pf}}{(Z_0 + Z_1 + Z_2)} \left[\left(\frac{3}{2} + j\frac{\sqrt{3}}{2} \right) Z_0 + j\sqrt{3}Z_2 \right] \\ \mathbf{V}_c &= -\frac{V_{pf}}{(Z_0 + Z_1 + Z_2)} \left[\left(\frac{3}{2} - j\frac{\sqrt{3}}{2} \right) Z_0 - j\sqrt{3}Z_2 \right] \end{aligned} \quad (6.13)$$

We can see that if all the sequence impedances were the same then, in magnitude, $V_b = V_c = V_{pf}$. However, their phases would differ.

6.2.3 Line-to-Line Fault

A line-to-line fault can be assumed, without loss of generality, to occur between lines b and c, as shown in [Figure 6.3c](#). The fault equations are

$$\mathbf{V}_b = \mathbf{V}_c, \quad \mathbf{I}_a = 0, \quad \mathbf{I}_c = -\mathbf{I}_b \quad (6.14)$$

From Equation 6.2 applied to voltages and currents, we get

$$\mathbf{V}_{a1} = \mathbf{V}_{a2}, \quad \mathbf{I}_{a0} = 0, \quad \mathbf{I}_{a2} = -\mathbf{I}_{a1} \quad (6.15)$$

Using Equations 6.4 and 6.15, we find

$$\mathbf{V}_{a0} = 0, \quad \mathbf{V}_{a1} = \mathbf{V}_{a2} = 0 = \mathbf{V}_{pf} - \mathbf{I}_{a1}(Z_1 + Z_2)$$

or

$$\mathbf{I}_{a1} = \frac{V_{pf}}{(Z_1 + Z_2)} = -\mathbf{I}_{a2}, \quad \mathbf{I}_{a0} = 0 \quad (6.16)$$

Using Equation 6.1 applied to currents, Equations 6.15 and 6.16, we get

$$\mathbf{I}_a = 0, \quad \mathbf{I}_c = \frac{j\sqrt{3}}{(Z_1 + Z_2)} V_{pf} = -\mathbf{I}_b \quad (6.17)$$

We can also determine the short-circuited phase voltages by the aforementioned methods.

$$\mathbf{V}_a = V_{\text{pf}} \left(\frac{2Z_2}{Z_1 + Z_2} \right), \quad \mathbf{V}_b = \mathbf{V}_c = -\frac{\mathbf{V}_a}{2} \quad (6.18)$$

The fault analysis does not involve the zero-sequence circuit, that is, there are no zero-sequence currents. The fault currents flow between the b and c phases. Also for transformers $Z_1 = Z_2$, so that $\mathbf{V}_a = V_{\text{pf}}$.

6.2.4 Double Line-to-Ground Fault

The double line-to-ground fault, as shown in [Figure 6.3d](#), can be regarded as involving lines b and c without loss of generality. The fault equations are

$$\mathbf{V}_b = \mathbf{V}_c = 0, \quad \mathbf{I}_a = 0 \quad (6.19)$$

From Equations 6.19 and 6.2, we find

$$\mathbf{V}_{a0} = \mathbf{V}_{a1} = \mathbf{V}_{a2} = \frac{\mathbf{V}_a}{3}, \quad \mathbf{I}_{a0} + \mathbf{I}_{a1} + \mathbf{I}_{a2} = 0 \quad (6.20)$$

Using Equations 6.4 and 6.20, we get

$$\mathbf{I}_{a0} + \mathbf{I}_{a1} + \mathbf{I}_{a2} = 0 = \frac{V_{\text{pf}}}{Z_1} - \mathbf{V}_{a1} \left(\frac{1}{Z_0} + \frac{1}{Z_1} + \frac{1}{Z_2} \right) \quad (6.21)$$

or

$$\mathbf{V}_{a1} = V_{\text{pf}} \left(\frac{Z_0 Z_2}{Z_0 Z_1 + Z_0 Z_2 + Z_1 Z_2} \right)$$

so that, from Equation 6.4:

$$\begin{aligned} \mathbf{I}_{a1} &= V_{\text{pf}} \left(\frac{Z_0 + Z_2}{Z_0 Z_1 + Z_0 Z_2 + Z_1 Z_2} \right) \\ \mathbf{I}_{a2} &= -V_{\text{pf}} \left(\frac{Z_0}{Z_0 Z_1 + Z_0 Z_2 + Z_1 Z_2} \right) \\ \mathbf{I}_{a0} &= -V_{\text{pf}} \left(\frac{Z_2}{Z_0 Z_1 + Z_0 Z_2 + Z_1 Z_2} \right) \end{aligned} \quad (6.22)$$

Substituting Equation 6.22 into Equation 6.1 applied to currents, we get

$$\begin{aligned} \mathbf{I}_a = 0, \quad \mathbf{I}_b = -V_{\text{pf}} \left[\frac{j\sqrt{3}Z_0 + \left(\frac{3}{2} + j\frac{\sqrt{3}}{2}\right)Z_2}{Z_0Z_1 + Z_0Z_2 + Z_1Z_2} \right] \\ \mathbf{I}_c = V_{\text{pf}} \left[\frac{j\sqrt{3}Z_0 - \left(\frac{3}{2} - j\frac{\sqrt{3}}{2}\right)Z_2}{Z_0Z_1 + Z_0Z_2 + Z_1Z_2} \right] \end{aligned} \quad (6.23)$$

Using Equations 6.1, 6.4, and 6.22, the fault-phase voltages are given by

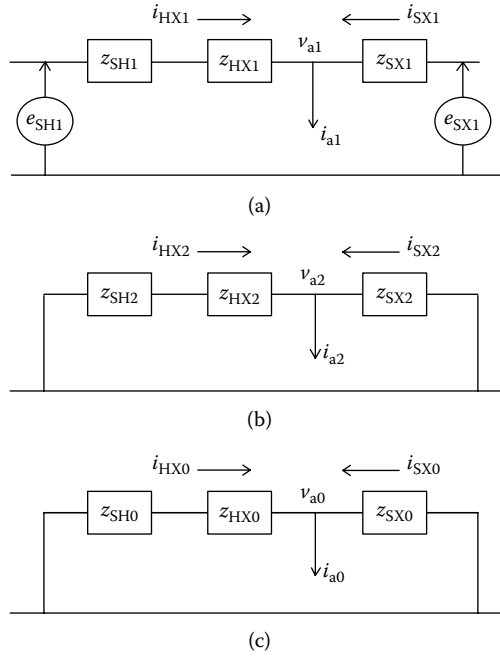
$$\mathbf{V}_a = V_{\text{pf}} \left(\frac{3Z_0Z_2}{Z_0Z_1 + Z_0Z_2 + Z_1Z_2} \right), \quad \mathbf{V}_b = \mathbf{V}_c = 0 \quad (6.24)$$

We see that if all the sequence impedances are equal, then $\mathbf{V}_a = V_{\text{pf}}$.

6.3 Fault Currents for Transformers with Two Terminals per Phase

A two-terminal transformer can be modeled by a single leakage reactance z_{HX} , where H and X indicate HV and LV terminals. All electrical quantities from this point on will be taken to mean per-unit quantities and will be written with small letters. This will enable us to better describe transformers, using a single circuit without the ideal transformer for each sequence.

The HV and LV systems external to the transformer are described by system impedances z_{SH} and z_{SX} and voltage sources e_{SH} and e_{SX} . In per-unit terms, the two voltage sources are the same. The resulting sequence circuit models are shown in Figure 6.4. Subscripts 0, 1, and 2 are used to label the sequence circuit parameters, since they can differ, although the positive and negative circuit parameters are equal for transformers but not necessarily for the systems. A fault on the X terminal is shown in Figure 6.4. The H terminal faults can be obtained by interchanging subscripts. In addition to the voltage source on the H system, we also see a voltage source attached to the X system. This can be a reasonable simulation of the actual system, or it can simply be regarded as a device for keeping the voltage v_{a1} at the fault point at the rated per-unit value. This also allows us to consider cases in which z_{SX} is small or zero in a limiting sense.

**FIGURE 6.4**

Sequence circuits for a fault on the low-voltage X terminal of a two-terminal per phase transformer, using per-unit quantities: (a) positive sequence, (b) negative sequence, and (c) zero sequence.

In order to use the previously developed general results, we need to compute the Thevenin impedances and pf voltage at the fault point. From Figure 6.4, we see that

$$z_1 = \frac{z_{SX1}(z_{HX1} + z_{SH1})}{z_{HX1} + z_{SH1} + z_{SX1}}, \quad z_2 = \frac{z_{SX2}(z_{HX2} + z_{SH2})}{z_{HX2} + z_{SH2} + z_{SX2}} \quad (6.25)$$

$$z_0 = \frac{z_{SX0}(z_{HX0} + z_{SH0})}{z_{HX0} + z_{SH0} + z_{SX0}}$$

and, since we are ignoring pf currents,

$$v_{pf} = e_{SH1} = 1 \quad (6.26)$$

where all the pf quantities are positive sequence. The pf voltage at the fault point will be taken as the rated voltage of the transformer and, in per-unit terms, is equal to one. Figure 6.4 and Equation 6.25 assume that both terminals are connected to the HV and LV systems. The system

beyond the fault point is not to be considered attached, then the Thevenin impedances become

$$z_1 = z_{HX1} + z_{SH1}, \quad z_2 = z_{HX2} + z_{SH2}, \quad z_0 = z_{HX0} + z_{SH0} \quad (6.27)$$

Using the computer, this can be accomplished by setting z_{SX1} , z_{SX2} , and z_{SX0} to large (i.e., open circuited) values in Equation 6.25. In this case, all the fault current flows through the transformer. Thus, considering the system not attached beyond the fault point amounts to assuming that the faulted terminal is open circuited before the fault occurs. In fact, the terminals associated with all three phases of the faulted terminal or terminals are open before the fault occurs. After the fault, one or more terminals are grounded or connected depending on the fault type. The other terminals, corresponding to the other phases, remain open when the system is not connected beyond the fault point.

The system impedances are sometimes set as zero. This increases the severity of the fault and is sometimes required for design purposes. It is not a problem mathematically for the system impedances on the nonfaulted terminal. However, with zero system impedances on the faulted terminal, Equation 6.25 shows that all the Thevenin impedances will equal zero, unless we consider the system not attached beyond the fault point and use Equation 6.27. Therefore, in this case, if we want to consider the system attached beyond the fault point, we must use very small system impedance values. Continuity is thereby assured when transitioning from rated system impedances to very small system impedances. Otherwise, a discontinuity may occur in the fault current calculation if one abruptly changes the circuit model from one with a system connected to one not connected beyond the fault point just because the system impedances become small.

Much simplification is achieved when the positive and negative system impedances are equal, if they are zero, or if they are small, since then $z_1 = z_2$ because $z_{HX1} = z_{HX2}$ for transformers. We will now calculate the sequence currents for a general case in which all the sequence impedances are different. We can then apply Equation 6.1, expressed in terms of currents, to determine the phase currents for the general case. However, in this last step, we assume that the positive and negative impedances are the same. This will simplify the formulas for the phase currents and is closer to the real situation for transformers.

To obtain the currents in the transformer during the fault, according to Figure 6.4 we need to find i_{HX1} , i_{HX2} , and i_{HX0} for the standard faults. Since i_{a1} , i_{a2} , and i_{a0} have already been obtained for the standard faults, we must find the transformer currents in terms of these known fault currents. From Figure 6.4, using Equation 6.26, we see that

$$\begin{aligned} v_{a1} &= v_{pf} - i_{HX1}(z_{HX1} + z_{SH1}), & v_{a2} &= -i_{HX2}(z_{HX2} + z_{SH2}) \\ v_{a0} &= -i_{HX0}(z_{HX0} + z_{SH0}) \end{aligned} \quad (6.28)$$

Substituting the per-unit version of Equations 6.4 into 6.28, we get

$$\begin{aligned} i_{\text{HX1}} &= i_{\text{a1}} \left(\frac{z_1}{z_{\text{HX1}} + z_{\text{SH1}}} \right), & i_{\text{HX2}} &= i_{\text{a2}} \left(\frac{z_2}{z_{\text{HX2}} + z_{\text{SH2}}} \right) \\ i_{\text{HX0}} &= i_{\text{a0}} \left(\frac{z_0}{z_{\text{HX0}} + z_{\text{SH0}}} \right) \end{aligned} \quad (6.29)$$

6.3.1 Three-Phase Line-to-Ground Fault

For this fault case, we substitute the per-unit version of Equations 6.7 into 6.29 to get

$$i_{\text{HX1}} = \frac{v_{\text{pf}}}{(z_{\text{HX1}} + z_{\text{SH1}})}, \quad i_{\text{HX2}} = i_{\text{HX0}} = 0 \quad (6.30)$$

Then, using Equation 6.1 applied to currents, we find

$$i_{\text{HXa}} = i_{\text{HX1}}, \quad i_{\text{HXb}} = \alpha^2 i_{\text{HX1}}, \quad i_{\text{HXc}} = \alpha i_{\text{HX1}} \quad (6.31)$$

that is, the fault currents in the transformer form a positive-sequence set as expected.

6.3.2 Single-Phase Line-to-Ground Fault

For this type of fault, we substitute the per-unit versions of Equation 6.11 into 6.29 to get

$$\begin{aligned} i_{\text{HX1}} &= \frac{v_{\text{pf}}}{(z_0 + z_1 + z_2)} \left(\frac{z_1}{(z_{\text{HX1}} + z_{\text{SH1}})} \right) \\ i_{\text{HX2}} &= \frac{v_{\text{pf}}}{(z_0 + z_1 + z_2)} \left(\frac{z_2}{(z_{\text{HX2}} + z_{\text{SH2}})} \right) \\ i_{\text{HX0}} &= \frac{v_{\text{pf}}}{(z_0 + z_1 + z_2)} \left(\frac{z_0}{(z_{\text{HX0}} + z_{\text{SH0}})} \right) \end{aligned} \quad (6.32)$$

If the system beyond the fault point is neglected, using Equation 6.27, Equation 6.32 can be written as

$$i_{\text{HX1}} = \frac{v_{\text{pf}}}{(z_0 + z_1 + z_2)} = i_{\text{HX2}} = i_{\text{HX0}} \quad (6.33)$$

Assuming the positive and negative system impedances are equal, as is the case for transformers or if they are small or zero, and substituting Equation 6.32 into 6.1 applied to currents, we obtain the phase currents

$$\begin{aligned} i_{\text{HXa}} &= \frac{v_{\text{pf}}}{(z_0 + 2z_1)} \left[\frac{z_0}{(z_{\text{HX0}} + z_{\text{SH0}})} + \frac{2z_1}{(z_{\text{HX1}} + z_{\text{SH1}})} \right] \\ i_{\text{HXb}} &= \frac{v_{\text{pf}}}{(z_0 + 2z_1)} \left[\frac{z_0}{(z_{\text{HX0}} + z_{\text{SH0}})} - \frac{z_1}{(z_{\text{HX1}} + z_{\text{SH1}})} \right] \\ i_{\text{HXc}} &= \frac{v_{\text{pf}}}{(z_0 + 2z_1)} \left[\frac{z_0}{(z_{\text{HX0}} + z_{\text{SH0}})} - \frac{z_1}{(z_{\text{HX1}} + z_{\text{SH1}})} \right] \end{aligned} \quad (6.34)$$

If we ignore the system beyond the fault point and substitute Equation 6.27 into 6.34, then

$$i_{\text{HXa}} = \frac{3v_{\text{pf}}}{(z_0 + 2z_1)}, \quad i_{\text{HXb}} = i_{\text{HXc}} = 0 \quad (6.35)$$

This is also seen more directly using Equations 6.33 and 6.1. This makes sense because, according to Equation 6.12, all of the fault current flows through the transformer and none is shared with the system side of the fault point.

If the system impedance beyond the fault point is not ignored, fault current occurs in phases b and c inside the transformer even though the fault is on phase a. These b and c fault currents are of a lower magnitude than the phase a fault current.

6.3.3 Line-to-Line Fault

For this type of fault, we substitute the per-unit versions of Equation 6.16 into 6.29 to get

$$\begin{aligned} i_{\text{HX1}} &= \frac{v_{\text{pf}}}{(z_{\text{HX1}} + z_{\text{SH1}})} \left(\frac{z_1}{z_1 + z_2} \right) \\ i_{\text{HX2}} &= -\frac{v_{\text{pf}}}{(z_{\text{HX2}} + z_{\text{SH2}})} \left(\frac{z_2}{z_1 + z_2} \right) \\ i_{\text{HX0}} &= 0 \end{aligned} \quad (6.36)$$

If we ignore the system beyond the fault point, this becomes

$$i_{\text{HX1}} = \frac{v_{\text{pf}}}{(z_1 + z_2)} = -i_{\text{HX2}}, \quad i_{\text{HX0}} = 0 \quad (6.37)$$

For the phase currents, using Equation 6.1 applied to currents and Equation 6.36 and assuming the positive and negative system impedances are equal or zero, we get

$$\begin{aligned} i_{\text{HXa}} &= 0 \\ i_{\text{HXb}} &= -j \frac{\sqrt{3}}{2} \frac{v_{\text{pf}}}{(z_{\text{HX1}} + z_{\text{SH1}})} \\ i_{\text{HXc}} &= j \frac{\sqrt{3}}{2} \frac{v_{\text{pf}}}{(z_{\text{HX1}} + z_{\text{SH1}})} \end{aligned} \quad (6.38)$$

If we ignore the system beyond the fault point, Equation 6.38 becomes

$$i_{\text{HXa}} = 0, \quad i_{\text{HXc}} = j\sqrt{3} \frac{v_{\text{pf}}}{2z_1} = -i_{\text{HXb}} \quad (6.39)$$

In this case, with the fault between phases b and c, phase a is unaffected. Also, as we saw from Equations 6.36 and 6.37, no zero-sequence currents are involved in this type of fault.

6.3.4 Double Line-to-Ground Fault

For this fault, we substitute Equation 6.22 expressed in per-unit terms into Equation 6.29:

$$\begin{aligned} i_{\text{HX1}} &= \frac{v_{\text{pf}}}{(z_{\text{HX1}} + z_{\text{SH1}})} \left(\frac{z_0 z_1 + z_1 z_2}{z_0 z_1 + z_0 z_2 + z_1 z_2} \right) \\ i_{\text{HX2}} &= -\frac{v_{\text{pf}}}{(z_{\text{HX2}} + z_{\text{SH2}})} \left(\frac{z_0 z_2}{z_0 z_1 + z_0 z_2 + z_1 z_2} \right) \\ i_{\text{HX0}} &= -\frac{v_{\text{pf}}}{(z_{\text{HX0}} + z_{\text{SH0}})} \left(\frac{z_0 z_2}{z_0 z_1 + z_0 z_2 + z_1 z_2} \right) \end{aligned} \quad (6.40)$$

If we ignore the system beyond the fault point, Equation 6.40 becomes

$$\begin{aligned} i_{\text{HX1}} &= v_{\text{pf}} \left(\frac{z_0 + z_2}{z_0 z_1 + z_0 z_2 + z_1 z_2} \right) \\ i_{\text{HX2}} &= -v_{\text{pf}} \left(\frac{z_0}{z_0 z_1 + z_0 z_2 + z_1 z_2} \right) \\ i_{\text{HX0}} &= -v_{\text{pf}} \left(\frac{z_2}{z_0 z_1 + z_0 z_2 + z_1 z_2} \right) \end{aligned} \quad (6.41)$$

Using Equation 6.1 applied to currents, and Equation 6.40 and assuming equal positive and negative system impedances or zero system impedances, we get for the phase currents

$$\begin{aligned} i_{\text{HXa}} &= \frac{v_{\text{pf}}}{(2z_0 + z_1)} \left[\frac{z_1}{(z_{\text{HX1}} + z_{\text{SH1}})} - \frac{z_0}{(z_{\text{HX0}} + z_{\text{SH0}})} \right] \\ i_{\text{HXb}} &= \frac{v_{\text{pf}}}{(2z_0 + z_1)} \left[\frac{\alpha^2 z_1 - j\sqrt{3}z_0}{(z_{\text{HX1}} + z_{\text{SH1}})} - \frac{z_0}{(z_{\text{HX0}} + z_{\text{SH0}})} \right] \\ i_{\text{HXc}} &= \frac{v_{\text{pf}}}{(2z_0 + z_1)} \left[\frac{\alpha z_1 + j\sqrt{3}z_0}{(z_{\text{HX1}} + z_{\text{SH1}})} - \frac{z_0}{(z_{\text{HX0}} + z_{\text{SH0}})} \right] \end{aligned} \quad (6.42)$$

If we ignore the system beyond the fault point, using Equations 6.27 and 6.41, Equation 6.42 becomes

$$\begin{aligned} i_{\text{HXa}} &= 0 \\ i_{\text{HXb}} &= -\frac{v_{\text{pf}}}{(2z_0 + z_1)} \left[\left(\frac{3}{2} + j\frac{\sqrt{3}}{2} \right) + j\sqrt{3} \frac{z_0}{z_1} \right] \\ i_{\text{HXc}} &= \frac{v_{\text{pf}}}{(2z_0 + z_1)} \left[\left(-\frac{3}{2} + j\frac{\sqrt{3}}{2} \right) + j\sqrt{3} \frac{z_0}{z_1} \right] \end{aligned} \quad (6.43)$$

6.3.5 Zero-Sequence Circuits

Zero-sequence circuits require special consideration because certain transformer three-phase connections, such as the delta connection, block the flow of zero-sequence currents at the terminals and hence provide an essentially infinite impedance to their passage; this is also true of the ungrounded Y connection. This occurs because the zero-sequence currents, which are all in phase, require a return path in order to flow. The delta connection provides an internal path for the flow of these currents, circulating around the delta, but blocks their flow through the external lines. These considerations do not apply to positive- or negative-sequence currents, which sum to zero vectorially and so require no return path.

For transformers, since the amp-turns must be balanced for each sequence, in order for zero-sequence currents to be present they must flow in both windings. For example in a grounded Y-delta unit, zero-sequence currents can flow within the transformer but cannot flow in the external circuit connected to the delta side. Similarly, zero-sequence currents cannot flow in either winding if one of them is an ungrounded Y.

Figure 6.5 shows some examples of zero-sequence circuit diagrams for different transformer connections. These can be compared with Figure 6.4c, which applies when both windings have grounded Y connections. Where a break in a line occurs in Figure 6.5, imagine that an infinite impedance is inserted. Mathematically, we should let the impedance approach infinity or a very large value as a limiting process in the formulas.

No zero-sequence current can flow into the terminals for the connection in Figure 6.5a because the fault is on the delta side terminals. The Thevenin impedance, looking in from the fault point, is $z_0 = z_{SX0}$. In this case, no zero-sequence current can flow in the transformer and only flows in the external circuit on the LV side.

We find for the connection in Figure 6.5b that $z_0 = z_{HX0}z_{SX0}/(z_{HX0} + z_{SX0})$, that is, the parallel combination of z_{HX0} and z_{SX0} . In this case, zero-sequence current flows in the transformer, but no zero-sequence current flows into the system impedance on the HV side.

In Figure 6.5c, because of the ungrounded Y connection, no zero-sequence current flows in the transformer. This is true regardless of which side of the transformer has an ungrounded Y connection. In Figure 6.5d, no zero-sequence current can flow into the transformer from the external circuit, and thus, no zero-sequence current flows in the transformer.

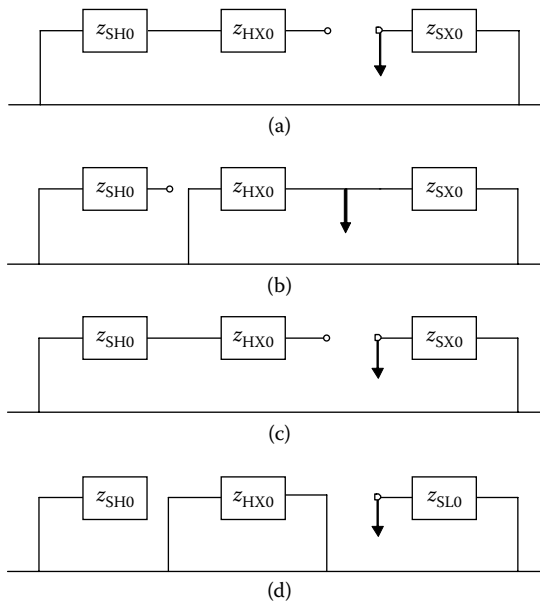


FIGURE 6.5

Some examples of zero-sequence impedance diagrams for two-terminal transformers: (a) Y_g/δ , (b) δ/Y_g , (c) Y_g/Y_u , and (d) δ/δ . The arrow indicates the fault point. Y_g = grounded Y, Y_u = ungrounded Y.

Another issue is the value of the zero-sequence impedances themselves when they are fully in the circuit. These values tend to differ from the positive-sequence impedances in transformers because the magnetic flux patterns associated with them can be quite different from the positive-sequence flux distribution. This difference is taken into account by multiplying factors that multiply the positive-sequence impedances to produce the zero-sequence values. For three-phase core form transformers, these multiplying factors tend to be ≈ 0.85 ; however, they can differ for different three-phase connections and are usually found by experimental measurements.

If there is an impedance between the neutral and ground, for example at a Y-connected neutral, then three times this impedance value should be added to the zero-sequence transformer impedance. This is because identical zero-sequence current flows in the neutral from all three phases, so in order to account for the single-phase voltage drop across the neutral impedance, its value must be increased by a factor of three in the single-phase circuit diagram.

6.3.6 Numerical Example for a Single Line-to-Ground Fault

As a numerical example, consider a single line-to-ground fault on the X terminal of a 24-MVA three-phase transformer. Assume that the H and X terminals have line-to-line voltages of 112 and 20 kV, respectively, and that they are connected to delta and grounded-Y windings. Let $z_{HX1} = 10\%$, $z_{HX0} = 8\%$, $z_{SH1} = z_{SX1} = 0.01\%$, $z_{SH0} = 0\%$, and $z_{SX0} = 0.02\%$. The system impedance on the HV side is set to zero because it is a delta winding. It is perhaps better to work in per-unit values by dividing these impedances by 100, however if we work with per-unit impedances in percentages, we must also set $v_{pf} = 100\%$, assuming that it has its rated value. This will give us fault currents per-unit (not percentages). Then, assuming the system is connected beyond the fault point, we get from Equation 6.25, $z_1 = 9.99 \times 10^{-3}\%$ and $z_2 = 1.995 \times 10^{-2}\%$. Solving for the currents from Equation 6.34, we get $i_{HXa} = 11.24$, $i_{HXb} = 3.746$, and $i_{HXc} = 3.746$. These currents are per-unit values and are not percentages. For a 45-MVA three-phase transformer with a HV delta-connected winding with a line-to-line voltage of 112 kV, the base MVA per phase is 15 and the base winding voltage is 112 kV. Thus, the base current is $(15/112) \times 10^3 = 133.9$ A. The fault currents on the HV side of the transformer are $I_{HXa} = 1505$ A, $I_{HXb} = 501.7$ A, and $I_{HXc} = 501.7$ A.

If we assume that the system is not connected beyond the fault point, then we get $z_1 = 10.01\%$ and $z_0 = 8\%$ from Equation 6.27, so that from Equation 6.35, we get $i_{HXa} = 10.71$ and $I_{HXa} = 1434$ A. The other phase currents are zero. This a-phase current is slightly lower than the a-phase current, assuming the system is connected beyond the fault point.

6.4 Fault Currents for Transformers with Three Terminals per Phase

A three-terminal transformer can be represented in terms of three single-winding impedances. Figure 6.6 shows the sequence circuits for such a transformer, where H, X, and Y label the transformer impedances and SH, SX, and SY label the associated system impedances. Per-unit quantities are shown in Figure 6.6. The systems are represented by impedances in series with voltage sources. The positive sense of the currents is into the transformer terminals. Although the fault is shown on the X-terminal, by interchanging subscripts, the formulas that follow can apply to faults on any terminal. We again label the sequence impedances with subscripts 0, 1, and 2, even though the positive- and negative-sequence impedances are equal for transformers. However, they are not necessarily equal for the systems. The zero-sequence

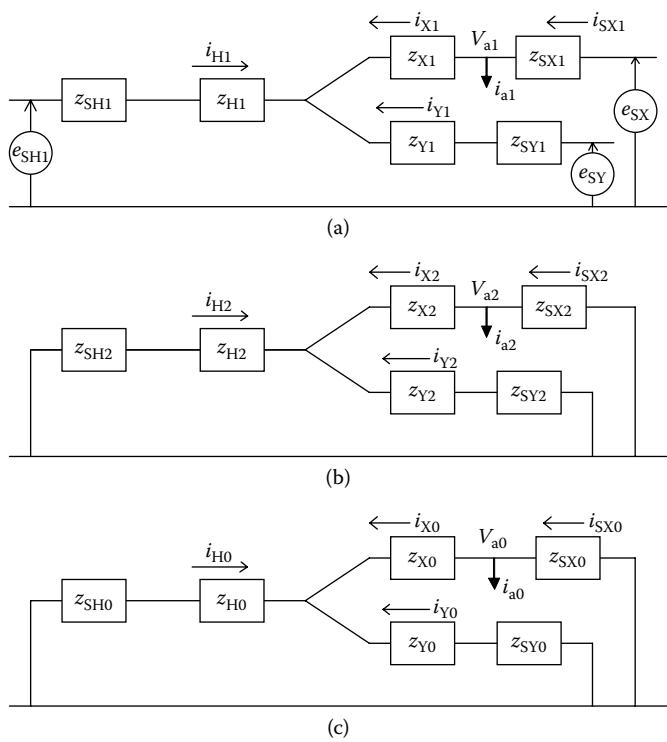


FIGURE 6.6 Sequence circuits for a fault on the X terminal of a three-terminal per phase transformer, using per-unit quantities: (a) positive-sequence circuit, (b) negative-sequence circuit, and (c) zero-sequence circuit.

impedances usually differ from their positive-sequence counterparts for transformers as well as for the systems.

We will calculate the sequence currents assuming possible unequal sequence impedances; however, we will calculate the phase currents assuming equal positive and negative system impedances. This is true for transformers and transmission lines. This is also true for cases in which small or zero system impedances are assumed, a situation that is often a requirement in fault analysis. Equation 6.1 can be applied to the sequence currents to get the phase currents.

From [Figure 6.6](#), looking into the circuits from the fault point, the Thevenin impedances are

$$\begin{aligned}
 z_1 &= \frac{z_{SX1}(z_{X1} + w_1)}{z_{X1} + z_{SX1} + w_1} & \text{where } w_1 &= \frac{(z_{H1} + z_{SH1})(z_{Y1} + z_{SY1})}{z_{H1} + z_{Y1} + z_{SH1} + z_{SY1}} \\
 z_2 &= \frac{z_{SX2}(z_{X2} + w_2)}{z_{X2} + z_{SX2} + w_2} & \text{where } w_2 &= \frac{(z_{H2} + z_{SH2})(z_{Y2} + z_{SY2})}{z_{H2} + z_{Y2} + z_{SH2} + z_{SY2}} \\
 z_0 &= \frac{z_{SX0}(z_{X0} + w_0)}{z_{X0} + z_{SX0} + w_0} & \text{where } w_0 &= \frac{(z_{H0} + z_{SH0})(z_{Y0} + z_{SY0})}{z_{H0} + z_{Y0} + z_{SH0} + z_{SY0}}
 \end{aligned} \tag{6.44}$$

If the system beyond the fault point is ignored, the Thevenin impedances become

$$z_1 = z_{X1} + w_1, \quad z_2 = z_{X2} + w_2, \quad z_0 = z_{X0} + w_0 \tag{6.45}$$

where the w 's remain the same. This amounts mathematically to set z_{SX1} , z_{SX2} , and z_{SX0} equal to large values. When the system impedances must be set to zero, then the system impedances must be set to small values if we wish to consider the system connected beyond the fault point, as was the case for two-terminal transformers.

At this point, we will consider some common transformer connections and conditions that require special consideration, including changes in some of the above impedances. For example, if one of the terminals is not loaded, this amounts to setting the system impedance for that terminal to a large value. The large value should be infinity, but since these calculations are usually performed on a computer, we just need to make it large when compared with the other impedances. If the unloaded terminal is the faulted terminal, this results in changing z_1 and z_2 to the values in Equation 6.45. In other words, it is equivalent to ignoring the system beyond the fault point. If the unloaded terminal is an unfaulted terminal, then w_1 and w_2 will be changed when z_{SH1} , z_{SH2} or z_{SY1} , z_{SY2} are set to large values. This amounts to having an open circuit replace that part of the positive or negative system circuit associated with the open terminal. If the open terminal connection is a Y connection, then the

zero-sequence system impedance should also be set to a large value and the zero-sequence circuit associated with the unloaded terminal becomes an open circuit and w_0 will change. However, if the open circuit is delta connected, as for a buried delta connection, then the zero-sequence system impedance should be set to zero. This will also change w_0 but only slightly, because zero-sequence currents can circulate in delta-connected windings even in an open terminal situation, whereas zero-sequence currents cannot flow in Y-connected windings if the terminals are unloaded.

Working in the per-unit system, the pf voltages are given by

$$v_{pf} = e_{SH1} = e_{SX1} = e_{SY1} = 1 \quad (6.46)$$

We ignore pf currents, which can always be added later. We assume all the pf voltages are equal to their rated values or to one in per-unit terms. We also have

$$i_H + i_X + i_Y = 0 \quad (6.47)$$

Equation 6.47 applies to all the sequence currents. From [Figure 6.6](#),

$$\begin{aligned} v_{a1} &= e_{SH1} - i_{H1}(z_{H1} + z_{SH1}) + i_{X1}z_{X1} = e_{SY1} - i_{Y1}(z_{Y1} + z_{SY1}) + i_{X1}z_{X1} \\ v_{a2} &= -i_{H2}(z_{H2} + z_{SH2}) + i_{X2}z_{X2} = -i_{Y2}(z_{Y2} + z_{SY2}) + i_{X2}z_{X2} \\ v_{a0} &= -i_{H0}(z_{H0} + z_{SH0}) + i_{X0}z_{X0} = -i_{Y0}(z_{Y0} + z_{SY0}) + i_{X0}z_{X0} \end{aligned} \quad (6.48)$$

Solving Equation 6.48, together with Equations 6.44, 6.46, 6.47, and 6.4 expressed in per-unit terms, we obtain the winding sequence currents in terms of the fault sequence currents:

$$\begin{aligned} i_{H1} &= i_{a1} \left(\frac{z_1}{z_{X1} + w_1} \right) \left(\frac{w_1}{z_{H1} + z_{SH1}} \right), \quad i_{H2} = i_{a2} \left(\frac{z_2}{z_{X2} + w_2} \right) \left(\frac{w_2}{z_{H2} + z_{SH2}} \right) \\ i_{H0} &= i_{a0} \left(\frac{z_0}{z_{X0} + w_0} \right) \left(\frac{w_0}{z_{H0} + z_{SH0}} \right) \\ i_{X1} &= -i_{a1} \left(\frac{z_1}{z_{X1} + w_1} \right), \quad i_{X2} = -i_{a2} \left(\frac{z_2}{z_{X2} + w_2} \right) \\ i_{X0} &= -i_{a0} \left(\frac{z_0}{z_{X0} + w_0} \right) \\ i_{Y1} &= i_{a1} \left(\frac{z_1}{z_{X1} + w_1} \right) \left(\frac{w_1}{z_{Y1} + z_{SY1}} \right), \quad i_{Y2} = i_{a2} \left(\frac{z_2}{z_{X2} + w_2} \right) \left(\frac{w_2}{z_{Y2} + z_{SY2}} \right) \\ i_{Y0} &= i_{a0} \left(\frac{z_0}{z_{X0} + w_0} \right) \left(\frac{w_0}{z_{Y0} + z_{SY0}} \right) \end{aligned} \quad (6.49)$$

For Equation 6.49, if we ignore the system beyond the fault point and use Equation 6.45, we get

$$\begin{aligned}
 i_{H1} &= i_{a1} \left(\frac{w_1}{z_{H1} + z_{SH1}} \right), & i_{H2} &= i_{a2} \left(\frac{w_2}{z_{H2} + z_{SH2}} \right), & i_{H0} &= i_{a0} \left(\frac{w_0}{z_{H0} + z_{SH0}} \right) \\
 i_{X1} &= -i_{a1}, & i_{X2} &= -i_{a2}, & i_{X0} &= -i_{a0} \\
 i_{Y1} &= i_{a1} \left(\frac{w_1}{z_{Y1} + z_{SY1}} \right), & i_{Y2} &= i_{a2} \left(\frac{w_2}{z_{Y2} + z_{SY2}} \right), & i_{Y0} &= i_{a0} \left(\frac{w_0}{z_{Y0} + z_{SY0}} \right)
 \end{aligned} \tag{6.50}$$

We will use these equations, together with the fault current equations, to obtain the currents in the transformer for the various types of fault. Equation 6.1 applied to currents may be used to obtain the phase currents in terms of the sequence currents.

6.4.1 Three-Phase Line-to-Ground Fault

For this type of fault, we substitute the per-unit version of Equations 6.7 into 6.49 to get

$$\begin{aligned}
 i_{H1} &= \frac{v_{pf}}{(z_{X1} + w_1)} \left(\frac{w_1}{z_{H1} + z_{SH1}} \right), & i_{H2} &= i_{H0} = 0 \\
 i_{X1} &= -\frac{v_{pf}}{(z_{X1} + w_1)}, & i_{X2} &= i_{X0} = 0 \\
 i_{Y1} &= \frac{v_{pf}}{(z_{X1} + w_1)} \left(\frac{w_1}{z_{Y1} + z_{SY1}} \right), & i_{Y2} &= i_{Y0} = 0
 \end{aligned} \tag{6.51}$$

If we ignore the system beyond the fault point, we get the same sequence equations as Equation 6.51. Thus, the system beyond the fault has no influence on three-phase fault currents. The phase currents corresponding to Equation 6.51 are

$$\begin{aligned}
 i_{Ha} &= \frac{v_{pf}}{(z_{X1} + w_1)} \left(\frac{w_1}{z_{H1} + z_{SH1}} \right), & i_{Hb} &= \alpha^2 i_{Ha}, & i_{Hc} &= \alpha i_{Ha} \\
 i_{Xa} &= -\frac{v_{pf}}{(z_{X1} + w_1)}, & i_{Xb} &= \alpha^2 i_{Xa}, & i_{Xc} &= \alpha i_{Xa} = 0 \\
 i_{Ya} &= \frac{v_{pf}}{(z_{X1} + w_1)} \left(\frac{w_1}{z_{Y1} + z_{SY1}} \right), & i_{Yb} &= \alpha^2 i_{Ya}, & i_{Yc} &= \alpha i_{Ya} = 0
 \end{aligned} \tag{6.52}$$

These form a positive-sequence set as expected for a three-phase fault.

6.4.2 Single-Phase Line-to-Ground Fault

For this fault, we substitute the per-unit version of Equation 6.11 into Equation 6.49 to get

$$\begin{aligned}
 i_{H1} &= \frac{v_{pf}}{(z_0 + z_1 + z_2)} \left(\frac{z_1}{z_{X1} + w_1} \right) \left(\frac{w_1}{z_{H1} + z_{SH1}} \right) \\
 i_{H2} &= \frac{v_{pf}}{(z_0 + z_1 + z_2)} \left(\frac{z_2}{z_{X2} + w_2} \right) \left(\frac{w_2}{z_{H2} + z_{SH2}} \right) \\
 i_{H0} &= \frac{v_{pf}}{(z_0 + z_1 + z_2)} \left(\frac{z_0}{z_{X0} + w_0} \right) \left(\frac{w_0}{z_{H0} + z_{SH0}} \right) \\
 i_{X1} &= -\frac{v_{pf}}{(z_0 + z_1 + z_2)} \left(\frac{z_1}{z_{X1} + w_1} \right) \\
 i_{X2} &= -\frac{v_{pf}}{(z_0 + z_1 + z_2)} \left(\frac{z_2}{z_{X2} + w_2} \right) \\
 i_{X0} &= -\frac{v_{pf}}{(z_0 + z_1 + z_2)} \left(\frac{z_0}{z_{X0} + w_0} \right) \\
 i_{Y1} &= \frac{v_{pf}}{(z_0 + z_1 + z_2)} \left(\frac{z_1}{z_{X1} + w_1} \right) \left(\frac{w_1}{z_{Y1} + z_{SY1}} \right) \\
 i_{Y2} &= \frac{v_{pf}}{(z_0 + z_1 + z_2)} \left(\frac{z_2}{z_{X2} + w_2} \right) \left(\frac{w_2}{z_{Y2} + z_{SY2}} \right) \\
 i_{Y0} &= \frac{v_{pf}}{(z_0 + z_1 + z_2)} \left(\frac{z_0}{z_{X0} + w_0} \right) \left(\frac{w_0}{z_{Y0} + z_{SY0}} \right)
 \end{aligned} \tag{6.53}$$

We can simplify these equations by omitting the second term on the right side of Equation 6.53, if the system beyond the fault point is ignored:

$$\begin{aligned}
 i_{H1} &= \frac{v_{pf}}{(z_0 + z_1 + z_2)} \left(\frac{w_1}{z_{H1} + z_{SH1}} \right) \\
 i_{H2} &= \frac{v_{pf}}{(z_0 + z_1 + z_2)} \left(\frac{w_2}{z_{H2} + z_{SH2}} \right) \\
 i_{H0} &= \frac{v_{pf}}{(z_0 + z_1 + z_2)} \left(\frac{w_0}{z_{H0} + z_{SH0}} \right) \\
 i_{X1} &= -\frac{v_{pf}}{(z_0 + z_1 + z_2)} = i_{X2} = i_{X0}
 \end{aligned}$$

$$\begin{aligned}
i_{Y1} &= \frac{v_{pf}}{(z_0 + z_1 + z_2)} \left(\frac{w_1}{z_{Y1} + z_{SY1}} \right) \\
i_{Y2} &= \frac{v_{pf}}{(z_0 + z_1 + z_2)} \left(\frac{w_2}{z_{Y2} + z_{SY2}} \right) \\
i_{Y0} &= \frac{v_{pf}}{(z_0 + z_1 + z_2)} \left(\frac{w_0}{z_{Y0} + z_{SY0}} \right)
\end{aligned} \tag{6.54}$$

Using the per-unit version of Equation 6.1 and assuming equal positive and negative system impedances, we can obtain the phase currents from Equation 6.53:

$$\begin{aligned}
i_{Ha} &= \frac{v_{pf}}{(z_0 + 2z_1)} \left[2 \left(\frac{z_1}{z_{X1} + w_1} \right) \left(\frac{w_1}{z_{H1} + z_{SH1}} \right) + \left(\frac{z_0}{z_{X0} + w_0} \right) \left(\frac{w_0}{z_{H0} + z_{SH0}} \right) \right] \\
i_{Hb} &= \frac{v_{pf}}{(z_0 + 2z_1)} \left[- \left(\frac{z_1}{z_{X1} + w_1} \right) \left(\frac{w_1}{z_{H1} + z_{SH1}} \right) + \left(\frac{z_0}{z_{X0} + w_0} \right) \left(\frac{w_0}{z_{H0} + z_{SH0}} \right) \right] \\
i_{Hc} &= \frac{v_{pf}}{(z_0 + 2z_1)} \left[- \left(\frac{z_1}{z_{X1} + w_1} \right) \left(\frac{w_1}{z_{H1} + z_{SH1}} \right) + \left(\frac{z_0}{z_{X0} + w_0} \right) \left(\frac{w_0}{z_{H0} + z_{SH0}} \right) \right] \\
i_{Xa} &= - \frac{v_{pf}}{(z_0 + 2z_1)} \left[2 \left(\frac{z_1}{z_{X1} + w_1} \right) + \left(\frac{z_0}{z_{X0} + w_0} \right) \right] \\
i_{Xb} &= - \frac{v_{pf}}{(z_0 + 2z_1)} \left[- \left(\frac{z_1}{z_{X1} + w_1} \right) + \left(\frac{z_0}{z_{X0} + w_0} \right) \right] \\
i_{Xc} &= - \frac{v_{pf}}{(z_0 + 2z_1)} \left[- \left(\frac{z_1}{z_{X1} + w_1} \right) + \left(\frac{z_0}{z_{X0} + w_0} \right) \right] \\
i_{Ya} &= \frac{v_{pf}}{(z_0 + 2z_1)} \left[2 \left(\frac{z_1}{z_{X1} + w_1} \right) \left(\frac{w_1}{z_{Y1} + z_{SY1}} \right) + \left(\frac{z_0}{z_{X0} + w_0} \right) \left(\frac{w_0}{z_{Y0} + z_{SY0}} \right) \right] \\
i_{Yb} &= \frac{v_{pf}}{(z_0 + 2z_1)} \left[- \left(\frac{z_1}{z_{X1} + w_1} \right) \left(\frac{w_1}{z_{Y1} + z_{SY1}} \right) + \left(\frac{z_0}{z_{X0} + w_0} \right) \left(\frac{w_0}{z_{Y0} + z_{SY0}} \right) \right] \\
i_{Yc} &= \frac{v_{pf}}{(z_0 + 2z_1)} \left[- \left(\frac{z_1}{z_{X1} + w_1} \right) \left(\frac{w_1}{z_{Y1} + z_{SY1}} \right) + \left(\frac{z_0}{z_{X0} + w_0} \right) \left(\frac{w_0}{z_{Y0} + z_{SY0}} \right) \right]
\end{aligned} \tag{6.55}$$

We have used the fact that $\alpha^2 + \alpha = -1$, along with $w_1 = w_2$ and $z_1 = z_2$ to get Equation 6.55.

For cases in which the system beyond the fault point is ignored, again, restricting ourselves to the case where the positive- and negative-sequence impedances are equal, using Equation 6.54, the phase currents are given by

$$\begin{aligned}
i_{Ha} &= \frac{v_{pf}}{(z_0 + 2z_1)} \left(\frac{2w_1}{z_{H1} + z_{SH1}} + \frac{w_0}{z_{H0} + z_{SH0}} \right) \\
i_{Hb} &= \frac{v_{pf}}{(z_0 + 2z_1)} \left(-\frac{w_1}{z_{H1} + z_{SH1}} + \frac{w_0}{z_{H0} + z_{SH0}} \right) \\
i_{Hc} &= \frac{v_{pf}}{(z_0 + 2z_1)} \left(-\frac{w_1}{z_{H1} + z_{SH1}} + \frac{w_0}{z_{H0} + z_{SH0}} \right) \\
i_{xa} &= -\frac{3v_{pf}}{(z_0 + 2z_1)}, \quad i_{xb} = 0, \quad i_{xc} = 0 \\
i_{Ya} &= \frac{v_{pf}}{(z_0 + 2z_1)} \left(\frac{2w_1}{z_{Y1} + z_{SY1}} + \frac{w_0}{z_{Y0} + z_{SY0}} \right) \\
i_{Yb} &= \frac{v_{pf}}{(z_0 + 2z_1)} \left(-\frac{w_1}{z_{Y1} + z_{SY1}} + \frac{w_0}{z_{Y0} + z_{SY0}} \right) \\
i_{Yc} &= \frac{v_{pf}}{(z_0 + 2z_1)} \left(-\frac{w_1}{z_{Y1} + z_{SY1}} + \frac{w_0}{z_{Y0} + z_{SY0}} \right)
\end{aligned} \tag{6.56}$$

6.4.3 Line-to-Line Fault

For this fault condition, we substitute the per-unit version of Equation 6.16 into 6.49 to get

$$\begin{aligned}
i_{H1} &= \frac{v_{pf}}{(z_1 + z_2)} \left(\frac{z_1}{z_{X1} + w_1} \right) \left(\frac{w_1}{z_{H1} + z_{SH1}} \right) \\
i_{H2} &= -\frac{v_{pf}}{(z_1 + z_2)} \left(\frac{z_2}{z_{X2} + w_2} \right) \left(\frac{w_2}{z_{H2} + z_{SH2}} \right) \\
i_{H0} &= 0 \\
i_{X1} &= -\frac{v_{pf}}{(z_1 + z_2)} \left(\frac{z_1}{z_{X1} + w_1} \right) \\
i_{X2} &= \frac{v_{pf}}{(z_1 + z_2)} \left(\frac{z_2}{z_{X2} + w_2} \right) \\
i_{X0} &= 0 \\
i_{Y1} &= \frac{v_{pf}}{(z_1 + z_2)} \left(\frac{z_1}{z_{X1} + w_1} \right) \left(\frac{w_1}{z_{Y1} + z_{SY1}} \right) \\
i_{Y2} &= -\frac{v_{pf}}{(z_1 + z_2)} \left(\frac{z_2}{z_{X2} + w_2} \right) \left(\frac{w_2}{z_{Y2} + z_{SY2}} \right) \\
i_{Y0} &= 0
\end{aligned} \tag{6.57}$$

If we ignore the system beyond the fault point, Equation 6.57 becomes

$$\begin{aligned}
 i_{H1} &= \frac{v_{pf}}{(z_1 + z_2)} \left(\frac{w_1}{z_{H1} + z_{SH1}} \right) \\
 i_{H2} &= -\frac{v_{pf}}{(z_1 + z_2)} \left(\frac{w_2}{z_{H2} + z_{SH2}} \right) \\
 i_{H0} &= 0 \\
 i_{X1} &= -\frac{v_{pf}}{(z_1 + z_2)}, \quad i_{X2} = \frac{v_{pf}}{(z_1 + z_2)}, \quad i_{X0} = 0 \\
 i_{Y1} &= \frac{v_{pf}}{(z_1 + z_2)} \left(\frac{w_1}{z_{Y1} + z_{SY1}} \right) \\
 i_{Y2} &= -\frac{v_{pf}}{(z_1 + z_2)} \left(\frac{w_2}{z_{Y2} + z_{SY2}} \right) \\
 i_{Y0} &= 0
 \end{aligned} \tag{6.58}$$

Assuming equal positive and negative system impedances and using the per-unit version of Equation 6.1, we can obtain the phase currents from Equation 6.57:

$$\begin{aligned}
 i_{Ha} &= 0, \quad i_{Hb} = -j \frac{\sqrt{3}}{2} \frac{v_{pf}}{(z_{X1} + w_1)} \left(\frac{w_1}{z_{H1} + z_{SH1}} \right) = -i_{Hc} \\
 i_{Xa} &= 0, \quad i_{Xb} = j \frac{\sqrt{3}}{2} \frac{v_{pf}}{(z_{X1} + w_1)} = -i_{Xc} \\
 i_{Ya} &= 0, \quad i_{Yb} = -j \frac{\sqrt{3}}{2} \frac{v_{pf}}{(z_{X1} + w_1)} \left(\frac{w_1}{z_{Y1} + z_{SY1}} \right) = -i_{Yc}
 \end{aligned} \tag{6.59}$$

For cases in which we ignore the system beyond the fault point, we can obtain the phase currents from Equation 6.58:

$$\begin{aligned}
 i_{Ha} &= 0, \quad i_{Hb} = -j \frac{\sqrt{3}}{2} \frac{v_{pf}}{z_1} \left(\frac{w_1}{z_{H1} + z_{SH1}} \right) = -i_{Hc} \\
 i_{Xa} &= 0, \quad i_{Xb} = j \frac{\sqrt{3}}{2} \frac{v_{pf}}{z_1} = -i_{Xc} \\
 i_{Ya} &= 0, \quad i_{Yb} = -j \frac{\sqrt{3}}{2} \frac{v_{pf}}{z_1} \left(\frac{w_1}{z_{Y1} + z_{SY1}} \right) = -i_{Yc}
 \end{aligned} \tag{6.60}$$

6.4.4 Double Line-to-Ground Fault

For this fault, we substitute the per-unit version of Equation 6.22 into 6.49, to get

$$\begin{aligned}
 i_{H1} &= v_{\text{pf}} \left(\frac{z_0 + z_2}{\Delta} \right) \left(\frac{z_1}{z_{X1} + w_1} \right) \left(\frac{w_1}{z_{H1} + z_{SH1}} \right) \\
 i_{H2} &= -v_{\text{pf}} \left(\frac{z_0}{\Delta} \right) \left(\frac{z_2}{z_{X2} + w_2} \right) \left(\frac{w_2}{z_{H2} + z_{SH2}} \right) \\
 i_{H0} &= -v_{\text{pf}} \left(\frac{z_2}{\Delta} \right) \left(\frac{z_0}{z_{X0} + w_0} \right) \left(\frac{w_0}{z_{H0} + z_{SH0}} \right) \\
 i_{X1} &= -v_{\text{pf}} \left(\frac{z_0 + z_2}{\Delta} \right) \left(\frac{z_1}{z_{X1} + w_1} \right) \\
 i_{X2} &= v_{\text{pf}} \left(\frac{z_0}{\Delta} \right) \left(\frac{z_2}{z_{X2} + w_2} \right) \\
 i_{X0} &= v_{\text{pf}} \left(\frac{z_2}{\Delta} \right) \left(\frac{z_0}{z_{X0} + w_0} \right) \\
 i_{Y1} &= v_{\text{pf}} \left(\frac{z_0 + z_2}{\Delta} \right) \left(\frac{z_1}{z_{X1} + w_1} \right) \left(\frac{w_1}{z_{Y1} + z_{SY1}} \right) \\
 i_{Y2} &= -v_{\text{pf}} \left(\frac{z_0}{\Delta} \right) \left(\frac{z_2}{z_{X2} + w_2} \right) \left(\frac{w_2}{z_{Y2} + z_{SY2}} \right) \\
 i_{Y0} &= -v_{\text{pf}} \left(\frac{z_2}{\Delta} \right) \left(\frac{z_0}{z_{X0} + w_0} \right) \left(\frac{w_0}{z_{Y0} + z_{SY0}} \right)
 \end{aligned} \tag{6.61}$$

where $\Delta = z_0 z_1 + z_0 z_2 + z_1 z_2$.

For the system not attached beyond the fault point, by using Equation 6.45, Equation 6.61 becomes

$$\begin{aligned}
 i_{H1} &= v_{\text{pf}} \left(\frac{z_0 + z_2}{\Delta} \right) \left(\frac{w_1}{z_{H1} + z_{SH1}} \right) \\
 i_{H2} &= -v_{\text{pf}} \left(\frac{z_0}{\Delta} \right) \left(\frac{w_2}{z_{H2} + z_{SH2}} \right) \\
 i_{H0} &= -v_{\text{pf}} \left(\frac{z_2}{\Delta} \right) \left(\frac{w_0}{z_{H0} + z_{SH0}} \right) \\
 i_{X1} &= -v_{\text{pf}} \left(\frac{z_0 + z_2}{\Delta} \right), \quad i_{X2} = v_{\text{pf}} \left(\frac{z_0}{\Delta} \right), \quad i_{X0} = v_{\text{pf}} \left(\frac{z_2}{\Delta} \right)
 \end{aligned}$$

$$\begin{aligned}
i_{Y1} &= v_{pf} \left(\frac{z_0 + z_2}{\Delta} \right) \left(\frac{w_1}{z_{Y1} + z_{SY1}} \right) \\
i_{Y2} &= -v_{pf} \left(\frac{z_0}{\Delta} \right) \left(\frac{w_2}{z_{Y2} + z_{SY2}} \right) \\
i_{Y0} &= -v_{pf} \left(\frac{z_2}{\Delta} \right) \left(\frac{w_0}{z_{Y0} + z_{SY0}} \right)
\end{aligned} \tag{6.62}$$

For cases in which the system is connected beyond the fault point and we assume equal positive- and negative-sequence impedances, we obtain the phase currents from Equations 6.61 and 6.1 applied to currents:

$$\begin{aligned}
i_{Ha} &= \frac{v_{pf}}{2z_0 + z_1} \left[\left(\frac{z_1}{z_{X1} + w_1} \right) \left(\frac{w_1}{z_{H1} + z_{SH1}} \right) - \left(\frac{z_0}{z_{X0} + w_0} \right) \left(\frac{w_0}{z_{H0} + z_{SH0}} \right) \right] \\
i_{Hb} &= \frac{v_{pf}}{2z_0 + z_1} \left[\left(\alpha^2 - j\sqrt{3} \frac{z_0}{z_1} \right) \left(\frac{z_1}{z_{X1} + w_1} \right) \left(\frac{w_1}{z_{H1} + z_{SH1}} \right) - \left(\frac{z_0}{z_{X0} + w_0} \right) \left(\frac{w_0}{z_{H0} + z_{SH0}} \right) \right] \\
i_{Hc} &= \frac{v_{pf}}{2z_0 + z_1} \left[\left(\alpha + j\sqrt{3} \frac{z_0}{z_1} \right) \left(\frac{z_1}{z_{X1} + w_1} \right) \left(\frac{w_1}{z_{H1} + z_{SH1}} \right) - \left(\frac{z_0}{z_{X0} + w_0} \right) \left(\frac{w_0}{z_{H0} + z_{SH0}} \right) \right] \\
i_{Xa} &= -\frac{v_{pf}}{2z_0 + z_1} \left[\left(\frac{z_1}{z_{X1} + w_1} \right) - \left(\frac{z_0}{z_{X0} + w_0} \right) \right] \\
i_{Xb} &= -\frac{v_{pf}}{2z_0 + z_1} \left[\left(\alpha^2 - j\sqrt{3} \frac{z_0}{z_1} \right) \left(\frac{z_1}{z_{X1} + w_1} \right) - \left(\frac{z_0}{z_{X0} + w_0} \right) \right] \\
i_{Xc} &= -\frac{v_{pf}}{2z_0 + z_1} \left[\left(\alpha + j\sqrt{3} \frac{z_0}{z_1} \right) \left(\frac{z_1}{z_{X1} + w_1} \right) - \left(\frac{z_0}{z_{X0} + w_0} \right) \right] \\
i_{Ya} &= \frac{v_{pf}}{2z_0 + z_1} \left[\left(\frac{z_1}{z_{X1} + w_1} \right) \left(\frac{w_1}{z_{Y1} + z_{SY1}} \right) - \left(\frac{z_0}{z_{X0} + w_0} \right) \left(\frac{w_0}{z_{Y0} + z_{SY0}} \right) \right] \\
i_{Yb} &= \frac{v_{pf}}{2z_0 + z_1} \left[\left(\alpha^2 - j\sqrt{3} \frac{z_0}{z_1} \right) \left(\frac{z_1}{z_{X1} + w_1} \right) \left(\frac{w_1}{z_{Y1} + z_{SY1}} \right) - \left(\frac{z_0}{z_{X0} + w_0} \right) \left(\frac{w_0}{z_{Y0} + z_{SY0}} \right) \right] \\
i_{Yc} &= \frac{v_{pf}}{2z_0 + z_1} \left[\left(\alpha + j\sqrt{3} \frac{z_0}{z_1} \right) \left(\frac{z_1}{z_{X1} + w_1} \right) \left(\frac{w_1}{z_{Y1} + z_{SY1}} \right) - \left(\frac{z_0}{z_{X0} + w_0} \right) \left(\frac{w_0}{z_{Y0} + z_{SY0}} \right) \right]
\end{aligned} \tag{6.63}$$

For cases in which the system is not connected beyond the fault point, Equation 6.63 becomes, using Equation 6.45,

$$\begin{aligned}
i_{Ha} &= \frac{v_{pf}}{2z_0 + z_1} \left[\left(\frac{w_1}{z_{H1} + z_{SH1}} \right) - \left(\frac{w_0}{z_{H0} + z_{SH0}} \right) \right] \\
i_{Hb} &= \frac{v_{pf}}{2z_0 + z_1} \left[\left(\alpha^2 - j\sqrt{3} \frac{z_0}{z_1} \right) \left(\frac{w_1}{z_{H1} + z_{SH1}} \right) - \left(\frac{w_0}{z_{H0} + z_{SH0}} \right) \right]
\end{aligned}$$

$$\begin{aligned}
i_{Hc} &= \frac{v_{pf}}{2z_0 + z_1} \left[\left(\alpha + j\sqrt{3} \frac{z_0}{z_1} \right) \left(\frac{w_1}{z_{H1} + z_{SH1}} \right) - \left(\frac{w_0}{z_{H0} + z_{SH0}} \right) \right] \\
i_{Xa} &= 0 \\
i_{Xb} &= -\frac{v_{pf}}{2z_0 + z_1} \left[\left(\alpha^2 - j\sqrt{3} \frac{z_0}{z_1} \right) - 1 \right] \\
i_{Xc} &= -\frac{v_{pf}}{2z_0 + z_1} \left[\left(\alpha + j\sqrt{3} \frac{z_0}{z_1} \right) - 1 \right] \\
i_{Ya} &= \frac{v_{pf}}{2z_0 + z_1} \left[\left(\frac{w_1}{z_{Y1} + z_{SY1}} \right) - \left(\frac{w_0}{z_{Y0} + z_{SY0}} \right) \right] \\
i_{Yb} &= \frac{v_{pf}}{2z_0 + z_1} \left[\left(\alpha^2 - j\sqrt{3} \frac{z_0}{z_1} \right) \left(\frac{w_1}{z_{Y1} + z_{SY1}} \right) - \left(\frac{w_0}{z_{Y0} + z_{SY0}} \right) \right] \\
i_{Yc} &= \frac{v_{pf}}{2z_0 + z_1} \left[\left(\alpha + j\sqrt{3} \frac{z_0}{z_1} \right) \left(\frac{w_1}{z_{Y1} + z_{SY1}} \right) - \left(\frac{w_0}{z_{Y0} + z_{SY0}} \right) \right]
\end{aligned} \tag{6.64}$$

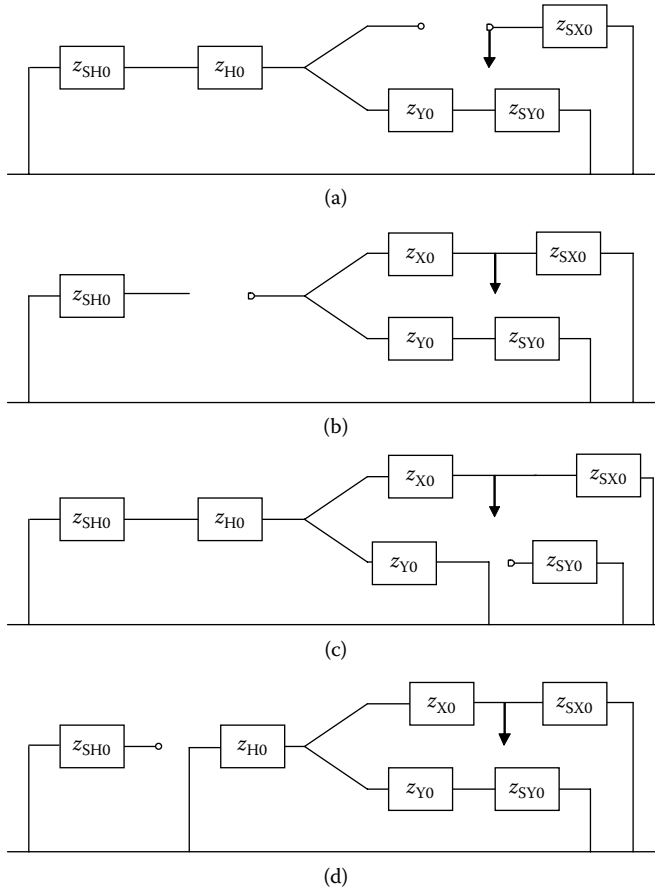
6.4.5 Zero-Sequence Circuits

Figure 6.7 lists some examples of zero-sequence circuits for three-terminal transformers. An infinite impedance is represented by a break in the circuit. When substituting into the preceding formulas, a large-enough value must be used. Although there are many more possibilities than are shown in Figure 6.7, those shown can serve to illustrate the method of accounting for the different three-phase connections. The zero-sequence circuit in Figure 6.6c represents a transformer with all grounded Y terminal connections.

In Figure 6.7a, we have $z_{X0} \rightarrow \infty$, so that no zero-sequence current flows into the transformer. This can also be seen in Equation 6.49. In Figure 6.7b, we see that $z_{H0} \rightarrow \infty$ since no zero-sequence current flows into an ungrounded Y winding. This implies that $w_0 = z_{Y0} + z_{SY0}$, that is, the parallel combination of the H and Y impedances is replaced by the Y impedances. In Figure 6.7c, no zero-sequence current flows into or out of the terminals of a delta winding, so the delta terminal system impedance must be set to zero. This allows the current to circulate within the delta. In Figure 6.7d, we see that zero-sequence current flows in all the windings but not out of the HV delta winding terminals. We just need to set $z_{SH0} = 0$ in all the formulas, and this only affects w_0 .

6.4.6 Numerical Examples

At this point, we will calculate the fault currents for a single line-to-ground fault on the X terminal. This is a common type of fault. Consider a grounded-Y (H), grounded-Y (X), and buried-delta (Y) transformer, which has a three-phase MVA = 45 (15 MVA/phase). The line-to-line terminal voltages are

**FIGURE 6.7**

Some examples of zero-sequence circuit diagrams for three-terminal transformers. The arrow indicates the fault point. (a) $Y_g/Y_u/Y_g$, (b) $Y_u/Y_g/Y_g$, (c) $Y_g/Y_g/\Delta$, and (d) $\Delta/Y_g/Y_g \cdot Y_g =$ grounded Y , $Y_u =$ ungrounded Y .

H: 125 kV, X: 20 kV, Y: 10 kV. The base winding currents are therefore: $I_{bH} = 15/72.17 \times 10^3 = 207.8$ A, $I_{bX} = 15/11.55 \times 10^3 = 1299$ A, and $I_{bY} = 15/10 \times 10^3 = 1500$ A. The winding-to-winding leakage reactances are given in [Table 6.1](#).

From these, we calculate the single-winding leakage reactances as

$$z_H = \frac{1}{2}(z_{HX} + z_{HY} - z_{XY}) = 11\%$$

$$z_X = \frac{1}{2}(z_{HX} + z_{XY} - z_{HY}) = 1\%$$

TABLE 6.1Leakage Reactances for a Y_g, Y_g , Delta Transformer

Winding 1	Winding 2	Positive/Negative Leakage Reactance (%)		Zero-Sequence Leakage Reactance (%)	
H	X	12	z_{HX}	10.2	z_{HX0}
H	Y	25	z_{HY}	21.25	z_{HY0}
X	Y	15	z_{XY}	12.75	z_{XY0}

$$z_Y = \frac{1}{2}(z_{HY} + z_{XY} - z_{HX}) = 14\%$$

$$z_{H0} = \frac{1}{2}(z_{HX0} + z_{HY0} - z_{XY0}) = 9.35\%$$

$$z_{X0} = \frac{1}{2}(z_{HX0} + z_{XY0} - z_{HY0}) = 0.85\%$$

$$z_{Y0} = \frac{1}{2}(z_{HY0} + z_{XY0} - z_{HX0}) = 16.4\%$$

We drop the subscript 1 in these calculations for the positive/negative reactances. We assume that the zero-sequence reactances are 0.85 times the positive/negative reactances. This factor can vary with the winding connection and other factors and is usually determined by experience. The zero-sequence reactances can also be measured.

Because the Y winding is a buried delta, no positive- or negative-sequence currents can flow into the terminals of this winding. Therefore, it is necessary to set z_{SY} to a large value in the formulas. Zero-sequence current can circulate around the delta so z_{SY0} is set to zero.

We do not want to consider system impedances in our calculations. However, if the system is connected beyond the fault point, we need to set the system impedances to very small values. Considering a system not attached beyond the fault point amounts to having the faulted terminal unloaded before the fault occurs. We will perform the calculation both ways.

We will assume system impedances of

$$z_{SH} = z_{SX} = 0.001\%, \quad z_{SY} = 1,000,000\%$$

$$z_{SH0} = z_{SX0} = 0.002\%, \quad z_{SY0} = 0\%$$

Again, the large value for z_{SY} and zero value for z_{SY0} are necessary because it is a buried delta. We assume here that the system zero-sequence reactances are a factor of two times the system positive-or negative-sequence reactances. This is a reasonable assumption for transmission lines because these constitute a major part of the system [Ste62a]. Using these values, from Equation 6.44, we get

$w_1 = 11.00088\%, \quad w_0 = 5.23663\%$

For the system connected beyond the fault point, from Equation 6.44, we get

$z_1 = 0.001\%, \quad z_0 = 0.002\%$

and for the system not connected beyond the fault point, from Equation 6.45, we get

$z_1 = 12.00088\%, \quad z_0 = 6.08663\%$

Using these values, along with the impedances in Table 6.1, we can calculate the per-unit phase and phase currents in the transformer from Equations 6.53 through 6.56 for the two cases. Since we are working with percentages, we must set $v_{pf} = 100\%$. These currents are given in Table 6.2 for the two cases.

The per-unit values in the Table 6.2 are not percentages. They should sum to zero for each phase. These values would differ somewhat if different multiplying factors were used to get the zero-sequence winding impedances

TABLE 6.2
Per-Unit and Phase Currents Compared for System Connected or Not Connected Beyond the Fault Point and Small System Impedances

	Phase A	Phase B	Phase C
<i>System connected beyond fault</i>			
Per-unit currents			
H	8.766	2.516	2.516
X	−12.380	−6.130	−6.130
Y	3.614	3.614	3.614
Phase currents			
H	1822	523	523
X	−16082	−7963	−7963
Y	5422	5422	5422
<i>System not connected beyond fault</i>			
Per-unit currents			
H	8.508	−1.463	−1.463
X	−9.971	0	0
Y	1.463	1.463	1.463
Phase currents			
H	1768	−304	−304
X	−12952	0	0
Y	2194	2194	2194

The currents are somewhat lower for a system not connected beyond the fault point compared with the currents for a system connected beyond the fault point. In fact, the delta winding current is significantly lower. These results do not change much as the system impedances increase toward their rated values in the 1% range. Thus, the discontinuity in the currents between the two cases remains as the system sequence impedances increase. If the system is considered connected while its impedance has its rated value, it would be awkward to consider the system disconnected when the system impedances approach zero.

These currents do not include the asymmetry factor, which accounts for initial transient effects when the fault occurs.

6.5 Asymmetry Factor

A factor multiplying the currents calculated above is necessary to account for a transient overshoot when the fault occurs. This factor, called the asymmetry factor, was discussed in Chapter 2, and is given by

$$K = \sqrt{2} \left\{ 1 + \exp \left[- \left(\phi + \frac{\pi}{2} \right) \frac{r}{x} \right] \sin \phi \right\} \quad (6.65)$$

where x is the reactance looking into the terminal, r is the resistance, and $\phi = \tan^{-1}(x/r)$ in radians. The system impedances are usually ignored when calculating these quantities, so that for a two-terminal unit

$$\frac{x}{r} = \frac{\text{Im}(z_{\text{HX}})}{\text{Re}(z_{\text{HX}})} \quad (6.66)$$

and for a three-terminal unit with a fault on the X terminal

$$x = \text{Im}(z_X) + \frac{\text{Im}(z_H)\text{Im}(z_Y)}{\text{Im}(z_H) + \text{Im}(z_Y)}, \quad r = \text{Re}(z_X) + \frac{\text{Re}(z_H)\text{Re}(z_Y)}{\text{Re}(z_H) + \text{Re}(z_Y)} \quad (6.67)$$

with corresponding expressions for the other terminals should the fault be on them. When K in Equation 6.65 multiplies the rms short-circuit current, it yields the maximum peak short-circuit current.

7

Phase-Shifting and Zig-Zag Transformers

7.1 Introduction

Phase-shifting transformers are used in power systems to help control power flow and line losses. They shift the input voltages and currents by an angle that can be adjusted using a tap changer. They operate by adding a $\pm 90^\circ$ voltage to the input voltage, that is, in quadrature. For three-phase transformers, the quadrature voltage to be added to a given phase voltage can be derived by interconnecting the other phases, which can be done in many ways; this gives rise to a large number of configurations for these transformers. We will deal with only a few common types of configurations in this chapter. The phase-shifting capability can be combined with voltage magnitude control in the same transformer. This results in a more complex unit involving two sets of tap changers; however, we will not discuss this in this chapter.

The use of phase-shift transformers can be illustrated by considering the feeding of a common load from two voltage sources that are out of phase with each other, as shown in [Figure 7.1](#). Solving for the currents, we get

$$\mathbf{I}_1 = \mathbf{V}_1 \frac{(Z_2 + Z_L)}{K} - \mathbf{V}_2 \frac{Z_L}{K}, \quad \mathbf{I}_2 = \mathbf{V}_2 \frac{(Z_1 + Z_L)}{K} - \mathbf{V}_1 \frac{Z_L}{K} \quad (7.1)$$

where $K = Z_1 Z_2 + Z_1 Z_L + Z_2 Z_L$. The current into the load, \mathbf{I}_L , is

$$\mathbf{I}_L = \mathbf{I}_1 + \mathbf{I}_2 = \mathbf{V}_1 \frac{Z_2}{K} + \mathbf{V}_2 \frac{Z_1}{K} \quad (7.2)$$

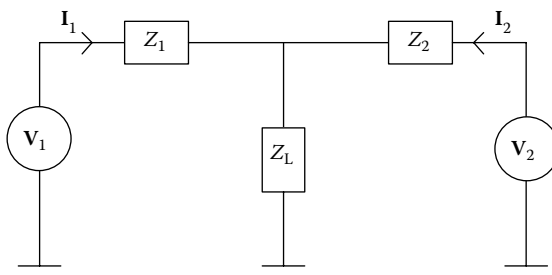
and the voltage across the load, \mathbf{V}_L , is

$$\mathbf{V}_L = \mathbf{V}_1 - \mathbf{I}_1 Z_1 = \frac{Z_L}{K} (\mathbf{V}_1 Z_2 + \mathbf{V}_2 Z_1) \quad (7.3)$$

Thus, the complex power delivered to the load is

$$\mathbf{V}_L \mathbf{I}_L^* = \frac{Z_L}{|K|^2} |\mathbf{V}_1 Z_2 + \mathbf{V}_2 Z_1|^2 \quad (7.4)$$

where * denotes complex conjugation.

**FIGURE 7.1**

Two possibly out-of-phase sources feeding a common load.

Consider a case in which $Z_1 = Z_2 = Z$, $V_1 = V$, $V_2 = Ve^{j\theta}$. Then, Equation 7.4 becomes

$$V_L I_L^* = \frac{2Z_L |Z|^2 V^2}{|K|^2} (1 + \cos\theta) \quad (7.5)$$

Thus, the maximum power is transferred when $\theta = 0$. In this case, a phase-shifting transformer can be used to adjust the phase of V_2 so that it equals that of V_1 .

In modern interconnected power systems the need for these devices has increased. Other methods for introducing a quadrature voltage are being developed, for instance, by means of power electronic circuits in conjunction with AC–DC converters, which can act much faster than on-load tap changers. However they are presently more costly than phase-shifting transformers and are used primarily when response time is important. (Electronic on-load tap changers are also being developed for fast response-time applications.)

In this chapter, we will develop a circuit model description for three common types of phase-shifting transformers. This is useful to understand the regulation behavior of such devices, that is, how much the output voltage magnitude and phase change are when the unit is loaded as compared with that of the no-load voltage output. In the process, we will also find that the phase angle depends on the tap position, a relationship that can be nonlinear. In addition to the positive-sequence circuit model, which describes normal operations, we will also determine the negative- and zero-sequence circuit models for use in short-circuit fault current analysis, which is carried out for the standard types of faults for two phase-shifting transformers.

Very little has been published on phase-shifting transformers in the open literature beyond general interconnection diagrams and how they are used in specific power grids. References that emphasize the basic principles include [Hob39, Cle39, Kra98, Wes64].

7.2 Basic Principles

The basic principles have been discussed in Chapters 3 through 6, but we will repeat some of them here for easier reference. We neglect the exciting current and model the individual phases in terms of their leakage impedances. For a two-winding phase, we use the circuit model shown in Figure 7.2. Z_{12} is the two-winding leakage impedance, referred to as side 1. Most of the development described here is carried out in terms of impedances in Ohms. Because of the differences in per-unit bases for the input and winding quantities, per-unit quantities are not as convenient in this analysis. We indicate the appropriate places where the per-unit quantities might prove useful. We assume that positive currents flow into their respective windings. With N_1 equal to the number of turns on side 1 and N_2 , the number of turns on side 2, the ideal transformer voltages satisfy

$$\frac{E_1}{E_2} = \frac{N_1}{N_2} \quad (7.6)$$

and the currents satisfy

$$\frac{I_1}{I_2} = -\frac{N_2}{N_1} \quad (7.7)$$

For three windings per phase, we use the model shown in Figure 7.3. In this case, the ideal transformer voltages satisfy

$$\frac{E_1}{N_1} = \frac{E_2}{N_2} = \frac{E_3}{N_3} \quad (7.8)$$

and the currents satisfy

$$N_1 I_1 + N_2 I_2 + N_3 I_3 = 0 \quad (7.9)$$

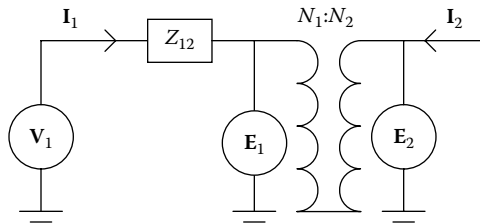
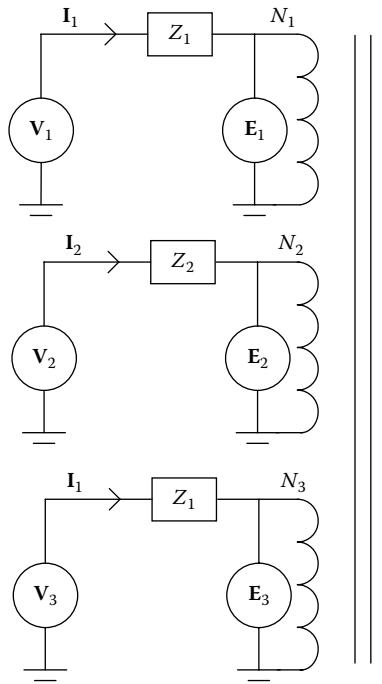


FIGURE 7.2

Model of a two-winding transformer phase.

**FIGURE 7.3**

Model of a three-winding transformer phase. The vertical lines connecting the circuits represent the common core.

The single-winding impedances are given in terms of the two-winding impedances by

$$\begin{aligned}
 Z_1 &= \frac{1}{2} \left[Z_{12} + Z_{13} - \left(\frac{N_1}{N_2} \right)^2 Z_{23} \right] \\
 Z_2 &= \frac{1}{2} \left(\frac{N_2}{N_1} \right)^2 \left[Z_{12} + \left(\frac{N_1}{N_2} \right)^2 Z_{23} - Z_{13} \right] \\
 Z_3 &= \frac{1}{2} \left(\frac{N_3}{N_1} \right)^2 \left[Z_{13} + \left(\frac{N_1}{N_2} \right)^2 Z_{23} - Z_{12} \right]
 \end{aligned} \tag{7.10}$$

Here, the first subscript refers to the winding for which the two-winding impedance is measured and the second subscript refers to the winding that will be shorted when measuring the impedance. To refer impedances to the opposite winding, we use

$$Z_{ij} = \left(\frac{N_i}{N_j} \right)^2 Z_{ji} \quad (7.11)$$

For a three-phase system, the positive-sequence quantities correspond to the order of the unit phasors shown in Figure 7.4. We let

$$\alpha = e^{j120^\circ} = -\frac{1}{2} + j\frac{\sqrt{3}}{2} \quad (7.12)$$

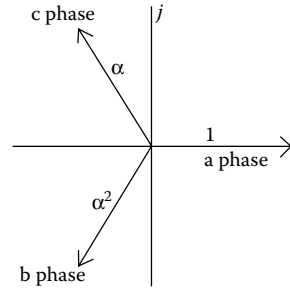


FIGURE 7.4
Positive-sequence unit phasors.

Then, the ordering is 1, α^2 , and α . This corresponds to the phase ordering a, b, and c for the windings and 1, 2, and 3 for the terminals. Negative-sequence ordering is 1, α , and α^2 , which corresponds to the phase ordering a, c, and b or 1, 3, and 2 for the windings or terminals, respectively. This is obtained by interchanging two phases. Note that

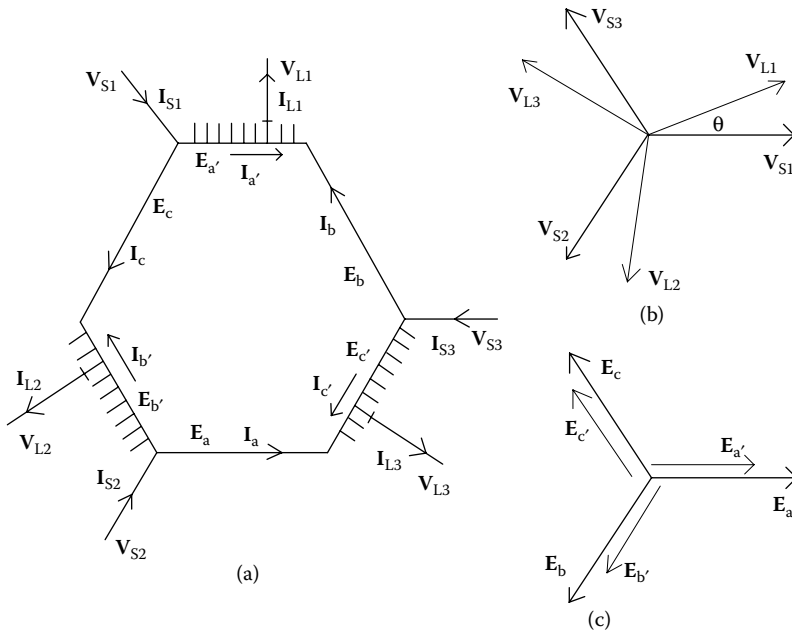
$$\alpha^2 = e^{j240^\circ} = e^{-j120^\circ} = \alpha^* = -\frac{1}{2} - j\frac{\sqrt{3}}{2} \quad (7.13)$$

The zero-sequence quantities are all in phase with each other.

We will choose interconnections to produce a positive phase shift at a positive tap setting. By interchanging two phases, we can produce a negative phase shift at a positive tap setting. Interchanging two phases is equivalent to imputing a negative-sequence set of voltages. This implies that negative-sequence circuits have the opposite phase shift in relation to positive-sequence circuits. Zero-sequence circuits have zero phase shifts. By positive phase shift, we mean that output voltages and currents lead the input voltages and currents, that is, output quantities are rotated counterclockwise on a phasor diagram relative to the input quantities.

7.3 Squashed Delta Phase-Shifting Transformer

One of the simplest phase shifters to analyze is the squashed delta configuration shown in Figure 7.5, where S denotes the source or input quantities and L indicates the load or output quantities. The input and output set of voltages and the corresponding currents form a balanced positive-sequence set. In this study, we take the S currents as positive into the terminals and the L currents as positive out of the terminals. The input and output voltage

**FIGURE 7.5**

Squashed delta configuration, with the phase quantities labeled: (a) circuit, (b) input and output phasors, and (c) internal phasors. The ideal transformer voltages, the E 's, increase in the opposite direction of the assumed current flow. θ is a positive phase-shift angle.

phasor diagram is shown in Figure 7.5b. These are the voltages to ground; the currents form a similar set but are not shown. Similarly, the internal voltages and corresponding currents form a positive-sequence set, as shown in Figure 7.5c for the voltages. Note that Figures 7.5b and 7.5c can be rotated relative to each other if shown on a common phasor diagram. Information on their relative orientation is not contained in the figure although the phase order is consistent between the figures. This applies to the corresponding current phasors as well. a , a' , and so on refer to windings on the same leg, with the prime labeling the tapped winding. The two-winding impedances, that is, $Z_{aa'}$, and so on, will be referred to the unprimed coil. Because all these impedances are the same by symmetry, we need only one symbol. This transformer can be designed with a single three-phase core and is generically referred to as a single-core design. It is also best adapted to phase-angle shifts in one direction.

Using the two-winding phase model described in the [Section 7.2](#), adapting it to the present labeling scheme, and concentrating on one input–output pair, we can write

$$\begin{aligned} V_{S1} - V_{L1} &= E_{a'}, & V_{S1} - V_{L2} &= I_c Z_{aa'} + E_c \\ I_{S1} &= I_c + I_{a'}, & I_{L1} &= I_{a'} + I_b \end{aligned} \quad (7.14)$$

Note that, in Equation 7.14, the two-winding leakage impedance is assigned to the unprimed side of the transformer. We also have the following transformer relations:

$$\begin{aligned} \mathbf{E}_{a'} &= \frac{N_{a'}}{N_a} \mathbf{E}_a = \frac{1}{n} \mathbf{E}_a = \frac{e^{-j120^\circ}}{n} \mathbf{E}_c \\ \mathbf{I}_{a'} &= -\frac{N_a}{N_{a'}} \mathbf{I}_a = -n \mathbf{I}_a = -n e^{-j120^\circ} \mathbf{I}_c \end{aligned} \quad (7.15)$$

where we define $n = N_a/N_{a'}$, the turns ratio. We also have the following relationships:

$$\begin{aligned} \mathbf{V}_{S1} - \mathbf{V}_{S2} &= (1 - \alpha^2) \mathbf{V}_{S1} = \sqrt{3} e^{j30^\circ} \mathbf{V}_{S1} \\ \mathbf{V}_{S2} - \mathbf{V}_{L2} &= \mathbf{E}_{b'} = e^{-j120^\circ} \mathbf{E}_{a'} = \frac{e^{j120^\circ}}{n} \mathbf{E}_c \end{aligned} \quad (7.16)$$

A detailed solution of these equations is essential because we will need some of the intermediate results later. We assume that \mathbf{V}_{S1} and \mathbf{I}_{S1} are given. From Equations 7.14 and 7.15, we get

$$\mathbf{I}_c = \frac{1}{1 - n e^{-j120^\circ}} \mathbf{I}_{S1}, \quad \mathbf{I}_{a'} = -\frac{n e^{-j120^\circ}}{1 - n e^{-j120^\circ}} \mathbf{I}_{S1} = \frac{n}{n - e^{j120^\circ}} \mathbf{I}_{S1} \quad (7.17)$$

We also have

$$\mathbf{I}_{L1} = \mathbf{I}_{a'} + \mathbf{I}_b = \mathbf{I}_{a'} + e^{j120^\circ} \mathbf{I}_c = \left(\frac{n - e^{-j120^\circ}}{n - e^{j120^\circ}} \right) \mathbf{I}_{S1} = e^{j\theta} \mathbf{I}_{S1}$$

where

$$\theta = 2 \tan^{-1} \left(\frac{\sqrt{3}}{2n + 1} \right) \quad (7.18)$$

Because n is determined by the tap position, this shows that θ is a nonlinear function of the tap position, assuming the taps are evenly spaced.

Adding Equation 7.16 and using Equation 7.14, we get

$$\mathbf{V}_{S1} - \mathbf{V}_{L2} = \sqrt{3} e^{j30^\circ} \mathbf{V}_{S1} + \frac{e^{j120^\circ}}{n} \mathbf{E}_c = \mathbf{I}_c Z_{aa'} + \mathbf{E}_c$$

Solving for \mathbf{E}_c and using Equation 7.17, we get

$$\mathbf{E}_c = \frac{\sqrt{3} n e^{j30^\circ}}{n - e^{j120^\circ}} \mathbf{V}_{S1} + \frac{n e^{j120^\circ} Z_{aa'}}{(n - e^{j120^\circ})^2} \mathbf{I}_{S1} \quad (7.19)$$

Combining this equation with the first expressions of Equations 7.14 and 7.15, we get

$$\mathbf{V}_{L1} = \left[\mathbf{V}_{S1} - \left(\frac{Z_{aa'}}{n^2 + n + 1} \right) \mathbf{I}_{S1} \right] e^{j\theta} \quad (7.20)$$

where θ is given by Equation 7.18. Although the current shifts by θ in all cases, in general, the voltage shifts by θ only under no load conditions.

The circuit model suggested by Equation 7.20 is shown in Figure 7.6. By symmetry, this applies to all three phases with appropriate labeling. The equivalent impedance shown in Figure 7.6 is given by

$$Z_{eq} = \frac{Z_{aa'}}{n^2 + n + 1} \quad (7.21)$$

Figure 7.6 is a positive-sequence circuit model. The negative-sequence model is obtained simply by changing θ to $-\theta$, with Z_{eq} unchanged. Note that Z_{eq} depends on the tap setting.

Although the input power per phase is $P_{in} = \mathbf{V}_{S1} \mathbf{I}_{S1}^*$, the transformed or winding power per phase P_{wdg} is relatively less. Ignoring impedance drops, from Equations 7.17 and 7.19, we have

$$P_{wdg} = \mathbf{E}_c \mathbf{I}_c^* = j \left(\frac{n\sqrt{3}}{n^2 + n + 1} \right) P_{in} \quad (7.22)$$

where the factor j shows that the transformed power is in quadrature with the input power. As a numerical example, let $\theta = 30^\circ$. Then, from Equations 7.18 and 7.22, we have

$$\tan\left(\frac{\theta}{2}\right) = \frac{\sqrt{3}}{2n+1} \Rightarrow n = 2.732 \Rightarrow P_{wdg} = j0.4227 P_{in} \quad (7.23)$$

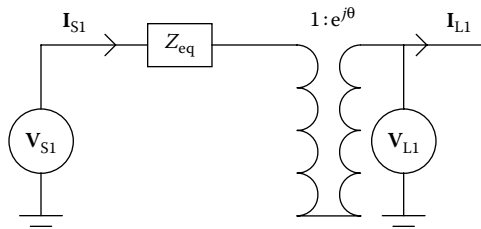


FIGURE 7.6

Circuit model of one phase of a phase-shifting transformer for a positive sequence. For a negative sequence, change θ to $-\theta$.

We can express Equation 7.20 in per-unit terms; however, because of the difference between the input power and voltage base and that of the windings, we must be careful to specify the base used. As usual, we take the power base to be the terminal power base. This is the terminal power per phase. Thus, the rated input power base is $P_{b,in}$; the rated input voltage base is $V_{b,in}$; and the rated input current base that can be derived from the power and voltage base is $I_{b,in} = P_{b,in}/V_{b,in}$. Similarly, we can derive the input impedance base from the power and voltage base, $Z_{b,in} = V_{b,in}/I_{b,in} = (V_{b,in})^2/P_{b,in}$. Because the transformation ratio is 1:1 in terms of magnitude, the output base values are the same as the input base values. Thus, Equation 7.20 can be written as follows:

$$\frac{\mathbf{V}_{L1}}{V_{b,in}} = \left[\frac{\mathbf{V}_{S1}}{V_{b,in}} - Z_{eq} \frac{\mathbf{I}_{S1}}{I_{b,in}} \left(\frac{I_{b,in}}{V_{b,in}} \right) \right] e^{j\theta} = \left[\frac{\mathbf{V}_{S1}}{V_{b,in}} - \frac{Z_{eq}}{Z_{b,in}} \frac{\mathbf{I}_{S1}}{I_{b,in}} \right] e^{j\theta} \quad (7.24)$$

or

$$\mathbf{v}_{L1} = [\mathbf{v}_{S1} - z_{eq} \mathbf{i}_{S1}] e^{j\theta}$$

where lowercase letters are used to denote the per-unit quantities.

Assuming the rated input power per phase to be the common power base, the winding and input impedance bases are proportional to the square of the respective voltage magnitudes. Using Equation 7.19 and ignoring impedance drops, we have

$$\frac{Z_{b,wdg}}{Z_{b,in}} = \left| \frac{\mathbf{E}_c}{\mathbf{V}_{S1}} \right|^2 = \frac{3n^2}{n^2 + n + 1} \quad (7.25)$$

Thus, using Equation 7.21, z_{eq} can be expressed as

$$z_{eq} = \frac{Z_{eq}}{Z_{b,in}} = \frac{1}{n^2 + n + 1} \left(\frac{Z_{b,wdg}}{Z_{b,in}} \right) \left(\frac{Z_{aa'}}{Z_{b,wdg}} \right) = \frac{3n^2}{(n^2 + n + 1)^2} z_{aa'} \quad (7.26)$$

where z_{eq} is on an input base and $z_{aa'}$ is on a winding base. Note that the winding base depends on the turns ratio, as indicated in Equation 7.25. Thus, this base is perhaps most useful for design purposes when n refers to the maximum phase angle. At the other extreme, with $\theta = 0$, we have $n = \infty$, so that $Z_{eq} = z_{eq} = 0$. In this case, the input is directly connected to the output, bypassing the coils.

7.3.1 Zero-Sequence Circuit Model

The zero-sequence circuit model may be derived with reference to [Figure 7.5](#), assuming all quantities are of zero sequence. Thus, Figures 7.5b and 7.5c

should be replaced by diagrams with all phasors in parallel. Using a zero subscript for zero-sequence quantities, we can write

$$\begin{aligned} \mathbf{V}_{S1,0} - \mathbf{V}_{L1,0} &= \mathbf{E}_{a',0}, & \mathbf{V}_{S1,0} - \mathbf{V}_{L2,0} &= \mathbf{I}_{c,0}Z_{aa',0} + E_{c,0} \\ \mathbf{I}_{S1,0} &= \mathbf{I}_{c,0} + \mathbf{I}_{a',0}, & \mathbf{I}_{L1,0} &= \mathbf{I}_{a',0} + \mathbf{I}_{b,0} \end{aligned} \quad (7.27)$$

and

$$\begin{aligned} \mathbf{E}_{a',0} &= \frac{N_{a'}}{N_a} \mathbf{E}_{a,0} = \frac{1}{n} \mathbf{E}_{a,0} = \frac{1}{n} \mathbf{E}_{c,0} \\ \mathbf{I}_{a',0} &= -\frac{N_a}{N_{a'}} \mathbf{I}_{a,0} = -n \mathbf{I}_{a,0} = -n \mathbf{I}_{c,0} \end{aligned} \quad (7.28)$$

Because $\mathbf{I}_{b,0} = \mathbf{I}_{c,0}$, Equation 7.27 shows that

$$\mathbf{I}_{L1,0} = \mathbf{I}_{S1,0} \quad (7.29)$$

so the current is not phase-shifted. We also have

$$\mathbf{V}_{S1,0} - \mathbf{V}_{S2,0} = 0, \quad \mathbf{V}_{S2,0} - \mathbf{V}_{L2,0} = \mathbf{E}_{b',0} = \frac{1}{n} \mathbf{E}_{b,0} = \frac{1}{n} \mathbf{E}_{c,0} \quad (7.30)$$

Solving the above zero-sequence equations, we get

$$\mathbf{I}_{c,0} = \frac{\mathbf{I}_{S1,0}}{1-n}, \quad \mathbf{E}_{c,0} = \frac{n}{1-n} \mathbf{I}_{c,0} Z_{aa',0} = \frac{n}{(1-n)^2} \mathbf{I}_{S1,0} Z_{aa',0} \quad (7.31)$$

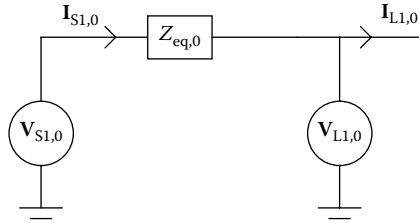
and

$$\mathbf{V}_{L1,0} = \mathbf{V}_{S1,0} - \frac{Z_{aa',0}}{(1-n)^2} \mathbf{I}_{S1,0} \quad (7.32)$$

The circuit model for Equation 7.32 is shown in [Figure 7.7](#), where we define

$$Z_{eq,0} = \frac{Z_{aa',0}}{(1-n)^2} \quad (7.33)$$

$Z_{eq,0}$ has a different dependence on n compared to the positive-sequence circuit and becomes infinite when $n = 1$. This is reasonable because, from Equation 7.28, $\mathbf{I}_{a',0} = -\mathbf{I}_{c,0}$ when $n = 1$; therefore, from Equation 7.27, $\mathbf{I}_{S1,0} = 0$. Thus, no zero-sequence current can flow into the squashed delta transformer when $n = 1$. Internal current can, however, circulate around the delta. From Equation 7.18, $\theta = 60^\circ$ when $n = 1$.

**FIGURE 7.7**

Zero-sequence circuit model of one phase of a squashed delta phase-shifting transformer.

Equation 7.32 can be rewritten in per-unit terms referring to the same input base as used for the positive sequence:

$$\mathbf{v}_{L1,0} = \mathbf{v}_{S1,0} - \mathbf{z}_{eq,0} \mathbf{i}_{S1,0} \quad (7.34)$$

Using the positive-sequence winding base for the two-winding zero-sequence impedance, $Z_{aa',0}$, we can write

$$\mathbf{z}_{eq,0} = \frac{3n^2}{(n^2 + n + 1)(1 - n)^2} \mathbf{z}_{aa',0} \quad (7.35)$$

This expression is primarily useful in designs in which the winding base is used for the maximum phase-shift angle.

We will postpone both a discussion of the regulation effects and calculations of the short-circuit current until other types of phase-shifting transformers are treated because the positive-, negative-, and zero-sequence circuit diagrams for all the cases treated will have the same appearance, although Z_{eq} or \mathbf{z}_{eq} and θ differ among the various types.

7.4 Standard Delta Phase-Shifting Transformer

As opposed to the squashed delta design, the standard delta design uses an unsquashed delta winding but is still a single-core design. The connection diagram is given in [Figure 7.8](#). The tapped windings are on the same core as the corresponding parallel windings on the delta. The taps are symmetrically placed with respect to the point of contact at the delta vertex. This ensures that there is no change in the current or no-load voltage magnitude from the input to the output. It also means that $\mathbf{E}_{a'} = \mathbf{E}_{a''}$, and so on, for the other phases. Each phase really consists of three windings: the two tap windings and the winding opposite and parallel in [Figure 7.8](#), where primes

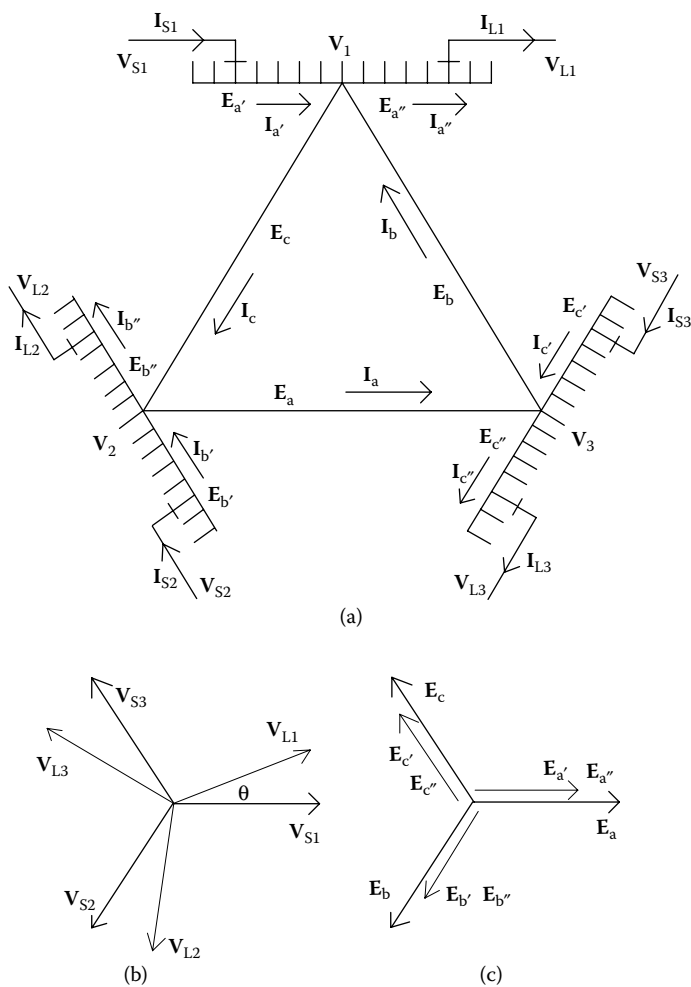


FIGURE 7.8 Standard delta configuration, with the phase quantities labeled: (a) circuit, (b) input and output phasors, and (c) internal phasors. The ideal transformer voltages, the E 's, increase in the opposite direction of the assumed current flow. The taps are symmetrically positioned.

and double primes are used to distinguish them. Thus, a three-winding per-phase model is needed. $Z_a, Z_{a'}$, and $Z_{a''}$ will be used to label the single-winding impedances for phase a. Because all the phases have equivalent impedances by symmetry, the same designations will be used for the other phases as well. The same remarks apply to the phasor diagrams as in the squashed delta case. Although not shown, the current phasor diagrams have the same sequence order as their corresponding voltage-phaser diagrams; however, the two diagrams can be rotated relative to each other.

In Figure 7.8a, \mathbf{V}_1 , \mathbf{V}_2 , and \mathbf{V}_3 designate the phasor voltages to ground at the delta vertices. Thus, using $\mathbf{E}_{a'} = \mathbf{E}_{a''}$ and so on, and $\mathbf{I}_{a'} = \mathbf{I}_{S1}$; $\mathbf{I}_{a''} = \mathbf{I}_{L1}$, and so on, we have

$$\begin{aligned}\mathbf{V}_{S1} - \mathbf{V}_1 &= \mathbf{I}_{S1}Z_{a'} + \mathbf{E}_{a'}, & \mathbf{V}_1 - \mathbf{V}_{L1} &= \mathbf{I}_{L1}Z_{a''} + \mathbf{E}_{a'} \\ \mathbf{V}_2 - \mathbf{V}_3 &= (\alpha^2 - \alpha)\mathbf{V}_1 = -j\sqrt{3}\mathbf{V}_1 = \mathbf{I}_a Z_a + \mathbf{E}_a \\ \mathbf{I}_{S1} - \mathbf{I}_{L1} &= \mathbf{I}_c - \mathbf{I}_b = (\alpha - \alpha^2)\mathbf{I}_a = j\sqrt{3}\mathbf{I}_a\end{aligned}\quad (7.36)$$

In addition, we have the following transformer relations:

$$\begin{aligned}\frac{\mathbf{E}_a}{\mathbf{E}_{a'}} &= \frac{N_a}{N_{a'}} = n \\ N_a \mathbf{I}_a + N_{a'} \mathbf{I}_{S1} + N_{a''} \mathbf{I}_{L1} &= 0 \quad \text{or} \quad n \mathbf{I}_a + \mathbf{I}_{S1} + \mathbf{I}_{L1} = 0\end{aligned}\quad (7.37)$$

where we define the turns ratio n as the ratio between the turns in one of the delta windings to the turns in one of the tap windings. Both tap windings have the same number of turns. Solving for \mathbf{I}_a in the last equation in Equation 7.36 and inserting it into the last equation in Equation 7.37, we get

$$\mathbf{I}_{L1} = e^{j\theta} \mathbf{I}_{S1} \quad \text{with} \quad \theta = 2 \tan^{-1} \left(\frac{\sqrt{3}}{n} \right) \quad (7.38)$$

We also have

$$\mathbf{I}_a = - \frac{2}{n \left(1 - j \frac{\sqrt{3}}{n} \right)} \mathbf{I}_{S1} \quad (7.39)$$

From Equations 7.36 through 7.39, we get

$$\mathbf{E}_a = - \frac{j\sqrt{3}}{\left(1 - j \frac{\sqrt{3}}{n} \right)} \mathbf{V}_{S1} + \frac{j\sqrt{3}}{\left(1 - j \frac{\sqrt{3}}{n} \right)} \left[Z_{a'} - \frac{2jZ_a}{\sqrt{3}n \left(1 - j \frac{\sqrt{3}}{n} \right)} \right] \mathbf{I}_{S1} \quad (7.40)$$

and

$$\mathbf{V}_{L1} = \left[\mathbf{V}_{S1} - \left(Z_{a'} + Z_{a''} + \frac{4Z_a}{n^2 + 3} \right) \mathbf{I}_{S1} \right] e^{j\theta} \quad (7.41)$$

with θ as given in Equation 7.38. This is the no-load phase-angle shift. This conforms to the circuit model shown in Figure 7.6 with

$$Z_{eq} = Z_{a'} + Z_{a''} + \frac{4Z_a}{n^2 + 3} \quad (7.42)$$

or in terms of two-winding impedances, using Equation 7.10:

$$Z_{eq} = Z_{a'a''} + \left(\frac{2}{n^2 + 3} \right) (Z_{aa'} + Z_{aa''} - n^2 Z_{a'a''}) \quad (7.43)$$

This is the positive-sequence circuit. Again, the negative-sequence circuit is found by changing θ to $-\theta$ without any change in Z_{eq} .

We again determine the winding power per phase P_{wdg} in terms of the input power per phase $P_{in} = \mathbf{V}_{S1} \mathbf{I}_{S1}^*$. Similarly, ignoring the impedance drops, we get

$$P_{wdg} = \mathbf{E}_a \mathbf{I}_a^* = j \left(\frac{2\sqrt{3}n}{n^2 + 3} \right) P_{in} \quad (7.44)$$

where j indicates that the transformed power is in quadrature with the input power. Using trigonometric identities, we can show that

$$P_{wdg} = j \sin \theta P_{in} \quad (7.45)$$

with θ as given in Equation 7.38. (This relation does not hold for the squashed delta design.) Thus, for $\theta = 30^\circ$, $|P_{wdg}| = 0.5 |P_{in}|$.

In per-unit terms, based on input quantities, Equation 7.41 can be cast in the form of Equation 7.24. Again, we need to determine the relationship between the winding bases and the input base for impedances. The two-winding impedances given above are referred to by either the a or a' winding. Their bases are related to the input base by maintaining the power base the same as the input power per phase:

$$Z_{b,a \text{ wdg}} = \left| \frac{E_a}{V_{S1}} \right|^2 = \left(\frac{3n^2}{n^2 + 3} \right) Z_{b,in}, \quad Z_{b,a' \text{ wdg}} = \left| \frac{E_{a'}}{V_{S1}} \right|^2 = \left(\frac{3}{n^2 + 3} \right) Z_{b,in} \quad (7.46)$$

Thus, in per-unit terms, Z_{eq} in Equation 7.43 becomes

$$z_{eq} = \left(\frac{3n^2}{n^2 + 3} \right) \left[\frac{z_{a'a''}}{n^2} + \frac{2(z_{aa'} + z_{aa''} - z_{a'a''})}{(n^2 + 3)} \right] \quad (7.47)$$

Again, this is primarily useful for design purposes when n refers to the maximum phase angle. At zero phase shift, $n = \infty$, Equation 7.47 indicates that $z_{eq} = 0$. At this tap position, the tap windings are effectively out of the circuit, and the input is directly connected to the output.

7.4.1 Zero-Sequence Circuit Model

The zero-sequence circuit model can be derived with reference to [Figure 7.8](#) but with all phasors taken to be zero sequence. Rewriting Equations 7.36 and 7.37 accordingly and appending a zero subscript, we get

$$\begin{aligned} \mathbf{V}_{S1,0} - \mathbf{V}_{1,0} &= \mathbf{I}_{S1,0} \mathbf{Z}_{a',0} + \mathbf{E}_{a',0}, & \mathbf{V}_{1,0} - \mathbf{V}_{L1,0} &= \mathbf{I}_{L1,0} \mathbf{Z}_{a'',0} + \mathbf{E}_{a'',0} \\ \mathbf{V}_{2,0} - \mathbf{V}_{3,0} &= 0 = \mathbf{I}_{a,0} \mathbf{Z}_{a,0} + \mathbf{E}_{a,0}, & \mathbf{I}_{S1,0} - \mathbf{I}_{L1,0} &= \mathbf{I}_{c,0} - \mathbf{I}_{b,0} = 0 \\ \frac{\mathbf{E}_{a,0}}{\mathbf{E}_{a',0}} &= \frac{N_a}{N_{a'}} = n, & n\mathbf{I}_{a,0} + \mathbf{I}_{S1,0} + \mathbf{I}_{L1,0} &= 0 \end{aligned} \quad (7.48)$$

Solving, we find that

$$\mathbf{I}_{L1,0} = \mathbf{I}_{S1,0} \quad (7.49)$$

thus, the zero-sequence current undergoes no phase shift. We also have

$$\mathbf{E}_{a,0} = -\mathbf{I}_{a,0} \mathbf{Z}_{a,0}, \quad \mathbf{I}_{a,0} = -\frac{2}{n} \mathbf{I}_{S1,0} \quad (7.50)$$

and

$$\mathbf{V}_{L1,0} = \mathbf{V}_{S1,0} - \left(\mathbf{Z}_{a',0} + \mathbf{Z}_{a'',0} + \frac{4}{n^2} \mathbf{Z}_{a,0} \right) \mathbf{I}_{S1,0} \quad (7.51)$$

Thus, the voltage undergoes no phase shift at no-load. The circuit model of [Figure 7.7](#) applies here, with

$$\mathbf{Z}_{eq} = \mathbf{Z}_{a',0} + \mathbf{Z}_{a'',0} + \frac{4}{n^2} \mathbf{Z}_{a,0} \quad (7.52)$$

or, in terms of two winding impedances

$$\mathbf{Z}_{eq,0} = \mathbf{Z}_{a'a'',0} + \frac{2}{n^2} (\mathbf{Z}_{aa',0} + \mathbf{Z}_{aa'',0} - n^2 \mathbf{Z}_{a'a'',0}) \quad (7.53)$$

On a per-unit basis, using rated input quantities, Equation 7.51 has the same appearance as Equation 7.34. The equivalent per-unit impedance is given by

$$\mathbf{z}_{eq,0} = \left(\frac{3}{n^2 + 3} \right) [2(\mathbf{z}_{aa',0} + \mathbf{z}_{aa'',0}) - \mathbf{z}_{a'a'',0}] \quad (7.54)$$

Again, this is primarily useful when n refers to the maximum phase angle shift. At zero phase shift, the output is directly connected to the input as was the case for the positive sequence.

7.5 Two-Core Phase-Shifting Transformer

Phase shifters for large power applications are often designed as two units—the series unit and the excitor unit, each with its own core and associated coils. Depending on their size, the two units can be housed inside the same tank or in separate tanks. This construction is largely dictated by tap-changer limitations. A commonly used circuit diagram is shown in Figure 7.9. The phasor diagrams refer to the positive-sequence quantities and, although the phase ordering is consistent among the diagrams, their relative orientation is not specified. Currents have the same phase ordering as their associated voltages. The series unit uses a three-winding model, whereas the excitor unit uses a two-winding model. We have used two different labeling schemes for the series and excitor units. Subscript letters are used for the series quantities, and subscript numbers are used for the excitor quantities. Primes and double primes are used to distinguish different windings associated with the same phase. Note that the input–output coils in Figure 7.9 are a part of the series unit but are attached to the excitor unit at their midpoints. The input and output voltages are voltages to ground. We assume the input voltage and current phasors are given.

Following an analysis similar to that of the Section 7.4 for the series unit, and using $\mathbf{E}_{a'} = \mathbf{E}_{a''}$, and so on, we can write

$$\begin{aligned} \mathbf{V}_{S1} - \mathbf{V}_1 &= \mathbf{I}_{S1}Z_{a'} + \mathbf{E}_{a'}, & \mathbf{V}_1 - \mathbf{V}_{L1} &= \mathbf{I}_{L1}Z_{a''} + \mathbf{E}_{a'} \\ \mathbf{E}_{2'} - \mathbf{E}_{3'} &= (\alpha^2 - \alpha)\mathbf{E}_{1'} = -j\sqrt{3}\mathbf{E}_{1'} = \mathbf{I}_a Z_a + \mathbf{E}_a \\ \mathbf{V}_1 &= \mathbf{I}_1 Z_{11'} + \mathbf{E}_{1'}, & \mathbf{I}_1 &= \mathbf{I}_{S1} - \mathbf{I}_{L1}, & \mathbf{I}_{2'} &= \mathbf{I}_c - \mathbf{I}_a \end{aligned} \quad (7.55)$$

We also have the following transformer relations:

$$\begin{aligned} \frac{\mathbf{E}_a}{\mathbf{E}_{a'}} &= \frac{N_a}{N_{a'}} = n_s, & \frac{\mathbf{E}_1}{\mathbf{E}_{1'}} &= \frac{N_1}{N_{1'}} = n_e, & \frac{\mathbf{I}_{1'}}{\mathbf{I}_1} &= -\frac{N_1}{N_{1'}} = -n_e \\ N_a \mathbf{I}_a + N_{a'} \mathbf{I}_{S1} + N_{a''} \mathbf{I}_{L1} &= 0 & \text{or} & & n_s \mathbf{I}_a + \mathbf{I}_{S1} + \mathbf{I}_{L1} &= 0 \end{aligned} \quad (7.56)$$

where we define the turns ratio of the series unit, n_s , as the ratio of the turns in a coil of the delta to the turns in the first or the second half of the input–output winding, that is, from the input to the midpoint or from the output to the midpoint. We have also defined the excitor-winding ratio, n_e , as the ratio of the turns in the winding connected to the midpoint of the input–output winding to the turns in the tapped winding. The latter ratio will depend on the tap position. From Equations 7.55 and 7.56 and the phasor diagrams, we get

$$\mathbf{I}_{2'} = e^{-j120^\circ} \mathbf{I}_1 = -n_e e^{-j120^\circ} \mathbf{I}_1 = \mathbf{I}_c - \mathbf{I}_a = (\alpha - 1) \mathbf{I}_a = -\sqrt{3} e^{-j30^\circ} \mathbf{I}_a \quad (7.57)$$

which implies

$$\mathbf{I}_1 = j \frac{\sqrt{3}}{n_e} \mathbf{I}_a$$

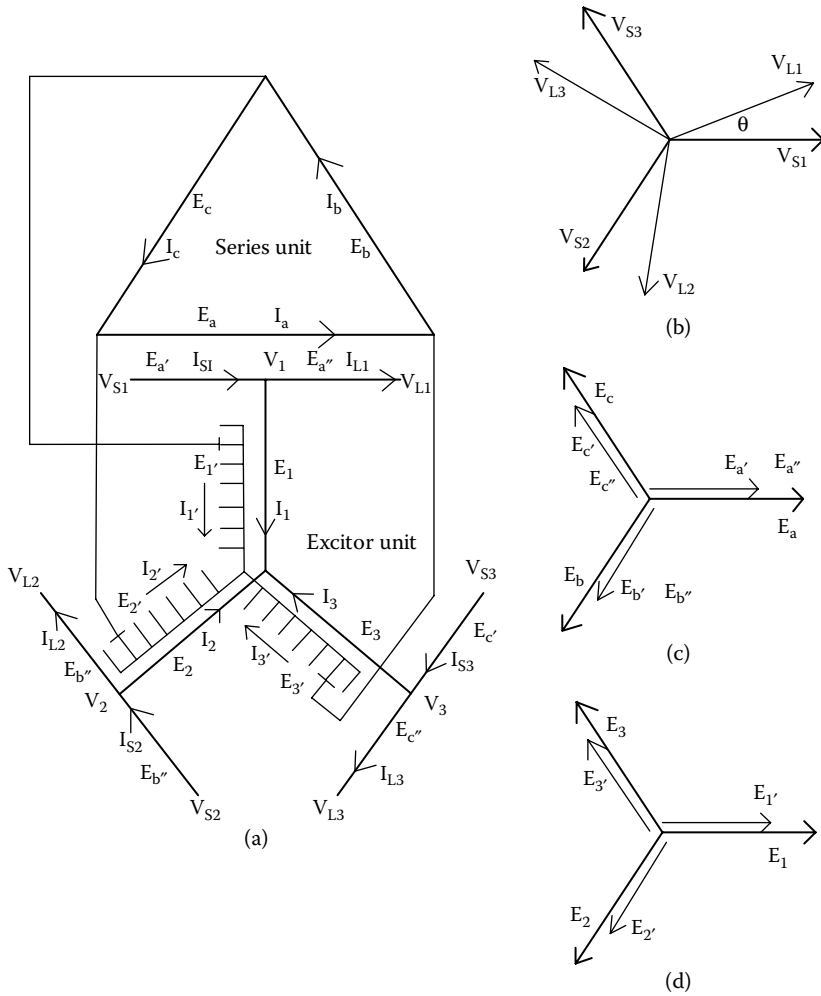


FIGURE 7.9

Circuit diagram of a two-core phase-shifting transformer: (a) circuit, (b) input and output phasors, (c) internal phasors for series, and (d) internal phasors for excitor. The ideal transformer voltages, the E 's, increase in the opposite direction of the assumed current flow. The input-output coil is equally divided.

Substituting \mathbf{I}_1 from Equation 7.55 and \mathbf{I}_a from Equation 7.56 into Equation 7.57, we get

$$\mathbf{I}_{L1} = \left[\frac{1 + j \left(\frac{\sqrt{3}}{n_e n_s} \right)}{1 - j \left(\frac{\sqrt{3}}{n_e n_s} \right)} \right] \mathbf{I}_{S1} = e^{j\theta} \mathbf{I}_{S1} \quad \text{where} \quad \theta = 2 \tan^{-1} \left(\frac{\sqrt{3}}{n_e n_s} \right) \quad (7.58)$$

Thus, in terms of the known input current, using Equations 7.55 and 7.56, we can write

$$\mathbf{I}_1 = - \frac{2j \left(\frac{\sqrt{3}}{n_e n_s} \right)}{\left[1 - j \left(\frac{\sqrt{3}}{n_e n_s} \right) \right]} \mathbf{I}_{S1}, \quad \mathbf{I}_a = - \frac{2}{n_s \left[1 - j \left(\frac{\sqrt{3}}{n_e n_s} \right) \right]} \mathbf{I}_{S1} \quad (7.59)$$

From the initial set of equations, we also get

$$\mathbf{E}_1 = j \frac{n_e}{\sqrt{3}} (\mathbf{I}_a Z_a + \mathbf{E}_a) \quad (7.60)$$

Substituting Equations 7.57 and 7.60 into the expression for \mathbf{V}_1 in Equation 7.55, we find that

$$\mathbf{V}_1 = \left(Z_{11'} + \frac{n_e^2}{3} Z_a \right) \mathbf{I}_1 + j \frac{n_e}{\sqrt{3}} \mathbf{E}_a \quad (7.61)$$

Substituting this into the first relationship of Equation 7.55, and using Equation 7.56 and the first equation of Equation 7.59, we get

$$\mathbf{E}_a = - \frac{j \left(\frac{\sqrt{3}}{n_e} \right)}{\left[1 - j \left(\frac{\sqrt{3}}{n_e n_s} \right) \right]} \mathbf{V}_{S1} + \left\{ \frac{\frac{6n_s}{(n_e n_s)^2}}{\left[1 - j \left(\frac{\sqrt{3}}{n_e n_s} \right) \right]^2} \left(Z_{11'} + \frac{n_e^2}{3} Z_a \right) + \frac{j \frac{\sqrt{3}}{n_e}}{\left[1 - j \left(\frac{\sqrt{3}}{n_e n_s} \right) \right]} Z_{a'} \right\} \mathbf{I}_{S1} \quad (7.62)$$

Adding the first two expressions in Equation 7.55 and using Equation 7.62, we get

$$\mathbf{V}_{L1} = \left\{ \mathbf{V}_{S1} - \left[Z_{a'} + Z_{a''} + \frac{12}{(n_e n_s)^2 + 3} \left(Z_{11'} + \frac{n_e^2}{3} Z_a \right) \right] \mathbf{I}_{S1} \right\} e^{j\theta} \quad (7.63)$$

where θ is given in Equation 7.58. Equation 7.63 can be represented with the same circuit model as [Figure 7.6](#) by applying the following relation:

$$Z_{eq} = Z_{a'} + Z_{a''} + \left[\frac{12}{(n_e n_s)^2 + 3} \right] \left(Z_{11'} + \frac{n_e^2}{3} Z_a \right) \quad (7.64)$$

or, in terms of the two-winding impedances, we can express it as

$$Z_{eq} = Z_{a'a''} + \left(\frac{12}{(n_e n_s)^2 + 3} \right) \left[Z_{11'} + \frac{n_e^2}{6} (Z_{aa'} + Z_{aa''} - n_s^2 Z_{a'a''}) \right] \quad (7.65)$$

Using Equations 7.59 and 7.60 and ignoring impedance drops, we can show that the winding power per phase is the same for the series and excitor units, that is,

$$P_{wdg} = \mathbf{E}_1 \mathbf{I}_1^* = \mathbf{E}_a \mathbf{I}_a^* = j \left[\frac{2\sqrt{3}n_e n_s}{(n_e n_s)^2 + 3} \right] P_{in} \quad (7.66)$$

where $P_{in} = \mathbf{V}_{S1} \mathbf{I}_{S1}^*$. In terms of the phase shift θ given in Equation 7.58, Equation 7.66 can be written as

$$P_{wdg} = j \sin \theta P_{in} \quad (7.67)$$

similar to the case for the standard delta phase shifter.

In per-unit terms, keeping the power base constant at the rated input power, Equation 7.63 can be cast in the form of Equation 7.24. To do this, we need to find the ratio of the impedance bases for both the series and excitor windings to the input or terminal impedance base. Using the above formulas, we find that

$$\begin{aligned} Z_{b,a\,wdg} &= \left| \frac{\mathbf{E}_a}{\mathbf{V}_{S1}} \right|^2 = \left[\frac{3n_s^2}{(n_e n_s)^2 + 3} \right] Z_{b,in} \\ Z_{b,a'\,wdg} &= \left| \frac{\mathbf{E}_{a'}}{\mathbf{V}_{S1}} \right|^2 = \left[\frac{3}{(n_e n_s)^2 + 3} \right] Z_{b,in} \\ Z_{b,1\,wdg} &= \left| \frac{\mathbf{E}_1}{\mathbf{V}_{S1}} \right|^2 = \left[\frac{(n_e n_s)^2}{(n_e n_s)^2 + 3} \right] Z_{b,in} \end{aligned} \quad (7.68)$$

Applying these relations, the per-unit equivalent impedance can be written as

$$z_{eq} = \frac{3}{[(n_e n_s)^2 + 3]} \left\{ z_{a'a''} + \frac{4(n_e n_s)^2}{[(n_e n_s)^2 + 3]} \left[z_{11'} + \frac{1}{2}(z_{aa'} + z_{aa''} - z_{a'a''}) \right] \right\} \quad (7.69)$$

The negative-sequence circuit has the same equivalent impedance, but it has a phase-angle shift in the opposite direction to the positive-sequence circuit.

7.5.1 Zero-Sequence Circuit Model

The zero-sequence circuit model is derived with reference to [Figure 7.9](#) by assuming that all quantities are zero sequence. Thus, we simply rewrite the basic equations, appending a zero subscript:

$$\begin{aligned} \mathbf{V}_{S1,0} - \mathbf{V}_{1,0} &= \mathbf{I}_{S1,0} Z_{a',0} + \mathbf{E}_{a',0}, & \mathbf{V}_{1,0} - \mathbf{V}_{L1,0} &= \mathbf{I}_{L1,0} Z_{a'',0} + \mathbf{E}_{a'',0} \\ \mathbf{E}_{2',0} - \mathbf{E}_{3',0} &= 0 = \mathbf{I}_{a,0} Z_{a,0} + \mathbf{E}_{a,0} \\ \mathbf{V}_{1,0} &= \mathbf{I}_{1,0} Z_{11',0} + \mathbf{E}_{1,0}, & \mathbf{I}_{1,0} &= \mathbf{I}_{S1,0} - \mathbf{I}_{L1,0}, & \mathbf{I}_{2',0} &= \mathbf{I}_{c,0} - \mathbf{I}_{a,0} = 0 \end{aligned} \quad (7.70)$$

and

$$\begin{aligned} \frac{\mathbf{E}_{a,0}}{\mathbf{E}_{a',0}} &= \frac{N_a}{N_{a'}} = n_s, & \frac{\mathbf{E}_{1,0}}{\mathbf{E}_{1',0}} &= \frac{N_1}{N_{1'}} = n_e, & \frac{\mathbf{I}_{1',0}}{\mathbf{I}_{1,0}} &= -\frac{N_1}{N_{1'}} = -n_e \\ N_a \mathbf{I}_{a,0} + N_{a'} \mathbf{I}_{S1,0} + N_{a'} \mathbf{I}_{L1,0} &= 0 & \text{or} & & n_s \mathbf{I}_{a,0} + \mathbf{I}_{S1,0} + \mathbf{I}_{L1,0} &= 0 \end{aligned} \quad (7.71)$$

Solving, we find that

$$\begin{aligned} \mathbf{I}_{1,0} &= 0, & \mathbf{I}_{S1,0} &= \mathbf{I}_{L1,0}, & \mathbf{I}_{a,0} &= -\frac{2}{n_s} \mathbf{I}_{S1} \\ \mathbf{E}_{a,0} &= \frac{2}{n_s} \mathbf{I}_{S1,0} Z_{a,0}, & \mathbf{V}_{1,0} &= \mathbf{E}_{1,0} \end{aligned} \quad (7.72)$$

Notice that, even if both the Y windings of the excitor are grounded, no zero-sequence current flows into the excitor because the secondary current from the tap winding would have to flow into the closed delta of the series unit, and this is not possible for zero-sequence currents.

From the above formulas, we get

$$\mathbf{V}_{L1,0} = \mathbf{V}_{S1,0} - \left(Z_{a',0} + Z_{a'',0} + \frac{4}{n_s^2} Z_{a,0} \right) \mathbf{I}_{S1,0} \quad (7.73)$$

Thus, we see that the zero-sequence current and no-load voltage have no phase angle shift and the circuit of Figure 7.7 applies with

$$Z_{eq,0} = Z_{a',0} + Z_{a'',0} + \frac{4}{n_s^2} Z_{a,0} \quad (7.74)$$

or, in terms of two-winding impedances

$$Z_{eq,0} = Z_{a'a'',0} + \frac{2}{n_s^2} (Z_{aa'} + Z_{aa''} - n_s^2 Z_{a'a''}) \quad (7.75)$$

Using the same basis as for the positive sequence, the per-unit version of this equation is

$$z_{eq,0} = \frac{3}{[(n_e n_s)^2 + 3]} [2(z_{aa'} + z_{aa''}) - z_{a'a''}] \quad (7.76)$$

7.6 Regulation Effects

Because all the phase-shifting transformers examined here have the same basic positive-sequence (as well as negative- and zero-sequence) circuits (Figure 7.6), with different expressions for Z_{eq} or z_{eq} and θ , the effect of a load on the output can be studied in common. The relevant circuit model is shown in Figure 7.10.

We assume a balanced positive-sequence system. Since all phases are identical, we exclude the phase subscript. We use per-unit quantities for this development, which can be accomplished by simply changing from upper- to lowercase letters and using a unit turns ratio. The ideal transformer is included in the figure to account for the phase shift. From the figure, we see that

$$\mathbf{v}_L = (\mathbf{v}_S - z_{eq} \mathbf{i}_S) e^{j\theta} = \mathbf{i}_L z_L = e^{j\theta} \mathbf{i}_S z_L \quad (7.77)$$

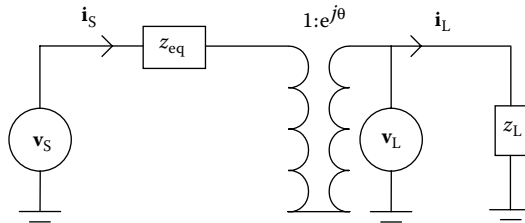


FIGURE 7.10

One phase of a phase-shifting transformer under load, represented using per-unit quantities.

where z_L is the per-unit load impedance. Solving for i_s , we find that

$$i_s = \frac{v_s}{(z_{eq} + z_L)} \quad (7.78)$$

so that

$$v_L = v_s \left[1 - \frac{z_{eq}}{(z_{eq} + z_L)} \right] e^{j\theta} = v_s \left[\frac{1}{1 + \frac{z_{eq}}{z_L}} \right] e^{j\theta} \quad (7.79)$$

Thus, any shift in the phase angle or magnitude from the no-load conditions is due to a nonzero z_{eq}/z_L . Because z_{eq} is almost entirely inductive, a purely inductive or capacitive load will not affect θ but will result only in a magnitude change in the voltage. On the contrary, a resistive or complex load will lead to shifts in both magnitude and phase angle.

Under no-load (NL) conditions ($z_L = \infty$), Equation 7.79 shows that

$$v_{L,NL} = v_s e^{j\theta} \quad (7.80)$$

Thus, taking ratios, we see that

$$\frac{v_L}{v_{L,NL}} = \frac{1}{\left(1 + \frac{z_{eq}}{z_L} \right)} \quad (7.81)$$

Therefore, the presence of a load will lower the magnitude and shift the phase, depending on the phase of the above ratio of impedances. This analysis is similar to that given in Chapter 3, except there we ignored the shift in phase. Because these transformers are designed to shift the phase by a given amount under no-load conditions, finding the additional shift in this phase caused by transformer loading is important. Let $z_{eq}/z_L = pe^{j\beta}$. Then, Equation 7.81 becomes

$$\frac{v_L}{v_{L,NL}} = \frac{1}{\sqrt{1 + 2p\cos\beta + p^2}} e^{-j\theta \tan^{-1}\left(\frac{p\sin\beta}{1+p\cos\beta}\right)} \quad (7.82)$$

As an example, let z_{eq} be a 10% inductive leakage impedance and z_L be a 100% resistive load. Then, $z_{eq}/z_L = 0.1e^{j90^\circ}$ and $v_L/v_{L,NL} = 0.995 \angle -5.71^\circ$, where \angle indicates the angular dependence of the complex number. This angle of nearly 6° will be subtracted from the phase angle of the transformer output, so the behavior of the phase under load is quite important. In the above example,

the magnitude will only be lowered by 0.5%. Because the transformer impedance varies with the tap setting (or phase shift), the angle shift due to loading also varies with the tap setting.

7.7 Fault Current Analysis

The phase-shifting transformers discussed in this section are all two-terminal transformers that have a single reactance, Z_{eq} or $Z_{eq,0}$, for positive- or negative- and zero-sequence circuits, respectively. We assume that the positive- and negative-sequence reactances are the same and do not distinguish them with subscripts. Thus, the theory developed in Chapter 6 can be applied to these phase-shifting transformers with the recognition that negative-sequence currents have a phase shift opposite of the positive-sequence currents. We retain the notations source, S , and load, L , used above instead of H and X . We assume the fault is on the L or output terminal. The fault currents at the fault position are the same for the various fault types, as shown in Chapter 6.

The faults of interest are as listed below:

1. Three-phase line-to-ground fault
2. Single-phase line-to-ground fault
3. Line-to-line fault
4. Double line-to-ground fault

We will summarize the fault currents for the above types here. We will use per-unit notation.

For fault type 1, we have

$$i_{a1} = \frac{v_{pf}}{z_1}, \quad i_{a2} = i_{a0} = 0 \quad (7.83)$$

For fault type 2, we assume that the a-phase line is shorted, so that

$$i_{a1} = \frac{v_{pf}}{(z_0 + z_1 + z_2)} = i_{a2} = i_{a0} \quad (7.84)$$

For fault type 3, assuming that the b and c lines are shorted together, we have

$$i_{a1} = \frac{v_{pf}}{(z_1 + z_2)} = -i_{a2}, \quad i_{a0} = 0 \quad (7.85)$$

For fault type 4, assuming that the b and c lines are shorted to ground, we get

$$\begin{aligned} i_{a1} &= v_{\text{pf}} \left(\frac{z_0 + z_2}{z_0 z_1 + z_0 z_2 + z_1 z_2} \right) \\ i_{a2} &= -v_{\text{pf}} \left(\frac{z_0}{z_0 z_1 + z_0 z_2 + z_1 z_2} \right) \\ i_{a0} &= -v_{\text{pf}} \left(\frac{z_2}{z_0 z_1 + z_0 z_2 + z_1 z_2} \right) \end{aligned} \quad (7.86)$$

Assuming equal positive and negative reactances for the transformer and the systems, we have the following expressions for the Thevenin impedances:

$$z_1 = z_2 = \frac{z_{\text{SL}}(z_{\text{eq}} + z_{\text{SS}})}{z_{\text{eq}} + z_{\text{SS}} + z_{\text{SL}}}, \quad z_0 = \frac{z_{\text{SL},0}(z_{\text{eq},0} + z_{\text{SS},0})}{z_{\text{eq},0} + z_{\text{SS},0} + z_{\text{SL},0}} \quad (7.87)$$

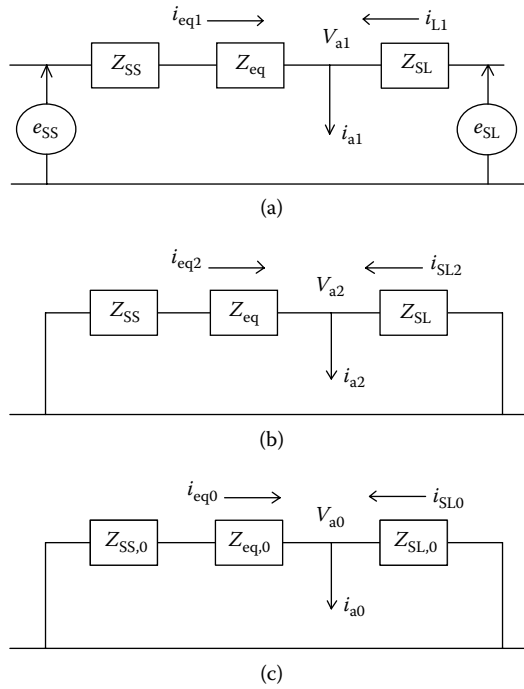
The per-unit currents feeding the fault from the transformer side are given by

$$\begin{aligned} i_{\text{eq}1} &= i_{a1} \left(\frac{z_1}{z_{\text{eq}} + z_{\text{SS}}} \right), & i_{\text{eq}2} &= i_{a2} \left(\frac{z_1}{z_{\text{eq}} + z_{\text{SS}}} \right) \\ i_{\text{eq}0} &= i_{a0} \left(\frac{z_0}{z_{\text{eq},0} + z_{\text{SS},0}} \right) \end{aligned} \quad (7.88)$$

Figure 7.11 shows the terminal circuit diagrams for the three sequences, covering all the fault types. For simplicity, we assume that no current flows in the prefault condition. These can always be added later.

As shown in Figure 7.11, the per-unit currents flowing out of the transformer into the fault are on the load side of the transformer and are given by Equation 7.88 in terms of the fault sequence currents. Thus, in terms of finding the fault currents in the individual windings, we need to find their expressions in terms of the load currents. However, in a phase-shifting transformer, positive- and negative-sequence currents experience opposite phase shifts. This makes the analysis of fault currents within these transformers quite different from the fault currents in a standard two-winding transformer.

We have already considered the currents in the windings of a phase-shifting transformer when we derived their equivalent impedance for positive-, negative-, and zero-sequence circuits. Now, we use those results and the fact that negative-sequence currents within a phase-shifting transformer can be obtained from the positive-sequence currents by changing their phase shift to its negative. Note that i_{eq} in Equation 7.88 equals i_{S1} in per-unit terms. We now apply the fault formulas from Equation 7.88 to the phase-shifting transformers described in Sections 7.3 through 7.5. Because the per-unit notation is used, we need to express the formulas for the currents

**FIGURE 7.11**

Sequence circuits showing system impedances and transformer equivalent impedances. The fault is on the load-side terminal: (a) positive sequence, (b) negative sequence, and (c) zero sequence.

in per-unit terms. Considering the lengths of the formulas, we only present the results for the winding-sequence currents.

7.7.1 Squashed Delta Fault Currents

From Equation 7.17, we see that

$$\mathbf{I}_{a'} = \frac{n}{n - e^{j120^\circ}} \mathbf{I}_{S1} = \frac{n}{n - e^{j120^\circ}} e^{-j\theta} \mathbf{I}_{L1} \quad (7.89)$$

where

$$\theta = 2 \tan^{-1} \left(\frac{\sqrt{3}}{2n + 1} \right) \quad (7.90)$$

Using Equation 7.90, Equation 7.89 can be manipulated to the following form:

$$\mathbf{I}_{a'} = \frac{n}{\sqrt{n^2 + n + 1}} e^{-j\frac{\theta}{2}} \mathbf{I}_{L1} \quad (7.91)$$

To convert this expression to the per-unit form, we need the ratios of the current bases. These are the reciprocals of the ratios of the voltage bases, assuming the same power level for both bases. This is given by

$$\frac{I_{b,L1}}{I_{b,a'}} = \frac{V_{b,a'}}{V_{b,L1}} = \frac{\sqrt{3}}{\sqrt{n^2 + n + 1}} \quad (7.92)$$

Using this relation, we can convert Equation 7.91 to the per-unit form:

$$\mathbf{i}_{a'} = \frac{n\sqrt{3}}{n^2 + n + 1} e^{-j\frac{\theta}{2}} \mathbf{i}_{L1} \quad (7.93)$$

Because this is a two-winding transformer, $\mathbf{i}_a = -\mathbf{i}_{a'}$.

For the zero-sequence currents, from Equations 7.28 and 7.31, we have

$$\mathbf{I}_{a',0} = -n\mathbf{I}_{c,0} = \frac{n}{n-1} \mathbf{I}_{L1} \quad (7.94)$$

Note that the zero-sequence current is the same in all the phases. Using the base transformation given in Equation 7.92, this can be converted to per-unit form:

$$\mathbf{i}_{a',0} = \frac{n\sqrt{3}}{(n-1)\sqrt{n^2 + n + 1}} \mathbf{i}_{L1} \quad (7.95)$$

We also have $\mathbf{i}_{a0} = -\mathbf{i}_{a'0}$.

Using Equation 7.88 and the fact that negative-sequence currents have an opposite phase shift from positive-sequence currents, we can find the sequence currents in the windings as follows:

$$\begin{aligned} \mathbf{i}_{a',1} &= i_{a1} e^{-j\frac{\theta}{2}} \left(\frac{n\sqrt{3}}{n^2 + n + 1} \right) \left(\frac{z_1}{z_{eq} + z_{ss}} \right) \\ \mathbf{i}_{a',2} &= i_{a2} e^{j\frac{\theta}{2}} \left(\frac{n\sqrt{3}}{n^2 + n + 1} \right) \left(\frac{z_1}{z_{eq} + z_{ss}} \right) \\ \mathbf{i}_{a',0} &= i_{a0} \left(\frac{n\sqrt{3}}{(n-1)\sqrt{n^2 + n + 1}} \right) \left(\frac{z_0}{z_{eq,0} + z_{ss,0}} \right) \end{aligned} \quad (7.96)$$

Here, i_{a1} , i_{a2} , and i_{a0} are the fault sequence currents for the various fault types described in Chapter 6. These can then be transformed to the phase or winding currents by using Equation 6.1.

7.7.2 Standard Delta Fault Currents

This transformer has three windings. From Equation 7.39, we have

$$\mathbf{I}_a = -\frac{2}{n\left(1 - j\frac{\sqrt{3}}{n}\right)}\mathbf{I}_{S1} = -\frac{2}{n\left(1 - j\frac{\sqrt{3}}{n}\right)}e^{-j\theta}\mathbf{I}_{L1} = -\frac{2}{\sqrt{n^2 + 3}}e^{-j\frac{\theta}{2}}\mathbf{I}_{L1} \quad (7.97)$$

where

$$\mathbf{I}_{L1} = e^{j\theta}\mathbf{I}_{S1} \quad \text{and} \quad \theta = 2\tan^{-1}\left(\frac{\sqrt{3}}{n}\right) \quad (7.98)$$

Converting to the per-unit system, we find for the ratio of current bases:

$$\frac{I_{b,L1}}{I_{b,a}} = \frac{E_a}{V_{L1}} = \frac{n\sqrt{3}}{\sqrt{n^2 + 3}} \quad (7.99)$$

Using this ratio, Equation 7.97 becomes (in per-unit terms)

$$\mathbf{i}_a = -\frac{2n\sqrt{3}}{n^2 + 3}e^{-j\frac{\theta}{2}}\mathbf{i}_{L1} \quad (7.100)$$

We also have

$$\mathbf{I}_{a'} = e^{-j\theta}\mathbf{I}_{L1}, \quad \mathbf{I}_{a''} = \mathbf{I}_{L1} \quad (7.101)$$

The ratio of current bases is the same for the currents in Equation 7.101 and is given by

$$\frac{I_{b,L1}}{I_{b,a'}} = \frac{E_{a'}}{V_{L1}} = \frac{\sqrt{3}}{\sqrt{n^2 + 3}} \quad (7.102)$$

Using this, Equation 7.101 becomes (in per-unit terms),

$$\mathbf{i}_{a'} = \frac{\sqrt{3}}{\sqrt{n^2 + 3}}e^{-j\theta}\mathbf{i}_{L1}, \quad \mathbf{i}_{a''} = \frac{\sqrt{3}}{\sqrt{n^2 + 3}}\mathbf{i}_{L1} \quad (7.103)$$

Using trigonometric identities and the formula for θ from Equation 7.98, we can show that $\mathbf{i}_a + \mathbf{i}_{a'} + \mathbf{i}_{a''} = 0$.

For the zero-sequence currents, from Equations 7.49 and 7.50, we get

$$\mathbf{I}_{a,0} = -\frac{2}{n}\mathbf{I}_{L1,0}, \quad I_{a',0} = \mathbf{I}_{L1,0}, \quad I_{a'',0} = \mathbf{I}_{L1,0} \quad (7.104)$$

Putting these on a per-unit basis, using the same current bases as for the positive-sequence case, we get

$$\mathbf{i}_{a,0} = -\frac{2\sqrt{3}}{\sqrt{n^2+3}}\mathbf{i}_{L1,0}, \quad \mathbf{i}_{a',0} = \frac{\sqrt{3}}{\sqrt{n^2+3}}\mathbf{i}_{L1,0}, \quad \mathbf{i}_{a'',0} = \frac{\sqrt{3}}{\sqrt{n^2+3}}\mathbf{i}_{L1,0} \quad (7.105)$$

These zero-sequence per-unit currents also sum to zero, as expected.

Using Equation 7.88 and noting that i_{eq} corresponds to i_{L1} , we get the following expressions for the winding sequence currents:

$$\begin{aligned} \mathbf{i}_{a,1} &= -i_{a1} \frac{2n\sqrt{3}}{n^2+3} e^{-j\theta} \left(\frac{z_1}{z_{eq} + z_{SS}} \right), & \mathbf{i}_{a,2} &= -i_{a2} \frac{2n\sqrt{3}}{n^2+3} e^{j\frac{\theta}{2}} \left(\frac{z_1}{z_{eq} + z_{SS}} \right) \\ \mathbf{i}_{a,0} &= -i_{a0} \frac{2\sqrt{3}}{\sqrt{n^2+3}} \left(\frac{z_0}{z_{eq,0} + z_{SS,0}} \right) \\ \mathbf{i}_{a',1} &= i_{a1} \frac{\sqrt{3}}{\sqrt{n^2+3}} e^{-j\theta} \left(\frac{z_1}{z_{eq} + z_{SS}} \right), & \mathbf{i}_{a',2} &= i_{a2} \frac{\sqrt{3}}{\sqrt{n^2+3}} e^{j\theta} \left(\frac{z_1}{z_{eq} + z_{SS}} \right) \\ \mathbf{i}_{a',0} &= i_{a0} \frac{\sqrt{3}}{\sqrt{n^2+3}} \left(\frac{z_0}{z_{eq,0} + z_{SS,0}} \right) \\ \mathbf{i}_{a'',1} &= i_{a1} \frac{\sqrt{3}}{\sqrt{n^2+3}} \left(\frac{z_1}{z_{eq} + z_{SS}} \right), & \mathbf{i}_{a'',2} &= i_{a2} \frac{\sqrt{3}}{\sqrt{n^2+3}} \left(\frac{z_1}{z_{eq} + z_{SS}} \right) \\ \mathbf{i}_{a'',0} &= i_{a0} \frac{\sqrt{3}}{\sqrt{n^2+3}} \left(\frac{z_0}{z_{eq,0} + z_{SS,0}} \right) \end{aligned} \quad (7.106)$$

The per-unit currents for the various fault types can be inserted for i_{a1} , i_{a2} , and i_{a0} , as shown in Chapter 6. Accordingly, one can then get the winding phase currents in per-unit terms by applying Equation 6.1 for the various fault types.

7.7.3 Two-Core Phase-Shifting Transformer Fault Currents

We will quote the results for this transformer based on the formulas in [Section 7.5](#). This transformer has five windings, labeled 1, 1', a, a', and a''. The per-unit winding currents, expressed in terms of the output L1 current, are given by

$$\begin{aligned}
\mathbf{i}_1 &= -j \frac{2\sqrt{3}n_en_s}{(n_en_s)^2 + 3} e^{-j\frac{\theta}{2}} \mathbf{i}_{L1} = -\mathbf{i}_{1'}, & \mathbf{i}_a &= -\frac{2\sqrt{3}n_en_s}{(n_en_s)^2 + 3} e^{-j\frac{\theta}{2}} \mathbf{i}_{L1} \\
\mathbf{i}_{a'} &= \frac{\sqrt{3}}{\sqrt{(n_en_s)^2 + 3}} e^{-j\theta} \mathbf{i}_{L1}, & \mathbf{i}_{a''} &= \frac{\sqrt{3}}{\sqrt{(n_en_s)^2 + 3}} \mathbf{i}_{L1} \\
\mathbf{i}_{1,0} &= i_{1',0} = 0, & \mathbf{i}_{a,0} &= -\frac{2\sqrt{3}}{\sqrt{(n_en_s)^2 + 3}} \mathbf{i}_{L1,0} \\
\mathbf{i}_{a',0} &= \frac{\sqrt{3}}{\sqrt{(n_en_s)^2 + 3}} \mathbf{i}_{L1,0} = \mathbf{i}_{a'',0}
\end{aligned} \tag{7.107}$$

The winding sequence currents are given by

$$\begin{aligned}
\mathbf{i}_{1,1} &= -j \frac{2\sqrt{3}n_en_s}{(n_en_s)^2 + 3} e^{-j\frac{\theta}{2}} \mathbf{i}_{L1,1}, & \mathbf{i}_{1',2} &= j \frac{2\sqrt{3}n_en_s}{(n_en_s)^2 + 3} e^{j\frac{\theta}{2}} \mathbf{i}_{L1,2} \\
\mathbf{i}_{1,0} &= i_{1',0} = 0 \\
\mathbf{i}_{a,1} &= -\frac{2\sqrt{3}n_en_s}{(n_en_s)^2 + 3} e^{-j\frac{\theta}{2}} \mathbf{i}_{L1,1}, & \mathbf{i}_{a,2} &= -\frac{2\sqrt{3}n_en_s}{(n_en_s)^2 + 3} e^{j\frac{\theta}{2}} \mathbf{i}_{L1,2} \\
\mathbf{i}_{a,0} &= -\frac{2\sqrt{3}}{\sqrt{(n_en_s)^2 + 3}} \mathbf{i}_{L1,0} \\
\mathbf{i}_{a',1} &= \frac{\sqrt{3}}{\sqrt{(n_en_s)^2 + 3}} e^{-j\theta} \mathbf{i}_{L1,1}, & \mathbf{i}_{a',2} &= \frac{\sqrt{3}}{\sqrt{(n_en_s)^2 + 3}} e^{j\theta} \mathbf{i}_{L1,2} \\
\mathbf{i}_{a',0} &= \frac{\sqrt{3}}{\sqrt{(n_en_s)^2 + 3}} \mathbf{i}_{L1,0} \\
\mathbf{i}_{a'',1} &= \frac{\sqrt{3}}{\sqrt{(n_en_s)^2 + 3}} \mathbf{i}_{L1,1} = \mathbf{i}_{a'',2}, & \mathbf{i}_{a'',0} &= \frac{\sqrt{3}}{\sqrt{(n_en_s)^2 + 3}} \mathbf{i}_{L1,0}
\end{aligned} \tag{7.108}$$

Substituting the i_{eq} currents from Equation 7.88 for \mathbf{i}_{L1} into the formulas in Equation 7.108, we get the sequence currents in all the windings. Note that j in Equation 7.108 is a rotation by 90° in the complex plane, so in the negative-sequence current formula, it has to be replaced by $-j$ for a 90° rotation in the opposite direction.

7.8 Zig-Zag Transformer

A delta HV (*H*) winding and zig-zag low-voltage (*X*) winding transformer is analyzed. The complex currents are calculated, as well as the terminal positive- or negative- and zero-sequence impedances. Although explicit expressions for these impedances are given in terms of the two-winding impedances, they can also be obtained directly from a program that calculates the magnetic field associated with complex currents. These impedances can then be used to obtain fault currents for a short-circuit analysis.

The three-phase connections for the delta primary and zig-zag secondary windings are given schematically in Figure 7.12. Parallel lines denote the windings on the same phase. The delta winding phases are denoted *a*, *b*, and *c*. The zig-zag windings consist of windings from the two phases connected in series. Thus, the zig-zag *X*₁ terminal is attached to a series combination of windings from the *b* and *c* phases. The orientation of the zig-zag windings in Figure 7.12 is such that the terminal voltage of the *X* terminals to ground is in phase with the terminal voltage of the delta terminals *V* to ground. This requires the two separate windings of the zig-zag to have the same number of turns. A 180° phase shift between *X* and *V* can be achieved by winding the *X* windings in the opposite sense of the delta windings.

Figure 7.13 shows the positive-sequence phasors associated with the winding and terminal voltages of the delta winding. *E*_{*a*}, *E*_{*b*}, and *E*_{*c*} are a positive-sequence set of winding voltages, and *V*₁, *V*₂, and *V*₃ are a positive-sequence set of terminal-to-ground voltages. The *E*'s are no-load voltages due to the core excitation; the diagram in Figure 7.13 does not take into account the voltage drops caused by the currents and impedances. For the voltage drops,

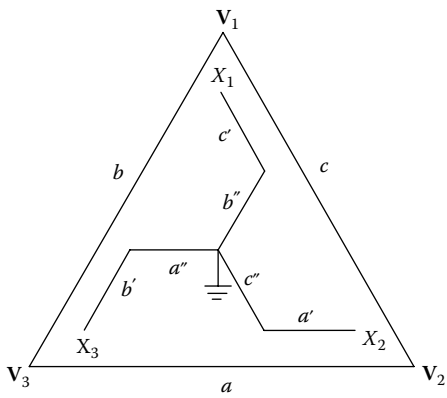
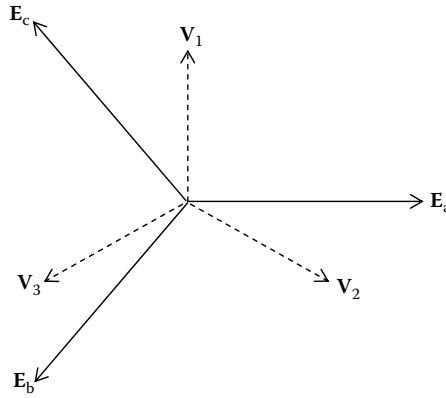


FIGURE 7.12
Schematic three-phase connection diagram of the zig-zag transformer.

**FIGURE 7.13**

Phasor diagram of the delta terminal and winding voltages.

we use a three-winding T-equivalent circuit model. The single-winding impedances are the same for all the three phases. Concentrating on the a phase, the winding voltages are given by

$$\begin{aligned} V_a &= E_a + I_a Z_a \text{ (Delta HV)} \\ V_{a'} &= E_{a'} + I_{a'} Z_{a'} \text{ (Zig-Y LV)} \\ V_{a''} &= E_{a''} + I_{a''} Z_{a''} \text{ (Zag-Y LV)} \end{aligned} \quad (7.109)$$

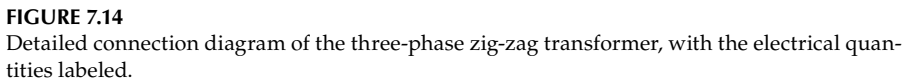
where the currents are taken to be positive into the winding terminals. The E 's are proportional to the winding turns and increase in the opposite sense to the current direction.

The connection diagram of the winding for all the three phases is shown in Figure 7.14. The subscripts a , a' , and a'' refer to the delta, zig, and zag windings, respectively, of the a phase. The b and c subscripts have the same significance for the b and c phases. The zig and zag windings are connected in such a way that their phase voltages are subtractive. This gives the maximum net voltage across both windings.

7.8.1 Calculation of Electrical Characteristics

Like the voltages, the currents I_1 , I_2 , and I_3 and $I_{a'}$, $I_{b'}$, and $I_{c'}$ form three-phase sets, as shown in Figure 7.14. From this figure, we have

$$\begin{aligned} I_1 &= I_c - I_b \\ I_2 &= I_a - I_c \\ I_3 &= I_b - I_a \end{aligned} \quad (7.110)$$


$$\begin{aligned} \mathbf{V}_1 - \mathbf{V}_2 &= \mathbf{E}_c + \mathbf{I}_c Z_a \\ \mathbf{V}_3 - \mathbf{V}_1 &= \mathbf{E}_b + \mathbf{I}_b Z_a \\ \mathbf{V}_2 - \mathbf{V}_3 &= \mathbf{E}_a + \mathbf{I}_a Z_a \end{aligned} \quad (7.111)$$

For the X1 terminal, from Figure 7.14, we see that

We let N_1 = the number of turns in the HV delta winding and N_2 = the number of turns in the zig winding = the number of turns in the zag winding; thus, we have

where we define n as the ratio of turns in the delta winding to turns in the zig or zag winding. Because of the phase relationship among the constituents of a positive-sequence set, we can write

$$\mathbf{E}_{c'} - \mathbf{E}_{b''} = \mathbf{E}_{a'}(e^{j120^\circ} - e^{-j120^\circ}) = j\sqrt{3}\mathbf{E}_{a'} = j\frac{\sqrt{3}}{n}\mathbf{E}_a \quad (7.114)$$

From Equation 7.111, we have

$$\mathbf{E}_a = (\mathbf{V}_2 - \mathbf{V}_3) - \mathbf{I}_a Z_a = (e^{-j120^\circ} - e^{j120^\circ})\mathbf{V}_1 - \mathbf{I}_a Z_a = -j\sqrt{3}\mathbf{V}_1 - \mathbf{I}_a Z_a \quad (7.115)$$

Substituting from Equations 7.114 and 7.115 into Equation 7.112, we get

$$\mathbf{V}_{x1} = \frac{3}{n}\mathbf{V}_1 - j\frac{\sqrt{3}}{n}\mathbf{I}_a Z_a + \mathbf{I}_{c'} Z_{a'} - \mathbf{I}_{b''} Z_{a''} \quad (7.116)$$

Due to the continuity of the current in the zig and zag windings, we must have

$$\begin{aligned} \mathbf{I}_{c'} &= -\mathbf{I}_{b''} \\ \mathbf{I}_{a'} &= -\mathbf{I}_{c''} \\ \mathbf{I}_{b'} &= -\mathbf{I}_{a''} \end{aligned} \quad (7.117)$$

so that Equation 7.116 can be rewritten as

$$\mathbf{V}_{x1} = \frac{3}{n}\mathbf{V}_1 - j\frac{\sqrt{3}}{n}\mathbf{I}_a Z_a + \mathbf{I}_{c'}(Z_{a'} + Z_{a''}) \quad (7.118)$$

Since the currents form a balanced set, we have

$$\mathbf{I}_{c'} = e^{j120^\circ}\mathbf{I}_{a'} \quad (7.119)$$

From amp-turn balance, we have

$$\begin{aligned} N_1\mathbf{I}_a + N_2\mathbf{I}_{a'} + N_2\mathbf{I}_{a''} &= 0 \\ n\mathbf{I}_a + \mathbf{I}_{a'} + \mathbf{I}_{a''} &= 0 \end{aligned} \quad (7.120)$$

From Equation 7.117, we have

$$\mathbf{I}_{a''} = -\mathbf{I}_{b'} = -e^{-j120^\circ}\mathbf{I}_{a'} \quad (7.121)$$

Thus, from Equations 7.119 through 7.121, we get

$$\mathbf{I}_{c'} = -j\frac{n}{\sqrt{3}}\mathbf{I}_a \quad (7.122)$$

Using this result, Equation 7.118 becomes

$$\mathbf{V}_{x1} = \frac{3}{n}\mathbf{V}_1 - j\frac{\sqrt{3}}{n}\mathbf{I}_a \left[Z_a + \frac{n^2}{3}(Z_{a'} + Z_{a''}) \right] \quad (7.123)$$

From Equation 7.110, we have

$$\mathbf{I}_1 = (\mathbf{e}^{j120^\circ} - \mathbf{e}^{-j120^\circ})\mathbf{I}_a = j\sqrt{3}\mathbf{I}_a \quad (7.124)$$

Substituting this into Equation 7.123, we get

$$\mathbf{V}_{X1} = \frac{3}{n}\mathbf{V}_1 - \frac{\mathbf{I}_1}{n} \left[Z_a + \frac{n^2}{3}(Z_{a'} + Z_{a''}) \right] \quad (7.125)$$

Thus, under no-load conditions, we see from Equation 7.125 that the terminal voltages are related by

$$\mathbf{V}_{X1} = \frac{3}{n}\mathbf{V}_1 \quad (7.126)$$

This shows that the no-load terminal voltages H and X are in phase, as desired. From Equations 7.122 and 7.124, the current into the $X1$ terminal is

$$\mathbf{I}_{X1} = \mathbf{I}_{c'} = -\frac{n}{3}\mathbf{I}_1 \quad (7.127)$$

Thus, we see that the power into the $X1$ terminal, ignoring the impedance drop, is

$$\mathbf{V}_{X1}\mathbf{I}_{X1}^* = -\mathbf{V}_1\mathbf{I}_1^* \quad (7.128)$$

where $*$ indicates complex conjugation. This equation shows that the power flows out of the $X1$ terminal and that it equals the power into the V_1 terminal. From Equations 7.115 and 7.124, ignoring the impedance drop, we also get

$$\mathbf{E}_a\mathbf{I}_a^* = \mathbf{V}_1\mathbf{I}_1^* \quad (7.129)$$

so that the delta winding power equals the input power. The a -phase winding currents can be obtained from Equations 7.120 and 7.121.

$$\begin{aligned} \mathbf{I}_{a'} &= n\mathbf{I}_a \left(-\frac{1}{2} + \frac{j}{2\sqrt{3}} \right) \\ \mathbf{I}_{a''} &= n\mathbf{I}_a \left(-\frac{1}{2} - \frac{j}{2\sqrt{3}} \right) \end{aligned} \quad (7.130)$$

Multiplying Equation 7.125 by $n/3$, we get

$$\frac{n}{3}\mathbf{V}_{X1} = \mathbf{V}_1 - \frac{\mathbf{I}_1}{3} \left[Z_a + \frac{n^2}{3}(Z_{a'} + Z_{a''}) \right] \quad (7.131)$$

Thus, as seen from the high-voltage (HV) side, the effective impedance, Z_{eff} , is given by

$$Z_{\text{eff}} = \frac{1}{3} \left[Z_a + \frac{n^2}{3} (Z_{a'} + Z_{a'}) \right] \quad (7.132)$$

7.8.2 Per-Unit Formulas

At this point, it is desirable to represent everything on per-unit bases. We will use the input power per phase as the power base. Using Equation 7.129, this also equals the delta winding power. Thus, $P_b = V_1 I_1 = E_a I_a$. The asterisks are not needed because these quantities are real. Thus, V_1 and I_1 are the voltage and current bases for the H terminal. We label these as $V_{b,1}$ and $I_{b,1}$. In terms of these and from Equations 7.126 and 7.127, the base voltage and current at the $X1$ terminal are

$$\begin{aligned} V_{b,X1} &= \frac{3}{n} V_{b,1} \\ I_{b,X1} &= \frac{n}{3} I_{b,1} \end{aligned} \quad (7.133)$$

Dividing Equation 7.131 by $V_{b,1}$ and using Equation 7.133, we find that

$$\mathbf{v}_{X1} = \mathbf{v}_1 - \mathbf{i}_1 z_{\text{eff}} \quad (7.134)$$

where lowercase letters have been used for per-unit quantities, and

$$z_{\text{eff}} = \frac{Z_{\text{eff}}}{Z_{b,1}} \quad (7.135)$$

where

$$Z_{b,1} = \frac{V_{b,1}}{I_{b,1}} = \frac{V_{b,1}^2}{P_b} \quad (7.136)$$

Since the H winding power equals the terminal power, we can resort to a winding base to calculate z_{eff} . From Equations 7.115 and 7.124, ignoring impedance reductions, we get

$$\begin{aligned} V_{b,a} &= \sqrt{3} V_{b,1} \\ I_{b,a} &= \frac{1}{\sqrt{3}} I_{b,1} \\ Z_{b,a} &= \frac{V_{b,a}}{I_{b,a}} = \frac{V_{b,a}^2}{P_b} = 3 Z_{b,1} \end{aligned} \quad (7.137)$$

For the a' and a'' windings, using Equation 7.113 and maintaining the same power base, we have

$$\begin{aligned} V_{b,a'} &= V_{b,a''} = \frac{V_{b,a}}{n} \\ Z_{b,a'} &= Z_{b,a''} = \frac{V_{b,a'}^2}{P_b} = \frac{Z_{b,a}}{n^2} \end{aligned} \quad (7.138)$$

From Equations 7.135 and 7.132, we can write

$$z_{\text{eff}} = \frac{Z_{\text{eff}}}{Z_{b,1}} = \frac{1}{3} \left[\left(\frac{Z_{b,a}}{Z_{b,1}} \right) \frac{Z_a}{Z_{b,a}} + \frac{n^2}{3} \left(\frac{Z_{b,a}}{Z_{b,1}} \right) \left(\frac{Z_{b,a'}}{Z_{b,a}} \right) \frac{(Z_{a'} + Z_{a''})}{Z_{b,a'}} \right] \quad (7.139)$$

Using Equations 7.137 and 7.138, we can put each winding on its own base to get

$$z_{\text{eff}} = z_a + \frac{1}{3}(z_{a'} + z_{a''}) \quad (7.140)$$

In terms of two-winding per-unit impedances, we have the standard formulas

$$\begin{aligned} z_a &= \frac{z_{aa'} + z_{aa''} - z_{a'a''}}{2} \\ z_{a'} &= \frac{z_{aa'} + z_{a'a''} - z_{aa''}}{2} \\ z_{a''} &= \frac{z_{aa''} + z_{a'a''} - z_{aa'}}{2} \end{aligned} \quad (7.141)$$

Substituting these into Equation 7.140, we get

$$z_{\text{eff}} = \frac{z_{aa'} + z_{aa''}}{2} - \frac{z_{a'a''}}{6} \quad (7.142)$$

Thus, the effective terminal impedance can be derived from the two-winding impedances.

7.8.3 Zero-Sequence Impedance

We can use a similar analysis to get the zero-sequence impedance, using a zero subscript to label the zero-sequence quantities. Thus, instead of Equation 7.112, we have

$$\mathbf{V}_{x1,0} = \mathbf{E}_{c',0} + \mathbf{I}_{c',0} Z_{a',0} - \mathbf{E}_{b'',0} - \mathbf{I}_{b'',0} Z_{a'',0} \quad (7.143)$$

However, $E_{c',0}$ and $E_{b'',0}$ are now in phase and have the same magnitude, and therefore, they cancel each other in Equation 7.143. In addition, using Equation 7.117, which also applies to zero-sequence currents, Equation 7.143 becomes

$$\mathbf{V}_{X1,0} = \mathbf{I}_{c',0} (Z_{a',0} + Z_{a'',0}) \quad (7.144)$$

From Equation 7.117 and the equality of the zero-phase currents in the three phases, we have

$$\mathbf{I}_{a',0} = \mathbf{I}_{b',0} = -\mathbf{I}_{a'',0} \quad (7.145)$$

Hence, applying Equation 7.120 to zero-phase currents, we get

$$\mathbf{I}_{a,0} = 0 \quad (7.146)$$

Thus, no zero-sequence current flows in the delta HV winding. Since $\mathbf{I}_{X1,0} = \mathbf{I}_{c',0}$, Equation 7.144 becomes

$$\mathbf{V}_{X1,0} = \mathbf{I}_{X1,0} (Z_{a',0} + Z_{a'',0}) \quad (7.147)$$

Reverting to per-unit quantities, we divide Equation 7.147 by $V_{b,X1}$ to get

$$\mathbf{v}_{X1,0} = \mathbf{i}_{X1,0} z_{\text{eff},0} \quad (7.148)$$

where

$$z_{\text{eff},0} = \left(\frac{Z_{a',0} + Z_{a'',0}}{Z_{b,X1}} \right) \quad (7.149)$$

and

$$Z_{b,X1} = \frac{V_{b,X1}^2}{P_b} = \left(\frac{V_{b,X1}}{V_{b,a'}} \right)^2 \frac{V_{b,a'}^2}{P_b} = 3Z_{b,a'} \quad (7.150)$$

Substituting this into Equation 7.149 and using Equation 7.141, we get

$$z_{\text{eff},0} = \frac{1}{3} (z_{a',0} + z_{a'',0}) = \frac{1}{3} z_{a'a'',0} \quad (7.151)$$

Thus, we can find the effective zero-sequence impedance from the per-unit two-winding zero-sequence impedance between the zig and zag windings. Normally, we calculate the positive-sequence impedance and adjust it, via an empirical factor, to get the zero-sequence impedance.

7.8.4 Fault Current Analysis

The phase-sequence diagrams are shown in Figure 7.15. We will calculate the sequence currents in the three windings in terms of the fault-sequence currents, which depend on the fault type. The phase currents can then be obtained by the transformation given in Equation 6.1. We will consider equal positive- and negative-sequence reactances for the transformer and the systems and will not distinguish them with subscripts. In addition, we will consider an X-terminal fault, which is fed from the HV line.

The Thevenin impedances, in terms of those given in Figure 7.15, are

$$z_1 = z_2 = \frac{z_{SX}(z_{eff} + z_{SH})}{z_{eff} + z_{SH} + z_{SX}}, \quad z_0 = \frac{z_{SX,0}(z_{eff,0} + z_{SH,0})}{z_{eff,0} + z_{SH,0} + z_{SX,0}} \quad (7.152)$$

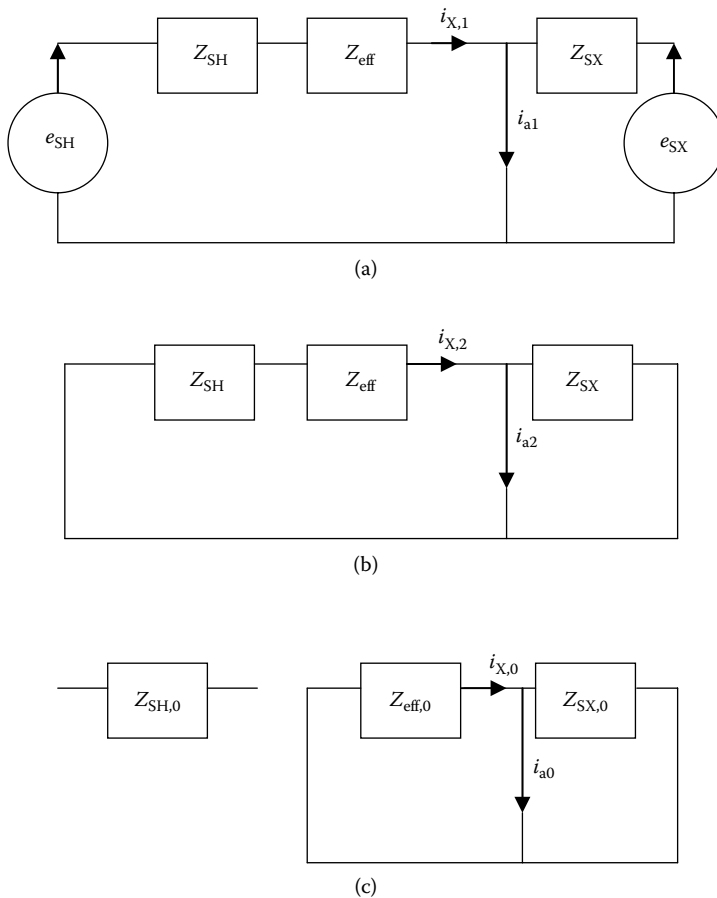


FIGURE 7.15

Sequence circuits for the zig-zag transformer: (a) positive sequence, (b) negative sequence, and (c) zero sequence.

$z_{SH,0}$ must be set equal to zero in the formulas. The per-unit sequence currents feeding the fault from the transformer side are given by

$$\begin{aligned} i_{X,1} &= i_{a1} \left(\frac{z_1}{z_{\text{eff}} + z_{SH}} \right), & i_{X,2} &= i_{a2} \left(\frac{z_1}{z_{\text{eff}} + z_{SH}} \right) \\ i_{X,0} &= i_{a0} \left(\frac{z_0}{z_{\text{eff},0} + z_{SH,0}} \right) \end{aligned} \quad (7.153)$$

We need to find the per-unit fault-sequence currents in the windings in terms of the fault-sequence currents out of the X1 terminal. The number 1 preceded by a comma in Equation 7.153 refers to a positive sequence, and so forth, whereas X1 refers to the X terminal number 1. From Equations 7.124, 7.127, and 7.130, we find that

$$\mathbf{I}_a = j \frac{\sqrt{3}}{n} \mathbf{I}_{X1}, \quad \mathbf{I}_{a'} = n \mathbf{I}_a \left(-\frac{1}{2} + j \frac{1}{2\sqrt{3}} \right), \quad \mathbf{I}_{a''} = n \mathbf{I}_a \left(-\frac{1}{2} - j \frac{1}{2\sqrt{3}} \right) \quad (7.154)$$

From Equations 7.133, 7.137, and 7.138, the current bases are related by

$$\frac{I_{b,X1}}{I_{b,a}} = \frac{n}{\sqrt{3}}, \quad \frac{I_{b,X1}}{I_{b,a'}} = \frac{I_{b,X1}}{I_{b,a''}} = \frac{1}{\sqrt{3}} \quad (7.155)$$

Using these base-current relations, Equation 7.154 can be written in per-unit terms as

$$\mathbf{i}_a = j \mathbf{i}_{X1}, \quad \mathbf{i}_{a'} = j \mathbf{i}_{X1} \left(-\frac{1}{2} + j \frac{1}{2\sqrt{3}} \right), \quad \mathbf{i}_{a''} = j \mathbf{i}_{X1} \left(-\frac{1}{2} - j \frac{1}{2\sqrt{3}} \right) \quad (7.156)$$

The three per-unit currents sum to zero as expected.

Replacing X1 by X,1, X,2, and X,0 for the sequence currents obtained from Equation 7.153 for the different fault types, we can obtain, from Equation 7.156, the fault-sequence currents in the various windings. From these, we can then obtain the phase currents from Equation 6.1.

8

Multiterminal Three-Phase Transformer Model

8.1 Introduction

This chapter closely follows our published papers “Applications of a Multiterminal Transformer Model Using Two Winding Leakage Inductances” [Del06] and “Multiterminal Three Phase Transformer Model With Balanced or Unbalanced Loading” [Del08].

In Chapters 3 and 4, we have shown that two- and three-terminal transformers can be modeled using leakage inductances or reactances associated with the leakage flux. The two-winding leakage inductance is the self-inductance of the two windings, assuming that the sum of the amp-turns is zero. It is easily measured by applying a voltage to the first winding, shorting the second winding, and measuring the reactance, while keeping other windings open circuited. It is also easily calculated with finite element codes or analytic methods.

To model the circuit for a two-winding transformer, we need an ideal transformer in series with the leakage inductance. For a three-winding transformer, we can combine the three pairs of leakage inductances to form three single winding inductances that, together with an ideal transformer, form a simple circuit without mutual couplings, called a T-equivalent circuit. For a four-winding transformer, a similar process leads to a much more complicated circuit, again without mutual couplings [Blu51]. There does not appear to be a circuit model without mutual couplings for a transformer with any number of terminals or windings. However, some methods use only the two-winding leakage inductances to model the transformer [Bra82], [deL92], [Mom02], [Shi63], [Aco89]. These have mutual couplings and assume an ideal or separately treated iron core. We explore such a method in this chapter and show how it lends itself naturally to matrix methods to obtain complicated connections among the windings on the same or different legs. The single-winding resistances are also included in the model for greater generality.

In this chapter, we derive the basic equations from first principles in order to highlight the assumptions in the model and to establish the terminology.

Most of the examples given are for two- or three-terminal transformers in order to show that the formulas do reduce to the familiar formulas derived by previous methods. We will restrict our discussion to sinusoidal conditions at power frequencies. We will also develop a theory initially for balanced conditions, and later extend the theory to account for unbalanced conditions, including short circuits. The latter development requires the inclusion of the core in order to get a solvable system. Both methods are useful, depending on the type of problem to be solved.

For higher-frequency applications, capacitances must be included [deL92a]. The inductances and, to a lesser extent, the leakage inductances, also vary with frequency. The resistances have a strong frequency dependence, and thus mutual resistances at higher frequencies must also be considered [Mom02]. However, we will only deal with the low-frequency inductive and resistive aspects of the windings in this chapter.

8.2 Theory

8.2.1 Two-Winding Leakage Inductance

We should briefly introduce some background material on two-winding leakage inductances for later reference and to establish notation. Because we are concerned with transformer operation at a fixed frequency and sinusoidal conditions, we will most often be dealing with reactances in our circuit models. We use X to denote a reactance, where $X = j\omega L$, in which L is the inductance, j is the unit imaginary, and $\omega = 2\pi f$, where f is the frequency in Hz. We also use $X = j\omega M$ to refer to mutual reactance. The subscript pair on X will distinguish self- from mutual reactances. These quantities are constants because they are associated with the leakage flux.

Ignoring the resistance, the general circuit equations for a two-winding transformer can be written as:

$$\begin{aligned} V_1 &= X_{11}I_1 + X_{12}I_2 + \mathbf{E}N_1 \\ V_2 &= X_{21}I_1 + X_{22}I_2 + \mathbf{E}N_2 \end{aligned} \tag{8.1}$$

Since the X 's are linear circuit elements, $X_{12} = X_{21}$. \mathbf{E} is the volts/turn and N is the number of turns, so $\mathbf{E}N$ refer to the voltages induced by the ideal transformer, V are the voltages, and I are the currents. We use phasor notation here. The currents are directed into the winding at the positive voltage end. Since the amp-turns sum to zero:

$$N_1\mathbf{I}_1 + N_2\mathbf{I}_2 = 0 \tag{8.2}$$

Substituting for \mathbf{I}_2 from Equation 8.2 and \mathbf{E} from the second equation in Equation 8.1, we get

$$\mathbf{V}_1 = \frac{N_1}{N_2} \mathbf{V}_2 + \left[X_{11} - 2 \frac{N_1}{N_2} X_{12} + \left(\frac{N_1}{N_2} \right)^2 X_{22} \right] \mathbf{I}_1 \quad (8.3)$$

The leakage reactance is

$$Z_{12} = \frac{\mathbf{V}_1}{\mathbf{I}_1} \bigg|_{V_2=0} \quad (8.4)$$

The term in brackets in Equation 8.3 is the leakage reactance between windings 1 and 2 in that order, denoted by Z_{12} :

$$Z_{12} = X_{11} - 2 \frac{N_1}{N_2} X_{12} + \left(\frac{N_1}{N_2} \right)^2 X_{22} \quad (8.5)$$

The order is important. We have:

$$Z_{21} = \left(\frac{N_2}{N_1} \right)^2 Z_{12} \quad (8.6)$$

We can also note from Equation 8.5 that $Z_{11} = 0$, that is, when the subscripts are equal, the two-winding leakage reactance vanishes. The circuit model for a two-winding transformer will consist of the leakage reactance in series with an ideal transformer.

8.2.2 Multiwinding Transformers

We can use the same approach to model a multiwinding transformer. However, we will include the winding resistances for greater generality. The circuit equations are

$$\mathbf{V}_j = R_j \mathbf{I}_j + \sum_{k=1}^n X_{jk} \mathbf{I}_k + \mathbf{E} N_j \quad (8.7)$$

$$j = 1, \dots, n$$

and

$$\sum_{k=1}^n N_k \mathbf{I}_k = 0 \quad (8.8)$$

Here, n is the number of windings, and the other symbols are the same as before.

Using Equation 8.8, we can eliminate one voltage equation in Equation 8.7, as we did for the two-winding transformer, in which the winding 2 equation was chosen for elimination. Here we choose the winding 1 equation for elimination. Substituting for \mathbf{I}_1 from Equation 8.8 and \mathbf{E} from the winding 1 equation of Equation 8.7, for the remaining equations we get

$$\mathbf{V}_j = \frac{N_j}{N_1} \mathbf{V}_1 + R_j \mathbf{I}_j + \sum_{k=2}^n \left(\frac{N_j N_k}{N_1^2} R_1 + D_{1jk} \right) \mathbf{I}_k \quad (8.9)$$

$$j = 2, \dots, n$$

where

$$D_{1jk} = X_{jk} - \frac{N_k}{N_1} X_{j1} + \frac{N_j N_k}{N_1^2} X_{11} - \frac{N_j}{N_1} X_{1k} \quad (8.10)$$

We rewrite this as

$$D_{1jk} = \frac{1}{2} \left(2X_{jk} - 2\frac{N_k}{N_1} X_{j1} + 2\frac{N_j N_k}{N_1^2} X_{11} - 2\frac{N_j}{N_1} X_{1k} \right) \quad (8.11)$$

We then add and subtract $\frac{N_j}{N_k} X_{kk} + \frac{N_k}{N_j} X_{jj}$ from the terms in parentheses in Equation 8.11. After some rearrangement, we get

$$D_{1jk} = \frac{1}{2} \left\{ \frac{N_j N_k}{N_1^2} \left[X_{11} - 2\frac{N_1}{N_j} X_{1j} + \left(\frac{N_1}{N_j} \right)^2 X_{jj} \right] \right. \\ \left. + \frac{N_j N_k}{N_1^2} \left[X_{11} - 2\frac{N_1}{N_k} X_{1k} + \left(\frac{N_1}{N_k} \right)^2 X_{kk} \right] \right. \\ \left. - \frac{N_k}{N_j} \left[X_{jj} - 2\frac{N_j}{N_k} X_{jk} + \left(\frac{N_j}{N_k} \right)^2 X_{kk} \right] \right\} \quad (8.12)$$

Using the definition of two-winding leakage reactance given in Equation 8.5, we can rewrite Equation 8.12 as

$$\begin{aligned}
D_{1jk} &= \frac{1}{2} \left\{ \frac{N_j N_k}{N_1^2} (Z_{1j} + Z_{1k}) - \frac{N_k}{N_j} Z_{jk} \right\} \\
&= \frac{N_j N_k}{N_1^2} \frac{1}{2} \left[Z_{1j} + Z_{1k} - \left(\frac{N_1}{N_j} \right)^2 Z_{jk} \right] \\
&= \frac{N_j N_k}{N_1^2} Z_{1jk}
\end{aligned} \tag{8.13}$$

where we have defined the quantity

$$Z_{1jk} = \frac{1}{2} \left[Z_{1j} + Z_{1k} - \left(\frac{N_1}{N_j} \right)^2 Z_{jk} \right] \tag{8.14}$$

This is just the single-winding leakage impedance of winding 1 as part of a three-winding system, represented by a T-equivalent circuit. It is usually denoted by Z_1 when two other windings are understood to be 2 and 3. We need the additional subscript labeling here because there can be more than three windings. Substituting Equation 8.13 into Equation 8.9, the circuit equations become

$$\begin{aligned}
\mathbf{V}_j &= \frac{N_j}{N_1} \mathbf{V}_1 + R_j \mathbf{I}_j + \sum_{k=2}^n \frac{N_j N_k}{N_1^2} (R_1 + Z_{1jk}) \mathbf{I}_k \\
&\text{for } j = 2, \dots, n
\end{aligned} \tag{8.15}$$

The circuit Equation 8.15 contains only two-winding leakage reactances via the term Z_{1jk} . The first term, containing \mathbf{V}_1 , expresses the voltage transfer across the ideal transformer. Winding 1, with voltage \mathbf{V}_1 , is on one side of the ideal transformer, and its voltage is assumed to be known. All the other windings are on the other side of the ideal transformer. They are coupled to each other via the cross terms in Equation 8.15. The presence of winding 1 is reflected in these terms. From Equation 8.6, with j, k substituted for 1, 2, we get

$$Z_{1jk} = Z_{1kj} \tag{8.16}$$

that is, Z_{1jk} is symmetric in j and k . From the discussion following Equation 8.6, we note that

$$Z_{1jj} = Z_{1j} \tag{8.17}$$

that is, when the second and third indices are equal, Z_{1jj} reduces to the two-winding leakage reactance.

To simplify the notation further, we define a new quantity:

$$W_{1jk} = \frac{N_j N_k}{N_1^2} (R_1 + Z_{1jk}) \quad (8.18)$$

so that Equation 8.15 becomes

$$\mathbf{V}_j = \frac{N_j}{N_1} \mathbf{V}_1 + R_j \mathbf{I}_j + \sum_{k=2}^n W_{1jk} \mathbf{I}_k \quad (8.19)$$

for $j = 2, \dots, n$

W_{1jk} is a complex quantity because it contains resistive and reactive elements. From Equation 8.16, we see that

$$W_{1jk} = W_{1kj} \quad (8.20)$$

so that it is symmetric in j and k . We also see, from Equation 8.17, that when $j = k$,

$$W_{1jj} = \left(\frac{N_j}{N_1} \right)^2 (R_1 + Z_{1j}) \quad (8.21)$$

A circuit diagram of a four-winding and terminal transformer, illustrating the meaning of Equation 8.19, is shown in [Figure 8.1](#). Note that the impedances are on the secondary side of the transformer.

Although the Z 's were treated as inductive elements, the formulas in this chapter will be unchanged, with the Z 's containing mutual resistances. This can be useful in high-frequency work [Mom02].

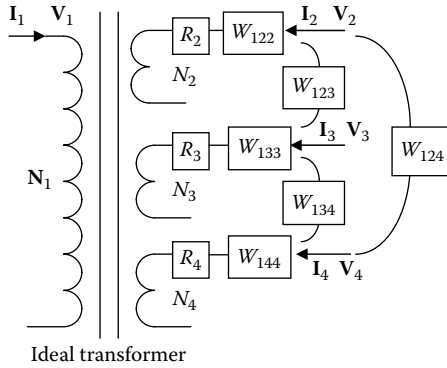
The per-unit system is often simpler. Using lowercase letters for per-unit quantities, in this system Equation 8.19 becomes

$$\mathbf{v}_j = \mathbf{v}_1 + r_j \mathbf{i}_j + \sum_{k=2}^n w_{1jk} \mathbf{i}_k \quad (8.22)$$

for $j = 2, \dots, n$

where

$$\begin{aligned} w_{1jk} &= r_1 + z_{1jk} \\ z_{1jk} &= \frac{1}{2} (z_{1j} + z_{1k} - z_{jk}) \end{aligned} \quad (8.23)$$

**FIGURE 8.1**

Circuit model of a four-winding transformer using only two-winding leakage reactances and an ideal transformer. (From Del Vecchio, R. M. 2006. *IEEE Trans Power Deliv* 21(3):1300–8. With permission.)

We prefer to derive formulas in the regular system of units because it is relatively easy to convert them to the per-unit system. Much of the literature is written in the per-unit system, which we will use to perform calculations.

8.2.3 Transformer Loading

In the following applications, we consider winding 1 to be the primary winding with known voltage and windings $j = 2, \dots, n$ to be secondary windings. When the secondary windings are loaded, the voltages V_j are applied across a load Z_{Lj} . This load is usually a complex number, containing resistive and reactive terms. The load current flows into the load and out of the secondary terminal. Because we assume that the winding currents flow into the terminal, the load current is the negative of the winding currents. Therefore, we have

$$\mathbf{V}_j = -Z_{Lj}\mathbf{I}_j \quad (8.24)$$

Substituting this into Equation 8.19, the circuit equations with load become

$$(R_j + Z_{Lj})\mathbf{I}_j + \sum_{k=2}^n W_{1jk}\mathbf{I}_k = -\frac{N_j}{N_1}\mathbf{V}_1 \quad (8.25)$$

for $j = 2, \dots, n$

If we use the load currents, instead of the winding currents, the term on the right in Equation 8.25 will be positive. This can be written as a matrix equation, where the matrix is complex and symmetric, and solved by

standard methods. \mathbf{V}_1 , N 's, resistances, two-winding leakage reactances, and the load impedances are assumed known. Therefore, we can solve for the \mathbf{I} 's.

8.3 Transformers with Winding Connections within a Phase

We have thus far discussed a single-phase transformer or one phase of a three-phase transformer with uncoupled phases. The windings have been simple, with no internal interconnections. We will now apply this theory to more complicated transformers, in which the windings can be interconnected within a single phase. In general, a multiterminal transformer with n windings may have less than $n - 1$ secondary terminals. Because the number of equations we need to solve equals the number of secondary terminals, we may have fewer than $n - 1$ equations to solve.

8.3.1 Two Secondary Windings in Series

This is a common situation. For example, a tap winding is often connected to a secondary winding. In some cases, two series-connected low-voltage (LV) windings are used. Let p and q be the series-connected secondary windings. Let s denote the terminal to which one of these windings is attached. We have

$$\begin{aligned}\mathbf{V}_s &= \mathbf{V}_p + \mathbf{V}_q \\ \mathbf{I}_s &= \mathbf{I}_p = \mathbf{I}_q\end{aligned}\tag{8.26}$$

Adding the $j = p$ and $j = q$ equations in Equation 8.19 yields for the resulting system

$$\begin{aligned}\mathbf{V}_s &= \left(\frac{N_p + N_q}{N_1} \right) \mathbf{V}_1 + (R_p + R_q) \mathbf{I}_s + (W_{1pp} + 2W_{1pq} + W_{1qq}) \mathbf{I}_s \\ &\quad + \sum_{k=2, k \neq p, k \neq q}^n (W_{1pk} + W_{1qk}) \mathbf{I}_k \\ \mathbf{V}_j &= \frac{N_j}{N_1} \mathbf{V}_1 + R_j \mathbf{I}_j + (W_{1jp} + W_{1jq}) \mathbf{I}_s + \sum_{k=2, k \neq p, k \neq q}^n W_{1jk} \mathbf{I}_k \\ &\text{for } j = 2, \dots, n, j \neq p, j \neq q\end{aligned}\tag{8.27}$$

Thus, the equations for windings p and q are eliminated and an equation for terminal s is added, resulting in one less secondary terminal equation to solve.

As an example, consider a three-winding system with windings 2 and 3 in series. Then, Equation 8.27 reduces to one equation, the s terminal equation, which becomes

$$\mathbf{V}_s = \left(\frac{N_2 + N_3}{N_1} \right) \mathbf{V}_1 + (R_2 + R_3 + W_{122} + 2W_{123} + W_{133}) \mathbf{I}_s \quad (8.28)$$

If we omit the resistance terms from the W 's in Equation 8.28, we obtain an effective reactance on the secondary side:

$$Z_{\text{eff}} = \frac{N_2(N_2 + N_3)}{N_1^2} Z_{12} + \frac{N_3(N_2 + N_3)}{N_1^2} Z_{13} - \frac{N_3}{N_2} Z_{23} \quad (8.29)$$

This is the effective leakage reactance of this two-terminal transformer on the secondary side. We obtained a formula for the reactance for this connection in Chapter 4, in which the joined windings were windings 1 and 2. Here, the joined windings are windings 2 and 3. By relabeling the indices, substituting for the single-winding reactances, and transferring the reactance to the secondary side, Equation 4.106 reduces to Equation 8.29.

8.3.2 Primary Winding in Series with a Secondary Winding

This is also a fairly common situation. We can have two high-voltage (HV) primary windings connected in series or an HV winding connected in series with a tap winding. This requires special consideration because we have singled out the primary winding in the above treatment. Let winding p be in series with winding 1. We have

$$\begin{aligned} \mathbf{V}_s &= \mathbf{V}_1 + \mathbf{V}_p \\ \mathbf{I}_1 &= \mathbf{I}_p = -\frac{1}{(N_1 + N_p)} \sum_{k=2, k \neq p}^n N_k \mathbf{I}_k \end{aligned} \quad (8.30)$$

We have used the amp-turn balance condition here. Substituting for \mathbf{I}_p in Equation 8.19, we get

$$\begin{aligned} \mathbf{V}_j &= \frac{N_j}{N_1} \mathbf{V}_1 + R_j \mathbf{I}_j + \sum_{k=2, k \neq p}^n \left[W_{1jk} - \left(\frac{N_k}{N_1 + N_p} \right) W_{1jp} \right] \mathbf{I}_k \\ &\text{for } j = 2, \dots, n, j \neq p \\ \mathbf{V}_p &= \frac{N_p}{N_1} \mathbf{V}_1 + \sum_{k=2, k \neq p}^n \left[W_{1pk} - \left(\frac{N_k}{N_1 + N_p} \right) (R_p + W_{1pp}) \right] \mathbf{I}_k \end{aligned} \quad (8.31)$$

We therefore get for \mathbf{V}_s

$$\mathbf{V}_s = \left(\frac{N_1 + N_p}{N_1} \right) \mathbf{V}_1 + \sum_{k=2, k \neq p}^n \left[W_{1pk} - \left(\frac{N_k}{N_1 + N_p} \right) (R_p + W_{1pp}) \right] \mathbf{I}_k \quad (8.32)$$

Solving Equation 8.32 for \mathbf{V}_1 and substituting into the \mathbf{V}_j equations, we get

$$\begin{aligned} \mathbf{V}_j = & \left(\frac{N_j}{N_1 + N_p} \right) \mathbf{V}_s + R_j \mathbf{I}_j \\ & + \sum_{k=2, k \neq p}^n \left[W_{1jk} - \left(\frac{N_k}{N_1 + N_p} \right) W_{1jp} + \frac{N_j N_k}{(N_1 + N_p)^2} (R_p + W_{1pp}) - \left(\frac{N_j}{N_1 + N_p} \right) W_{1pk} \right] \mathbf{I}_k \end{aligned}$$

for $j = 2, \dots, n, j \neq p$ (8.33)

Equation 8.33 shows that the two windings in series are placed on one side of the ideal transformer and that their series voltage \mathbf{V}_s is assumed known. The presence of both windings is reflected in the terms in Equation 8.33 on the secondary side.

As an example, consider a three-winding transformer with windings 1 and 2 in series. There is just one equation, Equation 8.33, for winding 3. Dropping the resistance terms in Equation 8.33, we obtain an effective leakage reactance of

$$Z_{\text{eff}} = \left(\frac{N_3}{N_1 + N_2} \right)^2 \left[-\frac{N_2}{N_1} Z_{12} + \left(\frac{N_1 + N_2}{N_1} \right) Z_{13} + \left(\frac{N_1 + N_2}{N_2} \right) Z_{23} \right] \quad (8.34)$$

This is similar to the previous example except that the joined windings are windings 1 and 2. The formula in Chapter 4 applies directly to this connection without relabeling the indices, except that the reactance must be transformed to the secondary side. This transference is carried out by the term

$\left(\frac{N_3}{N_1 + N_2} \right)^2$ in Equation 8.34.

8.3.3 Autotransformer

An autotransformer connection is shown in [Figure 8.2](#). We let winding 1 be the series or HV winding and winding p be the common or LV winding. The current at the common terminal is positive into the terminal by the convention used here and is labeled \mathbf{I}_{Tp} . The voltage at the HV terminal is labeled \mathbf{V}_s .

From Figure 8.2, we can see that

$$\begin{aligned} \mathbf{V}_s &= \mathbf{V}_1 + \mathbf{V}_p \\ \mathbf{I}_{Tp} &= \mathbf{I}_p - \mathbf{I}_1 \\ &= \left(\frac{N_1 + N_p}{N_1} \right) \mathbf{I}_p + \frac{1}{N_1} \sum_{k=2, k \neq p}^n N_k \mathbf{I}_k \end{aligned} \quad (8.35)$$

where we have used amp-turn balance. Proceeding as we did in Section 8.3.2, we find for the secondary terminal equations:

$$\begin{aligned} \mathbf{V}_j &= \left(\frac{N_j}{N_1 + N_p} \right) \mathbf{V}_s + R_j \mathbf{I}_j + \left(\frac{N_1}{N_1 + N_p} \right) \left[W_{1jp} - \left(\frac{N_j}{N_1 + N_p} \right) (R_p + W_{1pp}) \right] \mathbf{I}_{Tp} \\ &\quad + \sum_{k=2, k \neq p}^n \left\{ W_{1jk} - \left(\frac{N_k}{N_1 + N_p} \right) \left[W_{1jp} + \frac{N_j}{N_k} W_{1pk} - \left(\frac{N_j}{N_1 + N_p} \right) (R_p + W_{1pp}) \right] \right\} \mathbf{I}_k \end{aligned} \quad (8.36)$$

for $j = 2, \dots, n, j \neq p$

$$\begin{aligned} V_p &= \left(\frac{N_p}{N_1 + N_p} \right) V_s + \left(\frac{N_1}{N_1 + N_p} \right)^2 (R_p + W_{1pp}) I_{Tp} \\ &\quad + \left(\frac{N_1}{N_1 + N_p} \right) \sum_{k=2, k \neq p}^n \left[W_{1pk} - \left(\frac{N_k}{N_1 + N_p} \right) (R_p + W_{1pp}) \right] I_k \end{aligned} \quad (8.37)$$

Here, \mathbf{V}_s , the primary terminal voltage, is assumed to be given. It is on one side of the ideal transformer, and the secondary voltages, with their impedances and couplings, are on the other side. All of the direct and coupling terms are expressed in terms of winding resistances and leakage reactances.

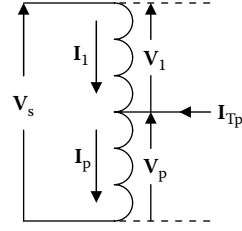


FIGURE 8.2

Autotransformer connection. (From Del Vecchio, R. M. 2006. *IEEE Trans Power Deliv* 21(3):1300–8. With permission.)

8.4 Multiphase Transformers

At this point, some simplification in notation is useful. We will recast Equation 8.19 using vector and matrix notation. Vectors will be denoted by bold-faced type and matrices by italicized type. Since the voltage and current vectors are vectors of phasors, this is consistent with our phasor notation; however, the elements of these vectors will be denoted in ordinary type. Other vectors, such as the turn vectors, are not vectors of phasors but will still be denoted with boldface. The vector notation will supersede our

previous phasor notation here. Let \mathbf{V} , \mathbf{I} , and \mathbf{N} be vectors of winding secondary voltages, currents, and turns divided by N_1 :

$$\begin{aligned}\mathbf{V} &= (V_2, V_3, \dots, V_n)^T \\ \mathbf{I} &= (I_2, I_3, \dots, I_n)^T \\ \mathbf{N} &= \left(\frac{N_2}{N_1}, \frac{N_3}{N_1}, \dots, \frac{N_n}{N_1} \right)^T\end{aligned}\quad (8.38)$$

Here, superscript T denotes transpose because these are column vectors. Let R denote the diagonal matrix of secondary winding resistances:

$$R = \begin{pmatrix} R_2 & 0 & 0 & 0 \\ 0 & R_3 & 0 & 0 \\ 0 & 0 & \ddots & 0 \\ 0 & 0 & 0 & R_n \end{pmatrix}\quad (8.39)$$

Let W denote the matrix W_{jk} with rows labeled j and columns k , for $j, k = 2, \dots, n$. Then, Equation 8.19 becomes

$$\mathbf{V} = \mathbf{N}V_1 + (R + W)\mathbf{I}\quad (8.40)$$

This equation refers to a single phase. For a three-phase system, we label the phases a, b, and c. The unit phasors, associated with these respective phases, are, as before, denoted by 1, α^2 , and α . They are 120° apart in the complex plane and, for convenience, are given here and shown in [Figure 8.3](#).

$$\begin{aligned}1 \\ \alpha^2 &= -\frac{1}{2} - j\frac{\sqrt{3}}{2} \\ \alpha &= -\frac{1}{2} + j\frac{\sqrt{3}}{2}\end{aligned}\quad (8.41)$$

where j is the imaginary unit.

Using a, b, and c as subscripts to label the phase quantities, we must expand Equation 8.40 for a three-phase system:

$$\begin{pmatrix} \mathbf{V}_a \\ \mathbf{V}_b \\ \mathbf{V}_c \end{pmatrix} = \begin{pmatrix} \mathbf{N}V_{1a} \\ \mathbf{N}V_{1b} \\ \mathbf{N}V_{1c} \end{pmatrix} + \begin{pmatrix} R + W & 0 & 0 \\ 0 & R + W & 0 \\ 0 & 0 & R + W \end{pmatrix} \begin{pmatrix} \mathbf{I}_a \\ \mathbf{I}_b \\ \mathbf{I}_c \end{pmatrix}\quad (8.42)$$

The vectors of each phase are now considered phasors. In particular, $V_{1a} = V_1$, $V_{1b} = V_1\alpha^2$, and $V_{1c} = V_1\alpha$ since V_1 is the driving voltage. However, V_a , V_b , and V_c or I_a , I_b , and I_c cannot be expressed so simply because of the complex nature of the matrix in Equation 8.42. The V 's and I 's will still form a balanced three-phase system, but there may be an overall phase shift from the input V_1 system.

The extended vectors shown in Equation 8.42 are of dimension $3(n - 1)$ for an n -winding system. Equation 8.42 represents a system of uncoupled phases. We will now explore several possibilities for coupling the phases, for which this matrix formalism is very useful. In our further discussion, the vectors \mathbf{V} , \mathbf{NV}_1 , and \mathbf{I} will refer to the three-phase system and we will assume the matrix $\mathbf{R} + \mathbf{W}$ to have the expanded form in Equation 8.42. We will now treat \mathbf{NV}_1 as a three-phase vector entity, since \mathbf{V}_1 contains phase information, and hence, \mathbf{V}_1 is in boldface here. Thus, in our abbreviated notation, Equation 8.42 is expressed as

$$\mathbf{V} = \mathbf{NV}_1 + (\mathbf{R} + \mathbf{W})\mathbf{I} \quad (8.43)$$

This is basically the same as Equation 8.40, except that the vector quantities refer to all three phases and \mathbf{V}_1 is a phasor vector. Here we will deal with three-phase quantities, unless otherwise noted, with \mathbf{V}_1 representing a balanced three-phase system of phasors.

8.4.1 Delta Connection

The delta connection diagram for a set of windings from three phases is shown in Figure 8.4. This is a -30° delta because the terminal voltages are shifted by -30° relative to the phase voltages.

The voltages at the terminals are labeled V_{T1} and so on. The terminal voltages are assumed to be relative to ground potential. Since there is no ground point or reference voltage in the delta connection, we assume there is one at the middle of the delta as shown in Figure 8.4(b). Relative to this, the voltage relationships can be expressed in matrix form:

$$\begin{pmatrix} V_{T1} \\ V_{T2} \\ V_{T3} \end{pmatrix} = \begin{pmatrix} 1/3 & 0 & -1/3 \\ -1/3 & 1/3 & 0 \\ 0 & -1/3 & 1/3 \end{pmatrix} \begin{pmatrix} V_a \\ V_b \\ V_c \end{pmatrix} \quad (8.44)$$

$$\begin{pmatrix} V_a \\ V_b \\ V_c \end{pmatrix} = \begin{pmatrix} 1 & -1 & 0 \\ 0 & 1 & -1 \\ -1 & 0 & 1 \end{pmatrix} \begin{pmatrix} V_{T1} \\ V_{T2} \\ V_{T3} \end{pmatrix}$$

V_{T1} and so on are phasors. By convention, we assume that positive currents flow into the terminals and, within the winding, they are opposite to the direction of voltage increase. The voltage representation in the first equation of Equation 8.44 assumes balanced three-phase delta voltages. It is not the inverse of the matrix in the second equation in Equation 8.44, which applies to balanced or unbalanced voltages.

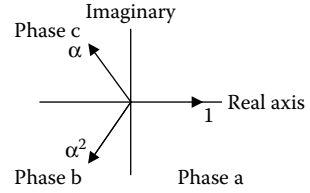
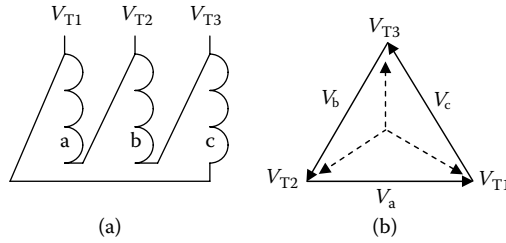


FIGURE 8.3
Unit phasors of a three-phase system.

**FIGURE 8.4**

Delta connection: (a) winding phase and (b) phasor relationships. (From Del Vecchio, R. M. 2006. *IEEE Trans Power Deliv* 21(3):1300–8. With permission.)

Labeling the terminal currents I_{T1} and so on the winding and terminal currents are related by

$$\begin{pmatrix} I_{T1} \\ I_{T2} \\ I_{T3} \end{pmatrix} = \begin{pmatrix} 1 & 0 & -1 \\ -1 & 1 & 0 \\ 0 & -1 & 1 \end{pmatrix} \begin{pmatrix} I_a \\ I_b \\ I_c \end{pmatrix} \quad (8.45)$$

$$\begin{pmatrix} I_a \\ I_b \\ I_c \end{pmatrix} = \begin{pmatrix} 1/3 & -1/3 & 0 \\ 0 & 1/3 & -1/3 \\ -1/3 & 0 & 1/3 \end{pmatrix} \begin{pmatrix} I_{T1} \\ I_{T2} \\ I_{T3} \end{pmatrix}$$

Here again, the I_T 's are phasors. The second current equation in Equation 8.45 assumes balanced three-phase currents in the delta. The two matrices in Equation 8.45 are not inverses. The first equation in Equation 8.45 applies to balanced or unbalanced delta currents.

We assume winding p is delta connected, and let M_v be a unit diagonal matrix of dimension $3(n-1)$ for an n -winding system. We then modify the p -winding rows for all three phases by inserting the entries from the first matrix in Equation 8.44 in the appropriate slots; for example, we place $1/3$ in the p -winding diagonal position for all three phases, $-1/3$ in the a-phase row and in the c-phase column for winding p , and so on. For example, if the p winding were winding 3 of a transformer with two secondary windings, 2 and 3 (winding 1 is the primary winding that has been eliminated from the matrix), we would have

$$M_v = \begin{pmatrix} 1 & 0 & 0 & 0 & 0 & 0 \\ 0 & 1/3 & 0 & 0 & 0 & -1/3 \\ 0 & 0 & 1 & 0 & 0 & 0 \\ 0 & -1/3 & 0 & 1/3 & 0 & 0 \\ 0 & 0 & 0 & 0 & 1 & 0 \\ 0 & 0 & 0 & -1/3 & 0 & 1/3 \end{pmatrix} \quad (8.46)$$

Let M_I be a similar matrix corresponding to the second matrix of Equation 8.45 for the currents, for example for winding 3 of a transformer with two secondaries:

$$M_I = \begin{pmatrix} 1 & 0 & 0 & 0 & 0 & 0 \\ 0 & 1/3 & 0 & -1/3 & 0 & 0 \\ 0 & 0 & 1 & 0 & 0 & 0 \\ 0 & 0 & 0 & 1/3 & 0 & -1/3 \\ 0 & 0 & 0 & 0 & 1 & 0 \\ 0 & -1/3 & 0 & 0 & 0 & 1/3 \end{pmatrix} \quad (8.47)$$

Thus, assuming the expanded three-phase notation, we have

$$\mathbf{V}_T = M_V \mathbf{V}, \quad \mathbf{I} = M_I \mathbf{I}_T \quad (8.48)$$

Here, T labels the terminal quantities. In some cases, this is the same as the winding quantity. Applying these to Equation 8.43, we get

$$\mathbf{V}_T = M_V(\mathbf{N}\mathbf{V}_1) + M_V(R + W)\mathbf{M}_I \mathbf{I}_T \quad (8.49)$$

Equation 8.49 now applies to terminal quantities. We can impose a load on these as was done in [Section 8.2.3](#) and solve the resulting equations to get the terminal currents. The terminal voltages can then be found from Equation 8.49 or from the load voltage drop equation, that is, Equation 8.24. The phase voltages and currents can then be found by applying the appropriate matrix in Equations 8.44 and 8.45 in an expanded form.

8.4.2 Zig-Zag Connection

The zig-zag connection is often used for grounding purposes. It affords a low impedance to zero-sequence currents. The zig-zag connection involves interconnecting two secondary windings from different phases. The diagram is shown in Figure 8.5, in which the secondary windings are labeled 2a, b, and c and 3a, b, and c.

The diagram assumes the winding voltages increase upwards. Therefore, the windings are connected so that their phasor voltages subtract. The currents in the connected windings are of opposite signs based on our sign convention. This also can be viewed from the phasor diagram viewpoint, as shown in [Figure 8.6](#).

Assuming the transformer has only two secondary windings, the matrices connecting the terminal to the winding voltages and currents, M_V and M_I as defined in Equation 8.48 are

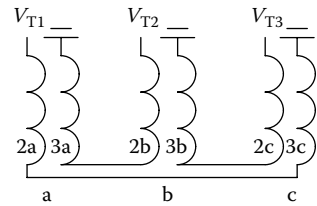
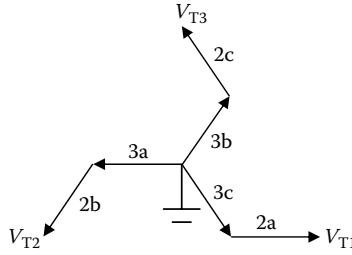


FIGURE 8.5

Zig-zag winding connection. (From Del Vecchio, R. M. 2006. *IEEE Trans Power Deliv* 21(3): 1300–8. With permission.)

**FIGURE 8.6**

Zig-zag phasor relationships. (From Del Vecchio, R. M. 2006. *IEEE Trans Power Deliv* 21(3):1300–8. With permission.)

$$\begin{aligned}
 M_V &= \begin{pmatrix} 1 & 0 & 0 & 0 & 0 & -1 \\ 0 & -1 & 1 & 0 & 0 & 0 \\ 0 & 0 & 0 & -1 & 1 & 0 \end{pmatrix} \\
 M_I &= \begin{pmatrix} 1 & 0 & 0 \\ 0 & -1 & 0 \\ 0 & 1 & 0 \\ 0 & 0 & -1 \\ 0 & 0 & 1 \\ -1 & 0 & 0 \end{pmatrix} \quad (8.50)
 \end{aligned}$$

These are no longer square matrices. The column dimension of M_V is six because it operates on the voltages in the original configuration consisting of three phases with two secondary terminal windings per phase. The row dimension is three because there are three phases with only one terminal per phase after the zig-zag connection is made. The opposite is true for M_I because it operates on the terminal currents after the zig-zag connection is made to produce the currents in the two separate windings. Note that windings 2 and 3 have the same number of turns in this connection. Let $N_z = N_2 = N_3$ be the common number of turns. Using this and Equations 8.50 in 8.49 and dropping the resistance terms, we find

$$\begin{pmatrix} V_{T1} \\ V_{T2} \\ V_{T3} \end{pmatrix} = \frac{N_z}{N_1} \sqrt{3} V_1 \begin{pmatrix} e^{-j30^\circ} \\ e^{-j150^\circ} \\ e^{j90^\circ} \end{pmatrix} + \begin{pmatrix} W_{122} + W_{133} & -W_{123} & -W_{123} \\ -W_{123} & W_{122} + W_{133} & -W_{123} \\ -W_{123} & -W_{123} & W_{122} + W_{133} \end{pmatrix} \begin{pmatrix} I_{T1} \\ I_{T2} \\ I_{T3} \end{pmatrix} \quad (8.51)$$

If we use the fact that the I_T 's form a balanced set, that is $I_{T1} + I_{T2} + I_{T3} = 0$, we find that this reduces to a set of three uncoupled equations. The first of these is

$$V_{T1} = \frac{N_z}{N_1} \sqrt{3} V_1 e^{-j30^\circ} + (W_{122} + W_{133} + W_{123}) I_{T1} \quad (8.52)$$

Using the definition of the W 's and ignoring the resistance terms, the effective impedance term multiplying I_{T1} is

$$Z_{\text{eff}} = \frac{3}{2} \left(\frac{N_z}{N_1} \right)^2 (Z_{12} + Z_{13}) - \frac{1}{2} Z_{23} \quad (8.53)$$

This agrees with Equation 7.132 found in Chapter 7, expressed in terms of two-winding reactances and transferred to the zig-zag side of the ideal transformer.

After applying a load as in [Section 8.2.3](#), the resulting equations may be solved for the terminal currents. Then, the version of Equation 8.51 that includes the resistance terms and possibly other secondary windings, in conjunction with the load voltage drop equation (Equation 8.24), can be used to find the terminal voltages. By applying M_I to the terminal current vector, we can find the currents in the windings. Then, Equation 8.42 can be used to find the voltages across the individual windings.

8.5 Generalizing the Model

The procedure outlined in [Section 8.4](#) for the multiphase transformers can be generalized. For example, the addition of two windings in series from the same phase can be accomplished by applying the appropriate matrices M_V and M_I to Equation 8.40. In this case, we need not work with the expanded three-phase Equation 8.43 because the phases are uncoupled. For two secondary windings, labeled 2 and 3, with the terminal T_1 at the positive end of winding 2, the appropriate matrix transformations are

$$V_{T1} = (1 \ 1) \begin{pmatrix} V_2 \\ V_3 \end{pmatrix}, \quad \begin{pmatrix} I_2 \\ I_3 \end{pmatrix} = \begin{pmatrix} 1 \\ 1 \end{pmatrix} (I_{T1}) \quad (8.54)$$

where

$$M_V = (1 \ 1), \quad M_I = \begin{pmatrix} 1 \\ 1 \end{pmatrix}$$

If the two secondary voltages are part of a larger system of secondaries, the matrices M_V and M_I must be expanded with unit diagonal elements for the other windings, and the 1's in Equation 8.54 should be inserted into the appropriate slots.

In general, we can consider a series of winding interconnections for the secondaries, each described by matrices that we label 1, 2, ..., s , corresponding to the order in which they are applied and where s is the number of separate connections. This results in the series

$$\begin{aligned}
 \mathbf{V}_{T1} &= M_{V1} \mathbf{V}, \quad \mathbf{V}_{T2} = M_{V2} \mathbf{V}_{T1}, \quad \dots \quad \mathbf{V}_{Ts} = M_{Vs} \mathbf{V}_{Ts-1} \\
 \Rightarrow \mathbf{V}_{Ts} &= M_{Vs} M_{Vs-1} \dots M_{V1} \mathbf{V} \\
 \mathbf{I} &= M_{I1} \mathbf{I}_{T1}, \quad \mathbf{I}_{T1} = M_{I2} \mathbf{I}_{T2}, \quad \dots \quad \mathbf{I}_{Ts-1} = M_{Is} \mathbf{I}_{Ts} \\
 \Rightarrow \mathbf{I} &= M_{I1} M_{I2} \dots M_{Is} \mathbf{I}_{Ts}
 \end{aligned} \tag{8.55}$$

In this case, the resulting matrices

$$\begin{aligned}
 M_V &= M_{Vs} M_{Vs-1} \dots M_{V2} M_{V1} \\
 M_I &= M_{I1} M_{I2} \dots M_{Is-1} M_{Is}
 \end{aligned} \tag{8.56}$$

should be used in Equation 8.49. Notice that the M_V steps are applied in reverse order to the M_I steps. Here, the matrices and Equation 8.49 could refer to a single phase if there are no phase-to-phase interconnections, or to a system including all three phases if there are phase-to-phase interconnections.

This procedure will lead to a set of terminal equations to which the loads may be attached to get an equation for the terminal currents, as in Equation 8.25. Let the loading condition be given, in vector matrix form, by

$$\mathbf{V}_L = Z_L \mathbf{I}_L \tag{8.57}$$

where \mathbf{V}_L is a vector of load voltages at the various terminals and \mathbf{I}_L is a vector of load currents out of the various terminals. In general, \mathbf{V}_L and \mathbf{I}_L can be three-phase vectors. The load impedance matrix, Z_L , is generally complex and may not necessarily be diagonal. By our convention, $\mathbf{I}_L = -\mathbf{I}_T$, and setting $\mathbf{V}_T = \mathbf{V}_L$, the terminal equations to solve are

$$[Z_L + M_V(R + W)M_I] \mathbf{I}_T = -M_V(\mathbf{N}\mathbf{V}_1) \tag{8.58}$$

Once the terminal currents are found, the winding currents can be found by applying M_I to the terminal current vector. The terminal voltages can be found from Equation 8.57 and the winding voltages by substituting the winding currents into Equations 8.43 or 8.40 for a single-phase system.

When singling out a particular winding, for example the HV winding, as winding 1, any interconnections involving this winding must be handled separately from the way the secondary winding interconnections were handled, as it was previously for the case of a winding in series with winding 1 or in the case of an autotransformer. However, after this winding's interconnections are accounted for, the above procedure can be applied to the modified equations to account for any additional interconnections among the secondaries.

Note that M_I is the transpose of M_V . We also saw this in Equation 8.50 for the zig-zag connection, in Equations 8.46 and 8.47 for a delta connection, and in Equation 8.54. This follows from our convention regarding the current direction in a winding. Thus, if $R + W$ is symmetric, then $M_V(R + W)M_I$ will also be symmetric.

8.6 Regulation and Terminal Impedances

Regulation effects can be obtained by comparing the output terminal voltages with the no-load terminal voltages. The output terminal voltages can be determined using Equation 8.57 once the load currents are solved for. The no-load terminal voltages are given by the negative of the right-hand side of Equation 8.58. One can obtain the voltage magnitude drop and angle shift from no-load to load conditions from these voltage vectors.

As an example, consider a Y-Y autotransformer with X-line taps and a delta-connected tertiary. This is a three-phase, 60-MVA unit. The HV winding also has no-load taps within the winding. The two-winding leakage reactances when the HV winding no-load taps are in the center position are given in Table 8.1 in per-unit percent.

Single-winding resistances in per-unit percent were also used in the calculation and are shown in Table 8.2.

TABLE 8.1

Two-Winding Leakage Reactances

Winding 1	Winding 2	Per-Unit %
HV	LV	23.12
HV	Taps	44.22
HV	TV	45.71
LV	Taps	16.53
LV	TV	19.44
Taps	TV	11.77

Source: Del Vecchio, R. M. 2006. *IEEE Trans Power Deliv* 21(3):1300–8. With permission.

TABLE 8.2

Winding Resistances (Per-Unit %)

Winding	HV	LV	Taps	TV
Resistance	0.391	0.254	1.3	0.62

Source: Del Vecchio, R. M. 2006. *IEEE Trans Power Deliv* 21(3):1300–8. With permission.

TABLE 8.3

Regulation as Percentage Drop

Power Factor %	100	90	80	70
Calculation	0.47	3.55	4.63	5.36
Test	0.5	3.71	4.88	5.68

Source: Del Vecchio, R. M. 2006. *IEEE Trans Power Deliv* 21(3):1300–8.
With permission.

Regulation effects at different power factor loads with the on-load taps out, expressed as a percent voltage drop from no-load conditions, are given in Table 8.3, in which the calculations are compared with the test results. The calculated results were obtained by the methods described here, using the per-unit reactances and resistances given in Tables 8.1 and 8.2. These per-unit quantities were converted to Ohmic quantities for the calculation.

These regulation effects can also be obtained at other tap positions, but were not measured. However, we can use them to get the terminal-to-terminal reactances at various tap positions, which were measured.

To obtain the terminal-to-terminal impedances, Z_{tt} , the regulation R can be expressed as a voltage ratio, using the simplified model discussed in Chapter 3 in Figure 3.12, where $Z_{2,eq}$ is replaced by Z_{tt}

$$R = \frac{V_{\text{Term, load}}}{V_{\text{Term, no-load}}} = \frac{1}{\left(1 + \frac{Z_{tt}}{Z_L}\right)} \quad (8.59)$$

Here, Z_L is the load impedance, assumed known, which can be expressed in terms of its real and imaginary parts. Z_{tt} contains unknown real and imaginary parts, so there are two unknowns. The no-load terminal voltages are known, and the load terminal voltages are obtained by solving Equation 8.58 and then using Equation 8.57. The ratio of these two quantities, R , contains magnitude and phase information. The magnitude is used to obtain the regulation expressed as a percentage drop as given in Table 8.3. The phase shift from the no-load condition is the phase of R . These two calculated quantities allow us to solve Equation 8.59 for the two unknowns in Z_{tt} . The imaginary part of Z_{tt} is the terminal-to-terminal reactance. We compare this with test values of the HV to LV reactance in Table 8.4. The two-winding leakage reactances between the HV and the other windings change slightly at the different no-load tap settings. These were used in the calculations in Table 8.4 for the all-in and all-out no-load tap positions.

The HV to TV terminal-to-terminal reactances can be found using the same methods. They are compared with the test results in Table 8.5. They were only measured with the load taps out. This type of calculated information is valuable at the design stage to help determine whether regulation and impedance requirements will be met.

TABLE 8.4

HV-LV Terminal Reactances (Per-Unit %)

Load/No-Load Taps	All In	Center	All Out
Boost	8.46 C	7.94 C	7.68 C
	8.53 T	8.08 T	7.74 T
Out	8.11 C	7.56 C	7.28 C
	8.04 T	7.56 T	7.20 T
Buck	8.05 C	7.48 C	7.16 C
	8.07 T	7.56 T	7.16 T

C, calculation; T, test.

Source: Del Vecchio, R. M. 2006. *IEEE Trans Power Deliv* 21(3):1300–8. With permission.**TABLE 8.5**

HV-TV Reactances (Per-Unit %)

Load/No-Load Taps	All In	Center	All Out
Out	29.35 C	28.81 C	28.54 C
	29.54 T	29.05 T	28.58 T

C, calculation; T, test.

Source: Del Vecchio, R. M. 2006. *IEEE Trans Power Deliv* 21(3):1300–8. With permission.

8.7 Multiterminal Transformer Model for Balanced and Unbalanced Load Conditions

Thus far, the multiterminal model developed required balanced loading, particularly if delta windings were present. The model also singled out the input (HV) winding for special treatment, leading to complications when the input winding is interconnected with the other windings. In this section, both of these issues are addressed so that a more general treatment emerges. This generalization can accommodate balanced or unbalanced loading, including short circuits.

The starting point for the circuit model is the calculation (or measurement) of the two-winding leakage reactances between all pairs of windings. Both the positive- and zero-sequence reactances are needed, though the latter are often estimated from the positive-sequence reactances. This contrasts with the previous development, in which only the positive-sequence reactances were needed. We will assume that the positive- and negative-sequence reactances are equal. The two-winding leakage reactances combine to form a reduced reactance matrix. This matrix is called “reduced” because it excludes one of the windings. We also want to make this distinction because we will later add back the excluded winding so all of the windings can be treated

equally. This reduced matrix is the same matrix as that for which the matrix elements were given in Equation 8.18 for the balanced model, but is given a slightly different notation here. The matrix is then inverted to get an admittance matrix. An amp-turn balance condition is imposed on the admittance matrix, which extends it to a matrix involving all of the windings. This full admittance matrix is singular.

Although we can work in the admittance representation, it is often convenient to solve problems in the impedance representation. To invert the full admittance matrix, we add the core excitation data. Since the resulting matrix is close to being singular, the inversion must be carried out with high accuracy.

Superposed on this overall scheme, we will make winding interconnections as needed via voltage and current transfer matrices. We will then show how these transfer matrices can be used to obtain winding currents and voltages after the terminal loading problem has been solved.

Our main concern here is with power frequency steady-state alternating current (AC) applications. We will therefore work with reactances rather than inductances. We will include single-winding resistances and ignore mutual resistances, which may be present at high frequencies [Mom02].

8.7.1 Theory

The starting point for this development is Equation 8.19, relating voltages and currents developed earlier, in which we singled out winding 1 (usually the HV winding) for exclusion. Including the single-winding resistances, the basic formula is given by Equation 8.15, which we repeat here

$$\mathbf{V}_j = \frac{N_j}{N_1} \mathbf{V}_1 + R_j \mathbf{I}_j + \sum_{k=2}^n \frac{N_j N_k}{N_1^2} (R_1 + Z_{1jk}) \mathbf{I}_k \quad (8.60)$$

for $j = 2, \dots, n$

where n is the number of windings. The \mathbf{V}_j 's, \mathbf{I}_j 's, R_j 's, and N_j 's are the single-winding voltages, currents, resistances, and turns, respectively. Z_{1jk} is a leakage reactance matrix, derived from two-winding positive-sequence leakage reactances. It is given by

$$Z_{1jk} = \frac{1}{2} \left[Z_{1j} + Z_{1k} - \left(\frac{N_1}{N_j} \right)^2 Z_{jk} \right] \quad (8.61)$$

$j, k = 2, \dots, n$

where the Z_{ij} are the two-winding positive-sequence leakage reactances.

It is useful to introduce separate matrices for the real and imaginary parts of Equation 8.60. Since the R 's are real and the Z 's are imaginary, we define the reduced matrices as

$$\begin{aligned} R_{jk}^r &= R_j \delta_{jk} + \frac{N_j N_k}{N_1^2} R_1 \\ W_{jk}^r &= \frac{N_j N_k}{N_1^2} Z_{1jk} \\ j, k &= 2, \dots, n \end{aligned} \quad (8.62)$$

where $\delta_{jk} = 1$ if $j = k$ and 0 otherwise. The superscript r indicates a reduced quantity. Previously, W , without the superscript r , included the resistance of winding 1. We define the reduced vectors as

$$\mathbf{V}^r = \begin{pmatrix} V_2 \\ V_3 \\ \vdots \\ V_n \end{pmatrix}, \quad \mathbf{I}^r = \begin{pmatrix} I_2 \\ I_3 \\ \vdots \\ I_n \end{pmatrix}, \quad \mathbf{N}^r = \begin{pmatrix} N_2 \\ N_3 \\ \vdots \\ N_n \end{pmatrix} \quad (8.63)$$

where r again denotes reduced. Using this notation, Equation 8.60 becomes

$$\mathbf{V}^r - \frac{V_1}{N_1} \mathbf{N}^r = (R^r + jW^r) \mathbf{I}^r \quad (8.64)$$

As mentioned earlier, italicized quantities represent matrices and bold-faced quantities represent vectors. We have inserted the imaginary unit j to take into account the complex nature of the reduced reactance matrix, and therefore we consider W^r to be real.

Extending this to three phases, labeled a, b, and c, we have

$$\begin{pmatrix} \mathbf{V}_a^r - \frac{V_{1a}}{N_1} \mathbf{N}^r \\ \mathbf{V}_b^r - \frac{V_{1b}}{N_1} \mathbf{N}^r \\ \mathbf{V}_c^r - \frac{V_{1c}}{N_1} \mathbf{N}^r \end{pmatrix} = \left[\begin{pmatrix} R^r & 0 & 0 \\ 0 & R^r & 0 \\ 0 & 0 & R^r \end{pmatrix} + j \begin{pmatrix} W^r & 0 & 0 \\ 0 & W^r & 0 \\ 0 & 0 & W^r \end{pmatrix} \right] \begin{pmatrix} \mathbf{I}_a^r \\ \mathbf{I}_b^r \\ \mathbf{I}_c^r \end{pmatrix} \quad (8.65)$$

The 0s in Equation 8.65 are zero matrices of the same size as the W^r 's and R^r 's.

At this point we are interested in unbalanced conditions in general, so we should include the zero-sequence two-winding leakage reactances, $Z_{0,ij}$. Using these in an expression similar to Equation 8.61, we obtain the analogous quantities $Z_{0,ijk}$ and the analogous matrix W_{0r}^r , defined by an expression similar to W^r in Equation 8.62. Following [Bra82], we should modify the three-phase W^r matrix in Equation 8.65. We do this by replacing the W^r matrices along the diagonal in Equation 8.65 by

$$W_S^r = \frac{1}{3}(W_0^r + 2W^r) \quad (8.66)$$

We also replace the off-diagonal 0 matrices in Equation 8.65 by

$$W_M^r = \frac{1}{3}(W_0^r - W^r) \quad (8.67)$$

The R^r matrices remain unchanged in this procedure. Thus, the three-phase W^r matrix in Equation 8.65 becomes

$$W^{3r} = \begin{pmatrix} W_S^r & W_M^r & W_M^r \\ W_M^r & W_S^r & W_M^r \\ W_M^r & W_M^r & W_S^r \end{pmatrix} \quad (8.68)$$

This method is slightly different from that in [Bra82] in the way the matrix Equation 8.68 is organized. For balanced conditions, set $W_0^r = W^r$ and the matrix in Equation 8.68 reduces to that in Equation 8.65. Labeling the quantities in Equation 8.65 with a superscript 3 to indicate that three phases are involved, we rewrite it in simplified notation:

$$\mathbf{V}^{3r} - \frac{V_1^3}{N_1} \mathbf{N}^{3r} = (R^{3r} + jW^{3r}) \mathbf{I}^{3r} \quad (8.69)$$

The relabeled vectors and matrices correspond to the expanded versions in Equation 8.65, with W^{3r} given by Equation 8.68.

8.7.2 Admittance Representation

To include all the windings on a similar footing, we must invert Equation 8.69. The matrix will then become an admittance matrix, which requires the inversion of a complex matrix. Working with real-matrix inverses only, this can be done via the formula

$$(M_{\text{Re}} + jM_{\text{Im}})^{-1} = (M_{\text{Re}} + M_{\text{Im}}M_{\text{Re}}^{-1}M_{\text{Im}})^{-1} - j(M_{\text{Im}} + M_{\text{Re}}M_{\text{Im}}^{-1}M_{\text{Re}})^{-1} \quad (8.70)$$

Here, M_{Re} and M_{Im} are the real and imaginary components of a general complex matrix and both are assumed invertible. If either component matrix

is zero, this reduces to the usual matrix inverse, except that j changes sign for the imaginary component. This procedure is unnecessary if software is available for dealing with complex matrix algebra and inverses.

Complex matrices and vectors can be handled by treating them as enlarged real matrices and vectors according to the following equation:

$$M = \begin{pmatrix} M_{\text{Re}} & -M_{\text{Im}} \\ M_{\text{Im}} & M_{\text{Re}} \end{pmatrix}, \quad \mathbf{V} = \begin{pmatrix} \mathbf{V}_{\text{Re}} \\ \mathbf{V}_{\text{Im}} \end{pmatrix} \quad (8.71)$$

where M_{Re} is the real part and M_{Im} is the imaginary part of the complex matrix, and the same is true for the vector \mathbf{V} . Matrix algebra can be carried out using these, as if they were real matrices and vectors. The real and imaginary parts of the vectors can then be extracted as needed, with the real part at the top and the imaginary part at the bottom of the column vector.

Inverting Equation 8.69, we get

$$\mathbf{I}^{3r} = Y^{3r} \left(\mathbf{V}^{3r} - \frac{V_1^3}{N_1} \mathbf{N}^{3r} \right) \quad (8.72)$$

where Y^{3r} is the complex inverse of $R^{3r} + jW^{3r}$ in Equation 8.69.

To include winding 1 on an equal footing with the other windings, we use amp-turn balance to get its current. Thus,

$$I_1 = -\frac{N_2}{N_1} I_2 - \frac{N_3}{N_1} I_3 - \dots - \frac{N_n}{N_1} I_n \quad (8.73)$$

We can transform the reduced current vector in Equation 8.63 to a full current vector \mathbf{I} using the following matrix:

$$\begin{pmatrix} I_1 \\ I_2 \\ I_3 \\ \vdots \\ I_n \end{pmatrix} = \begin{pmatrix} -\frac{N_2}{N_1} & -\frac{N_3}{N_1} & \dots & -\frac{N_n}{N_1} \\ 1 & 0 & \dots & 0 \\ 0 & 1 & \dots & 0 \\ \vdots & \vdots & \ddots & 0 \\ 0 & 0 & 0 & 1 \end{pmatrix} \begin{pmatrix} I_2 \\ I_3 \\ \vdots \\ I_n \end{pmatrix} \quad (8.74)$$

This matrix has n rows and $n - 1$ columns and applies to a single phase. By tripling it along the diagonal, we get a matrix that applies to all three phases. Calling this matrix A^3 for amp-turn balance matrix (3 for all three phases), we can rewrite Equation 8.74:

$$\mathbf{I}^3 = A^3 \mathbf{I}^{3r} \quad (8.75)$$

where \mathbf{I}^3 stands for the full three-phase current vector of dimension $3n$.

Using the transpose of the matrix in Equation 8.74, we can express one phase of the reduced voltage vector in Equation 8.72 in terms of the full voltage vector:

$$\begin{pmatrix} V_2 - \frac{N_2}{N_1} V_1 \\ V_3 - \frac{N_3}{N_1} V_1 \\ \vdots \\ V_n - \frac{N_n}{N_1} V_1 \end{pmatrix} = \begin{pmatrix} -\frac{N_2}{N_1} & 1 & 0 & 0 \\ -\frac{N_3}{N_1} & 0 & 1 & 0 \\ \vdots & \vdots & \vdots & \vdots \\ -\frac{N_n}{N_1} & 0 & 0 & 1 \end{pmatrix} \begin{pmatrix} V_1 \\ V_2 \\ V_3 \\ \vdots \\ V_n \end{pmatrix} \quad (8.76)$$

By tripling the matrix in Equation 8.76 along the diagonal so that it applies to all three phases and calling the resulting matrix A^{3t} , we can write:

$$\left(\mathbf{V}^{3r} - \frac{V_1^3}{N_1} \mathbf{N}^{3r} \right) = A^{3t} \mathbf{V}^3 \quad (8.77)$$

Here, \mathbf{V}^3 is the voltage vector for all the windings and all three phases of dimension $3n$. Using these transformations, Equation 8.72 can be put in a form which includes all the windings as follows:

$$\mathbf{I}^3 = A^3 Y^{3r} A^{3t} \mathbf{V}^3 \quad (8.78)$$

Let $Y^3 = A^3 Y^{3r} A^{3t}$, then, Equation (8.78) can be written more succinctly as

$$\mathbf{I}^3 = Y^3 \mathbf{V}^3 \quad (8.79)$$

Y^3 is a $3n$ by $3n$ complex matrix.

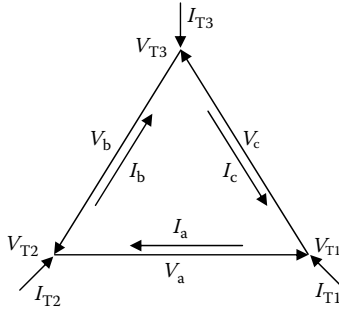
At this point, we will drop the superscript 3 because all the matrix equations we deal with from here on will involve all three phases unless otherwise noted. Thus, Equation 8.79 becomes

$$\mathbf{I} = Y \mathbf{V} \quad (8.80)$$

8.7.2.1 Delta Winding Connection

As we know from the introduction to this chapter, the matrix Y is singular. We would usually add the core excitation shunt admittances to Y^3 to render it invertible as discussed in [Bra82]. However, at this point, it is natural to make the delta connections so that balanced loading need not be assumed. [Figure 8.7](#) shows a delta connection with the labeling convention assumed for the phase and terminal voltages and currents.

The terminal currents are positive into the terminals. The phase currents are opposite the direction of phase voltage increase. With these conventions,

**FIGURE 8.7**

Delta winding connection with the phase and terminal quantities labeled. T is the terminal quantities and small letters are the phase quantities. (From Del Vecchio, R. M. 2008. *IEEE Trans Power Deliv* 23(3):1439–47. With permission.)

the terminal and phase voltages and currents are related using the following equations;

$$\begin{pmatrix} V_a \\ V_b \\ V_c \end{pmatrix} = \begin{pmatrix} 1 & -1 & 0 \\ 0 & 1 & -1 \\ -1 & 0 & 1 \end{pmatrix} \begin{pmatrix} V_{T1} \\ V_{T2} \\ V_{T3} \end{pmatrix} \quad (8.81)$$

$$\begin{pmatrix} I_{T1} \\ I_{T2} \\ I_{T3} \end{pmatrix} = \begin{pmatrix} 1 & 0 & -1 \\ -1 & 1 & 0 \\ 0 & -1 & 1 \end{pmatrix} \begin{pmatrix} I_a \\ I_b \\ I_c \end{pmatrix} \quad (8.82)$$

These were given in Equations 8.44 and 8.45; however, they were not used for the balanced terminal model. We need them here to allow for unbalanced conditions. Note that the matrices in Equations 8.81 and 8.82 are transposes of each other. This transformation needs to be embedded in a general transformation matrix that includes all the other windings and all three phases. The other winding currents and voltages are left unchanged, so they are transformed by a unit matrix. Thus, we embed the delta transformations in a unit matrix for the other windings. For example, if we have a two-winding transformer and winding 2 is a delta winding, Equation 8.82 is embedded as

$$\begin{pmatrix} I_{1,T1} \\ I_{2,T1} \\ I_{1,T2} \\ I_{2,T2} \\ I_{1,T3} \\ I_{2,T3} \end{pmatrix} = \begin{pmatrix} 1 & 0 & 0 & 0 & 0 & 0 \\ 0 & 1 & 0 & 0 & 0 & -1 \\ 0 & 0 & 1 & 0 & 0 & 0 \\ 0 & -1 & 0 & 1 & 0 & 0 \\ 0 & 0 & 0 & 0 & 1 & 0 \\ 0 & 0 & 0 & -1 & 0 & 1 \end{pmatrix} \begin{pmatrix} I_{1,a} \\ I_{2,a} \\ I_{1,b} \\ I_{2,b} \\ I_{1,c} \\ I_{2,c} \end{pmatrix} \quad (8.83)$$

Here, all the windings in one phase are listed consecutively, followed by the next phase, and so on. The corresponding voltage transformation in Equation 8.81 is embedded by transposing the matrix in Equation 8.83.

Denoting the matrix as M_y in Equation 8.83, where y indicates admittance representation, Equation 8.83 and the corresponding voltage transformation can be written to include all the windings:

$$\begin{aligned} \mathbf{I}_T &= M_y \mathbf{I} \\ \mathbf{V} &= M_y^t \mathbf{V}_T \end{aligned} \quad (8.84)$$

If there is more than one delta winding (say K), we label the transforming matrices, $M_{y1}, M_{y2}, \dots, M_{yK}$. Then, the transformed currents and voltages become

$$\begin{aligned} \mathbf{I}_{T1} &= M_{y1} \mathbf{I}, \quad \mathbf{I}_{T2} = M_{y2} \mathbf{I}_{T1}, \quad \dots \quad \mathbf{I}_{TK} = M_{yK} \mathbf{I}_{TK-1} \\ \mathbf{V} &= M_{y1}^t \mathbf{V}_{T1}, \quad \mathbf{V}_{T1} = M_{y2}^t \mathbf{V}_{T2}, \quad \dots \quad \mathbf{V}_{TK-1} = M_{yK}^t \mathbf{V}_{TK} \end{aligned} \quad (8.85)$$

Combining these, we get

$$\begin{aligned} \mathbf{I}_{TK} &= M_{yK} \dots M_{y2} M_{y1} \mathbf{I} = M_Y \mathbf{I} \\ \mathbf{V} &= M_{y1}^t M_{y2}^t \dots M_{yK}^t \mathbf{V}_{TK} = M_Y^t \mathbf{V}_{TK} \end{aligned} \quad (8.86)$$

where we have defined the product matrix M_Y . After the delta transformations, Equation 8.80 becomes

$$\mathbf{I}_{TK} = M_Y Y M_Y^t \mathbf{V}_{TK} \quad (8.87)$$

Using the resulting matrix in Equation 8.87 Y_{mod} to indicate that Y has been modified to include the deltas, we have

$$\mathbf{I}_{TK} = Y_{\text{mod}} \mathbf{V}_{TK} \quad (8.88)$$

The delta connection treated here is a -30° delta because the terminal voltages are shifted by -30° relative to the phase voltages. A $+30^\circ$ delta connection can also be treated by a similar procedure.

If there are squashed delta windings, they should also be handled in the admittance representation in order to allow unbalanced loading. This connection is discussed in Chapter 7. Those transformations are a bit more complicated than the delta transformations and will not be dealt with here. Also note that parallel winding connections can be handled in the admittance representation.

8.7.3 Impedance Representation

Although we can work in the admittance representation, it is often convenient to make winding connections and solve terminal equations in the impedance

representation. Note that even with the matrix transformation in Equation 8.87 the resulting matrix is still singular. To invert it, we must make some modifications. This is done by adding the core excitation characteristics [Bra82].

Let $Y_{\text{exc}-1}$ and $Y_{\text{exc}-0}$ be the positive and zero-sequence core excitation shunt admittances, respectively. These are used to construct diagonal and off-diagonal admittances for unbalanced conditions, similar to Equations 8.66 through 8.68:

$$\begin{aligned} Y_S &= -j\frac{1}{3}(Y_{\text{exc}-0} + 2Y_{\text{exc}-1}) \\ Y_M &= -j\frac{1}{3}(Y_{\text{exc}-0} - Y_{\text{exc}-1}) \end{aligned} \quad (8.89)$$

These can be added to a single winding or $1/n$ times these to all the windings. They are added to the imaginary part of Y_{mod} .

If the core losses are known, they can be used to obtain the core conductance, which also should be added to a single winding, or $1/n$ times it to all the windings. This is a real quantity and should be added to the diagonal terms in the real part of Y_{mod} .

Once this is done, the matrix Y_{mod} becomes invertible. If this is a complex matrix, complex inversion must be used. If Y_{mod} has real and imaginary parts, both must be modified using the above procedure in order to get an invertible matrix. Thus, core losses are needed if winding resistances are included. Because the resulting matrix is close to being singular, a double precision inversion may be needed.

Inverting Equation 8.88 with these modifications, we get

$$\mathbf{V}_{\text{TK}} = \mathbf{Z}_{\text{mod}} \mathbf{I}_{\text{TK}} \quad (8.90)$$

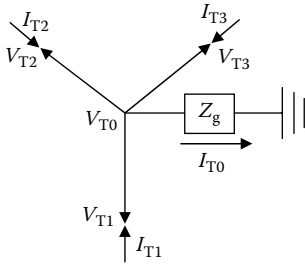
where \mathbf{Z}_{mod} is the inverse of the core-modified version of Y_{mod} and is an impedance matrix. It is in this representation that most of the other winding connections can be made more naturally without sacrificing unbalanced loading.

8.7.3.1 Ungrounded Y Connection

The ungrounded Y connection can be generalized to include Y connections with an impedance connecting the neutral point to ground as shown in Figure 8.8. For a true ungrounded Y connection, this impedance is set to a large enough value to keep the neutral current close to zero. If the value is too large, numerical instabilities may occur when the problem is solved.

Another equation must be added to Equation 8.90 to account for the additional branch to ground. It now becomes

$$\begin{pmatrix} \mathbf{V}_{\text{TK}} \\ V_{T0} \end{pmatrix} = \begin{pmatrix} \mathbf{Z}_{\text{mod}} & 0 \\ 0 & Z_g \end{pmatrix} \begin{pmatrix} \mathbf{I}_{\text{TK}} \\ I_{T0} \end{pmatrix} \quad (8.91)$$

**FIGURE 8.8**

Y connection grounded through an impedance. (From Del Vecchio, R. M. 2008. *IEEE Trans Power Deliv* 23(3):1439–47. With permission.)

The vectors in Equation 8.90 have been enlarged to include one more component and are of a dimension $3n + 1$. The matrix in Equation 8.90 has also been enlarged to a $3n + 1 \times 3n + 1$ matrix. The current equation

$$I_{T0} = I_{T1} + I_{T2} + I_{T3} \quad (8.92)$$

can be added via the matrix

$$\begin{pmatrix} I_{T1} \\ I_{T2} \\ I_{T3} \\ I_{T0} \end{pmatrix} = \begin{pmatrix} 1 & 0 & 0 \\ 0 & 1 & 0 \\ 0 & 0 & 1 \\ 1 & 1 & 1 \end{pmatrix} \begin{pmatrix} I_{S1} \\ I_{S2} \\ I_{S3} \end{pmatrix} \quad (8.93)$$

We have relabeled the new terminal currents with S instead of T to distinguish the different terminal situations. As before, the new terminal currents must be embedded in a larger unit matrix to include all the other windings. The transformed voltages are given by transposing the matrix in Equation 8.93:

$$\begin{pmatrix} V_{S1} \\ V_{S2} \\ V_{S3} \end{pmatrix} = \begin{pmatrix} 1 & 0 & 0 & 1 \\ 0 & 1 & 0 & 1 \\ 0 & 0 & 1 & 1 \end{pmatrix} \begin{pmatrix} V_{T1} \\ V_{T2} \\ V_{T3} \\ V_{T0} \end{pmatrix} \quad (8.94)$$

Here, we see that the new terminal voltages are given in terms of the old terminal voltages by $V_{S1} = V_{T1} + V_{T0}$, and so on. The matrices in Equations 8.93 and 8.94 are not square matrices. In both cases, the new terminal voltage and current vectors have one less component than the original vectors.

We need to embed Equation 8.94 in a larger matrix that leaves the other winding terminal voltages unchanged and do the same for the currents in Equation 8.93. Calling this enlarged matrix M_{zu} in Equation 8.94, with z standing for impedance representation and u for ungrounded Y, we can rewrite Equations 8.93 and 8.94 to include all the windings as

$$\begin{aligned} \mathbf{V}_S &= M_{zu} \begin{pmatrix} \mathbf{V}_{TK} \\ V_{T0} \end{pmatrix} \\ \begin{pmatrix} \mathbf{I}_{TK} \\ I_{T0} \end{pmatrix} &= M_{zu}^t \mathbf{I}_S \end{aligned} \quad (8.95)$$

where t indicates transpose. Then, Equation 8.91 is transformed into

$$\mathbf{V}_S = M_{zu} \begin{pmatrix} Z_{\text{mod}} & 0 \\ 0 & Z_g \end{pmatrix} M_{zu}^t \mathbf{I}_S \quad (8.96)$$

The terminal voltage and current vectors in Equation 8.96 include all the terminals and all three phases but exclude the neutral terminals. We use the S label for the terminals in the transformed situation. This procedure can be generalized for other ungrounded Y-connected windings (or those grounded through an impedance). Simply enlarge the matrix in Equation 8.91 to include other grounding impedances along the diagonal, labeled Z_{g1} , Z_{g2} , and so forth, and enlarge the matrices M_{zu} and M_{zu}^t appropriately. As in Equation 8.96, the resulting matrix will be a $3n \times 3n$ matrix and have the same terminals as before the grounding impedances were added. It is convenient to refer to the enlarged matrix in Equation 8.96 as $Z_{\text{mod-g}}$ so that the equation can be written:

$$\mathbf{V}_S = M_{zu} Z_{\text{mod-g}} M_{zu}^t \mathbf{I}_S \quad (8.97)$$

If there are no ungrounded or impedance grounded Y's, $Z_{\text{mod-g}}$ becomes Z_{mod} and Equation 8.97 reduces to Equation 8.90.

8.7.3.2 Series-Connected Windings from the Same Phase

This is a common connection, particularly for tap windings. The windings can be connected so that the voltages add or subtract. For simplicity, consider connecting windings 1 and 2, with winding 1 retaining its terminal status. The voltage addition is shown in Figure 8.9. Here the label 1, S1 refers to winding 1 in phase 1 and so forth.

The new terminal quantities will be labeled U. They are $V_{1,U1} = V_{1,S1} + V_{2,S1}$ and $I_{1,S1} = I_{1,U1}$, $I_{2,S1} = I_{1,U1}$ and can be expressed in matrix form, including the other phases, as

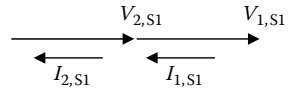


FIGURE 8.9

Voltage addition of two windings of the same phase. (From Del Vecchio, R. M. 2008. *IEEE Trans Power Deliv* 23(3):1439–47. With permission.)

$$\begin{pmatrix} V_{1,U1} \\ V_{1,U2} \\ V_{1,U3} \end{pmatrix} = \begin{pmatrix} 1 & 1 & 0 & 0 & 0 & 0 \\ 0 & 0 & 1 & 1 & 0 & 0 \\ 0 & 0 & 0 & 0 & 1 & 1 \end{pmatrix} \begin{pmatrix} V_{1,S1} \\ V_{2,S1} \\ V_{1,S2} \\ V_{2,S2} \\ V_{1,S3} \\ V_{2,S3} \end{pmatrix} \quad (8.98)$$

The currents are transformed by the transpose of the matrix in Equation 8.98 and are

$$\begin{pmatrix} I_{1,S1} \\ I_{2,S1} \\ I_{1,S2} \\ I_{2,S2} \\ I_{1,S3} \\ I_{2,S3} \end{pmatrix} = \begin{pmatrix} 1 & 0 & 0 \\ 1 & 0 & 0 \\ 0 & 1 & 0 \\ 0 & 1 & 0 \\ 0 & 0 & 1 \\ 0 & 0 & 1 \end{pmatrix} \begin{pmatrix} I_{1,U1} \\ I_{1,U2} \\ I_{1,U3} \end{pmatrix} \quad (8.99)$$

The matrices in Equations 8.98 and 8.99 are not square. They reduce the size of the three-phase voltage and current vectors by 3. We need to embed the matrices in Equations 8.98 and 8.99 into enlarged matrices that include the other windings without changing their terminal voltages and currents, that is, a unit matrix. If different winding numbers are connected in series, then the patterns in these matrices must be inserted in the appropriate positions of the final full winding matrix. We will call the enlarged matrix M_{zs} , corresponding to the voltage transformation matrix in Equation 8.98, where z refers to impedance representation and s to series connection. Then, we have

$$\begin{aligned} \mathbf{V}_U &= M_{zs} \mathbf{V}_S \\ \mathbf{I}_S &= M_{zs}^t \mathbf{I}_U \end{aligned} \quad (8.100)$$

This transforms Equation 8.97 into

$$\mathbf{V}_U = M_{zs} M_{zu} Z_{\text{mod-g}} M_{zu}^t M_{zs}^t \mathbf{I}_U \quad (8.101)$$

This has fewer terminals than before the series addition.

From Equations 8.95 and 8.100, we see that

$$\begin{aligned} \mathbf{V}_U &= M_{zs} M_{zu} \begin{pmatrix} \mathbf{V}_{TK} \\ V_{T0} \end{pmatrix} \\ \begin{pmatrix} \mathbf{I}_{TK} \\ I_{T0} \end{pmatrix} &= M_{zu}^t M_{zs}^t \mathbf{I}_U \end{aligned} \quad (8.102)$$

If there are more series-connected windings, these are handled in the same way and we end up with additional transformation matrices, for example M_{zs1} , M_{zs2} , and so on. Similarly, we can add more than two windings together by adding the additional windings to the previous ones using similar matrices operating on the previous terminal quantities.

We now see the general pattern. The voltages and currents are transformed by matrices that are usually transposes of each other and typically non-square. These also transform the terminal equations as in Equation 8.101.

From here on, we will only calculate the transformation matrices M for the terminal voltages and currents and assume that they are used similarly

to Equations 8.100 and 8.101. To avoid notational difficulties, we will assume that the starting terminal quantities are labeled S and the transformed are labeled U. The S-terminal quantities will be, in general, the result of multiple previous transformations.

8.7.3.3 Zig-Zag Winding Connection

This is a series connection involving two windings from different phases and is treated in a similar manner as in [Section 8.7.3.2](#). The connection is shown in [Figure 8.10](#), in which we assume that windings 1 and 2 are involved in the connection and winding 1 is the final terminal winding. This connection was given previously in [Figure 8.5](#), but here the labeling is different and winding 1 is part of the zig-zag connection.

The connection is one of voltage subtraction and results in the elimination of the terminal voltages and currents associated with winding 2. The transformed voltages are given by

$$\begin{pmatrix} V_{1,U1} \\ V_{1,U2} \\ V_{1,U3} \end{pmatrix} = \begin{pmatrix} 1 & 0 & 0 & 0 & 0 & -1 \\ 0 & -1 & 1 & 0 & 0 & 0 \\ 0 & 0 & 0 & -1 & 1 & 0 \end{pmatrix} \begin{pmatrix} V_{1,S1} \\ V_{2,S1} \\ V_{1,S2} \\ V_{2,S2} \\ V_{1,S3} \\ V_{2,S3} \end{pmatrix} \quad (8.103)$$

and the transformed currents by the transpose

$$\begin{pmatrix} I_{1,S1} \\ I_{2,S1} \\ I_{1,S2} \\ I_{2,S2} \\ I_{1,S3} \\ I_{2,S3} \end{pmatrix} = \begin{pmatrix} 1 & 0 & 0 \\ 0 & -1 & 0 \\ 0 & 1 & 0 \\ 0 & 0 & -1 \\ 0 & 0 & 1 \\ -1 & 0 & 0 \end{pmatrix} \begin{pmatrix} I_{1,U1} \\ I_{1,U2} \\ I_{1,U3} \end{pmatrix} \quad (8.104)$$

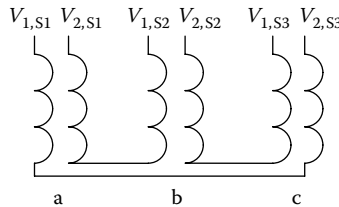
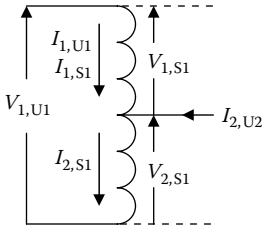


FIGURE 8.10

Zig-zag winding connection. The phases are labeled a, b, and c. (From Del Vecchio, R. M. 2008. *IEEE Trans Power Deliv* 23(3):1439–47. With permission.)

**FIGURE 8.11**

Autotransformer connection.
(From Del Vecchio, R. M.
2008. *IEEE Trans Power Deliv*
23(3):1439–47. With permission.)

Because the positive current direction is into the terminals, we see that the current in winding 2 is the negative of the current into winding 1, to which it is connected. These matrices can be extended to include all the windings and can be used to transform the terminal equation. This will result in a terminal equation with three fewer terminals. Label the full voltage transformation matrix $M_{zz'}$ corresponding to that in Equation 8.104, where the second z stands for zig-zag connection.

8.7.3.4 Autoconnection

This connection involves two windings from the same phase as shown in Figure 8.11. We will assume, again without loss of generality, that windings 1 and 2 are involved in this connection.

For simplicity, we will only consider the transformations for one phase, as shown in Figure 8.11. The other phases will simply be repeats along the diagonal of the complete matrix. The voltage terminal transformation is

$$\begin{pmatrix} V_{1,U1} \\ V_{2,U1} \end{pmatrix} = \begin{pmatrix} 1 & 1 \\ 0 & 1 \end{pmatrix} \begin{pmatrix} V_{1,S1} \\ V_{2,S1} \end{pmatrix} \quad (8.105)$$

and the currents are transformed by the transpose matrix

$$\begin{pmatrix} I_{1,S1} \\ I_{2,S1} \end{pmatrix} = \begin{pmatrix} 1 & 0 \\ 1 & 1 \end{pmatrix} \begin{pmatrix} I_{1,U1} \\ I_{2,U1} \end{pmatrix} \quad (8.106)$$

This leaves the number of terminals unchanged. Label the full voltage transformation, including all the windings and phases, $M_{za'}$ with a standing for auto.

Notice how much more simple the autotransformation is when all the windings are treated the same, compared with the autoconnection discussed for the balanced model when winding 1 is the series winding in this connection.

8.7.3.5 Three Windings Joined

Here the three windings are connected at a common point. This is an important connection for phase-shifting transformers or autotransformers with X-line taps. The three windings can be from different phases and the voltage connections can generally be additive or subtractive. This transformation can be performed in two steps. First, we join two of the windings but retain both terminals as is done in the autoconnection. Second, we join the third winding

to one of the terminals of the first two joined windings as in the series connection. This can be generalized if the windings are on different phases.

8.7.4 Terminal Loading

The various winding connections so far have been represented by matrices, which transform the terminal voltages and currents and are typically transposes of each other. In the impedance representation, we labeled these with a z for impedance and another letter to indicate the type of connection. To generalize this, here we will label these z_1, z_2 , and so on, with the number indicating the order in which they are applied. We will also label the terminal vectors S_1, S_2, S_3 , and so on, with the number corresponding to the matrix transformation order. For simplicity, we will ignore ungrounded Y connections, but their inclusion is straightforward and is discussed in [Section 8.7.3.1](#). Thus, we will start with Equation 8.90.

In the impedance representation, the multiple voltage and current transformations result in

$$\begin{aligned} \mathbf{V}_{S_1} &= M_{z_1} \mathbf{V}_{TK}, & \mathbf{V}_{S_2} &= M_{z_2} \mathbf{V}_{S_1}, & \cdots & \mathbf{V}_{S_L} = M_{z_L} \mathbf{V}_{S_{L-1}} \\ \mathbf{I}_{TK} &= M_{z_1}^t \mathbf{I}_{S_1}, & \mathbf{I}_{S_1} &= M_{z_2}^t \mathbf{I}_{S_2}, & \cdots & \mathbf{I}_{S_{L-1}} = M_{z_L}^t \mathbf{I}_{S_L} \end{aligned} \quad (8.107)$$

We consider a total of L transformations of various types. When applied successively, they result in

$$\begin{aligned} \mathbf{V}_{S_L} &= M_{z_L} \cdots M_{z_2} M_{z_1} \mathbf{V}_{TK} = M_Z \mathbf{V}_{TK} \\ \mathbf{I}_{TK} &= M_{z_1}^t M_{z_2}^t \cdots M_{z_L}^t \mathbf{I}_{S_L} = M_Z^t \mathbf{I}_{S_L} \end{aligned} \quad (8.108)$$

Here, we defined the total transformation matrix M_Z . The terminal Equation 8.90 that we started with is transformed into

$$\mathbf{V}_{S_L} = M_Z Z_{\text{mod}} M_Z^t \mathbf{I}_{S_L} \quad (8.109)$$

If ungrounded Y s are present, then $Z_{\text{mod-g}}$ should replace Z_{mod} in Equation 8.109 and \mathbf{V}_{TK} and \mathbf{I}_{TK} should be expanded to include \mathbf{V}_{T_0} and \mathbf{I}_{T_0} as in Equation 8.95 or additional neutral-to-ground impedances, voltages, and currents if more than one ungrounded Y is present.

We assume that terminal 1 is the input terminal having a given voltage. The other terminals are loaded with some impedance. In general, we can write

$$\mathbf{V}_{S_L} = -Z_{Ld} \mathbf{I}_{S_L} + \mathbf{V}_{Ld} \quad (8.110)$$

Here, Z_{Ld} is a complex load matrix that is typically diagonal. The minus sign is necessary because the terminal currents are assumed to flow into the transformer while the load currents flow out of it. \mathbf{V}_{Ld} is an applied voltage load vector that typically includes only a nonzero terminal 1 voltage. However, it may be nonzero for other terminals in some situations.

As an example, if there are three terminals, which we will label 1, 2, and 3, and terminal 1 is driven by a voltage V_0 , Equation 8.110 would take the form, for one phase

$$\begin{pmatrix} V_1 \\ V_2 \\ V_3 \end{pmatrix} = - \begin{pmatrix} 0 & 0 & 0 \\ 0 & Z_{Ld,2} & 0 \\ 0 & 0 & Z_{Ld,3} \end{pmatrix} \begin{pmatrix} I_1 \\ I_2 \\ I_3 \end{pmatrix} + \begin{pmatrix} V_0 \\ 0 \\ 0 \end{pmatrix} \quad (8.111)$$

This must be enlarged to include the other phases. The diagonal matrix entries are the complex load impedances for terminals 2 and 3. The voltage V_0 will change for the different phases if, for example, the input is a three-phase balanced set of voltages. The Z_{Ld} 's will be the same for the different phases under balanced conditions but will be different for unbalanced loading. In fact, we should include the zero-sequence load impedances if they differ from the positive-sequence impedances, using the procedure given in Equations 8.66 through 8.68.

Combining Equations 8.110 and 8.109, we get

$$(M_Z Z_{mod} M_Z^t + Z_{Ld}) \mathbf{I}_{SL} = \mathbf{V}_{Ld} \quad (8.112)$$

This terminal equation must be solved. If a real-matrix solver is used, then this must be cast in the form of Equation 8.71 to separate the real and imaginary parts.

8.7.5 Solution Process

8.7.5.1 Terminal Currents and Voltages

In general, Equation 8.112 is complex, so complex solution techniques must be employed, unless the methods discussed in [Section 8.7.2](#) are used. Most scientific or math libraries have matrix equation solvers. We recommend a double precision matrix equation solver.

Once the terminal currents, \mathbf{I}_{SL} , are found, the terminal voltages, \mathbf{V}_{SL} , can be found using Equations 8.110 or 8.109. From these quantities, we can also obtain the power into and out of the various terminals. In addition, we can obtain regulation effects and transformer terminal impedances using the methods outlined for balanced loading.

8.7.5.2 Winding Currents and Voltages

Equation 8.108 can be used to obtain \mathbf{I}_{TK} from the terminal currents \mathbf{I}_{SL} . If ungrounded Y's are present, then the I_{T0} 's are also obtained. Then, Equation 8.90 or 8.91, depending on whether ungrounded Y's are present, can be used to determine \mathbf{V}_{TK} from \mathbf{I}_{TK} . Equation 8.86 can then be used to obtain \mathbf{V} from

\mathbf{V}_{TK} , where \mathbf{V} contains the winding voltages under load. Finally, Equation 8.80 can be used to get the winding currents \mathbf{I} from \mathbf{V} , and this is summarized in the following steps:

$$\begin{aligned}\mathbf{I}_{TK} &= \mathbf{M}_Z^t \mathbf{I}_{SL} \\ \mathbf{V}_{TK} &= \mathbf{Z}_{mod} \mathbf{I}_{TK} \\ \mathbf{V} &= \mathbf{M}_Y^t \mathbf{V}_{TK} \\ \mathbf{I} &= \mathbf{YV}\end{aligned}\tag{8.113}$$

These are slightly modified if ungrounded Y's are present. In this case, the neutral currents and voltages are also obtained.

8.7.6 Unbalanced Loading Examples

The examples given here will be for a single line-to-ground fault. If the unfaulted terminals are open, they are given a very high load impedance. For unfaulted loaded terminals, we assume that the load impedances are very low, about 0.01%, but that the load voltages stay at their rated values. A full or partial load generally can be added to the unfaulted terminals. For the faulted terminal, we assume that the load impedance and voltage are zero. In general, the a-phase terminal is faulted. The b- and c-phase terminals corresponding to the faulted terminal are given very low impedances, and their voltages are set to their rated values. These terminal conditions correspond to those used in the sequence analysis calculations for cases in which the system is connected beyond the fault point. If the system is not connected beyond the fault point, then the b- and c-phase terminals corresponding to the faulted terminal are given very high impedances to signify an unloaded condition. The results obtained by the methods discussed here will be compared with the results of the sequence analysis method.

It is also convenient to use per-unit impedance and admittance quantities as inputs for a computer program that performs the above calculations. However, they are converted to ohms or mhos before performing the analysis. We have also kept the exciting admittances low, typically about 0.05%, to minimize the influence of the core for better comparison with the sequence results. We also ignore resistance effects in this analysis. The fault currents are rms amps with no asymmetry factor correction.

8.7.6.1 Autotransformer with Buried Delta Tertiary and Fault on Low-Voltage Terminal

The autotransformer is a three-phase, 50-MVA unit, Y connected with a buried delta. The line-to-line voltages, expressed in kilovolts (kV), are as follows: HV 154.63, LV 69.28, and TV 7.2. The per-unit winding-to-winding

TABLE 8.6

Winding-to-Winding Leakage Reactances in Per-Unit % for the 50-MVA Autotransformer

Winding	Positive Sequence		Zero Sequence	
	LV	TV	LV	TV
HV	24.518	40.428	20.842	30.508
LV		11.090		9.430

Source: Del Vecchio, R. M. 2008. *IEEE Trans Power Deliv* 23(3):1439–47. With permission.

TABLE 8.7

Comparison of Terminal and Winding Fault Currents for the 50-MVA Autotransformer

	Present Method Phase			Sequence Analysis Phase		
	A	B	C	a	B	c
<i>Terminal</i>						
HV	2650	154	154	2654	154	154
LV	7401	1830	1830	7412	1833	1833
TV	0.27	0.27	0	0	0	0
<i>Winding</i>						
Series	2650	154	154	2654	154	154
Common	4754	1678	1678	4759	1679	1679
TV	8274	8264	8264	8274	8274	8274

Source: Del Vecchio, R. M. 2008. *IEEE Trans Power Deliv* 23(3):1439–47. With permission.

leakage reactances are given in Table 8.6. Note that these are winding-to-winding leakage reactances and not terminal-to-terminal leakage reactances, because the method presented here is based on winding-to-winding leakage reactances. The relationship between winding-to-winding and terminal-to-terminal leakage reactances for autotransformers was given in Chapter 4.

The single line-to-ground fault is on phase a of the LV terminal. The terminal and winding currents obtained by the present method are compared with the sequence analysis results given in Table 8.7. Only the current magnitudes are given. The neutral current is 8104 A (amps) by the present method and 8117 A by the sequence analysis method.

8.7.6.2 Power Transformer with Fault on Delta Tertiary

This is a three-phase, 16.8-MVA power transformer with line-to-line voltages expressed in kilovolts: HV 138, LV 13.8, and TV 7.22. The HV and LV windings

TABLE 8.8

Winding-to-Winding Leakage Reactances in Per-Unit % for the 16.8-MVA Power Transformer

Winding	Positive Sequence		Zero Sequence	
	LV	TV	LV	TV
HV	10.00	17.40	8.50	13.92
LV		7.10		6.39

Source: Del Vecchio, R. M. 2008. *IEEE Trans Power Deliv* 23(3):1439-47. With permission.

TABLE 8.9

Comparison of Terminal and Winding Fault Currents for the 16.8-MVA Power Transformer

	Present Method Phase			Sequence Analysis Phase		
	a	B	c	A	b	c
<i>Terminal</i>						
HV	8.7	0	8.7	8.6	0	8.6
LV	5804	0.23	5804	5803	0	5803
TV	12,628	6314	6314	12,627	6313	6313
<i>Winding</i>						
HV	8.6	0	8.6	8.6	0	8.6
LV	5803	0	5803	5803	0	5803
TV	6314	0	6314	6313	0	6313

Source: Del Vecchio, R. M. 2008. *IEEE Trans Power Deliv* 23(3):1439-47. With permission.

are Y connected, and the TV is delta connected. The leakage reactances are given in Table 8.8.

The single line-to-ground fault is on phase a of the loaded delta tertiary, and no line-to-line loads are present. The comparison of the fault currents by the present and sequence analysis methods is shown in Table 8.9, in which only the current magnitudes are given.

The terminal currents sum to zero for the delta. There are no neutral currents for either analysis method because this will be a zero-sequence current that cannot flow out of the delta. If the system is not connected beyond the fault point, there are no short-circuit currents in any of the windings, as was discussed in Chapter 6.

8.7.6.3 Power Transformer with Fault on Ungrounded Y Secondary

This is a three-phase, 40-MVA power transformer with line-to-line voltages expressed in kilovolts: HV 242.93, LV 34.5, and TV 13.2. The HV is a

TABLE 8.10

Winding-to-Winding Leakage Reactances in Per-Unit % for the 40-MVA Power Transformer

Winding	Positive Sequence		Zero Sequence	
	LV	TV	LV	TV
HV	8.45	12.62	7.18	10.10
LV		3.3		3.00

Source: Del Vecchio, R. M. 2008. *IEEE Trans Power Deliv* 23(3):1439–47. With permission.

TABLE 8.11

Comparison of Terminal and Winding Fault Currents for the 40-MVA Power Transformer

	Present Method Phase			Sequence Analysis Phase		
	A	B	c	a	b	C
<i>Terminal</i>						
HV	854	427	427	852	426	426
LV	20,281	10,140	10,140	20,162	10,081	10,081
TV	32,300	32,300	0.2	32,063	32,063	0
<i>Winding</i>						
HV	852	426	426	852	426	426
LV	20,167	10,084	10,084	20,162	10,081	10,081
TV	21,382	10,691	10,691	21,375	10,688	10,688

Source: Del Vecchio, R. M. 2008. *IEEE Trans Power Deliv* 23(3):1439–47. With permission.

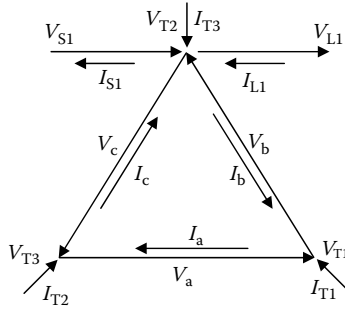
grounded Y, the LV is an ungrounded Y, and the TV is a loaded delta. The leakage reactances are given in Table 8.10.

The single line-to-ground fault is on phase a of the ungrounded Y secondary. The terminal and winding current magnitudes are given in Table 8.11 for both methods. There are no neutral currents in either method of analysis. If the system is not connected beyond the fault point, there are no fault currents in the transformer, as discussed in Chapter 6 and shown by this method.

8.7.7 Balanced Loading Example

8.7.7.1 Standard Delta Phase-Shifting Transformer

This type of transformer was discussed in Chapter 7, so we know the analytic expressions for the phase shift, terminal and winding currents, and effective leakage reactance for comparison with the values determined by this method. The connection is shown in [Figure 8.12](#).

**FIGURE 8.12**

Standard delta phase shifter. S₁ and L₁ label the input and output terminals of the A phase. The other input and output terminals are not shown. The delta is at +30°. (From Del Vecchio, R. M. 2008. *IEEE Trans Power Deliv* 23(3):1439–47. With permission.)

The secondary windings are loaded with their rated terminal resistance on all three phases. The delta is a +30° delta. The current transformation, corresponding to the +30° delta is

$$\begin{pmatrix} I_{T1} \\ I_{T2} \\ I_{T3} \end{pmatrix} = \begin{pmatrix} 1 & -1 & 0 \\ 0 & 1 & -1 \\ -1 & 0 & 1 \end{pmatrix} \begin{pmatrix} I_a \\ I_b \\ I_c \end{pmatrix} \quad (8.114)$$

The voltages are transformed by transposing the matrix in Equation 8.114 with the vectors interchanged. The −30° delta transformation was given in Equation 8.82. Note that the S₁ winding is connected negatively to the delta terminal, while the L₁ winding is connected positively to the delta terminal.

The transformer is a three-phase, 75-MVA unit. Labeling the input and output windings S and L, respectively, and the delta winding T, the winding phase voltages expressed in kilovolts are as follows: S 8.0, L 8.0, and T 38.0. The positive-sequence leakage reactances are, in per-unit percents, $Z_{SL} = 20$, $Z_{ST} = 10$, and $Z_{LT} = 10$. The zero-sequence reactances are the same, as balanced loading is assumed.

The parameter n is the ratio of delta winding turns to turns in the S or L winding, which are assumed equal. The parameter for this unit is 4.76. The phase shift is given by

$$\theta = 2 \tan^{-1} \left(\frac{\sqrt{3}}{n} \right) \quad (8.115)$$

For the value of n given, this is 40°. The present method gives the same value for no-load conditions but a value of 38.66° for load conditions.

The magnitude of the terminal voltage is given by

$$|V_{L1}| = \sqrt{\frac{n^2 + 3}{3n^2}} |V_a| \quad (8.116)$$

This is equal to 23.396 kV for this unit. The present method gives this value for no-load conditions, but a value of 23.389 for load conditions. The angle and voltage magnitude shift under load conditions are regulation effects. Based on the input power and terminal voltage, the terminal current S1 is 1068.6 A. The current in the delta is given by

$$|I_a| = \frac{2}{\sqrt{n^2 + 3}} |I_{S1}| \quad (8.117)$$

This gives a value of 421.9 A compared with a value of 422.6 A by the present method.

The winding power is smaller than the input power:

$$P_{\text{wdg}} = \sin\theta P_{\text{in}} \quad (8.118)$$

For P_{in} of 75 MVA, P_{wdg} is 48.21 MVA. The present method gives 48.26 MVA.

The effective per-unit leakage reactance, as given in Chapter 7, is

$$z_{\text{eff}} = \left(\frac{3n^2}{n^2 + 3} \right) \left[\frac{z_{\text{SL}}}{n^2} + \frac{2(z_{\text{TS}} + z_{\text{TL}} - z_{\text{SL}})}{n^2 + 3} \right] \quad (8.119)$$

This gives 2.34%. Using the technique discussed in [Section 8.6](#), we obtain 2.324% for this quantity by the analysis method presented here.

8.7.8 Discussion

The method we propose presents a systematic way of modeling transformers for circuit analysis, especially the ones with complicated winding interconnections. The inputs required are 1) the winding-to-winding positive- and zero-sequence leakage reactances, with only the positive ones required for balanced conditions, 2) winding turns, 3) the core excitation conditions for unbalanced loading, 4) winding resistances and core losses if desired, 5) quantities such as MVA and volts per turn, and 6) the winding interconnections.

Our method then permits the calculation of terminal voltages and currents and winding voltages and currents under load, regardless of whether the loading is balanced or unbalanced. This is particularly important for unbalanced faults, because the winding currents are needed for subsequent force and stress analysis. For balanced conditions, the method can give terminal-to-terminal leakage reactances and regulation effects. For the

terminal-to-terminal per-unit leakage reactances, only two terminals should be loaded, one primary and one secondary, at its rated load. The other windings should be loaded with a very large impedance to simulate an unloaded condition.

The main purpose of the examples given is to show that this method agrees with other types of analysis for which comparisons can be made. We do not claim that the methods proposed here are more accurate than other methods of analysis, when they are feasible; rather we expect that these methods are more general and can be applied to more complicated winding configurations than is possible or reasonable with more standard methods such as sequence analysis methods.

The terminal Equation 8.112 can be integrated into a larger system, for example, for power flow analysis. As part of a larger network, only the terminal quantities of the transformer are of interest. However, once the network equations are solved, we can obtain the internal winding currents by the methods described in this chapter. These can be used, for example, for loss or short-circuit analysis.

If transient analysis is desired, then inductance matrices can be used from the start instead of reactance matrices. The procedures described here can be carried out with inductance matrices, eliminating the imaginary unit j . These matrices will then be incorporated into a differential matrix equation in time. Nonlinear core characteristics can be added as discussed in [Bra82]. This will mainly be used in transient analysis and is most easily inserted in the admittance representation. However, [Bra82] also discusses a method for inserting nonlinear core characteristics in the impedance representation. Also note that two core transformers can be modeled using the methods described in this chapter. In this case, it is necessary to add any connections between terminals on different cores. Voltage and current transfer matrices can be constructed to accomplish this.

9

Rabins' Method for Calculating Leakage Fields, Leakage Inductances, and Forces in Transformers

9.1 Introduction

Modern general-purpose computer programs are available for calculating the magnetic field inside the complex geometry of a transformer. These numerical methods generally use finite elements or boundary elements, and geometric details such as the tank wall and clamping structure can be included. While three-dimensional programs are available, two-dimensional programs using an axisymmetric geometry are adequate for most purposes. Although inputting the geometry, the ampere-turns (amp-turns) in the winding sections, and the boundary conditions can be tedious, parametric procedures are often available to simplify this task. Along with the magnetic field, associated quantities such as inductances and forces can be calculated by these methods. In addition, eddy currents in structural parts and their accompanying losses can be obtained with an appropriate alternating current (AC) solver.

Despite these modern advances in computational methods, older procedures can often be profitably used to obtain quantities of interest very quickly and with minimum input. One of these is Rabins' method, which assumes an idealized transformer geometry [Rab56]. This simplified geometry enables the development of analytic formulas for calculating the magnetic field and other useful quantities. The geometry consists of a single leg of a single- or three-phase transformer. The leg consists of a core and surrounding coils, which are assumed to be axisymmetric, along with yokes, which are assumed to be of infinite extent at the top and bottom of the leg. The entire axisymmetric geometry is of infinite extent radially and thus has no tank walls or clamping structures. In addition, the core and yokes are assumed to be infinitely permeable.

Despite these simplifications, Rabins' method accurately calculates the magnetic field in the immediate vicinity of the windings. Thus, it also accurately obtains forces and inductances, which depend largely on the field near

the windings. This can be shown by a direct comparison with a finite element solution applied to a more complex geometry, including a tank wall and clamps. Although the finite element procedure can obtain losses in structural parts, Rabins’ method is not suited for this. However, because the magnetic field near or inside the windings is obtained accurately, the eddy current losses in the windings and their spatial distribution can be accurately obtained from formulas based on this leakage field.

In this chapter, we present Rabins’ method and show how it can be used to obtain the leakage magnetic field, forces, leakage inductances, and mutual inductances between winding sections, for use in detailed circuit models of transformers such as those needed in impulse calculations.

9.2 Theory

We will model a cylindrical coil or section of a coil surrounding a core leg with top and bottom yokes as shown in Figure 9.1. The yokes are really boundaries of the geometry, which extends infinitely far radially. We assume the coils are composed of stranded conductors so that no eddy current effects are modeled. Thus, we can assume direct current (DC) conditions. We assume the current density in the coil to be piecewise constant axially and uniform radially, as shown in Figure 9.2. As indicated in the figure, there

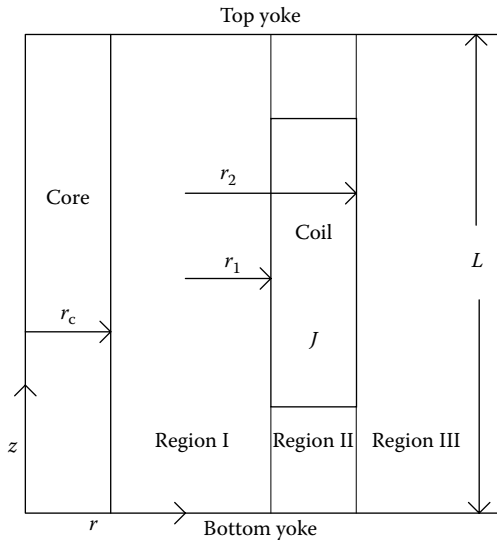


FIGURE 9.1
Geometry of iron core, yokes, and coil or coil section.

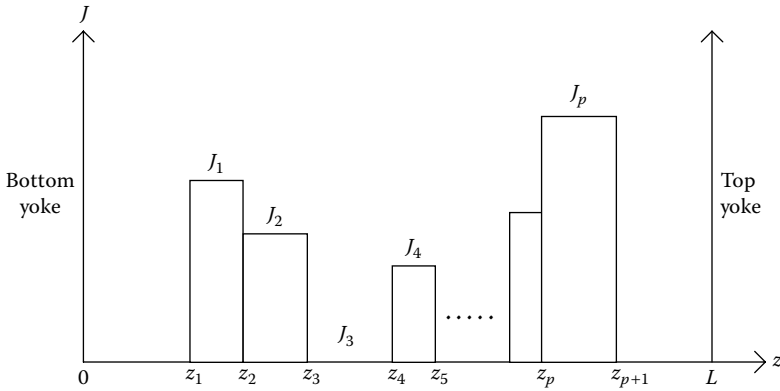


FIGURE 9.2
Axial distribution of current density in the coil.

can be regions within the coil where the current density decreases to zero. Because there are no nonlinear effects within the geometry modeled, the fields from several coils can be added vectorially so that it is only necessary to model one coil at a time.

Maxwell's equations for the magnetic field (in SI units), applied to the geometry outside the core and yokes and assuming static conditions, are

$$\nabla \times \mathbf{H} = \mathbf{J} \quad (9.1)$$

$$\nabla \cdot \mathbf{B} = 0 \quad (9.2)$$

where \mathbf{H} is the magnetic field, \mathbf{B} is the induction, and \mathbf{J} is the current density. Defining a vector potential \mathbf{A} by

$$\mathbf{B} = \nabla \times \mathbf{A} \quad (9.3)$$

Equation 9.2 is automatically satisfied. We also have

$$\mathbf{B} = \mu_0 \mathbf{H} \quad (9.4)$$

in the region of interest where μ_0 is the permeability of vacuum, oil, or air, which are all nearly the same. Substituting Equations 9.3 and 9.4 into Equation 9.1, we obtain

$$\nabla \times (\nabla \times \mathbf{A}) = \nabla (\nabla \cdot \mathbf{A}) - \nabla^2 \mathbf{A} = \mu_0 \mathbf{J} \quad (9.5)$$

The vector potential is not completely defined by Equation 9.3. It contains some arbitrariness that can be removed by setting

$$\nabla \cdot \mathbf{A} = 0 \quad (9.6)$$

Using this, Equation 9.5 becomes

$$\nabla^2 \mathbf{A} = -\mu_0 \mathbf{J} \quad (9.7)$$

The current density vector is azimuthal so that

$$\mathbf{J} = J_\phi \mathbf{a}_\phi \quad (9.8)$$

where \mathbf{a}_ϕ is the unit vector in the azimuthal direction. Because of the axisymmetric geometry, all the field quantities are independent of ϕ . With these assumptions, in cylindrical coordinates, Equation 9.7 becomes

$$\frac{\partial^2 A_\phi}{\partial r^2} + \frac{1}{r} \frac{\partial A_\phi}{\partial r} - \frac{A_\phi}{r^2} + \frac{\partial^2 A_\phi}{\partial z^2} = -\mu_0 J_\phi \quad (9.9)$$

Thus, \mathbf{A} and \mathbf{J} have only a ϕ component and we drop this subscript for simplicity in the following equations.

We write the current density as a Fourier series in terms of a fundamental spatial period of length L , the yoke-to-yoke distance, or window height.

$$J = J_0 + \sum_{n=1}^{\infty} J_n \cos\left(\frac{n\pi z}{L}\right) \quad (9.10)$$

where

$$J_0 = \frac{1}{L} \int_0^L J dz, \quad J_n = \frac{2}{L} \int_0^L J \cos\left(\frac{n\pi z}{L}\right) dz \quad (9.11)$$

For the current density described in [Figure 9.2](#), for example, we have

$$J = \begin{cases} 0, & 0 \leq z \leq z_1 \\ J_1, & z_1 \leq z \leq z_2 \\ \vdots & \\ J_i, & z_i \leq z \leq z_{i+1} \\ \vdots & \\ J_p, & z_p \leq z \leq z_{p+1} \\ 0, & z_{p+1} \leq z \leq L \end{cases} \quad (9.12)$$

Using Equation 9.12, the integrals in Equation 9.11 can be evaluated to get

$$\begin{aligned} J_0 &= \frac{1}{L} \sum_{i=1}^p J_i (z_{i+1} - z_i) \\ J_n &= \frac{2}{n\pi} \sum_{i=1}^p J_i \left[\sin\left(\frac{n\pi z_{i+1}}{L}\right) - \sin\left(\frac{n\pi z_i}{L}\right) \right] \end{aligned} \quad (9.13)$$

Thus, for one section with a constant current density J , we have

$$\begin{aligned} J_0 &= J \frac{(z_2 - z_1)}{L} \\ J_n &= \frac{2J}{n\pi} \left[\sin\left(\frac{n\pi z_2}{L}\right) - \sin\left(\frac{n\pi z_1}{L}\right) \right] \end{aligned} \quad (9.14)$$

L is best taken to be about three times the window height of the transformer and not the winding height, although we treat it like a winding height with zero current densities in the top and bottom sections of the winding. To some extent, this compensates for the fact that real core yokes are not of infinite extent.

As shown in [Figure 9.1](#), we have divided the solution space into three regions:

$$\begin{aligned} \text{Region I} & \quad r_c \leq r \leq r_1, \quad 0 \leq z \leq L \\ \text{Region II} & \quad r_1 \leq r \leq r_2, \quad 0 \leq z \leq L \\ \text{Region III} & \quad r_2 \leq r \leq \infty, \quad 0 \leq z \leq L \end{aligned}$$

In regions I and III, dropping the subscript ϕ , the current density is 0 so that Equation 9.9 becomes

$$\frac{\partial^2 A}{\partial r^2} + \frac{1}{r} \frac{\partial A}{\partial r} - \frac{A}{r^2} + \frac{\partial^2 A}{\partial z^2} = 0 \quad (9.15)$$

This is a homogeneous partial differential equation. We will look for a solution of the form

$$A(r, z) = R(r)Z(z) \quad (9.16)$$

Substituting this into Equation 9.15 and dividing by RZ , we get

$$\frac{1}{R} \frac{\partial^2 R}{\partial r^2} + \frac{1}{rR} \frac{\partial R}{\partial r} - \frac{1}{r^2} + \frac{1}{Z} \frac{\partial^2 Z}{\partial z^2} = 0 \quad (9.17)$$

This equation contains terms that are only a function of r and terms that are only a function of z , whose sum is a constant = 0. Therefore, each set of terms must separately equal a constant whose sum is zero. Let the constant be m^2 , a positive number. Then

$$\frac{1}{R} \frac{\partial^2 R}{\partial r^2} + \frac{1}{rR} \frac{\partial R}{\partial r} - \frac{1}{r^2} = m^2, \quad \frac{1}{Z} \frac{\partial^2 Z}{\partial z^2} = -m^2 \quad (9.18)$$

Rearranging the terms, we get

$$r^2 \frac{\partial^2 R}{\partial r^2} + r \frac{\partial R}{\partial r} - (m^2 r^2 + 1)R = 0, \quad \frac{\partial^2 Z}{\partial z^2} + m^2 Z = 0 \quad (9.19)$$

We need to consider the cases $m = 0$ and $m > 0$ separately.

For $m = 0$, the solution to the z equation that satisfies the boundary conditions at the top and bottom yokes is a constant independent of z , and the r equation in Equation 9.19 becomes

$$r^2 \frac{\partial^2 R}{\partial r^2} + r \frac{\partial R}{\partial r} - R = 0 \quad (9.20)$$

The solution to this equation is

$$R_0 = Sr + \frac{T}{r} \quad (9.21)$$

where S and T are constants to be determined by the boundary conditions and where we label the solution with a subscript zero.

For $m > 0$, the solution to the z equation in Equation 9.19 can be written

$$Z = Z_m \cos(mz + \phi_m) \quad (9.22)$$

where Z_m and ϕ_m are constants to be determined by the boundary conditions. Because we assume that the yoke material has infinite permeability, the B-field must be perpendicular to the yoke surfaces. Using Equation 9.3, in cylindrical coordinates, we have

$$\mathbf{B} = -\frac{\partial A}{\partial z} \mathbf{a}_r + \left(\frac{\partial A}{\partial r} + \frac{A}{r} \right) \mathbf{k} \quad (9.23)$$

where \mathbf{a}_r and \mathbf{k} are unit vectors in the r and z directions, respectively. For \mathbf{B} to be perpendicular to the upper and lower yokes, the \mathbf{a}_r component of the B-field must vanish at these yoke positions. Thus,

$$\frac{\partial A}{\partial z} = 0 \quad \Rightarrow \quad \frac{\partial Z}{\partial z} = 0 \quad \text{at} \quad z = 0, L \quad (9.24)$$

Using this, Equation 9.22 must have the form

$$Z = Z_n \cos(mz), \quad m = \frac{n\pi}{L}, \quad n = 1, 2, \dots \quad (9.25)$$

Here, we use n rather than m to label the constant. m also depends on n , but we omit this reference for simplicity.

For $m > 0$, the radial equation in Equation 9.19 can be written, with the substitution $x = mr$, as

$$x^2 \frac{\partial^2 R}{\partial x^2} + x \frac{\partial R}{\partial x} - R(x^2 + 1) = 0 \quad (9.26)$$

The solution to this equation is

$$R_n = C_n I_1(x) + D_n K_1(x) \quad (9.27)$$

where I_1 and K_1 are modified Bessel functions of the first and second kind, respectively, of order 1 [Dwi61]. We have also labeled the constants C and D with the subscript n because the solution depends on n through m , which occurs in x .

In general, the solution to Equation 9.15 can be expressed as a sum of these individual solutions, each a product of an R and Z term:

$$A = Sr + \frac{T}{r} + \sum_{n=1}^{\infty} [C_n I_1(mr) + D_n K_1(mr)] \cos(mz), \quad m = \frac{n\pi}{L} \quad (9.28)$$

where the Z solution constants have been absorbed in the overall constants shown. This solution satisfies the boundary condition at $z = 0, L$. Because we also assume an infinitely permeable core, the B-field must be normal to the core surface. Thus, from Equation 9.23, the \mathbf{k} -component must vanish at the core surface (region I):

$$\frac{\partial A}{\partial r} + \frac{A}{r} = 0 \quad \text{at} \quad r = r_c \quad (9.29)$$

Substituting Equation 9.28 into Equation 9.29, we get

$$2S + \sum_{n=1}^{\infty} \left[mC_n \frac{\partial I_1}{\partial x} + mD_n \frac{\partial K_1}{\partial x} + m \frac{(C_n I_1 + D_n K_1)}{x} \right] \cos(mz) = 0 \quad \text{at} \quad x = mr_c \quad (9.30)$$

Although Equation 9.30 seems to require that $S = 0$, when all the windings are considered with their amp-turns that sum to zero, we can satisfy this boundary condition with $S \neq 0$ for each winding. Assuming the S term will ultimately vanish, the remaining terms in Equation 9.30 must vanish for all z . These remaining terms constitute a Fourier expansion in $\cos(n\pi z/L)$.

For these terms to vanish for all z , the individual Fourier coefficients must vanish. This requires

$$mC_n \left(\frac{\partial I_1}{\partial x} + \frac{I_1}{x} \right) + mD_n \left(\frac{\partial K_1}{\partial x} + \frac{K_1}{x} \right) = mC_n I_0 - mD_n K_0 = 0 \quad (9.31)$$

where we have used modified Bessel function identities to get the first equality in Equation 9.31 [Rab56]. I_0 and K_0 are modified Bessel functions of order 0. Thus, from Equation 9.31, we have

$$D_n = C_n \frac{I_0(mr_c)}{K_0(mr_c)} \quad (9.32)$$

Labeling the unknown constants with the region number as superscript, Equation 9.28 becomes

$$A^I = S^I r + \sum_{n=1}^{\infty} C_n^I \left[I_1(mr) + \frac{I_0(mr_c)}{K_0(mr_c)} K_1(mr) \right] \cos(mz), \quad m = \frac{n\pi}{L} \quad (9.33)$$

We have dropped the T/r term because it approaches infinity as the core radius approaches zero and it is not needed to satisfy the boundary conditions in this region. Labeling the solution constants in this region with superscript I , this amounts to setting $T^I = 0$ in this region.

In region III, A must be finite as $r \rightarrow \infty$. Since $I_1 \rightarrow \infty$ as $r \rightarrow \infty$ and the Sr term also $\rightarrow \infty$, from Equation 9.28 and using the appropriate region label, we have

$$A^{\text{III}} = \frac{T^{\text{III}}}{r} + \sum_{n=1}^{\infty} D_n^{\text{III}} K_1(mr) \cos(mz) \quad (9.34)$$

Labeling the solution constants in this region with superscript III, this amounts to setting $S^{\text{III}} = 0$ and $C_n^{\text{III}} = 0$.

In region II, we must keep the current density term in Equation 9.9. Substituting the Fourier series Equation 9.10 into Equation 9.9 and dropping the ϕ subscript in region II, we have

$$\frac{\partial^2 A}{\partial r^2} + \frac{1}{r} \frac{\partial A}{\partial r} - \frac{A}{r^2} + \frac{\partial^2 A}{\partial z^2} = -\mu_0 \left[J_0 + \sum_{n=1}^{\infty} J_n \cos(mz) \right] \quad (9.35)$$

We look for a solution to this equation in the form of a series expansion:

$$A = \sum_{n=0}^{\infty} R_n(r) \cos(mz), \quad m = \frac{n\pi}{L} \quad (9.36)$$

Substituting into Equation 9.35, we get

$$\sum_{n=0}^{\infty} \left(\frac{\partial^2 R_n}{\partial r^2} + \frac{1}{r} \frac{\partial R_n}{\partial r} - \frac{R_n}{r^2} \right) \cos(mz) - m^2 \sum_{n=1}^{\infty} R_n \cos(mz) = -\mu_0 \left[J_0 + \sum_{n=1}^{\infty} J_n \cos(mz) \right] \quad (9.37)$$

Because the cosine functions are orthogonal, we can equate corresponding coefficients on both sides of this equation. We obtain

$$\begin{aligned} \frac{\partial^2 R_0}{\partial r^2} + \frac{1}{r} \frac{\partial R_0}{\partial r} - \frac{R_0}{r^2} &= -\mu_0 J_0 \\ \frac{\partial^2 R_n}{\partial r^2} + \frac{1}{r} \frac{\partial R_n}{\partial r} - \frac{R_n}{r^2} - m^2 R_n &= -\mu_0 J_n \end{aligned} \quad (9.38)$$

The solution to the $n = 0$ equation can be written in terms of a solution of the homogeneous equation, which was found earlier, plus a particular solution:

$$R_0 = Sr + \frac{T}{r} - \frac{\mu_0 J_0 r^2}{3} \quad (9.39)$$

The solution to the $n > 0$ equations in Equation 9.38 consists of a homogeneous solution that was found previously and a particular solution:

$$R_n = C_n I_1(mr) + D_n K_1(mr) - \frac{\pi \mu_0 J_n}{2m^2} L_1(mr) \quad (9.40)$$

where L_1 is a modified Struve function of order 1 [Abr72]. Thus, the solution Equation 9.36 in region II is given explicitly as

$$A^{\text{II}} = S^{\text{II}} r + \frac{T^{\text{II}}}{r} - \frac{\mu_0 J_0 r^2}{3} + \sum_{n=1}^{\infty} \left[C_n^{\text{II}} I_1(mr) + D_n^{\text{II}} K_1(mr) - \frac{\pi \mu_0 J_n}{2m^2} L_1(mr) \right] \cos(mz) \quad (9.41)$$

where we have labeled the constants with the region number as superscripts.

This equation already satisfies the boundary conditions at $z = 0, L$, as do the other region equations. The unknown constants must be determined by satisfying the boundary conditions at $r = r_1, r_2$ (Figure 9.1). The vector potential must be continuous across the interfaces. Otherwise, the B-field given by Equation 9.23 will contain infinities. Thus, at $r = r_1$, using Equations 9.33 and 9.41,

$$\begin{aligned} S^{\text{I}} r_1 + \sum_{n=1}^{\infty} C_n^{\text{I}} \left[I_1(mr_1) + \frac{I_0(mr_c)}{K_0(mr_c)} K_1(mr_1) \right] \cos(mz) &= S^{\text{II}} r_1 + \frac{T^{\text{II}}}{r_1} - \frac{\mu_0 J_0 r_1^2}{3} \\ &+ \sum_{n=1}^{\infty} \left[C_n^{\text{II}} I_1(mr_1) + D_n^{\text{II}} K_1(mr_1) - \frac{\pi \mu_0 J_n}{2m^2} L_1(mr_1) \right] \cos(mz) \end{aligned} \quad (9.42)$$

Since this must be satisfied for all z , we obtain

$$S^I r_1 = S^{II} r_1 + \frac{T^{II}}{r_1} - \frac{\mu_o J_0 r_1^2}{3}$$

$$C_n^I \left[I_1(x_1) + \frac{I_0(x_c)}{K_0(x_c)} K_1(x_1) \right] = C_n^{II} I_1(x_1) + D_n^{II} K_1(x_1) - \frac{\pi \mu_o J_n}{2m^2} L_1(x_1) \quad (9.43)$$

where $x_1 = mr_1$, $x_c = mr_c$.

Similarly at $r = r_2$, using Equations 9.34 and 9.41, we get

$$\frac{T^{III}}{r_2} = S^{II} r_2 + \frac{T^{II}}{r_2} - \frac{\mu_o J_0 r_2^2}{3}$$

$$D_n^{III} K_1(x_2) = C_n^{II} I_1(x_2) + D_n^{II} K_1(x_2) - \frac{\pi \mu_o J_n}{2m^2} L_1(x_2) \quad (9.44)$$

where $x_2 = mr_2$.

In addition to the continuity of \mathbf{A} at the interfaces between regions, according to Maxwell's equations, the normal component of \mathbf{B} and the tangential component of \mathbf{H} should be continuous across these interfaces. According to Equation 9.23, the normal \mathbf{B} components (\mathbf{a}_r components) are already continuous across these interfaces because all regional solutions have the same z dependence and because the A 's are continuous. Since \mathbf{B} is proportional to \mathbf{H} in all regions of interest here, the tangential \mathbf{B} components must be continuous. Thus, from Equation 9.23, we require that

$$\frac{\partial A}{\partial r} + \frac{A}{r} = \frac{1}{r} \frac{\partial}{\partial r} (rA) = \frac{m}{x} \frac{\partial}{\partial x} (xA) \quad (9.45)$$

be continuous at $r = r_1, r_2$ ($x = x_1, x_2$). Using this equation, we obtain the additional conditions on the unknown constants:

$$2S^I = 2S^{II} - \mu_o J_0 r_1, \quad 2S^{II} - \mu_o J_0 r_2 = 0$$

$$C_n^I \left\{ \frac{\partial}{\partial x} [xI_1(x)] + \frac{I_0(x_c)}{K_0(x_c)} \frac{\partial}{\partial x} [xK_1(x)] \right\} = C_n^{II} \frac{\partial}{\partial x} [xI_1(x)]$$

$$+ D_n^{II} \frac{\partial}{\partial x} [xK_1(x)] - \frac{\pi \mu_o J_n}{2m^2} \frac{\partial}{\partial x} [xL_1(x)] \quad \text{at } x = x_1 = mr_1 \quad (9.46)$$

$$C_n^{II} \frac{\partial}{\partial x} [xI_1(x)] + D_n^{II} \frac{\partial}{\partial x} [xK_1(x)] - \frac{\pi \mu_o J_n}{2m^2} \frac{\partial}{\partial x} [xL_1(x)]$$

$$= D_n^{III} \frac{\partial}{\partial x} [xK_1(x)] \quad \text{at } x = x_2 = mr_2$$

Using the identities [Rab56, Abr72]

$$\frac{\partial}{\partial x}[xI_1(x)] = xI_0(x), \quad \frac{\partial}{\partial x}[xK_1(x)] = -xK_0(x), \quad \frac{\partial}{\partial x}[xL_1(x)] = xL_0(x) \quad (9.47)$$

we obtain for the last two equations in Equation 9.46:

$$\begin{aligned} C_n^I \left[I_0(x_1) - \frac{I_0(x_c)}{K_0(x_c)} K_0(x_1) \right] &= C_n^{II} I_0(x_1) - D_n^{II} K_0(x_1) - \frac{\pi \mu_o J_n}{2m^2} L_0(x_1) \\ C_n^{II} I_0(x_2) - D_n^{II} K_0(x_2) - \frac{\pi \mu_o J_n}{2m^2} L_0(x_2) &= -D_n^{III} K_0(x_2) \end{aligned} \quad (9.48)$$

Solving for the S and T constants from Equations 9.43, 9.44, and 9.46, we get

$$\begin{aligned} S^I &= \frac{\mu_o J_0(r_2 - r_1)}{2}, \quad S^{II} = \frac{\mu_o J_0 r_2}{2} \\ T^{II} &= -\frac{\mu_o J_0 r_1^3}{6}, \quad T^{III} = \frac{\mu_o J_0(r_2^3 - r_1^3)}{6} \end{aligned} \quad (9.49)$$

Solving for the C_n and D_n constants from Equations 9.43, 9.44, and 9.46, we get

$$\begin{aligned} C_n^{II} &= \frac{\pi \mu_o J_n}{2m^2} \left[\frac{K_0(x_2)L_1(x_2) + K_1(x_2)L_0(x_2)}{K_0(x_2)I_1(x_2) + K_1(x_2)I_0(x_2)} \right] \\ C_n^I &= C_n^{II} - \frac{\pi \mu_o J_n}{2m^2} \left[\frac{K_0(x_1)L_1(x_1) + K_1(x_1)L_0(x_1)}{K_0(x_1)I_1(x_1) + K_1(x_1)I_0(x_1)} \right] \\ D_n^{II} &= \frac{I_0(x_c)}{K_0(x_c)} C_n^I + \frac{\pi \mu_o J_n}{2m^2} \left[\frac{I_0(x_1)L_1(x_1) - I_1(x_1)L_0(x_1)}{K_0(x_1)I_1(x_1) + K_1(x_1)I_0(x_1)} \right] \\ D_n^{III} &= D_n^{II} - \frac{\pi \mu_o J_n}{2m^2} \left[\frac{I_0(x_2)L_1(x_2) - I_1(x_2)L_0(x_2)}{K_0(x_2)I_1(x_2) + K_1(x_2)I_0(x_2)} \right] \end{aligned} \quad (9.50)$$

Using the identities [Rab56]

$$\begin{aligned} I_0(x)K_1(x) + I_1(x)K_0(x) &= \frac{1}{x} \\ x \left[L_0(x)K_1(x) + L_1(x)K_0(x) \right] &= \frac{2}{\pi} \int_0^x t K_1(t) dt \\ x \left[L_0(x)I_1(x) - L_1(x)I_0(x) \right] &= \frac{2}{\pi} \int_0^x t I_1(t) dt \end{aligned} \quad (9.51)$$

we can transform Equation 9.50 into the form

$$\begin{aligned}
 C_n^{\text{II}} &= \frac{\mu_0 J_n}{m^2} \int_0^{x_2} t K_1(t) dt \\
 C_n^{\text{I}} &= \frac{\mu_0 J_n}{m^2} \int_{x_1}^{x_2} t K_1(t) dt \\
 D_n^{\text{II}} &= \frac{\mu_0 J_n}{m^2} \left[\frac{I_0(x_c)}{K_0(x_c)} \int_{x_1}^{x_2} t K_1(t) dt - \int_0^{x_1} t I_1(t) dt \right] \\
 D_n^{\text{III}} &= \frac{\mu_0 J_n}{m^2} \left[\frac{I_0(x_c)}{K_0(x_c)} \int_{x_1}^{x_2} t K_1(t) dt + \int_{x_1}^{x_2} t I_1(t) dt \right]
 \end{aligned} \tag{9.52}$$

Summarizing and simplifying the notation slightly, the solutions in the three regions are given by

$$\begin{aligned}
 A^{\text{I}} &= \frac{\mu_0 J_0 (r_2 - r_1)}{2} r + \mu_0 \sum_{n=1}^{\infty} \frac{J_n}{m^2} [C_n I_1(x) + D_n K_1(x)] \cos(mz) \\
 A^{\text{II}} &= \mu_0 J_0 \left(\frac{r_2 r}{2} - \frac{r_1^3}{6r} - \frac{r^2}{3} \right) + \mu_0 \sum_{n=1}^{\infty} \frac{J_n}{m^2} \left[E_n I_1(x) + F_n K_1(x) - \frac{\pi}{2} L_1(x) \right] \cos(mz) \\
 A^{\text{III}} &= \frac{\mu_0 J_0 (r_2^3 - r_1^3)}{6r} + \mu_0 \sum_{n=1}^{\infty} \frac{J_n}{m^2} G_n K_1(x) \cos(mz)
 \end{aligned} \tag{9.53}$$

where $m = n\pi/L$, $x = mr$, and

$$\begin{aligned}
 C_n &= \int_{x_1}^{x_2} t K_1(t) dt, \quad D_n = \frac{I_0(x_c)}{K_0(x_c)} C_n \\
 E_n &= \int_0^{x_2} t K_1(t) dt, \quad F_n = \frac{I_0(x_c)}{K_0(x_c)} \int_{x_1}^{x_2} t K_1(t) dt - \int_0^{x_1} t I_1(t) dt \\
 G_n &= \frac{I_0(x_c)}{K_0(x_c)} \int_{x_1}^{x_2} t K_1(t) dt + \int_{x_1}^{x_2} t I_1(t) dt
 \end{aligned} \tag{9.54}$$

Here, $x_1 = mr_1$ and $x_2 = mr_2$.

Using Equation 9.23, the axial component of the induction vector at the core radius is

$$B_z(r_c, z) = \mu_0 J_0 (r_2 - r_1) \tag{9.55}$$

This is μ_0 times the average current density times the radial build of the winding. If we multiply and divide Equation 9.55 by the winding height L ,

we see that B_z is proportional to the amp-turns in the winding with proportionality constant μ_0/L . Since the axial height L is the same for all the windings, when we add this axial component for all the windings we will get zero, assuming amp-turn balance. Thus, the flux will enter the core radially as required.

Although the modified Bessel functions generally are available in mathematical computer libraries, the modified Struve functions are not as easily obtained. Therefore, we indicate here some methods for obtaining these and the integrals in Equation 9.54 in terms of readily available functions or easily evaluated integrals. From [Abr72], the modified Struve functions are given in integral form as

$$\begin{aligned} L_0(x) &= \frac{2}{\pi} \int_0^{\pi/2} \sinh(x \cos \theta) d\theta \\ L_1(x) &= \frac{2x}{\pi} \int_0^{\pi/2} \sinh(x \cos \theta) \sin^2 \theta d\theta \end{aligned} \quad (9.56)$$

From Equation 9.56, we can see that these functions become asymptotically large as $x \rightarrow \infty$. Such large values of x occur when evaluating the higher harmonics in Equation 9.53. We indicate here a way of avoiding these large values by looking for a means of cancellation. [Abr72] gives integral expressions for the modified Bessel functions. In particular, we have

$$\begin{aligned} I_0(x) &= \frac{1}{\pi} \int_0^\pi e^{\pm x \cos \theta} d\theta = \frac{1}{\pi} \int_0^{\pi/2} (e^{x \cos \theta} + e^{-x \cos \theta}) d\theta \\ I_1(x) &= \frac{x}{\pi} \int_0^\pi e^{\pm x \cos \theta} \sin^2 \theta d\theta = \frac{x}{\pi} \int_0^{\pi/2} (e^{x \cos \theta} + e^{-x \cos \theta}) \sin^2 \theta d\theta \end{aligned} \quad (9.57)$$

These also become asymptotically large as x increases. However, by defining the difference functions:

$$M_0(x) = I_0(x) - L_0(x), \quad M_1(x) = I_1(x) - L_1(x) \quad (9.58)$$

we can show that

$$\begin{aligned} M_0(x) &= \frac{2}{\pi} \int_0^{\pi/2} e^{-x \cos \theta} d\theta \\ M_1(x) &= \frac{2x}{\pi} \int_0^{\pi/2} e^{-x \cos \theta} \sin^2 \theta d\theta = \frac{2}{\pi} \left[1 - \int_0^{\pi/2} e^{-x \cos \theta} \cos \theta d\theta \right] \end{aligned} \quad (9.59)$$

The last equality in Equation 9.59 is obtained by integration by parts. The integrals in Equation 9.59 are well behaved as x increases and can be evaluated numerically. In subsequent developments, we will also need the integral of M_0 . This is readily determined from Equation 9.59 as

$$\int_0^x M_0(t)dt = \frac{2}{\pi} \int_0^{\pi/2} \frac{(1 - e^{-x \cos \theta})}{\cos \theta} d\theta \quad (9.60)$$

The integrand approaches x as $\theta \rightarrow \pi/2$, and so the integral is also well behaved. For high x values, asymptotic series for some of these functions can be found in [Abr72]. This reference also lists a table of the difference functions defined in Equation 9.58 and the integral given in Equation 9.60.

Now we will write other expressions of interest in terms of the M functions and modified Bessel functions. Using Equations 9.51 and 9.58, we can write

$$\begin{aligned} \int_0^x tI_1(t)dt &= \frac{\pi}{2} x [M_1(x)I_0(x) - M_0(x)I_1(x)] \\ \int_0^x tK_1(t)dt &= \frac{\pi}{2} \{1 - x [M_1(x)K_0(x) + M_0(x)K_1(x)]\} \end{aligned} \quad (9.61)$$

We will also need a similar integral for the modified Struve function. We need the following identities, given in [Rab56]:

$$\frac{d}{dt} L_0(t) = \frac{2}{\pi} + L_1(t), \quad \frac{d}{dt} I_0(t) = I_1(t) \quad (9.62)$$

Multiplying these by t and integrating from 0 to x , we get

$$\begin{aligned} xL_0(x) - \int_0^x L_0(t)dt &= \frac{x^2}{\pi} + \int_0^x tL_1(t)dt \\ xI_0(x) - \int_0^x I_0(t)dt &= \int_0^x tI_1(t)dt \end{aligned} \quad (9.63)$$

Substituting for L_0 in terms of the M_0 function and rearranging, we get

$$\int_0^x tL_1(t)dt = -xM_0(x) - \frac{x^2}{\pi} + \int_0^x M_0(t)dt + \int_0^x tI_1(t)dt \quad (9.64)$$

Thus, all the functions needed to determine the vector potential are obtainable in terms of the modified Bessel functions and the M functions. We will need Equation 9.64 to obtain derived quantities such as magnetic energies.

The vector potential must be determined for all the coils of interest using the appropriate radii and current density distribution for each coil. Because Maxwell's equations are linear in the fields and potentials in the region

outside the core and yokes, we can simply add the potentials or fields from the various coils vectorially at each point to get the net potential or field. Note that a given point may not be in the same region number (I, II, or III) for the different coils.

9.3 Rabins' Formula for Leakage Reactance

The leakage inductance for a two-winding transformer can be obtained from the total magnetic energy, as discussed in Chapter 4, when there is amp-turn balance. We use Equation 4.9 for the magnetic energy, W , which is repeated here:

$$W = \frac{1}{2} \int_{\text{volume of circuits}} \mathbf{A} \cdot \mathbf{J} dV \quad (9.65)$$

This equation together with Equation 4.23, can be used to obtain the leakage inductance. Here, \mathbf{A} is the total vector potential due to both windings. Because \mathbf{A} and \mathbf{J} are both azimuthally directed, the dot product becomes simply the ordinary product. We also drop the implied ϕ subscript on J and A .

9.3.1 Rabins' Method Applied to Calculate the Leakage Reactance between Two Windings That Occupy Different Radial Positions

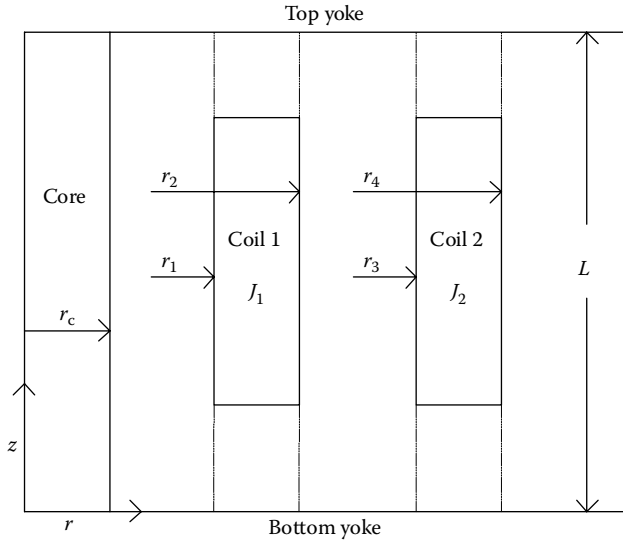
We assume that the two windings occupy different radial positions as shown in [Figure 9.3](#).

Writing A_1, A_2 for the vector potential due to coils 1 and 2 and J_1, J_2 for their current densities, Equation 9.65 becomes

$$\begin{aligned} 2W &= \int_{V_1} (A_1 + A_2) J_1 dV_1 + \int_{V_2} (A_1 + A_2) J_2 dV_2 \\ &= \int_{V_1} A_1 J_1 dV_1 + \int_{V_1} A_2 J_1 dV_1 + \int_{V_2} A_1 J_2 dV_2 + \int_{V_2} A_2 J_2 dV_2 \end{aligned} \quad (9.66)$$

For the $A_1 J_1$ or $A_2 J_2$ integrals, we must use the region II solution corresponding to each coil. Assuming coil 1 is the inner coil, the $A_2 J_1$ integral requires that we use the region I solution for A_2 , while the $A_1 J_2$ integral requires that we use the region III solution for A_1 .

From Equations 9.53 and 9.10 and using a second subscript to distinguish the coil 1 quantities from the coil 2 ones, we get

**FIGURE 9.3**

Geometry for the two-coil leakage inductance calculation.

$$\int_{V_1} A_1 J_1 dV_1 = 2\pi \int_{r_1}^{r_2} r dr \int_0^L dz \left[J_{0,1} + \sum_{p=1}^{\infty} J_{p,1} \cos\left(\frac{p\pi z}{L}\right) \right] \left\{ \mu_0 J_{0,1} \left(\frac{r_2 r}{2} - \frac{r_1^3}{6r} - \frac{r^2}{3} \right) \right. \\ \left. + \mu_0 \sum_{n=1}^{\infty} \frac{J_{n,1}}{m^2} \left[E_{n,1} I_1(mr) + F_{n,1} K_1(mr) - \frac{\pi}{2} L_1(mr) \right] \cos\left(\frac{n\pi z}{L}\right) \right\} \quad (9.67)$$

Note that the subscript 1 on the I and K are not related to the labeling for winding 1. Also note that $E_{n,1}$ and $F_{n,1}$ are the same as E_n and F_n in Equation 9.54 and are also the same for the other coefficients. However, when we consider winding 2, $E_{n,2}$ and $F_{n,2}$, and so on the integration limits in Equation 9.54 must be changed from x_1, x_2 to x_3, x_4 . Performing the z integration first, we notice that product terms that contain a single cosine term vanish, that is,

$$\int_0^L \cos\left(\frac{n\pi z}{L}\right) dz = \frac{L}{n\pi} \sin\left(\frac{n\pi z}{L}\right) \Big|_0^L = 0 \quad (9.68)$$

Product terms that contain two cosine factors have the value

$$\int_0^L \cos\left(\frac{n\pi z}{L}\right) \cos\left(\frac{p\pi z}{L}\right) dz = \begin{cases} 0, & n \neq p \\ L/2, & n = p \end{cases} \quad (9.69)$$

After performing the z integration, Equation 9.67 becomes

$$\int_{V_1} A_1 J_1 dV_1 = 2\pi \int_{r_1}^{r_2} r dr \left\{ \mu_0 L J_{0,1}^2 \left(\frac{r_2 r}{2} - \frac{r_1^3}{6r} - \frac{r^2}{3} \right) + \frac{\mu_0 L}{2} \sum_{n=1}^{\infty} \frac{J_{n,1}^2}{m^2} \left[E_{n,1} I_1(mr) + F_{n,1} K_1(mr) - \frac{\pi}{2} L_1(mr) \right] \right\} \quad (9.70)$$

Performing the r -integration, we get

$$\begin{aligned} \int_{V_1} A_1 J_1 dV_1 &= 2\pi \mu_0 L \left\{ J_{0,1}^2 \left(\frac{r_1^4}{4} + \frac{r_2^4}{12} - \frac{r_2 r_1^3}{3} \right) + \frac{1}{2} \sum_{n=1}^{\infty} \frac{J_{n,1}^2}{m^2} \left[E_{n,1} \int_{r_1}^{r_2} r I_1(mr) dr + F_{n,1} \int_{r_1}^{r_2} r K_1(mr) dr - \frac{\pi}{2} \int_{r_1}^{r_2} r L_1(mr) dr \right] \right\} \\ &= 2\pi \mu_0 L \left\{ J_{0,1}^2 \left(\frac{r_1^4}{4} + \frac{r_2^4}{12} - \frac{r_2 r_1^3}{3} \right) + \frac{1}{2} \sum_{n=1}^{\infty} \frac{J_{n,1}^2}{m^4} \left[E_{n,1} \int_{x_1}^{x_2} x I_1(x) dx + F_{n,1} \int_{x_1}^{x_2} x K_1(x) dx - \frac{\pi}{2} \int_{x_1}^{x_2} x L_1(x) dx \right] \right\} \quad (9.71) \end{aligned}$$

In the second equality above, the r integrals have been converted to integrals in $x = mr$. Formulas for the x integrals above have been given in Equations 9.61 and 9.64 in terms of known or easily calculated quantities.

The $A_2 J_2$ term in Equation 9.66 is given by Equation 9.71 with a subscript 2 and with the r -integration from r_3 to r_4 (Figure 9.3). Thus, we have

$$\begin{aligned} \int_{V_2} A_2 J_2 dV_2 &= 2\pi \mu_0 L \left\{ J_{0,2}^2 \left(\frac{r_3^4}{4} + \frac{r_4^4}{12} - \frac{r_4 r_3^3}{3} \right) + \frac{1}{2} \sum_{n=1}^{\infty} \frac{J_{n,2}^2}{m^4} \left[E_{n,2} \int_{x_3}^{x_4} x I_1(x) dx + F_{n,2} \int_{x_3}^{x_4} x K_1(x) dx - \frac{\pi}{2} \int_{x_3}^{x_4} x L_1(x) dx \right] \right\} \quad (9.72) \end{aligned}$$

The $A_2 J_1$ integral in Equation 9.66 is given by

$$\begin{aligned} \int_{V_1} A_2 J_1 dV_1 &= 2\pi \int_{r_1}^{r_2} r dr \int_0^L dz \left[J_{0,1} + \sum_{p=1}^{\infty} J_{p,1} \cos \left(\frac{p\pi z}{L} \right) \right] \left\{ \frac{\mu_0 J_{0,2}}{2} (r_4 - r_3) r + \mu_0 \sum_{n=1}^{\infty} \frac{J_{n,2}}{m^2} [C_{n,2} I_1(mr) + D_{n,2} K_1(mr)] \cos \left(\frac{n\pi z}{L} \right) \right\} \quad (9.73) \end{aligned}$$

Using the previous method for carrying out the cos integrals, we get

$$\int_{V_1} A_2 I_1 dV_1 = 2\pi\mu_0 L \left\{ \frac{J_{0,1}J_{0,2}}{6} (r_4 - r_3)(r_2^3 - r_1^3) + \frac{1}{2} \sum_{n=1}^{\infty} \frac{J_{n,1}J_{n,2}}{m^4} \left[C_{n,2} \int_{x_1}^{x_2} x I_1(x) dx + D_{n,2} \int_{x_1}^{x_2} x K_1(x) dx \right] \right\} \quad (9.74)$$

Similarly, the $A_1 I_2$ integral in Equation 9.66 is given by

$$\int_{V_2} A_1 I_2 dV_2 = 2\pi\mu_0 L \left\{ \frac{J_{0,1}J_{0,2}}{6} (r_4 - r_3)(r_2^3 - r_1^3) + \frac{1}{2} \sum_{n=1}^{\infty} \frac{J_{n,1}J_{n,2}}{m^4} G_{n,1} \int_{x_3}^{x_4} x K_1(x) dx \right\} \quad (9.75)$$

Despite their different appearances, Equations 9.74 and 9.75 are the same. We can see this from the definition of the coefficients in Equation 9.54, remembering that the subscript 1 on the coefficients is associated with x_1, x_2 and the subscript 2 with x_3, x_4 . This is an example of a reciprocity relation that holds for linear systems.

Summing up the terms in Equation 9.66 and after some algebraic manipulation, we get

$$\begin{aligned} 2W = & \frac{\pi\mu_0 L}{6} \left\{ J_{0,1}^2 (r_2 - r_1)^2 [(r_1 + r_2)^2 + 2r_1^2] + J_{0,2}^2 (r_4 - r_3)^2 [(r_3 + r_4)^2 + 2r_3^2] \right. \\ & + 4J_{0,1}J_{0,2} (r_2 - r_1)(r_4 - r_3)(r_1^2 + r_1 r_2 + r_2^2) \Big\} \\ & + \pi\mu_0 L \sum_{n=1}^{\infty} \left\{ \frac{J_{n,1}^2}{m^4} \left[E_{n,1} \int_{x_1}^{x_2} x I_1(x) dx + F_{n,1} \int_{x_1}^{x_2} x K_1(x) dx - \frac{\pi}{2} \int_{x_1}^{x_2} x L_1(x) dx \right] \right. \\ & + \frac{J_{n,2}^2}{m^4} \left[E_{n,2} \int_{x_3}^{x_4} x I_1(x) dx + F_{n,2} \int_{x_3}^{x_4} x K_1(x) dx - \frac{\pi}{2} \int_{x_3}^{x_4} x L_1(x) dx \right] \\ & \left. + 2 \frac{J_{n,1}J_{n,2}}{m^4} G_{n,1} \int_{x_3}^{x_4} x K_1(x) dx \right\} \quad (9.76) \end{aligned}$$

When the coefficients E_n and F_n , and so on have a subscript 1, then the expressions given by Equation 9.54 apply with x_1, x_2 for the integration limits. However, when the second subscript is 2, then x_3, x_4 must be substituted for x_1, x_2 in the formulas.

The leakage inductance, with respect to coil 1 as given in Chapter 4, Equation 4.23, is given by $2W/I_1^2$. For I_1^2 , we can write $(NI)^2/N^2$. This makes the formula work for either winding as the reference winding because $(NI)^2$ is

the same for both windings, and whatever winding's N is chosen will make that the reference winding. Using Equation 9.76, this is

$$\begin{aligned}
 L_{\text{leak}} = & \frac{\pi\mu_0 LN^2}{6(NI)^2} \left\{ J_{0,1}^2 (r_2 - r_1)^2 [(r_1 + r_2)^2 + 2r_1^2] \right. \\
 & + J_{0,2}^2 (r_4 - r_3)^2 [(r_3 + r_4)^2 + 2r_3^2] + 4J_{0,1}J_{0,2}(r_2 - r_1)(r_4 - r_3)(r_1^2 + r_1r_2 + r_2^2) \Big\} \\
 & + \frac{\pi\mu_0 LN^2}{(NI)^2} \sum_{n=1}^{\infty} \left\{ \frac{J_{n,1}^2}{m^4} \left[E_{n,1} \int_{x_1}^{x_2} x I_1(x) dx + F_{n,1} \int_{x_1}^{x_2} x K_1(x) dx - \frac{\pi}{2} \int_{x_1}^{x_2} x L_1(x) dx \right] \right. \\
 & + \frac{J_{n,2}^2}{m^4} \left[E_{n,2} \int_{x_3}^{x_4} x I_1(x) dx + F_{n,2} \int_{x_3}^{x_4} x K_1(x) dx - \frac{\pi}{2} \int_{x_3}^{x_4} x L_1(x) dx \right] \\
 & \left. + 2 \frac{J_{n,1}J_{n,2}}{m^4} G_{n,1} \int_{x_3}^{x_4} x K_1(x) dx \right\} \quad (9.77)
 \end{aligned}$$

To get the leakage reactance, multiply L_{leak} by $\omega = 2\pi f$.

9.3.2 Rabins' Method Applied to Calculate the Leakage Reactance between Two Axially Stacked Windings

In some transformer designs, the two coils are stacked axially and therefore occupy the same radial position. In these cases, the coil radial builds are usually the same, and often the coils are duplicates. Rabins' method can be used to find the leakage inductance in these situations. The current densities for each coil will be nonzero within the different axial regions, but the Fourier decomposition should reflect this. In this case, only the region II solution is needed for both coils, and Equation 9.66 still holds. In this case, $r_3 = r_1$ and $r_4 = r_2$. Evaluating the terms in Equation 9.66, we find that the A_1J_1 and A_2J_2 terms are the same as before except that we must replace r_3, r_4, x_3 , and x_4 by r_1, r_2, x_1 , and x_2 .

The A_2J_1 integral is

$$\begin{aligned}
 \int_{V_1} A_2 J_1 dV_1 = & 2\pi \int_{r_1}^{r_2} r dr \int_0^L dz \left[J_{0,1} + \sum_{p=1}^{\infty} J_{p,1} \cos\left(\frac{p\pi z}{L}\right) \right] \left\{ \mu_0 J_{0,2} \left(\frac{r_2 r}{2} - \frac{r_1^3}{6r} - \frac{r^2}{3} \right) \right. \\
 & \left. + \mu_0 \sum_{n=1}^{\infty} \frac{J_{n,2}}{m^2} \left[E_{n,1} I_1(mr) + F_{n,1} K_1(mr) - \frac{\pi}{2} L_1(mr) \right] \cos\left(\frac{n\pi z}{L}\right) \right\} \quad (9.78)
 \end{aligned}$$

We can use subscript 1 on E_n and F_n in Equation 9.78 because the radial extent of the two windings is the same; however, subscript 2 is needed on J_n because

the current distributions are different. Carrying out the z and r integrations, we get

$$\int_{V_1} A_2 J_1 dV_1 = 2\pi\mu_0 L \left\{ J_{0,1} J_{0,2} \left(\frac{r_1^4}{4} + \frac{r_2^4}{12} - \frac{r_2 r_1^3}{3} \right) + \frac{1}{2} \sum_{n=1}^{\infty} \frac{J_{n,1} J_{n,2}}{m^4} \left[E_{n,1} \int_{x_1}^{x_2} x I_1(x) dx + F_{n,1} \int_{x_1}^{x_2} x K_1(x) dx - \frac{\pi}{2} \int_{x_1}^{x_2} x L_1(x) dx \right] \right\} \quad (9.79)$$

This expression is also equal to the $A_1 J_2$ term. Hence, by combining all the terms in Equation 9.66, we get

$$\begin{aligned} 2W = & \frac{\pi\mu_0 L}{6} \left\{ (J_{0,1}^2 + J_{0,2}^2 + 2J_{0,1} J_{0,2}) (r_2 - r_1)^2 [(r_1 + r_2)^2 + 2r_1^2] \right. \\ & + \pi\mu_0 L \sum_{n=1}^{\infty} \left\{ \frac{(J_{n,1}^2 + J_{n,2}^2 + 2J_{n,1} J_{n,2})}{m^4} \right. \\ & \times \left[E_{n,1} \int_{x_1}^{x_2} x I_1(x) dx + F_{n,1} \int_{x_1}^{x_2} x K_1(x) dx - \frac{\pi}{2} \int_{x_1}^{x_2} x L_1(x) dx \right] \left. \right\} \end{aligned} \quad (9.80)$$

The leakage inductance between these two coils is then given by

$$\begin{aligned} L_{\text{leak axially stacked coils}} = & \frac{\pi\mu_0 L N^2}{6(NI)^2} \left\{ (J_{0,1}^2 + J_{0,2}^2 + 2J_{0,1} J_{0,2}) (r_2 - r_1)^2 [(r_1 + r_2)^2 + 2r_1^2] \right. \\ & + \frac{\pi\mu_0 L N^2}{(NI)^2} \sum_{n=1}^{\infty} \left\{ \frac{(J_{n,1}^2 + J_{n,2}^2 + 2J_{n,1} J_{n,2})}{m^4} \right. \\ & \times \left[E_{n,1} \int_{x_1}^{x_2} x I_1(x) dx + F_{n,1} \int_{x_1}^{x_2} x K_1(x) dx - \frac{\pi}{2} \int_{x_1}^{x_2} x L_1(x) dx \right] \left. \right\} \end{aligned} \quad (9.81)$$

We note that $J_{0,1}$ and $J_{0,2}$ are the average current densities in windings 1 and 2, and $(r_2 - r_1)L$ is the cross-sectional area of either winding. Thus, since the amp-turns are balanced between the two windings, we have

$$N_1 I_1 = J_{0,1} (r_2 - r_1) L = -N_2 I_2 = -J_{0,2} (r_2 - r_1) L \quad (9.82)$$

In this equation, we see that the first set of terms in Equation 9.81 vanishes. Thus, for the leakage inductance we get

$$\begin{aligned} L_{\text{leak axially displaced coils}} = & \frac{\pi\mu_0 L N^2}{(NI)^2} \sum_{n=1}^{\infty} \left\{ \frac{(J_{n,1}^2 + J_{n,2}^2 + 2J_{n,1} J_{n,2})}{m^4} \right. \\ & \times \left[E_{n,1} \int_{x_1}^{x_2} x I_1(x) dx + F_{n,1} \int_{x_1}^{x_2} x K_1(x) dx - \frac{\pi}{2} \int_{x_1}^{x_2} x L_1(x) dx \right] \left. \right\} \end{aligned} \quad (9.83)$$

We obtain the leakage reactance by multiplying L_{leak} by $\omega = 2\pi f$. Note that both coils extend the full axial height L . However, the top coil will have a large section below it, where the bottom winding is located, with zero current density, and similarly, the bottom coil will have a large section above it, where the top winding is located, with zero current density.

9.3.3 Rabins' Method Applied to Calculate the Leakage Reactance for a Collection of Windings

Rabins' method can be used to find the leakage reactance for a collection of any number of coils. The amp-turns of the coils must sum to zero. Assuming coil 1 is the reference winding, we can obtain the leakage induction from

$$W = \frac{1}{2} \int_{\text{volume of circuits}} \mathbf{A} \cdot \mathbf{J} dV = \frac{1}{2} L_{\text{leak},1} I_1^2 \quad (9.84)$$

In this case, for the magnetic energy of N_w windings, Equation 9.66 becomes

$$\begin{aligned} 2W &= \int_{V_1} \left(\sum_{j=1}^{N_w} A_j \right) J_1 dV_1 + \int_{V_2} \left(\sum_{j=1}^{N_w} A_j \right) J_2 dV_2 + \cdots \\ &= \sum_{k=1}^{N_w} \int_{V_k} \left(\sum_{j=1}^{N_w} A_j \right) J_k dV_k = \sum_{k=1}^{N_w} \sum_{j=1}^{N_w} \int_{V_k} A_j J_k dV_k \end{aligned} \quad (9.85)$$

Care must be taken to use the solution of the vector potential for a given winding in the appropriate region. The double sum in Equation 9.85 can be simplified by noting that

$$\int_{V_k} A_j J_k dV_k = \int_{V_j} A_k J_j dV_j \quad (9.86)$$

The leakage inductance relative to winding 1 is then given by

$$\begin{aligned} L_{\text{leak},1} &= \frac{1}{I_1^2} \sum_{k=1}^{N_w} \sum_{j=1}^{N_w} \int_{V_k} A_j J_k dV_k \\ &= \frac{1}{I_1^2} \left(\sum_{j=1}^{N_w} \int_{V_k} A_j J_j dV_k + 2 \sum_{j < k=1}^{N_w} \int_{V_k} A_j J_k dV_k \right) \end{aligned} \quad (9.87)$$

We can then obtain the leakage reactance by multiplying $L_{\text{leak},1}$ by $\omega = 2\pi f$.

9.4 Application of Rabins' Method to Calculate the Self-Inductance of and Mutual Inductance between Coil Sections

Here, we will consider a collection of coils subdivided into coil sections. A coil section, for our purposes, consists of a part of a coil that has a uniform current density. In this case, Equation 9.14 holds for the Fourier coefficients, whereas in all other respects, it is treated like a full coil of height L . Later, we will apply these results to obtain a detailed model of the transformer for impulse simulation studies.

For these calculations, we will use the vector potential solution for each winding section obtained by Rabins' method. However, this requires amp-turn balance in order to satisfy the B-field boundary condition at the core surface. Although the self-inductance calculation of a coil section cannot satisfy this boundary condition when taken individually, when considering a pair of coil sections, amp-turn balance can be achieved so that the self- and mutual inductances associated with this pair of coil sections are valid within the context of Rabins' method. Thus, the self-inductances, mutual inductance, and leakage inductance of the coil section pair satisfy the relation between these quantities given in Equation 4.23.

These Rabins' inductances tend to be about an order of magnitude higher than the corresponding air core inductances and mutual inductances, which are often used in impulse simulation studies. We find that the Rabins' method inductances tend to give good agreement with impulse data obtained via recurrent surge oscillograph (RSO) methods.

Wilcox et al. [Wil88, Wil89] obtained analytic expressions for the mutual and self-impedances and inductances of coils on a ferromagnetic core. These can also be used in simulation studies. However, the self-inductance of a single coil on a high-permeability ferromagnetic core increases with the core permeability and can become quite large, as finite element methods show. Self- and mutual inductances determined in this manner tend to be about an order of magnitude higher than those obtained by Rabins' method. Because the permeability is not very well known for a transformer core with joints and so on, this can present difficulties when deciding which value to use.

Having obtained Rabins' solution for the vector potential, this solution can be directly applied to the calculation of self- and mutual inductances. The mutual induction between two coil sections is given by Equation 4.26 in Chapter 4, which we repeat here:

$$M_{12} = \frac{1}{I_1 I_2} \int_{V_1} \mathbf{A}_2 \cdot \mathbf{J}_1 dV_1 \quad (9.88)$$

Here again, except for the uniform current density in one coil section, we treat the coil sections as if they were full coils of height L in applying Rabins' method.

If the sections are on the same coil or two coils axially displaced, then A_2 is the solution in region II. The A_2J_1 integral was already done in this case and is given in Equation 9.79. Thus, after some algebraic manipulation of the J_0 radial terms, we have

$$M_{12, \text{ same radial position}} = \frac{\pi\mu_0 L}{6I_1 I_2} J_{0,1} J_{0,2} (r_2 - r_1)^2 [(r_2 + r_1)^2 + 2r_1^2] + \frac{\pi\mu_0 L}{I_1 I_2} \sum_{n=1}^{\infty} \frac{J_{n,1} J_{n,2}}{m^4} \left[E_{n,1} \int_{x_1}^{x_2} x I_1(x) dx + F_{n,1} \int_{x_1}^{x_2} x K_1(x) dx - \frac{\pi}{2} \int_{x_1}^{x_2} x L_1(x) dx \right] \quad (9.89)$$

Since

$$N_1 I_1 = J_{0,1} (r_2 - r_1) L, \quad N_2 I_2 = J_{0,2} (r_2 - r_1) L \quad (9.90)$$

we can rewrite Equation 9.89 as

$$M_{12, \text{ same radial position}} = \frac{\pi\mu_0 N_1 N_2}{6L} [(r_2 + r_1)^2 + 2r_1^2] + \frac{\pi\mu_0 L N_1 N_2}{(N_1 I_1)(N_2 I_2)} \times \sum_{n=1}^{\infty} \frac{J_{n,1} J_{n,2}}{m^4} \left[E_{n,1} \int_{x_1}^{x_2} x I_1(x) dx + F_{n,1} \int_{x_1}^{x_2} x K_1(x) dx - \frac{\pi}{2} \int_{x_1}^{x_2} x L_1(x) dx \right] \quad (9.91)$$

When the coil sections are part of different coils, radially displaced, we can assume that 1 is the inner and 2 is the outer coil. The result will be independent of this assumption. Thus, we need the region I solution for coil 2. The A_2J_1 integral has already been done, and the result is given in Equation 9.74. We have

$$M_{12, \text{ different radial positions}} = \frac{\pi\mu_0 L J_{0,1} J_{0,2}}{3I_1 I_2} (r_4 - r_3)(r_2^3 - r_1^3) + \frac{\pi\mu_0 L}{I_1 I_2} \sum_{n=1}^{\infty} \frac{J_{n,1} J_{n,2}}{m^4} \left[C_{n,2} \int_{x_1}^{x_2} x I_1(x) dx + D_{n,2} \int_{x_1}^{x_2} x K_1(x) dx \right] \quad (9.92)$$

In this case, the amp-turns can be expressed as

$$N_1 I_1 = J_{0,1} (r_2 - r_1) L, \quad N_2 I_2 = J_{0,2} (r_4 - r_3) L \quad (9.93)$$

Using this, we can rewrite Equation 9.92 as

$$M_{12, \text{different radial positions}} = \frac{\pi\mu_0 N_1 N_2}{3L} (r_1^2 + r_1 r_2 + r_2^2) + \frac{\pi\mu_0 L N_1 N_2}{(N_1 I_1)(N_2 I_2)} \sum_{n=1}^{\infty} \frac{J_{n,1} J_{n,2}}{m^4} \left[C_{n,2} \int_{x_1}^{x_2} x I_1(x) dx + D_{n,2} \int_{x_1}^{x_2} x K_1(x) dx \right] \quad (9.94)$$

If we assume the coil consists of a single section of uniform current density so that Equation 9.14 applies, J in that equation is equal to NI/area of the section. Thus, when $J_{n,1}$ or $J_{n,2}$ are substituted in Equation 9.91 or 9.94, $N_1 I_1$ and $N_2 I_2$ in the denominators will be replaced by the respective section areas. Of course, the other factors in Equation 9.14 will need to be inserted. Although amp-turn balance is assumed, it does not matter in these formulas because mutual inductances are normalized by the two currents. If the coil sections are oppositely wound, then the mutual inductances should be multiplied by -1 . This can be done by replacing N by $-N$ for an oppositely wound coil section.

For a single coil, for example coil 1, the self-inductance can be obtained from

$$W = \frac{1}{2} \int_{V_1} \mathbf{A}_1 \cdot \mathbf{J}_1 dV = \frac{1}{2} L_1 I_1^2 \Rightarrow L_1 = \frac{1}{I_1^2} \int_{V_1} \mathbf{A}_1 \cdot \mathbf{J}_1 dV \quad (9.95)$$

This was discussed in Chapter 4. In this case, we use the solution for A in region II because the current density here is nonzero. The integral in Equation 9.95 has already been carried out in Equation 9.89, so we have

$$L_1 = \frac{\pi\mu_0 L}{6I_1^2} J_{0,1}^2 (r_2 - r_1)^2 [(r_2 + r_1)^2 + 2r_1^2] + \frac{\pi\mu_0 L}{I_1^2} \sum_{n=1}^{\infty} \frac{J_{n,1}^2}{m^4} \left[E_{n,1} \int_{x_1}^{x_2} x I_1(x) dx + F_{n,1} \int_{x_1}^{x_2} x K_1(x) dx - \frac{\pi}{2} \int_{x_1}^{x_2} x L_1(x) dx \right] \quad (9.96)$$

Since

$$N_1 I_1 = J_{0,1} (r_2 - r_1) L \quad (9.97)$$

we can rewrite Equation 9.96 as

$$L_1 = \frac{\pi\mu_0 N_1^2}{6L} [(r_2 + r_1)^2 + 2r_1^2] + \frac{\pi\mu_0 L N_1^2}{(N_1 I_1)^2} \sum_{n=1}^{\infty} \frac{J_{n,1}^2}{m^4} \left[E_{n,1} \int_{x_1}^{x_2} x I_1(x) dx + F_{n,1} \int_{x_1}^{x_2} x K_1(x) dx - \frac{\pi}{2} \int_{x_1}^{x_2} x L_1(x) dx \right] \quad (9.98)$$

9.5 Determining the B-Field

Determining the B-field within the windings is important in order to obtain the electromagnetic forces acting within the windings as a result of a fault and associated high-winding currents. The B-field present for rated currents can also be useful for estimating the losses in various parts of the transformer, including the eddy losses of the windings.

Before calculating the B-field, a plot of the flux lines can be obtained directly from the vector potential. This type of plot gives a visual sense of the B-field. In the r - z geometry, the appropriate flux lines are lines of constant rA_ϕ , that is, radius \times the azimuthal vector potential. The B-field points along these lines of constant rA_ϕ . In addition, the flux per radian between two lines equals the difference in the values of rA_ϕ on the two lines. Therefore, if lines of equally spaced values of rA_ϕ are plotted, the B-field is strongest where the lines are closest to each other because the average B-field is the flux per unit area or distance between the flux lines in this case. Hence, these give a good sense of what the flux is doing in the transformer. A flux plot, using Rabins' method, is given in Figure 9.4 for a two-winding transformer.

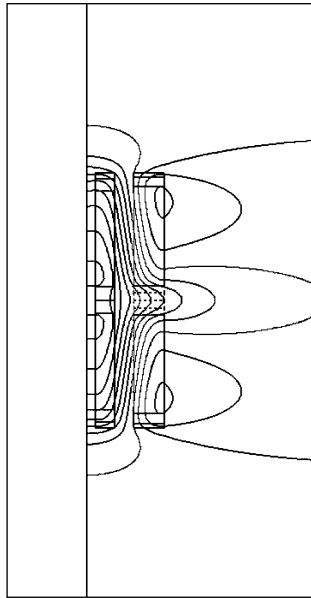


FIGURE 9.4

Flux plot for a two-winding transformer based on Rabins' method. The amp-turns are not uniform along the windings, resulting in radially directed flux, especially at the winding center where the center taps are out. The vertical and radial dimensions are not necessarily to the same scale.

The B-field or induction vector is given by Equation 9.23. We need to evaluate it in the three regions using Equation 9.53. Using the region label as superscript, the radial component is

$$\begin{aligned}
 B_r^I &= \mu_0 \sum_{n=1}^{\infty} \frac{J_n}{m} [C_n I_1(x) + D_n K_1(x)] \sin(mz) \\
 B_r^{II} &= \mu_0 \sum_{n=1}^{\infty} \frac{J_n}{m} \left[E_n I_1(x) + F_n K_1(x) - \frac{\pi}{2} L_1(x) \right] \sin(mz) \\
 B_r^{III} &= \mu_0 \sum_{n=1}^{\infty} \frac{J_n}{m} G_n K_1(x) \sin(mz)
 \end{aligned} \tag{9.99}$$

Using Equation 9.47 and

$$B_z = \frac{1}{r} \frac{\partial}{\partial r} (rA) = \frac{m}{x} \frac{\partial}{\partial x} (xA) \tag{9.100}$$

the axial component is

$$\begin{aligned}
 B_z^I &= \mu_0 J_0 (r_2 - r_1) + \mu_0 \sum_{n=1}^{\infty} \frac{J_n}{m} [C_n I_0(x) - D_n K_0(x)] \cos(mz) \\
 B_z^{II} &= \mu_0 J_0 (r_2 - r) + \mu_0 \sum_{n=1}^{\infty} \frac{J_n}{m} \left[E_n I_0(x) - F_n K_0(x) - \frac{\pi}{2} L_0(x) \right] \cos(mz) \\
 B_z^{III} &= -\mu_0 \sum_{n=1}^{\infty} \frac{J_n}{m} G_n K_0(x) \cos(mz)
 \end{aligned} \tag{9.101}$$

To find the net B-field associated with a collection of coils, we add their components at the point in question, keeping in mind what region the point is in relative to each coil.

9.6 Determination of Winding Forces

The force density vector, \mathbf{F} (in SI units, N/m^3), is given by

$$\mathbf{F} = \mathbf{J} \times \mathbf{B} \tag{9.102}$$

Because \mathbf{J} is azimuthal and \mathbf{B} has only r and z components, this reduces to

$$\mathbf{F} = JB_z \mathbf{a}_r - JB_r \mathbf{k} \quad (9.103)$$

where \mathbf{a}_r is the unit vector in the radial direction and \mathbf{k} is the unit axial vector. We have omitted the ϕ subscript on J . Thus, the radial forces occur due to the axial field component and vice versa.

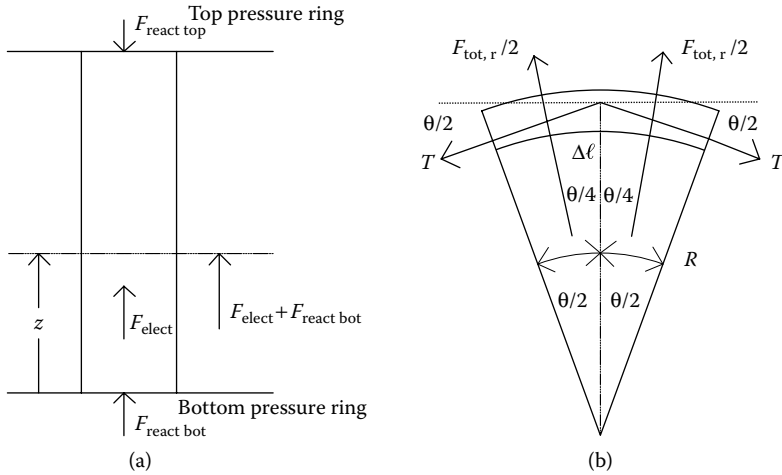
In Equation 9.103, the B -field values result from all the coils and J is the current density at the point in question. This force density is nonzero only over those parts of the winding that carry current. To obtain net forces over all or part of a winding, we need to integrate Equation 9.103 over the winding or winding part. For this, the winding can be subdivided into as fine a mesh as desired and \mathbf{F} computed at the centroids of these subdivisions, and the resulting values \times the mesh volume element added.

The compressive force acts axially at each axial position along the winding. We assume that the windings are constrained at the two ends by pressure rings of some type, and we ignore gravity here. Starting from the bottom, we integrate the axial forces upward along the winding and stop when the sum of the downward acting forces reaches a maximum. This is the net downward force on the bottom pressure ring, which is countered by an equal upward force on the winding exerted by the pressure ring. We do the same thing, starting from the top of the winding and integrating the axial forces until the largest upward-acting summed force is reached. This constitutes the net upward force acting on the top pressure ring, which is countered by an equal downward force exerted by the pressure ring. Including the reaction forces of the pressure rings, we then integrate upward, starting for example at the bottom of the winding, and at each vertical position, the compressive force will be calculated at that position because there will be an equal and opposite force acting from above. This is illustrated in [Figure 9.5a](#).

Another force of interest for coil design is the radial force, which results in hoop stress, tensile or compressive, on the winding. Because of the cylindrical symmetry, the radial forces vectorially add to zero. Therefore, we must handle them a bit differently if we are to arrive at a useful resultant for hoop stress calculations. In [Figure 9.5b](#), we isolate a small portion of the winding and show the forces acting in a horizontal section. We show the radial forces acting outward and the tensile forces applied by the missing part of the winding, which are necessary to maintain equilibrium. If the radial forces act inward, then the rest of the winding will need to apply compressive forces to maintain equilibrium, and all the force arrows in [Figure 9.5b](#) will be reversed. The calculation will, however, proceed similarly.

In [Figure 9.5b](#), θ is assumed to be a very small angle. The force balance in the upward direction in the figure is

$$2 \frac{F_{\text{tot},r}}{2} \cos\left(\frac{\theta}{4}\right) = 2T \sin\left(\frac{\theta}{2}\right) \quad (9.104)$$

**FIGURE 9.5**

Forces on the winding needed for stress analysis: (a) compressive force at each axial position and (b) hoop forces (tensile shown) from the radial forces.

$F_{\text{tot}, r}$ is the sum of the radial electromagnetic forces acting on the winding section shown, and T is the total tensile force acting on the cross section of the winding. For a small θ , this reduces to

$$F_{\text{tot}, r} = T\theta \quad (9.105)$$

$\theta = \Delta\ell/R$, where $\Delta\ell$ is the circumferential length of the winding section shown and R is its average radius. θ is in radians. The average tensile stress is $\sigma = T/A$, where A is the cross-sectional area of the winding section. The volume of the winding section is $\Delta V = A\Delta\ell$. Using these relations and Equation 9.105, we can obtain the tensile (or compressive) stress as

$$\sigma = R \frac{F_{\text{tot}, r}}{\Delta V} \quad (9.106)$$

Thus, the average tensile stress in the winding is the average radius multiplied by the average radial force density, assuming the radial forces act outward. For inward radial forces, σ is negative, that is, compressive. The average radial force density at a particular axial position z can be found by computing the radial component of Equation 9.103 at several radial positions in the winding, keeping z fixed, and taking their average. We should weight these by the volume element, which is proportional to r .

Other forces of interest can be found from the known force densities.

9.7 Numerical Considerations

The infinite sums in the various expressions given in this chapter have to be first reduced to finite sums without significant loss of accuracy. Because the n th term is reduced by some power of n , they tend to get smaller as the value of n becomes larger. We found that a set of 200 terms provides sufficient accuracy. The sums should also be carried out in double precision.

We have used a mathematical library for the modified Bessel functions of the first and second kinds of order zero and one. The library gives two forms for these functions, one for the function itself and another to express the function as an exponential times a remainder. For instance, the following exponential forms should be used:

$$\begin{aligned} I_0(x) &= e^x \times \text{Remainder}_{I_0}, & I_1(x) &= e^x \times \text{Remainder}_{I_1} \\ K_0(x) &= e^{-x} \times \text{Remainder}_{K_0}, & K_1(x) &= e^{-x} \times \text{Remainder}_{K_1} \end{aligned} \quad (9.107)$$

When these functions occur in some combination, the exponentials can be combined and the exponents usually cancel to a large extent.

The modified Struve function does not appear in our mathematical library, so we obtained it via the difference functions defined in Equation 9.58 and their integral expressions given in Equations 9.59 and 9.60. These integrals can be done with high accuracy, and they have finite values of reasonably small magnitudes for the various values of x . These expressions can then be used in Equations 9.61 and 9.64 to obtain the integrals of the modified Bessel and Struve functions, respectively.

10

Mechanical Design

10.1 Introduction

Transformers must be designed to withstand the large forces that occur during fault conditions. Fault currents for the standard fault types such as single line to ground, line to line, double line to ground, and all three lines to ground must be calculated. Since these faults can occur during any part of the alternating current (AC) cycle, the worst-case transient overcurrent must be used to determine the forces. This can be calculated and is specified in the standards as an asymmetry factor, which multiplies the rms steady-state currents. The asymmetry factor is given by [IEE93]:

$$K = \sqrt{2} \left[1 + e^{-\left(\phi + \frac{\pi}{2}\right) \frac{r}{x}} \sin \phi \right] \quad (10.1)$$

where $\phi = \tan^{-1}(x/r)$ and x/r is the ratio of the effective AC reactance to resistance. These are part of the total impedance, which limits the fault current in the transformer when a short circuit occurs. Using this factor, the resulting currents are used to obtain the magnetic field (leakage field) surrounding the coils and, in turn, the resulting forces on the windings. Analytic methods such as Rabins' method [Rab56], discussed in Chapter 9, or finite element methods can be used to calculate the magnetic field. An example of a leakage field is shown in [Figure 10.1](#), which was generated by the finite element program Maxwell Version 12 (Ansoft Corp., Pittsburgh, PA). Since this finite element calculation uses the two-dimensional option, Figure 10.1 is cylindrically symmetrical about the core center line, and only the bottom half of the windings and core are shown because we assume symmetry about a horizontal center plane. Although details such as clamps and shields can be included in the calculation by using a finite element approach, they are not part of Rabins' analytical method, which assumes a simpler idealized geometry. However, calculations show that the magnetic field in the windings and hence the forces are nearly identical in the two cases. [Figure 10.2](#) shows a flux plot

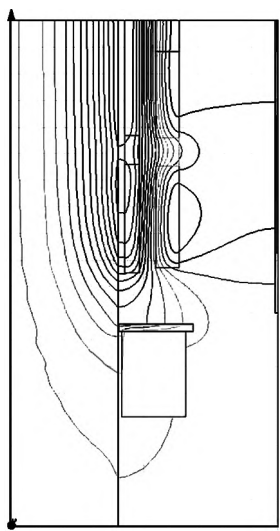


FIGURE 10.1 Plot of transformer leakage flux. Only the bottom half is shown. The figure is assumed to be cylindrically symmetrical about the core center line. A bottom clamp with shunts on top and tank shunts on the right are shown.

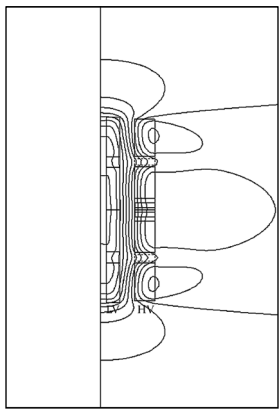


FIGURE 10.2 Flux plot generated from the Rabins' method solution for the same transformer and currents as shown in [Figure 10.1](#). The full coil geometry is shown. The horizontal and vertical scales are not necessarily the same for this plot.

generated from the Rabins' method solution for the same transformer and currents as are shown in Figure 10.1. Figure 10.2 shows the entire coil geometry, but the bottom clamp and tank shunt are absent. Nevertheless, the similarity is apparent when we compare the bottom half of Figure 10.2 with Figure 10.1.

The force density (force per unit volume), \mathbf{f} , generated in the windings by the magnetic induction, \mathbf{B} , is given by the Lorentz force law:

$$\mathbf{f} = \mathbf{J} \times \mathbf{B} \quad (10.2)$$

where \mathbf{J} is the current density in SI units. These force densities can be integrated to get total forces, forces per unit length, or pressures depending on the type of integration performed. The resulting values or the maxima of these values can then be used to obtain stresses or maximum stresses in the winding materials.

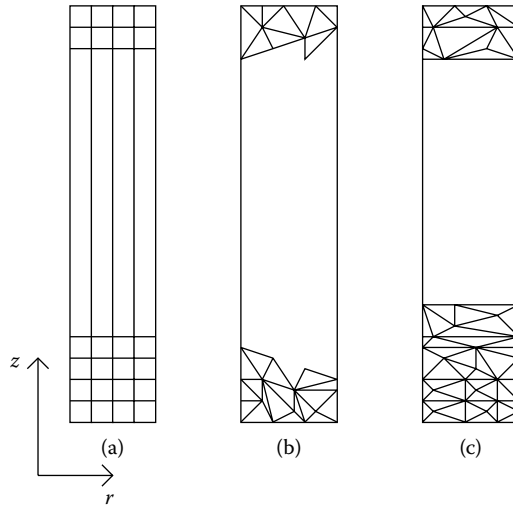
The procedure described above is static in that the field and force calculations assume steady-state conditions, even though the currents are multiplied by an asymmetry factor to account for a transient overshoot. Because the fault currents are applied suddenly, the resulting forces or pressures are also applied suddenly. This can result in transient mechanical effects such as the excitation of mechanical resonances, which can produce higher forces for a brief period than those obtained by a steady-state calculation. A few studies have been done on these transient mechanical effects in transformers [Hir71], [Bos72], [Pat80], and [Tho79]. Although these studies are approximate, we can use an appropriate enhancement factor to multiply the steady-state force where they have indicated a large effect primarily due to the excitation of a mechanical resonance. In other cases, studies have indicated little or no transient effects and no correction is necessary.

Because controlled short-circuit tests are rarely performed on large transformers to validate a transformer's mechanical design, there are few empirical studies that directly test the theoretical calculations. To some extent, our confidence in these calculations comes from tests on smaller units and the fact that, in recent years, very few field failures have been directly attributable to mechanical causes.

10.2 Force Calculations

The electromagnetic forces acting on the coils can be obtained using an analytic or finite element magnetic field calculation in conjunction with the Lorentz force law. In our analytic calculation using Rabins' method [Rab56], each coil carrying current is subdivided into four radial sections and 100 axial sections as shown in Figure 10.3a. In the case of the finite element method, the cross-section of the coil is subdivided into an irregular net of triangles as shown in Figure 10.3b. The principles used to determine the forces or pressures needed in the stress calculation are similar for the two cases, so we will focus on the analytic method.

The current density is uniform in each block as shown in Figure 10.3a, but it can vary axially from block to block due to tapping out sections of the coil

**FIGURE 10.3**

Coil subdivisions in (a) analytic and (b) finite element calculations of the magnetic field. (c) A modified finite element mesh, which is more useful for subsequent stress analysis.

or thinning of sections of the winding to achieve a better amp-turn balance with tapped-out sections in adjacent winding. These sections of reduced or zero current density produce radially bulging flux lines, as shown in [Figure 10.1](#). We know from the Lorentz force law that since the current is azimuthally directed, radially directed flux produces axial forces and axially directed flux produces radial forces. There are no azimuthal forces because we assume the geometry is cylindrically symmetric.

The radial and axial forces are computed for each block in Figure 10.3a. Because of the cylindrical symmetry, each block in the figure is actually a ring. Think of the radial force as a pressure acting inward or outward on the ring, depending on its sign. If these forces are summed over the four radial blocks and then divided by the area of the cylindrical surface at the average radius of the winding, we obtain an effective total radial pressure acting on the coil at the axial position of the block. The maximum pressure in absolute value for the 100 axial positions is the worst-case radial pressure and is used in subsequent stress analysis. Note that these forces are radially directed so that integrating them vectorially over 360° will produce zero. This integration must therefore be done regardless of their vectorial nature.

We also need the axially directed force summed over the four radial blocks. The maximum absolute value of this force for the 100 axial positions is a worst-case force used in the stress analysis. These axial forces are also summed, starting at the bottom of the coil. The total of these axial forces (summed over all the blocks of the coil) is a net upward or downward force depending on its sign. This force is countered by an equal and opposite force exerted by

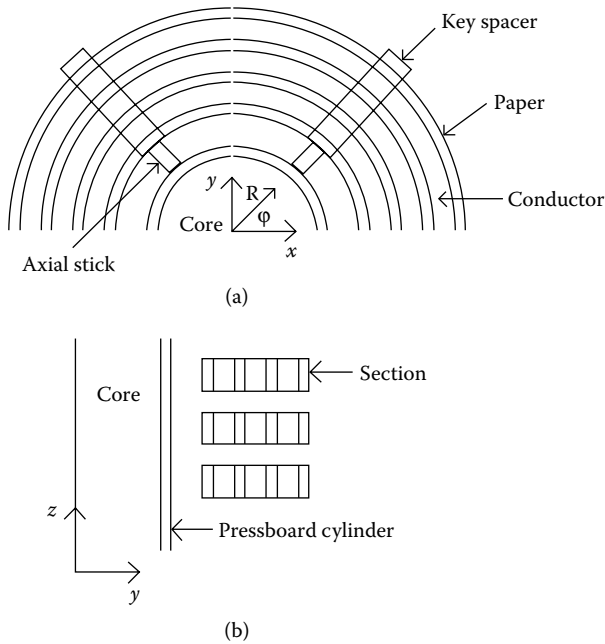
the pressure ring. If this net force acts downward, then the bottom pressure ring exerts an equal upward force on the coil. If it acts upward, then the top pressure ring exerts an equal downward force. In the former case, the top ring exerts no force on the coil, and in the latter case, the bottom ring exerts no force on the coil. We ignore the gravitational forces in comparison with the electromagnetic forces here. If we start with the force exerted upward, if any, by the bottom pressure ring, and keep adding to this the forces produced by the horizontal layers of four blocks starting from the bottom row, we will arrive at a maximum net upward force at some vertical position along the winding. This force is called the maximum compressive force and is a worst-case force used in stress analysis.

The total axial forces on the windings are added together if they are upward (positive). Similarly, windings having downward (negative) total axial forces contribute to the total downward force. These total upward or downward forces should be equal in absolute value because the net electromagnetic force acting axially must be zero. In practice, there are slight differences in these calculated quantities due to rounding errors. The net upward or downward axial force is called the total end thrust and is used in sizing the pressure rings. If the windings are symmetric about a horizontal center plane, the total axial force on each winding is nearly zero, so there is little or no end thrust. However, when one or more windings are offset vertically from the others, even slightly, net axial forces develop on each winding, which push some windings up and some down. We should include some offset, for example, 6.35–12.7 mm, in the calculations to take into account possible misalignment in the transformer's construction.

As we can see from the way forces needed for stress analysis were extracted from the block forces in [Figure 10.3a](#), the finite element mesh shown in [Figure 10.3c](#) will be more useful for obtaining the needed forces. Here, the coil is subdivided into a series of axial blocks, which can be of different heights, before the triangular mesh is generated. Then, the forces can be summed for all the triangles within each block to correspond to the forces obtained from the four radial blocks at the same axial height in [Figure 10.3a](#).

10.3 Stress Analysis

Now we will relate the forces discussed in [Section 10.2](#) to the stresses in the coil in order to determine whether the coil can withstand them without permanently deforming or buckling. The coils have a rather complex structure as indicated in [Figure 10.4](#), which shows a disk-type coil. Helical windings are disk windings with only one turn per section and thus are a special case of those shown [Figure 10.4](#). The sections are separated vertically by key spacers made of pressboard. These are spaced around the coil so as to

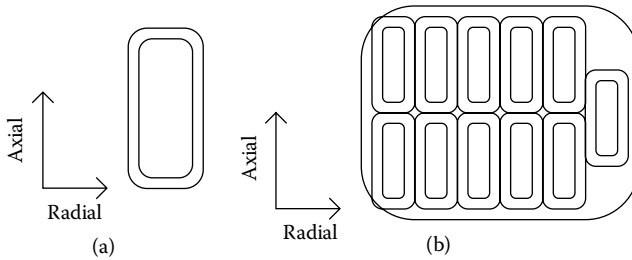
**FIGURE 10.4**

Details of a typical disk winding: (a) horizontal view (x, y) plane and (b) vertical view (y, z) plane.

allow cooling oil to flow between them. The coils are supported radially by means of axial sticks and pressboard cylinders or barriers. These brace the coil on the inside against an inner coil or against the core. There are similar support structures on the outside of the coil, except for the outermost coil. Spaces between the sticks allow cooling oil to flow vertically. Because of the dissimilar materials used, such as pressboard, paper, and copper for the conductors, and because of the many openings for the cooling oil, the stress analysis will be very complicated unless suitable approximations are made.

Although we can see distinct separate axial sections in Figure 10.4, in reality, the wires must maintain electrical continuity from section to section so that the coil has a helical (spring-like) structure. For the stress analysis, we generally assume that the helical pitch is small enough that the coil can be considered to have distinct horizontal sections as shown in Figure 10.4. Moreover, these sections are assumed to close on themselves, forming rings.

Another approximation concerns the cable that comprises the winding turns. Figure 10.5 shows the two most common types. The magnet wire consists of a single strand of copper surrounded by a paper covering and is treated almost without approximation in the stress analysis. The continuously transposed cable (CTC) consists of multiple enamel-coated copper strands arranged in a nearly rectangular pattern as shown. The figure

**FIGURE 10.5**

Types of wire or cable used in transformer coils: (a) magnet wire and (b) transposed cable.

does not show how the transpositions are made. The transpositions rotate the different strands so that they each occupy all the positions shown as one moves along the wire. The transpositions give some rigidity to the collection of strands. In addition, a bonded cable is often used. In a bonded cable, all the strands are bonded together by an epoxy coating over the enamel, which is subjected to a heat treatment. In this case, the cable can be treated as a rigid structure, although there is some question as to how to evaluate its material properties. With or without bonding, some approximations must be made as to how to model the cable for stress analysis purposes. For radial force considerations without bonding, we assume that the cable has a radial thickness equivalent to two radial strands. With bonding, we assume a radial thickness equivalent to 80% of the actual radial build.

We will first look at the stresses produced by the axial forces, and then we will consider stresses due to the radial forces. We need to examine worst-case stresses in the copper winding turns, key spacers, pressure rings, and tie plates, which are attached to the top and bottom clamps.

10.3.1 Compressive Stress in the Key Spacers

The maximum axial compressive force is used to determine the worst-case compressive stress in the key spacers. This force, F_c , obtained for each coil from the magnetic field analysis program, is divided by the area of the key spacers covering one 360° disk section in order to obtain the key spacer compressive stress σ_{ks} :

$$\sigma_{ks} = \frac{F_c}{N_{ks} W_{ks} B} \quad (10.3)$$

where N_{ks} is the number of key spacers around one 360° section, W_{ks} is the width of a key spacer, and B is the radial build of the coil. We use key spacers made of precompressed pressboard that can withstand a maximum compressive stress of 310 MPa (MPa = N/mm²). Therefore, the stress calculated by Equation 10.3 should not exceed this number and is usually restricted to much less.

10.3.2 Axial Bending Stress per Strand

The maximum axial force over the 100 vertical subdivisions is computed for each coil. For greater generality, we will let N_v = the number of vertical subdivisions. We call this maximum force F_a . To compute the bending stress, we need to know the force per unit length along an individual strand because these forces are continuously distributed along the strand. The number of strands in the entire coil N_s is given by

$$N_s = N_t N_h N_w N_{st} \quad (10.4)$$

where N_t is the number of turns per leg, N_h is the number of cables per turn high (radially), N_w is the number of cables per turn wide (axially), and N_{st} is the number of strands per cable. We allow for the fact that each turn can consist of several cables in parallel, some radially and some axially positioned, and each having N_{st} strands. If the coil consists of two separate windings stacked axially (center fed) with each having N_e electrical turns, then $N_t = 2N_e$. Because the section with the maximum axial force is only $1/N_v$ of the coil, it has only $1/N_v$ of the above number of strands. Hence, the maximum force per unit length on a single strand q_{st} is given by

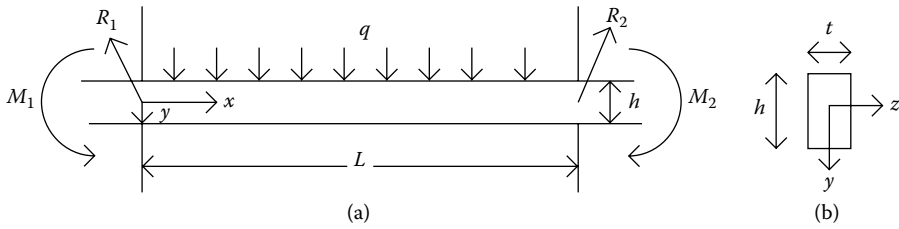
$$q_{st} = \frac{N_v F_a}{N_s \pi D_m} \quad (10.5)$$

where D_m is the mean diameter of the coil.

The problem can be analyzed as a uniformly loaded rectangular beam with built-in ends, as shown in Figure 10.6a. There are six unknowns—the horizontal and vertical components of the reaction forces and the bending moments at the two built-in ends—but only three equations of statics, making this a statically indeterminate problem. The two horizontal reaction forces are equal and opposite and produce a tensile stress in the beam, which is small for small deflections and will be ignored. The vertical reaction forces are equal and share the downward load equally. Therefore, they are given by $R_{1,up} = R_{2,up} = qL/2$, where $q = q_{st}$ is the downward force per unit length along the beam and L is the length of the beam. By symmetry, the bending moments M_1 and M_2 shown in Figure 10.6a are equal and produce a constant bending moment along the beam. In addition, a bending moment as a function of position is also present, resulting in a total bending moment at position x :

$$M(x) = \frac{qLx}{2} - \frac{qx^2}{2} - M_1 \quad (10.6)$$

using the sign convention of [Tim55].

**FIGURE 10.6**

Uniformly loaded beam with built-in ends: (a) side view and (b) cross-sectional view.

To solve for the unknown M_1 , we need to solve the equation of the beam's deflection curve [Tim55].

$$\frac{d^2y}{dx^2} = -\frac{M(x)}{EI_z} \quad (10.7)$$

where E is Young's modulus for the beam material, I_z is the area moment of inertia about the z axis, and y is the downward deflection of the beam. Substituting Equation 10.6 into 10.7, we have

$$\frac{d^2y}{dx^2} = \frac{1}{EI_z} \left(M_1 - \frac{qLx}{2} + \frac{qx^2}{2} \right) \quad (10.8)$$

Integrating once, we get

$$\frac{dy}{dx} = \frac{1}{EI_z} \left(M_1x - \frac{qLx^2}{4} + \frac{qx^3}{6} \right) + C \quad (10.9)$$

where C is a constant of integration. Since the beam is rigidly clamped at the ends, the slope $dy/dx = 0$ at $x = 0$ and $x = L$. Setting $dy/dx = 0$ at $x = 0$ in Equation 10.9 yields $C = 0$. Setting $dy/dx = 0$ at $x = L$, we find that

$$M_1 = \frac{qL^2}{12} \quad (10.10)$$

Substituting these values into Equation 10.9, we get

$$\frac{dy}{dx} = \frac{q}{EI_z} \left(\frac{L^2x}{12} - \frac{Lx^2}{4} + \frac{x^3}{6} \right) \quad (10.11)$$

Integrating again, we get

$$y = \frac{q}{EI_z} \left(\frac{L^2 x^2}{24} - \frac{Lx^3}{12} + \frac{x^4}{24} \right) = \frac{qx^2(L-x)^2}{24EI_z} \quad (10.12)$$

where the constant of integration was set to zero because $y = 0$ at $x = 0$ and $x = L$.

Inserting Equation 10.10 into Equation 10.6, the bending moment as a function of position along the beam is

$$M(x) = \frac{q}{2} \left[x(L-x) - \frac{L^2}{6} \right] \quad (10.13)$$

The maximum positive value occurs at $x = L/2$ and is $M_{\max} = qL^2/24$. The minimum value occurs at $x = 0$ or $x = L$ and is $M_{\min} = -qL^2/12$. Because the minimum bending moment is larger in absolute value, we use it in the formula to obtain the stress due to the bending in the beam [Tim55]:

$$\sigma_x = \frac{My}{I_z} \quad (10.14)$$

where y is measured downward from the centroid of the beam's cross section, as shown in Figure 10.6b. For a given x , σ_x is the maximum or minimum when $y = \pm h/2$, where h is the beam height in the bending direction. If σ_x is positive, the stress is tensile; if σ_x is negative, the stress is compressive. Inserting M_{\min} into Equation 10.14, taking $y = -h/2$, and using

$$I_z = \frac{th^3}{12} \quad (10.15)$$

for the area moment of inertia for a rectangular cross section with respect to the z -axis through the centroid (Figure 10.6b), we get

$$\sigma_{x,\max} = \frac{q}{2t} \left(\frac{L}{h} \right)^2 \quad (10.16)$$

where t is the thickness of the beam perpendicular to the bending plane. This is a tensile stress and occurs at the top of the beam at the supports. There is a compressive stress of equal magnitude at the bottom of the beam at the supports.

Inserting the actual load from Equation 10.5 into Equation 10.16, the maximum axial bending stress is

$$\sigma_{\max, \text{axial}} = \frac{N_v F_a}{2N_s \pi D_m t} \left(\frac{L}{h} \right)^2 \quad (10.17)$$

The span length L can be determined from the number of key spacers, their width, and the mean circumference:

$$L = \frac{\pi D_m - N_{ks} W_{ks}}{N_{ks}} = \frac{\pi D_m}{N_{ks}} - W_{ks} \quad (10.18)$$

The strand height h and thickness t apply to a single strand, whether as a part of a cable having many strands or as a single strand in a magnet wire. If the cable is bonded, the maximum axial bending stress in Equation 10.17 is divided by 3. This is simply an empirical correction made to take into account the greater rigidity of bonded cable.

We can also get the maximum downward deflection of the beam from Equation 10.12, which occurs at $x = L/2$. Inserting Equation 10.15 for I_z into Equation 10.12, the maximum deflection y_{\max} is

$$y_{\max} = \frac{q}{32E} \left(\frac{L^4}{th^3} \right) = \frac{N_v F_a}{32N_s \pi D_m E} \left(\frac{L^4}{th^3} \right) \quad (10.19)$$

where we have used Equation 10.5 to obtain the second equality.

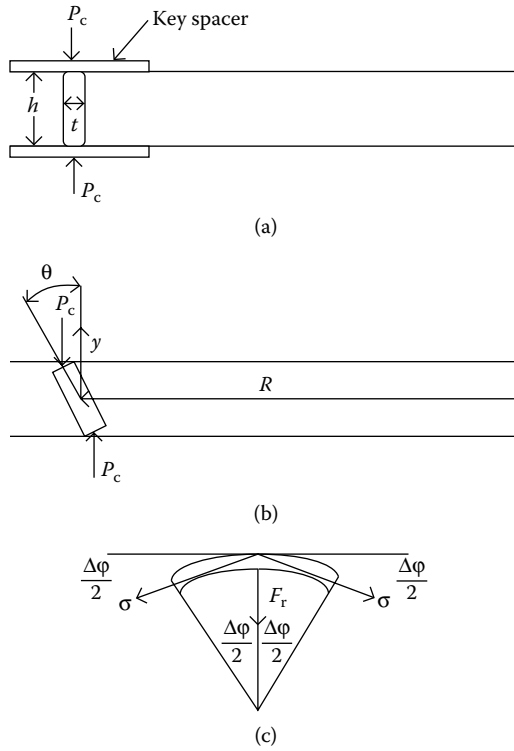
10.3.3 Tilting Strength

The axial compressive force that is applied to the key spacers can cause the individual strands of the conductors, which are pressed under the key spacers, to tilt if the force is large enough. Figure 10.7 shows an idealized geometry of this situation: an individual strand that has the form of a closed ring acted on by a uniform axial compressive pressure P_c . We assume initially that the strand has rounded ends that do not dig into the adjacent key spacers to prevent or oppose the tilting shown. (There can be several layers of strands in the axial direction separated by paper, which plays the same role as the key spacers Figure 10.7.)

Analyzing a small section in the azimuthal direction of length $\Delta\ell$, the applied pressure exerts a torque τ_c given by

$$\tau_c = P_c (t\Delta\ell) h \sin \theta \quad (10.20)$$

where t is the radial thickness of the strand and $t\Delta\ell$ is the area on which the pressure P_c acts. The axial height of the strand is h , and θ is the tilting angle from the vertical, which we assume is small. The tilting causes the

**FIGURE 10.7**

Geometry of strand tilting due to the axial compressive force: (a) untilted strand between key spacers, (b) tilted strand with the angle of tilt indicated, and (c) the inward radial force produced by the hoop stress in the tilted strand. The strand is ring-shaped when viewed in the axial direction.

material of the ring to stretch above its axial center and to compress below it. This produces stresses in the ring, which in turn produce a torque that opposes the torque calculated above. To calculate this opposing torque, let y be the distance above the axial center of the strand, as shown in Figure 10.7b. The increase in the radius at distance y above the center line is $y \tan \theta$. Therefore, the strain at position y is

$$\epsilon = \frac{y \tan \theta}{R} \quad (10.21)$$

where ϵ is an azimuthal strain. This produces an azimuthal tensile stress (hoop stress) given by

$$\sigma = E\epsilon = \frac{Ey \tan \theta}{R} \quad (10.22)$$

where E is Young's modulus for the conductor material. This hoop stress results in an inward force F_r on the section of strand given by (Figure 10.7c)

$$F_r = 2\sigma(t\Delta y) \sin\left(\frac{\Delta\phi}{2}\right) \equiv \sigma(t\Delta y)\Delta\phi = \sigma(t\Delta y)\frac{\Delta\ell}{R} \quad (10.23)$$

In Equation 10.23, $t\Delta y$ is the area at height y over which the stress σ acts, and $\Delta\phi$ is the angle subtended by the azimuthal section of strand of length $\Delta\ell$. Also, $\Delta\ell = R\Delta\phi$ is used, and the small angle approximation of the sin function is used.

The inward force F_r produces a counter torque $\Delta\tau$ on the small section of height Δy , which for small θ is given by

$$\Delta\tau = F_r y = \frac{\sigma t \Delta\ell y \Delta y}{R} \quad (10.24)$$

Using Equation 10.22, counter torque $\Delta\tau$ becomes

$$\Delta\tau = \frac{Et\Delta\ell \tan\theta y^2 \Delta y}{R^2} \quad (10.25)$$

Letting Δy become infinitesimal and integrating from $y = 0$ to $h/2$, we get

$$\tau = \frac{Et\Delta\ell \tan\theta h^3}{24R^2} \quad (10.26)$$

Analyzing the portion of the strand below the center line, the hoop stress is compressive and will result in an outward force on the strand. This will create a torque of the same magnitude and sense as that in Equation 10.26, so to take the whole strand into account, we just need to multiply Equation 10.26 by two. In equilibrium, this resulting torque equals the applied torque given by Equation 10.20. Equating these two expressions and using $\sin\theta \approx \tan\theta \approx \theta$ for small θ , we get

$$P_c = \frac{E}{12} \left(\frac{h}{R}\right)^2 \quad (10.27)$$

When the conductor strand has squared ends, there is an additional resistance to tilting because the ends dig into the key spacers or paper. This results in an additional resisting torque of magnitude [Ste62], [Wat66]:

$$C \frac{f_{ks} t^3 \sin\theta \Delta\ell}{6} \quad (10.28)$$

where C is a constant depending on the spacer material and f_{ks} is the fraction of the coil average circumference occupied by key spacers. If there are no key spacers, set $f_{ks} = 1$. This should be added to $2 \times$ Equation 10.26 and their sum equated to Equation 10.20, resulting in a tilting pressure of

$$P_c = \frac{E}{12} \left(\frac{h}{R} \right)^2 + \frac{C}{6} \left(\frac{f_{ks} t^2}{h} \right) \quad (10.29)$$

If the strand has rounded corners of radius R_{corn} , then t in Equation 10.29 is reduced by $2R_{\text{corn}}$ so only its flat portion is considered. Therefore, the resulting critical axial pressure is

$$P_c = \frac{E}{12} \left(\frac{h}{R} \right)^2 + \frac{C}{6} \left[\frac{f_{ks} (t - 2R_{\text{corn}})^2}{h} \right] \quad (10.30)$$

In Equation 10.30, E is the initial Young's modulus for copper and is essentially independent of the hardness. It has a value of 1.10×10^5 MPa. C is assumed to be equal to 2.44×10^3 MPa/mm. The second term in Equation 10.30 is called the bedding term.

This equation is often modified to take into account other factors based on experimental data, such as the proof strength of copper and whether the cable is made of the magnet wire or CTC. A possible modified version is

$$P_c = C_1 C_2 \left\{ \frac{E}{8\pi} \left(\frac{h}{R} \right)^2 + \frac{C_3}{6} \left[\frac{f_{ks} (t - 2R_{\text{corn}})^2}{h} \right] \right\} \quad (10.31)$$

where C_1 depends on the proof strength of the copper and varies from 1.0 for regular copper to 1.4 for very hard copper. For magnet wire, $C_2 = 1$ for $f_{ks} = 1$ and $C_2 = 1.4$ for $f_{ks} < 1$. For CTC, $C_2 = 1.2$ for $f_{ks} = 1$, and $C_2 = 2.0$ for $f_{ks} < 1$. $C_3 = 270$ MPa/mm for magnet wire and $C_3 = 132$ MPa/mm for CTC.

To compare this with the applied maximum axial compressive force, we multiply Equation 10.30 or 10.31 by the radial surface area of the strands in one horizontal layer A_{layer} . This is

$$A_{\text{layer}} = 2\pi R t N_d N_h N_{\text{st,radial}} \quad (10.32)$$

where N_d is the number of turns in a disk or section, N_h is the number of cables in parallel radially per turn, and $N_{\text{st,radial}}$ is the number of strands in the radial direction per cable. $N_{\text{st,radial}} = 1$ for magnet wire and, as shown in [Figure 10.5b](#), $N_{\text{st,radial}} = (N_{\text{st}} - 1)/2$ for CTC. Thus, the critical axial force is

$$F_{\text{cr}} = P_c A_{\text{layer}} \quad (10.33)$$

This applies to unbonded cable. For bonded cable, we take $F_{cr} = \infty$ because in this case we assume that tilting is very unlikely. We compare Equation 10.33 with the maximum applied axial compressive force F_c by taking the ratio F_{cr}/F_c . This ratio must be >1 for a viable design, that is, F_c must be $<F_{cr}$.

The expression for A_{layer} does not take into account the fractional area coverage of the key spacers because the force is applied to the key spacer area. However, except for the bedding term, the calculation involves an averaging process over all the strands in the layer. The bedding term already includes the fractional key spacer area coverage.

10.3.4 Stress in the Tie Bars

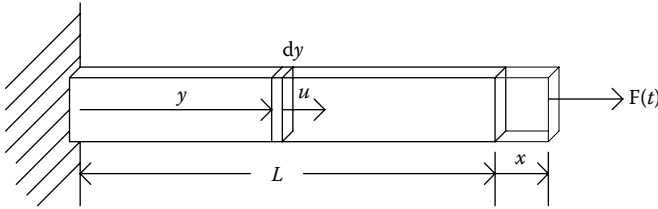
The tie bars or tie plates are used to join the upper and lower clamping structures, which keep the coils under compression. They are generally long rectangular bars of steel that are placed along the sides of the core legs. They are under mild tension during normal transformer operations. During short circuit, the tensile stresses can increase considerably. Also, when the transformer is lifted, the tie bars support the entire weight of the core and coils.

The short-circuit stress in the tie bars is due to the total end thrust produced by all the coils on a single leg. This is the sum of the total upward or downward forces acting on the coils. Because of the three-phase current, the maximum force will not appear on all legs simultaneously. For a single line-to-ground fault, one of the legs will have the highest currents and forces. This leg is therefore singled out for the stress calculation. For a three-phase fault, the maximum force acts on all three legs but not simultaneously so that, even in this case, the force associated with only one leg may be used in the stress analysis. Although this force acts on a single leg, we can assume that all the tie bars participate in countering this force. Other assumptions or even tests can be made to determine how this force is distributed among the tie bars.

The total end thrust is the result of a static force calculation. Because of the possible dynamic effects associated with the sudden application of a force to an elastic system, the end thrust can be considerably higher for a short period after the force application. To see what the dynamic force enhancement might be, we will analyze an elastic bar subjected to a suddenly applied force, as illustrated in [Figure 10.8](#). Let x be the change in length produced by the force, relative to the unstressed bar of length L . A bar under stress stores elastic energy U , which is given by [Tim55]

$$U = \frac{EA}{2L} x^2 \quad (10.34)$$

where E is Young's modulus for the bar material and A is the cross-sectional area of the bar. The applied force causes the bar material to move so that it acquires a kinetic energy. The bar is fixed at one end and moves with

**FIGURE 10.8**

Elastic bar fixed at one end and subject to an applied force at the other end.

maximum velocity at the other end. Because each portion of the bar moves with a different velocity, we must integrate the kinetic energy of each segment along the bar to get the total. In Figure 10.8, a bar segment at distance y from the fixed end of thickness dy is isolated. The parameter u measures the displacement of this bar segment, and its velocity is therefore du/dt . However, the strain ϵ is uniform along the bar, so we have $\epsilon = u/y = x/L$. Therefore, $u = xy/L$ and $du/dt = (y/L) dx/dt$. The segment's kinetic energy is

$$d(\text{KE}) = \frac{1}{2} \rho A dy \left(\frac{y}{L} \frac{dx}{dt} \right)^2 = \frac{1}{2} \frac{\rho A}{L^2} \left(\frac{dx}{dt} \right)^2 y^2 dy \quad (10.35)$$

where ρ is the mass density of the bar material. Integrating over the bar, we get

$$\text{KE} = \frac{1}{2} \frac{\rho AL}{3} \left(\frac{dx}{dt} \right)^2 \quad (10.36)$$

Effectively one-third of the mass of the bar is moving with the end velocity dx/dt . We use Lagrange's method to obtain the equation of motion of the bar. The Lagrangian is $L = \text{KE} - U$ (KE is kinetic energy), and the equation of motion is

$$\frac{d}{dt} \left[\frac{\partial L}{\partial (dx/dt)} \right] - \frac{\partial L}{\partial x} = F \quad (10.37)$$

Using Equations 10.34 and 10.36, this becomes

$$\frac{d^2 x}{dt^2} + \frac{3E}{\rho L^2} x = \left(\frac{3}{\rho AL} \right) F \quad (10.38)$$

The force applied to the tie bars during a fault is produced by the coils. Although the forces applied to the coils are proportional to the current squared, because of the coil's internal structure, the force transmitted to the

tie bars may be modified. However, assuming the coils are well clamped, we expect that the force transmitted to the tie bars is also proportional to the current squared to a good approximation. The fault current has the approximate form [Wat66]:

$$I = I_0(e^{-at} - \cos \omega t)u(t) \quad (10.39)$$

where a is a constant, which is a measure of the resistance in the circuit, ω is the angular frequency, and $u(t)$ is the unit step function, which is zero for $t < 0$ and 1 for $t \geq 0$. The force has the form

$$F = F_0 \left(\frac{1}{2} + e^{-2at} - 2e^{-at} \cos \omega t + \frac{1}{2} \cos 2\omega t \right) u(t) \quad (10.40)$$

which results from squaring Equation 10.39 and using a trigonometric identity. This function is plotted in [Figure 10.9a](#) for $a = 22.6$ and $\omega = 2\pi(60)$. To simplify matters and maintain a worst-case position, assume $a = 0$, so Equation 10.40 reduces to

$$F = F_0 \left(\frac{3}{2} - 2 \cos \omega t + \frac{1}{2} \cos 2\omega t \right) u(t) \quad (10.41)$$

This is plotted in [Figure 10.9b](#). It achieves a maximum of $F_{\max} = 4F_0$, whereas Equation 10.40 reaches a maximum value of about $3.3F_0$ for the parameters used. If this maximum force were acting in a steady-state manner, according to Hooke's law, the bar's displacement will be

$$x_{\max} = \frac{L}{EA} 4F_0 = \frac{L}{EA} F_{\max} \quad (10.42)$$

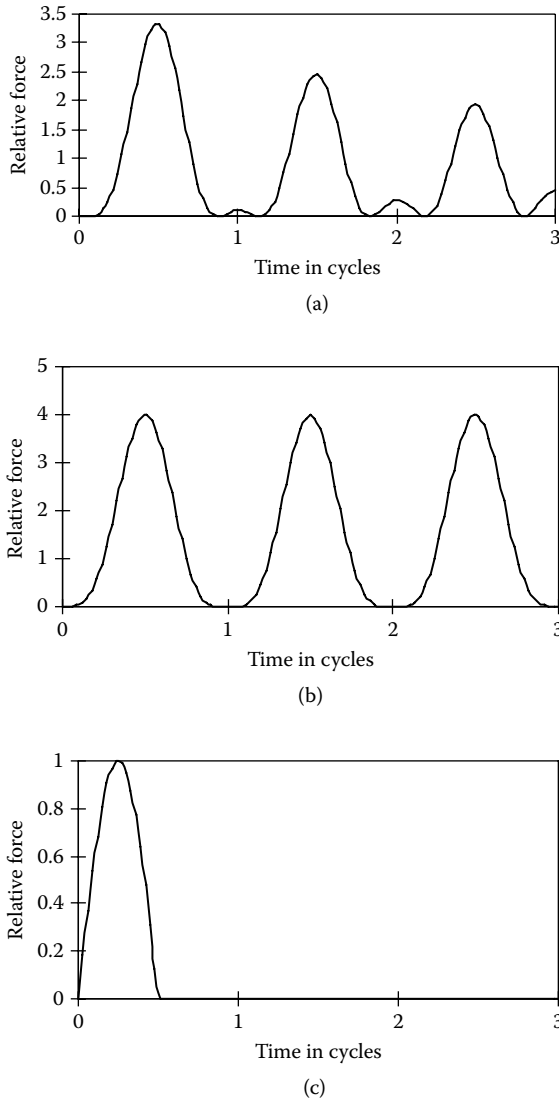
We compare this with the dynamical solution of Equation 10.38 to get the enhancement factor.

To solve Equation 10.38, we take Laplace transforms (LTs) using the boundary conditions $x(t = 0^-) = 0$ and $dx/dt(t = 0^-) = 0$. We get

$$\left(s^2 + \frac{3E}{\rho L^2} \right) \text{LT}(x) = \left(\frac{3}{\rho AL} \right) \text{LT}(F) \quad (10.43)$$

The LT of Equation 10.41 is

$$\text{LT}(F) = F_0 \left[\frac{3}{2} \left(\frac{1}{s} \right) - 2 \left(\frac{s}{s^2 + \omega^2} \right) + \frac{1}{2} \left(\frac{s}{s^2 + 4\omega^2} \right) \right] \quad (10.44)$$

**FIGURE 10.9**

Graphs of some tie bar forces versus time in cycles: (a) plot of Equation 10.40, (b) plot of Equation 10.41, and (c) plot of Equation 10.48.

Substituting into Equation 10.43, for the LT of x , we get

$$\text{LT}(x) = \left(\frac{3}{\rho AL} \right) \frac{F_0}{s^2 + b^2} \left[\frac{3}{2} \left(\frac{1}{s} \right) - 2 \left(\frac{s}{s^2 + \omega^2} \right) + \frac{1}{2} \left(\frac{s}{s^2 + 4\omega^2} \right) \right] \quad (10.45)$$

where

$$b^2 = \frac{3E}{\rho L^2}$$

Using algebra to rewrite Equation 10.45 and taking inverse transforms, we get

$$x(t) = \left(\frac{L}{EA} \right) F_{\max} u(t) \left\{ \frac{1}{4} \left[\frac{3}{2} (1 - \cos bt) + \frac{2}{1 - (\omega/b)^2} (\cos bt - \cos \omega t) - \frac{1}{2} \left(\frac{1}{1 - 4(\omega/b)^2} \right) (\cos bt - \cos 2\omega t) \right] \right\} \quad (10.46)$$

where the quantity in curly brackets is the enhancement factor.

We need to compare the natural angular frequency b with the applied angular frequencies $\omega = 2\pi f = 377$ Rads/s, assuming $f = 60$ Hz, and $2\omega = 754$ Rads/s to see whether a resonance problem might occur. For steel bars, $E = 2.07 \times 10^5$ MPa, $\rho = 7837$ kg/m³. Using Equation 10.45 for b , we get

$$b = \sqrt{\frac{3E}{\rho L^2}} = \frac{8902}{L(m)} \text{ Rads/seconds} \quad (10.47)$$

For a 2.54-m long tie bar, the typical length, $b = 3504$ Rads/s. Since this is much larger than ω or 2ω , we are far from resonance. Thus, $(\omega/b)^2$ can be ignored relative to 1 in Equation 10.46, and this equation simplifies to $x(t) = (L/EA)F$ with F given by Equation 10.41. Hence, x_{\max} is the same as in the steady-state case, and the enhancement factor is 1. Thus, unless the applied or twice the applied frequency is close to the tie bar's natural frequency, there is no dynamic enhancement. By numerically checking over a large grid of times and electrical frequencies, a maximum enhancement of about 1.66 is produced if the time does not exceed one period ($\omega t < 2\pi$). However, as time increases, the maximum enhancement factor gradually increases when we are near resonance. This is to be expected because there is no damping in the problem and no cutoff of the force.

Another perhaps more realistic approximation to the applied force is provided by a half-wave pulse given by

$$F(t) = F_{\max} \left[u(t) \sin \omega t + u \left(t - \frac{\pi}{\omega} \right) \sin \omega \left(t - \frac{\pi}{\omega} \right) \right] \quad (10.48)$$

where $u(t)$ is a unit step at $t = 0$ and $u(t - \pi/\omega)$ is a unit step at $t = \pi/\omega$. This is illustrated in Figure 10.9c. The LT of Equation 10.48 is

$$\text{LT}(F) = \frac{\omega \left(1 + e^{-\frac{\pi}{\omega}s} \right)}{s^2 + \omega^2} \quad (10.49)$$

Substituting this into Equation 10.43, we get the LT of x :

$$\text{LT}(x) = \left(\frac{3}{\rho AL} \right) F_{\max} \frac{\omega \left(1 + e^{-\frac{\pi}{\omega}s} \right)}{(s^2 + b^2)(s^2 + \omega^2)} \quad (10.50)$$

Taking the inverse transform, we get

$$\begin{aligned} x = & \left(\frac{L}{EA} \right) F_{\max} \left[\frac{1}{1 - \left(\frac{\omega}{b} \right)^2} \right] \times \left\{ u(t) \left(\sin \omega t - \frac{\omega}{b} \sin bt \right) \right. \\ & \left. + u \left(t - \frac{\pi}{\omega} \right) \left[\sin \omega \left(t - \frac{\pi}{\omega} \right) - \frac{\omega}{b} \sin b \left(t - \frac{\pi}{\omega} \right) \right] \right\} \end{aligned} \quad (10.51)$$

where the quantity after $(L/EA)F_{\max}$ is the enhancement factor. For $b \gg \omega$, we get the static response $x = (L/EA)F$, with F given by Equation 10.48, that is, the bar extension is just proportional to the force with no enhancement. By numerically checking over a large grid of times and electrical frequencies, the maximum enhancement factor obtained is 1.77.

In practice, we use a force of 1.8 times the end thrust, provided it is more than 0.8 times the maximum compressive force over all the windings. Otherwise, we use 0.8 times the maximum compressive force over all the windings. Since the tie bars must support the weight of the core and coils during lifting, we check the stress in the tie bars produced by lifting. During lifting, we assume that the tie bars associated with the outer legs are stressed because the lifting hooks are positioned there. Both the short-circuit dynamic stresses and the lifting stresses must be below a maximum allowable stress in the tie bar material. We assume this maximum allowable stress to be 620 MPa if low carbon steel is used, and 414 MPa if a stainless steel is used for the tie bar material.

10.3.5 Stress in the Pressure Ring

The pressure ring receives the total end thrust of the windings. In our designs, it is made of pressboard about 38–63.5 mm thick. The ring covers the radial build of the windings with a small overhang. During a fault, the ring must support the full dynamic end thrust of the windings, which according to the previous section is 1.8 times the maximum total end thrust per leg or 0.8 times the maximum compressive force in all the windings, whichever is larger.

The end thrust or force is distributed over the end ring, producing an effective pressure:

$$P_{\text{ring}} = \frac{F_{\text{ring}}}{A_{\text{ring}}} \quad (10.52)$$

where we use “ring” to label the end force (F_{ring}) and the ring area (A_{ring}). The ring area is given by

$$A_{\text{ring}} = \frac{\pi}{4} (D_{\text{ring,out}}^2 - D_{\text{ring,in}}^2) \quad (10.53)$$

in terms of the outer and inner diameters of the ring. The ring is supported on radial blocks with space between them for the leads. This produces an unsupported span of a certain length, L_u . The problem is similar to that discussed in [Section 10.3.2](#) for the axial bending of a strand of wire. Thus, we can use Equation 10.16 for the maximum stress in the end ring, with $L = L_u$, $t = (1/2)(D_{\text{ring,out}} - D_{\text{ring,in}})$ the radial build of the ring, $h = h_{\text{ring}}$ the ring’s thickness, and $q = P_{\text{ring}}$ the force per unit length along the unsupported span. We get

$$\sigma_{x,\text{max}} = \frac{P_{\text{ring}}}{2} \left(\frac{L_u}{h_{\text{ring}}} \right)^2 = \frac{F_{\text{ring}}}{2A_{\text{ring}}} \left(\frac{L_u}{h_{\text{ring}}} \right)^2 \quad (10.54)$$

For pressboard rings, the maximum bending stress permissible is $\sigma_{\text{bend,max}} = 103$ MPa. Substituting this value for $\sigma_{x,\text{max}}$ and solving for F_{ring} corresponding to this limiting stress, we find

$$F_{\text{ring,max}} = \sigma_{\text{bend,max}} \left(\frac{\pi}{2} \right) (D_{\text{ring,out}}^2 - D_{\text{ring,in}}^2) \left(\frac{h_{\text{ring}}}{L_u} \right)^2 \quad (10.55)$$

This is the maximum end force the pressure ring can sustain, and it must be greater than the applied maximum end force.

The maximum deflection can be obtained by appropriate substitution into Equation 10.19.

10.3.6 Hoop Stress

The maximum radial pressure acting on the winding, as obtained from the force program, creates a hoop stress in the winding conductor. The hoop stress is tensile or compressive, depending on whether the pressure acts radially outward or inward. In Figure 10.10, we treat the winding as an ideal cylinder or ring subjected to a radially inward pressure, P_r . Let R_m be the mean radius of the cylinder and H its axial height. In Figure 10.10b, we show two compressive reaction forces F in the winding, sustaining the force applied to half the cylinder. The x -directed force produced by the pressure P_r cancels out by symmetry, and the net y -directed force acting downward is given by

$$F_y = P_r H R_m \int_0^\pi \sin \phi d\phi = 2 P_r H R_m \quad (10.56)$$

This is balanced by a force of $2F$ acting upward, so equating these we get $F = P_r H R_m$. Dividing this by the cross-sectional area A of the material sustaining the force, we get the compressive stress in the material:

$$\sigma_{\text{hoop}} = \frac{F}{A} = \frac{P_r H R_m}{A} \quad (10.57)$$

For $A = HB$, where B is the radial build of the cylinder, we get

$$\sigma_{\text{hoop}} = \frac{P_r R_m}{B} \quad (10.58)$$

Equation 10.58 assumes that the cylinder is made of a homogeneous material. If the cylinder is made of conductors and insulating materials, the conductors

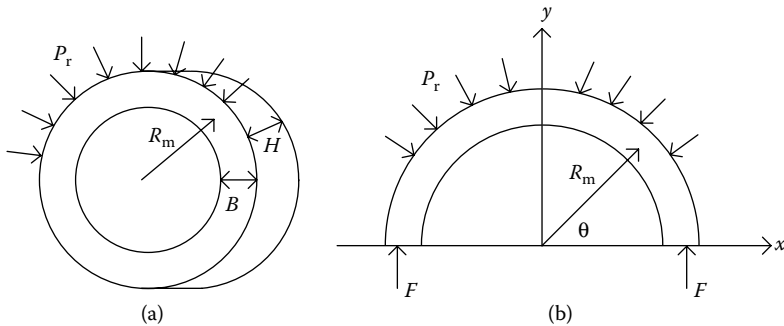


FIGURE 10.10

Geometry for determining the hoop stress in a cylinder acted on by a radially inward pressure: (a) the full cylinder and (b) half the cylinder showing the internal forces needed to maintain equilibrium.

primarily support the forces. In this case, A should equal the cross-sectional area of all the conductors in the winding, that is, $A = A_t N_t$, where A_t is the cross-sectional area of the conductors in a turn and N_t is the total number of turns in the winding. If the winding is center fed, that is, consists of two parallel windings on the same leg, and N_t refers to the total turns per leg or twice the number of electrical turns, then A_t should be half the turn area, that is, the area of the cable in either half of the winding. Substituting this into Equation 10.57 and using $D_m = 2R_m$, we get

$$\sigma_{\text{hoop}} = \frac{P_r H D_m}{2 A_t N_t} \quad (10.59)$$

for the hoop stress. This is compressive for P_r acting inward and tensile for P_r acting outward. In either case, this stress should not exceed the proof stress of the winding material.

When the radial pressure acts inward, the winding is apt to buckle before the proof stress is exceeded. This inward radial buckling is a complex process and will be discussed in [Section 10.4](#).

10.3.7 Radial Bending Stress

Windings have inner radial supports such as sticks made of pressboard or other material, which are spaced uniformly along their circumference and extend the height of the winding. When an inward radial pressure acts on the winding, the sections of the winding between supports act like a curved beam subjected to a uniform loading. A similar situation occurs in the case of a rotating flywheel with radial spokes. In the flywheel case, the loading (centrifugal force) acts outward, but otherwise, the analysis is similar. The flywheel example is analyzed by Timoshenko [Tim55], and we follow this here with minor changes.

We need to use Castigliano's theorem, which states that if the material of a system follows Hooke's law, that is, remains within the elastic limit, and if the displacements are small, then the partial derivative of the strain energy with respect to any force equals the displacement corresponding to the force. Here, force and displacement have a generalized meaning, that is, they can refer to torques or moments and angular displacements, as well as their usual meanings of force and length displacements. Also, the strain energy must be expressed as a quadratic function of the forces. For example, the strain energy U_{tensile} associated with tensile or compressive forces N in a beam of length L with elastic modulus E is

$$U_{\text{tensile}} = \int_0^L \frac{N^2}{2EA} dx \quad (10.60)$$

where N , A , and E can be functions of position along the beam x . The strain energy U_{bending} associated with a bending moment M in a beam of length L is

$$U_{\text{bending}} = \int_0^L \frac{M^2}{2EI} dx \quad (10.61)$$

where M , I , and E can be functions of position x and I is the area moment of inertia.

Figure 10.11a shows a portion of the winding with the inner radial supports spaced an angle 2α apart. There is a normal force X acting radially outward at the supports, and this counters the inward pressure, which has been converted to a force per unit length q acting on the coil section. The coil section is assumed to form a closed ring of radial build h , axial height t , and mean radius R .

Figure 10.11b shows a further isolated portion of the ring that extends in the adjacent midsections between the supports because there is no radially

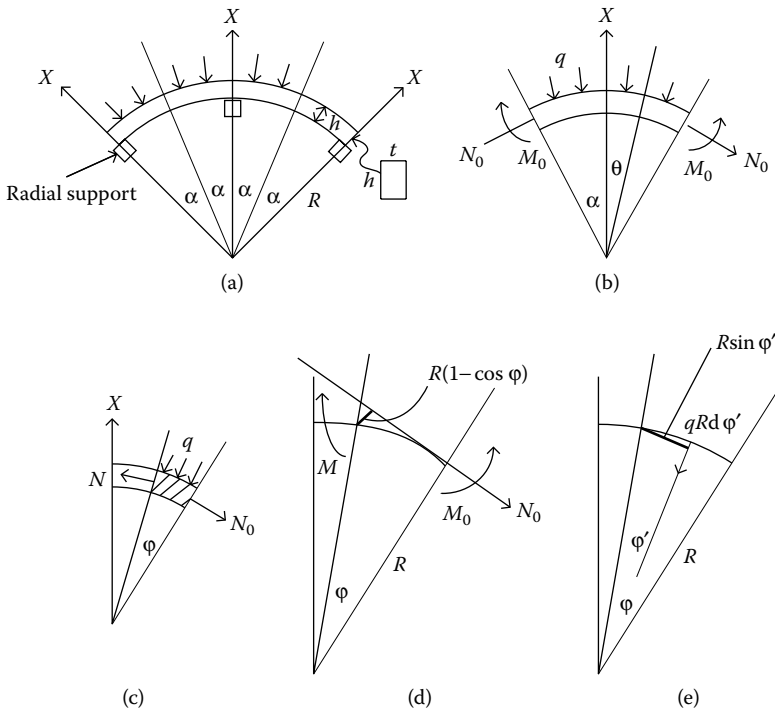


FIGURE 10.11

Geometry for determining the radial bending stresses: (a) pie-shaped section of winding covering two sections between radial supports, (b) section of winding between radial supports, (c) section of winding halfway between supports, (d) same as (c) but showing details of variables used in calculations, (e) same as (c) but showing further details of variables used in calculations.

directed (shearing) force acting on these mid-cross sections. This is because the distributed load between the midsections must balance the outward force at the included support through symmetry. Thus, the only reactions at the midsections are an azimuthally directed force N_0 and a couple M_0 , which need to be found.

Balancing the vertical forces, we have

$$X - 2N_0 \sin \alpha - 2qR \int_0^{\alpha} \cos \theta d\theta = 0 \quad (10.62)$$

Performing the integration and solving for N_0 , we get

$$N_0 = \frac{X}{2 \sin \alpha} - qR \quad (10.63)$$

At any cross section, as shown in [Figure 10.11c](#), by measuring angles from the midsection position with the variable ϕ we can obtain the normal force N from the static equilibrium requirement:

$$N = N_0 \cos \phi - qR \int_0^{\phi} \sin \phi' d\phi' \quad (10.64)$$

Integrating and substituting for N_0 from Equation 10.63, we get

$$N = \frac{X \cos \phi}{2 \sin \alpha} - qR \quad (10.65)$$

Similarly, using [Figures 10.11d](#) and 10.11e, we can obtain the bending moment at the cross section of angle ϕ from the midsection by balancing the moments:

$$M = M_0 - N_0 R (1 - \cos \phi) - qR^2 \int_0^{\phi} \sin \phi' d\phi' \quad (10.66)$$

Performing the integration and substituting for N_0 from Equation 10.63, we get

$$M = M_0 + \frac{XR(\cos \phi - 1)}{2 \sin \alpha} \quad (10.67)$$

Equations 10.65 and 10.67 express the normal force and bending moments as functions of position along the beam (arc in this case). These can be used in the energy expressions: Equations 10.60 and 10.61. Castigliano's theorem can then be used to solve for the unknowns. However, we are missing the strain energy associated with the supports. The radial supports consist of several different materials, as illustrated in [Figure 10.12](#). We assume that they can be treated as

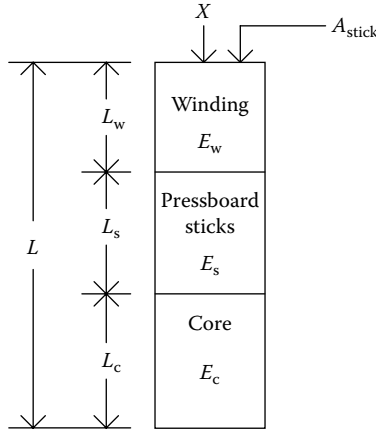


FIGURE 10.12
Radial support structure.

a column of uniform cross-sectional area A_{stick} . In general, the column consists of winding material (copper), pressboard sticks, and core steel. However, for an innermost winding, the winding material is not present as part of the support column. For such a composite structure, we derive an equivalent Young's modulus E_{eq} by using the fact that the stress is the same throughout the column and only the strain differs from material to material. We get

$$E_{\text{eq}} = \frac{L}{\frac{L_w}{E_w} + \frac{L_s}{E_s} + \frac{L_c}{E_c}} \quad (10.68)$$

where L_w is the length of the winding portion and E_w is its Young's modulus. Similarly, s refers to the stick and c refers to the core. $L = L_w + L_s + L_c$ is the total column length.

Retaining only the portion shown in [Figure 10.11b](#), since the entire ring energy is simply a multiple of this, the total strain energy for our system can be written

$$U = 2 \int_0^\alpha \frac{N^2 R}{2EA} d\phi + 2 \int_0^\alpha \frac{M^2 R}{2EI} d\phi + \frac{X^2 L}{2E_{\text{eq}} A_{\text{stick}}} \quad (10.69)$$

where N and M are given by Equations 10.65 and 10.67, A is the cross-sectional area of the ring ($A = th$), I is its bending moment ($I = th^3/12$), and the infinitesimal length along the bar $Rd\phi$ is used. The two unknowns are X and M_0 . At the fixed end of the support column (the center of the core), the displacement is zero, and hence by Castigliano's theorem $\partial U / \partial X = 0$. Also, the bending moment at the midsection of the span between the supports

produces no angular displacement by symmetry. Hence, by Castigliano's theorem, $\partial U / \partial M_0 = 0$. Differentiating Equation 10.69, we get

$$\frac{\partial U}{\partial X} = \frac{2R}{EA} \int_0^\alpha N \frac{\partial N}{\partial X} d\varphi + \frac{2R}{EI} \int_0^\alpha M \frac{\partial M}{\partial X} d\varphi + \frac{XL}{E_{eq} A_{stick}} = 0 \quad (10.70)$$

and

$$\frac{\partial U}{\partial M_0} = \frac{2R}{EA} \int_0^\alpha N \frac{\partial N}{\partial M_0} d\varphi + \frac{2R}{EI} \int_0^\alpha M \frac{\partial M}{\partial M_0} d\varphi = 0 \quad (10.71)$$

Substituting for N and M from Equations 10.65 and 10.67, we get

$$\begin{aligned} \frac{2R}{EA} \int_0^\alpha \left(\frac{X \cos \varphi}{2 \sin \alpha} - qR \right) \frac{\cos \varphi}{2 \sin \alpha} d\varphi + \frac{2R}{EI} \int_0^\alpha \left[M_0 + \frac{XR(\cos \varphi - 1)}{2 \sin \alpha} \right] \frac{R(\cos \varphi - 1)}{2 \sin \alpha} d\varphi \\ + \frac{XL}{E_{eq} A_{stick}} = 0 \end{aligned} \quad (10.72)$$

and

$$\frac{2R}{EI} \int_0^\alpha \left[M_0 + \frac{XR(\cos \varphi - 1)}{2 \sin \alpha} \right] d\varphi = 0 \quad (10.73)$$

Integrating Equations 10.72 and 10.73, we get

$$M_0 = \frac{XR}{2} \left(\frac{1}{\sin \alpha} - \frac{1}{\alpha} \right) \quad (10.74)$$

and

$$X = \frac{qR}{\frac{1}{4 \sin^2 \alpha} \left(\alpha + \frac{\sin 2\alpha}{2} \right) + \frac{AR^2}{I} \left[\frac{1}{4 \sin^2 \alpha} \left(\alpha + \frac{\sin 2\alpha}{2} \right) - \frac{1}{2\alpha} \right] + \frac{EA}{E_{eq} A_{stick}}} \quad (10.75)$$

where we have used the fact that $L = R$. Substituting this into Equations 10.65 and 10.67 and defining

$$\begin{aligned} f_1(\alpha) &= \frac{1}{4 \sin^2 \alpha} \left(\alpha + \frac{\sin 2\alpha}{2} \right) \\ f_2(\alpha) &= \frac{1}{4 \sin^2 \alpha} \left(\alpha + \frac{\sin 2\alpha}{2} \right) - \frac{1}{2\alpha} \end{aligned} \quad (10.76)$$

for N and M , we get

$$N = qR \left\{ \frac{\cos \phi}{2 \sin \alpha} \left[\frac{1}{f_1(\alpha) + \frac{AR^2}{I} f_2(\alpha) + \frac{EA}{E_{eq} A_{stick}}} \right] - 1 \right\} \quad (10.77)$$

$$M = \frac{qR^2}{2} \left(\frac{\cos \phi}{\sin \alpha} - \frac{1}{\alpha} \right) \left[\frac{1}{f_1(\alpha) + \frac{AR^2}{I} f_2(\alpha) + \frac{EA}{E_{eq} A_{stick}}} \right] \quad (10.78)$$

We also have

$$\frac{AR^2}{I} = 12 \left(\frac{R}{h} \right)^2 \quad (10.79)$$

where h is the radial build of the ring.

N gives rise to a normal stress:

$$\sigma_N = \frac{N}{A} = \frac{qR}{A} \left\{ \frac{\cos \phi}{2} \left(\frac{1}{\sin \alpha} \right) \left[\frac{1}{f_1(\alpha) + 12 \left(\frac{R}{h} \right)^2 f_2(\alpha) + \frac{EA}{E_{eq} A_{stick}}} \right] - 1 \right\} \quad (10.80)$$

and M gives rise to a bending stress that varies over the cross section, achieving a maximum tensile or compressive value of (Equation 10.14)

$$\sigma_M = \frac{Mh}{2I} = \frac{qR}{A} \left(\frac{3R}{h} \right) \left(\cos \phi - \frac{\sin \alpha}{\alpha} \right) \left(\frac{1}{\sin \alpha} \right) \left[\frac{1}{f_1(\alpha) + 12 \left(\frac{R}{h} \right)^2 f_2(\alpha) + \frac{EA}{E_{eq} A_{stick}}} \right] \quad (10.81)$$

We have factored out the term qR/A since this can be shown to be the hoop stress in the ring. (In Equation 10.57, PH corresponds to q and R_m to R in our development here.) Thus, σ_{hoop} will be substituted in the following equations for qR/A , where σ_{hoop} is given by Equation 10.59.

TABLE 10.1Tabulated Values for $f_1(\alpha)$ and $f_2(\alpha)$ and $\sin \alpha$ Times These Quantities

No. of Sticks/Circle	α (°)	$f_1(\alpha)$	$f_2(\alpha)$	$\sin \alpha f_1(\alpha)$	$\sin \alpha f_2(\alpha)$
2	90	0.3927	0.07439	0.3927	0.07439
4	45	0.6427	0.006079	0.4545	0.004299
6	30	0.9566	0.001682	0.4783	0.0008410
8	22.5	1.2739	0.0006931	0.4875	0.0002652
10	18	1.5919	0.0003511	0.4919	0.0001085
12	15	1.9101	0.0002020	0.4944	0.00005228
18	10	2.8648	0.00005942	0.4975	0.00001032
24	7.5	3.8197	0.00002500	0.4986	0.00000326
30	6	4.7747	0.00001279	0.4991	0.00000134

We now need to add σ_N and σ_M in such a way to produce the worst-case stress in the ring. The quantity

$$\frac{1}{\sin \alpha \left[f_1(\alpha) + 12 \left(\frac{R}{h} \right)^2 f_2(\alpha) + \frac{EA}{E_{eq} A_{stick}} \right]} \quad (10.82)$$

occurs in both stress formulas. We have tabulated $f_1(\alpha)$, $f_2(\alpha)$, and $\sin \alpha$ times these in Table 10.1 for a range of α values.

For any other choice of parameters, Equation 10.82 is positive. In Equation 10.81, the magnitude of σ_M for fixed α is determined by the term $(\cos \varphi - \sin \alpha / \alpha)$, where φ can range from 0 to α . This achieves a maximum in absolute value at $\varphi = \alpha$. The stress can have either sign depending on whether it is on the inner or outer radial surface of the ring. In Equation 10.80, the magnitude of σ_N achieves a maximum at $\varphi = \alpha$ for virtually any other parameters. It has a negative sign consistent with the compressive nature of the applied force. Thus, σ_N and σ_M should be added with each having a negative sign at $\varphi = \alpha$ to get the maximum stress. We get

$$\sigma_{\max} = \sigma_{\text{hoop}} \left\{ \frac{\cos \alpha}{2 \sin \alpha} \left[\frac{1}{f_1(\alpha) + 12 \left(\frac{R}{h} \right)^2 f_2(\alpha) + \frac{EA}{E_{eq} A_{stick}}} \right] \right. \quad (10.83)$$

$$\left. - 1 + \frac{3R}{h} \left(\cos \alpha - \frac{\sin \alpha}{\alpha} \right) \left(\frac{1}{\sin \alpha} \right) \left[\frac{1}{f_1(\alpha) + 12 \left(\frac{R}{h} \right)^2 f_2(\alpha) + \frac{EA}{E_{eq} A_{stick}}} \right] \right\}$$

This stress is negative, although it is usually quoted as a positive number. It occurs at the support.

We have analyzed a ring subjected to a hoop stress having radial supports. A coil is usually not a monolithic structure but consists of a number of cables radially distributed. The cables can consist of a single strand of conductor as in the case of magnet wire or be multistranded, which can also be bonded. The average hoop stress in the winding will be nearly the same in all the cables because the paper insulation tends to equalize it. We will examine this in more detail in [Section 10.5](#). The radial thickness h in the equations should refer to a single cable. If it is a magnet wire, then its radial thickness should be used. If it is a multistranded transposed cable, then something less than its radial thickness should be used because this is not a homogeneous material. If it is unbonded, we use twice the thickness of an individual strand as its effective radial build. If it is bonded, we use 80% of its actual radial thickness as its effective radial build.

10.4 Radial Buckling Strength

Buckling occurs when a sufficiently high force causes a structure to deform its shape to the point where it becomes destabilized and may collapse. The accompanying stresses may in fact be small and well below the proof stress of the material. An example is a slender column subjected to an axial compressive force. At a certain value of the force, a slight lateral bulge in the column can precipitate a collapse. Another example is that of a thin ring subjected to a uniform compressive radial pressure. A slight deformation in the circular shape of the ring can cause a collapse if the radial pressure is high enough. This critical radial pressure produces a hoop stress (see [Section 10.3.6](#)), called the critical hoop stress, which can be well below the proof stress of the material. In general, the smaller the ratio of the radial build to the radius of the ring, the smaller the critical hoop stress. Thus, buckling is essentially an instability problem and is analyzed by assuming a small distortion in the shape of the system under study and determining under what conditions this leads to collapse.

We examine the possible buckling of a winding subjected to an inward radial pressure. We will treat an individual cable of the winding as a closed ring as was done in [Section 10.3](#), since the cables are not bonded to each other. In free unsupported radial buckling, the assumption is that there are no inner supports. Thus, the sticks spaced around the inside circumference of a winding are assumed to be absent. We can argue that there is sufficient looseness in this type of support that the onset of buckling occurs as if these supports were absent, and once started, the buckling process continues toward collapse or permanent deformation. We can also argue that even

though buckling may begin in the absence of supports, before it progresses very far the supports are engaged and from then on it becomes a different type of buckling, called forced or constrained buckling. The key to the last argument is that even though free buckling has begun, the stresses in the material are quite low, resulting in no permanent deformation, and the process is halted before collapse.

10.4.1 Free Unsupported Buckling

Timoshenko [Tim55] analyzes free buckling of a circular ring in some detail and quotes the results for forced buckling. The lowest-order shape distortion away from a circle is taken to be an ellipse. This is shown in [Figure 10.13](#) along with the parameters used to describe the system. R is the radius of the ring, h is the radial thickness, and q is the uniform inward force per unit length along the ring's outer surface. The analysis assumes a thin ring so that R can be taken to be a mean radius. It also assumes that the ring is uniform in the direction along the ring's axis.

For this lowest buckling mode, the critical load, that is, the critical force per unit length q_{crit} which will precipitate buckling, is given by

$$q_{\text{crit}} = \frac{3EI}{R^3} \quad (10.84)$$

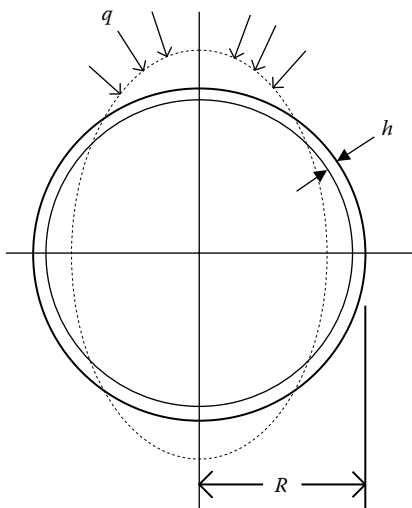


FIGURE 10.13

Buckling of a circular ring. The distorted elliptical shape, which is the lowest buckling mode, and the system parameters are shown.

where E is Young's modulus of the hoop material and I is the area moment of inertia, $I = th^3/12$, and t is the thickness of the ring in the direction of the ring's axis. We can convert q_{crit} to a critical pressure by dividing by t . This pressure P_{crit} is given by

$$P_{\text{crit}} = \frac{3EI}{tR^3} \quad (10.85)$$

We can then use this in Equation 10.58 and substitute h for B to get

$$\sigma_{\text{crit}} = \frac{3EI}{thR^2} = \frac{1}{4}E\left(\frac{h}{R}\right)^2 \quad (10.86)$$

This is the critical hoop stress. It depends geometrically only on the ratio of the radial build to the radius of the ring.

Since buckling occurs after the stress has built up in the ring to the critical value and increases incrementally beyond it, the appropriate modulus to use in Equation 10.86 is the tangential modulus since this is associated with incremental changes. This argument for using the tangential modulus is based on an analogous argument for the buckling of slender columns together with supporting experimental evidence given in [Tim55]. We will assume it applies to thin rings as well.

The tangential modulus can be obtained graphically from the stress-strain curve for the material, as illustrated in Figure 10.14a. However, the

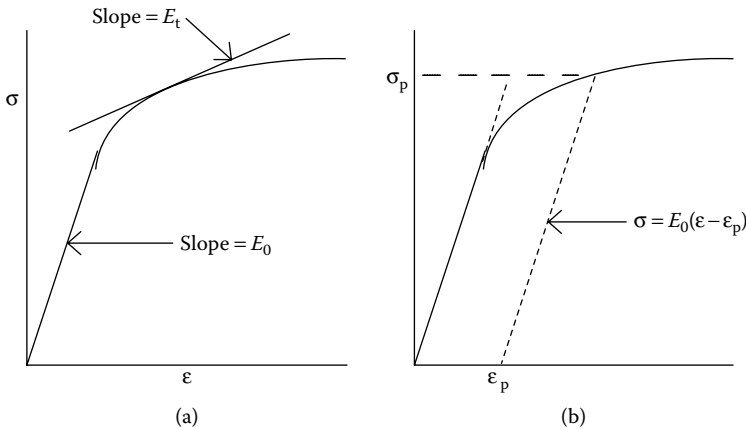


FIGURE 10.14

Stress-strain curve and derived quantities: (a) initial (E_0) and tangential (E_t) moduli and (b) proof stress.

stress–strain curve can be parametrized for copper, the material of interest here, of different hardnesses according to [Tho79] by

$$\sigma = \frac{E_0 \epsilon}{\left[1 + k \left(\frac{\sigma}{\sigma_0} \right)^m \right]} \quad (10.87)$$

where $k = 3/7$, $m = 11.6$, and $E_0 = 1.10 \times 10^5$ MPa. σ_0 depends on the hardness of copper. The tangential modulus obtained from this is

$$E_t = \frac{d\sigma}{d\epsilon} = \frac{E_0}{\left[1 + \gamma \left(\frac{\sigma}{\sigma_0} \right)^m \right]} \quad (10.88)$$

where $\gamma = k(m + 1) = 5.4$. Substituting E_t from Equation 10.88 for E in Equation 10.86, we obtain a formula for self-consistently determining the critical stress:

$$\sigma_{\text{crit}}^{m+1} + \frac{\sigma_0^m}{\gamma} \sigma_{\text{crit}} - \frac{\sigma_0^m}{4\gamma} E_0 \left(\frac{h}{R} \right)^2 = 0 \quad (10.89)$$

This can be solved by Newton–Raphson iteration.

The parameter σ_0 is generally not provided by the wire or cable supplier. It can be obtained by fitting a supplied stress–strain curve. Alternatively and more simply, it can be obtained from the proof stress of the material that is generally provided or specified. As we move along a stress–strain curve and then remove the stress, the material does not move back toward zero stress along the same curve it followed when the stress increased, but rather it follows a straight line parallel to the initial slope of the stress–strain curve, as illustrated in [Figure 10.14b](#). This leaves a residual strain (ϵ_p) in the material, corresponding to the stress σ_p , which was the highest stress achieved before it was removed. For $\epsilon_p = 0.002$ (0.2%), σ_p is called the proof stress. Some people use $\epsilon_p = 0.001$ in this definition.

Thus, the proof stress is determined from the intersection of the recoil line:

$$\sigma = E_0(\epsilon - \epsilon_p) \quad (10.90)$$

with the stress–strain curve given by Equation 10.87. Solving Equations 10.87 and 10.90 simultaneously, we find

$$\sigma_0 = \left(\frac{k}{E_0 \epsilon_p} \right)^{1/m} \sigma_p^{(m+1)/m} \quad (10.91)$$

This permits us to find σ_0 from a given proof stress σ_p corresponding to the appropriate ϵ_p . For a proof stress of 170 MPa at 0.2% strain ($\epsilon_p = 0.002$), we obtain $\sigma_0 = 154.5$ MPa for copper.

10.4.2 Constrained Buckling

Forced or constrained buckling is when the axial supports (sticks) are engaged in the buckling process. Since there is some looseness in the supports because they do not rigidly clamp the winding cable, they can be considered a hinged type of support. Because this type of support allows a freer pivoting action, this type of buckling may also be referred to as free supported buckling. In this case, the lowest-order buckling mode is shown in Figure 10.15. The corresponding critical force per unit length q_{crit} is given by [Tim55]

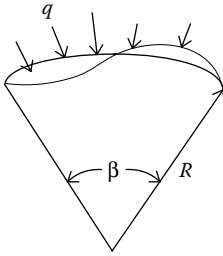


FIGURE 10.15
Buckling of a circular hinged arch.

$$q_{\text{crit}} = \frac{EI}{R^3} \left[\left(\frac{2\pi}{\beta} \right)^2 - 1 \right] \quad (10.92)$$

where β is the angle between the outer supports. This corresponds to a critical hoop stress of

$$\sigma_{\text{crit}} = \frac{E_t}{12} \left(\frac{h}{R} \right)^2 \left[\left(\frac{2\pi}{\beta} \right)^2 - 1 \right] \quad (10.93)$$

where h is the radial build of the arch. This will exceed the free buckling critical stress (Equation 10.86) when $\beta < \pi$. $\beta = \pi$ corresponds to two end supports. Thus, for most cases where $\beta \ll \pi$, the constrained buckling stress is much larger than the free buckling stress. Both buckling types depend on the radial build of the ring or arch. We will adopt the same procedure for determining the effective radial build of a cable as we used for the radial bending stress determination at the end of [Section 10.3.7](#).

Since we can also imagine that a loose or hinged support exists at the center point of the arch in Figure 10.15, we should take β as twice the angle between supports (sticks). Letting n be the number of radial supports around the winding circumference so that $\beta = 4\pi/n$, we can write Equation 10.93 as

$$\sigma_{\text{crit}} = \frac{E_t}{12} \left(\frac{h}{R} \right)^2 \left[\frac{n^2}{4} - 1 \right] \quad (10.94)$$

Substituting the tangential modulus from Equation 10.88 into this formula, we obtain a formula for self-consistently determining the critical stress:

$$\sigma_{\text{crit}}^{m+1} + \frac{\sigma_0^m}{\gamma} \sigma_{\text{crit}} - \frac{\sigma_0^m}{12\gamma} E_0 \left(\frac{h}{R} \right)^2 \left[\frac{n^2}{4} - 1 \right] = 0 \quad (10.95)$$

This is similar to the procedure used to get Equation 10.89. Equation 10.95 can be solved by Newton–Raphson iteration.

Arched buckling with this value of β appears to provide a more realistic value of buckling strength in practice than totally free unsupported buckling. There is increasing experimental evidence for this [Sar00]. One such experiment will be described in the next section.

10.4.3 Experiment to Determine Buckling Strength

This section is largely based on a presentation at a Doble Conference [Del01]. A small (5-MVA), three-phase, two-winding per phase, three-leg core transformer was designed with the inner low-voltage (LV) windings on each leg wound with different conductors. It had terminal line-to-line voltages of 13.2 kV for the high-voltage (HV) winding and 3.6 kV for the LV winding and was Y-Y connected. The leakage impedance was 5.8% at 5 MVA. There were no taps, so the windings were uniform except for crossovers. The outer HV winding was the same for all the legs. Details concerning the HV winding and the two inner windings that failed by buckling are given in Table 10.2. The LV windings that failed by buckling were on the outer two legs of the transformer, labeled LV1 and LV2.

TABLE 10.2

Geometric and Other Parameters for the Windings

Winding	HV	LV1	LV2
Inner diameter (mm)	444.5	343	343
Radial build (mm)	35	25.4	25.4
Height (mm)	1041	1067	1067
Number of disks	72	76	76
Electrical turns/disk	4	1	1
Total turns	288	76	76
Wire type	Magnet	Magnet	Magnet
Copper strand thickness (mm)	3.56	3.68	2.67
Copper strand width (mm)	10.9	10.2	10.2
Paper thickness (two-sided) (mm)	0.762	0.305	0.305
Number of strands/disk	8	6	8
Number of radial supports (sticks)	12	12	12
Proof stress (MPa)	207	194	348

The unit was tested at the Powertech Labs in Surrey, British Columbia, Canada. The phases (legs) were tested separately and sequentially at each power level, starting from 80% of the design voltage and increasing in steps of ~10% until failure occurred. The voltage was applied to the HV winding, with the LV winding shorted to ground before the unit was energized. The voltage application was timed to produce maximum offset in the current. A typical voltage-current readout is shown in Figure 10.16. The total duration of the short-circuit event was ~0.25 seconds. Two shots per leg were performed before going to the next voltage level. A visual inspection of the windings was conducted after each shot via a Plexiglas window in the transformer tank. In addition, the impedance was calculated after each test from the ratio of voltage to current.

A frequency response analysis (FRA) was performed on each leg after the two shot sequences or after a single shot if an impedance change occurred. The FRA was performed by applying a sharp impulse to the HV winding and measuring the current in the LV winding. The results were displayed as a transfer admittance versus frequency. The transferred admittance plot was then compared with that obtained initially before the tests began. [Figure 10.17](#)

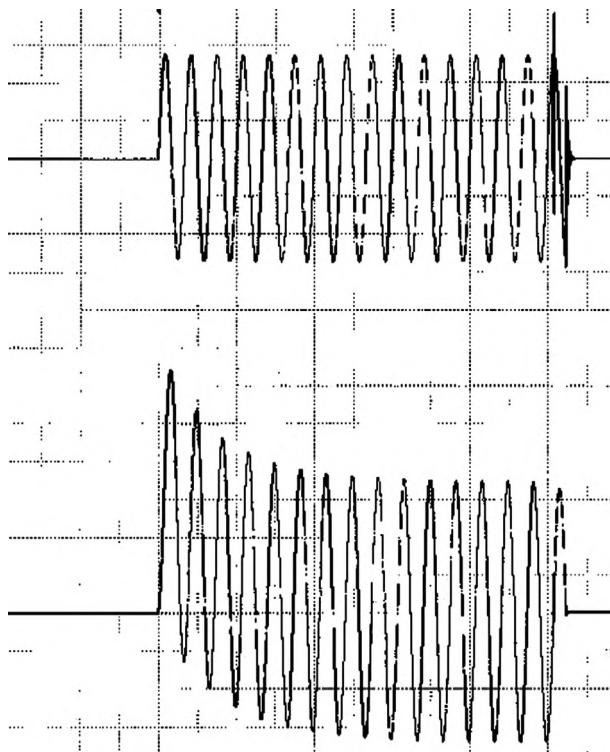


FIGURE 10.16

Short-circuit HV applied phase voltage (top) and resulting current (bottom) for a typical test.

shows such a comparison when the leg was considered to have passed the short-circuit event, while Figure 10.18 shows a comparison when the unit failed. No further tests were performed after a failure based on the FRA occurred. An impedance change of 2% and 13% also occurred in the two legs when an FRA failure was indicated. Prior to failure, the impedance changes were <1% and were possibly due to measurement uncertainties.

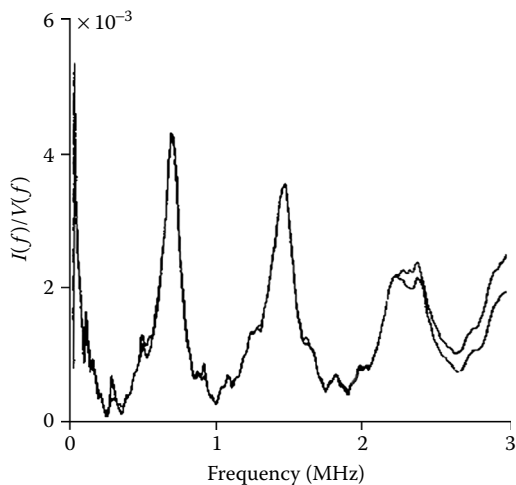


FIGURE 10.17

Comparison of the admittance versus frequency plot measured after a shot with the initial admittance plot for a passing case.

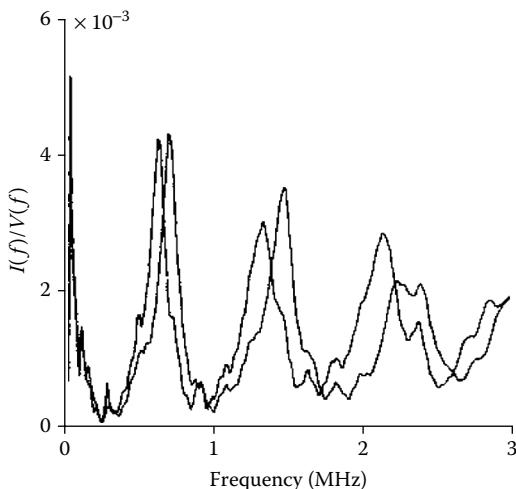


FIGURE 10.18

Comparison of the admittance versus frequency plot measured after a shot with the initial admittance plot for a failed case.

The middle leg failed in an axial mode. This failure, in addition to a large impedance and FRA change, was visually obvious because the outer winding of this leg collapsed. The failure mode of the two outer legs was only evident from the impedance and FRA changes, since the outer windings appeared normal after the failure. We shipped the unit back to our plant and disassembled it to find the cause of the failure. As Figures 10.19 and 10.20 show, the failure mode was radial buckling of the inner winding. It is also clear, from the position of the sticks relative to the winding distortion, that the sticks were actively involved in the failure. We can see in both figures that the winding bulges outward between two adjacent sticks and inward between adjacent sticks on opposite sides of the bulge. It can also be seen that all the turns participate in the buckling, that is, the entire radial build appears to buckle as a unit. The torn paper in the figures occurred while disassembling the windings.

Both inner windings failed in buckling at nearly the same current, which had a peak value at maximum offset in the HV winding of 13,300 A. Using this current and the LV current required for amp-turn balance in our computer program that calculates the magnetic flux, forces, and stresses, we

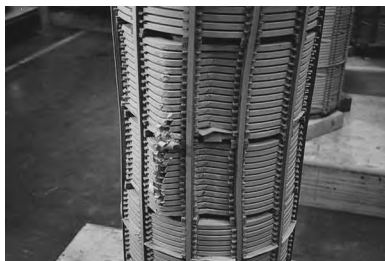


FIGURE 10.19

(See color insert following page 338.) View of the inner winding of LV1, which buckled over about the middle-third of its axial height.



FIGURE 10.20

(See color insert following page 338.) View of the inner winding of LV2, which buckled in two different areas, both radially and axially displaced from each other. One area is facing the viewer, and the other can be seen in silhouette on the upper right of the winding. Each buckling area covered about one-third of the winding's axial height.

TABLE 10.3
Measured and Calculated Buckling Hoop Stresses in the Inner Windings

Winding and modulus ratio	LV1	E_t/E_0	LV2	E_t/E_0
Max hoop stress at test failure (MPa)	88.4		90.4	
Buckling stress				
Free unsupported (MPa)	11.0	1.0	5.8	1.0
Constrained ($\beta = 360^\circ/6$) (MPa)	121.2	0.942	67.5	1.0
Constrained ($\beta = 360^\circ/12$) (MPa)	164.8	0.313	244.1	0.885

obtain the maximum compressive hoop stresses in the LV windings given in Table 10.3. A calculation of how the stress is distributed across the radial build of the winding, taking the paper layers into account, produced a variation of $\pm 2\%$, with the higher stress on the inner conductor. This calculation is similar to that in [Tho79].

In applying the buckling formulas, h was chosen to be the radial build of a bare copper strand and R was chosen as the average winding radius. The tangential modulus E_t was obtained by the method proposed here. It is given Table 10.3 as a ratio with respect to the initial modulus E_0 , where $E_0 = 1.10 \times 10^5$ MPa for copper.

As we can see in Table 10.3, the free unsupported buckling stress is far below the actual hoop stress at failure. This buckling mode also has an elliptical shape that is not observed. The constrained buckling mode stress with $\beta = 360^\circ/12$, the angle between the radial supports, is much too high when compared with the actual failure stress. The buckling shape also does not agree with the observed shape. The constrained buckling stress with $\beta = 360^\circ/6$, twice the angle between the radial supports, is fairly close to the actual failure stress. In addition, the buckling shape for this mode agrees with observation.

10.5 Stress Distribution in a Composite Wire–Paper Winding Section

The hoop stress calculated for a winding section or disk in [Section 10.3.6](#) was an average over the disk. In reality, for the innermost winding, the axial magnetic field varies from nearly zero on the inside of the winding to close to its maximum value at the outer radius of the winding. Because the current density is uniform, the force density also varies in the same fashion as the magnetic field. Thus, we might expect higher hoop stresses in the outermost turns as compared with the inner turns. However, because of the layered structure with paper insulation between turns, all of the turns tend to share the stresses more equally. This effect will be examined next in order to determine the

extent of the stress nonuniformity so that, if necessary, corrective action can be taken.

We will now analyze an ideal ring geometry, as shown in Figure 10.21, where r_{ci} denotes the inner radius of the i th conductor layer and r_{pi} is the inner radius of the i th paper layer, where $i = 1, \dots, n$ for the conductors and $i = 1, \dots, n - 1$ for the paper layers. Because of the assumed close contact, the outer radius of the i th conductor layer equals the inner radius of the i th paper layer, and the outer radius of the i th paper layer equals the inner radius of the $i + 1$ th conductor layer. We do not need to include the innermost or outermost paper layers because they are essentially stress free.

We assume that the radial force density varies linearly from the innermost to outermost conductor layers. Thus,

$$f_{ci} = \frac{f_o i}{n} \quad (10.96)$$

where f_o is the maximum force density at the outermost conductor. We wish to express this in terms of the average force density, f_{ave} . We have

$$f_{ave} = \frac{1}{n} \sum_{i=1}^n f_{ci} = \frac{f_o}{n^2} \sum_{i=1}^n i = \frac{f_o(n+1)}{2n} \quad (10.97)$$

Solving for f_o and substituting into Equation 10.96, we get

$$f_{ci} = \frac{2f_{ave}}{n+1} i \quad (10.98)$$

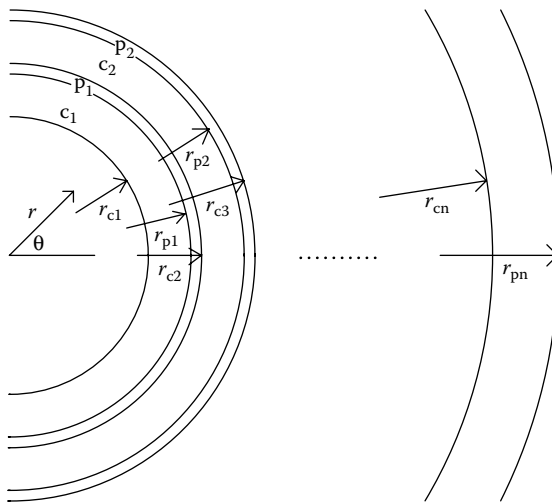


FIGURE 10.21

Conductor-paper-layered ring winding section. ci refers to conductor i and pi to paper layer i .

It is even more convenient to relate f_{ci} to the average hoop stress in the winding that results from these radial forces. We related this stress to the radial pressure in Equation 10.58, but the average force density is just the average radial pressure divided by the winding radial build. Therefore, from Equation 10.58, we find

$$\sigma_{\text{ave,hoop}} = \frac{P_r R_m}{B} = f_{\text{ave}} R_m \quad (10.99)$$

where R_m is the mean radius of the winding. Thus, Equation 10.98 can be written

$$f_{ci} = \frac{2\sigma_{\text{ave,hoop}}}{R_m(n+1)} i \quad (10.100)$$

We assume that the winding section can be analyzed as a two-dimensional stress distribution problem, that is, stress variations in the axial direction are assumed to be small. For this type of problem in polar coordinates, in which only radial forces are acting and the geometry is cylindrically symmetric [Tim70], the governing equation is

$$\frac{\partial \sigma_r}{\partial r} + \frac{\sigma_r - \sigma_\phi}{r} + f_r = 0 \quad (10.101)$$

where σ_r is the radial stress, σ_ϕ is the azimuthal stress, and f_r is the radial force density. The stresses are related to the strains for the two-dimensional plane stress case by

$$\sigma_r = \frac{E}{1-\nu^2} (\epsilon_r + \nu \epsilon_\phi), \quad \sigma_\phi = \frac{E}{1-\nu^2} (\epsilon_\phi + \nu \epsilon_r) \quad (10.102)$$

where E is Young's modulus and ν is Poisson's ratio ($\nu = 0.25$ for most materials). The radial and azimuthal strains, ϵ_r and ϵ_ϕ , are related to the radial displacement u , in the cylindrically symmetric case, by

$$\epsilon_r = \frac{du}{dr}, \quad \epsilon_\phi = \frac{u}{r} \quad (10.103)$$

Substituting Equations 10.102 and 10.103 into 10.101, we get

$$r^2 \frac{d^2 u}{dr^2} + r \frac{du}{dr} - u + \frac{f_r (1-\nu^2)}{E} r^2 = 0 \quad (10.104)$$

with the general solution

$$u = Ar + \frac{B}{r} + Kr^2 \quad (10.105)$$

where A and B are constants to be determined by the boundary conditions and

$$K = -\frac{f_r(1 - \nu^2)}{3E} \quad (10.106)$$

Note that for our problem, f_r is negative (radially inward) so that K is positive. In the paper layers, $K = 0$ since there is no force density there. Using Equation 10.105 for u in Equation 10.103, we obtain for Equation 10.102

$$\begin{aligned} \sigma_r &= \frac{E}{1 - \nu^2} \left[A(1 + \nu) - \frac{B}{r^2}(1 - \nu) + Kr(2 + \nu) \right] \\ \sigma_\phi &= \frac{E}{1 - \nu^2} \left[A(1 + \nu) + \frac{B}{r^2}(1 - \nu) + Kr(1 + 2\nu) \right] \end{aligned} \quad (10.107)$$

Equations 10.105 through 10.107 apply to each layer of conductor or paper. We therefore need to introduce labels to distinguish the layers. Let A_{ci} and B_{ci} apply to conductor layer i and A_{pi} and B_{pi} apply to paper layer i . Let c_i and p_i also label the displacements, u , and the stresses σ_r and σ_ϕ for the corresponding layer. At the conductor–paper interface, the displacements must match:

$$\begin{aligned} u_{ci}(r_{pi}) &= u_{pi}(r_{pi}), \quad i = 1, \dots, n-1 \\ u_{ci}(r_{ci}) &= u_{p(i-1)}(r_{ci}), \quad i = 2, \dots, n \end{aligned} \quad (10.108)$$

There are $2(n-1)$ such equations (Figure 10.21). Also at the interface, the radial stresses must match:

$$\begin{aligned} \sigma_{r,ci}(r_{pi}) &= \sigma_{r,pi}(r_{pi}), \quad i = 1, \dots, n-1 \\ \sigma_{r,ci}(r_{ci}) &= \sigma_{r,p(i-1)}(r_{ci}), \quad i = 2, \dots, n \end{aligned} \quad (10.109)$$

There are also $2(n-1)$ such equations. At the innermost and outermost radii, we also have

$$\sigma_{r,c1}(r_{c1}) = 0, \quad \sigma_{r,cn}(r_{pn}) = 0 \quad (10.110)$$

This provides two more equations, and thus, altogether we have $4n-2$ equations. There are two unknowns, A_{ci} and B_{ci} , associated with each conductor layer for a total of $2n$ unknowns and two unknowns, A_{pi} and B_{pi} , associated with each paper layer for a total of $2(n-1)$ unknowns because there are only $n-1$ paper layers. Thus, there are altogether $4n-2$ unknowns to solve for; this matches the number of equations. In Equation 10.107, we must use

the appropriate material constants for the conductor or paper layer, that is, $E = E_c$ or E_p is the conductor's or paper's Young's modulus and $\nu = \nu_c$ or ν_p for the conductor's or paper's Poisson's ratio. In addition, K needs to be labeled according to the layer, that is, K_{ci} , and in the case of a paper layer, $K_{pi} = 0$.

The resulting set of $4n - 2$ equations in $4n - 2$ unknowns is a linear system and can be solved using standard methods. Once the solution is obtained, Equation 10.107 can be used to find the stresses. The σ_ϕ can then be compared with the average hoop stress to see how much deviation from a uniform distribution exists. Table 10.4 shows a sample calculation. The average stresses are calculated for the conductor and paper, and then the stresses in the layers are expressed as multipliers of this average stress. These multipliers are

TABLE 10.4

Sample Stress Distribution in a Composite Conductor–Paper Disk

Input				
Winding inner radius	381 mm			
Winding outer radius	457 mm			
Number of radial turns	10			
Conductor layer radial thickness	6.35 mm			
Paper layer radial thickness	1.27 mm			
Average hoop stress	124.1 MPa			
$E_c = 1.1 \times 10^5$ MPa				
$E_p = 2.07 \times 10^2$ MPa				
$\nu_c = \nu_p = 0.25$				
Output				
Average hoop stress in conductor layers	127.6 MPa			
Average hoop stress in paper layers	1.08 MPa			
Average radial stress in conductor layers	3.03 MPa			
Average radial stress in paper layers	3.38 MPa			
Average stress multipliers				
Layer	Conductor		Paper	
	Hoop	Radial	Hoop	Radial
1	0.90	0.28	0.60	0.51
2	0.91	0.78	0.89	0.89
3	0.93	1.13	1.10	1.15
4	0.96	1.36	1.23	1.30
5	0.99	1.47	1.27	1.35
6	1.03	1.47	1.24	1.30
7	1.06	1.35	1.12	1.14
8	1.08	1.12	0.92	0.87
9	1.09	0.76	0.63	0.50
10	1.08	0.28		

averages for the layers since the stresses vary across a layer. The input is the geometric data and the average hoop stress in the conductor, which is obtained from the radial pressure via Equation 10.99. The calculated average hoop stress in the conductor does not quite agree with the input, probably because of numerical approximations in the averaging method. The hoop stress in the conductors varies by about 20% from the inner to the outer layers. The other stresses are small in comparison although they show considerable variation across the winding. The stresses are shown as positive, even though they are compressive and therefore negative.

10.6 Additional Mechanical Considerations

During a short circuit, the leads or busbars are subjected to an increased force due to the higher fault current they carry and its interaction with the higher leakage flux from the main windings and from nearby leads. These forces will depend on the detailed positioning of the leads with respect to the main windings and with respect to each other and will therefore vary considerably from design to design. The leads must be braced properly so that they do not deform or move much during a fault. The leakage flux in the vicinity of the lead can be obtained from a finite element calculation. The flux produced by neighboring leads can be determined using the Biot–Savart law. From these, the forces on the leads can be determined, and the adequacy of the bracing can be checked. In general, the bracing should contain sufficient margin based on past experience so that the above rather laborious analysis will only be necessary for unusual or novel designs.

We have neglected gravitational forces in this chapter, except for the effect of the core and coil weight on the tie bar stress during lifting. Gravitational forces will affect the compressive force on the key spacers and on the downward end thrust, which acts on the bottom pressure ring. Another force that was neglected is the compressive force, which is initially placed on the coils by pretensioning the tie bars. This force adds to the compressive force on the key spacers and to the top and bottom thrust on the pressure ring, and adds some initial tension to the tie bars. Because the compressive forces on the key spacers are involved in conductor tilting, this design criterion will also be affected. These additional forces are present during normal operation and will add to the fault forces when a fault occurs.

We have treated the axial and radial stress calculations independently, but in reality, axial and radial forces are applied simultaneously, resulting in a biaxial stress condition. The results of such a combined analysis for a circular arched wire segment between supports have been reported and agree with experimental results [Ste72]. In this type of analysis, the worst-case stress condition is not necessarily due to the largest axial or radial forces because

these do not usually occur at the same position along the winding; it is rather due to some combination of the two, which should be examined at each position along the winding at which the forces are calculated.

The axial and radial analyses can be performed separately as long as the materials remain linear, that is, they obey Hooke's law, and the displacements are small. The resulting stresses can then be combined appropriately to obtain the overall stress state, and various criteria for failure can be applied to this overall stress state. Our strategy of looking at the worst-case stresses produced by the axial and radial forces separately and then applying a failure criterion to each is probably a good approximation, especially since the worst-case axial and radial forces typically occur at different positions along the winding. The radial forces are produced by axial flux, which is high in the middle of the winding, whereas the axial forces are produced by radial flux, which is high at the ends of the winding.

Some authors study dynamical effects, particularly the axial response of a winding to a suddenly applied short-circuit current [Bos72], [Ste72]. They have found that the level of prestress is important. When the prestress is low (~10% of normal), the winding literally bounces against the upper support, resulting in a much higher than expected force. The enhancement factor over the expected nondynamical maximum force is about 4. However, when the prestress is normal or above, there is no enhancement over the expected maximum force. The prestress also affects the natural frequency of the winding to oscillations in the axial direction. Higher prestress tends to shift this frequency toward higher values, away from the frequencies in the short-circuit forces. Hence, little dynamical enhancement is expected under these conditions. Thus, if sufficient prestress is applied to clamp the windings in the axial direction, there will be little or no enhancement of the end thrust over the expected value based on the maximum fault currents. However, as the unit ages, the prestress can decrease. With modern precompressed pressboard key spacers, this effect is small. However, we allow an enhancement factor of 1.8 in design.

An area of some uncertainty is how to treat transposed cable, with or without bonding, in the stress calculations. It is not exactly a solid homogeneous material, yet it is not simply a loose collection of individual strands. We believe that we have taken a conservative approach in our calculations. However, further experimental work in this area will be useful.

11

Electric Field Calculations

11.1 Simple Geometries

We can often obtain a good estimation of the electric field in a certain region of a transformer by idealizing the geometry to such an extent that the field can be calculated analytically. This has the advantage of exhibiting the field as a function of several parameters so that we can appreciate the effect of changing these and how this affects the field. Such insight is often worth the price of the slight inaccuracy that may exist in the numerical value of the field.

11.1.1 Planar Geometry

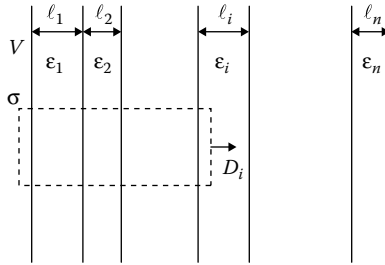
As a first example, we consider a layered insulation structure having a planar geometry, as shown in [Figure 11.1](#). This can represent the major insulation structure between two cylindrical windings having large radii compared with the gap separation. We further approximate the disk structure as a smooth surface so that the resulting field calculation will represent the field away from the corner of the disks. We treat this corner field in [Section 11.2](#).

We use one of Maxwell's equations in integral form to solve this:

$$\oint_S \mathbf{D} \cdot d\mathbf{S} = q \quad (11.1)$$

where \mathbf{D} is the displacement vector, $d\mathbf{S}$ is the vectorial surface area with an outward normal, and q is the charge enclosed by the closed surface S . Because of the assumed ideal planar geometry, the surface charge density on the electrode at potential V is uniform and is designated as σ in [Figure 11.1](#). An opposite surface charge of $-\sigma$ exists on the ground electrode. Both electrode potentials can be raised by an equal amount without changing the results. Only the potential difference matters. We also assume that the materials have linear electrical characteristics so that

$$\mathbf{D} = \epsilon \mathbf{E} \quad (11.2)$$

**FIGURE 11.1**

Geometry of a planar layered insulation structure.

holds within each material, where the permittivity ϵ can differ within the various layers, as shown in Figure 11.1.

Because of the planar geometry, the \mathbf{D} and \mathbf{E} fields are directed perpendicular to the planes of the electrodes and layers and are uniform along these planes. If we take our closed surface as the dotted rectangle shown in Figure 11.1, which has some depth, so that the two vertical sides represent surfaces, then the only contribution to the integral in Equation 11.1, which is nonzero, is the part over the right vertical surface. This is because the electric field and hence the displacement vector is zero inside the conductor on the left and is parallel to the upper and lower surfaces. Therefore, the displacement vector has the uniform value labeled D_i in Figure 11.1 on the right vertical surface of the dotted rectangle. Thus, for this closed surface, Equation 11.1 becomes

$$D_i S = q = \sigma S \Rightarrow D_i = \sigma \quad (11.3)$$

Using Equation 11.2 applied to layer i , Equation 11.3 becomes

$$E_i = \frac{\sigma}{\epsilon_i} \quad (11.4)$$

In terms of the potential V , we can write by definition

$$V = -\int \mathbf{E} \cdot d\boldsymbol{\ell} \quad (11.5)$$

where the line integral starts at the zero-potential electrode and ends on the V -potential electrode. In terms of the E fields in the different materials and their thicknesses ℓ_i , Equation 11.5 becomes

$$V = E_1 \ell_1 + E_2 \ell_2 + \cdots = \sum_{j=1}^n E_j \ell_j \quad (11.6)$$

Using Equation 11.4, we can write

$$V = \sigma \sum_{j=1}^n \frac{\ell_j}{\epsilon_j} \quad (11.7)$$

Solving for σ and substituting into Equation 11.4, we get

$$E_i = \frac{V}{\epsilon_i \left(\sum_{j=1}^n \frac{\ell_j}{\epsilon_j} \right)} \quad (11.8)$$

Letting ℓ be the total distance between the electrodes so that $\ell = \ell_1 + \ell_2 + \dots + \ell_n$ and defining the fractional lengths, $f_j = \ell_j / \ell$, Equation 11.8 can be expressed as

$$E_i = \frac{(V/\ell)}{\epsilon_i \left(\sum_{j=1}^n \frac{f_j}{\epsilon_j} \right)} = \frac{E_0}{\epsilon_i \left(\sum_{j=1}^n \frac{f_j}{\epsilon_j} \right)} \quad (11.9)$$

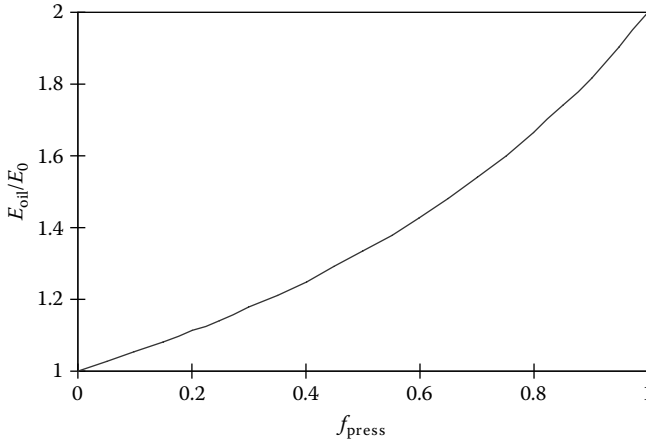
where E_0 is the electric field that would exist between the electrodes if there was only one layer of uniform material between them. E_i/E_0 is called an enhancement factor for the material of permittivity ϵ_i , especially when it is greater than 1. It is given by

$$\frac{E_i}{E_0} = \frac{1}{\epsilon_i \left(\sum_{j=1}^n \frac{f_j}{\epsilon_j} \right)} \quad (11.10)$$

The enhancement factor is the value of the field when there are multiple dielectrics between the conducting planes relative to the field when there is a single dielectric between them. Notice that only the ratios of permittivities are involved in Equations 11.8 through 11.10 so that only relative permittivities are required.

We apply these results to an oil–pressboard insulation system. Even if there are many layers of pressboard used to subdivide the oil gap, only the total fractional thickness f_{press} matters in the calculation because they all have the same permittivity. Similarly, the subdivided oil gap's total fractional thickness, $f_{\text{oil}} = 1 - f_{\text{press}}$, is all that is needed to perform the calculation. For this situation, Equation 11.9 becomes

$$E_{\text{oil}} = \frac{E_0}{\epsilon_{\text{oil}} \left(\frac{f_{\text{oil}}}{\epsilon_{\text{oil}}} + \frac{f_{\text{press}}}{\epsilon_{\text{press}}} \right)}, \quad E_{\text{press}} = \frac{E_0}{\epsilon_{\text{press}} \left(\frac{f_{\text{oil}}}{\epsilon_{\text{oil}}} + \frac{f_{\text{press}}}{\epsilon_{\text{press}}} \right)} \quad (11.11)$$

**FIGURE 11.2**

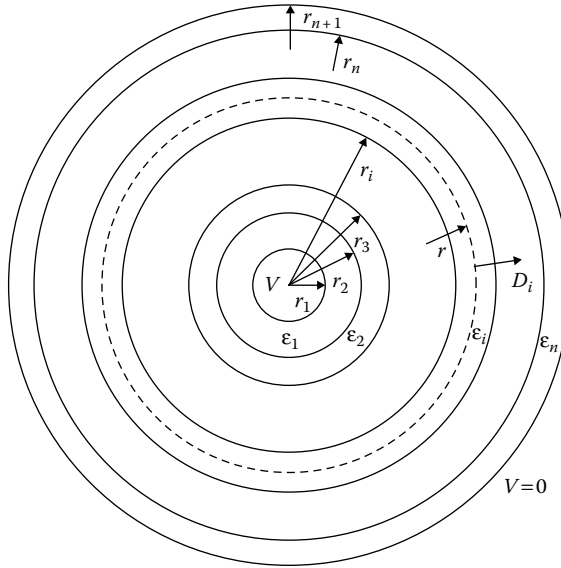
Relative electric field in the oil in a planar oil gap as a function of the fractional amount of pressboard.

Since the relative permittivities of pressboard and oil are $\epsilon_{\text{press}} \cong 4.4$ and $\epsilon_{\text{oil}} \cong 2.2$; the electric field in the oil is about twice as high as the electric field in the pressboard for a given oil–pressboard combination. Thus, the oil’s electric field is the most important factor for purposes of estimating breakdown. This is further reinforced by the fact that oil breaks down at a significantly lower field than pressboard. We plot E_{oil}/E_0 versus f_{press} in Figure 11.2. We see from Figure 11.2 that for a given oil gap, the lowest field results when there is no pressboard. As more pressboard displaces the oil, the field in the oil increases, approaching twice its total oil value when the gap is nearly filled with pressboard. E_{oil}/E_0 is the enhancement factor for the oil.

11.1.2 Cylindrical Geometry

A somewhat better estimate can be made of the electric field in the major insulation structure between two coils if we consider approximating the geometry as an ideal cylindrical geometry. This geometry is also useful for approximating the field around a long cable of circular cross section. Consider the general case of a multilayer concentric cylindrical insulation structure, as shown in Figure 11.3. The innermost cylinder is at potential V and the outermost at zero potential although only their potential difference matters.

We see from symmetry that the \mathbf{D} and \mathbf{E} fields are directed radially. We assume that there is a surface charge per unit length \cong along the inner cylinder (Figure 11.3). In Figure 11.3, we apply Equation 11.1 to the dashed line cylindrical surface that is assumed to extend a distance L along the axis with

**FIGURE 11.3**

Ideal layered cylindrical insulation structure. This can be reinterpreted to refer to a spherical geometry.

disk-like surfaces on either end. The only contribution to the integral is along the cylindrical surface of the cylinder and we find

$$2\pi r L D_i = \lambda L \Rightarrow D_i = \frac{\lambda}{2\pi r} \quad (11.12)$$

Assuming the linear relation Equation 11.2, for layer i , we get

$$E_i = \frac{\lambda}{2\pi \epsilon_i r} \quad (11.13)$$

Using Equation 11.5 and starting the line integral from the outer zero-potential electrode, using Equation 11.13, we have

$$\begin{aligned} V &= -\frac{\lambda}{2\pi} \left[\frac{1}{\epsilon_n} \int_{r_{n+1}}^{r_n} \frac{dr}{r} + \frac{1}{\epsilon_{n-1}} \int_{r_n}^{r_{n-1}} \frac{dr}{r} + \cdots + \frac{1}{\epsilon_1} \int_{r_2}^{r_1} \frac{dr}{r} \right] \\ &= \frac{\lambda}{2\pi} \sum_{j=1}^n \frac{1}{\epsilon_j} \ln \left(\frac{r_{j+1}}{r_j} \right) \end{aligned} \quad (11.14)$$

Solving for λ and substituting into Equation 11.13, we get

$$E_i = \frac{V}{\epsilon_i r \left[\sum_{j=1}^n \frac{1}{\epsilon_j} \ln \left(\frac{r_{j+1}}{r_j} \right) \right]} \quad (11.15)$$

For any given layer, the maximum field, $E_{i,\max}$, occurs at its inner radius, so we have

$$E_{i,\max} = \frac{V}{\epsilon_i r_i \left[\sum_{j=1}^n \frac{1}{\epsilon_j} \ln \left(\frac{r_{j+1}}{r_j} \right) \right]} \quad (11.16)$$

From Equations 11.15 and 11.16, we see that for a given layer, the electric field is inversely proportional to the permittivity. Thus, an oil layer at a given position will see about twice the electric field of a pressboard layer at the same position. Since the maximum field in a layer is also inversely proportional to the radius of the layer, this field can be reduced by increasing the radius of the layer. Thus, for a cable surrounded by solid insulation, such as paper, and immersed in oil, the critical field will probably occur in the oil at the outer surface of the paper. To reduce this, we can increase its radius by adding more paper or start with a larger radius cylindrical conductor to begin with.

If there were a single dielectric between the inner cylinder of radius r_1 and outer cylinder of radius r_{n+1} , then Equation 11.15 would become

$$E_0(r) = \frac{V}{r \ln \left(\frac{r_{n+1}}{r_1} \right)} \quad (11.17)$$

Substituting V from Equation 11.17 into Equation 11.15, we get

$$E_i(r) = \frac{\ln \left(\frac{r_{n+1}}{r_1} \right)}{\epsilon_i \left[\sum_{j=1}^n \frac{1}{\epsilon_j} \ln \left(\frac{r_{j+1}}{r_j} \right) \right]} E_0(r) \quad (11.18)$$

The enhancement factor for the material in layer i with permittivity ϵ_i for this geometry is given by

$$\frac{E_i(r)}{E_0(r)} = \frac{\ln \left(\frac{r_{n+1}}{r_1} \right)}{\epsilon_i \left[\sum_{j=1}^n \frac{1}{\epsilon_j} \ln \left(\frac{r_{j+1}}{r_j} \right) \right]} \quad (11.19)$$

11.1.3 Spherical Geometry

Another geometry of some interest is the spherical geometry. A general multilayered spherical insulation structure is shown in [Figure 11.3](#). We have interpreted it as a cross section through a spherical system of insulators. In this case, the D and E fields are again directed radially by symmetry, and the charge on the inner conductor at potential V is taken as q . The dashed circle in Figure 11.3 now defines a spherical surface, and when we apply Equation 11.1 we get

$$E_i = \frac{q}{4\pi\epsilon_i r^2} \quad (11.20)$$

From Equations 11.5 and 11.20, we obtain

$$\begin{aligned} V &= -\frac{q}{4\pi} \left[\frac{1}{\epsilon_n} \int_{r_{n+1}}^{r_n} \frac{dr}{r^2} + \frac{1}{\epsilon_{n-1}} \int_{r_n}^{r_{n-1}} \frac{dr}{r^2} + \cdots + \frac{1}{\epsilon_1} \int_{r_2}^{r_1} \frac{dr}{r^2} \right] \\ &= \frac{q}{4\pi} \sum_{j=1}^n \frac{1}{\epsilon_j} \left(\frac{1}{r_j} - \frac{1}{r_{j+1}} \right) \end{aligned} \quad (11.21)$$

Solving for q and substituting into Equation 11.20, we obtain

$$E_i = \frac{V}{\epsilon_i r^2 \left[\sum_{j=1}^n \frac{1}{\epsilon_j r_j} \left(1 - \frac{r_j}{r_{j+1}} \right) \right]} \quad (11.22)$$

The maximum field in layer i , $E_{i,\max}$, occurs at the inner radius and is given by

$$E_{i,\max} = \frac{V}{\epsilon_i r_i^2 \left[\sum_{j=1}^n \frac{1}{\epsilon_j r_j} \left(1 - \frac{r_j}{r_{j+1}} \right) \right]} \quad (11.23)$$

This expression can be used to approximate the field near a sharp bend in a cable immersed in oil with the various radii defined appropriately. We see that as the radius of the layer increases, the field in it decreases. Thus, the field in the oil can be reduced by adding more insulation or decreasing the sharpness of the bend.

When there is a single dielectric between the inner and outer electrodes, Equation 11.22 becomes

$$E_0(r) = \frac{V}{r^2 \left(1 - \frac{r_1}{r_{n+1}} \right)} \quad (11.24)$$

Substituting for V from Equation 11.24 into Equation 11.22, we obtain

$$E_i(r) = \frac{\frac{1}{r_1} \left(1 - \frac{r_1}{r_{n+1}} \right)}{\epsilon_i \left[\sum_{j=1}^n \frac{1}{\epsilon_j r_j} \left(1 - \frac{r_j}{r_{j+1}} \right) \right]} E_0(r) \quad (11.25)$$

Therefore, the enhancement factor for the material in layer i for this geometry is given by

$$\frac{E_i(r)}{E_0(r)} = \frac{\frac{1}{r_1} \left(1 - \frac{r_1}{r_{n+1}} \right)}{\epsilon_i \left[\sum_{j=1}^n \frac{1}{\epsilon_j r_j} \left(1 - \frac{r_j}{r_{j+1}} \right) \right]} \quad (11.26)$$

11.1.4 Cylinder–Plane Geometry

Cylinder–plane geometry is a reasonable approximation to a commonly occurring configuration in transformers in which a cable or lead runs parallel to the tank wall. The geometry and its parameterization are shown in Figure 11.4. The cylinder and plane extend infinitely far in the direction perpendicular to the page. The radius of the cylinder is R , and the distance of its center from the plane is h . The cylinder is at a potential V_0 while the plane is at zero potential.

The potential and electric field distribution for this problem can be obtained by the method of images [Pug62], [Kul04]. Two equal and opposite line charges can be placed symmetrically about the zero-potential plane, as shown in Figure 11.5. Their charge per unit length is λ and their distance from the plane is s . The potential and electric field are desired at a point

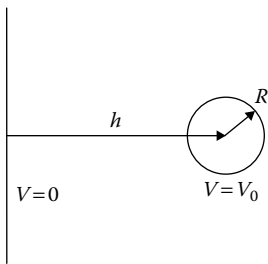


FIGURE 11.4

Cylinder–plane geometry and parameterization.

P shown in Figure 11.5, which is a distance r_1 from the negative charge and r_2 from the positive charge. The negative charge is behind the plane and the positive charge will be found to be located inside the charged cylinder. These image charges do not occur within the solution space of interest, which is outside the cylinder and to the right of the zero-potential plane. Therefore, from Maxwell's equations in this region, we have

$$\nabla \cdot \mathbf{E} = 0, \quad \mathbf{E} = -\nabla V \Rightarrow \nabla^2 V = 0 \quad (11.27)$$

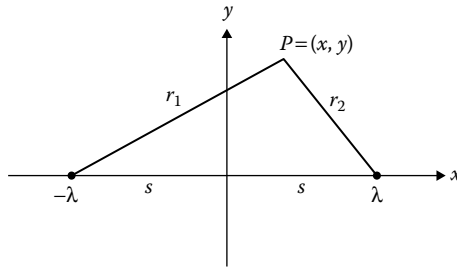
**FIGURE 11.5**

Image line charges for the cylinder–plane geometry.

Equation 11.27 is Laplace's equation and is valid in the space of interest here. The solution of this equation that satisfies the boundary conditions is unique.

The electric field due to a line charge is

$$\mathbf{E} = \frac{\lambda}{2\pi\epsilon_0 r} \mathbf{a}_r \quad (11.28)$$

where \mathbf{a}_r is the outward unit vector from the charge. The potential relative to a distant point, for example, at $r = C$ is

$$V = -\int_C^r \mathbf{E} \cdot d\mathbf{r} = -\frac{\lambda}{2\pi\epsilon_0} \int_C^r \frac{dr'}{r'} = \frac{\lambda}{2\pi\epsilon_0} [\ln(C) - \ln(r)] \quad (11.29)$$

Thus, the potential due to the equal and opposite line charges at distances r_1 and r_2 from the charges, as shown in Figure 11.5, is given by

$$V = \frac{\lambda}{2\pi\epsilon_0} [\ln(r_1) - \ln(r_2)] = \frac{\lambda}{2\pi\epsilon_0} \ln\left(\frac{r_1}{r_2}\right) \quad (11.30)$$

Here, we assume that the distance C is the same from either line charge because we assume it to be much larger than their separation. In any event, an overall constant may be added to a potential distribution without affecting any quantities of physical interest. The sign difference in Equation 11.30 comes from the different signs of λ on the two line charges.

From Equation 11.30, we immediately see that when $r_1 = r_2$, the potential equals zero. Thus, the boundary condition of zero potential on the plane between the two charged lines is satisfied. We need to satisfy the other boundary condition of potential V_0 on the cylinder, which is on the positive x -axis side of the zero-potential plane. We rewrite the potential in Equation 11.30 at the generic point P in Figure 11.5 as

$$V = A \ln\left(\frac{r_1}{r_2}\right) = \frac{A}{2} \ln\left(\frac{r_1}{r_2}\right)^2 = \frac{A}{2} \ln\left(\frac{r_1^2}{r_2^2}\right) = \frac{A}{2} \ln\left[\frac{(x+s)^2 + y^2}{(x-s)^2 + y^2}\right] \quad (11.31)$$

For V to be a constant, as is needed on the cylinder, we need to have (r_1/r_2) equal a constant, for example m . Thus,

$$\left(\frac{r_1}{r_2}\right)^2 = \left[\frac{(x+s)^2 + y^2}{(x-s)^2 + y^2}\right] = m^2 \quad (11.32)$$

Working through the algebra, we get

$$\left[x - \left(\frac{m^2 + 1}{m^2 - 1}\right)s\right]^2 + y^2 = \left(\frac{2ms}{m^2 - 1}\right)^2 \quad (11.33)$$

However, this is just the equation of a circle centered at $x = \left(\frac{m^2 + 1}{m^2 - 1}\right)s$, $y = 0$ with a radius of $\left(\frac{2ms}{m^2 - 1}\right)$, which we need to satisfy the boundary condition on the cylinder. For this, as indicated in [Figure 11.4](#), we set

$$h = \left(\frac{m^2 + 1}{m^2 - 1}\right)s, \quad R = \frac{2ms}{m^2 - 1} \quad (11.34)$$

Solving these last two equations for s and m , we obtain

$$s = h\sqrt{1 - \left(\frac{R}{h}\right)^2}, \quad m = \frac{h}{R} \left[1 + \sqrt{1 - \left(\frac{R}{h}\right)^2}\right] = \frac{h+s}{R} \quad (11.35)$$

The first equation in Equation 11.35 shows that $s < h$. We can also show that $s > h - R$. Thus, the positive line charge is inside the cylinder and out of the region where the potential distribution is required. The negative line charge is also outside this region.

For the value of m in Equation 11.35, we require $V = V_0$. Using this in Equation 11.31, we can get the value of A :

$$V_0 = A \ln(m) = A \ln\left(\frac{h+s}{R}\right) \Rightarrow A = \frac{V_0}{\ln\left(\frac{h+s}{R}\right)} \quad (11.36)$$

where $s = h\sqrt{1 - \left(\frac{R}{h}\right)^2}$.

Thus, the potential distribution is

$$V = \frac{V_0}{2 \ln\left(\frac{h+s}{R}\right)} \ln\left[\frac{(x+s)^2 + y^2}{(x-s)^2 + y^2}\right] \quad (11.37)$$

The electric field is obtained from the potential according to

$$\mathbf{E} = -\nabla V = -\frac{\partial V}{\partial x} \mathbf{i} - \frac{\partial V}{\partial y} \mathbf{j} \quad (11.38)$$

where \mathbf{i} and \mathbf{j} are unit vectors in the x and y directions. Carrying out the differentiations, we find for the x and y components of \mathbf{E}

$$\begin{aligned} E_x &= \frac{2sV_0}{\ln\left(\frac{h+s}{R}\right)} \left[\frac{(x^2 - s^2) - y^2}{(x^2 - s^2)^2 + 2y^2(x^2 + s^2) + y^4} \right] \\ E_y &= \frac{2sV_0}{\ln\left(\frac{h+s}{R}\right)} \left[\frac{2xy}{(x^2 - s^2)^2 + 2y^2(x^2 + s^2) + y^4} \right] \end{aligned} \quad (11.39)$$

Using these, we can show that

$$\nabla^2 V = \frac{\partial^2 V}{\partial x^2} + \frac{\partial^2 V}{\partial y^2} = 0 \quad (11.40)$$

so that Laplace's equation is satisfied.

We see from Equation 11.39 that, when $y = 0$, $E_y = 0$ so there is only an x -component of the field. The x -component of \mathbf{E} for $y = 0$ is given by

$$E_x(y=0) = \frac{2sV_0}{\ln\left(\frac{h+s}{R}\right)} \left(\frac{1}{x^2 - s^2} \right) \quad (11.41)$$

Notice that along the x -axis from the zero-potential plane to the cylinder, $x < s$, so that E_x is negative if V_0 is positive, as expected, since \mathbf{E} should point away from the positive potential toward the zero-potential plane.

To check on these formulas, the cylinder-plane geometry was modeled with a finite element analysis program, Ansoft's Maxwell (Ansoft Corp., Pittsburgh, PA). We modeled the geometry for $R = 10$ mm and $h = 100$ mm and chose $V_0 = 1000$ V. The equipotential contours are shown in [Figure 11.6](#), and the electric field vectors are shown in [Figure 11.7](#).

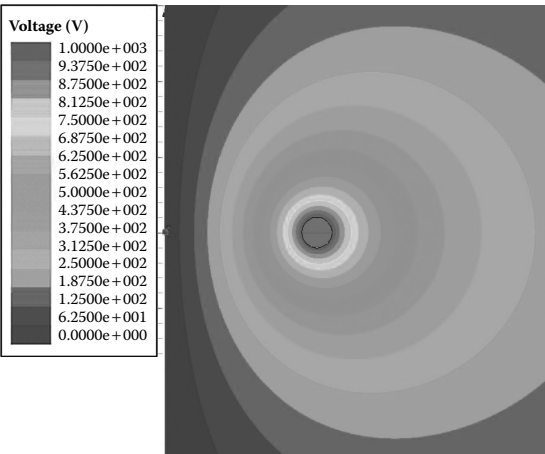


FIGURE 11.6
(See color insert following page 338.) Cylinder–plane equipotential contours obtained with a finite element program.

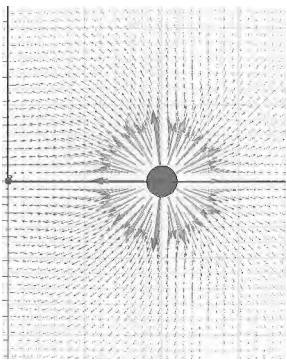
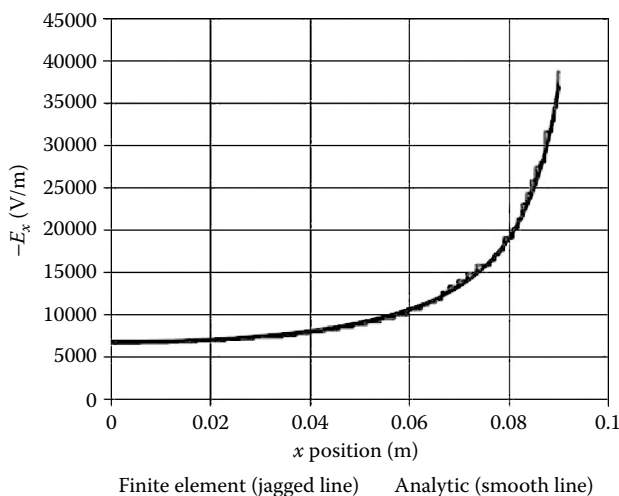


FIGURE 11.7
(See color insert following page 338.) Electric field vectors for the cylinder–plane geometry modeled with finite elements.

The negative of the electric field was plotted along the x -axis from the finite element program and compared with the analytic formula given in Equation 11.41. The results are shown in Figure 11.8. The fields are given in volts/meter and the distance in meters, and the agreement is good.

No dielectric barriers or paper covering of the cylinder were included in the cylinder–plane geometry. Including these barriers for the other geometries considered earlier resulted in enhancement effects on the electric fields. We can approximate the enhancement effect due to such barriers for the

**FIGURE 11.8**

Negative of the x -component of the electric field along the x -axis from the zero-potential plane at $x = 0$ to the cylinder at $x = 90 \text{ mm} = 0.09 \text{ m}$. The finite element and analytic results are compared.

cylinder–plane geometry by using the cylinder enhancement factor given in Equation 11.19 and treating the plane as a cylinder at a radial distance of h from the cylinder center. This approach can be refined, if necessary, based on a parametric study using a finite element program.

11.2 Electric Field Calculations Using Conformal Mapping

11.2.1 Physical Basis

In a region of space without charge, Maxwell's electrostatic equation is

$$\nabla \cdot \mathbf{D} = 0 \quad (11.42)$$

where \mathbf{D} is the electric displacement. If the region has a uniform permittivity ϵ , then $\mathbf{D} = \epsilon \mathbf{E}$, where \mathbf{E} is the electric field. Hence, Equation 11.42 becomes

$$\nabla \cdot \mathbf{E} = 0 \quad (11.43)$$

Introducing a potential function V , where

$$\mathbf{E} = -\nabla V \quad (11.44)$$

From Equation 11.43, we get

$$\nabla^2 V = 0 \quad (11.45)$$

In two dimensions, using Cartesian coordinates, Equation 11.45 reads

$$\frac{\partial^2 V}{\partial x^2} + \frac{\partial^2 V}{\partial y^2} = 0 \quad (11.46)$$

The solution of Equation 11.46, including boundary conditions, can then be used to determine the electric field via Equation 11.44.

Boundary conditions are generally of two types: Dirichlet or Neumann. A Dirichlet boundary condition specifies the voltage along a boundary. This voltage is usually a constant, as would be appropriate for a metallic surface. A Neumann boundary condition specifies the normal derivative along a boundary. The normal derivative is usually taken to be zero, which indicates that the equipotential surfaces (surfaces of constant V) or lines in two dimensions intersect the boundary at right angles. This type of boundary is often used to enforce symmetry.

In the theory of functions of a complex variable, analytic functions play a special role. Analytic functions are functions that are continuous and differentiable in some region of the complex plane. Functions which satisfy Equation 11.46 are called harmonic functions. In addition, analytic mappings from one complex plane to another have properties that allow a solution of Equation 11.46 in a relatively simple geometry in one complex plane to be transformed to a solution of this equation in a more complicated geometry in another complex plane. We briefly describe some of the important properties of these functions that are needed in the present application. See [Chu60] for further details.

11.2.2 Conformal Mapping

Let $z = x + iy$ denote a complex variable, where $i = \sqrt{-1}$ is the unit imaginary (i rather than j is used for the unit imaginary in this context). We can write function $f(z)$ in terms of its real and imaginary parts as

$$f(z) = u(x, y) + iv(x, y) \quad (11.47)$$

where u and v are real functions of two variables. If f is analytic, it is differentiable at points z in its domain of definition. Since we are in the z -plane, the derivative can be taken in many directions about a given point and the value must be independent of direction. Taking this derivative

in the x direction and then in the iy direction and equating the results, we obtain the Cauchy–Riemann equations:

$$\frac{\partial u}{\partial x} = \frac{\partial v}{\partial y}, \quad \frac{\partial u}{\partial y} = -\frac{\partial v}{\partial x} \quad (11.48)$$

Differentiating the first of these equations with respect to x and the second with respect to y , we have

$$\frac{\partial^2 u}{\partial x^2} = \frac{\partial^2 v}{\partial x \partial y}, \quad \frac{\partial^2 u}{\partial y^2} = -\frac{\partial^2 v}{\partial y \partial x} \quad (11.49)$$

Because the mixed partial derivatives on the right-hand sides of these equations are equal for differentiable functions, when we add these equations, we get

$$\frac{\partial^2 u}{\partial x^2} + \frac{\partial^2 u}{\partial y^2} = 0 \quad (11.50)$$

Thus, u is a harmonic function. By differentiating the first part of Equation 11.48 with respect to y , the second with respect to x , and adding, we similarly find that v is a harmonic function.

The solution of the potential problem, Equation 11.46 with boundary conditions, is often needed in a rather geometrically complicated region. The idea behind using complex variable theory is to formulate the problem in a simpler geometric region where the solution is easy and then use an analytic function to map the easy solution onto the more complicated geometric region. The possibility of doing this derives from several additional properties of analytic functions.

First of all, an analytic function of an analytic function is also analytic. Because the real and imaginary parts of the original and composite functions are harmonic, harmonic functions are transformed into harmonic functions by means of analytic transformations. In terms of formulas, if $f(z)$ is an analytic function of z and $z = g(w)$ expresses z in terms of an analytic mapping from the w -plane, where $w = u + iv$, then $f(g(w))$ is an analytic function of w . The real and imaginary parts of f are transformed into harmonic functions of the new variables u and v .

Given an analytic mapping from the z - to w -plane ($w = f(z)$), the inverse mapping $z = F(w)$ is analytic at points, where $f'(z) = df/dz \neq 0$. Moreover, at such points,

$$F'(w) = \frac{1}{f'(z)} \quad \text{or} \quad \frac{dz}{dw} = \frac{1}{dw/dz} \quad (11.51)$$

This result will be useful in later applications to the electrostatic problem.

Perhaps the most important characteristic of analytic mappings in the present context is that they are conformal mappings. This means that if two curves intersect at an angle α in the z -plane, their images in the w -plane under an analytic mapping $w = f(z)$ intersect at the same angle α at the transformed point. To see this, we use the fact that an analytic function can be expanded about a point z_0 using a Taylor's series expansion:

$$\begin{aligned} w &= f(z) = f(z_0) + f'(z_0)(z - z_0) + \cdots \\ &= w_0 + f'(z_0)(z - z_0) + \cdots \end{aligned} \quad (11.52)$$

where we assume that $f'(z_0) \neq 0$. Writing $\Delta w = w - w_0$ and $\Delta z = z - z_0$, for small Δz , Equation 11.52 becomes

$$\Delta w = f'(z_0)\Delta z \quad (11.53)$$

If Δz is an incremental distance along a curve in the z -plane, Δw is the corresponding incremental distance along the transformed curve in the w -plane (Figure 11.9). Because we can write any complex number in polar form:

$$z = |z|e^{i\phi} \quad (11.54)$$

In terms of its magnitude $|z|$ and argument ϕ , Equation 11.53 can be expressed as

$$|\Delta w|e^{i\beta} = |f'(z_0)||\Delta z|e^{i(\psi_0 + \alpha)} \quad (11.55)$$

where $\psi_0 = \text{argument}(f'(z_0))$, and α and β are shown in Figure 11.9. Thus, from Equation 11.55, we see that

$$\beta = \psi_0 + \alpha \quad (11.56)$$

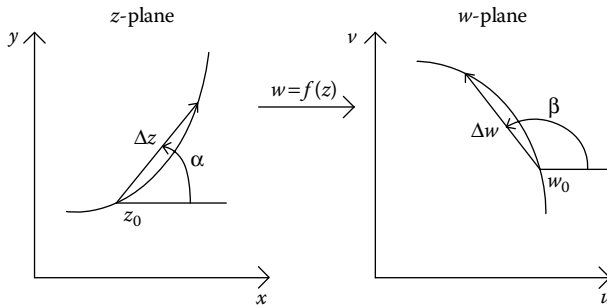


FIGURE 11.9

Analytic mapping of a curve from the z - to the w -plane.

As Δz and Δw approach zero, their directions approach that of the tangent to their respective curves. Thus, the angle that the transformed curve makes with the horizontal axis β is equal to the angle that the original curve made with its horizontal axis α rotated by the amount ψ_0 . Since ψ_0 is characteristic of the derivative $f'(z_0)$, which is independent of the curve passing through z_0 , any curve through z_0 will be rotated by the same angle ψ_0 . Thus, since any two intersecting curves are rotated by the same angle under the transformation, the angle between the curves will be preserved.

In terms of the electrostatic problem, this last mapping characteristic indicates that a set of equipotential (nonintersecting) curves in one geometry will remain nonintersecting in the transformed geometry obtained from the first by means of an analytic map. Similarly, the orthogonal relationship between the equipotentials and the electric field lines will be preserved in the new geometry.

Finally, we need to look at the boundary conditions. If H is a harmonic function, which is constant along some curve or boundary, then

$$H(x, y) = C \quad (11.57)$$

Changing variables by $z = f(w)$, in the new variables, this becomes

$$H(x(u, v), y(u, v)) = C \quad (11.58)$$

that is, a transformed curve along which H has the same constant value. Thus, the Dirichlet boundary conditions are transformed into Dirichlet boundary conditions with the same boundary value along the transformed curve.

A Neumann boundary condition means that the normal derivative of H along the boundary vanishes. Since the normal derivative is the scalar product of the gradient and unit normal vector, the vanishing of this derivative means that the gradient vector points along the boundary, that is, it is tangential to it. However, the gradient vector is perpendicular to curves along which H is constant. Therefore, these curves of constant H are perpendicular to the boundary curve. Under a conformal mapping, this perpendicularity is preserved so that the transformed boundary curve is normal to the transformed curves of constant H . Therefore, the gradient of these transformed curves is parallel to the transformed boundary so that their normal derivative vanishes in the transformed geometry. Thus, Neumann boundary conditions are preserved under analytic transformations.

Because a solution of Equation 11.46 that satisfies Dirichlet or Neumann boundary conditions is unique, under an analytic mapping, the transformed solution subject to the transformed boundary conditions will also be unique in the new geometry.

11.2.3 Schwarz–Christoffel Transformation

This transformation is an analytic mapping (except for a few isolated points) from the upper-half plane to the interior of a closed polygon. The closed polygon can be degenerate in the sense that some of its vertices may be at infinity. This type of polygon includes the type of interest here.

We will consider the general case, as illustrated in [Figure 11.10](#). Part of the x -axis from x_1 to $x_n = \infty$ is mapped onto the boundary of a closed polygon in the w plane. We have also drawn unit tangent vectors \mathbf{s} and \mathbf{t} along corresponding boundary curves in the z - and w -planes. We showed earlier that the angle that the transformed curve makes with the horizontal axis at a point is given by the angle that the original curve makes with its horizontal plus the argument of the derivative of the mapping. In this case, the original curve is along the x -axis in the positive sense and so makes zero angle with this axis. Therefore, the transformed curve makes an angle with its axis given by $\arg(f'(z))$, where \arg denotes “argument of.” Thus, if the mapping has a constant argument between two consecutive points along the x -axis, the transformed boundary curve will have a constant argument also and therefore be a straight line. However, as the w value moves along the boundary through a point w_i where the polygon transitions from one side to another, the argument of the tangent abruptly changes value. At these points, the mapping cannot be analytic (or conformal). However, there are only n such points for an n -sided polygon.

A mapping that has the above characteristics is given, in terms of its derivative, by

$$f'(z) = A(z - x_1)^{-k_1} (z - x_2)^{-k_2} \cdots (z - x_{n-1})^{-k_{n-1}} \quad (11.59)$$

where $x_1 < x_2 < \dots < x_{n-1}$. Since

$$(z - x_i)^{-k_i} = \left[|z - x_i| e^{i \arg(z - x_i)} \right]^{-k_i} = |z - x_i|^{-k_i} e^{-k_i \arg(z - x_i)} \quad (11.60)$$

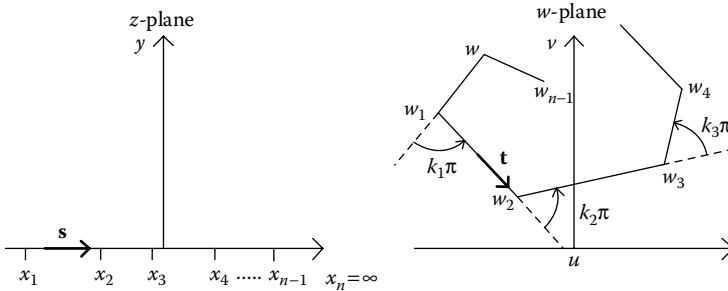


FIGURE 11.10
Schwarz–Christoffel mapping geometry.

and since the argument of a product of terms is the sum of their arguments

$$\arg(f'(z)) = \arg A - k_1 \arg(z - x_1) - k_2 \arg(z - x_2) - \cdots - k_{n-1} \arg(z - x_{n-1}) \quad (11.61)$$

When $z = x < x_1$, then

$$\arg(x - x_1) = \arg(x - x_2) = \cdots = \arg(x - x_{n-1}) = \pi \quad (11.62)$$

However, when $z = x$ moves to the right of x_1 , $\arg(x - x_1) = 0$ but $\arg(x - x_i) = \pi$ for $i > 2$. Thus, the argument of $f(z)$ abruptly changes by $k_1\pi$ as $z = x$ moves to the right of x_1 . This is shown in [Figure 11.10](#). Similarly, when $z = x$ passes through x_2 , $\arg(x - x_1) = \arg(x - x_2) = 0$ and all the rest equal π so that $\arg(f'(z))$ jumps by $k_2\pi$. These jumps are the exterior angles of the polygon traced in the w -plane. As such, they can be restricted to $-\pi \leq k_i\pi \leq \pi$ so that

$$-1 \leq k_i \leq 1 \quad (11.63)$$

Because the sum of the exterior angles of a closed polygon equals 2π , for the point at infinity, we have

$$k_n\pi = 2\pi - (k_1 + k_2 + \cdots + k_{n-1})\pi \quad (11.64)$$

so that

$$k_1 + k_2 + \cdots + k_n = 2 \quad (11.65)$$

Note that the point x_n can be a finite point, in which case it must be included in Equation 11.59. However, the transformation is simplified if it is at infinity.

To obtain the Schwarz–Christoffel transformation, we must integrate Equation 11.59 to get

$$w = f(z) = A \int^z (\zeta - x_1)^{-k_1} (\zeta - x_2)^{-k_2} \cdots (\zeta - x_{n-1})^{-k_{n-1}} d\zeta + B \quad (11.66)$$

The complex constants A and B and the x_i values can be chosen to achieve the desired map. The choice of these values is somewhat arbitrary, and this freedom should be used to simplify the calculations. With this brief background, we will now proceed to determine the mapping of interest here. [Chu60] or other standard books on complex variables contain further details and proofs.

11.2.4 Conformal Map for the Electrostatic Field Problem

Figure 11.11 shows the w -plane geometry of interest for the electrostatic field problem and the corresponding z -plane boundary points. The disk-to-disk separation is $2g$, and the disk-to-ground plane gap is h . The x, y and u, v coordinate systems are indicated in Figure 11.11, and the axes intersect at their respective origins. Note that some of the image points (w_2, w_3 , and w_5) are at infinity, albeit in different directions in the complex plane. These are shown at finite positions in Figure 11.11 for representational purposes. In assigning values to x_1, x_2, x_3 , and x_4 , we have taken advantage of the symmetry in the w -plane geometry. In fact, we chose the coordinate systems to exploit this symmetry. In Figure 11.10, we chose the positive direction for the exterior angles so that if we are moving along a side toward the next vertex, the angle increases if we make a left turn and decreases if we make a right turn. In Figure 11.11, as we move through the vertex w_1 from w_5 , we turn to the right by 90° , hence $k_1 = -1/2$. Moving through w_2 , we make a 180° turn to the left, so $k_2 = 1$. Passing through w_3 , we again make a 180° left turn, so $k_3 = 1$. We turn right by 90° when we go through w_4 , so $k_4 = -1/2$. The angular change through w_5 is 180° to the left so $k_5 = 1$. Thus, $k_1 + k_2 + k_3 + k_4 + k_5 = -1/2 + 1 + 1 - 1/2 + 1 = 2$ as required.

From Equation 11.59, the derivative of the transformation is

$$f'(z) = A \frac{(z+a)^{1/2}(z-a)^{1/2}}{(z+1)(z-1)} = A \frac{(z^2-a^2)^{1/2}}{(z^2-1)} \quad (11.67)$$

where $a > 1$. The integral can be carried out by writing

$$\frac{1}{z^2-1} = \frac{1}{2} \left(\frac{1}{z-1} - \frac{1}{z+1} \right) \quad (11.68)$$

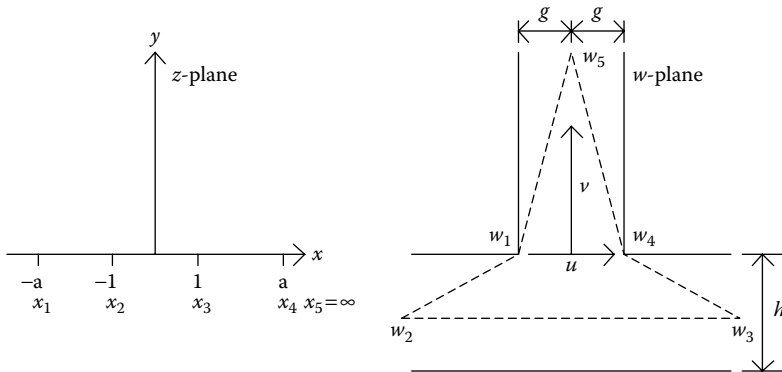


FIGURE 11.11

Schwarz-Christoffel transformation for the electrostatic problem.

Substituting into Equation 11.67, we get

$$f'(z) = \frac{A}{2} \left[\frac{(z^2 - a^2)^{1/2}}{z-1} - \frac{(z^2 - a^2)^{1/2}}{z+1} \right] \quad (11.69)$$

Using tables of integrals and the definitions of the complex version of the standard functions [Dwi61], we can integrate this to get

$$w = f(z) = A \left\{ \ln(2\sqrt{z^2 - a^2} + 2z) - \frac{\sqrt{a^2 - 1}}{2} \left[\sin^{-1} \left(\frac{z - a^2}{a(z-1)} \right) + \sin^{-1} \left(\frac{z + a^2}{a(z+1)} \right) \right] \right\} + B \quad (11.70)$$

where \ln is the natural logarithm. This solution can be verified by taking its derivative.

To fix the constants, we must match the image points w_1, w_2 , and so forth to their corresponding x -axis points. Thus, we must get $w_1 = -g$ when $z = x_1 = -a$. Substituting into Equation 11.70, we find

$$-g = A \left\{ \ln(-2a) - \frac{\sqrt{a^2 - 1}}{2} [\sin^{-1}(1) + \sin^{-1}(-1)] \right\} + B \quad (11.71)$$

Since

$$\ln z = \ln|z| + i \arg(z)$$

where we are using the principal value of the logarithm, Equation 11.71 becomes

$$-g = A[\ln(2a) + i\pi] + B \quad (11.72)$$

since $\arg(-2a) = \pi$. Similarly, we must have $w_4 = g$ correspond to $x_4 = a$. Substituting into Equation 11.70, we find

$$\begin{aligned} g &= A \left\{ \ln(2a) - \frac{\sqrt{a^2 - 1}}{2} [\sin^{-1}(-1) + \sin^{-1}(1)] \right\} + B \\ &= A \ln(2a) + B \end{aligned} \quad (11.73)$$

Subtracting Equation 11.72 from Equation 11.73, we get

$$A = i \frac{2g}{\pi} \quad (11.74)$$

Adding Equations 11.72 and 11.73 and using Equation 11.74, we get

$$B = g - i \frac{2g}{\pi} \ln(2a) \quad (11.75)$$

Substituting A and B into Equation 11.70, we get

$$w = f(z) = i \frac{2g}{\pi} \left\{ \ln \left(2\sqrt{z^2 - a^2} + 2z \right) - \frac{\sqrt{a^2 - 1}}{2} \left[\sin^{-1} \left(\frac{z - a^2}{a(z - 1)} \right) + \sin^{-1} \left(\frac{z + a^2}{a(z + 1)} \right) \right] \right\} + g - i \frac{2g}{\pi} \ln(2a) \quad (11.76)$$

The log terms can be combined, resulting in

$$w = f(z) = i \frac{2g}{\pi} \left\{ \ln \left(\frac{\sqrt{z^2 - a^2} + z}{a} \right) - \frac{\sqrt{a^2 - 1}}{2} \left[\sin^{-1} \left(\frac{z - a^2}{a(z - 1)} \right) + \sin^{-1} \left(\frac{z + a^2}{a(z + 1)} \right) \right] \right\} + g \quad (11.77)$$

Further manipulation of the log term leads to

$$\begin{aligned} \ln \left(\frac{\sqrt{z^2 - a^2} + z}{a} \right) &= \ln \left(\sqrt{\left(\frac{z}{a} \right)^2 - 1} + \left(\frac{z}{a} \right) \right) = \ln \left(i \sqrt{1 - \left(\frac{z}{a} \right)^2} + \left(\frac{z}{a} \right) \right) \\ &= \ln \left[i \left(\sqrt{1 - \left(\frac{z}{a} \right)^2} - i \left(\frac{z}{a} \right) \right) \right] = i \frac{\pi}{2} + \ln \left[\sqrt{1 - \left(\frac{z}{a} \right)^2} - i \left(\frac{z}{a} \right) \right] \end{aligned} \quad (11.78)$$

where we used $\ln(i) = \ln(1) + i \arg(i) = i\pi/2$. Using the identity from [Dwi61]:

$$\sin^{-1}C = i \ln \left(\pm \sqrt{1 - C^2} - iC \right) \quad (11.79)$$

where C is a complex number, Equation 11.78 becomes,

$$\ln \left(\frac{\sqrt{z^2 - a^2} + z}{a} \right) = i \frac{\pi}{2} - i \sin^{-1} \left(\frac{z}{a} \right) \quad (11.80)$$

Substituting into Equation 11.77, we get

$$w = \frac{2g}{\pi} \sin^{-1} \left(\frac{z}{a} \right) - i \frac{g\sqrt{a^2 - 1}}{\pi} \left[\sin^{-1} \left(\frac{z - a^2}{a(z - 1)} \right) + \sin^{-1} \left(\frac{z + a^2}{a(z + 1)} \right) \right] \quad (11.81)$$

To determine the constant a , we must use the correspondence between another set of points, such as x_2, w_2 or x_3, w_3 . Using the x_3, w_3 pair, we note that as x approaches $x_3 = 1$ from below, w_3 must approach $\infty - ih$. Therefore, in Equation 11.81, we let $z = x \rightarrow 1$ from below. Here, we use another expression for the complex inverse sine function [Dwi61]:

$$\sin^{-1}(x \pm iy) = \sin^{-1}\left(\frac{2x}{p+q}\right) \pm i \cosh^{-1}\left(\frac{p+q}{2}\right) \quad (11.82)$$

where

$$p = \sqrt{(1+x)^2 + y^2}, \quad q = \sqrt{(1-x)^2 + y^2} \quad \text{and} \quad y \geq 0$$

where p and q are assumed to be positive. In Equation 11.82, we have taken the principal value of the inverse sine function, corresponding to $n = 0$ in [Dwi61]. If $y = 0$ and $x > 1$, $p = 1 + x$, $q = -(1 - x)$, and $p + q = 2x$. If $y = 0$ and $x < -1$, $p = -(1 + x)$, $q = 1 - x$, and $p + q = -2x$. If $y = 0$ and $|x| < 1$, $p = 1 + x$, $q = 1 - x$, and $p + q = 2$. This latter case corresponds to the real sine function. Note that the sign of the \cosh^{-1} term in Equation 11.82 is the sign of the imaginary part of the complex argument of the \sin^{-1} on the left-hand side of that equation.

Substituting $z \rightarrow 1$ into Equation 11.81, we get

$$\infty - ih = \frac{2g}{\pi} \sin^{-1}\left(\frac{1}{a}\right) - i \frac{g\sqrt{a^2 - 1}}{\pi} \left[\sin^{-1}(\infty) + \sin^{-1}\left(\frac{1+a^2}{2a}\right) \right] \quad (11.83)$$

where the infinities must be interpreted in a limiting sense. These infinities are real infinities and can be grouped with the real part of Equation 11.83. The imaginary part can be handled separately. The imaginary part is used to find the value of a . Keeping this in mind and using Equation 11.82, we find

$$\sin^{-1}(\infty) = \sin^{-1}(1) + i \cosh^{-1}(\infty) = \frac{\pi}{2} + i \cosh^{-1}(\infty) \quad (11.84)$$

For the other inverse sine term, since

$$\frac{1+a^2}{2a} = \frac{2a+(a-1)^2}{2a} = 1 + \frac{(a-1)^2}{2a} > 1 \quad (11.85)$$

we have

$$\sin^{-1}\left(\frac{1+a^2}{2a}\right) = \sin^{-1}(1) + i \cosh^{-1}\left(\frac{1+a^2}{2a}\right) = \frac{\pi}{2} + i \cosh^{-1}\left(\frac{1+a^2}{2a}\right) \quad (11.86)$$

Since $a > 1$, the first inverse sine term in Equation 11.83 is an ordinary real inverse sine function. Substituting into Equation 11.83, and neglecting finite real terms compared with ∞ , we get

$$\infty - ih = \infty - ig\sqrt{a^2 - 1} \quad (11.87)$$

Therefore, equating the imaginary parts of both sides of Equation 11.87, we get $\sqrt{a^2 - 1} = h/g$ and solving for a :

$$a = \sqrt{1 + \left(\frac{h}{g}\right)^2} \quad (11.88)$$

Thus, Equation 11.81 becomes

$$w = \frac{g}{\pi} \left\{ 2\sin^{-1}\left(\frac{z}{a}\right) - i\frac{h}{g} \left[\sin^{-1}\left(\frac{z - a^2}{a(z - 1)}\right) + \sin^{-1}\left(\frac{z + a^2}{a(z + 1)}\right) \right] \right\} \quad (11.89)$$

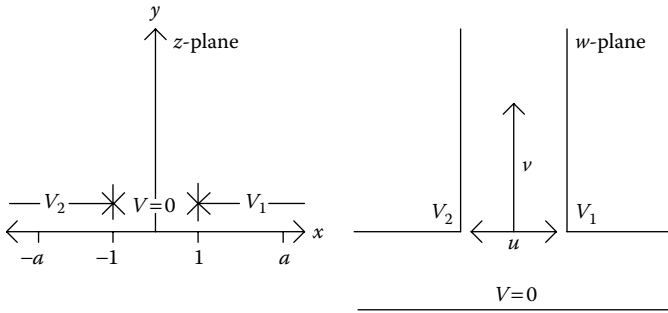
with a given by Equation 11.88. We can check other points of correspondence for consistency using similar procedures. In deriving Equation 11.89, the infinities contribute to the real part of Equation 11.81, whereas only the imaginary part is needed to obtain the value of a .

11.2.4.1 Electric Potential and Field Values

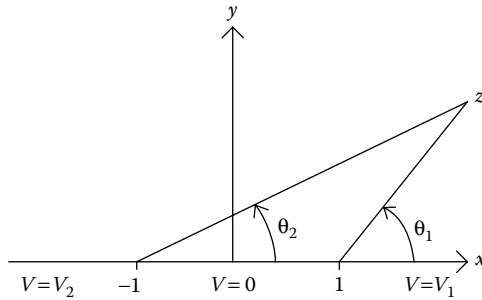
The boundary values of the potential in the w -plane (the plane of interest for the electrostatic problem) are shown in Figure 11.12. Two conductors are at potentials V_1 and V_2 relative to a plane at zero potential. This can be done without loss of generality, since if the plane were not at zero potential, its value could be subtracted from all the potential values without altering the values of the electric field. The corresponding boundary values in the z -plane are also shown in Figure 11.12. We will solve the problem in the simpler z -plane geometry and then use the conformal map given by Equation 11.89 to transfer the solution to the w -plane. Figure 11.13 suggests a method of doing this. θ_1 and θ_2 are angles between the vectors from points 1 and -1 to z . In terms of these angles, a potential that satisfies the boundary conditions in the z -plane is given by

$$V = V_1 - \frac{V_1}{\pi}\theta_1 + \frac{V_2}{\pi}\theta_2 \quad (11.90)$$

When $z = x > 1$, θ_1 and θ_2 are zero, so $V = V_1$. When $-1 < z = x < 1$, $\theta_1 = \pi$, and $\theta_2 = 0$, so $V = 0$. When $z = x < -1$, $\theta_1 = \theta_2 = \pi$, so $V = V_2$. Thus, the boundary conditions are satisfied.

**FIGURE 11.12**

Correspondence between potential boundary values for the z - and w -planes.

**FIGURE 11.13**

The potential function in the z -plane.

We must now show that V is a harmonic function. Note that

$$\theta_1 = \arg(z - 1), \quad \theta_2 = \arg(z + 1) \quad (11.91)$$

Note also that

$$\ln(z \pm 1) = \ln|z \pm 1| + i \arg(z \pm 1) \quad (11.92)$$

Because the log function is analytic, its real and imaginary components are harmonic functions as was shown for analytic functions. Thus, θ_1 and θ_2 are harmonic and so is V , since sums of harmonic functions are also harmonic.

In terms of x and y where $z = x + iy$, we can write Equation 11.90 as

$$V = V_1 - \frac{V_1}{\pi} \tan^{-1} \left(\frac{y}{x-1} \right) + \frac{V_2}{\pi} \tan^{-1} \left(\frac{y}{x+1} \right) \quad (11.93)$$

Since the transformation Equation 11.89 is analytic except at a few points, the inverse transformation is defined and analytic at all points where $w' = dw/dz \neq 0$. Thus, V can be considered a function of u, v through the dependence of x and y on these variables via the inverse transformation. This will enable us to obtain expressions for the electric field in the w -plane. We have

$$E_u = -\frac{\partial V}{\partial u}, \quad E_v = -\frac{\partial V}{\partial v} \quad (11.94)$$

Referring to Equation 11.93, note that

$$\frac{\partial}{\partial u} \tan^{-1} \left(\frac{y}{x-c} \right) = \frac{(x-c) \frac{\partial y}{\partial u} - y \frac{\partial x}{\partial u}}{(x-c)^2 + y^2} \quad (11.95)$$

Substituting $c = \pm 1$, corresponding to the two terms in Equation 11.93, and applying a similar formula for the v derivative, we get for the electric field components

$$\begin{aligned} E_u &= \frac{V_1}{\pi} \left[\frac{(x-1) \frac{\partial y}{\partial u} - y \frac{\partial x}{\partial u}}{(x-1)^2 + y^2} \right] - \frac{V_2}{\pi} \left[\frac{(x+1) \frac{\partial y}{\partial u} - y \frac{\partial x}{\partial u}}{(x+1)^2 + y^2} \right] \\ E_v &= \frac{V_1}{\pi} \left[\frac{(x-1) \frac{\partial y}{\partial v} - y \frac{\partial x}{\partial v}}{(x-1)^2 + y^2} \right] - \frac{V_2}{\pi} \left[\frac{(x+1) \frac{\partial y}{\partial v} - y \frac{\partial x}{\partial v}}{(x+1)^2 + y^2} \right] \end{aligned} \quad (11.96)$$

The derivatives in these formulas can be determined by Equations 11.51, 11.67, and 11.74. Thus,

$$\frac{dz}{dw} = \frac{1}{dw/dz} = -i \frac{\pi}{2g} \frac{(z^2 - 1)}{(z^2 - a^2)^{1/2}} \quad (11.97)$$

Because the square root of a complex number with argument θ changes its sign when θ increases to $\theta + 2\pi$, there is an ambiguity in the sign of Equation 11.97. Thus, we must make a branch cut in the complex plane, keeping the plus sign (+) for values on one side of the cut and – on the other. This cut is made along a ray from the origin, typically along $\theta = 0$. Expressing the square root term in the denominator of Equation 11.97 in polar form, we get

$$\begin{aligned} (z^2 - a^2)^{1/2} &= (x^2 - y^2 - a^2 + 2ixy)^{1/2} \\ &= \left(\sqrt{(x^2 - y^2 - a^2)^2 + 4x^2y^2} \right)^{1/2} e^{\frac{1}{2} \tan^{-1} \left(\frac{2xy}{x^2 - y^2 - a^2} \right)} \end{aligned} \quad (11.98)$$

We see that the argument is zero along the line $x = 0$, and it changes sign when x crosses this line from positive to negative or vice versa. Thus, we choose the $x = 0$ line as a branch cut. In our geometry, this is a line from the origin along the positive y -axis. We take the positive sign for $x \geq 0$ and the negative sign for $x < 0$.

Expressing Equation 11.97 in terms of x and y , converting the numerator and denominator to the polar form of a complex number, combining the exponentials, and separating into real and imaginary parts, we get

$$\begin{aligned} \frac{dz}{dw} = \frac{\pi}{2g} & \left\{ \frac{(x^2 - y^2 - 1)^2 + 4x^2y^2}{[(x^2 - y^2 - a^2)^2 + 4x^2y^2]^{1/2}} \right\}^{1/2} \\ & \times \left[\sin \left[\tan^{-1} \left(\frac{2xy}{x^2 - y^2 - 1} \right) - \frac{1}{2} \tan^{-1} \left(\frac{2xy}{x^2 - y^2 - a^2} \right) \right] \right. \\ & \left. - i \cos \left[\tan^{-1} \left(\frac{2xy}{x^2 - y^2 - 1} \right) - \frac{1}{2} \tan^{-1} \left(\frac{2xy}{x^2 - y^2 - a^2} \right) \right] \right] \end{aligned} \quad (11.99)$$

Now, using the uniqueness of the derivative when taken in the u or iv directions, which led to the Cauchy–Riemann equations (Equation 11.48), we can write

$$\frac{dz}{dw} = \frac{\partial x}{\partial u} + i \frac{\partial y}{\partial u} = \frac{\partial y}{\partial v} - i \frac{\partial x}{\partial v} \quad (11.100)$$

This, together with Equation 11.99, can be used to extract the appropriate derivatives for use in Equation 11.96. Thus,

$$\begin{aligned} \frac{\partial x}{\partial u} = \frac{\partial y}{\partial v} &= \frac{\pi}{2g} \left\{ \frac{(x^2 - y^2 - 1)^2 + 4x^2y^2}{[(x^2 - y^2 - a^2)^2 + 4x^2y^2]^{1/2}} \right\}^{1/2} \\ & \times \sin \left[\tan^{-1} \left(\frac{2xy}{x^2 - y^2 - 1} \right) - \frac{1}{2} \tan^{-1} \left(\frac{2xy}{x^2 - y^2 - a^2} \right) \right] \\ \frac{\partial y}{\partial u} = -\frac{\partial x}{\partial v} &= -\frac{\pi}{2g} \left\{ \frac{(x^2 - y^2 - 1)^2 + 4x^2y^2}{[(x^2 - y^2 - a^2)^2 + 4x^2y^2]^{1/2}} \right\}^{1/2} \\ & \times \cos \left[\tan^{-1} \left(\frac{2xy}{x^2 - y^2 - 1} \right) - \frac{1}{2} \tan^{-1} \left(\frac{2xy}{x^2 - y^2 - a^2} \right) \right] \end{aligned} \quad (11.101)$$

These apply when $x \geq 0$ and their negatives must be used when $x < 0$.

Thus, the electric field in the w -plane can be expressed completely in terms of x and y via Equations 11.96 and 11.101. However, we must invert

Equation 11.89 to do this. The first step is to express Equation 11.89 in terms of x and y and in terms of its real and imaginary parts. Thus, we write the first \sin^{-1} term, using Equation 11.82:

$$\sin^{-1}\left(\frac{z}{a}\right) = \sin^{-1}\left(\frac{x}{a} + i\frac{y}{a}\right) = \sin^{-1}\left[\frac{2\left(\frac{x}{a}\right)}{p+q}\right] + i \cosh^{-1}\left(\frac{p+q}{2}\right) \quad (11.102)$$

where

$$p = \sqrt{\left(1 + \frac{x}{a}\right)^2 + \left(\frac{y}{a}\right)^2}, \quad q = \sqrt{\left(1 - \frac{x}{a}\right)^2 + \left(\frac{y}{a}\right)^2}$$

The second \sin^{-1} term in Equation 11.89 can be written similarly:

$$\begin{aligned} \sin^{-1}\left[\frac{z-a^2}{a(z-1)}\right] &= \sin^{-1}\left\{\frac{(x-a^2)+iy}{a[(x-1)+iy]}\right\} \\ &= \sin^{-1}\left\{\frac{(x-a^2)(x-1)+y^2+iy(a^2-1)}{a[(x-1)^2+y^2]}\right\} \\ &= \sin^{-1}\left\{\frac{2[(x-a^2)(x-1)+y^2]}{a[(x-1)^2+y^2]} + i \cosh^{-1}\left(\frac{p_1+q_1}{2}\right)\right\} \quad (11.103) \end{aligned}$$

where

$$p_1 \Big\} = \sqrt{\left[1 \pm \frac{[(x-a^2)(x-1)+y^2]}{a[(x-1)^2+y^2]}\right]^2 + \left[\frac{y(a^2-1)}{a[(x-1)^2+y^2]}\right]^2}$$

with the upper sign referring to p_1 and the lower sign to q_1 . Treating the third \sin^{-1} term in Equation 11.89 similarly, we get

$$\begin{aligned} \sin^{-1}\left[\frac{z+a^2}{a(z+1)}\right] &= \sin^{-1}\left\{\frac{(x+a^2)+iy}{a[(x+1)+iy]}\right\} \\ &= \sin^{-1}\left\{\frac{(x+a^2)(x+1)+y^2-iy(a^2-1)}{a[(x+1)^2+y^2]}\right\} \\ &= \sin^{-1}\left\{\frac{2[(x+a^2)(x+1)+y^2]}{a[(x+1)^2+y^2]} - i \cosh^{-1}\left(\frac{p_2+q_2}{2}\right)\right\} \quad (11.104) \end{aligned}$$

where

$$p_2 \Big\} = \sqrt{\left[1 \pm \frac{[(x+a^2)(x+1)+y^2]}{a[(x+1)^2+y^2]}\right]^2 + \left[\frac{y(a^2-1)}{a[(x+1)^2+y^2]}\right]^2}$$

Again the upper sign in the expression for p_2 and q_2 refers to p_2 and the lower sign to q_2 . Also, the negative sign multiplies the \cosh^{-1} term because the imaginary part of the complex argument of the \sin^{-1} function is negative.

Using Equations 11.102 through 11.104 in Equation 11.89, we get

$$\begin{aligned}
 u &= \frac{g}{\pi} \left\{ 2 \sin^{-1} \left[\frac{2 \left(\frac{x}{a} \right)}{p+q} \right] + \frac{h}{g} \left[\cosh^{-1} \left(\frac{p_1+q_1}{2} \right) - \cosh^{-1} \left(\frac{p_2+q_2}{2} \right) \right] \right\} \\
 v &= \frac{g}{\pi} \left\{ 2 \cosh^{-1} \left(\frac{p+q}{2} \right) \right. \\
 &\quad \left. - \frac{h}{g} \left[\sin^{-1} \left(\frac{2[(x-a^2)(x-1)+y^2]}{a[(x-1)^2+y^2](p_1+q_1)} \right) + \sin^{-1} \left(\frac{2[(x+a^2)(x+1)+y^2]}{a[(x+1)^2+y^2](p_2+q_2)} \right) \right] \right\}
 \end{aligned} \tag{11.105}$$

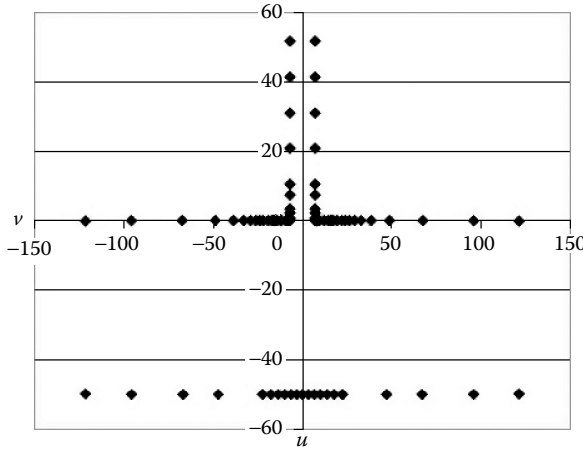
where

$$\begin{aligned}
 a &= \sqrt{1 + \left(\frac{h}{g} \right)^2} \\
 p \Bigg|_q &= \sqrt{\left(1 \pm \frac{x}{a} \right)^2 + \left(\frac{y}{a} \right)^2} \\
 p_1 \Bigg|_{q_1} &= \sqrt{\left\{ 1 \pm \frac{[(x-a^2)(x-1)+y^2]}{a[(x-1)^2+y^2]} \right\}^2 + \left\{ \frac{y(a^2-1)}{a[(x-1)^2+y^2]} \right\}^2} \\
 p_2 \Bigg|_{q_2} &= \sqrt{\left\{ 1 \pm \frac{[(x+a^2)(x+1)+y^2]}{a[(x+1)^2+y^2]} \right\}^2 + \left\{ \frac{y(a^2-1)}{a[(x-1)^2+y^2]} \right\}^2}
 \end{aligned}$$

The upper and lower signs refer to the p 's and q 's, respectively.

At this point, we can map Equation 11.105 in order to see how it behaves, particularly at the critical points of $x = \pm 1$ and $x = \pm a$, $y = 0$. This map is shown in [Figure 11.14](#) for a number of points along the x -axis and for $g = 7$ mm and $h = 50$ mm.

We will trace a point on the x -axis as it moves from +1,000,000 to -1,000,000. At $x = +1,000,000$, the point in the w -plane is only 51.4 mm above the u -axis on the right side of the gap between the two disks. As x decreases and approaches $+a$ from the right, the point moves down the v -axis and reaches the right corner at $x = a$. As x passes through a , it then moves right along the positive u -axis increasing toward $+\infty$ as x approaches $+1$. As x continues to decrease and passes through $+1$, it abruptly switches from $v = 0$ to $v = -h = -50$ mm in this case. That is, it jumps from the top of the horizontal gap

**FIGURE 11.14**

Map of Equation 11.105 for points along the x -axis in the z -plane to points in the w -plane.

to the bottom of the gap. The point then proceeds along the bottom of the horizontal gap toward $-\infty$ as x approaches -1 from the right. As x passes through -1 , the w -plane point abruptly switches to the top of the horizontal gap, where $v = 0$ and $u = -\infty$. As x continues toward $-a$, the mapped point heads toward the left corner point at $u = -g$ and $v = 0$. Then, as x heads toward $-\infty$, the point moves up the left side of the vertical gap between the two disks, reaching $v = 51.4$ mm at $x = -1,000,000$.

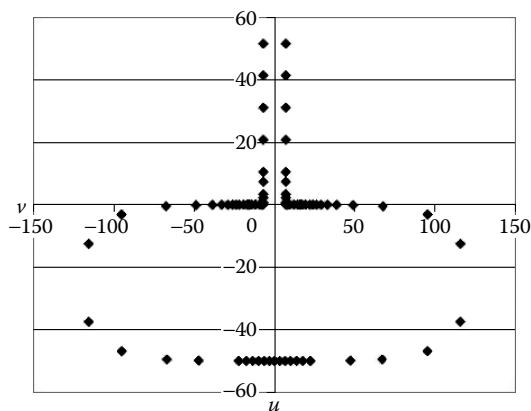
To see how this map behaves for $y > 0$, we plot the same x -axis points but with $y = 0.001$ in Figure 11.15 and with $y = 0.1$ in Figure 11.16.

Given u and v , Equation 11.105 can be inverted by a Newton–Raphson procedure. Using this method, the problem reduces to one of solving the following equations:

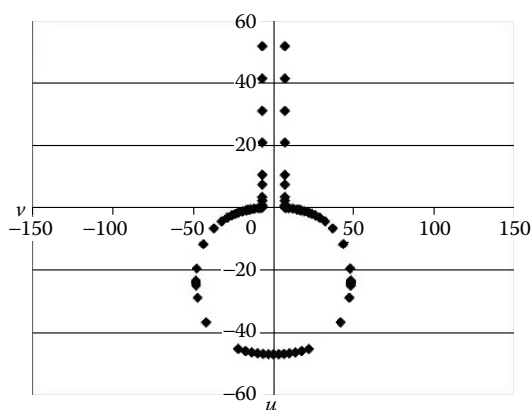
$$\begin{aligned} f_1(x, y) &= u(x, y) - u_0 = 0 \\ f_2(x, y) &= v(x, y) - v_0 = 0 \end{aligned} \quad (11.106)$$

where u_0 and v_0 are the desired coordinates at which the field in the w plane is evaluated. Since $\partial f_1 / \partial x = \partial u / \partial x$, and so forth, the Newton–Raphson equations for the increments Δx , Δy are

$$\begin{pmatrix} \Delta x \\ \Delta y \end{pmatrix} = \frac{-1}{\left[\left(\frac{\partial u}{\partial x} \right)^2 + \left(\frac{\partial u}{\partial y} \right)^2 \right]} \begin{pmatrix} \frac{\partial u}{\partial x} & -\frac{\partial u}{\partial y} \\ \frac{\partial u}{\partial y} & \frac{\partial u}{\partial x} \end{pmatrix} \begin{pmatrix} f_1(x, y) \\ f_2(x, y) \end{pmatrix} \quad (11.107)$$

**FIGURE 11.15**

Map of Equation 11.105 for points along the x -axis with $y = 0.001$ to points in the w -plane.

**FIGURE 11.16**

Map of Equation 11.105 for points along the x -axis with $y = 0.1$ to points in the w -plane.

where we have used the Cauchy–Riemann equations (Equation 11.48). At each iteration, we let $x_{\text{new}} = x_{\text{old}} + \Delta x$ and $y_{\text{new}} = y_{\text{old}} + \Delta y$ and stop when Δx and Δy are sufficiently small.

We can obtain the derivatives in Equation 11.107 by a procedure similar to that used to derive Equation 11.101. We use Equation 11.67 as a starting point with A from Equation 11.74:

$$\begin{aligned}
 f'(z) = \frac{dw}{dz} &= i \frac{2g}{\pi} \frac{(z^2 - a^2)^{1/2}}{(z^2 - 1)} = i \frac{2g}{\pi} \left\{ \frac{[(x + iy)^2 - a^2]^{1/2}}{(x + iy)^2 - 1} \right\} \\
 &= i \frac{2g}{\pi} \left\{ \frac{[(x^2 - y^2 - a^2) + i2xy]^{1/2}}{(x^2 - y^2 - 1) + i2xy} \right\}
 \end{aligned} \tag{11.108}$$

$$\begin{aligned}
&= \frac{2g}{\pi} \left\{ \frac{[(x^2 - y^2 - a^2)^2 + 4x^2y^2]^{1/2}}{(x^2 - y^2 - 1)^2 + 4x^2y^2} \right\}^{1/2} \\
&\quad \times \left\{ -\sin \left[\frac{1}{2} \tan^{-1} \left(\frac{2xy}{x^2 - y^2 - a^2} \right) - \tan^{-1} \left(\frac{2xy}{x^2 - y^2 - 1} \right) \right] \right. \\
&\quad \left. + i \cos \left[\frac{1}{2} \tan^{-1} \left(\frac{2xy}{x^2 - y^2 - a^2} \right) - \tan^{-1} \left(\frac{2xy}{x^2 - y^2 - 1} \right) \right] \right\}
\end{aligned}$$

Again, because of the square root function in Equation 11.108, we must make a branch cut along the line $x = 0$ and take the positive sign for $x > 0$ and the negative sign for $x < 0$. Since

$$\frac{dw}{dz} = \frac{\partial u}{\partial x} + i \frac{\partial v}{\partial x} = \frac{\partial v}{\partial y} - i \frac{\partial u}{\partial y} \quad (11.109)$$

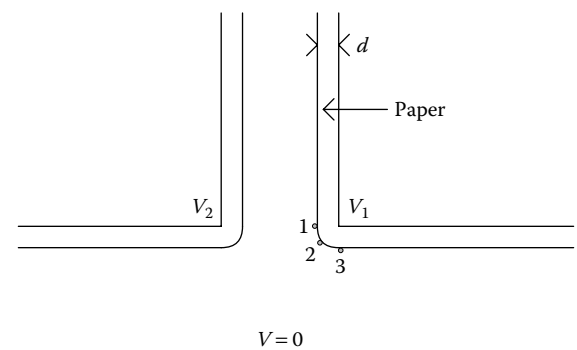
the partial derivatives for use in Equation 11.107 can be extracted from Equation 11.108 using Equation 11.109. We find

$$\begin{aligned}
\frac{\partial u}{\partial x} &= -\frac{2g}{\pi} \left\{ \frac{[(x^2 - y^2 - a^2)^2 + 4x^2y^2]^{1/2}}{(x^2 - y^2 - 1)^2 + 4x^2y^2} \right\}^{1/2} \\
&\quad \times \sin \left[\frac{1}{2} \tan^{-1} \left(\frac{2xy}{x^2 - y^2 - a^2} \right) - \tan^{-1} \left(\frac{2xy}{x^2 - y^2 - 1} \right) \right] \\
\frac{\partial u}{\partial y} &= -\frac{2g}{\pi} \left\{ \frac{[(x^2 - y^2 - a^2)^2 + 4x^2y^2]^{1/2}}{(x^2 - y^2 - 1)^2 + 4x^2y^2} \right\}^{1/2} \\
&\quad \times \cos \left[\frac{1}{2} \tan^{-1} \left(\frac{2xy}{x^2 - y^2 - a^2} \right) - \tan^{-1} \left(\frac{2xy}{x^2 - y^2 - 1} \right) \right]
\end{aligned} \quad (11.110)$$

Again, these are used when $x \geq 0$ and their negatives when $x < 0$.

11.2.4.2 Calculations and Comparison with a Finite Element Solution

A computer program was written to implement the above procedure for calculating the electric field. The field is infinite at the corners of the conductors. However, because real corners are not perfectly sharp, the field remains finite in practice. In transformer applications, the conductors are usually covered with an insulating layer of paper and the remaining space is filled with transformer oil. Because the paper has a much higher breakdown stress than

**FIGURE 11.17**

Points near the corner of the highest potential conductor where the electric field is calculated.

the oil, the field in the oil is usually critical for design purposes. The highest oil fields will occur at least a paper's thickness away from the corner of the highest potential conductor, which we assume is at potential V_1 . We have accordingly calculated the field at the three points shown in Figure 11.17, which are a paper's thickness (d) away from the corner of the V_1 potential conductor.

The presence of the paper, which has a different dielectric constant than oil, will modify the electric field. In general, it will increase it in the oil and decrease it in the paper. We will attempt to estimate this oil enhancement factor later. Here, we compare the analytic results with results from a finite element calculation without the presence of paper but with the fields calculated at the points shown in Figure 11.17, a paper's distance away from the corner. We compare the magnitudes of the fields E , where

$$E = \sqrt{E_u^2 + E_v^2} \quad (11.111)$$

The results for several different potential combinations and conductor separations are shown in Table 11.1. The agreement is very good, especially with the sharp corner finite element results. Finite element results for a 0.5-mm radius on the corners are also shown for comparison. These are also reasonably close to the analytic results and show that the sharpness or smoothness of the corners is washed out at distances greater than or equal to a paper's distance away. The field deep in the gap between the V_1 and V_2 conductors was also calculated with the analytic formulas and produced the expected result, $E = (V_2 - V_1)/2g$ (not shown in Table 11.1).

The enhancement factors in Table 11.1 are shown in parentheses. We can obtain these by performing the finite element calculations with paper having a dielectric constant $\epsilon = 4.0$ and then repeating it with the paper layer given the dielectric constant of oil $\epsilon = 2.2$ and taking the ratio of the field

TABLE 11.1

Comparison of Analytic and Finite Element Electric Field Magnitudes at Points 1, 2, and 3 of [Figure 11.17](#)

	Conformal Mapping	Finite Element (Sharp Corner)	Finite Element (Rounded Corner) ^a
(a) $V_1 = 825, V_2 = 725, g = 6.6, h = 63.5, d = 0.635$			
E_1	27.7	27.7 (1.08)	27.6 (1.12)
E_2	27.9	28.2 (1.22)	28.6 (1.14)
E_3	28.3	28.5 (1.08)	28.4 (1.14)
(b) $V_1 = 850, V_2 = 750, g = 5.08, h = 63.5, d = 0.508$			
E_1	32.7	32.7 (1.06)	32.4 (1.14)
E_2	32.4, 28.7 ^b	29.0 ^b (1.29)	32.9 (1.15)
E_3	32.6	32.6 (1.05)	32.6 (1.13)
(c) $V_1 = 800, V_2 = 800, g = 5.08, h = 63.5, d = 0.508$			
E_1	11.3	11.4 (0.90)	12.3 (1.04)
E_2	13.3, 12.2 ^b	12.4 ^b (1.17)	13.5 (1.16)
E_3	15.0	15.2 (1.04)	14.6 (1.09)
(d) $V_1 = 100, V_2 = -50, g = 12.7, h = 63.5, d = 0.508$			
E_1	17.8	17.6 (1.07)	17.2 (1.14)
E_2	16.9, 15.0 ^b	15.1 ^b (1.33)	16.9 (1.14)
E_3	16.1	16.0 (1.03)	16.0 (1.13)

Enhancement factors are shown in parentheses.
Lengths are in mm, potentials in kV, and fields in kV/mm.

^a The rounded corner conductor radius = 0.5.

^b $d = 0.71$.

magnitudes in the two cases. This is normally greater than one; however, in one case it is 0.90, as shown in Table 11.1. This is probably due to discretization inaccuracies in the finite element calculation or possibly in pinpointing the exact location of where to evaluate the field in the two cases since this was done with the cursor. There seems to be a tendency for greater enhancement factors at corner point 2 than on either side of it for a sharp corner.

The conformal mapping technique does not apply to the paper-oil situation so other approximate approaches must be employed to account for the oil enhancement. The equipotential contour plot for a finite element calculation with paper present is shown in [Figure 11.18](#). This is for the conditions given in Table 11.1a with sharp corners. [Figure 11.19](#) is a plot of the vector field for the same case.



FIGURE 11.18
(See color insert following page 338.) Equipotential contour plot in the oil from a finite element calculation showing the geometry near the corner for the conditions given in Table 11.1a with sharp corners and paper cover. The potential varies from high (red) near the upper disk to low (blue) near the zero-potential plane.

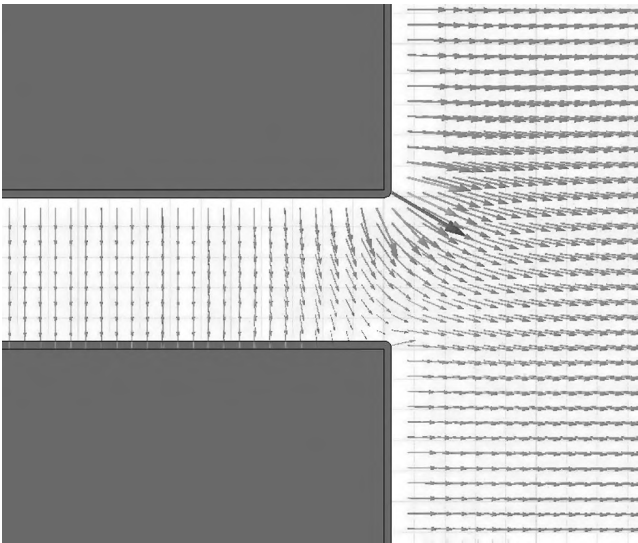
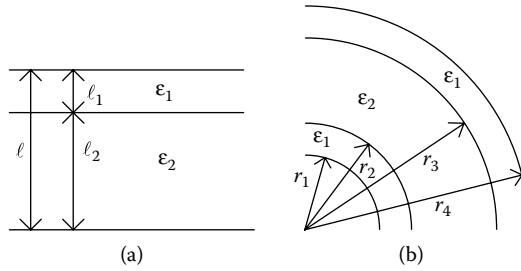


FIGURE 11.19
(See color insert following page 338.) Electric field vector plot from a finite element calculation showing an enlarged region near the conductor's corners for the same conditions as Figure 11.18.

**FIGURE 11.20**

Paper-oil configurations for (a) planar and (b) cylindrical geometries resulting in enhanced fields in the oil compared with the all oil case.

11.2.4.3 Estimating Enhancement Factors

For a paper-oil layering in a planar geometry as shown in Figure 11.20a, all the paper can be lumped into one layer for calculational purposes. Letting 1 refer to the paper layer and 2 refer to the oil layer, the enhancement factor for the oil (η = the ratio of the field in the oil with and without a paper layer) is

$$\eta = \frac{1}{\epsilon_2 \left(\frac{f_1}{\epsilon_1} + \frac{f_2}{\epsilon_2} \right)} \quad (11.112)$$

where $f_1 = \ell_1/\ell$, $f_2 = \ell_2/\ell$ with $\ell = \ell_1 + \ell_2$ are the fractional lengths of materials 1 and 2, respectively. We assume that when the paper is absent, it is replaced by oil, keeping the total distance ℓ between the metal surfaces the same.

In cylindrical cases, shown in Figure 11.20b, the position of the paper layer or layers is important in calculating the enhancement factors. We will assume that one paper layer is next to the inner conductor and one is next to the outer conductor. When additional layers are present, such as pressboard barriers, their position must be known, and they can be included in the calculation. The oil enhancement factor for the situation shown in Figure 11.20b is

$$\eta = \frac{\ln\left(\frac{r_4}{r_1}\right)}{\epsilon_2 \left[\frac{1}{\epsilon_1} \ln\left(\frac{r_2}{r_1}\right) + \frac{1}{\epsilon_2} \ln\left(\frac{r_3}{r_2}\right) + \frac{1}{\epsilon_1} \ln\left(\frac{r_4}{r_3}\right) \right]} \quad (11.113)$$

The cylindrical enhancement factor is larger than the planar enhancement factor for the same paper and oil layer thicknesses. It reduces to the planar case when r_1 becomes large.

The cylindrical enhancement factors refer to ideal geometries. For the geometry of interest shown in Figure 11.17, the enhancement factors reduce to the planar case for field points away from the corner and deep into the $V_1 - V_2$ gap

TABLE 11.2Calculated Oil Enhancement Factors for the Cases in [Table 11.1](#)

Case	Planar		Cylindrical		Weighted Cylindrical	Table 11.1 Average Rounded
	$V_1 - V_2$ Gap	$V_1 - 0$ Gap	$V_1 - V_2$ Gap	$V_1 - 0$ Gap		
a	1.095	1.004	1.182	1.081	1.137	1.133
b	1.099	1.004	1.174	1.069	1.125	1.140
c	1.099	1.004	1.174	1.069	1.125	1.096
d	1.037	1.004	1.113	1.069	1.094	1.137

or the $V_1 - 0$ or $V_2 - 0$ gaps. This is borne out by the finite element calculations. However, the geometry is closer to the cylindrical case near the corner.

For a sharp corner corresponding to $r_1 = 0$, Equation 11.113 shows that $\eta \rightarrow \epsilon_1/\epsilon_2 = 1.82$ for a case of oil–paper. This is an upper limit on the enhancement factor and is more than enough to account for the sharp corner enhancement factors shown in Table 11.1. For our purposes, the rounded corner enhancement factors are the most relevant ones. Table 11.1 shows that these are nearly the same for the three corner points. Treating the rounded corner case as a cylindrical geometry, we can take $r_1 = 0.5$ mm. The proper radius to use for the outer conductor is less clear. In Table 11.2, we calculate the planar and cylindrical oil enhancement factors for the two different gaps, where the outer conductor radius is taken to be the inner conductor radius plus the gap length that is $2g$ or h for the two gaps ([Figure 11.11](#)). Thus, referring to [Figure 11.20b](#):

$$\begin{aligned} r_4(V_1 - V_2 \text{ gap}) &= r'_4 = r_1 + g \\ r_4(V_1 - 0 \text{ gap}) &= r''_4 = r_1 + h \end{aligned} \quad (11.114)$$

Note that the $V_1 - 0$ gap has only one layer of paper. We also show a weighted cylindrical enhancement factor that uses a weighted average of the above two radii. The weighting is taken to be inversely proportional to the radius so that the V_2 conductor, which is closest to the corner, is given the highest weighting. This results in an effective outer conductor radius of

$$r_4 = \frac{2r'_4 r''_4}{r'_4 + r''_4} \quad (11.115)$$

These weighted enhancements come closest to the corner enhancements determined by the finite element calculations in most cases. We will therefore use a cylindrical enhancement factor with this weighted outer conductor radius in our design calculations if it is above the $V_1 - V_2$ gap planar enhancement factor. Otherwise, the $V_1 - V_2$ gap planar enhancement factor will be used.

Summarizing the above results, the conformal mapping calculations of the electric field near the corner of one of a pair of conductors at different potentials relative to a neighboring ground plane agree well with calculations obtained by a finite element program. Since the electric field is infinite at the corner of a perfectly sharp conductor, the calculations were compared a small distance from the corner, taken to be the thickness of a paper layer in an actual transformer winding. The finite element calculations were made with sharp and rounded corners, and the resulting fields were nearly the same a paper's thickness away from the corner. Since the oil breakdown fields are the most critical in transformer design and these occur beyond the paper's thickness, this result shows that a conformal mapping calculation is appropriate for determining these fields.

The only problem with the conformal mapping approach is that it does not take into account the different dielectric constants of oil and paper. We have proposed a method to take these approximately into account by means of an oil enhancement factor. By comparing with a finite element calculation, we have developed a formula to obtain this enhancement factor.

11.3 Finite Element Electric Field Calculations

Finite element methods permit the calculation of electric potentials and fields for complicated geometries. Modern commercial finite element codes generally provide a set of drawing tools, which allow the user to input the geometry in as much detail as desired. More sophisticated versions even allow parametric input so that changes in one or more geometric parameters such as the distance between electrodes can be easily accomplished without redoing the entire geometry. Both 2D and three-dimensional (3D) versions are available although the input to the 3D versions is, of course, more complicated. For many problems, a 2D geometry can be an adequate approximation to the real configuration. 2D versions usually allow an axis-symmetric geometry by inputting a cross section of it. In this sense, a 3D problem, which happens to have cylindrical symmetry, is solved. The x - y 2D geometry is really modeling an infinitely long object having the specified 2D cross section.

The basic geometry, which the user inputs, is then subdivided into a triangular mesh. Smaller triangles are used in regions where the potential is expected to change most rapidly. Larger triangles can adequately describe more slowly varying potential regions. Some programs automatically perform the triangular meshing and, through an iterative process, even refine the mesh in critical regions until the desired solution accuracy is achieved. When linear triangles are used, the potential is solved for only at the triangle

nodes and a linear interpolation scheme is used to approximate it inside the triangle. For higher-order triangles, additional nodes are added per triangle, and higher-order polynomial approximations are used to find the potential inside the triangles. Some programs use only second-order triangles because these provide sufficient accuracy for reasonable computer memory and execution times.

Some art is required even for the geometric input. Complete detail often is unnecessary to determine the fields in critical regions. Thus, the user must know when it is reasonable to ignore certain geometric details that are irrelevant to the problem. This not only saves on the labor involved in inputting the geometry, but it can also considerably reduce required computer memory and solution times.

Finite element programs require that the user input sources and the appropriate boundary conditions for the problem at hand. In the case of electric potential calculations, the sources are electric charges and the boundary conditions include specifying the voltage at one or more electrode surfaces. These are often the surfaces of metallic objects and have a constant potential throughout; therefore modeling their interiors is not necessary. Typically, the program will allow the user to declare such metallic objects nonexistent or perfect conductors so that the solution is not solved for over their interiors. Their surface, however, is still included as an equipotential surface. Sometimes the equipotential surface is a boundary surface so it already has no interior. A metallic object can also be allowed to float so that its potential is part of the problem solution.

On external boundaries where no specification is made, we assume that these have natural or Neumann boundary conditions. This means that the normal derivative of the potential vanishes along them. This implies that the potential lines (in 2D) or surfaces (in 3D) enter the boundary at right angles. These types of boundary are usually used to express some symmetry condition. For instance, a long conducting cylinder centered inside a rectangular grounded box can be modeled by a circle inside the box. However, by symmetry, only a quarter of the geometry centered on the circle needs to

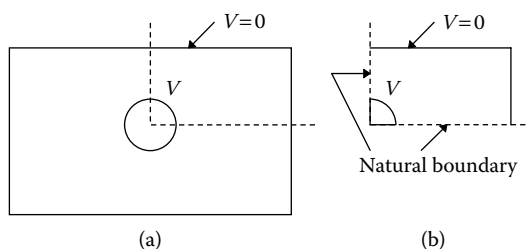


FIGURE 11.21

Using symmetry to simplify the finite element problem: (a) full geometry and (b) $\frac{1}{4}$ geometry.

be modeled, and natural boundary conditions must be imposed on the new boundaries created by isolating this region. This is depicted in [Figure 11.21](#).

The method works here because the potential lines are concentric ovoids about the conducting cylinder and therefore enter the dotted line boundaries in the 1/4 geometry at right angles. Although the problem depicted in Figure 11.21 is relatively simple to solve in the full geometry so that the use of symmetry does not save much in input or solution times, this technique can save much effort when more complicated geometries are involved.

Another boundary condition that some programs allow is the balloon boundary. This type of boundary is like specifying that the boundary does not exist and the solution continues beyond it as if there were empty space out far in that direction. There is a practical necessity for this type of boundary condition, because the finite element technique requires that the entire solution space of interest be subdivided into triangles or elements. When this solution space extends far enough that the geometric region of interest will be dwarfed relative to the whole space, we can specify such balloon boundaries rather than model vast regions of empty space. In practice, the program actually models a much larger region of space but with much coarser elements far away from the geometry of interest. This process is transparent to the user.

We will now give some examples of solving electrostatic problems with a finite element program using Ansoft's Maxwell 2D software. The first is a varistor stack assembly shown in Figure 11.22; this is an axisymmetric geometry. The varistors themselves are modeled as two continuous cylinders separated by a metallic region in the center that is floating. The ends

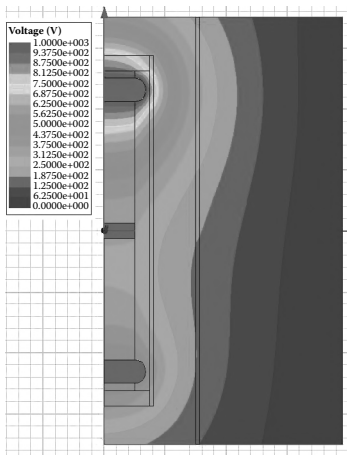


FIGURE 11.22
(See color insert following page 338.) Axisymmetric model of a varistor stack with equipotential contours. The top metal cap was at 1000 V and the bottom cap at 500 V.

consist of shaped metal electrodes to help reduce the end fields. There are pressboard disks that mechanically hold the assembly together inside a pressboard cylinder. There is another pressboard cylinder on the outside followed by the ground cylinder that defines the outermost boundary. The top and bottom boundaries are balloon boundaries. Although the geometry of the varistor stack itself is really cylindrical, the ground may not, in fact, be a concentric cylinder as modeled. For example, it may be a tank wall. However, it is sufficiently far away that a cylindrical approximation is reasonable.

The varistor cylinders, the pressboard elements, and the oil were given appropriate permittivities. The metallic end caps and center region were declared to be perfect conductors. Different voltages were specified on the two end caps, and the outer boundary cylinder was given a zero voltage. The center metallic conductor was floating. The equipotential lines obtained by solving this problem are shown in [Figure 11.22](#). Since the electric field is the gradient of the potential, the field is highest where the lines are closely spaced. The field itself can be calculated and displayed vectorially as shown in [Figure 11.23](#). The field can also be obtained numerically at specified points, along specified lines, or within specified regions.

The second example is of a region near the tops of the low-voltage (LV) and high-voltage (HV) windings with a static ring on top of the HV winding. These rings are used to moderate the electric fields near the tops of the windings by providing a surface of relatively large curvature compared with the sharper corners that occur at the windings disks. The static rings are at the same potential as the top disk. These are most effective when close

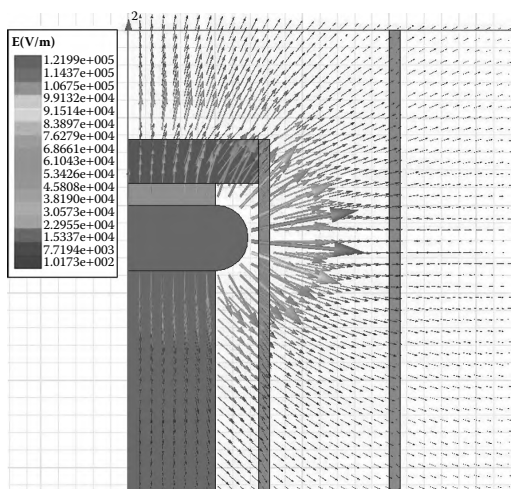


FIGURE 11.23
(See color insert following page 338.) Electric field vectors near the top metal cap.

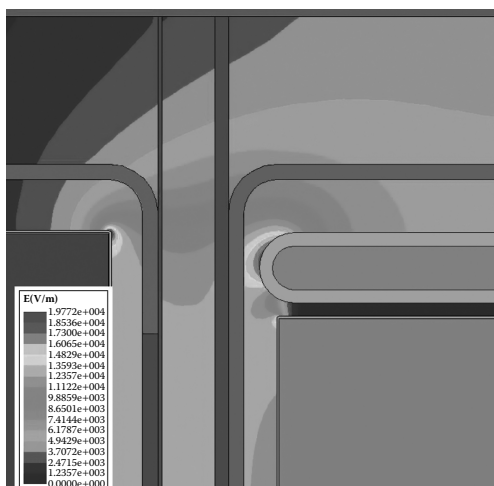


FIGURE 11.24

(See color insert following page 338.) Electric field magnitude contours in the oil near the tops of an LV winding at ground potential on the left and an HV winding at 450 kV on the right topped by a static ring at the same potential. The model is axisymmetric. The key is in kV/m.

to the top disk. In the example shown in Figure 11.24, the static ring is a few millimeters from the top disk. Since only the fields near the top disks of the two windings and static ring are of interest, the rest of the windings were modeled as solid blocks at the same potential as the top disks. Pressboard collars and cylinders that are used to subdivide the large oil gaps to lower the electrical breakdown probabilities are also shown. A cylindrically symmetric model was used, but only a blowup of the region near the top of the two windings is shown in Figure 11.24.

Notice that the static ring has diminished the corner field at the top of the HV winding on the right, but that the corner field on the LV winding on the left is fairly high. It can probably also benefit by having its own static ring.

12

Capacitance Calculations

12.1 Introduction

Under impulse conditions, very fast voltage pulses are applied to a transformer. These contain high-frequency components, eliciting capacitive effects that are absent at normal operating frequencies. In order to simulate the behavior of a transformer under impulse conditions, we must determine the capacitances for use in circuit or traveling-wave models [Mik78, Rud40].

The highest electrical stresses usually occur at the high-voltage end of the winding so that modifications of the first few disks are sometimes required to meet the voltage breakdown limits. This modification can take the form of the addition of one or more static rings so that their effect on the disk capacitance must be determined. Other methods such as the use of wound-in shields and interleaving are effective in increasing the disk capacitance, which is desirable for a better voltage distribution. We discuss wound-in shields in this chapter, but we discuss interleaving only for a particular variety used in multistart tap windings.

We use an energy method to determine the capacitance or, in general, the capacitance matrix. This method is a generalization of the method used by Stein to determine the disk capacitance of a disk embedded in a winding of similar disks [Ste64]. It utilizes a continuum model of a disk so that disks having many turns are considered. We also compare capacitances determined in this manner with capacitances determined using a more conventional approach. The conventional method also works for helical windings, that is, windings having one turn per disk, so that it is useful in its own right.

For completeness, we also calculate winding–winding, winding–core, and winding–tank capacitances that are all qualitatively similar. These are based on a cruder model and assume an infinitely long coil, ignoring end effects. They are really capacitances per unit length.

12.2 Distributive Capacitance along a Winding or Disk

We will try to be as general as possible here so that we may apply the results to a variety of situations. Thus, we will consider a disk or coil section having a series capacitance per unit length, c_s , and shunt capacitances per unit length, c_a and c_b to the neighboring objects on either side of the disk or coil section, as shown in Figure 12.1. For generality, we assume these neighboring objects to have linear voltage distributions given by

$$\begin{aligned} V_a(x) &= V_{a1} + \frac{x}{L}(V_{a2} - V_{a1}) \\ V_b(x) &= V_{b1} + \frac{x}{L}(V_{b2} - V_{b1}) \end{aligned} \quad (12.1)$$

where L is the length of the disk or coil section and x measures the distance from the high-voltage end at V_1 to the low-voltage end at V_2 . Setting $V_{a1} = V_{a2} = V_a$ and $V_{b1} = V_{b2} = V_b$ gives these neighboring objects a constant voltage.

Applying current conservation to the node at x in Figure 12.1 and assuming the current directions shown, we have

$$i_{x-\Delta x} - i_{x+\Delta x} = i_a + i_b \quad (12.2)$$

Using the current-voltage relationship for a capacitor, $i = C dV/dt$, and letting $V(x)$ denote voltages along the vertical centerline of Figure 12.1, we can rewrite Equation 12.2:

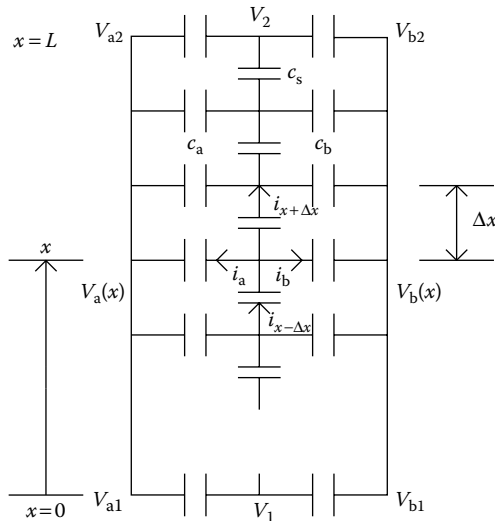


FIGURE 12.1

Approximately continuous capacitance distribution of a coil section.

$$\begin{aligned}
& c_s \Delta x \frac{d}{dt} [V(x - \Delta x) - V(x)] - c_s \Delta x \frac{d}{dt} [V(x) - V(x + \Delta x)] \\
& = c_a \Delta x \frac{d}{dt} [V(x) - V_a(x)] + c_b \Delta x \frac{d}{dt} [V(x) - V_b(x)] \quad (12.3)
\end{aligned}$$

Rearranging this equation, we get

$$\begin{aligned}
\frac{d}{dt} \{ c_s [V(x + \Delta x) - 2V(x) + V(x - \Delta x)] - c_a [V(x) - V_a(x)] \\
- c_b [V(x) - V_b(x)] \} = 0 \quad (12.4)
\end{aligned}$$

Thus, the quantity in curly brackets is a constant in time and may be set to 0 for all practical purposes. (For an applied pulse, all the voltages are zero after a very long time, so the constant must be zero.) Dividing the constant (= 0) curly bracket term in Equation 12.4 by $c_s(\Delta x)^2$, we get

$$\frac{V(x + \Delta x) - 2V(x) + V(x - \Delta x)}{(\Delta x)^2} - \frac{(c_a + c_b)}{c_s(\Delta x)^2} V(x) + \frac{[c_a V_a(x) + c_b V_b(x)]}{c_s(\Delta x)^2} = 0 \quad (12.5)$$

The first term in Equation 12.5 is the finite difference approximation to d^2V/dx^2 . The combination

$$\frac{(c_a + c_b)}{c_s(\Delta x)^2} \quad (12.6)$$

can be expressed in terms of the total series capacitance C_s and total shunt capacitances C_a and C_b , using

$$C_s = \frac{c_s \Delta x}{N}, \quad C_a = c_a \Delta x N, \quad C_b = c_b \Delta x N \quad (12.7)$$

where N is the number of subdivisions of the total length L into units of size Δx , $N = L/\Delta x$. Hence, Equation 12.7 becomes

$$C_s = \frac{c_s(\Delta x)^2}{L}, \quad C_a = c_a L, \quad C_b = c_b L \quad (12.8)$$

Substituting this into Equation 12.6, we get

$$\frac{(c_a + c_b)}{c_s(\Delta x)^2} = \frac{C_a + C_b}{C_s L^2} = \frac{\alpha^2}{L^2} \quad (12.9)$$

where

$$\alpha = \sqrt{\frac{C_a + C_b}{C_s}} \quad (12.10)$$

Similarly,

$$\frac{c_a}{c_s(\Delta x)^2} = \frac{C_a}{C_s L^2}, \quad \frac{c_b}{c_s(\Delta x)^2} = \frac{C_b}{C_s L^2} \quad (12.11)$$

Substituting Equations 12.9 and 12.11 into Equation 12.5 and taking the limit to be $\Delta x \rightarrow 0$ results in the differential equation

$$\frac{d^2 V}{dx^2} - \left(\frac{\alpha}{L} \right)^2 V = -\frac{1}{C_s L^2} [C_a V_a(x) + C_b V_b(x)] \quad (12.12)$$

The solution to the homogeneous part of Equation 12.12 is

$$V = A e^{\frac{\alpha}{L}x} + B e^{-\frac{\alpha}{L}x} \quad (12.13)$$

where A and B are constants to be determined by the boundary conditions. For the inhomogeneous part of Equation 12.12, we use

$$V = F + Gx \quad (12.14)$$

where F and G are determined by substituting them into Equation 12.12 and using Equation 12.1

$$-\left(\frac{\alpha}{L} \right)^2 (F + Gx) = -\frac{1}{C_s L^2} \left\{ C_a V_{a1} + C_b V_{b1} + \frac{x}{L} [C_a (V_{a2} - V_{a1}) + C_b (V_{b2} - V_{b1})] \right\} \quad (12.15)$$

Collecting terms, we find

$$\begin{aligned} F &= \frac{1}{\alpha^2 C_s} (C_a V_{a1} + C_b V_{b1}) \\ G &= \frac{1}{\alpha^2 C_s L} [C_a (V_{a2} - V_{a1}) + C_b (V_{b2} - V_{b1})] \end{aligned} \quad (12.16)$$

Thus, the general solution to Equation 12.12 is

$$\begin{aligned} V(x) &= A e^{\frac{\alpha}{L}x} + B e^{-\frac{\alpha}{L}x} + \frac{1}{\alpha^2 C_s} (C_a V_{a1} + C_b V_{b1}) \\ &\quad + \frac{1}{\alpha^2 C_s} \left(\frac{x}{L} \right) [C_a (V_{a2} - V_{a1}) + C_b (V_{b2} - V_{b1})] \end{aligned} \quad (12.17)$$

Using the boundary conditions $V = V_1$ at $x = 0$ and $V = V_2$ at $x = L$, we can solve Equation 12.17 for A and B . Performing the algebra, the solution can be cast in the following form:

$$\begin{aligned} V(x) = & (\gamma_a V_{a1} + \gamma_b V_{b1}) + \left(\frac{x}{L}\right) [\gamma_a (V_{a2} - V_{a1}) + \gamma_b (V_{b2} - V_{b1})] \\ & + \frac{1}{\sinh \alpha} \left\{ [V_2 - (\gamma_a V_{a2} + \gamma_b V_{b2})] \sinh \left(\alpha \frac{x}{L} \right) \right. \\ & \left. + [V_1 - (\gamma_a V_{a1} + \gamma_b V_{b1})] \sinh \left[\alpha \left(1 - \frac{x}{L} \right) \right] \right\} \end{aligned} \quad (12.18)$$

where

$$\gamma_a = \frac{C_a}{C_a + C_b}, \quad \gamma_b = \frac{C_b}{C_a + C_b} \quad (12.19)$$

so that $\gamma_a + \gamma_b = 1$. We need the derivative of this expression for evaluating the energy and for obtaining turn–turn voltages. It is

$$\begin{aligned} \frac{dV}{dx} = & \frac{1}{L} [\gamma_a (V_{a2} - V_{a1}) + \gamma_b (V_{b2} - V_{b1})] \\ & + \frac{\alpha}{L \sinh \alpha} \left\{ [V_2 - (\gamma_a V_{a2} + \gamma_b V_{b2})] \cosh \left(\alpha \frac{x}{L} \right) \right. \\ & \left. - [V_1 - (\gamma_a V_{a1} + \gamma_b V_{b1})] \cosh \left[\alpha \left(1 - \frac{x}{L} \right) \right] \right\} \end{aligned} \quad (12.20)$$

To determine the capacitance, we must evaluate the stored electrostatic energy. This energy is given by $C = \frac{1}{2} C (\Delta V)^2$, where C is the capacitance and ΔV is the voltage across the capacitor. Reverting to the original discrete notation, the energy in the series capacitance is

$$E_{\text{series}} = \frac{1}{2} \sum_1^N c_s \Delta x (\Delta V)^2 \quad (12.21)$$

Using Equation 12.8, this becomes

$$E_{\text{series}} = \frac{C_s L}{2} \sum_1^N \frac{1}{\Delta x} (\Delta V)^2 \quad (12.22)$$

Substituting $\Delta V = (dV/dx) \Delta x$ into Equation 12.22 and letting $\Delta x \rightarrow 0$, we get

$$E_{\text{series}} = \frac{C_s L}{2} \int_0^L \left(\frac{dV}{dx} \right)^2 dx \quad (12.23)$$

The energy in the shunt capacitances can be found similarly:

$$E_{\text{shunt}} = \frac{1}{2} \sum_1^N c_a \Delta x [V(x) - V_a(x)]^2 + \frac{1}{2} \sum_1^N c_b \Delta x [V(x) - V_b(x)]^2 \quad (12.24)$$

Again, using Equation 12.8 and taking the limit as $\Delta x \rightarrow 0$, we get

$$E_{\text{shunt}} = \frac{C_a}{2L} \int_0^L [V(x) - V_a(x)]^2 dx + \frac{C_b}{2L} \int_0^L [V(x) - V_b(x)]^2 dx \quad (12.25)$$

Combining Equations 12.23 and 12.25, the total energy is

$$E = \frac{C_s L}{2} \int_0^L \left(\frac{dV}{dx} \right)^2 dx + \frac{C_a}{2L} \int_0^L [V(x) - V_a(x)]^2 dx + \frac{C_b}{2L} \int_0^L [V(x) - V_b(x)]^2 dx \quad (12.26)$$

Substituting Equations 12.18 and 12.20 into Equation 12.26 and performing the integrations, we get

$$\begin{aligned} E = \frac{C_s}{2} \left\{ [(V_1 - \beta_1)^2 + (V_2 - \beta_2)^2] \frac{\alpha}{\tanh \alpha} - 2(V_1 - \beta_1)(V_2 - \beta_2) \frac{\alpha}{\sinh \alpha} \right. \\ - \eta^2 - 2\eta(V_1 - V_2) \\ + \alpha^2 \gamma_a \left[(\beta_1 - V_{a1})^2 + (\beta_1 - V_{a1})[\eta - (V_{a2} - V_{a1})] + \frac{1}{3}[\eta - (V_{a2} - V_{a1})]^2 \right] \\ \left. + \alpha^2 \gamma_b \left[(\beta_1 - V_{b1})^2 + (\beta_1 - V_{b1})[\eta - (V_{b2} - V_{b1})] + \frac{1}{3}[\eta - (V_{b2} - V_{b1})]^2 \right] \right\} \quad (12.27) \end{aligned}$$

where

$$\beta_1 = \gamma_a V_{a1} + \gamma_b V_{b1}, \quad \beta_2 = \gamma_a V_{a2} + \gamma_b V_{b2}, \quad \eta = \beta_2 - \beta_1 \quad (12.28)$$

For most of the applications of interest here, the side objects on which the shunt capacitances terminate are at a constant potential. Thus, to achieve this, we should set

$$V_{a1} = V_{a2} = V_a, \quad V_{b1} = V_{b2} = V_b \quad (12.29)$$

From this and Equation 12.28, we see that

$$\beta_1 = \beta_2 = \beta = \gamma_a V_a + \gamma_b V_b, \quad \eta = 0 \quad (12.30)$$

For this case, Equation 12.18 becomes

$$V(x) = \frac{1}{\sinh \alpha} \left\{ (V_2 - \beta) \sinh \left(\alpha \frac{x}{L} \right) + (V_1 - \beta) \sinh \left[\alpha \left(1 - \frac{x}{L} \right) \right] \right\} + \beta \quad (12.31)$$

Also, Equation 12.20 becomes

$$\frac{dV}{dx} = \frac{\alpha}{L \sinh \alpha} \left\{ (V_2 - \beta) \cosh \left(\alpha \frac{x}{L} \right) - (V_1 - \beta) \cosh \left[\alpha \left(1 - \frac{x}{L} \right) \right] \right\} \quad (12.32)$$

The energy expression in Equation 12.27 reduces to

$$E = \frac{C_s}{2} \left\{ [(V_1 - \beta)^2 + (V_2 - \beta)^2] \frac{\alpha}{\tanh \alpha} - 2(V_1 - \beta)(V_2 - \beta) \frac{\alpha}{\sinh \alpha} + \alpha^2 [\gamma_a (\beta - V_a)^2 + \gamma_b (\beta - V_b)^2] \right\} \quad (12.33)$$

12.3 Stein's Disk Capacitance Formula

As an example of Stein's disk capacitance formula, we can apply the above results to the case considered by Stein [Ste64] consisting of a disk embedded in a coil of similar disks (Figure 12.2). Assuming V is the voltage drop across

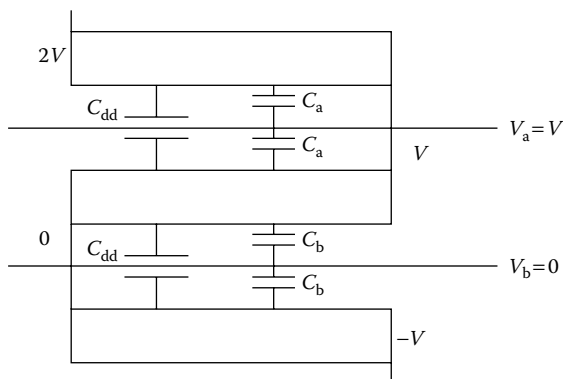


FIGURE 12.2

Disk embedded in a coil of similar disks with V the voltage drop along a disk.

an individual disk, we can take $V_1 = V$ and $V_2 = 0$. This applies to the middle disk in Figure 12.2. Starting from the right side of the bottom disk at potential $-V_1$ and proceeding upwards in the direction of voltage increase, we see that the voltage on the inner side of the bottom disk is zero. This is the same as the voltage on the inner side of the middle disk since they are connected at that point. Proceeding along the middle disk, the voltage reaches V outside that disk, but this side is connected to the outside of the top disk, so its voltage is also V . Proceeding along the top disk, we reach a voltage of $2V$ at its inner side. We assume that neighboring disks have the same voltage drop. Thus, we can imagine equipotential planes between the disks with the values for the middle disk $V_a = V$ and $V_b = 0$, as shown in Figure 12.2. As we move along the middle disk, these values are the average of the potential on the middle disk and the potential on the neighboring disk and can be taken as representing the potential value midway between them. The capacitances to the midplane are twice the disk–disk capacitance, $C_a = C_b = 2C_{dd}$. Since the two capacitances are equal, $\gamma_a = \gamma_b = \frac{1}{2}$ and $\beta = V/2$. For these values, the energy from Equation 12.33 becomes

$$E = \frac{C_s V^2}{2} \left[\frac{1}{2} \frac{\alpha}{\tanh \alpha} + \frac{1}{2} \frac{\alpha}{\sinh \alpha} + \frac{\alpha^2}{4} \right] \quad (12.34)$$

The effective disk capacitance is found from $E = 1/2 CV^2$ and is

$$C_{\text{Stein}} = C_s \left[\frac{1}{2} \frac{\alpha}{\tanh \alpha} + \frac{1}{2} \frac{\alpha}{\sinh \alpha} + \frac{\alpha^2}{4} \right] \quad (12.35)$$

where C_s is the series capacitance of the turns and

$$\alpha = \sqrt{\frac{C_a + C_b}{C_s}} = \sqrt{\frac{4C_{dd}}{C_s}} \quad (12.36)$$

C_{dd} is the disk–disk capacitance.

We compare this result with the more conventional approach. This assumes that the voltage drop along the disk is linear so that

$$V(x) = V \left(1 - \frac{x}{L} \right) \quad (12.37)$$

Substituting the derivative of Equation 12.37 into Equation 12.23, we get the energy in the series turns:

$$E_{\text{series}} = \frac{1}{2} C_s V^2 \quad (12.38)$$

We must consider the shunt energy with respect to the equipotential midplanes since we want the energy associated with a single disk. This is, using Equation 12.25,

$$E_{\text{shunt}} = \frac{1}{2} \left(\frac{2C_{\text{dd}}}{L} \right) \int_0^L \left\{ \left[V \left(1 - \frac{x}{L} \right) - V \right]^2 + \left[V \left(1 - \frac{x}{L} \right) - 0 \right]^2 \right\} dx \quad (12.39)$$

Evaluating this expression, we find

$$E_{\text{shunt}} = \frac{1}{2} \left(\frac{4}{3} C_{\text{dd}} \right) V^2 \quad (12.40)$$

Combining Equations 12.38 and 12.40 and extracting the effective disk capacitance, we get

$$C_{\text{conv}} = C_s + \frac{4}{3} C_{\text{dd}} \quad (12.41)$$

This expression can be applied to a helical winding (one turn per disk) by taking $C_s = 0$.

To compare Equation 12.35 with Equation 12.41, we normalize Equation 12.35 by dividing it by C_s . Thus,

$$\frac{C_{\text{Stein}}}{C_s} = \frac{1}{2} \frac{\alpha}{\tanh \alpha} + \frac{1}{2} \frac{\alpha}{\sinh \alpha} + \frac{\alpha^2}{4} \quad (12.42)$$

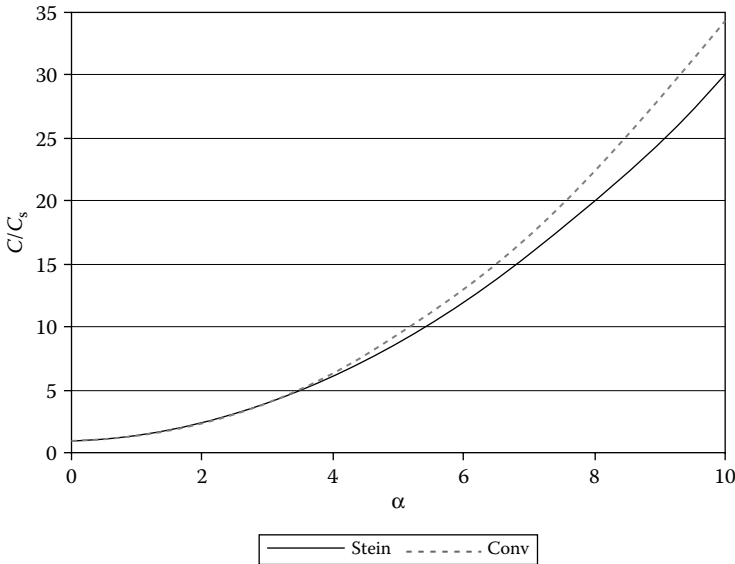
and

$$\frac{C_{\text{conv}}}{C_s} = 1 + \frac{4}{3} \frac{C_{\text{dd}}}{C_s} \quad (12.43)$$

From Equation 12.36, the right-hand side of Equation 12.42 is a function of C_{dd}/C_s , as is the right-hand side of Equation 12.43. Alternatively, both right-hand sides are functions of α . For small α , Equation 12.42 approaches Equation 12.43. For larger α , the comparison is shown graphically in [Figure 12.3](#). The difference becomes noticeable at values of $\alpha > 5$. At $\alpha = 10$, the conventional capacitance is about 15% larger than that obtained using Stein's method.

The voltage distribution along the disk using Stein's method can be obtained from Equation 12.31 by substituting $V_1 = V$, $V_2 = 0$, and $\beta = V/2$:

$$V(x) = \frac{V}{2} \left\{ 1 + \frac{1}{\sinh \alpha} \left[\sinh \left[\alpha \left(1 - \frac{x}{L} \right) \right] - \sinh \left(\alpha \frac{x}{L} \right) \right] \right\} \quad (12.44)$$

**FIGURE 12.3**

Comparison of Stein's and conventional capacitance formulas.

This is plotted in Figure 12.4 in normalized form. As we can see, the voltage becomes increasingly less uniform as α increases. The $\alpha = 1$ case closely approximates the linear distribution given in Equation 12.37 and used for the conventional capacitance calculation.

The voltage gradient is obtained from Equation 12.32 with the appropriate substitutions and is

$$\frac{dV}{dx} = -\frac{\alpha V}{2L \sinh \alpha} \left\{ \cosh \left[\alpha \left(1 - \frac{x}{L} \right) \right] + \cosh \left(\alpha \frac{x}{L} \right) \right\} \quad (12.45)$$

This is always negative, as Figure 12.4 indicates. Its largest value, in absolute terms, occurs at either end of the disk:

$$\left| \frac{dV}{dx} \right|_{\max} = \frac{\alpha V}{2L \sinh \alpha} (1 + \cosh \alpha) = \frac{\alpha V}{2L \tanh(\alpha/2)} \quad (12.46)$$

As $\alpha \rightarrow 0$, this approaches the uniform value of V/L . This voltage gradient is equal to the stress (electric field magnitude) in the turn–turn insulation, which must be able to handle it without breakdown. From Figure 12.4, we can see that the absolute value of the voltage gradient is a minimum at the center of the disk.

In this and later applications, the series and shunt or disk–disk capacitances can only be approximated for use in the formulas since in reality we

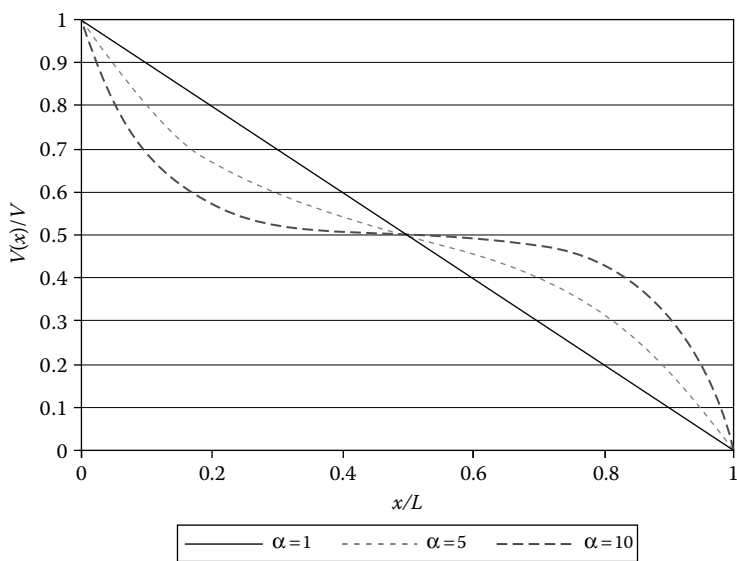


FIGURE 12.4
Normalized voltage along the disk for various values of alpha in Stein’s example.

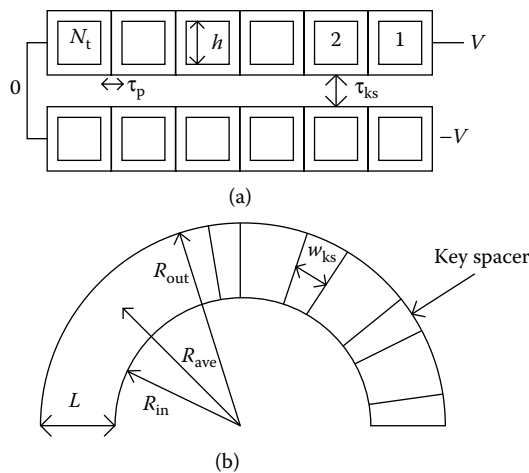


FIGURE 12.5
Geometry of a practical disk coil: (a) side view and (b) top view.

do not have a continuous distribution of capacitances as the model assumes. As shown in Figure 12.5, a disk consists of N_t turns, usually rectangular in cross section, with paper thickness τ_p between turns. τ_p is the two-sided paper thickness of a turn. The disks are separated by key spacers of thickness τ_{ks} and width w_{ks} spaced around the circumference.

The turn–turn capacitance C_{tt} is given approximately by

$$C_{tt} = \epsilon_0 \epsilon_p \frac{2\pi R_{ave} (h + 2\tau_p)}{\tau_p} \quad (12.47)$$

where ϵ_0 is the permittivity of vacuum, which is 8.8542×10^{-12} F/m in the SI system, ϵ_p is the relative permittivity of paper (≈ 3.5 for oil-soaked paper), R_{ave} is the average radius of the disk, and h is the bare copper or conductor height. The addition of $2\tau_p$ to h is designed to take into account fringing effects. There are $N_t - 1$ turn–turn capacitances in series, which results in a total series capacitance of $C_{tt}/(N_t - 1)$. However, the turn–turn capacitances do not have the full disk voltage drop across them, but only the fraction $(N_t - 1)/N_t$. Thus, the capacitive energy is

$$E = \frac{1}{2} \left(\frac{C_{tt}}{N_t - 1} \right) \left(\frac{N_t - 1}{N_t} \right)^2 V^2 \quad (12.48)$$

Based on the full voltage drop V , the equivalent series capacitance is

$$C_s = C_{tt} \frac{(N_t - 1)}{N_t^2} \quad (12.49)$$

This makes sense because for $N_t = 1$, we get $C_s = 0$.

The disk–disk capacitance can be considered to be two capacitances in parallel, namely the capacitance of the portion, containing the key spacers, and the capacitance of the remainder, containing an oil or air thickness instead of key spacers. We let f_{ks} be the key spacer fraction:

$$f_{ks} = \frac{N_{ks} w_{ks}}{2\pi R_{ave}} \quad (12.50)$$

where N_{ks} is the number of key spacers spaced around the circumference and w_{ks} is their width. Typically, $f_{ks} \approx 1/3$. The key spacer fraction of the disk–disk space is filled with two dielectrics—paper and pressboard—the latter being the usual key spacer material. For a planar capacitor containing two dielectric layers of permittivity ϵ_1 and ϵ_2 , according to electrostatic theory, the capacitance is

$$C = \frac{A}{\left(\frac{\ell_1}{\epsilon_1} + \frac{\ell_2}{\epsilon_2} \right)} \quad (12.51)$$

where A is the area and ℓ_1 and ℓ_2 are the thicknesses of the layers. Applying this to the disk-disk capacitance, we get

$$C_{dd} = \epsilon_0 \pi (R_{out}^2 - R_{in}^2) \left[\frac{f_{ks}}{\left(\frac{\tau_p}{\epsilon_p} + \frac{\tau_{ks}}{\epsilon_{ks}} \right)} + \frac{(1-f_{ks})}{\left(\frac{\tau_p}{\epsilon_p} + \frac{\tau_{ks}}{\epsilon_{oil}} \right)} \right] \quad (12.52)$$

Here, ϵ_{ks} is the relative permittivity of the key spacer material ($= 4.5$ for oil-soaked pressboard) and ϵ_{oil} is the relative permittivity of oil ($= 2.2$ for transformer oil). R_{in} and R_{out} are the inner and outer radii of the disk, respectively.

We conducted a finite element simulation to test the Stein capacitance (Equation 12.35). We modeled a 16-turn disk, as shown in Figure 12.6, and used static rings to define the equipotential surfaces assumed in Stein's method. The upper static ring is at potential V , and the bottom is at $V = 0$. The rightmost disk is at potential V , and the leftmost disk is at $V = 0$.

The model shown is an enlargement of the region near the disk. The full model is axisymmetric, and the distance from the leftmost disk to the center line is 300 mm. The radial build of the disk is 70 mm, and the disk height, including the paper, is 11 mm.

The bare conductor dimensions of a single turn are 10 mm high by 3.375 mm wide. The two-sided paper thickness is 1 mm. The distance from the paper to the nearest equipotential is 2.5 mm so that the disk-disk

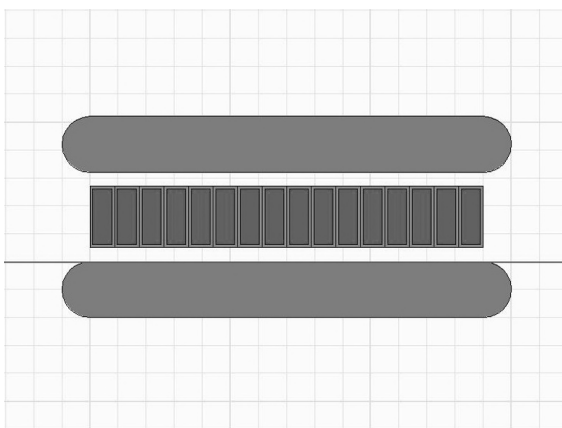


FIGURE 12.6

(See color insert following page 338.) Disk coil of 16 turns with static rings on either side supplying equipotential surfaces at the voltages assumed in Stein's method.

spacing is 5 mm. Because the model is axisymmetric, the disk–disk material is all oil (there are no key spacers). From these dimensions, we can calculate C_{tt} given in Equation 12.47. This formula requires that the parameters be in SI units, so we have $R_{ave} = 0.335$ m, $h = 0.01$ m, $\tau_p = 0.001$ m, and $\epsilon_p = 3.5$. ϵ_0 is given above. We obtain $C_{tt} = 7.8275 \times 10^{-10}$ F. Since there are $N_t = 16$ turns, we get $C_s = 4.5864 \times 10^{-11}$ F from Equation 12.49.

We can obtain C_{dd} from Equation 7.52, using $R_{in} = 0.3$ m, $R_{out} = 0.37$ m, $f_{ks} = 0$, $\tau_p = 0.001$ m, $\epsilon_p = 3.5$, $\tau_{ks} = 0.005$ m, and $\epsilon_{oil} = 2.2$. We get $C_{dd} = 5.0991 \times 10^{-10}$ F.

Using Equation 12.36, we see that $\alpha = 6.6687$. Inserting this value of α and C_s into Stein's capacitance Equation 12.35, we get $C_{Stein} = 6.6322 \times 10^{-10}$ F.

For the finite element calculation, we used $V = 100$ V. We distributed the voltage along the turns according to Equation 12.44 using $\alpha = 6.6687$. We can visualize this using Figure 12.4. The equipotential contour plot is shown in Figure 12.7. We chose balloon boundary conditions for the outer boundaries. These, along with the center line of the axisymmetric geometry, are not shown.

From the solution, the total energy was calculated as 4.1864×10^{-6} J. The capacitance can be extracted from the following formula: energy = $\frac{1}{2} C (\Delta V)^2$. We then get $C_{Finite\ Element} = 8.373 \times 10^{-10}$ F. This is 26% higher than the value obtained using Stein's formula. We can see from Figure 12.3 that, for this value of α , the conventional capacitance formula is about 10% higher than Stein's formula, so it will apparently agree more with the finite element result. However, the conventional capacitance formula assumes a linear voltage distribution along the winding. If we use a linear voltage distribution along the winding in the finite element calculation, we find that the capacitance

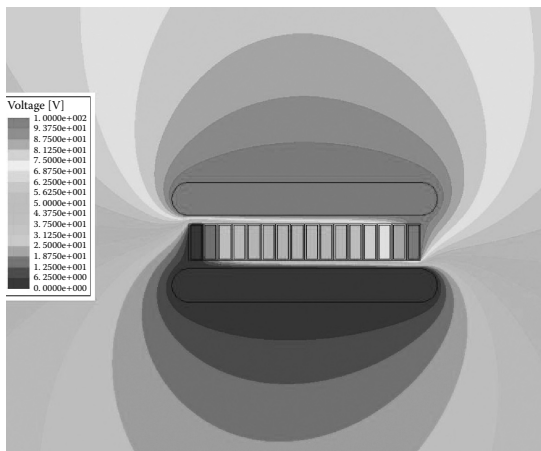


FIGURE 12.7

(See color insert following page 338.) Equipotential plot near the disk as a test of Stein's capacitance formula.

is about 26% higher than the conventional capacitance formula. There is no apparent advantage in using the conventional formula over Stein's formula, based on the finite element results.

12.4 General Disk Capacitance Formula

Generally, if the disk-disk spacings on either side of the main disk are unequal so that $C_a \neq C_b$, as shown in Figure 12.8, then from Equation 12.33 we have

$$C_{\text{general}} = C_s \left[(\gamma_a^2 + \gamma_b^2) \frac{\alpha}{\tanh \alpha} + 2\gamma_a \gamma_b \frac{\alpha}{\sinh \alpha} + \gamma_a \gamma_b \alpha^2 \right] \quad (12.53)$$

where

$$\gamma_a = \frac{C_{\text{dd1}}}{C_{\text{dd1}} + C_{\text{dd2}}}, \quad \gamma_b = \frac{C_{\text{dd2}}}{C_{\text{dd1}} + C_{\text{dd2}}}, \quad \alpha = \sqrt{\frac{2(C_{\text{dd1}} + C_{\text{dd2}})}{C_s}} \quad (12.54)$$

where C_{dd1} and C_{dd2} are the unequal disk-disk capacitances.

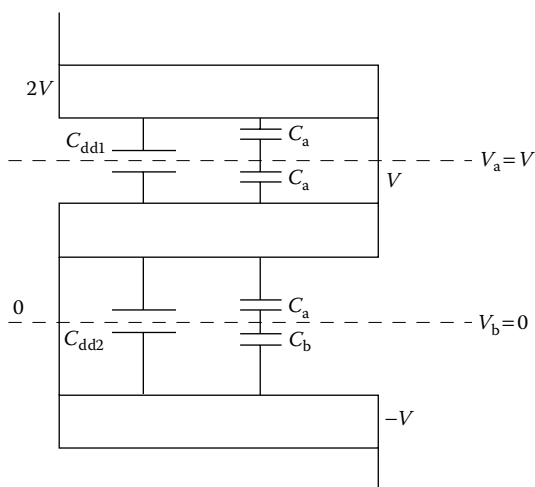


FIGURE 12.8

More general case of a disk embedded in a coil of similar disks.

12.5 Coil Grounded at One End with Grounded Cylinders on Either Side

An early impulse model for a coil assumed the coil consisted of a uniformly distributed chain of series capacitances connected to ground cylinders on either side by shunt capacitances, that is, the model shown in [Figure 12.1](#) but with $V_{a1} = V_{a2} = V_{b1} = V_{b2} = 0$ [Blu51]. The V_1 terminal is impulsed with a voltage V and the V_2 terminal is grounded. From Equation 12.30, we have $\beta = 0$ and Equation 12.31 becomes

$$V(x) = V \frac{\sinh \left[\alpha \left(1 - \frac{x}{L} \right) \right]}{\sinh \alpha} \quad (12.55)$$

with $\alpha = \sqrt{C_g/C_s}$. Here, C_g is the total ground capacitance (both sides) and C_s is the series capacitance of the coil. This is shown in normalized form in [Figure 12.9](#) for several values of α .

We expect this voltage distribution to exist immediately after the application of the impulse voltage, but before inductive effects come into play. Later, oscillations can cause voltage swings above the values shown in [Figure 12.9](#).

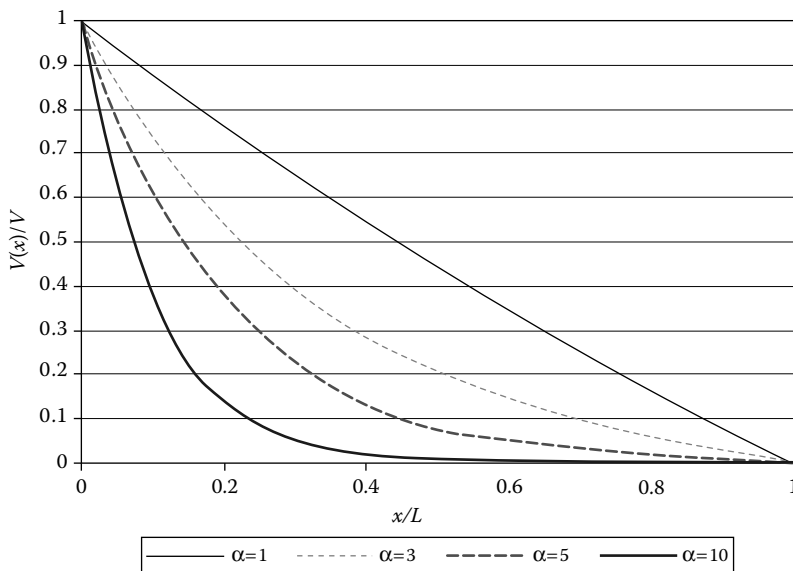


FIGURE 12.9

Graph of normalized voltage along a coil for several values of α .

The voltage gradient is given by

$$\frac{dV}{dx} = -\frac{\alpha V}{L \sinh \alpha} \cosh \left[\alpha \left(1 - \frac{x}{L} \right) \right] \quad (12.56)$$

The maximum gradient occurs at the line end ($x = 0$) and is

$$\left| \frac{dV}{dx} \right|_{\max} = \frac{\alpha V}{L \tanh \alpha} \quad (12.57)$$

Thus, the maximum disk–disk voltage immediately after impulse is approximately equal to Equation 12.57 multiplied by the disk–disk spacing.

From Equation 12.33, the coil's total capacitance to ground is

$$C_{\text{coil}} = C_s \frac{\alpha}{\tanh \alpha} \quad (12.58)$$

The series capacitance is due to N_d disks in series. If we obtain the disk capacitances by the Stein formula, we have

$$C_s = \frac{C_{\text{Stein}}}{N_d} \quad (12.59)$$

For an inner coil, we would usually take the surfaces of the neighboring coils to be the ground cylinders. For the innermost coil, the core determines the ground on one side, while for an outermost coil, the tank is the ground on one side. In general, the distance to ground is filled with various dielectric materials, including oil or air. One such structure is shown in [Figure 12.10](#). There are usually multiple pressboard layers, but for convenience these are grouped into a single layer in the figure.

The sticks provide spacing for cooling oil or air to flow. This composite structure is similar to that analyzed in Equation 12.52 for the disk–disk capacitance. The ground spacing is usually small relative to the coil radius for power transformers so that we may assume an approximately planar geometry. The ground capacitance on one side of the coil, C_{g1} , is obtained by

$$C_{g1} = \epsilon_0 2\pi R_{\text{gap}} H \left[\frac{f_s}{\left(\frac{\tau_{\text{press}}}{\epsilon_{\text{press}}} + \frac{\tau_s}{\epsilon_s} \right)} + \frac{(1-f_s)}{\left(\frac{\tau_{\text{press}}}{\epsilon_{\text{press}}} + \frac{\tau_s}{\epsilon_{\text{oil}}} \right)} \right] \quad (12.60)$$

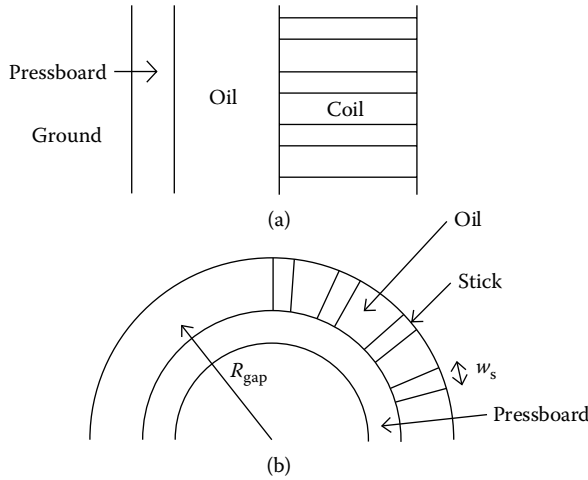


FIGURE 12.10
Ground capacitance geometry: (a) side view and (b) top view.

where f_s is the fraction of the space occupied by sticks (vertical spacers):

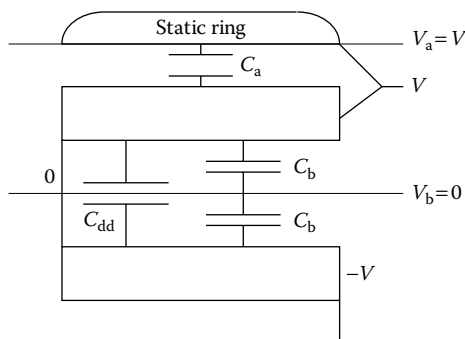
$$f_s = \frac{N_s w_s}{2\pi R_{\text{gap}}} \quad (12.61)$$

Where R_{gap} is the mean gap radius, w_s is the stick width, N_s is the number of sticks around the circumference, H is the coil height, τ_{press} is the pressboard thickness, ϵ_{press} is the pressboard relative permittivity, and τ_s , ϵ_s are the corresponding quantities for the sticks. The ground capacitances of both gaps, C_{g1} and C_{g2} , are added to obtain the total ground capacitance, C_g .

12.6 Static Ring on One Side of a Disk

If a static ring is present on one side of a disk and connected to the terminal voltage as shown in Figure 12.11, then we have a situation similar to that considered in Section 12.4 on general disk capacitance. The only difference is that C_a is the disk-static ring capacitance since the static ring is an equipotential surface. Thus, Equation 12.53 applies with

$$\gamma_a = \frac{C_a}{C_a + 2C_{\text{dd}}}, \quad \gamma_b = \frac{2C_{\text{dd}}}{C_a + 2C_{\text{dd}}}, \quad \alpha = \sqrt{\frac{C_a + 2C_{\text{dd}}}{C_s}} \quad (12.62)$$


FIGURE 12.11

Static ring on one side of a disk at the end of a coil.

where C_{dd} is the disk–disk capacitance to the lower disk and C_s is the single-disk series capacitance.

This case would be identical to Stein’s if the static ring were spaced at half of the normal disk–disk spacing or whatever is required to achieve $C_a = 2C_{dd} = C_b$. Then, $\gamma_a = \gamma_b = 1/2$, $\alpha = \sqrt{4C_{dd}/C_s}$ and Equation 12.53 would reduce to Equation 12.35. Thus, the end disk would have the same capacitance as any other disk.

12.7 Terminal Disk without a Static Ring

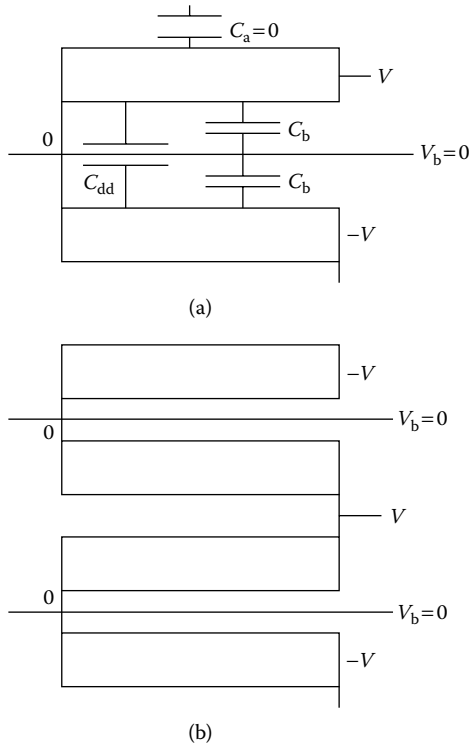
If the end disk does not have an adjacent static ring, we assume that the shunt capacitance on the end side is essentially zero. Then, we have the situation shown in Figure 12.12a. We have $C_a = 0$ so that $\gamma_a = 0$, $\gamma_b = 1$ and from Equation 12.53,

$$C_{\text{end}} = C_s \frac{\alpha}{\tanh \alpha} \quad (12.63)$$

with

$$\alpha = \sqrt{\frac{2C_{dd}}{C_s}} \quad (12.64)$$

This situation also applies to a center-fed winding without a static ring. In this case, as Figure 12.12b shows, there is no capacitive energy between the two center disks so that effectively $C_a = 0$. This result would also follow if

**FIGURE 12.12**

Terminal disk without a static ring: (a) top fed and (b) center fed.

both center disks were considered a unit and the energy was divided equally between them.

12.8 Capacitance Matrix

Before proceeding to other cases of interest, we need to introduce the capacitance matrix. For a system of conductors having voltages V_i and total electrostatic energy E , from the general theory of linear capacitors [Smy68], we have

$$\begin{aligned}
 \frac{\partial E}{\partial V_1} &= Q_1 = C_{11}V_1 + C_{12}V_2 + \cdots \\
 \frac{\partial E}{\partial V_2} &= Q_2 = C_{21}V_1 + C_{22}V_2 + \cdots \\
 &\vdots
 \end{aligned}
 \tag{12.65}$$

where Q_i is the charge on conductor i , C_{ii} is the self-capacitance of conductor i , and C_{ij} is the mutual capacitance between conductors i and j . The C 's can be grouped into a capacitance matrix, which is symmetric, $C_{ij} = C_{ji}$. The diagonal terms are positive, while the off-diagonal terms are negative because if V_k is a positive voltage while all other voltages are zero, that is, the other conductors are grounded, then the charge on conductor k must be positive, $Q_k = C_{kk}V_k > 0 \Rightarrow C_{kk} > 0$. By charge conservation, the charges induced on the other conductors must be negative so $Q_j = C_{jk}V_k < 0 \Rightarrow C_{jk} < 0$. By charge conservation, again assuming $V_k > 0$ and all other V 's = 0,

$$\sum_i Q_i = \sum_{i,j} C_{ij}V_j = \sum_i C_{ik}V_k = 0 \quad (12.66)$$

From the last equality in Equation 12.66, we have

$$C_{kk} = -\sum_{i \neq k} C_{ik} \quad (12.67)$$

that is, the negative of the sum of the off-diagonal terms equals the diagonal term.

We apply this to the general energy Equation 12.27 and consider the V_1 voltage node:

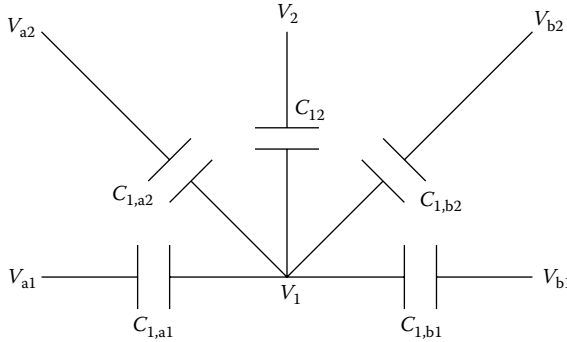
$$\begin{aligned} \frac{\partial E}{\partial V_1} &= Q_1 = \frac{C_s}{2} \left[2(V_1 - \beta_1) \frac{\alpha}{\tanh \alpha} - 2(V_2 - \beta_2) \frac{\alpha}{\sinh \alpha} - 2(\beta_2 - \beta_1) \right] \\ &= C_s \left[V_1 \frac{\alpha}{\tanh \alpha} - V_2 \frac{\alpha}{\sinh \alpha} - \gamma_a \left(\frac{\alpha}{\tanh \alpha} - 1 \right) V_{a1} - \gamma_a \left(1 - \frac{\alpha}{\sinh \alpha} \right) V_{a2} \right. \\ &\quad \left. - \gamma_b \left(\frac{\alpha}{\tanh \alpha} - 1 \right) V_{b1} - \gamma_b \left(1 - \frac{\alpha}{\sinh \alpha} \right) V_{b2} \right] \end{aligned} \quad (12.68)$$

Using the labeling scheme 1,2,3,4,5,6 \leftrightarrow 1,2,a1,a2,b1,b2 and Equation 12.68, the off-diagonal mutual capacitances are

$$\begin{aligned} C_{1,2} &= -C_s \frac{\alpha}{\sinh \alpha} \\ C_{1,a1} &= -C_s \gamma_a \left(\frac{\alpha}{\tanh \alpha} - 1 \right), \quad C_{1,a2} = -C_s \gamma_a \left(1 - \frac{\alpha}{\sinh \alpha} \right) \\ C_{1,b1} &= -C_s \gamma_b \left(\frac{\alpha}{\tanh \alpha} - 1 \right), \quad C_{1,b2} = -C_s \gamma_b \left(1 - \frac{\alpha}{\sinh \alpha} \right) \end{aligned} \quad (12.69)$$

These are all negative and the negative of their sum is C_{11} , which is

$$C_{11} = C_s \frac{\alpha}{\tanh \alpha} \quad (12.70)$$

**FIGURE 12.13**

Lumped capacitance model of a general lattice capacitor network. The C 's are taken to be positive.

This is an example of Equation 12.67.

The capacitance diagram corresponding to this situation is shown in Figure 12.13, which shows only the capacitances attached to voltage node V_1 . The other mutual capacitances can be filled in by a similar procedure. If the side voltages are constant so that $V_{a1} = V_{a2} = V_a$ and $V_{b1} = V_{b2} = V_b$, then there is only one mutual capacitance connecting 1 to a , given by

$$C_{1,a} = C_{1,a1} + C_{1,a2} = -C_s \gamma_a \left(\frac{\alpha}{\tanh \alpha} - \frac{\alpha}{\sinh \alpha} \right) \quad (12.71)$$

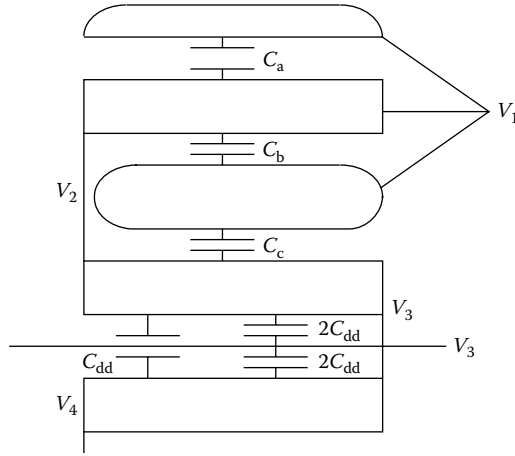
A similar equation holds for $C_{1,b}$. For small α , this approaches

$$C_{1,a} = -C_s \gamma_a \frac{\alpha^2}{2} = -\frac{C_a}{2} \quad (12.72)$$

so that on the capacitance diagram (Figure 12.13), half the shunt capacitance is attached to the V_1 node. If we carry through the analysis, we find that half of the shunt capacitance would also be attached to the V_2 node, producing a π capacitance diagram.

12.9 Two Static Rings

When two static rings are positioned at the end of a coil, they are situated as shown in Figure 12.14. Both are attached to the terminal voltage V_1 . This situation also applies to a center-fed coil with three static rings because adjacent pairs are configured similarly with respect to the top or bottom coil. We must

**FIGURE 12.14**

Two static rings at the end of a coil.

analyze more than one disk at a time since their electrostatic energies are coupled via the static rings. We allow for the possibility of different spacings between the static rings and adjacent disks and between disks by letting the disk–static ring and disk–disk capacitances be different.

The energy associated with the first or top disk is found using Equation 12.33 with $V_a = V_b = V_1$ so that $\beta = V_1$:

$$E_{1\text{st Disk}} = \frac{C_s}{2} (V_2 - V_1)^2 \frac{\alpha}{\tanh \alpha} \quad (12.73)$$

where $\alpha = \sqrt{(C_a + C_b)/C_s}$ and C_a and C_b are the disk–static ring capacitances. Assuming the same series capacitance C_s , the energy of the second disk is obtained from Equation 12.33 with the substitutions $V_a = V_1$, $V_b = V_3$ so that $\beta = \gamma_a V_1 + \gamma_b V_3$. For this disk, the high-voltage end is at voltage V_2 and the low-voltage end at voltage V_3 . Therefore, in Equation 12.33, we must associate $V_1 \leftrightarrow V_2$ and $V_2 \leftrightarrow V_3$. We find

$$\begin{aligned} E_{2\text{nd Disk}} = \frac{C_s}{2} \left\{ \left[(V_2 - \gamma_a V_1 - \gamma_b V_3)^2 + (V_3 - \gamma_a V_1 - \gamma_b V_3)^2 \right] \frac{\alpha_1}{\tanh \alpha_1} \right. \\ \left. - 2(V_2 - \gamma_a V_1 - \gamma_b V_3)(V_3 - \gamma_a V_1 - \gamma_b V_3) \frac{\alpha_1}{\sinh \alpha_1} \right. \\ \left. + \alpha_1^2 [\gamma_a (V_1 - \gamma_a V_1 - \gamma_b V_3)^2 + \gamma_b (V_3 - \gamma_a V_1 - \gamma_b V_3)^2] \right\} \quad (12.74) \end{aligned}$$

Here, $\alpha_1 = \sqrt{(C_c + 2C_{dd})/C_s}$, $\gamma_a = C_c/(C_c + 2C_{dd})$, and $\gamma_b = 2C_{dd}/(C_c + 2C_{dd})$. Using $\gamma_a + \gamma_b = 1$, this can be simplified as follows:

$$E_{2\text{nd Disk}} = \frac{C_s}{2} \left\{ [(V_2 - \gamma_a V_1 - \gamma_b V_3)^2 + \gamma_a^2 (V_3 - V_1)^2] \frac{\alpha_1}{\tanh \alpha_1} + 2\gamma_a (V_2 - \gamma_a V_1 - \gamma_b V_3)(V_1 - V_3) \frac{\alpha_1}{\sinh \alpha_1} + \alpha_1^2 \gamma_a \gamma_b (V_1 - V_3)^2 \right\} \quad (12.75)$$

Thus, the total energy in the first two disks with static rings is

$$E_{\text{Both Disk}} = \frac{C_s}{2} \left\{ (V_2 - V_1)^2 \frac{\alpha}{\tanh \alpha} + [(V_2 - \gamma_a V_1 - \gamma_b V_3)^2 + \gamma_a^2 (V_3 - V_1)^2] \frac{\alpha_1}{\tanh \alpha_1} + 2\gamma_a (V_2 - \gamma_a V_1 - \gamma_b V_3)(V_1 - V_3) \frac{\alpha_1}{\sinh \alpha_1} + \alpha_1^2 \gamma_a \gamma_b (V_1 - V_3)^2 \right\} \quad (12.76)$$

The lumped capacitance network associated with this configuration can be obtained by the procedure described in [Section 12.8](#). Thus,

$$\begin{aligned} \frac{\partial E_{\text{Both Disk}}}{\partial V_1} &= C_s \left\{ (V_1 - V_2) \frac{\alpha}{\tanh \alpha} + [-\gamma_a (V_2 - \gamma_a V_1 - \gamma_b V_3) + \gamma_a^2 (V_1 - V_3)] \frac{\alpha_1}{\tanh \alpha_1} + \gamma_a [(V_2 - \gamma_a V_1 - \gamma_b V_3) - \gamma_a (V_1 - V_3)] \frac{\alpha_1}{\sinh \alpha_1} + \alpha_1^2 \gamma_a \gamma_b (V_1 - V_3) \right\} \\ &= C_s \left\{ \left[\frac{\alpha}{\tanh \alpha} + 2\gamma_a^2 \left(\frac{\alpha_1}{\tanh \alpha_1} - \frac{\alpha_1}{\sinh \alpha_1} \right) + \alpha_1^2 \gamma_a \gamma_b \right] V_1 - \left[\frac{\alpha}{\tanh \alpha} + \gamma_a \left(\frac{\alpha_1}{\tanh \alpha_1} - \frac{\alpha_1}{\sinh \alpha_1} \right) \right] V_2 - \left[\gamma_a (2\gamma_a - 1) \left(\frac{\alpha_1}{\tanh \alpha_1} - \frac{\alpha_1}{\sinh \alpha_1} \right) + \alpha_1^2 \gamma_a \gamma_b \right] V_3 \right\} \quad (12.77) \end{aligned}$$

Reading off the mutual capacitances from Equation 12.77, we find

$$\begin{aligned}
 C_{12} &= -C_s \left[\frac{\alpha}{\tanh \alpha} + \gamma_a \left(\frac{\alpha_1}{\tanh \alpha_1} - \frac{\alpha_1}{\sinh \alpha_1} \right) \right] \\
 C_{13} &= -C_s \left[\gamma_a (2\gamma_a - 1) \left(\frac{\alpha_1}{\tanh \alpha_1} - \frac{\alpha_1}{\sinh \alpha_1} \right) + \alpha_1^2 \gamma_a \gamma_b \right]
 \end{aligned}
 \tag{12.78}$$

These are negative, and minus their sum is the self-capacitance C_{11} .

We also need to find C_{23} , which is obtained by differentiating Equation 12.76 with respect to V_2

$$\begin{aligned}
 \frac{\partial E_{\text{Both Disk}}}{\partial V_2} &= C_s \left\{ -(V_1 - V_2) \frac{\alpha}{\tanh \alpha} + (V_2 - \gamma_a V_1 - \gamma_b V_3) \frac{\alpha_1}{\tanh \alpha_1} + \gamma_a (V_1 - V_3) \frac{\alpha_1}{\sinh \alpha_1} \right\} \\
 &= C_s \left\{ - \left[\frac{\alpha}{\tanh \alpha} + \gamma_a \left(\frac{\alpha_1}{\tanh \alpha_1} - \frac{\alpha_1}{\sinh \alpha_1} \right) \right] V_1 \right. \\
 &\quad \left. + \left[\frac{\alpha}{\tanh \alpha} + \frac{\alpha_1}{\tanh \alpha_1} \right] V_2 - \left[\gamma_b \frac{\alpha_1}{\tanh \alpha_1} + \gamma_a \frac{\alpha_1}{\sinh \alpha_1} \right] V_3 \right\}
 \end{aligned}
 \tag{12.79}$$

Extracting the mutual capacitances, we find

$$\begin{aligned}
 C_{21} &= -C_s \left[\frac{\alpha}{\tanh \alpha} + \gamma_a \left(\frac{\alpha_1}{\tanh \alpha_1} - \frac{\alpha_1}{\sinh \alpha_1} \right) \right] \\
 C_{23} &= -C_s \left[\gamma_b \frac{\alpha_1}{\tanh \alpha_1} + \gamma_a \frac{\alpha_1}{\sinh \alpha_1} \right]
 \end{aligned}
 \tag{12.80}$$

These are negative and the negative of their sum is C_{22} . Moreover, we see that, as expected, $C_{21} = C_{12}$ since the capacitance matrix is symmetric. Differentiating Equation 12.76 with respect to V_3 will give us no new information.

Thus, we can draw the lumped capacitance diagram for this configuration as shown in Figure 12.15. We assume that the capacitances shown are positive (the negative of the mutual capacitances). Hence, the total capacitance between the V_1 and V_3 terminals is given by

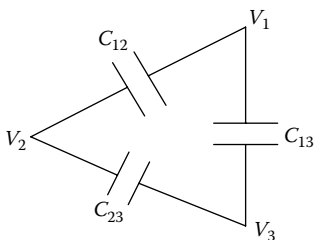


FIGURE 12.15

Lumped capacitance diagram for the two static ring configuration. Assume the C 's to be positive.

$$C_{\text{Both Disks}} = C_{13} + \frac{C_{12}C_{23}}{C_{12} + C_{23}} \quad (12.81)$$

In model impulse–voltage calculations, we can treat the first two disks as a unit having the capacitance given by Equation 12.81. Then, we can obtain the voltages across each disk from the overall voltage difference ($V_1 - V_3$) via

$$\begin{aligned} V_1 - V_2 &= \frac{C_{23}}{C_{12} + C_{23}}(V_1 - V_3) \\ V_2 - V_3 &= \frac{C_{12}}{C_{12} + C_{23}}(V_1 - V_3) \end{aligned} \quad (12.82)$$

12.10 Static Ring between the First Two Disks

A static ring is sometimes placed between the first two disks. This is usually considered only for center-fed windings so that there are two symmetrically spaced static rings, one for each of the two stacked coils. This case is very similar to the case studied in [Section 12.9](#). The only difference is that the energy in the first disk is given by

$$E_{\text{1st Disk}} = \frac{C_s}{2}(V_1 - V_2)^2 \frac{\alpha}{\tanh \alpha} \quad (12.83)$$

with $\alpha = \sqrt{C_b/C_s}$ since $C_a = 0$. Thus, the formulas of the last section apply with this value of α .

12.11 Winding Disk Capacitances with Wound-in Shields

This section closely follows our published paper [Del98]. To improve the voltage distribution along a transformer coil, that is, to reduce the maximum disk–disk voltage gradient, we must make the distribution constant, α , as small as possible, where $\alpha = \sqrt{C_g/C_s}$ with C_g the total ground capacitance and C_s the series capacitance of the coil. We can accomplish this by increasing C_s . Common methods for increasing the series capacitance include interleaving [Nuy78] and the use of wound-in shields [For69]. Both these techniques rely on inductive effects. Geometric methods for increasing C_s such as decreasing turn–turn or disk–disk clearances are generally ruled out by voltage withstand or cooling considerations.

Interleaving can produce large increases in C_s , which may be necessary in very high-voltage applications. However, it can be labor intensive and in practice tends to be limited to magnet wire applications. Wound-in shields tend to produce more modest increases in C_s when compared with interleaving. However, they require less labor and are suitable for use with transposed cable. In addition, they can easily provide a tapered capacitance profile to match the voltage stress profile of the winding.

We will present a simple analytic formula for calculating the disk capacitance with a variable number of wound-in shield turns. Since this formula rests on certain assumptions, we have developed a detailed circuit model to test these assumptions. Finally, we carry out experiments under a wide variety of conditions to check the formula.

12.11.1 Analytic Formula

Figure 12.16 shows the geometry of a pair of disks containing a wound-in shield. Also shown is the method of labeling turns of the coil and shield. Since the shield spans two disks, we must calculate the capacitance of the pair. Each disk has N turns and n wound-in-shield turns, where $n \leq N - 1$. The voltage across the pair of disks is V , and we assume that the rightmost turn of the top disk, $i = 1$, is at voltage V and the rightmost turn of the bottom disk, $j = 1$, is at 0 V, so that the coil is wound in a positive sense from outer to inner turn on the bottom disk and from inner to outer turn on the top disk. The shield turns are placed between the coil turns and are wound in the same sense as the coil. However, their crossover is at the outermost turn rather than the innermost one as is the case for the coil. This means that the positive voltage sense for the shield is from turn $j = 1$ to $j = n$ on the bottom disk and then from the leftmost turn, $i = n$ to turn $i = 1$ on the top disk.

We assume the voltage rise per turn is ΔV where

$$\Delta V = \frac{V}{2N}$$

(12.84)

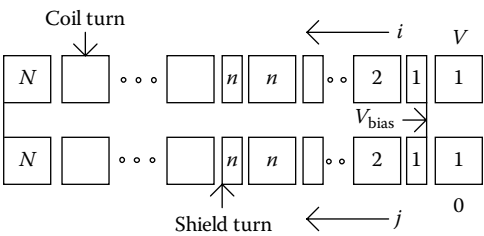


FIGURE 12.16 Disk pair with wound-in shields with labeling and other parameters indicated. (From Del Vecchio, R. M., B. Poulin, and R. Ahuja. 1998. *IEEE Trans Power Deliv* 13(2):503–9. With permission.)

We assume that the same volts per turn value also applies to the shield. For certainty, we assume that the voltage at the shield crossover point is V_{bias} , as shown in [Figure 12.16](#). Taking the voltage at the midpoint of a turn, we have for the top-disk coil turns,

$$V_c(i) = V - (i - 0.5)\Delta V \quad (12.85)$$

where $V_c(i)$ is the coil voltage for turn i , $i = 1, \dots, N$. Also for the top-disk wound-in shield turns

$$V_w(i) = V_{\text{bias}} - (i - 0.5)\Delta V \quad (12.86)$$

where $V_w(i)$ is the shield voltage for shield turn i , $i = 1, \dots, n$. For the bottom disk, we have

$$V_c(j) = (j - 0.5)\Delta V \quad (12.87)$$

for $j = 1, \dots, N$ and

$$V_w(j) = V_{\text{bias}} + (j - 0.5)\Delta V \quad (12.88)$$

for $j = 1, \dots, n$.

Letting c_w be the capacitance between a coil turn and adjacent shield turn, the energy stored in the capacitance between shield turn i and its adjacent coil turns is

$$\frac{1}{2} c_w \{ [V_c(i) - V_w(i)]^2 + [V_c(i+1) - V_w(i)]^2 \} \quad (12.89)$$

The two terms reflect the fact that there are two adjacent coil turns for every shield turn. Using the previous expressions for the V 's, Equation 12.89 becomes

$$\frac{1}{2} c_w [(V - V_{\text{bias}})^2 + (V - V_{\text{bias}} - \Delta V)^2] \quad (12.90)$$

This does not depend on i and so is the same for all n shield turns on the top disk. There are n such turns in the energy. For the bottom disk, Equation 12.89 applies, with j replacing i so the capacitive energy between shield turn j and its surrounding coil turns is

$$\frac{1}{2} c_w \{ [V - V_{\text{bias}} - 2N\Delta V]^2 + [V - V_{\text{bias}} - (2N - 1)\Delta V]^2 \} \quad (12.91)$$

This again does not depend on j and so is the same for all n shield turns on the bottom disk. Thus, there are n such terms in the energy.

We must add the capacitive energy of the turns without wound-in shields between them to the above energies. Letting c_t be the turn–turn capacitance, this energy is simply

$$\frac{1}{2}c_t(\Delta V)^2 \quad (12.92)$$

There are $2(N - n - 1)$ such terms in the energy. In addition, there is energy stored in the disk–disk capacitance, c_d . Since we assume that the voltage varies linearly along the disks, this capacitive energy is given by

$$\frac{1}{2}\left(\frac{c_d}{3}\right)V^2 \quad (12.93)$$

We ignore capacitive coupling to other disk pairs at this stage because our experimental setup consisted of an isolated disk pair. However, if this disk pair was embedded in a larger coil of similar disks, then we would need to double Equation 12.93 before adding to the energy.

The total capacitive energy of the disk pair is found by adding the above contributions. To simplify the formula, we define

$$\beta = \frac{V - V_{\text{bias}}}{\Delta V} \quad (12.94)$$

In terms of this parameter and the expression for ΔV given in Equation 12.84, the total capacitive energy, E_{tot} , is given by

$$\begin{aligned} E_{\text{tot}} &= \frac{1}{2} \left\{ c_w n (\Delta V)^2 \left[\beta^2 + (\beta - 1)^2 + \left(\frac{V_{\text{bias}}}{\Delta V} \right)^2 + \left(\frac{\Delta V - V_{\text{bias}}}{\Delta V} \right)^2 \right] \right\} \\ &\quad + \frac{1}{2} c_t (\Delta V)^2 2(N - n - 1) + \frac{1}{2} \left(\frac{c_d}{3} \right) V^2 \\ &= \frac{1}{2} V^2 \left\{ c_w \left(\frac{n}{4N^2} \right) \left[\beta^2 + (\beta - 1)^2 + (\beta - 2N)^2 + (\beta + 1 - 2N)^2 \right] \right. \\ &\quad \left. + c_t \left(\frac{N - n - 1}{2N^2} \right) + \frac{c_d}{3} \right\} \quad (12.95) \end{aligned}$$

Extracting the equivalent or total capacitance from Equation 12.95, we get

$$\begin{aligned} C_{\text{tot}} &= c_w \left(\frac{n}{4N^2} \right) \left[\beta^2 + (\beta - 1)^2 + (\beta - 2N)^2 + (\beta + 1 - 2N)^2 \right] \\ &\quad + c_t \left(\frac{N - n - 1}{2N^2} \right) + \frac{c_d}{3} \quad (12.96) \end{aligned}$$

At this point, V_{bias} and β is unspecified. The values of V_{bias} and β will depend on whether the shield is floating or whether it is attached at some point to a coil voltage. If the shield is floating, we expect $V_{\text{bias}} = V/2$. If the shield is attached at the crossover to the high-voltage terminal, then $V_{\text{bias}} = V$. If the leftmost or end-shield turn on the top disk ($i = n$) is attached to the high-voltage terminal, then $V_{\text{bias}} = V + (n - 0.5)\Delta V$. In terms of β :

$$\begin{aligned} \text{Shield floating} & \quad \beta = N \\ \text{Shield attached at crossover to } V & \quad \beta = 0 \\ \text{Shield attached at top left end to } V & \quad \beta = -(n - 0.5) \end{aligned} \quad (12.97)$$

We can consider other situations as well.

For the turn–turn capacitance, we used the expression (in SI units)

$$c_t = \frac{2\pi\epsilon_0\epsilon_p R_{\text{ave}}(h + 2\tau_p)}{\tau_p} \quad (12.98)$$

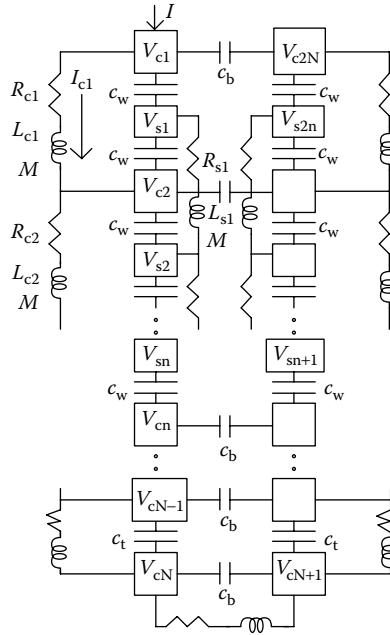
where R_{ave} is the average radius of the coil, h is the bare copper height of a coil turn in the axial direction, τ_p is the two-sided paper thickness of a coil turn, $\epsilon_0 = 8.8542 \times 10^{-12}$ F/m, and ϵ_p is the relative permittivity of paper. The addition of $2\tau_p$ to h is designed to take into account fringing effects. Also, the use of R_{ave} is a reasonably accurate approximation for coils with radial builds that are small compared to their radii. For the capacitance c_w , we use the same expression but with τ_p replaced by $0.5(\tau_p + \tau_w)$, where τ_w is the two-sided paper thickness of a shield turn. Since there are key spacers separating the disks and gaps between them, the disk–disk capacitance is given by

$$c_d = \pi\epsilon_0(R_o^2 - R_i^2) \left[\frac{f_{\text{ks}}}{\left(\frac{\tau_p}{\epsilon_p} + \frac{\tau_{\text{ks}}}{\epsilon_{\text{ks}}}\right)} + \frac{(1 - f_{\text{ks}})}{\left(\frac{\tau_p}{\epsilon_p} + \frac{\tau_{\text{ks}}}{\epsilon_{\text{air}}}\right)} \right] \quad (12.99)$$

where R_i and R_o are the inner and outer radii of the disk, respectively, f_{ks} is the fraction of the disk–disk space occupied by key spacers, τ_{ks} is the key spacer thickness, ϵ_{ks} is the key spacer relative permittivity, and ϵ_{air} is the relative permittivity of air (equal to 1) because the coils were tested in air.

12.11.2 Circuit Model

Since quite a few assumptions went into deriving the capacitance formula in the last section, we decided to model the disk pair by means of a circuit model, including capacitive, inductive, and resistive effects as sketched in

**FIGURE 12.17**

Circuit model for a disk pair with wound-in shields. The labeling scheme and circuit parameters are indicated.

Figure 12.17. We include all mutual couplings between the turns of the coil and wound-in-shield. We assume the circuit is excited by a current source that is nearly a step function. The circuit equations are

$$\begin{aligned} C \frac{d\mathbf{V}}{dt} &= A\mathbf{I} \\ M \frac{d\mathbf{I}}{dt} &= B\mathbf{V} - R\mathbf{I} \end{aligned} \quad (12.100)$$

where C is a capacitance matrix, M is an inductance matrix, R is a diagonal resistance matrix and A , B matrices are of ± 1 's and 0's. The voltage and current vectors, \mathbf{V} and \mathbf{I} , include the coil and shield turn voltages and currents. These equations are solved by means of a Runge–Kutta solver.

Since the experimental setup was in air, we used air core inductance and mutual inductance expressions. The mutual inductance between two thin wire coaxial loops of radii r_1 and r_2 spaced a distance d apart (in MKS units) is given by [Smy68]

$$M = \frac{2\mu_0}{k} \sqrt{r_1 r_2} \left[\left(1 - \frac{k^2}{2} \right) K(k) - E(k) \right] \quad (12.101)$$

with

$$k^2 = \frac{4r_1r_2}{[(r_1 + r_2)^2 + d^2]}$$

$K(k)$ and $E(k)$ are complete elliptic integrals of the first and second kinds, respectively, and $\mu_0 = 4\pi \times 10^{-7}$ H/m. For rectangular cross section coils, we can use Lyle's method in conjunction with Equation 12.101 for a more accurate determination of the mutual inductance [Gro73]. However, for the turn-turn mutual inductances in our experimental coils, treating the turns as thin circular loops was nearly as accurate as Lyle's method. The self-inductance of a single-turn circular coil of a square cross section with an average radius of a and square side length of c (in MKS units) is given by [Gro73]

$$L = \mu_0 a \left\{ \frac{1}{2} \left[1 + \frac{1}{6} \left(\frac{c}{2a} \right)^2 \right] \ln \left[\frac{8}{(c/2a)^2} \right] + 0.2041 \left(\frac{c}{2a} \right)^2 - 0.84834 \right\} \quad (12.102)$$

This applies for $c/2a \leq 0.2$. When the cross section is not a square, it can be subdivided into a number of squares and Equation 12.102 together with Equation 12.101 can be applied to compute the self-inductance more accurately. In our experimental coil, the turn dimensions were such that the simple formula with c taken as the square root of the turn area agreed with the more accurate calculation.

The turn-turn and turn-shield capacitances were the same as given in Section 12.11.1. The capacitance c_b in Figure 12.17 was taken as c_d/N . We did not include the capacitance between shield turns on neighboring disks in our final calculations, as their inclusion had little effect on the total capacitance.

The resistances used in the circuit model were based on the wire dimensions but were multiplied by a given factor to account for high-frequency losses. We can estimate this factor by examining the frequency dependence of the two main contributors to the coil loss, namely the Joule or I^2R loss and the eddy current loss due to stray flux carried by the conductor strands. Based on a formula for cylindrical conductors in [Smy68], the Joule loss is nearly independent of frequency at low frequencies, which includes 60 Hz for our conductor dimensions. At high frequencies, the loss divided by the DC or 60 Hz loss is given by

$$\frac{W_{\text{Joule}(f)}}{W_{\text{Joule}}(f=0)} = \frac{r_{\text{cond}}}{2} \sqrt{\pi \mu_0 \sigma f} \quad (12.103)$$

where r_{cond} is the radius of the conductor or in our case an effective radius based on the wire dimensions, σ is the wire's conductivity, and f

is the frequency in hertz. Based on our cable dimensions and for a typical frequency encountered in our calculations and experiment of ~ 0.15 MHz, we estimate that $W_{\text{Joule}}(f)/W_{\text{Joule}}(f=0) \sim 15.9$. The eddy current frequency dependence due to stray flux is given in [Lam66]. At low frequencies, this loss varies as f^2 , whereas at high frequencies, it varies as $f^{0.5}$. Taking the ratios of the high to low frequency eddy current loss, we get

$$\frac{W_{\text{Eddy}}(f)}{W_{\text{Eddy}}(60 \text{ Hz})} = \frac{6\sqrt{f}}{b^3(\pi\mu_0\sigma)^{1.5}(60)^2} \quad (12.104)$$

where b is the thickness of the lamination or strand in a direction perpendicular to the stray magnetic field. In our case, the cable was made of rectangular strands with dimensions $1.4 \text{ mm} \times 4.06 \text{ mm}$. For the 1.4 mm dimension, Equation 12.104 gives a ratio of 68,086, while for the 4.06 mm dimension, we get a ratio of 2766. A detailed field mapping is necessary to obtain the eddy current loss contribution at low frequencies, but typically this amounts to about 10% of the DC loss, depending on the cable construction. If we assume that the small and large dimension eddy losses are equal at low frequencies, that is, each is 5% of the DC loss, then we find that the ratio of high to low frequency total loss, based on the above ratios, is given by $W_{\text{tot}}(f)/W_{\text{tot}}(60 \text{ Hz}) = 3557$. This is only a crude estimate. Our data show that this ratio is about 1500 for our cable. Since the capacitance obtained from the simulation is nearly independent of the resistance used, we did not try to match the model's resistance with the experimental values. A sample output is shown in Figure 12.18.

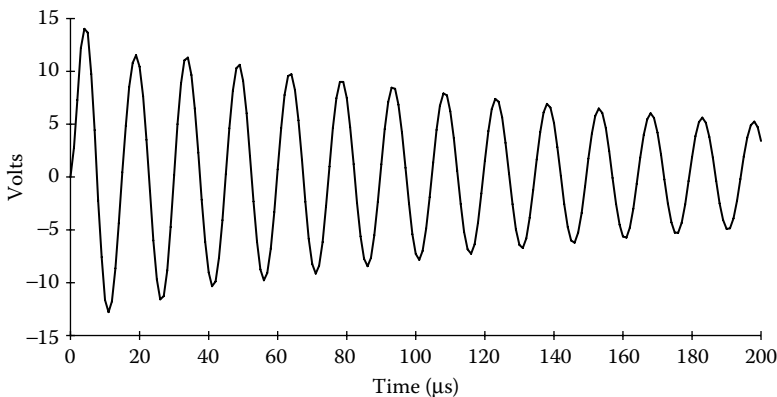


FIGURE 12.18

Voltage across the coil pair versus time from the detailed circuit model calculations. (From Del Vecchio, R. M., B. Poulin, and R. Ahuja. 1998. *IEEE Trans Power Deliv* 13(2):503–9. With permission.)

We used two methods to extract the equivalent total capacitance from the circuit model. Since we determined the voltages of each coil and shield turn at each time step, the capacitive energy was simply summed and the total capacitance determined via

$$E_{\text{tot}} = \frac{1}{2} C_{\text{tot}} V^2 \quad (12.105)$$

where V is the voltage of turn $i = 1$ at the particular time step. At the end of the total time duration of about 200 time steps, we calculated the average and median total capacitances. These two values generally agreed closely. The other method consisted of extracting the total capacitance from a simplified equivalent circuit as shown in Figure 12.19. We also used this latter method to obtain the total capacitance experimentally.

Using Laplace transforms, we can solve the circuit of Figure 12.19 analytically, assuming a step function current input of magnitude I . We get

$$V(t) = IR \left\{ 1 - e^{-\frac{R}{2L}t} \left[\cos(\omega_0 t) + \frac{1}{2} \left(\frac{R}{2L} \right) \left(\frac{1}{\omega_0} - \frac{\omega_0}{(R/2L)^2} \right) \sin(\omega_0 t) \right] \right\} \quad (12.106)$$

for $t \geq 0$. Here

$$\omega_0 = \sqrt{\frac{1}{LC} - \left(\frac{R}{2L} \right)^2} \quad (12.107)$$

In the limiting case as $R \rightarrow 0$, Equation 12.106 becomes

$$V(t) = I \sqrt{\frac{L}{C}} \sin(\omega_0 t) \quad (12.108)$$

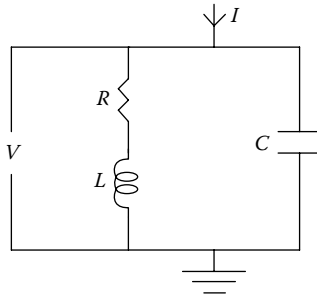


FIGURE 12.19

Simplified circuit model for capacitance determination.

In all the cases examined computationally or experimentally, the term $(R/2L)^2$ was much smaller than $1/LC$ so that it can be ignored in the expression for ω_0 . Thus, by measuring the oscillation frequency, we can determine the combination LC . To obtain C , we place an additional capacitance C_1 in parallel with the coil and determine a new oscillation frequency, ω_1 . Since this added capacitance does not change L , we have, taking ratios and squaring Equation 12.107,

$$\frac{C + C_1}{C} = \left(\frac{\omega_0}{\omega_1} \right)^2 \quad (12.109)$$

Since ω_0 and ω_1 can be measured or determined from the output of the circuit model and C_1 is known, C can be obtained. We find that the two methods of determining C closely agree.

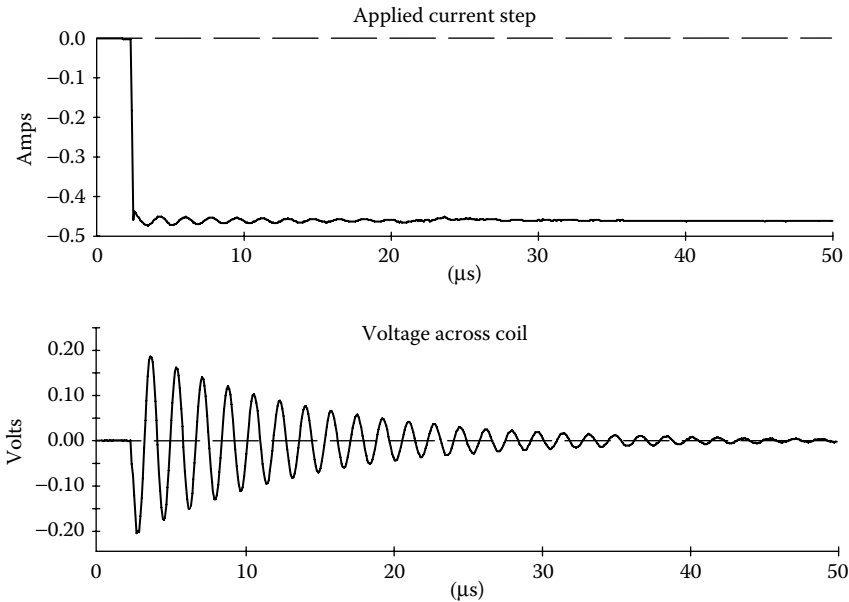
12.11.3 Experimental Methods

A coil containing two disk sections was made of transposed cable; there were 10 turns per disk. The cable turns were 11.7 mm radial build by 9.19 mm axial height, including a 0.76-mm (two-sided) paper cover. The inner radius was 249 mm; the outer radius depended on the number of shield turns but was approximately 392 mm. The wound-in-shield turns consisted of 3.55 mm radial build by 9.27 cm axial height magnet wire, including a 0.51-mm (two-sided) paper cover. The disks were separated by means of 18 key spacers equally spaced around the circumference. The key spacers were 44.5 mm wide by 4.19 mm thick.

The coil was excited by means of a current source that produced a near step function current. A sample of the current input and coil voltage output is shown in Figure 12.20. This voltage versus time plot was Fourier-analyzed to extract the resonant frequency. Frequencies were measured with and without an external capacitor of 10 nF across the coil in order to obtain the coil capacitance by the ratio method described previously.

Shield turns per disk of $n = 3, 5, 7, 9$ were tested as well as the no-shield case, $n = 0$. In addition, tests were performed for each n value with the shield floating, attached to the high-voltage terminal at the crossover, and attached to the high-voltage terminal at the end shield turn on the top disk. Other methods of attachment were also performed for the $n = 9$ case to test for expected symmetries.

Because the disk pair was not contained in a tightly wound coil, there tended to be some looseness in the winding. The looseness in the winding was determined by squeezing the disk turns tightly together and noting how much the radial build decreased. From this, we can determine how much looseness occurred in the insulation and correct for it. This amounted to about a 5% correction.

**FIGURE 12.20**

Experimental output from one of the test runs on the coil showing the input current and voltage across the coil versus time. (From Del Vecchio, R. M., B. Poulin, and R. Ahuja. 1998. *IEEE Trans Power Deliv* 13(2):503–9. With permission.)

12.11.4 Results

There are some uncertainties associated with the values of the relative permittivities that should be used in the capacitance calculations, particularly that of paper in air. For the pressboard key spacers, [Mos87] gives a method for determining its permittivity in terms of the board density, the permittivity of the fibers, and the permittivity of the substance filling the voids. Using this method for our key spacers in air, we obtain $\epsilon_{ks} = 4.0$. (For pressboard in oil, the value is $\epsilon_{ks} = 4.5$) For paper, [Cla62] presents a graph of the dielectric constant versus density in air and oil. Unfortunately, paper wrapping on cable is not as homogeneous a substance as pressboard. Its effective density will depend on how the wraps overlap and how loosely or tautly it is wound. In addition, for transposed cable, the paper–copper interface is not a clean rectilinear one. This is because of the extra unpaired strand on one side of the strand bundle. We found that a value of $\epsilon_p = 1.5$ was needed to obtain a good overall agreement with the test data. This will correspond to an effective paper density of 0.5 g/cm^3 according to the graph in [Cla62]. At that density, paper in oil will have $\epsilon_p = 3.0$ according to the same graph. For tightly wound paper in oil, values of $\epsilon_p = 3.5 - 4.0$ are typically used. Thus, a paper permittivity of 1.5 for paper in air is reasonable.

Table 12.1 shows the test results along with the calculated values of the capacitance for different numbers of shield turns and different shield biasing, which agree well overall. The trends are certainly well reproduced. Even for the floating shield case, which has the lowest capacitive enhancement, there is a capacitance increase over the unshielded case of a factor of 5 for three shield turns per disk and a factor of about 13 for nine shield turns per disk. By biasing the shield in different ways, we can achieve even greater increases.

Table 12.2 shows the coil-turn and shield-turn voltages as calculated by the circuit model at time $t = 30 \mu\text{s}$ for the $n = 9$ case with the shields floating. The table shows that the coil volts per turn are about the same as the shield volts per turn, verifying the assumption made by the analytic model. In addition, $V_{\text{bias}} \approx V/2$, as was also assumed in the simple model. Also, the voltage differences between the coil and shield turns fall into two groups of either ~ 12.8 or 11.5 V in this case. This also corresponds to the simple model prediction of either $N\Delta V = V/2$ or $(N-1)\Delta V = V/2 - \Delta V$ volts. Thus, in the case in which the shields are floating, the maximum shield turn-coil turn voltage is $V/2$. Based on the simple model, this holds regardless of the number of shield turns.

TABLE 12.1
Capacitance of Coil with Two Disks of 10 Turns per Disk and Variable Number of Wound-In-Shield Turns per Disk

Shield Turns (n)	C _{tot} (nF)			
	Calculation Method	Floating	Attached to V at Crossover	Attached to V at Top End
0	Measured	0.24		
	Analytic	0.264		
	Circuit model	0.287		
3	Measured	1.20	2.33	3.21
	Analytic	1.31	2.44	3.08
	Circuit model	1.41	2.66	3.31
5	Measured	1.78	3.53	6.07
	Analytic	2.03	3.94	6.04
	Circuit model	2.21	4.34	6.73
7	Measured	2.80	5.73	11.8
	Analytic	2.75	5.45	10.1
	Circuit model	2.99	6.01	11.4
9	Measured	3.17	6.82	16.1
	Analytic	3.49	6.99	15.5
	Circuit model	3.83	7.61	17.91

Source: Del Vecchio, R. M., B. Poulin, and R. Ahuja. 1998. *IEEE Trans Power Deliv* 13(2):503–9. With permission.

TABLE 12.2
Turn Voltages at $t = 30\text{ }\mu\text{s}$ for a Coil of Two Disks with 10 Turns per Disk and Nine Shield Turns per Disk with the Shield Floating

Coil Turns			Adjacent Shield Turn			Adjacent Shield Coil
No.	Volts	ΔV	No.	Volts	ΔV	$ \Delta V $
1	24.27		1	11.43		12.84, 11.49
2	22.92	1.35	2	10.12	1.31	12.80, 11.39
3	21.51	1.45	3	8.73	1.39	12.78, 11.35
4	20.08	1.43	4	7.30	1.43	12.78, 11.35
5	18.65	1.43	5	5.87	1.43	12.78, 11.46
6	17.24	1.41	6	4.45	1.42	12.79, 11.44
7	15.89	1.35	7	3.09	1.36	12.80, 11.53
8	14.62	1.27	8	1.79	1.30	12.83, 11.63
9	13.42	1.20	9	0.52	1.27	12.90, 11.77
10	12.29	1.13				
11	11.49	0.80				
12	10.50	0.99	10	23.43		12.93, 11.94
13	9.45	1.05	11	22.27	1.16	12.82, 11.77
14	8.28	1.17	12	21.08	1.19	12.80, 11.63
15	6.98	1.30	13	19.78	1.30	12.80, 11.50
16	5.64	1.34	14	18.39	1.39	12.75, 11.41
17	4.25	1.39	15	16.99	1.40	12.74, 11.35
18	2.83	1.42	16	15.56	1.43	12.73, 11.31
19	1.40	1.43	17	14.14	1.42	12.74, 11.31
20	0	1.40	18	12.75	1.39	12.75, 11.35

$V_{\text{bias}} = (V_{\text{shield turn 1}} + V_{\text{shield turn 18}})/2 = 12.09 \approx V/2 = 12.14$

Table 12.3 shows the corresponding output from the circuit model at $t = 150\text{ }\mu\text{s}$ for a case in which the shield is attached at the crossover to the high-voltage terminal. (It was actually attached to shield turn $i = 1$ in the model.) We see again that the coil volts per turn \approx shield volts per turn. According to the simple model prediction ($\beta = 0$), the voltage differences between shield and adjacent turn on the top disk are zero and ΔV as is also nearly the case for the circuit model. Along the bottom disk, the simple model gives voltage differences of $2N\Delta V = V$ and $(2N-1)\Delta V = V-\Delta V$ and this is also nearly the case for the circuit model. Thus, the maximum coil-turn to shield-turn voltage is V . According to the simple model, this holds regardless of the number of shield turns.

We can analyze a case in which the end turn of the shield on the top disk is attached to the high-voltage terminal similarly, although this configuration is harder to achieve in practice. This configuration also has a higher coil-turn to shield-turn voltage difference than the other methods of shield attachment.

TABLE 12.3
Turn Voltages at $t = 150\text{ }\mu\text{s}$ for a Coil of Two Disks with 10 Turns per Disk and Nine Shield Turns per Disk with the Shield Attached at the Crossover to the High-Voltage Terminal

Coil Turns			Adjacent Shield Turn			Adjacent Shield Coil
No.	Volts	ΔV	No.	Volts	ΔV	$/\Delta V/$
1	5.13		1	5.13		0, 0.29
2	4.84	0.29	2	4.87	0.26	0.03, 0.33
3	4.54	0.30	3	4.58	0.29	0.04, 0.35
4	4.23	0.31	4	4.28	0.30	0.05, 0.35
5	3.93	0.30	5	3.99	0.29	0.06, 0.36
6	3.63	0.30	6	3.69	0.30	0.06, 0.34
7	3.35	0.28	7	3.41	0.28	0.06, 0.33
8	3.08	0.27	8	3.14	0.27	0.06, 0.30
9	2.84	0.24	9	2.90	0.24	0.06, 0.28
10	2.62	0.22				
11	2.42	0.20				
12	2.24	0.18	10	7.52		5.28, 5.10
13	2.02	0.22	11	7.30	0.22	5.28, 5.06
14	1.77	0.25	12	7.05	0.25	5.28, 5.03
15	1.50	0.27	13	6.79	0.26	5.29, 5.02
16	1.22	0.28	14	6.51	0.28	5.29, 5.01
17	0.92	0.30	15	6.23	0.28	5.31, 5.01
18	0.62	0.30	16	5.94	0.29	5.32, 5.02
19	0.31	0.31	17	5.66	0.28	5.35, 5.04
20	0	0.31	18	5.38	0.28	5.38, 5.07

As expected, however, the price to pay for the higher capacitances is that there are higher coil-turn to shield-turn voltage differences.

Several symmetric situations are noted in the experimental data. These symmetries were only checked for the $n = 9$ case but should apply to all n values according to the simple model. We found that attaching the high-voltage terminal to the end shield turn on the top disk ($i = n$) produced the same capacitance as attaching the low-voltage terminal, at 0 V here, to the end turn on the bottom disk ($j = n$). This symmetry can be seen in the simple formula in Equation 12.96 by using the appropriate values for β . Attaching the top end shield turn to the low-voltage terminal produced the same capacitance as attaching the bottom end shield turn to the high-voltage terminal. This can also be shown by means of the simple formula. Also, the same capacitance was produced whether the shield crossover was attached to the high- or low-voltage terminal. This also follows from the simple model.

For consistency, the inductance of our coil was extracted from the experimental data and from the circuit model output. We found $L(\text{data}) = 280\text{ }\mu\text{H}$ and $L(\text{circuit model}) = 320\text{ }\mu\text{H}$. Using an algorithm from Grover [Gro73], we

obtained $L(\text{calc}) = 340 \mu\text{H}$. These are all within reasonable agreement. The decay constant $R/2L$ appearing in Equation 12.106 can be extracted from the data by analyzing the envelope of the damped sinusoid (Figure 12.20), and we found that it can be dropped in the formula for ω_0 (Equation 12.107). We also observed a significant resistance change when we changed the frequency by adding the external capacitance.

12.12 Multistart Winding Capacitance

Multistart windings are a simple example of an interleaved type of winding. They are commonly used as tap windings. In these windings, adjacent turns have voltage differences that can differ from the usual turn–turn voltage drop along typical disk or helical windings. Although multistart windings are helical windings, we can think of them as a collection of superposed series connected helical windings as shown in Figure 12.21.

These winding essentially start over again and again (this is where the name originates). Each start represents a constituent winding having a certain number of turns, called turns per start. The number of starts is the same as the number of constituent windings. By connecting taps between the starts, the turns per start become the number of tap turns. Their advantage as tap windings when compared with the standard type is that they allow a more balanced force distribution regardless of the tap setting and do not require thinning of adjacent windings.

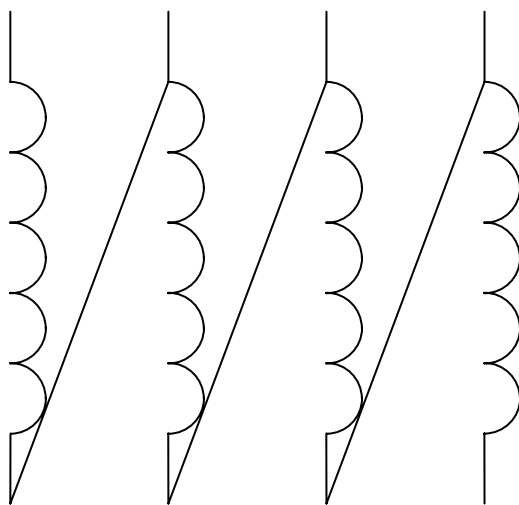


FIGURE 12.21

Schematic illustration of a multistart winding.

Although shown side by side in [Figure 12.21](#) for explanatory purposes, in reality the windings are superposed into one helical type of winding. The bottom-to-top connections are made external to this winding. The constituent windings are meshed in such a way that the voltage difference between adjacent turns in the composite winding is kept to one or two times the voltage drop along a constituent winding—really the best that can be done. Letting 1, 2, 3, ... label turns from the different constituent windings, [Figure 12.22](#) shows acceptable meshing schemes for various numbers of starts, N_s .

The turns are arranged along the winding according to Figure 12.22. The figure also indicates the voltage differences between adjacent turns, measured in units of the voltage drop between starts. We can see a pattern in the organization: Start with turn 1 from start coil 1. Put turn 2 from start coil 2 at the end of the group. Put turn 3 from start coil 3 below turn 1. Put turn 4 from start coil 4 above turn 2. Put turn 5 from start coil 5 below turn 3. Put turn 6 from start coil 6 above turn 4, and so on until you run out of start coils. Then, repeat the pattern until you run out of turns in the start coils.

The capacitance is obtained by summing up the capacitive energy associated with the winding configuration. Letting c_t be the turn-to-turn capacitance and ΔV_t the voltage difference between turns, the energy associated with a pair of adjacent turns is given by $\text{Energy}(\text{turn-turn}) = 1/2 c_t (\Delta V_t)^2$. Letting the voltage drop between starts be ΔV_s , the total energy is obtained by summing all the turn-turn energies. As we can see from Figure 12.22, each group of turns has two 1's except for the last group that has only one.

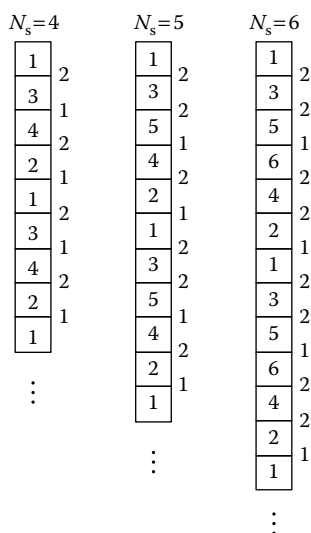


FIGURE 12.22

Winding schemes for multistart windings. The numbers beside the turns are the voltage differences between turns in units of the voltage drop between starts.

If there are n turns per start, there are n such groups. Hence, the energy for the 1's is $2n-1$ multiplied by the energy associated with voltage ΔV_s across capacitance c_t . The remaining turn–turn voltages in the group have a voltage of $2 \times \Delta V_s$ across them. There are N_s-2 such turns in the group. Since there are n such groups, the energy associated with these is $n \times (N_s-2)$ times the energy associated with a voltage of $2\Delta V_s$ across capacitance c_t . Combining these energies, we get at total energy of

$$\begin{aligned} E_{\text{total}} &= (2n-1)\frac{1}{2}c_t(\Delta V_s)^2 + n(N_s-2)\frac{1}{2}c_t(2\Delta V_s)^2 \\ &= \frac{1}{2}c_t(\Delta V)^2(4nN_s - 6n - 1) \end{aligned} \quad (12.110)$$

Since $\Delta V_s = V/N_s$, where V is the total voltage across the entire winding, by substituting this into Equation 12.110, we can extract a total capacitance for the winding, C_{ms} :

$$C_{\text{ms}} = c_t \frac{(4nN_s - 6n - 1)}{N_s^2} \quad (12.111)$$

c_t will depend on the insulation structure of the winding, that is, whether the turns are touching paper to paper in the manner of a layer winding or whether there is an oil gap separating them. In any case, the capacitance is much higher than that across a comparable helical winding in which the turn–turn voltages are much smaller.

13

Voltage Breakdown and High-Voltage Design

13.1 Introduction

A transformer's insulation system must be designed to withstand not only the alternating current (AC) operating voltages, with some allowance for an overvoltage of ~15%, but also the much higher voltages produced by lightning strikes or switching operations. These latter voltages can be limited by protective devices, such as lightning or surge arrestors, but these devices are usually set to protect at levels well above the normal AC operating voltage. Fortunately, the transformer's insulation can withstand higher voltages for the shorter periods of time that are characteristic of lightning or switching disturbances. Thus, insulation designed to be adequate at the operating voltage can also be sufficient for the short-duration higher voltages that may be encountered.

Insulation design is generally an iterative process. A particular winding type, such as disk, helix, or layer, is chosen for each of the transformer's windings. They must have the right number of turns to produce the desired voltage and must satisfy thermal, mechanical, and impedance requirements. The voltage distribution is then calculated throughout the windings using a suitable electrical model, together with the appropriate input such as a lightning impulse excitation. Voltage differences and/or electric fields are then calculated to determine whether they are high enough to cause breakdown, according to some specific breakdown criteria, across the assumed insulation structure. More elaborate path integrals are sometimes used to determine breakdown. If the breakdown criterion is exceeded at a specific location, the insulation is redesigned and the process repeated until the breakdown criteria are met. Insulation redesign can consist of adding more paper insulation to the wire or cable, increasing the size of the oil or air ducts, or resorting to interleaving the winding conductors or adding wound-in or other types of shields.

Although voltages and electric fields can be calculated to almost any desired accuracy assuming that the material properties are well known, the same cannot be said for the breakdown fields in solids or liquids. The theory of breakdown in gases is reasonably well established, but the theory of

breakdown for solids or liquids is relatively rudimentary. An oil breakdown model is presented here, which attempts to address this problem. Design rules have evolved based on experience. With suitable margins, these rules generally produce successful designs. Success is usually judged by whether a transformer passes a series of dielectric tests using standard impulse waveforms or AC power frequency voltages for specified periods without breakdown or excessive corona. These tests have been developed over the years in an effort to simulate a typical lightning or switching wave shape.

13.2 Principles of Voltage Breakdown

We briefly discuss some of the proposed mechanisms of voltage breakdown in solids, liquids, and gases, with primary emphasis on transformer oil, because in oil-filled transformers, due to the higher dielectric constant of the solid insulation, the highest electric stress tends to occur in the oil. In addition, the breakdown stress of the oil is generally much lower than that of the solid insulation. The same situation occurs in dry-type transformers; however, the breakdown mechanism in the gas is much better understood.

In gases, breakdown is thought to occur by electron avalanche, also called the Townsend mechanism [Kuf84]. In this process, the electric field imparts sufficient energy to the electrons between collisions with the atoms or molecules of the gas, helping them to release or ionize additional electrons upon subsequent collisions. These additional electrons, in turn, acquire sufficient energy between collisions to release more electrons in an avalanche process. The process depends in detail on the collision cross sections for the specific gas. These cross sections can lead to elastic scattering, ionization, and absorption, in addition to being highly energy dependent. They have been measured for a variety of gases. In principle, breakdown can be calculated from knowledge about these collision cross sections, together with corrections due to the influence of positive ions, photoexcitation, and so on. In practice, the theory has served to illuminate the parametric dependence of the breakdown process and, additionally, is in reasonable quantitative agreement for specific gases.

One of the major results of the theory of gaseous breakdown is that the breakdown voltage across a uniform gap depends on the product of pressure and gap thickness or, more generally, on the product of gas density and gap thickness. This relationship is called the Paschen curve. A sketch of such a curve is shown in [Figure 13.1](#). A common feature of such curves is the existence of a minimum. Thus, for a given gap distance and assuming we are to the right of the minimum, as the pressure is lowered the breakdown voltage will decrease and increase again as the pressure is lowered past the minimum. Care must be taken to ensure that the gap voltage is sufficiently far

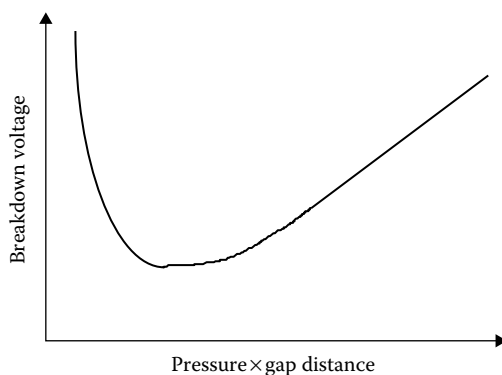


FIGURE 13.1
Schematic Paschen curve.

from the minimum to avoid breakdown. For a given gas pressure or, more accurately, density, the breakdown field depends only on the gap thickness.

During the avalanche process, because the negatively charged electrons move much more rapidly than the positively charged ions and because they are pulled toward opposite electrodes, a charge separation occurs in the gas. When the excess charge is large enough, as can occur in a well-developed avalanche for large gap distances or high values of pressure \times gap, the electric field produced by the excess charge approaches the applied field. When this occurs, the Townsend mechanism of breakdown gives way to a streamer type of breakdown. In this process, secondary breakdown paths or plasma channels form at the front of the avalanche, leading to a more rapid breakdown than can be accounted for by the Townsend mechanism alone. Theoretical calculations, based on idealized charge configurations, can account approximately for this type of breakdown.

In solids and liquids, in which the distance between electron collisions is much shorter than that in gases so that the electrons have a harder time acquiring enough energy to produce an avalanche, the Townsend mechanism is not considered operative, except possibly for extremely pure liquids. A streamer type of mechanism is considered much more likely but the theory is not as well developed. Moreover, especially in liquids, usually many types of impurities are found, and their presence even in small concentrations can lower the breakdown stress considerably. This is well established experimentally—further and further purifications lead to higher breakdown stresses to the point where the so-called intrinsic breakdown stress of a pure liquid can be reached, but has rarely been measured.

In solids and liquids, the breakdown stress does not appear to be strictly a function of the gap thickness but appears to depend on the area of the electrodes or the volume of the material under stress. This would argue against a strictly Townsend mechanism of breakdown according to which, with the nearly constant density of most solids and liquids, the breakdown should

depend on the gap distance only. However, the experimental evidence is fragmentary and sometimes contradictory.

The dependence of breakdown on an electrode area or volume is usually explained by means of a weak-link theory. According to this theory, a weak spot, imperfection, or imperfection-based mechanism causes the failure. Thus, as the size of the specimen grows, weaker spots or more and greater imperfections are uncovered, resulting in failure at lower electric stress. Support for this type of failure mechanism comes from studies of the statistics of breakdown. Experimental evidence shows that breakdown probabilities follow an extreme-value distribution, in particular, the Weibull distribution [Gum58]. This type of distribution is consistent with a weak-link mechanism. In fact, Weibull invented it to account for the statistics related to failure in fracture mechanics, which can be associated with material flaws. In its general form, the distribution function giving the probability of failure for a voltage $\leq V$, $P(V)$ is

$$P(V) = \begin{cases} 1 - e^{-\left(\frac{V-V_0}{a}\right)^k}, & V \geq V_0 \\ 0, & V < V_0 \end{cases} \quad (13.1)$$

where V_0 , a , and k are parameters >0 . The probability density function, which is the derivative of the distribution function, when multiplied by ΔV , gives the probability of failure in an assumed small interval ΔV about V . It is represented by

$$p(V) = \frac{dP(V)}{dV} = \frac{k}{a} \left(\frac{V - V_0}{a} \right)^{k-1} e^{-\left(\frac{V-V_0}{a}\right)^k} \quad (13.2)$$

The density function is generally asymmetric about the mode or the most probable value, and this asymmetry is usually taken as evidence that one is dealing with an extreme-value distribution, in contrast to a Gaussian density function, which is symmetric about the mode or mean in this case.

According to advocates of an electrode-area dependence on the breakdown stress, the weak link can be a protrusion on the electrode surface where the field is enhanced or an area of greater electron emissivity on the surface. Advocates of the volume dependence of breakdown emphasize the role of impurities in the material, which increase with volume [Wil53]. According to Kok [Kok61], impurities in liquids such as transformer oil tend to have a higher dielectric constant than the oil, particularly if they have absorbed some water. Thus, they are attracted to regions of higher electric field by the presence of gradients in the field. They tend to acquire an induced dipole moment so that other dipoles attach to them in a chain-like fashion. Such a chain can lead to a relatively high conductivity link between

the electrodes due to the presence of water and possibly dissolved ions, leading to breakdown. The probability of forming such a chain increases with the amount of impurity present and hence with the volume of liquid.

Other mechanisms that can account for some of the breakdown data, such as the formation of bubbles in the breakdown process, have been summarized in [Gall75]. We know from numerous experiments that the breakdown electric stress in transformer oil is lowered by the presence of moisture, particles such as cellulose fibers shed by paper or pressboard insulation, and the presence of dissolved gas. One experiment even showed that the breakdown stress between two electrodes depended on whether the electrodes were horizontal or vertical. Presumably, the dissolved gas and its tendency to form bubbles when the electric stress was applied influenced the results, since the bubbles would be trapped in the former orientation, whereas in the latter case, they could float away. In other experiments, allowing the oil to flow between the electrodes increased the breakdown stress compared with stationary oil. These influences make it difficult to compare breakdown results from different investigators. However, for a given investigator and using a standardized liquid or solid preparation and testing procedure, observed trends in the breakdown voltage or stress with other variables are probably valid.

Breakdown studies not concerned with time as a variable are generally done under impulse or AC power frequency conditions. In the latter case, the time duration is usually 1 minute. In impulse studies, the waveform is a unidirectional pulse having a rise time of $t_{\text{rise}} = 1\text{--}1.5\ \mu\text{s}$ and a fall time, to 50% of the peak value, of $t_{\text{fall}} = 40\text{--}50\ \mu\text{s}$ as sketched in Figure 13.2. In most such studies, the breakdown occurs on the tail of the pulse but the breakdown voltage level is considered the peak voltage. However, in front-of-wave breakdown studies, breakdown occurs on the rising part of the pulse and the breakdown voltage is taken as the voltage reached when breakdown occurs. Although the variability in time durations for the rise and fall of the pulse

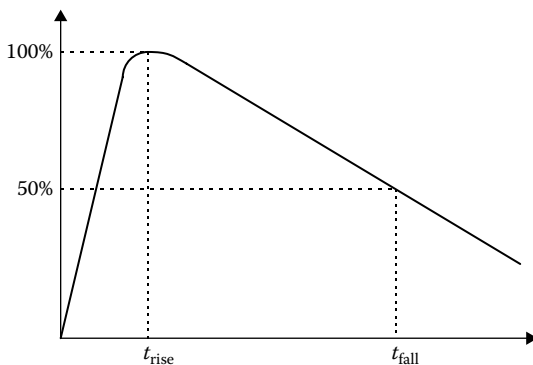


FIGURE 13.2
Impulse wave shape.

are not considered very significant when breakdown occurs on the tail of the pulse, front-of-wave breakdown voltages are generally higher than those occurring on the tail. The polarity of the impulse can also differ between studies, although the standard is negative polarity since that is the polarity of the usual lightning strike. There is also a fair degree of variability in the experimental conditions for AC power frequency breakdown studies. The frequency used can be 50 or 60 Hz, depending on the power frequency in the country where the study was performed. Holding times at this voltage can range between 1 and 3 minutes, or the breakdown can occur on a rising voltage ramp where the increase in volts per second can differ from study to study. These differences can lead to differences in the breakdown levels reported, but they should not amount to more than a few percent. The ratio between the full-wave impulse-breakdown voltage and the AC root mean square (rms) breakdown voltage is called the impulse ratio and is in the range of 2–3. This ratio applies to a combination of solid (pressboard) insulation and transformer oil, although it is not too different for either when considered separately.

There is some controversy concerning the breakdown mechanism in the different time regimes for transformer oil. Endicott and Weber [End57] found the same asymmetric probability density distributions for impulse and AC breakdown voltages, indicating that extreme-value statistics are operative. They also found that both types of breakdown depended on the electrode area. On the other hand, Bell [Bel77] found that the impulse (front-of-wave) breakdown voltages had a symmetrical Gaussian probability density, whereas the AC breakdowns had an asymmetric probability density. Bell found, nevertheless, that the impulse breakdown levels depended on the volume of stressed oil. According to this finding, the volume effect under impulse is not linked to extreme-value statistics. Palmer and Sharpley [Pal69] found that both impulse and AC breakdown voltages depended on the volume of stressed oil; however, breakdown statistics for both followed a Gaussian distribution. It appears from these and similar studies that the breakdown mechanism in transformer oil is not understood enough to conclude that different mechanisms are operative during the different time regimes.

One of the consequences of the theoretical uncertainty in transformer oil breakdown—and to a certain extent, in breakdown in solids—is that there is no accepted way to parameterize the data. Thus, although a few authors present graphs of breakdown voltage or stress versus electrode area, others show breakdown versus stressed oil volume, and still others represent breakdown versus gap thickness. An attractive compromise appears in the work of Danikas [Dan90]. In this work and others [Bel77], breakdown is studied as a function of both electrode area and gap thickness. This also allows for the possibility of a volume effect should the dependence be a function of area \times gap thickness. In [Dan90], the area effect appears to saturate for large areas; in other words, the breakdown level is unchanged as the

area increases beyond a given value. Thus, breakdown becomes purely a function of gap spacing at sufficiently large areas. Higaki et al. [Hig75] found that the breakdown electric stress becomes constant for large gap distances as well as for large volumes. This suggests caution in extrapolating experimental results in the direction of either larger or smaller parameter values from those covered by the experiment.

At this point, we present some of the breakdown data and parameter dependencies reported in the relevant literature. When graphs are presented, we have converted the best fit into an equation. Moreover, voltage values are converted to electric field values when the voltage is applied across a uniform gap. For consistency, we use kilovolts per millimeter (kV/mm) for breakdown stress, millimeter for gap thickness, and square millimeter (mm²) or cubic millimeter (mm³) for areas or volumes, respectively, in the formulas. This will allow us to compare different results not only with respect to parameter dependencies but also with respect to numerical values. Generally, the breakdown voltages are those for which the probability to have a breakdown is 50%. Thus, some margin below these levels is needed in actual design.

13.2.1 Breakdown in Solid Insulation

We begin with breakdown in solid insulation, namely, oil-saturated paper and pressboard. Samples are prepared by drying and vacuum impregnation and then tested under oil. For paper at 25°C, Blume et al. [Blu51] reported the breakdown voltage stress $E_{b,AC}$ versus thickness d for 60-Hz AC voltages as

$$E_{b,AC} \left(\frac{\text{kV}_{\text{rms}}}{\text{mm}} \right) = \frac{17.1}{d^{0.33}} \left(0.85 + \frac{0.15}{t^{1/4}} \right) \quad (13.3)$$

where thickness d is in millimeters and t is the duration of the voltage application, in minutes. Palmer and Sharpley [Pal69] reported the impulse breakdown for paper, $E_{b,imp}$, versus thickness d in millimeters at 90°C as

$$E_{b,imp} \left(\frac{\text{kV}_{\text{peak}}}{\text{mm}} \right) = \frac{79.43}{d^{0.275}} \quad (13.4)$$

In proceeding from 90 to 20°C, the impulse breakdown stress increases by about 10%, according to [Pal69]. Clark [Cla62] reported $E_{b,AC}$ for Kraft paper at room temperature and AC test conditions as

$$E_{b,AC} \left(\frac{\text{kV}_{\text{rms}}}{\text{mm}} \right) = \frac{32.8}{d^{0.33}} \quad (13.5)$$

Results from different investigators are difficult to compare because the thickness buildup is achieved by stacking thin layers of paper. The stacking processes can differ. Some use lapping with different amounts of overlap and different thicknesses of the individual layers. Other possible differences include the shape and size of the electrodes. Nevertheless, the exponent of the thickness dependence is nearly the same in different studies. Clark [Cla62] reported an area effect, but it is difficult to quantify. The impulse ratio for paper, corrected for temperature, based on Equations 13.4 and 13.5 is ~2.7.

For pressboard in oil at 25°C, Blume et al. [Blu51] reported the breakdown voltage to be

$$E_{b,AC} \left(\frac{\text{kV}_{\text{rms}}}{\text{mm}} \right) = \frac{25.7}{d^{0.33}} \left(\frac{1.75}{f^{0.137}} \right) \left(0.5 + \frac{0.5}{t^{1/4}} \right) \quad (13.6)$$

where the frequency f is in hertz and time duration t is in minutes. The frequency dependence was only tested in the range of 25 to 420 Hz but is expected to hold for even higher frequencies. For pressboard at room temperature, using 25-mm spherical electrodes, Moser [Mos79] reported

$$\begin{aligned} E_{b,AC} \left(\frac{\text{kV}_{\text{rms}}}{\text{mm}} \right) &= \frac{33.1}{d^{0.32}} \\ E_{b,\text{imp}} \left(\frac{\text{kV}_{\text{peak}}}{\text{mm}} \right) &= \frac{94.6}{d^{0.22}} \end{aligned} \quad (13.7)$$

Thus, the impulse ratio for pressboard obtained from Equation 13.7 is ~3.0. Palmer and Sharpley [Pal69] reported the following for pressboard in oil at 90°C:

$$\begin{aligned} E_{b,AC} \left(\frac{\text{kV}_{\text{rms}}}{\text{mm}} \right) &= \frac{27.5}{d^{0.26}} \\ E_{b,\text{imp}} \left(\frac{\text{kV}_{\text{peak}}}{\text{mm}} \right) &= \frac{91.2}{d^{0.26}} \end{aligned} \quad (13.8)$$

The impulse ratio for pressboard, based on Equation 13.8 is ~3.3. The data of [Mos79] and [Pal69] trends in the right direction because pressboard breakdown strength decreases with increasing temperature.

Based on the above data, significant differences do not appear to exist between the breakdown strength of oil-soaked paper or pressboard insulation either under AC- or impulse test conditions. Even the thickness dependencies are similar. Although Cygan and Laghari [Cyg87] found a dependence

of the area and thickness on the dielectric strength of polypropylene films, how this is applicable to paper or pressboard insulation is not known.

13.2.2 Breakdown in Transformer Oil

For transformer oil at 90°C, Palmer and Sharpley [Pal69] report breakdown electric fields that depend on volume Λ (in mm³) according to the equations

$$\begin{aligned} E_{b,AC} \left(\frac{\text{kV}_{\text{rms}}}{\text{mm}} \right) &= 34.9 - 1.74 \ln \Lambda \\ E_{b,\text{imp}} \left(\frac{\text{kV}_{\text{peak}}}{\text{mm}} \right) &= 82.5 - 3.69 \ln \Lambda \end{aligned} \quad (13.9)$$

This implies an impulse ratio for oil of ~2.5. In contrast to paper insulation, the breakdown strength of transformer oil increases slightly with temperature in the range of -5 to 100°C [Blu51]. Nelson [Nel89] summarizes earlier work on the volume effect for breakdown in oil by

$$E_{b,AC} \left(\frac{\text{kV}_{\text{rms}}}{\text{mm}} \right) = \frac{46.1}{\Lambda^{0.137}} \quad (13.10)$$

with Λ in mm³. The logarithmic dependence on volume given in Equation 13.9 cannot be valid as volume increases indefinitely because the breakdown stress would eventually become negative. In Equation 13.10, the breakdown stress becomes unrealistically close to zero as volume increases.

Endicott and Weber [End57] and [Web56] present breakdown strengths in oil versus electrode area A in the form:

$$\begin{aligned} (E_1 - E_2)_{b,AC} \left(\frac{\text{kV}_{\text{rms}}}{\text{mm}} \right) &= 1.74 \ln \left(\frac{A_2}{A_1} \right) \\ (E_1 - E_2)_{b,\text{imp}} \left(\frac{\text{kV}_{\text{peak}}}{\text{mm}} \right) &= 4.92 \ln \left(\frac{A_2}{A_1} \right) \end{aligned} \quad (13.11)$$

In Equation 13.11, E_1 refers to the breakdown voltage for A_1 and E_2 for A_2 . The gap spacing in both these studies was 1.9 mm. Although the impulse conditions in this study were of the front-of-wave type, the voltage ramp was maintained slow in an attempt to approximate full-wave conditions. Thus, we can reasonably obtain an impulse ratio of ~2.8 from Equation 13.11.

Moser [Mos79] gives the AC (50 Hz, 1 minute) partial-discharge inception electric stress, $E_{\text{pd},AC}$, for oil as a function of the gap thickness only. Although not strictly the breakdown strength, partial discharge maintained over a long

enough time can lead to breakdown and is therefore undesirable. Separate curves are given for gas-saturated or degassed oil and for insulated or non-insulated electrodes. Fitting the curves, we obtain

$$\begin{aligned}
 E_{\text{pd,AC}} \left(\frac{\text{kV}_{\text{rms}}}{\text{mm}} \right) &= \frac{14.2}{d^{0.36}} \quad (\text{gas-saturated oil, noninsulated electrodes}) \\
 E_{\text{pd,AC}} \left(\frac{\text{kV}_{\text{rms}}}{\text{mm}} \right) &= \frac{17.8}{d^{0.36}} \quad (\text{degassed oil, noninsulated electrodes}) \\
 E_{\text{pd,AC}} \left(\frac{\text{kV}_{\text{rms}}}{\text{mm}} \right) &= \frac{19.0}{d^{0.38}} \quad (\text{gas-saturated oil, insulated electrodes}) \\
 E_{\text{pd,AC}} \left(\frac{\text{kV}_{\text{rms}}}{\text{mm}} \right) &= \frac{21.2}{d^{0.36}} \quad (\text{degassed oil, insulated electrodes})
 \end{aligned} \tag{13.12}$$

with d in millimeters.

Trinh et al. [Tri82] analyzed transformer oil for dependence of dielectric strength on both area and volume. They conclude that both area and volume effects can be present, with the area effect becoming more important for ultra clean oil and the volume effect becoming more important for oil having higher particle content. Although the data show much scatter, they present curves for oils of different purities. For their technical-grade transformer oil, the middle grade of the three analyzed, the following formulas are approximate fits to their curves.

$$\begin{aligned}
 E_{\text{b,AC}} \left(\frac{\text{kV}_{\text{rms}}}{\text{mm}} \right) &= 5 \left(1 + \frac{10}{A^{0.2}} \right) \\
 E_{\text{b,imp}} \left(\frac{\text{kV}_{\text{peak}}}{\text{mm}} \right) &= 10 \left(1 + \frac{23.7}{A^{0.25}} \right)
 \end{aligned} \tag{13.13}$$

$$\begin{aligned}
 E_{\text{b,AC}} \left(\frac{\text{kV}_{\text{rms}}}{\text{mm}} \right) &= 5 \left(1 + \frac{7.9}{\Lambda^{0.14}} \right) \\
 E_{\text{b,imp}} \left(\frac{\text{kV}_{\text{peak}}}{\text{mm}} \right) &= 15 \left(1 + \frac{9.7}{\Lambda^{0.18}} \right)
 \end{aligned} \tag{13.14}$$

with A in mm^2 and Λ in mm^3 . They seem to propose that it is immaterial whether one describes breakdown in terms of an area or volume effect. However, the consequences of these two approaches are very different. For areas and volumes in the range of $\sim 10^3$ – 10^7 mm^2 or mm^3 , the impulse ratio implied by Equations 13.13 and 13.14 is in the range of ~ 2 – 3 . In these formulas,

as is also evident in [Dan90, Hig75], the dielectric strength approaches a constant value as the area or volume becomes very large. This is a reasonable expectation. On the other hand, dielectric strengths approach infinity as areas, volumes, and gap distances approach zero in Equations 13.10 through 13.14. This is surely inaccurate, although the formulas seem to hold for quite small values of these quantities.

By putting in typical values for d , A , and Λ as found in transformers in the above formulas, the dielectric strength of paper or pressboard can be seen to be approximately twice that of oil. However, the electric stress that occurs in the oil is typically greater than that which occurs in the paper or pressboard. For this reason, breakdown generally occurs in the oil gaps first. However, once the oil gaps break down, the solid insulation will experience a higher stress so that it could, in turn, break down. Even if the solid insulation can withstand the higher stress, the destructive effects of the oil breakdown, such as arcing or corona, would eventually puncture the solid insulation. Thus, it seems inappropriate to design a solid-oil insulation system so that the solid by itself could withstand the full voltage applied across the gap, as has sometimes been the practice in the past, unless the insulation is all solid. In fact, excess solid insulation, because of its higher dielectric constant than oil, increases the stress in the oil to levels above those in a design more sparing of the solid insulation.

Because of the gap and volume dependence of oil breakdown strength, it is common to subdivide large oil gaps, which occur for example between transformer windings, by means of one or more thin pressboard cylinders. Thus, a gap having a large distance or volume is reduced to several smaller gaps, each having higher breakdown strength. Hence, current practice favors a gap or volume effect over a pure area effect since gap subdivision will not be of benefit for an area effect. A combined gap-area or gap-volume effect will also be consistent with current practice.

The breakdown data refers to gaps that are uniform or as reasonably uniform as is practical. This situation is rarely achieved in design, so the question as to how to apply these results in actual practice arises. In volume-dependent breakdown, using only the oil volume encompassing electric field values between the maximum and 90% of the maximum is suggested [Pal69, Wil53]. Thus, for concentric cylinder electrodes, for example, only the volume between the inner cylinder and a cylinder at a specific fraction of the radial distance to the outer cylinder will be used in the volume-dependent breakdown formulas. For more complicated geometries, numerical methods such as finite elements can be used to determine this effective volume.

For gap distance-dependent breakdown, it is commonly suggested to subdivide a possible breakdown path into subdivisions of equal length and to calculate the average electric field over each subdivision. The maximum of these average fields is then compared with the breakdown value corresponding to a gap length equal to the subdivision length. If it exceeds the

breakdown value, breakdown is assumed to occur along the entire path length. This procedure is repeated for coarser and coarser subdivisions until a single subdivision consisting of the entire path is reached. Other possible breakdown paths are then chosen, and the procedure repeated [Nel89, Franc, private communication].

Another type of breakdown that can occur in insulation structures consisting of solids and liquids or solids and gases is creep breakdown. This occurs along a solid surface that is in contact with a liquid or gas. These potential breakdown surfaces are nearly unavoidable in insulation design. For example, the oil gaps present in the region between windings are kept uniform by means of sticks placed around the circumference. The surfaces of these sticks bridge the gap, providing a possible surface breakdown path. Because breakdown along such surfaces generally occurs at a lower stress than breakdown in the oil or air through the gap itself, surface breakdown is often design limiting. Palmer and Sharpley [Pal69] parameterized the surface creep breakdown stress along pressboard surfaces in oil at power frequency, $E_{cb,AC}$ in terms of the creep area A_c (in mm²), according to

$$E_{cb,AC} \left(\frac{\text{kV}_{\text{rms}}}{\text{mm}} \right) = 16.0 - 1.09 \ln A_c \quad (13.15)$$

On the other hand, Moser [Mos79] described creep breakdown along pressboard surfaces in oil in terms of the creep distance along the surface d_c (in mm), according to

$$E_{cb,AC} \left(\frac{\text{kV}_{\text{rms}}}{\text{mm}} \right) = \frac{16.6}{d_c^{0.46}} \quad (13.16)$$

For nonuniform field situations, the same procedure of path subdivision and comparison with the creep breakdown strength, calculated using Equation 13.16, is followed as described earlier for gap breakdown.

13.3 Geometric Dependence of Transformer-Oil Breakdown

One of the difficulties apparent in the discussion so far is that different theories explain breakdown in transformer oil or other liquids with different mechanisms. These theories do not provide detailed numerical predictions, as is the case for breakdown in gases, where the mechanism of breakdown is better understood on a fundamental level [Ree73]. At best, they point to a parameter dependence of the breakdown process, such as dependence on the

gap length, electrode area, or stressed volume. Experimental data are then used to fit a formula with the desired parameter dependence. This raises a problem. Does one choose the parameter dependence to fit the different physical configurations encountered in practice? This appears to be *ad hoc*. The method of gap subdivision described above comes closest to providing a general procedure to apply to all situations. The problem with this approach is that it does not appear to have any rational physical basis.

Often the same breakdown data can be fit to a gap, area, volume, or other parameter dependence. For example, in a recent series of papers detailing the breakdown process in transformer oil [Top02, Les02, Top02a], the authors found a dependence of the breakdown or corona-inception field on the electrode area over a wide range of areas. However, their own data were also fit to a breakdown field dependence on the radius of curvature of the electrode in the point or rod-plane geometry used.

Although statistically area or volume effects seem to play some role in the breakdown process, they do not provide a breakdown mechanism that can account for all the data. Indeed, no concrete breakdown mechanism seems to be associated with the area effect. In practice, designers of high-voltage (HV) core-form transformers subdivide the vertical gaps between the windings with a series of thin pressboard cylinder barriers, suggesting their belief in a gap dependence of the breakdown voltage. (This technique will also be effective for a volume-dependent breakdown voltage but not for an area-dependent one.) Gap-dependent partial-discharge inception curves, such as those provided by [Mos79], are relied upon in this designing process. On the other hand, there are geometries within a transformer that are not covered by a simple gap-dependent breakdown curve, for example, the stress at the corner of a disk that is part of a disk or helical winding. This also applies to leads or cables at high voltage next to the grounded transformer tank.

In this section, we develop a phenomenological theory of breakdown in oil, which can be applied to all geometries. By this we mean that we assume an underlying theory of breakdown but that the parameters of the theory are obtained experimentally. The theory derives its key parameters from planar gap breakdown but can be used to predict breakdown in other geometries. We will mainly consider the extension to cylindrical and spherical geometries since these can be derived analytically. However, a discussion of the more general approach will also be given with examples.

We assume a Townsend-type breakdown mechanism for the oil but do not attempt to link the parameters of the theory to any fundamental electronic or molecular processes. The parameters of the theory will be chosen to fit the gap-dependent planar breakdown data and then these same parameters will be applied to the cylindrical and spherical geometries. Data for these geometries can then provide a test of the theory. We use the term breakdown in this paper loosely to refer to actual breakdown or to corona- or partial discharge-inception voltage.

13.3.1 Theory

This section closely follows our previous published paper [Del04].

We will focus on the electrons produced in the avalanche process and assume that they move with a velocity \mathbf{v} proportional to the electric field \mathbf{E} .

$$\mathbf{v} = \mu \mathbf{E} \quad (13.17)$$

where μ is the mobility, assumed constant. (Here, as elsewhere, when we use the term electrons, we mean any charged complex or entity.) Actually, the electrons move opposite to the electric field, so the mobility can be considered negative or, in later discussions, the applied voltage can be considered negative. We assume that all the electrons, even the newly released ones, achieve this equilibrium velocity instantaneously or in extremely short times. Letting n be the number of electrons per unit volume, the continuity or conservation equation for electrons can be written [Dai73]:

$$\frac{\partial n}{\partial t} + \nabla \cdot (n\mathbf{v}) = \gamma \quad (13.18)$$

where γ is the number of electrons produced per unit volume per unit time. Ignoring diffusion effects, which should be extremely slow when compared with the breakdown process, and assuming steady-state conditions, Equation 13.18 becomes

$$\mathbf{v} \cdot \nabla n + n \nabla \cdot \mathbf{v} = \gamma \quad (13.19)$$

We will assume that γ depends on the electric field and has the form

$$\gamma = \beta n v g(E) \quad (13.20)$$

where β is a constant with the units of inverse length and $g(E)$ is a unitless field-dependent quantity. Note that $\beta g(E)$ is the number of electrons produced or released by a single electron in an electric field E per unit distance traveled. This depends on the magnitude of the electron velocity via Equation 13.17. The term $n v$ is the flux of electrons, that is, the number of electrons per unit area per unit time. Hence, the product γ is the number of secondary electrons released per unit volume per unit time.

13.3.2 Planar Geometry

Applying Equation 13.19 to a planar geometry as shown in [Figure 13.3](#), where the electric field is uniform in the x direction, so that $\nabla \cdot \mathbf{v} = 0$ according to Equation 13.17 and all quantities only depend on x , we have

$$v \frac{dn}{dx} = \beta n v g(E) \quad (13.21)$$

Canceling out v and rearranging, we get

$$\frac{dn}{n} = \beta g(E) dx \quad (13.22)$$

Note that we are ignoring the space-charge effects since, in general, $\nabla \cdot E = \rho/\epsilon$, where ρ is the charge density and ϵ the permittivity. This amounts to assuming that the electric field produced by any charge accumulation is small compared with the applied field and thus does not significantly distort it. Although this is probably a good approximation for the incipient breakdown conditions we consider here, it would probably not apply if the details of the breakdown process itself were being modeled. Equation 13.22 can be integrated to get

$$\frac{n(d)}{n_0} = e^{\beta \int_0^d g(E) dx} \quad (13.23)$$

where n_0 is the number density of electrons at $x = 0$ and the integral is over the thickness of the gap, d . Since E is constant, this becomes

$$\frac{n(d)}{n_0} = e^{\beta g(E)d} \quad (13.24)$$

We expect breakdown to occur when $n(d)/n_0$ is greater than a specific large number. However, this is equivalent to stating that

$$\beta g(E)d > N \quad (13.25)$$

where $N \sim 10$ since e^{10} is a large number. The exact value is not significant since we will soon eliminate it from the equations. Since β is a constant, we can write more succinctly

$$g(E)d > \frac{N}{\beta} = \kappa \quad (13.26)$$

where κ is a characteristic constant having units of length. We can think of κ as the number of electrons that must be released per unit electron times the distance over which this release must occur in order to cause breakdown. Thus, an energetic electron, which releases many secondary electrons, need

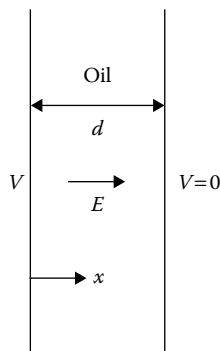


FIGURE 13.3

Planar geometry. (From Del Vecchio, R. M. 2004. *IEEE Trans Power Deliv* 19(2):652–6. With permission.)

only traverse a short distance to cause breakdown. On the other hand, a less energetic electron, which releases only a few secondary electrons, must traverse a longer distance to cause breakdown.

The planar-gap breakdown data for AC voltages and degassed oil with noninsulated electrodes are given in [Mos79]. It has been fit to the formula in Equation 13.12 and repeated here:

$$E_{\text{AC,planar}} \left(\frac{\text{kV}_{\text{rms}}}{\text{mm}} \right) = \frac{17.8}{d^{0.36}} \quad (13.27)$$

where the rms breakdown field is in kilovolts per millimeter and the gap distance d is in millimeters. Comparing Equations 13.26 and 13.27, we see that $g(E)$ must be of the form

$$g(E) = \left(\frac{E}{E_0} \right)^m \quad (13.28)$$

where E_0 is a constant chosen to make $g(E)$ unitless. Using Equation 13.28 in Equation 13.26, we get, for the breakdown field,

$$E = E_0 \left(\frac{\kappa}{d} \right)^{1/m} \quad (13.29)$$

We should take $1/m = 0.36$ or $m = 2.778$ in order to reproduce the exponential dependence in Equation 13.27. If we take the arbitrary constant $E_0 = 100$ kV/mm, we find that a value of $\kappa = 0.0083$ mm is needed to fit Equation 13.27.

For impulse waveforms, the impulse breakdown voltage for a given gap thickness has been shown by numerous experiments to be a constant multiple of the AC rms breakdown voltage, which on average is about 2.8. This is called the impulse ratio. Using this

$$E_{\text{Imp,planar}} \left(\frac{\text{kV}_{\text{peak}}}{\text{mm}} \right) = \frac{50}{d^{0.36}} \quad (13.30)$$

with d in millimeters. To fit this equation, m remains the same, but now $\kappa = 0.146$ mm. This implies that a greater electron avalanche is required to produce breakdown under short-duration impulse conditions, compared with the much longer AC breakdown conditions, for a given distance of electron travel. This has some intuitive appeal.

We expect that β —and hence κ —will depend on the quality or type of oil. In addition, m may depend on the same two factors. It is certainly well known that impurities in the oil affect the breakdown value.

13.3.3 Cylindrical Geometry

We now apply these same principles to a cylindrical geometry as shown in Figure 13.4. The electric field in the gap between the inner cylinder of radius a and outer cylinder of radius b is given by

$$\mathbf{E} = \frac{V}{r \ln\left(\frac{b}{a}\right)} \mathbf{a}_r \quad (13.31)$$

where \mathbf{a}_r is a unit radial vector, r is the radial coordinate, and V is the applied voltage.

Since \mathbf{v} is proportional to \mathbf{E} (by Equation 13.17), \mathbf{v} is also a radial r -dependent vector. In fact, because of the cylindrical symmetry, all quantities depend only on r . This greatly simplifies Equation 13.19 when expressed in cylindrical coordinates. Using Equations 13.17 and 13.31 and ignoring space-charge effects, we have $\nabla \cdot \mathbf{v} = 0$ in cylindrical coordinates. Expressing the remaining terms in Equation 13.19 in cylindrical coordinates, we have simply

$$\frac{dn}{dr} = \beta n g(E) \quad (13.32)$$

This is identical in form to Equation 13.22, except that $g(E)$ now depends on r . Thus, the breakdown condition becomes

$$\int_a^b \left(\frac{E(r)}{E_0} \right)^m dr > \frac{N}{\beta} = \kappa \quad (13.33)$$

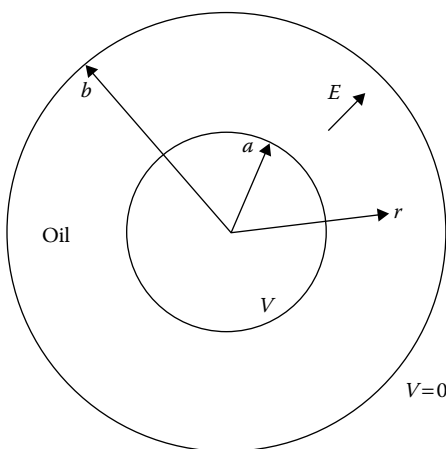


FIGURE 13.4

Cylindrical or spherical geometry. (From Del Vecchio, R. M. 2004. *IEEE Trans Power Deliv* 19(2):652–6. With permission.)

where m has been given numerically above. Getting $E(r)$ from Equation 13.31, we can perform the above integral to get the following expression as a breakdown condition:

$$\left(\frac{E_a}{E_0}\right)^m \left(\frac{a}{m-1}\right) \left[1 - \left(\frac{a}{b}\right)^{m-1}\right] = \kappa \quad (13.34)$$

where

$$E_a = \frac{V}{a \ln\left(\frac{b}{a}\right)} \quad (13.35)$$

is the electric field at the inner cylinder as well as the maximum field in the oil gap between the cylinders. Solving for E_a , we find

$$E_a = E_0 \left\{ \frac{(m-1)\kappa}{a \left[1 - \left(\frac{a}{b}\right)^{m-1}\right]} \right\}^{1/m} \quad (13.36)$$

For the same choice of E_0 , κ , and m used in the planar case, we get

$$E_{a,AC,cylindrical} \left(\frac{\text{kV}_{\text{rms}}}{\text{mm}} \right) = \frac{21.9}{\left\{ a \left[1 - \left(\frac{a}{b} \right)^{1.778} \right] \right\}^{0.36}} \quad (13.37)$$

and for impulse conditions, assuming an impulse ratio of 2.8, we get

$$E_{a,imp,cylindrical} \left(\frac{\text{kV}_{\text{peak}}}{\text{mm}} \right) = \frac{61.3}{\left\{ a \left[1 - \left(\frac{a}{b} \right)^{1.778} \right] \right\}^{0.36}} \quad (13.38)$$

where a and b are in millimeters.

13.3.4 Spherical Geometry

The spherical geometry is also depicted in [Figure 13.4](#), where a and b are now the radii of the inner and outer spheres, respectively. The electric field in the spherical gap is given by

$$\mathbf{E} = \frac{V}{r^2 \frac{1}{a} \left(1 - \frac{a}{b}\right)} \mathbf{a}_r \quad (13.39)$$

where the symbols have their usual meanings. Because of the spherical symmetry, all quantities depend only on r . Also, in view of Equations 13.17 and 13.39 and ignoring space-charge effects, $\nabla \cdot \mathbf{v} = 0$ in spherical coordinates, so that Equation 13.19 becomes, in these coordinates,

$$\frac{dn}{dr} = \beta n g(E) \quad (13.40)$$

Again, Equation 13.40 is of the same form as Equation 13.22, except that E is a function of r . Thus, the breakdown condition becomes identical to Equation 13.33, except that the $E(r)$ dependence is different. Substituting from Equation 13.39 and performing the integral, we get

$$\left(\frac{E_a}{E_0}\right)^m \left(\frac{a}{2m-1}\right) \left[1 - \left(\frac{a}{b}\right)^{2m-1}\right] = \kappa \quad (13.41)$$

where

$$E_a = \frac{V}{a \left(1 - \frac{a}{b}\right)} \quad (13.42)$$

is the field E at the inner sphere and the maximum field in the oil gap. Solving for E_a , we get

$$E_a = E_0 \left\{ \frac{(2m-1)\kappa}{a \left[1 - \left(\frac{a}{b}\right)^{2m-1}\right]} \right\}^{1/m} \quad (13.43)$$

Choosing E_0 , κ , and m from the planar fit, we have

$$E_{a,AC,spherical} \left(\frac{\text{kV}_{\text{rms}}}{\text{mm}} \right) = \frac{30.8}{\left\{ a \left[1 - \left(\frac{a}{b} \right)^{4.556} \right] \right\}^{0.36}} \quad (13.44)$$

For impulse waveforms, we have

$$E_{a,\text{imp,spherical}} \left(\frac{\text{kV}}{\text{mm}} \right) = \frac{86.2}{\left\{ a \left[1 - \left(\frac{a}{b} \right)^{4.556} \right] \right\}^{0.36}} \quad (13.45)$$

with a and b in millimeters.

13.3.5 Comparison with Experiment

Note that for an isolated cylinder or sphere, where $b \gg a$, from Equations 13.36 and 13.43, we have

$$E_{a,\text{cylinder}} = E_0 \left[\frac{(m-1)\kappa}{a} \right]^{1/m} \quad (13.46)$$

$$E_{a,\text{sphere}} = E_0 \left[\frac{(2m-1)\kappa}{a} \right]^{1/m} \quad (13.47)$$

with the ratio

$$\frac{E_{a,\text{sphere}}}{E_{a,\text{cylinder}}} = \left(\frac{2m-1}{m-1} \right)^{1/m} \quad (13.48)$$

This ratio should be constant and independent of (a) the radius of the cylinder or sphere and (b) the waveform, provided they are the same for the two cases. For $m = 2.778$, this ratio is 1.4.

Wilson [Wil53], citing data for oil obtained by Peek in 1915 [Pee29], shows this ratio to be nearly constant for different radii. However, the ratio found is 1.6. This can then reflect a different type of oil used, since m can depend on the type or quality of oil. Alternatively, it can reflect the fact that the necessarily finite-length cylinders used in the experiments were not a sufficiently close approximation to the ideal infinite-length ones analyzed here.

In the case of an isolated sphere ($b \gg a$), under impulse conditions, from Equation 13.45, we have

$$E_{a,\text{imp,sphere}} \left(\frac{\text{kV}}{\text{mm}} \right) = \frac{86.2}{a^{0.36}} \quad (13.49)$$

Breakdown data for impulse conditions obtained by Lesaint and Top [Les02] for point and rod electrodes reasonably far from the ground plane were fit to the expressions:

$$\begin{aligned} E_{\text{positive polarity}} \left(\frac{\text{kV}}{\text{mm}} \right) &= \frac{93}{a^{0.35}} \\ E_{\text{negative polarity}} \left(\frac{\text{kV}}{\text{mm}} \right) &= \frac{78}{a^{0.35}} \end{aligned} \quad (13.50)$$

where a is the radius of curvature of the tip in millimeters. Although the geometry is not quite that of an isolated sphere, it is reasonably close, so that the favorable comparison with Equation 13.49 is meaningful.

13.3.6 Generalization

The breakdown formulas for the cylindrical and spherical geometries reduce to the planar case when a and b become large. This is expected since, locally, the cylindrical and spherical gaps start looking increasingly like planar gaps. However, for small a , the breakdown formulas depart significantly from the planar case. In fact, for b being large compared with a , as Equation 13.49 indicates, the formulas depend only on the radius of curvature of the inner electrode. The gap or distance between a and b plays no role. As a decreases, the breakdown strength increases. Apart from the confirmation of this effect provided by Lesaint and Top [Les02], transformer designers know that the breakdown stress at the corners of the individual disks in a disk winding, where small radii of curvature are present, can be much higher than the allowable breakdown stress in the gaps between windings.

Although expressions for breakdown have been found for idealized geometries, in principle, Equation 13.19 can be solved for any geometry. This requires first solving for the electric field. Then, v and $g(E)$ become known, so that n can be found throughout the volume where E exists. By examining the boundary values of n , we can verify if it has been multiplied sufficiently from its starting electrode value to cause breakdown. The term, n , would need to be set at some specific value, say one, on the starting electrode.

Although the above procedure requires a considerable calculational effort, it may be possible to justify a simpler procedure for a general geometry. For example, having solved for the electric field, we might perform the integral

$$\int \left(\frac{E(s)}{E_0} \right)^m ds \quad (13.51)$$

along the possible breakdown paths and then compare it with κ , where $E_0 = 100$ kV/mm, $\kappa = 0.0083$ mm, and $m = 2.778$ are reasonable choices for standard transformer oil and AC voltages. Assuming an impulse ratio of 2.8,

we need to use $\kappa = 0.146$ mm for impulse conditions. When performing the above integral, we should always stay tangential to the electric field or perpendicular to the equipotential surfaces because we assume the electrons move in this manner. More specifically, the breakdown condition would become

$$\int_P \left(\frac{E(s)}{E_0} \right)^m ds \geq \kappa \quad (13.52)$$

where the integral is taken along a most likely breakdown path, P . This would then generalize Equation 13.33, which was used for cylindrical and spherical geometries, although in these two cases, the most likely breakdown path is clear. Note that the integral in Equation 13.52 is in millimeters, that is, the same unit as κ . Moreover, if insulation is present and $E(s)$ is calculated without including the enhancement effect of this insulation, then an enhancement factor should multiply $E(s)$ in Equation 13.52. If this can be considered constant along the path, then it can be factored out of the integral as an overall multiplier. Thus, if the constant enhancement factor is η , then η^m should multiply the integral.

Normally, we would calculate the electric fields for use in Equation 13.52 by assuming they are produced by a specified voltage V to ground. However, this may not correspond to the breakdown voltage. Often, we want to determine this breakdown voltage. When E is proportional to V , as is the case for the geometries considered above and is generally the case, Equation 13.52 can be written using an unknown factor X that multiplies the field E . This factor would also multiply the voltage V , so that XV is sufficient to produce breakdown. If there are multiple voltages involved, then X could be considered to multiply the maximum electric field along the breakdown path, so that XE is sufficient to produce breakdown. Using this factor, Equation 13.52 would become an equality, as shown below.

$$\int_P \left(\frac{XE(s)}{E_0} \right)^m ds = X^m \int_P \left(\frac{E(s)}{E_0} \right)^m ds = \kappa \quad (13.53)$$

Letting the integral in Equation 13.52 equal Intg , which is assumed known and includes any enhancement effects but without the factor X , we can solve Equation 13.53 for X .

$$X = \left(\frac{\kappa}{\text{Intg}} \right)^{1/m} \quad (13.54)$$

When this multiplies the voltage V used to calculate the integral in Equation 13.52 or multiplies the maximum electric field along the path in that integral, it will equal the breakdown voltage or breakdown electric field. When the

enhancement factor is constant, the net effect is to divide X , calculated without the enhancement factor, by the enhancement factor. This will decrease X and thus lower the breakdown voltage or field, as expected.

13.3.6.1 Breakdown for the Cylinder–Plane Geometry

The breakdown path is clear for the cylinder–plane geometry too. Here, the most likely breakdown path is from the point on the cylinder nearest the ground plane along the shortest straight line to the ground plane. The electric field along this line is given by Equation 11.41 in Chapter 11. As a numerical example, let the radius of the cylinder be 10 mm, with a 5-mm-thick paper covering. The distance from the center of the cylinder to the ground plane is allowed to vary. The breakdown path is therefore along a straight line from the ground plane to the paper cover. In this case, we use an enhancement factor for the cylinder geometry given in Equation 11.19. The enhancement factor varies with the distance to the ground plane but is about 1.05. We assume the gap to be filled with oil, and that the only solid insulation is the paper cover. The breakdown voltage level is calculated (in kV) and plotted versus the distance from the cylinder center to the ground plane, as shown in [Figure 13.5](#).

13.3.6.2 Breakdown for the Disk–Disk-to-Ground Plane Geometry

In Section 11.2.4.1, we calculated the electric field near the corner of the disk–disk-to-ground plane geometry using conformal mapping. We calculated the field at a paper distance away from the corner and included an enhancement factor to account for the paper (and other) insulation. We can use this solution method here to calculate the field along a possible breakdown path starting at the outer surface of the corner paper.

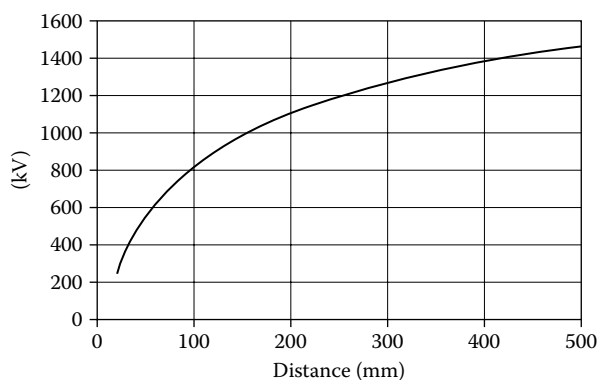
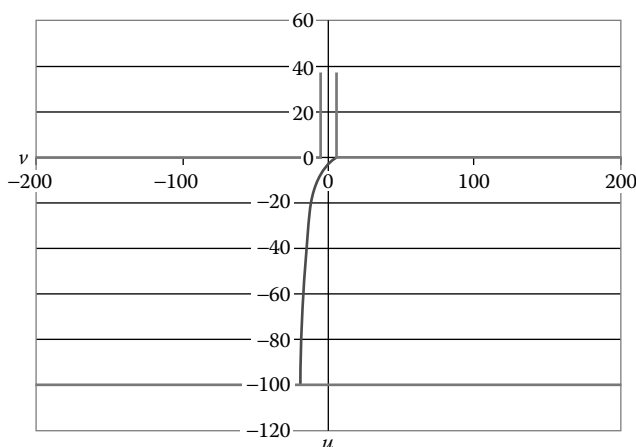


FIGURE 13.5 Breakdown voltage versus the distance from the cylinder center to the ground plane for a cylinder of radius = 10 mm and with a paper cover of 5 mm thickness.

**FIGURE 13.6**

(See color insert following page 338.) Breakdown path from outer paper cover of the disk-disk-to-ground plane geometry to the ground plane. Disk-disk gap = 10 mm, disk-ground plane = 100 mm, thickness of two-sided paper = 1 mm. Disk voltages are 100 and 80 kV.

In this method, the initial electric field vector defines a direction away from the paper surface. We set a sufficiently small step size and find the next point a step size away from the surface in the direction of the initial electric field. At this new point, we calculate a new electric field and use its direction to find the next point a step size away from the second field. Using the direction determined by the second electric field, we get a third point another step size away from the second point and calculate the third electric field here. This process is continued until we encounter a surface such as the ground plane or the paper surface of the second disk. An example of such a path is shown in Figure 13.6. In this example, the disk-disk separation is 10 mm, and the two-sided paper cover is 1 mm thick, so that the gap from disk metal to disk metal is 11 mm. The gap from the disk metal to the ground plane is 100.5 mm, including the one-sided paper cover. The two disks are at 100 and 80 kV. The path starts on the outer corner paper of the right disk at 100 kV and ends on the ground plane. The maximum corner electric field is selected as the starting point from the three positions shown in Chapter 11.

The integral in Equation 13.51 is performed along this path and the factor X is extracted using Equation 13.54 for the impulse value of $\kappa = 0.146$. Using the enhancement factor described in Chapter 11, which was 1.09 for this case, the calculated breakdown field is 30 kV/mm. The maximum field occurs at the outer paper surface at the disk corner.

As another example, the disk-disk gap is set to 21 mm, including a 1 mm two-sided paper cover, and the disk-to-ground plane distance is set to 150.5 mm, including a one-sided paper cover. The disk voltages are 100 and 50 kV. In this case, the breakdown path is from one disk to the other,

as shown in Figure 13.7. Here, the enhancement factor is 1.08, and the breakdown field is 34.0 kV/mm for impulse conditions.

Another example is to have a gap spacing of 4.5 mm, including a 0.5-mm two-sided paper cover, and a distance of 50.25 mm to the ground plane, which includes a 0.25-mm one-sided paper cover. The disk voltages are 100 and 80 kV. The breakdown path is shown in Figure 13.8. In this case, the

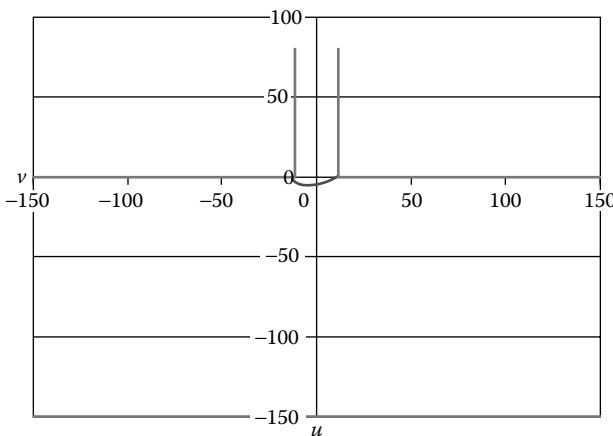


FIGURE 13.7
(See color insert following page 338.) Breakdown path from corner outer paper cover of one disk to the other disk. Disk-disk gap = 20 mm, disk-ground plane = 150 mm, thickness of two-sided paper = 1 mm. Disk voltages are 100 and 50 kV.

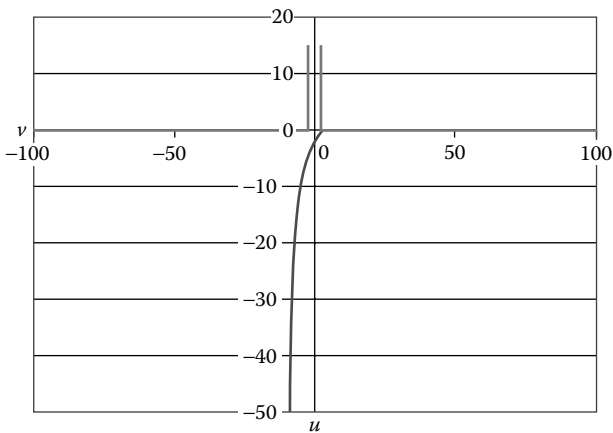
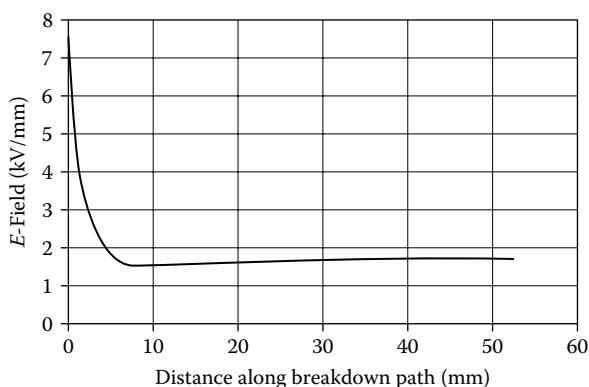


FIGURE 13.8
(See color insert following page 338.) Breakdown path from corner outer paper cover to the ground plane. Disk-disk gap = 4 mm, disk-ground plane = 50 mm, thickness of two-sided paper = 0.5 mm. Disk voltages are 100 and 80 kV.

**FIGURE 13.9**

Electric field along the breakdown path for the case shown in [Figure 13.8](#).

enhancement factor is 1.07, and the breakdown electric field is 40.0 kV/mm for impulse conditions.

The electric field along the breakdown path for this last case is plotted in [Figure 13.9](#). This field does not include the enhancement factor or the multiplier required to reach the breakdown level. This is the electric field tangential to the path, which is also the electric field magnitude because it is directed along the path.

The calculated breakdown fields for the larger disk–ground plane gaps are probably unrealistically low, because the two disks are assumed to extend indefinitely in the horizontal directions, thus maintaining their voltage levels. This means that higher fields are present over longer lengths of the breakdown paths than would normally occur in practice. This is not a concern when the breakdown path is between the two disks since, although the gap between the disks extends indefinitely in the vertical direction, the breakdown path length is relatively short and is confined to the region near the disk corner where the field calculation is more realistic. In practice, a limit is often placed on the corner electric field, which is in the range of 30–35 kV/mm. This is consistent with the above results.

When pressboard or other barriers are present, the breakdown path should only be taken up to the barrier because the breakdown avalanche would stop at this point. This is consistent with the practice of subdividing gaps to increase the breakdown electric-field levels.

13.3.7 Discussion

We have shown how, assuming a simple Townsend breakdown mechanism, it is possible to start from the planar geometry breakdown data in order to arrive at a prediction of the breakdown data in other geometries, which agrees well with the experimental data in these geometries. Although we

referred to electrons participating in the breakdown mechanism, this could clearly refer to any charged complex or entity and almost certainly not to bare electrons. Furthermore, although we referred to breakdown, this could also be interpreted as corona or partial discharge inception voltage.

This entire exercise highlights the unity of the breakdown process, regardless of the geometry in which it occurs. It is clearly unphysical to invoke area or volume effects to explain breakdown in curved geometries but not in planar geometries. Most of the data support a gap effect for planar geometries, which is characteristic of a Townsend-type mechanism. In addition, the common and effective practice of inserting pressboard barriers in large oil gaps to increase the breakdown voltage is a tacit acknowledgement of a gap effect.

This work has emphasized the need for more oil breakdown data in cylindrical and spherical geometries that are as close to ideal as possible, where mathematical methods may be applied without much approximation. The startling conclusion given in Equation 13.48 that the breakdown voltage ratio for spherical and cylindrical electrodes of the same radius subject to the same voltage waveform is a constant, independent of the radius of the electrode—provided they are sufficiently isolated—should be rechecked experimentally. Although ideal spherical geometries can be reasonably approximated, an ideal cylinder (infinitely long) is not easily accessible. Perhaps an equation similar to Equation 13.48 can be derived for finitely long cylinders, provided breakdown occurs near the center. This should approach the infinite case as the ratio of cylinder length to radius increases and would at least provide a guide as to when the cylinder is long enough.

There are essentially three parameters in the methodology discussed here, namely, m , β , and κ . (E_0 is really arbitrary.) The parameter m appears to be relatively insensitive to experimental breakdown conditions, whereas β and κ certainly depend on the breakdown waveform—whether one is considering full or partial breakdown—and on oil quality. Whether these parameters can be obtained in a more fundamental way from the properties of oil remains to be seen. At present, based on experimental data, one may expect to parameterize m , β , and, especially, κ in terms of waveform duration, the type of breakdown, and oil-impurity levels.

13.4 Insulation Coordination

Insulation coordination concerns matching the insulation design to the protective devices that are used to limit the voltages applied to the terminals of a transformer by lightning strikes or switching surges and possibly other potentially hazardous events. Since the insulation must withstand the normal operating voltages that are present continuously, as well as lightning or switching events that are of short duration, how the breakdown depends on

the time duration of the applied voltage is of major importance in insulation coordination. We have seen previously that the impulse ratio is $\sim 2\text{--}3$ for oil-filled transformer insulation. This means that the breakdown strength of a short-duration impulse voltage lasting $\sim 5\text{--}50\ \mu\text{s}$ is much higher than the breakdown strength of a long-duration (~ 1 minute) AC voltage. It appears that breakdown voltages or stresses generally decrease with the time duration of the voltage application for transformer insulation. The exact form of this breakdown versus time dependence is still somewhat uncertain, probably because of variations in factors, such as material purity and/or experimental methods, among different investigators.

Blume et al. [Blu51] and Clark [Cla62] showed a time-dependent behavior of the relative strength of oil or pressboard, which is schematically illustrated in Figure 13.10. Three regions are evident on the curve, labeled A, B, and C. For short durations, lasting $< 10\ \mu\text{s}$, there is a rapid falloff in the strength with increasing time. This is followed by a flat portion, B, which extends to about $1000\ \mu\text{s}$ for oil and to about $20,000\ \mu\text{s}$ for pressboard. In region A, there is a more gradual falloff, approaching an asymptotic value for long time intervals. The combination of an oil pressboard gap also produces a curve similar to that in Figure 13.10.

Using statistical arguments, that is, equating the probability of breakdown for time durations less than t for a fixed voltage across an oil gap under corona-free conditions, which equals $1 - \exp(-t/t_0)$, where t_0 is the average time taken for breakdown, to Equation 13.1 with V_0 taken to be zero, Kaufman and Meador [Kau68] obtained the relationship for breakdown voltage versus time for an oil gap in the form:

$$\frac{t_2}{t_1} = \left(\frac{V_1}{V_2} \right)^k \quad (13.55)$$

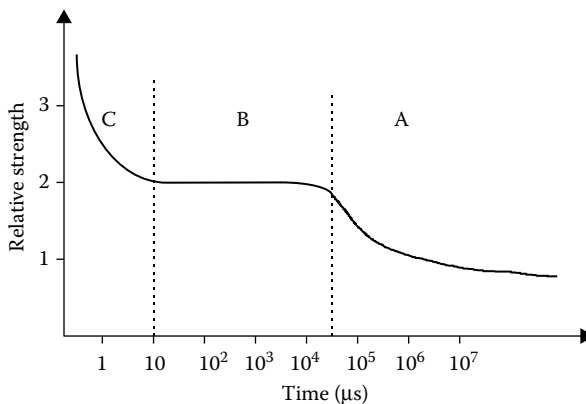


FIGURE 13.10

Schematic representation of oil or pressboard breakdown: relative strength versus time.

Experimentally, they found that for times from a few seconds to a few weeks, k ranges between 15 and 30. However, this relationship cannot hold for very long times since it predicts breakdown at zero voltage at infinite time. To correct this, one could use the same statistical argument to show that

$$\frac{t_2}{t_1} = \left(\frac{V_1 - V_0}{V_2 - V_0} \right)^k \quad (13.56)$$

where V_0 is the infinite time-breakdown voltage. This can be rearranged to the form

$$V_2 = V_0 + \frac{(V_1 - V_0)t_1^{1/k}}{t_2^{1/k}} \quad (13.57)$$

Picking a V_1 - t_1 pair, this can be written for a general V - t pair as

$$V = V_0 \left(1 + \frac{K}{t^{1/k}} \right) \quad (13.58)$$

Dividing by the gap thickness, this can be written in terms of the breakdown stress E_b as

$$E_b = E_{b,0} \left(1 + \frac{K}{t^{1/k}} \right) \quad (13.59)$$

where $E_{b,0}$ is the infinite time breakdown stress. This last equation is very similar to Equation 13.6 in its time dependence. As shown in [Figure 13.10](#), the time-dependent behavior of transformer oil breakdown is more complicated over a time span ranging from μ s to years than Equations 13.55 or 13.58 would suggest. Presumably, these expressions would apply to AC breakdown stress covering region A in the curve shown in [Figure 13.10](#).

At short times (in the μ s region), the breakdown voltage or stress versus time characteristic changes rapidly with time. Impulse wave shapes, as shown in [Figure 13.2](#), are somewhat complicated functions of time. To extract a single voltage-time duration pair from this wave shape for comparison with the breakdown curve, the common practice is to take the peak voltage and the time during which the voltage exceeds 90% of its peak value. Thus, a standard impulse wave, which increases to its peak value in 1.2 μ s and decays to 50% of its peak value in 50 μ s, spends about 10 μ s above its 90% voltage level. A switching surge test wave shape is similar to that of [Figure 13.2](#), but the rise time to peak value is ~ 100 μ s and the fall time to the 50% level is ~ 500 μ s. The time spent above 90% of peak voltage level is ~ 200 μ s. Therefore, we would expect breakdown to occur on a switching-surge test at a lower voltage than for a full wave-impulse test.

Two other types of impulse tests are the chopped-wave test and front-of-wave test, although the latter is considered unnecessary in view of modern methods of protection. A standard chopped wave, as shown in Figure 13.11, rises to its peak in $\sim 1.2 \mu\text{s}$ and abruptly falls to zero, with a slight undershoot, at the chop time of $\sim 3 \mu\text{s}$. It is above its 90% of peak voltage level for $\sim 3 \mu\text{s}$. The front-of-wave is chopped on the rising part of the wave and has a duration of $\sim 0.5 \mu\text{s}$ at levels above 90% of its maximum value. The generally accepted breakdown levels corresponding to these different times, normalized to the full wave-breakdown level, are given in Table 13.1.

We have included two other points in Table 13.1—the 1-minute AC test point and the essentially infinite time–nominal voltage point. For the 1-minute test point, we have used an impulse ratio of 2.8. Thus, the normalized breakdown peak voltage level is $1/2.8 \times \sqrt{2} = 0.5$, and the duration above 90% of the peak voltage is $0.287 \times 60 \text{ seconds} = 17.2 \text{ seconds}$. We have taken the nominal system voltage to be half the 1-minute test voltage. We could have chosen other values for these with equal justification. For instance, an impulse ratio of 2.4 is commonly assumed in setting test values and the nominal voltage can be

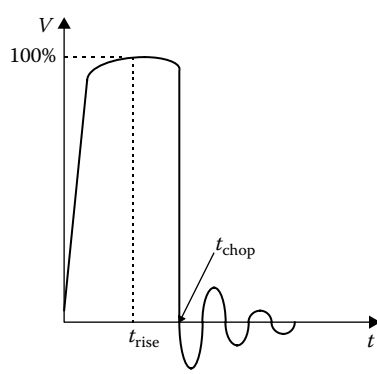


FIGURE 13.11
Chopped-wave impulse wave shape.

TABLE 13.1
Breakdown Voltages Normalized to the Full Wave–Impulse Level

Type	Duration (μs)	Breakdown Level
Front-of-wave	0.5	1.3
Chopped wave	3	1.1
Full wave	10	1.0
Switching surge	200	0.83
1-minute AC	17.2×106	0.5 peak
Nominal AC	∞	0.25 peak

a factor of 2.5–3.0 below the 1-minute test level. Note that the nominal system voltage used here is from terminal to ground.

We can produce a reasonable fit to the above tabular values with an equation of the form in Equation 13.58. Letting $V_{b,rel}$ be the breakdown levels relative to the full-wave level, we obtain

$$V_{b,rel} = 0.25 \left(1 + \frac{3.8}{t^{1/12}} \right) \quad (13.60)$$

with t in microseconds. Table 13.1 is based on results from practical experience in testing transformers. The numbers can only be regarded as approximate, and different choices are often made within a reasonable range about the values shown. This would influence the fit given in Equation 13.60 or possibly require a different parameterization. This parameterization may have no fundamental significance since it does not apply to any carefully controlled experiment. However, its form, which agrees with the more fundamental Equation 13.58, is noteworthy.

In practical applications, a table similar to Table 13.1 provides a way of linking the various test voltages to the full wave–impulse–voltage, which is also called the basic impulse level (BIL). Since the required impulse test levels are usually linked to the lightning or surge-arrestor protection level, whereas the AC test levels or nominal voltage level are not, they can be specified independently. For example, a 500-kV_{rms} line-to-line transformer (= 288 kV_{rms} line to ground = 408.2 kV_{peak} line to ground) would correspond to a full-wave impulse level of 1633 kV, according to Table 13.1. However, the user may have enough protection that only a 1300-kV impulse test is required. Nevertheless, the insulation would have to be designed to withstand a full-wave 1633-kV impulse test, even though not performed, since that level of protection is required to guarantee satisfactory operation at the nominal 500-kV_{rms} line-to-line voltage. As another example, we could have breakdown stress versus distance, area, or volume curves for 1-minute AC test conditions. To compare these to the stress levels generated in a simulated impulse-test calculation, one needs to know the relative breakdown level factors given in Table 13.1.

13.5 Continuum Model of Winding Used to Obtain the Impulse–Voltage Distribution

For very short times after the application of a voltage to a winding terminal, the voltage distribution along the winding is governed primarily by capacitive coupling because the winding inductance limits the flow of current initially.

13.5.1 Uniform Capacitance Model

In this approximation, a winding can be modeled by the capacitive ladder diagram shown in Figure 13.12a. Although discrete capacitances are shown, this is meant to be a continuum model. The winding is assumed uniform along its length. The calculation outlined here is similar to that given in Chapter 12. The calculation is somewhat more simple since the voltages on the neighboring windings, core, or tank are assumed to be at zero potential. Some of the steps are repeated here. Thus, as shown in Figure 13.12b, the series capacitors c_s are separated by a distance Δx , where Δx will eventually approach zero. The series capacitors are determined by the winding structure, including the number of disks, their spacing, and the number of turns per disk. The ground capacitors c_g are determined by the distance to the neighboring windings, the tank walls, or the core. These are all assumed to be at ground potential relative to the impulsed winding, which should be the case initially.

Analyzing a small portion of the winding at a distance x from the impulsed terminal (at the bottom of the figure), we can write Kirchhoff's current law at the center node shown in Figure 13.12b as

$$I(x - \Delta x) - I(x + \Delta x) = I_g(x) \quad (13.61)$$

However, using the voltage–current relationship for capacitors, we can express this as

$$c_s \frac{d}{dt} [V(x - \Delta x) - V(x)] - c_s \frac{d}{dt} [V(x) - V(x + \Delta x)] = c_g \frac{dV(x)}{dt} \quad (13.62)$$

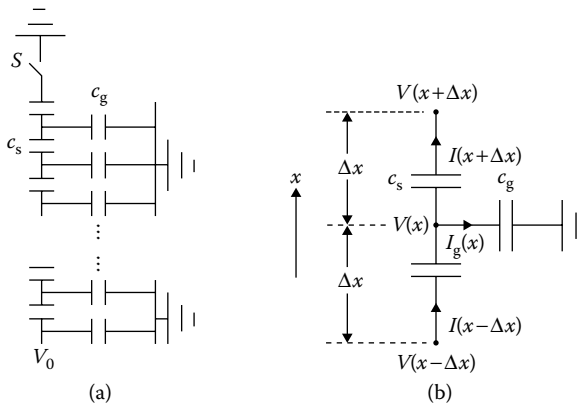


FIGURE 13.12

Initial voltage distribution winding model: (a) capacitive model of winding and (b) small section of winding used for analytical purposes.

Rearranging, we get

$$c_s \frac{d}{dt} \{ [V(x + \Delta x) - 2V(x) + V(x - \Delta x)] - c_g V(x) \} = 0 \quad (13.63)$$

The time derivative of the expression in curly brackets is zero, so this expression is a constant in time. The constant may be taken to be zero because the winding starts out at zero potential. Dividing by $(\Delta x)^2$, Equation 13.63 can be written as

$$\frac{V(x + \Delta x) - 2V(x) + V(x - \Delta x)}{(\Delta x)^2} = \frac{c_g}{c_s (\Delta x)^2} V(x) \quad (13.64)$$

The term on the left-hand side can be recognized as the second-order difference operator, which approaches the second derivative as $\Delta x \rightarrow 0$. If L is the length of the winding, there are $N = L/\Delta x$ series capacitors c_s and ground capacitors c_g . In terms of the total series and ground capacitances C_s and C_g , we have

$$C_s = \frac{c_s}{N} = \frac{c_s \Delta x}{L}, \quad C_g = N c_g = \frac{L c_g}{\Delta x} \quad (13.65)$$

Substituting into Equation 13.64 and letting $\Delta x \rightarrow 0$, we obtain

$$\frac{d^2 V}{dx^2} = \frac{C_g}{C_s L^2} V = \left(\frac{\alpha}{L} \right)^2 V \quad (13.66)$$

where the distribution constant α is defined as

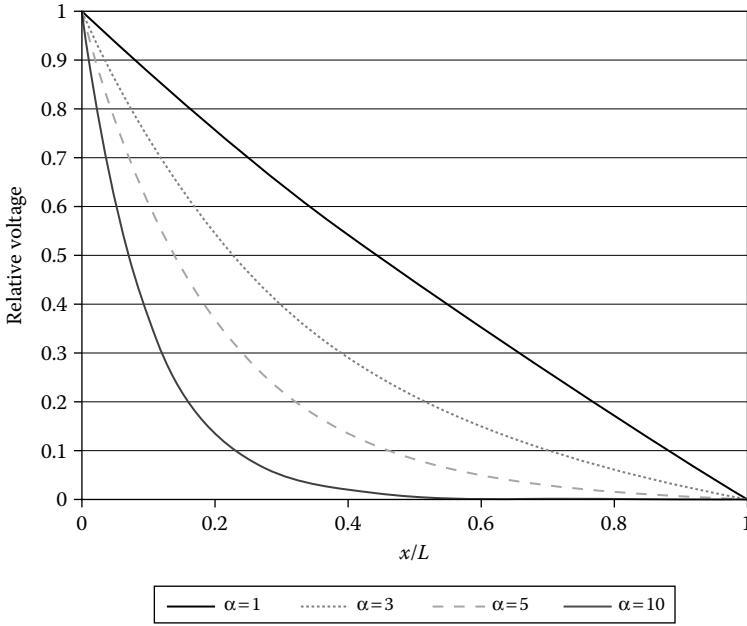
$$\alpha = \sqrt{\frac{C_g}{C_s}} \quad (13.67)$$

If the other end of the winding is grounded (with switch S closed in [Figure 13.12a](#)) and a voltage V_0 is applied at the line end, the solution to Equation 13.66 is

$$V(x) = V_0 \frac{\sinh \left[\alpha \left(1 - \frac{x}{L} \right) \right]}{\sinh \alpha} \quad (13.68)$$

When the switch S is open so that the nonimpulsed end of the winding is floating when the voltage V_0 is applied to the line end, the solution to Equation 13.66 is

$$V(x) = V_0 \frac{\cosh \left[\alpha \left(1 - \frac{x}{L} \right) \right]}{\cosh \alpha} \quad (13.69)$$

**FIGURE 13.13**

Initial voltage distribution along a winding grounded at one end for various values of α .

Equation 13.68 is plotted in Figure 13.13 for several values of α . We can see that as α increases, the slope of the curve becomes very steep at the line end. This implies that the disk-disk voltage, ΔV_d , increases with increasing α since this is given approximately as

$$\Delta V_d = \left| \frac{dV}{dx} \right| w = V_0 \alpha \left(\frac{w}{L} \right) \frac{\cosh \left[\alpha \left(1 - \frac{x}{L} \right) \right]}{\sinh \alpha} \quad (13.70)$$

where w is the disk-disk spacing, assumed small when compared with L . This has its maximum value at the line end, where $x = 0$.

$$\Delta V_{d,\text{line}} = V_0 \left(\frac{w}{L} \right) \frac{\alpha}{\tanh \alpha} \quad (13.71)$$

For the ungrounded or floating end winding, Equation 13.69 is plotted in Figure 13.14. The maximum stress again occurs at the line end and, using Equation 13.69, is given by

$$\Delta V_{d,\text{line}} = V_0 \left(\frac{w}{L} \right) \alpha \tanh \alpha \quad (13.72)$$

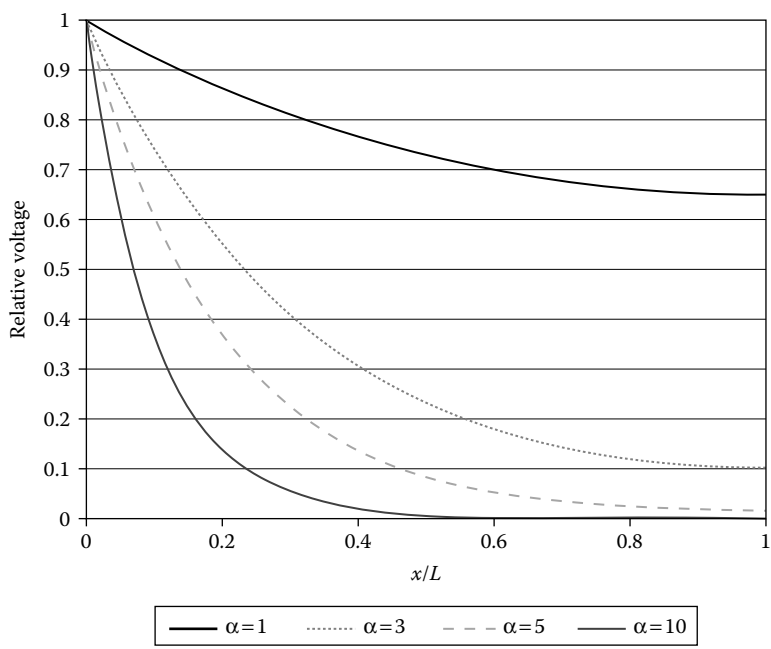


FIGURE 13.14 Initial voltage distribution along a winding that floats at one end for various values of α .

which is somewhat less than Equation 13.71, since $|\tanh\alpha| \leq 1$. When α is large, say > 3 , $\tanh\alpha \approx 1$, so Equations 13.71 and 13.72 are essentially equal. If α is small, say < 0.1 , $\Delta V_{d, \text{line}} = V_0(w/L)$ for the grounded end case, with $\Delta V_{d, \text{line}} \approx 0$ for the floating end case.

Since the disk–disk stress increases with α and, by implication, the turn–turn stress also increases, Equation 13.67 suggests that we need to increase C_s , decrease C_g , or both to reduce this stress. This has led to winding schemes such as interleaving, which can dramatically increase the series capacitance. Interleaving schemes can be quite complicated and need not be applied to the whole winding. In addition, the scheme may vary within a given winding. A multistart winding is an example of a simple interleaving scheme for increasing the series capacitance of a tap winding. Another method of increasing the series capacitance is by means of wound-in shields, which can be applied to a section of the winding near the line end where they are most needed. Decreasing C_g is not as promising since this would involve, in a simple approach, increasing the winding-to-winding or winding-to-tank distance for an outer winding or decreasing the winding height for a given radius. Such changes could interfere with impedance or cooling requirements.

13.5.2 Traveling Wave Theory

An improvement over the static capacitance model is the traveling wave theory developed by Rudenberg [Rud68, Rud40], which includes the approximate winding inductance. This is also a continuum uniform winding model, with the circuit parameters defined on a per-unit-length basis. A new variable, the inductance per unit length, is introduced to take inductive effects into account. This can only be regarded as approximate since it ignores the mutual inductance between the different sections of the winding. However, this approximation can be justified to some extent mathematically and by comparison with experiment.

Without going into all the details, which can be obtained from the references [Rud68] and [Rud40], the disk–disk voltages along the winding are given by

$$\Delta V_d = V_0 \alpha \left(\frac{w}{L} \right) \left(\frac{1}{2} e^{-\alpha \frac{x}{L}} + \frac{1}{\pi} \right) \quad (13.73)$$

with x , the distance along the winding, measured from the line end. This has its maximum at the line end, where $x = 0$, and is given by

$$\Delta V_{d, \text{line}} = 0.818 V_0 \alpha \left(\frac{w}{L} \right) \quad (13.74)$$

For $\alpha > 3$, which is relatively typical, $\tanh \alpha \approx 1$, so that, comparing Equation 13.74 with its counterparts in the purely capacitive cases, this disk–disk voltage drop is about 18% lower.

Norris [Nor48] proposed an improved version of Equation 13.73, which has the form

$$\Delta V_d = V_0 \alpha \left(\frac{w}{L} \right) \left(0.6 e^{-\alpha \frac{x}{L}} + 0.4 K_g \right) \quad (13.75)$$

where $K_g \leq 1$ can be found as a solution of the equation [Rud68, Rud40]:

$$\frac{\alpha}{\pi L} x = \begin{cases} \frac{1}{K_g^2} (1 + \sqrt{1 - K_g^2}), & x > \frac{\pi L}{\alpha} \\ 1, & x \leq \frac{\pi L}{\alpha} \end{cases} \quad (13.76)$$

This reduces to a quartic equation, which can be solved analytically for K_g as a function of x . At $x = 0$ and for $\alpha > 3$, Equation 13.75 is equal to the disk–disk voltage drop in the capacitive case, as can be seen by comparison with Equation 13.71. Norris also suggested corrections for incoming waves having finite rise and fall times and gives procedures for handling nonuniform windings.

13.6 Lumped-Parameter Model for Transient Voltage Distribution

In this section, we will develop a circuit model of the transformer, which includes capacitive, inductive, and resistive elements. The inductive elements include mutual inductances between elements in both the same and different windings and the effects of the iron core. The coils can be subdivided into as fine or coarse a manner as is consistent with the desired accuracy. Moreover, the subdivisions can be unequal so that accuracy in certain parts of the coil can be increased relative to that in other parts. The approach taken is similar to that of Miki et al. [Mik78], except that it includes the winding resistance and the effects of the iron core. In addition, the differential equations describing the circuit are organized in such a way that circuit symmetries can be exploited and other circuit elements such as nonlinear varistors may be included.

13.6.1 Circuit Description

A transformer is approximated as a collection of lumped circuit elements, as shown in Figure 13.15. Although not shown, we assume mutual inductances between all the inductors to be present. The subdivisions may correspond to distinctly different sections of the coil, having different insulation

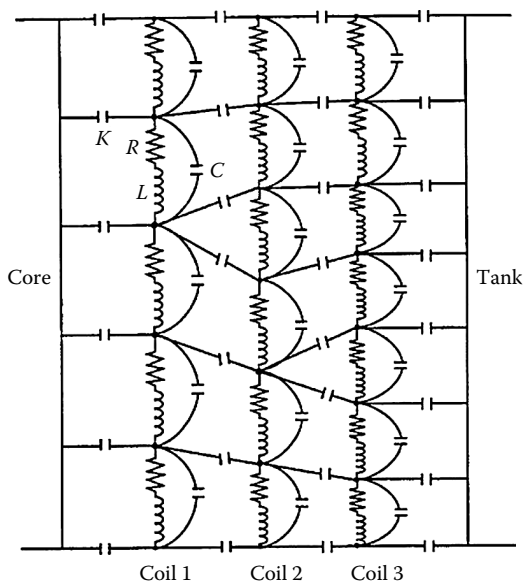


FIGURE 13.15

Circuit model of transformer. The number of coils and subdivisions within a coil are arbitrary.

thicknesses, for example, or may simply be present for increased accuracy. We assume the core and tank to be at ground potential. The presence of the tank only affects the capacitance to ground of the outer coil but not the inductance calculation. Other elements such as grounding resistors, capacitors, inductors, or nonlinear elements may be added. Terminals or nodes may be interconnected, shorted to ground, or connected to ground via a resistor, reactor, capacitor, or varistor.

To analyze the circuit of Figure 13.15, we isolate a representative portion, as shown in Figure 13.16. We adopt a node numbering scheme, starting from the bottom of the innermost coil and proceeding upward. Then, we continue from the bottom of the next coil, and so on. Similarly, we adopt a section or subdivision numbering scheme, starting from the bottom of the innermost coil, proceeding upward, and so on. These numbering schemes are related. In the figure, we have simply labeled the nodes along a winding with i (p 's, q 's, and s 's for nodes on adjacent windings) and the sections with j . Our circuit unknowns are the nodal voltages V_i and section currents I_j , directed upward as shown.

Considering the voltage drop from node $i - 1$ to node i , we can write

$$L_j \frac{dI_j}{dt} + \sum_{k \neq j} M_{jk} \frac{dI_k}{dt} + R_j I_j = V_{i-1} - V_i \quad (13.77)$$

where M_{jk} is the mutual inductance between sections j and k . Defining a section-current vector \mathbf{I} , a nodal-voltage vector \mathbf{V} , an inductance matrix M ,

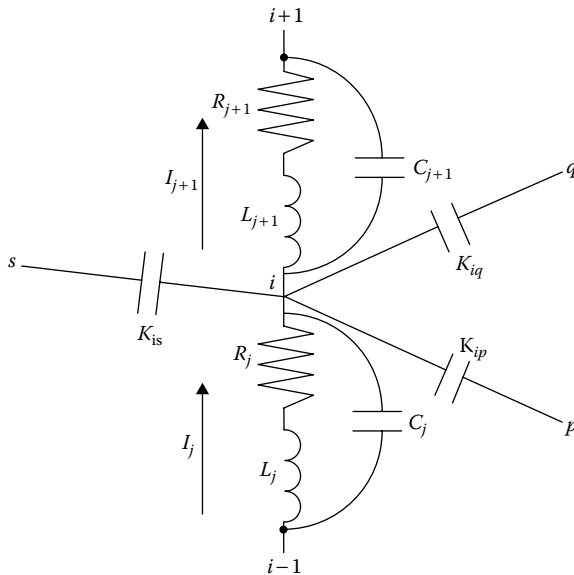


FIGURE 13.16
Representative portion of Figure 13.15.

where $M_{jj} = L_j$, and a diagonal resistance matrix R , we can compress Equation 13.77 as

$$M \frac{d\mathbf{I}}{dt} = B\mathbf{V} - R\mathbf{I} \quad (13.78)$$

where B is a rectangular matrix whose rows correspond to sections and whose columns correspond to nodes, such that $B_{ji-1} = 1$ and $B_{ji} = -1$, where nodes $i-1$ and i bracket section j . The inductance matrix M is a symmetric positive definite matrix. Equation 13.78 holds regardless of how the terminals are interconnected or what additional circuit elements are present.

Applying Kirchoff's current law to node i , we obtain

$$\left(C_j + C_{j+1} + \sum_p K_{ip} \right) \frac{dV_i}{dt} - C_j \frac{dV_{i-1}}{dt} - C_{j+1} \frac{dV_{i+1}}{dt} - \sum_p K_{ip} \frac{dV_p}{dt} = I_j - I_{j+1} \quad (13.79)$$

where the p sum is over all nodes, connected to node i via shunt capacitances K_{ip} . C_j is set to zero when node i is at the bottom of the coil, and $C_{j+1} = 0$ when node i is at the top of the coil, although a small value for capacitive coupling to the yokes could be used. The term $dV_p/dt = 0$ when node p is at ground potential such as for the core or tank. Defining a capacitance matrix C , Equation 13.79 can be rewritten as

$$C \frac{d\mathbf{V}}{dt} = A\mathbf{I} \quad (13.80)$$

where A is a rectangular matrix whose rows correspond to nodes and columns to sections and $A_{ij} = 1$ and $A_{ij+1} = -1$, with sections j and $j+1$ on either side of node i . One of these terms is zero when i is at the end of a coil.

When a nodal voltage V_i is specified, for example, at the impulsed terminal, as $V_i = V_s$, Equation 13.79 is replaced by

$$\frac{dV_i}{dt} = \frac{dV_s}{dt} \quad (13.81)$$

If $V_s = 0$ as for a grounded terminal, then Equation 13.81 becomes $dV_i/dt = 0$. When node i is shorted to ground via a resistor R_s , a term V_i/R_s is added to the left-hand side of Equation 13.79. If node i is grounded by means of a capacitor C_s , a term $C_s dV_i/dt$ is added to the left-hand side of Equation 13.79. For a shorting inductor L_s uncoupled from all the other inductors, the term $\int V_i dt/L_s$ is added to the left-hand side of Equation 13.79. Other situations, such as a resistor or varistor joining two nodes, can be easily accommodated.

When several nodes are joined together, say nodes i , r , s , and so on, their corresponding equations for Kirchoff's current law are simply added.

The resulting equation replaces the equation of node i . Then, the equations of the individual nodes, r , s , and so on are replaced by

$$\frac{dV_r}{dt} - \frac{dV_i}{dt} = 0, \quad \frac{dV_s}{dt} - \frac{dV_i}{dt} = 0, \quad \dots \quad (13.82)$$

The net result of all these circuit modifications is that the capacitance matrix in Equation 13.80 may be altered and the right-hand side may acquire additional terms, as for example, terms involving V for a resistor, $\int V dt$ for an inductor, and the impulsed voltage V_s . Thus, Equation 13.80 is replaced by

$$C \frac{dV}{dt} = A\mathbf{I} + f(V, V) \quad (13.83)$$

where C' is the new capacitance matrix and f depends on the added elements. The above procedure lends itself to straightforward computer implementation.

We can now solve Equations 13.78 and 13.83 simultaneously by means of a Runge-Kutta algorithm, for example, starting from a given initial state. Linear equations must be solved at each time step to determine $d\mathbf{I}/dt$ and dV/dt . Since M is a symmetric positive definite matrix, the Cholesky algorithm may be used to solve Equation 13.78, whereas Equation 13.83 may be solved by Gaussian elimination. Thus, we first perform LL^T or LU factorization on the respective matrices and use the factors to solve the linear equations at each time step, saving much computation time. L and U are lower and upper triangular matrices, respectively, involved in the Cholesky or Gaussian linear equation solution process.

13.6.2 Mutual and Self-Inductance Calculations

The geometry of the transformer core and coil, including the iron yokes, is assumed to have cylindrical symmetry. The iron is assumed to be infinitely permeable. A typical coil section is rectangular in cross section and carries a uniform azimuthally directed current density. The yokes extend outward to infinity, and the tank walls are ignored. This geometry corresponds to that used in the calculations of Rabins' self- and mutual inductances in Chapter 9, Section 9.4. Formulas for the mutual inductances between sections of coil on the same or different coils and for the self-inductances of coil sections are given in Section 9.4. These are used in the circuit model discussed here.

13.6.3 Capacitance Calculations

The series capacitances must consider the type of coil—whether helix, disk, multistart, or other types. Series and shunt capacitances incorporate details of the paper and pressboard insulation, the placement of key spacers and

sticks, and the oil duct geometry. Except when wound-in shields are present, the formula developed by Stein (see Chapter 12) is used for the series disk capacitances. This formula was found to produce the best results in work by Miki et al. [Mik78]. Simple standard formulas are used for helical and multi-start windings, as well as for shunt capacitances, as discussed in Chapter 12. Basically, a shunt capacitance per unit length is calculated, assuming the coils are infinitely long, and this is multiplied by the length of the section to get the section-to-section or section-to-ground shunt capacitances.

The series capacitance for a section containing several disks is obtained by adding the single-disk capacitances in series, that is, by dividing the single-disk capacitance by the number of disks in the section. Since the subdivisions need not contain an integral number of disks, fractional disks are allowed in this calculation. Other subdivision schemes, which restrict the sections to contain an integral number of disks, could be adopted. When wound-in shields are present, only an integral number of disk pairs are allowed in the subdivision. The finer the subdivisions or the greater their number, the greater is the expected accuracy. However, too fine a subdivision, say, less than the height of a disk, could be counterproductive. Fine subdivisions can also lead to convergence problems for the Fourier sums in the calculation of mutual inductance.

13.6.4 Impulse–Voltage Calculations and Experimental Comparisons

The standard impulse–voltage waveform can be mathematically represented as

$$V_s(t) = V_0(e^{-\kappa_1 t} - e^{-\kappa_2 t}) \quad (13.84)$$

where κ_1 , κ_2 , and V_0 are adjusted so that V_s increases to its maximum value in 1.2 μs and decays to half its value in 50 μs . We want to have an analytic formula that is smoothly differentiable, such as Equation 13.84, since the derivative is used in the solution process. Other waveforms such as a chopped wave may also be used. Procedures can be developed for extracting the parameters used in Equation 13.84 from the desired rise and fall times and peak voltage. In our experimental recurrent surge oscillograph (RSO) tests discussed below, the actual rise and fall times were 3 and 44 μs , respectively, and the parameters in Equation 13.84 were adjusted accordingly.

We tested a 45-MVA autotransformer having four windings, as shown in Figure 13.17. The HV (or series) winding consists of two coils in parallel with two ends joined at the center, where the impulse is applied. The other two ends are joined at the autotap with the low-voltage (LV or common) and X-line tap windings. The HV and LV windings are disk windings. The tap winding is a multistart winding and is grounded for the impulse test. The tertiary-voltage (TV) winding is a helical winding and is grounded at both ends for the impulse test. These windings represent one phase of a three-phase transformer, but the phases are essentially isolated from each other for the impulse test.

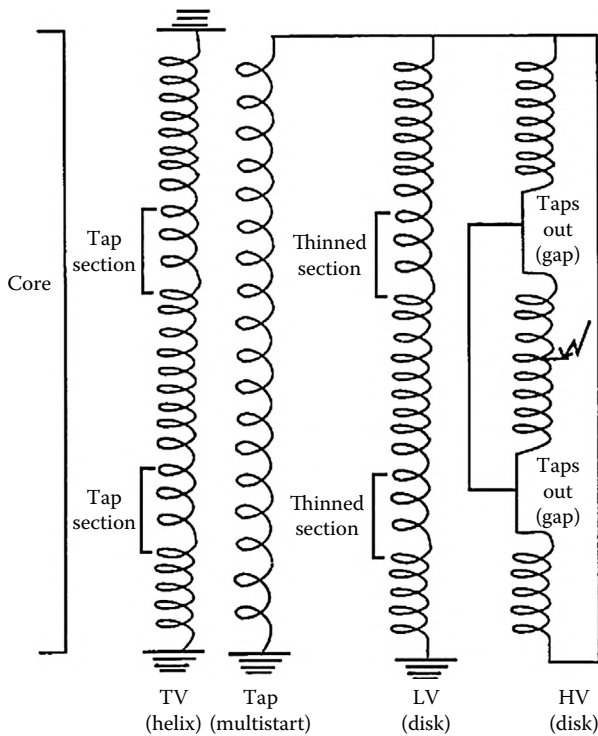


FIGURE 13.17
Schematic representation of impulsed autotransformer.

Both the HV and TV windings contain tapped sections along their lengths. The tap turns are out on the HV winding and in on the TV winding during the impulse test. In the calculations, a direct short is placed across the tapped-out sections. Near these tap sections, the turn density is lowered in the LV winding (thinning) for better short-circuit strength. In the calculations, these thinned areas are specified as one or more separate subdivisions with their own properties, which differ from those of the subdivisions in the rest of the winding.

Although nodal voltages and section currents are calculated throughout the transformer as a function of time, voltage differences can easily be obtained. In fact, disk-disk voltages are calculated throughout all the windings, and the maximum occurring during the time duration of the pulse can be printed out for each winding. The maximum voltage difference occurring between adjacent windings for the duration of the pulse can also be printed out. Secondary quantities, such as maximum electric fields in the oil and corner electric fields on the disks, can likewise be obtained.

Experimentally, only voltages along the HV coil and at the tap positions on the tertiary winding were easily accessible in the tests conducted. In an RSO

test, a repetitive series of pulses having the shape described by Equation 13.84 are applied to, in this case, the HV terminal. This repetitive input results in persistent oscilloscope displays of the output voltages for easy recording. The peak applied voltage is usually low, typically several hundred volts. This test simulates an impulse test done at much higher voltages to the extent that the system is linear. This is likely to be a good assumption provided the core does not saturate and that nonlinear circuit elements such as varistors do not come into play. In our RSO test, the transformer is outside the tank. Thus, the dielectric constant of air is used in the capacitance formulas. In addition, the tank distance, which affects the ground capacitance of the outer coil, is considered very large.

For the tests conducted here, the computer outputs of interest are the voltages to ground at the experimentally measured points. We present a sufficient number of these in the following figures to indicate the level of agreement between calculation and experiment. The input is then normalized to 100 at the peak of the impulse waveform. The units can therefore be interpreted as a percent of the BIL.

While comparing the simulations with experiment, it becomes apparent that the section resistances, which were obtained from the wire geometry and the direct current (DC) or power-frequency resistivity, are not adequate to account for the damping observed in the output waveforms. In fact, it is necessary to increase this resistivity by a factor of about 3000 to account for the damping. Such a factor is reasonable because the eddy currents induced by the stray flux associated with the impulse waveform contain high-frequency components that induce much higher losses than those occurring at power frequency. A factor of this magnitude was estimated in Chapter 12 for the experiment involving wound-in shields. A better approach, which we subsequently adopted, is to carry out Fourier analysis of the current waveforms and calculate the effective resistivity using the formula given in Chapter 12. This involves running the calculation at least twice: once to obtain the waveforms using an assumed resistivity, Fourier analyzing the waveforms to obtain a better estimate of the effective resistivity, and then repeating the calculation with the recalculated resistivity.

Each of the two halves of the HV coil has 52 disks with 12 radial turns each. The impulse is applied to the center of the leg, where the two halves are joined. Output voltages are recorded relative to this center point. [Figure 13.18](#) shows the experimental and calculated voltage waveform four disks below the impulsed terminal. The impulse voltage is also shown for comparison. [Figure 13.19](#) shows the voltage 12 disks below the impulsed terminal. The major oscillations agree well, but some differences can be seen in the lower amplitude higher frequency oscillations. [Figure 13.20](#) shows the experimental and theoretical voltages at the tap position about 30 disks below the impulsed terminal. [Figure 13.21](#) shows the voltage to ground at the upper tap position on the TV winding. This is a voltage transferred via capacitive and mutual inductive effects. The theory and experiment agree well in overall

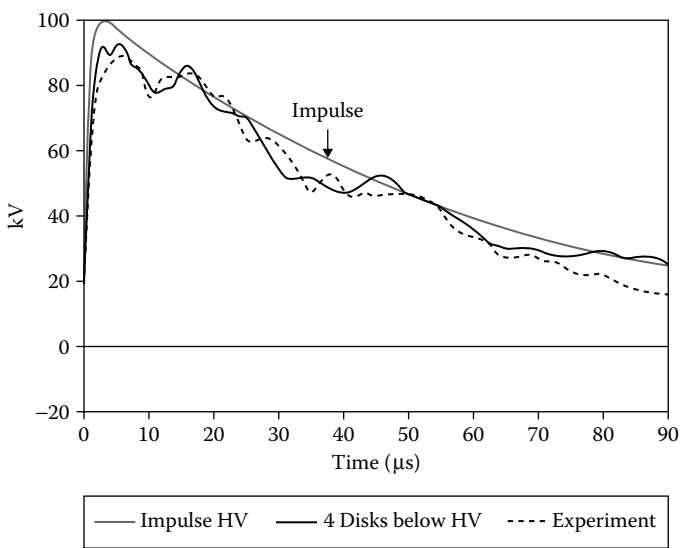


FIGURE 13.18
Experimental and calculated voltage to ground four disks below the HV-impulsed terminal. The impulse voltage is also shown.

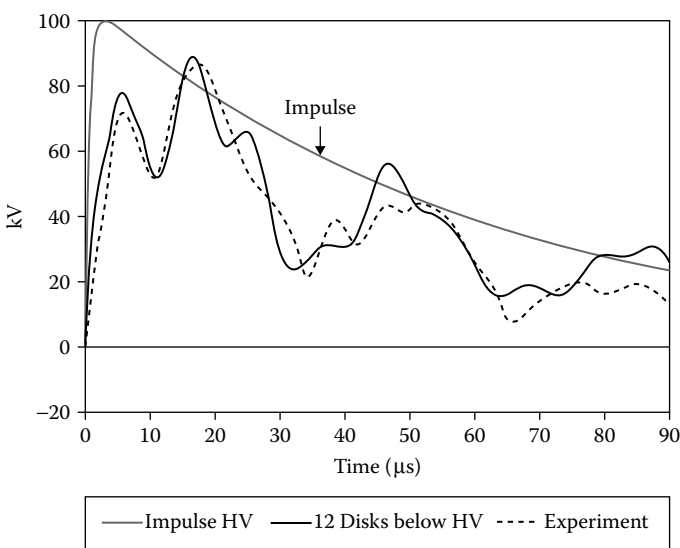


FIGURE 13.19
Experimental and calculated voltage to ground 12 disks below the HV-impulsed terminal.

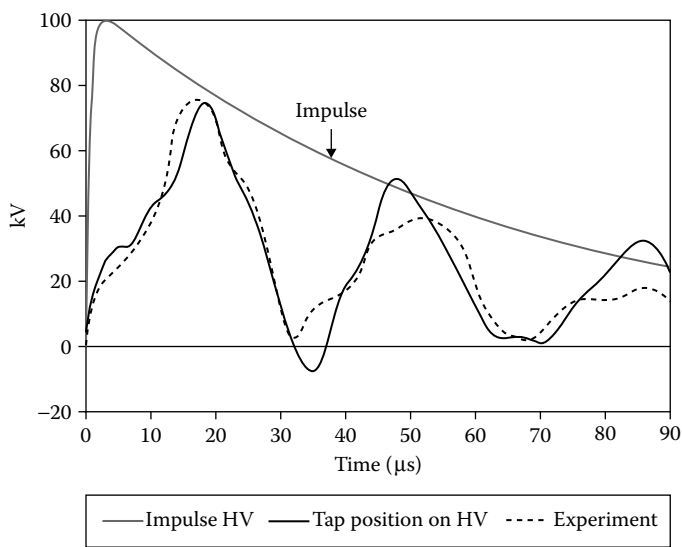


FIGURE 13.20
Experimental and calculated voltages to ground at the tap position on the HV winding, about 30 disks below the impulsed terminal.

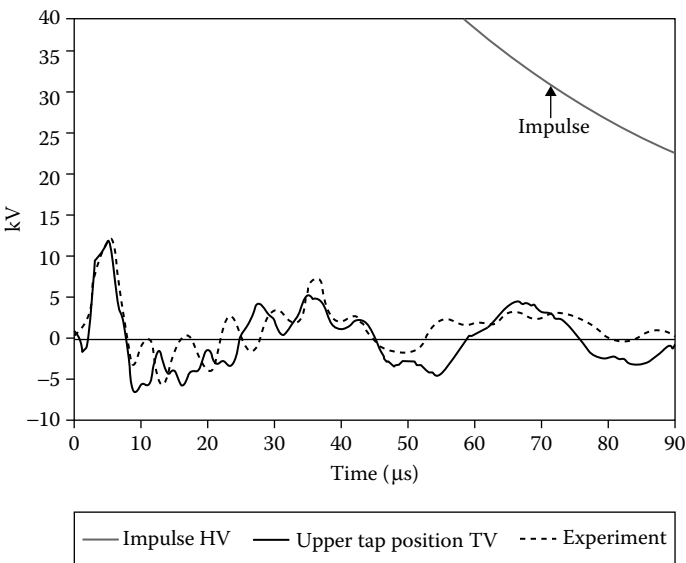


FIGURE 13.21
Experimental and calculated voltages to ground at the center of the upper tap position on the TV winding.

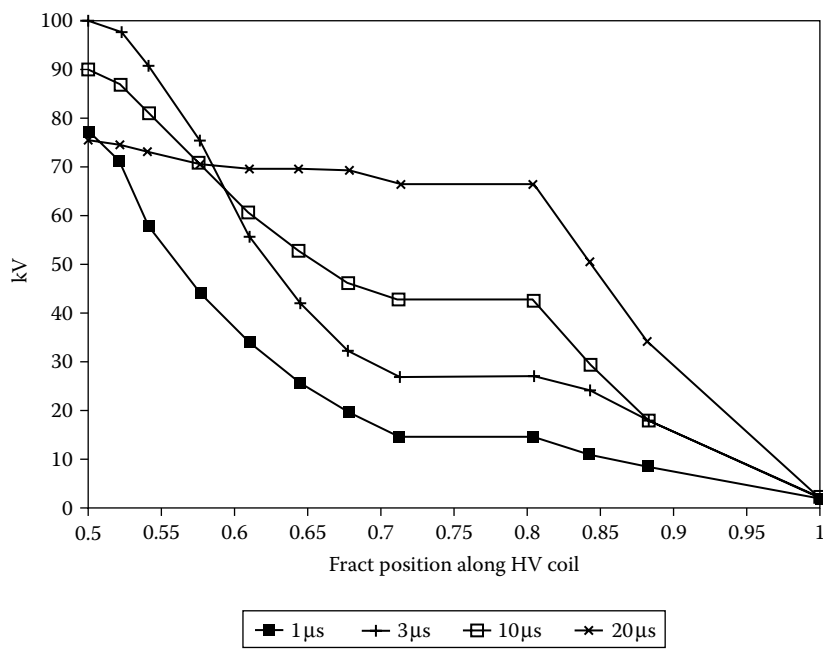


FIGURE 13.22
Calculated voltage profiles at various instants of time along the upper HV coil. The relative position of 0.5 is the impulsed terminal and 1 represents the top of the winding.

magnitude and major oscillations, but the high-frequency ripples are not as well predicted. Figure 13.22 shows another way to present the calculations. This shows the voltage as a function of relative coil position along the top HV winding at various instants of time. Note the flat portion of the curves at a relative position of ~0.75, which corresponds to the tap section with the taps out. Note also that the high capacitance of the multistart tap winding effectively grounds the autopoint. Maximum disk-disk voltages can be obtained by examining such curves although this is more easily done by programming.

13.6.5 Sensitivity Studies

We studied the sensitivity of the calculations for two of the inputs to which a small degree of uncertainty is attached, namely, the effective resistivity of copper and the number of subdivisions along the coils. The resistivity was increased from its DC value to 3000 times this DC value, and the waveform was studied at several locations along the HV winding. Increased resistivity increased the damping of the waveform at longer times but had little effect on the waveform at short times.

Generally, each coil has a minimum number of subdivisions dictated by the number of physically different coil sections. In our case, this was about 6–8 per coil. The multistart coil, however, has only one section. Because of its special construction, it cannot be meaningfully subdivided into axial sections similar to the other coils. In fact, the capacitances to neighboring coils must be coupled equally to both the top and bottom nodes because its voltage is not a unique function of position. We gradually increased the number of subdivisions from the minimum value of 7 up to 22. Once the number of subdivisions crosses 12 per coil, the results were insensitive to any further refinement. Thus, we did not have to be overly concerned about the number of subdivisions used, provided they are above a reasonable minimum, which in this case is ~12 per coil.

14

Losses

14.1 Introduction

Transformer losses are broadly classified as no-load and load losses. *No-load losses* occur when the transformer is energized with its rated voltage at one set of terminals, but the other sets of terminals are open circuited so that no through current or load current flows. In this case, full flux is present in the core, and only the necessary exciting current flows in the windings. The losses are predominately core losses due to hysteresis and eddy currents produced by the time-varying flux in the core steel. *Load losses* occur when the output is connected to a load so that current flows through the transformer from input to output terminals. Although core losses also occur in this case, they are not, by definition, considered part of the load losses. When measuring load losses, the output terminals are shorted to ground, and only a small impedance-related voltage is necessary to produce the desired full load current. In this case, the core losses are small because of the small core flux and do not significantly add to the measured losses. In operation, both types of losses are present and must be taken into account for cooling considerations.

Load losses are in turn broadly classified as I^2R losses due to Joule heating produced by current flow in the coils and as stray losses due to the stray flux as the stray flux encounters metal objects such as tank walls, clamps or bracing structures, and the coils themselves. Because the coil conductors are often stranded and transposed, the I^2R losses are usually determined by the DC resistance of the windings. The stray losses depend on the conductivity, permeability, and shape of the metal object encountered. These losses are primarily due to induced eddy currents in the object. Even though the object may be made of ferromagnetic material, such as the tank walls and clamps, their dimensions are such that hysteresis losses tend to be small relative to eddy current losses.

Although losses are usually a small fraction of the transformed power ($<0.5\%$ in large power transformers), they can produce localized heating that can compromise the operation of the transformer. Thus, it is important to understand how these losses arise and to calculate them as accurately as

possible so that necessary steps can be taken at the design stage to reduce them to a level that can be managed by the cooling system. Other incentives, such as the cost the customer attaches to the losses, can make it worthwhile to find ways of lowering the losses.

Modern methods of analysis, such as finite element or boundary element methods, have facilitated the calculation of stray flux losses in complex geometries. These methods are not yet routine in design because they require a fair amount of geometric input for each new geometry. However, some of these programs support the use of macros that can quickly generate a standard geometry based on key parameters, which can be changed for different designs. These methods can provide useful insights in cases where analytic methods are not available or are very crude. Occasionally, a parametric study using such methods can extend their usefulness beyond a specialized geometry. We will explore such methods, in particular the finite element method, when appropriate. However, we are mainly concerned here with analytic methods that can provide useful formulas covering wide parameter variations.

Typical power transformers have three-phase cores so that the stray flux produced arises from the currents in all three phases. Analytic formulas are generally based on single-phase assumptions. Although these formulas are based on physical principles, they usually require modifications obtained by comparison with test data. The need for such modifications can arise from the idealized geometries assumed in the calculation or from the ignored effects of three-phase flux. Three-dimensional (3D) finite element methods are now available for modeling all three phases, including the effects of three-phase flux. Even here, some approximations must be made to make the calculations tractable. We will explore this approach and compare it with other methods.

14.2 No-Load or Core Losses

Cores in power transformers are generally made of stacks of electrical steel laminations. These are usually in the range of 0.23–0.46 mm in thickness and up to 1 m wide or as wide as can be accommodated by the rolling mill. Modern electrical steels have a silicon content of about 3% that gives them a rather high resistivity, $\sim 50 \times 10^{-8} \Omega \cdot \text{m}$. Although higher silicon content can produce even higher resistivity, the brittleness increases with silicon content, and this makes it difficult to roll them in the mill as well as to handle them after. Special alloying, rolling, and annealing cycles produce the highly oriented Goss texture (cube on edge) with superior magnetic properties such as high permeability along the rolling direction. Thus, the designer should consider the orientation of the laminations in relation to the flux direction when designing a core.

Although thinness and high resistivity are desirable in the laminations to reduce (classical) eddy current losses, a high degree of orientation ($>95\%$) produces large magnetic domains parallel to the rolling direction, as shown in Figure 14.1. The lines between domains with magnetizations pointing up and down are called domain walls. These are narrow transition regions, where the magnetization vector rotates through 180° . During an alternating current (AC) cycle, the up domains increase in size at the expense of the down domains during one part of the cycle, and the opposite occurs during another part of the cycle. This requires the domain walls to move in the direction shown in Figure 14.1 for increasing the up magnetization. As the domain walls move, they generate eddy current losses. These losses were calculated by Pry and Bean [Pry58] for the idealized situation shown in Figure 14.1. They found that the losses were significantly higher than the losses obtained from a classical eddy current calculation, which assumes a homogeneous mixture of many small domains. These nonclassical losses depend on the size of the domains in the zero magnetization state where there are equal-sized up and down domains. This is because the maximum distance the walls move and hence their velocity depends on the zero magnetization domain size. The larger the size and hence the greater the domain wall's velocity, the greater the loss.

In order to decrease the nonclassical eddy current losses, we need to reduce the domain size. Laser or mechanical scribing will accomplish this. A laser or mechanical stylus is rastered across the domains (perpendicular to their magnetization direction) at a certain spacing. This introduces localized stresses at the surface because the scribe lines are not very deep. The domain size is dependent on the stress distribution in the laminations. Localized stresses help to refine the domains. Thus, after scribing, the laminations are not annealed since this would relieve the stress. Figure 14.2 shows the domain pattern in an oriented electrical steel sample before and after laser scribing. Specialized optical techniques make the domain patterns visible. We can clearly see the reduction in domain size as a result of laser scribing in Figure 14.2. The losses were reduced by $\sim 12\%$ as a result of laser scribing in this example.

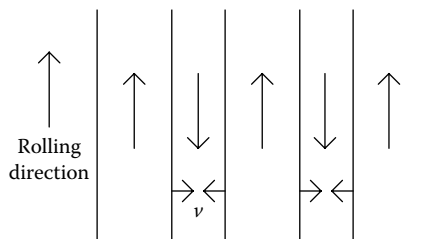
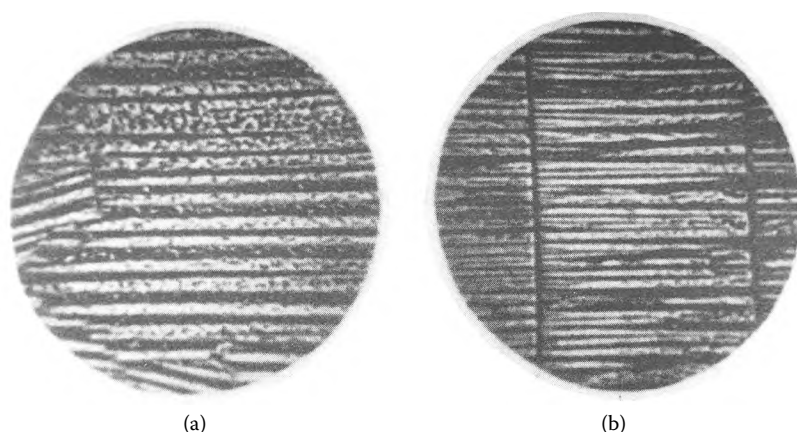


FIGURE 14.1

Idealized magnetic domain pattern in highly oriented electrical steel. The up and down arrows show the magnetization directions. The side-pointing small arrows show the direction of domain wall motion for increasing up magnetization. v is their velocity.

**FIGURE 14.2**

Effect of laser scribing on the domain wall spacing of an oriented electrical steel: (a) before scribing and (b) after scribing. (Courtesy of Armco Inc.)

Another type of loss in electrical steels is hysteresis loss. This results from the domain walls encountering obstructions during their motion. At an obstruction, which can be a crystal imperfection, an occlusion or impurity, or even a localized stress concentration, the domain wall is pinned temporarily. However, because of the magnetizing force driving its motion, it eventually breaks away from the pinning site. This process occurs very suddenly and the resulting high wall velocity generates localized eddy currents. These localized eddy current losses are thought to be the essence of what are called hysteresis losses. Thus, all losses in electrical steel are eddy current in nature. These hysteresis losses occur even at very low, essentially direct current (DC), cycle rates. This is because, although the domain walls move very slowly until they encounter an obstacle, the breakaway process is still very sudden. Thus, in loss separation studies, the hysteresis losses can be measured independently by going to low cycle rates, whereas the total loss, including hysteresis, is measured at high cycle rates. In high-quality electrical steel, the hysteresis and eddy current losses contribute about equally to the total loss.

A novel approach to eliminating hysteresis losses involves using the magnetic material at saturation. In this case, there are no domain walls and hence no wall pinning. Voltage is produced in coils surrounding the magnetic core by rotating the saturated flux vector so that the component linking the coil is sinusoidal [Kra88]. This can be accomplished by means of a toroidal core. This will not eliminate the classical eddy current losses and will require a material having a low excitation current to produce saturation to be practical.

The manufacturer or supplier of electrical steel generally provides the user with loss curves that show the total loss per kilogram or pound as a function of induction at the frequency of interest, usually 50 or 60 Hz. One of these

curves is shown in Figure 14.3a. This curve is generally measured under ideal conditions, that is, low stress on the laminations, and uniform, unidirectional, and sinusoidal flux in the laminations, so that it represents the absolute minimum loss per kilogram or pound to be expected in service. Another useful curve the manufacturer can provide is a curve of the exciting power per unit weight versus induction at the frequency of interest. A sample curve is shown in Figure 14.3b. Again this is an idealized curve, but it can be useful in estimating the power and current needed to energize the transformer.

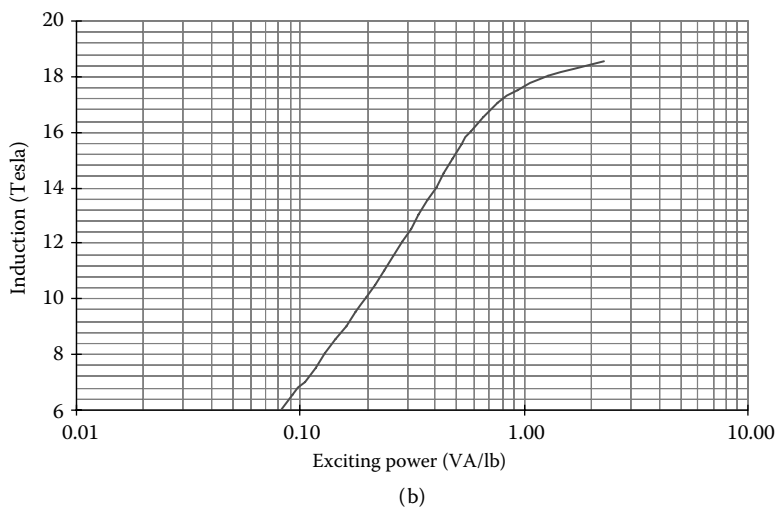
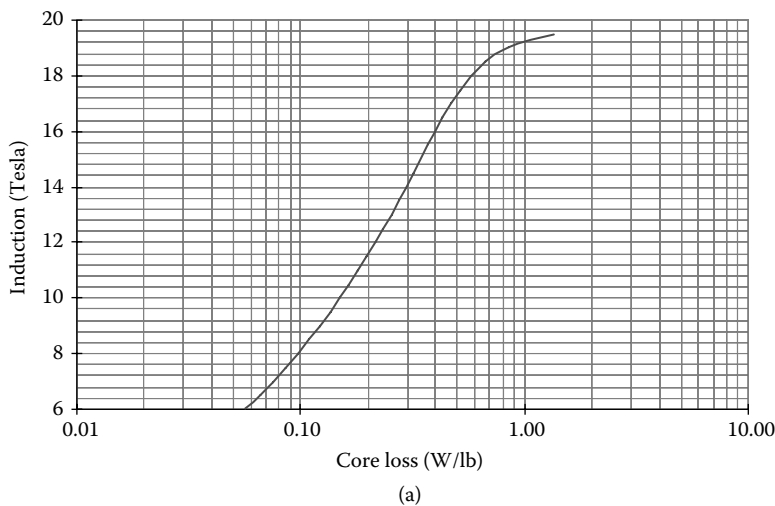


FIGURE 14.3
(a) Manufacturer's curve of specific core loss versus induction and (b) manufacturer's curve of specific exciting power versus induction based on a polynomial fit to data provided by Armco Inc. (Courtesy of Armco Inc.)

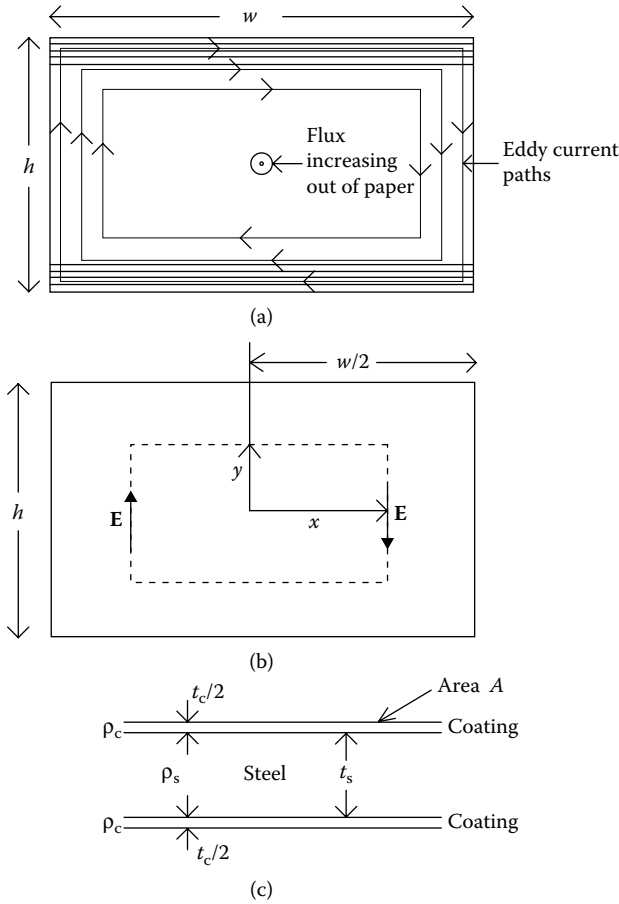
14.2.1 Building Factor

The specific core losses at the operating induction provided by the manufacturer are minimum expected losses so that multiplying by the core weight produces a total core loss lower than what is measured in practice. The discrepancy is a result of the fact that stacked cores require joints, where the induction must not only change the direction but also bridge a gap between different laminations. Also, stresses produced in the steel due to cutting and stacking operations increase the losses. There are other causes of this discrepancy, such as burrs produced by cutting, but all of these can be lumped into a building factor, which is simply a number that multiplies the ideal core loss to produce the measured core loss. These building factors are generally in the range of 1.2–1.4 and are roughly constant for a given core building practice.

Many attempts have been made to understand these extra losses, particularly in the region of the core joints; this has led to improved joint designs such as a step-lapped joint, in which the joint is made gradually in a step-like manner. In a three-phase core, studies have shown that near the joints where the flux changes its direction by 90° , the induction vector rotates and higher losses are generated. Thus, another approach to calculating the building factor is to apply a multiplier to the ideal losses for the amount of steel in the joint region only. This joint multiplier is higher than the average multiplier and can be as high as ~ 1.7 . The advantage of this approach is that cores having different fractions of their overall weight in the joint regions should receive more accurate average multipliers that reflect this difference.

14.2.2 Interlaminar Losses

The core laminations are coated with a glass-like insulating material. This is usually very thin (on the order of a few microns) to keep the space factor reasonably high ($>96\%$). Like any other material, the coating is not a perfect insulator. Thus, eddy currents driven by the bulk flux in the core can flow across the stacked laminations that comprise the core, that is, normal to their surfaces. These eddy currents for a core with a rectangular cross section are shown in [Figure 14.4](#). Of course, the eddy current paths are completed within the laminations where the resistance is much lower. The coating must be a good insulator to keep these losses low relative to the normal intralaminar losses. The insulative value of the coating is determined not only by the intrinsic resistivity of the coating material, which must be high, but also by its thickness. Although the thickness is usually not perfectly uniform, it should not vary so much that bald spots are produced. In high-quality electrical steels, two types of coatings are generally applied: a first glass-like coating and a second coat of special composition designed to apply a favorable stress to the steel. These two coatings help to prevent the occurrence of bald spots.

**FIGURE 14.4**

Interlaminar eddy currents produced by the bulk core flux: (a) eddy current paths in laminated core, (b) geometry for loss calculation, and (c) geometry for surface resistivity calculation.

The insulating value of the coating is determined by measuring the resistance across a stack of laminations or ideally a single lamination, as shown in Figure 14.4c. In terms of the parameters shown, the effective resistance across a lamination of area A is

$$R_{\text{eff}} = R_{\text{coating}} + R_{\text{steel}} = \frac{\rho_c t_c}{A} + \frac{\rho_s t_s}{A} = (\rho_c f_c + \rho_s f_s) \frac{t}{A} = \rho_{\text{eff}} \frac{t}{A} \quad (14.1)$$

where ρ_c is the coating resistivity and t_c is its two-sided thickness, ρ_s is the resistivity of steel, t_s is the thickness of steel, $t = t_c + t_s$ is the combined thickness, and f_c and f_s are fractional thicknesses of the coating and steel, respectively. It is often convenient to express the result in terms of a surface resistivity (SI unit $\Omega \cdot \text{m}^2$), $\sigma_{\text{surf}} = \rho_{\text{eff}} t$, where t is the thickness of one lamination.

We will now estimate the interlaminar losses with the help of the geometry shown in Figure 14.4b. Assume a rectangular stack of core steel of width w and height h and a uniform sinusoidal flux in the stack with peak induction B_0 and angular frequency ω . We use Faraday's law:

$$\oint \mathbf{E} \cdot d\ell = -\frac{d\Phi}{dt} = -\omega(4xy)B_0 \quad (14.2)$$

applied to the rectangle of area $4xy$, shown dashed in Figure 14.4b. By symmetry and Lenz's law, the electric field points as shown on the two vertical sides of the rectangle. The electric field is nearly zero along the horizontal sides because these occur within the metallic laminations. Thus, from Equation 14.2, we have

$$E(4y) = -\omega(4xy)B_0 \Rightarrow E = -\omega B_0 x \quad (14.3)$$

where E is the magnitude of the electric field, which points down on the right and up on the left sides of the rectangle. In these directions, we also have

$$E = \rho_{\text{eff}} J \quad (14.4)$$

where J is the current density and ρ_{eff} is the effective resistivity perpendicular to the stack of laminations derived previously.

The interlaminar losses are given by

$$\text{Loss}_{\text{int}} = \frac{1}{2} \int \rho_{\text{eff}} J^2 dV \quad (14.5)$$

where the volume integral is over the lamination stack and is assumed uniform in the direction into the paper (which we take to have unit length). The factor of $1/2$ comes from time averaging J , which we assume is expressed in terms of its peak value. Thus, from Equations 14.3 through 14.5, we get

$$\text{Loss}_{\text{int}} = \frac{\omega^2 B_0^2 h}{\rho_{\text{eff}}} \int_0^{w/2} x^2 dx = \frac{\omega^2 B_0^2 h w^3}{24 \rho_{\text{eff}}} = \left(\frac{\pi^2}{6} \right) \frac{f^2 B_0^2 h w^3}{\rho_{\text{eff}}} \quad (14.6)$$

where we have used $\omega = 2\pi f$. The specific loss (loss per unit volume) is given by

$$P_{\text{int}} = \frac{\text{Loss}_{\text{int}}}{hw} = \left(\frac{\pi^2}{6} \right) \frac{f^2 B_0^2 h w^2}{\rho_{\text{eff}}} \quad (14.7)$$

since we assumed unit length in the other dimension. To find the loss per unit weight or mass, divide the specific loss by the density of the core steel in the appropriate units. Equation 14.7 is in the SI system, where w is in meters, B_0 is in Tesla (T), ρ_{eff} is in ohm-meter ($\Omega\cdot\text{m}$), f is in hertz (Hz), and P_{int} is in watts per cubic meter (W/m^3).

The interlaminar loss should be compared with the normal loss at the same peak induction. For typical values of the parameters, this loss is generally much smaller than the normal loss and can be ignored. As a numerical example, let $f = 60$ Hz, $w = 0.75$ m, $B_0 = 1.7$ T, and $\rho_{\text{eff}} = 20 \Omega \cdot \text{m}$. We get $P_{\text{int}} = 481$ W/m³. The density of electrical steel is 7650 kg/m³ so that $P_{\text{int}} = 0.063$ W/kg. This is a fairly small loss compared with the normal losses at 1.7 T of ~ 1.3 W/kg. However, a high enough interlaminar resistance must be maintained to achieve these low losses.

14.3 Load Losses

14.3.1 I^2R Losses

I^2R losses in the coil conductors are generally the dominant source of load losses. They are normally computed using the DC value of resistivity. However, wires with large cross-sectional areas carrying AC current should generally be made of stranded and transposed conductors. To determine how AC current affects resistance, we will consider the resistance of an infinitely long cylinder of radius a , permeability μ , and DC conductivity $\sigma = 1/\rho$, where ρ is the DC resistivity. We let it carry current at an angular frequency $\omega = 2\pi f$. Then, the ratio of AC to DC resistance [Smy68] is given by

$$\frac{R_{\text{AC}}}{R_{\text{DC}}} = \frac{x}{2} \left[\frac{\text{ber } x \text{ bei}'x - \text{ber}'x \text{ bei } x}{(\text{ber}'x)^2 + (\text{bei}'x)^2} \right], \quad x = a\sqrt{\omega\mu\sigma} \quad (14.8)$$

The ber and bei functions along with their derivatives ber' and bei' are given in [Dwi61]. This resistance ratio, which can also be regarded as the ratio of an effective AC to DC resistivity, is plotted in Figure 14.5.

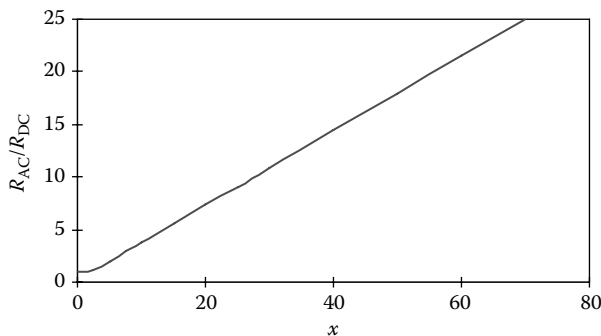


FIGURE 14.5

Plot of the AC to DC resistance ratio for an infinitely long cylinder.

As a numerical example, consider a copper cylinder with the following parameters: $a = 2.52$ cm, $\rho = 2 \times 10^{-8} \Omega \cdot \text{m}$, $\mu = 4\pi \times 10^{-7}$ H/m, and $f = 60$ Hz resulting in $x = 1.95$. Then, we find $R_{AC}/R_{DC} \approx 1.15$, that is, a 15% effect. Making the conductor out of strands that are insulated from each other is not sufficient to eliminate this effect. In addition, the strands must be transposed so that each strand occupies a given region of the cross-sectional area as often as any other strand. This is accomplished in modern transposed cables that use typically 5–50 strands.

With this remedy or the use of small wire sizes, I^2R losses can be calculated using the DC resistance formula:

$$I^2R \text{ Loss} = \frac{\rho \ell}{A} I^2 \quad (14.9)$$

where ρ is the resistivity at the temperature of interest, ℓ is the length of the conductor, A is its cross-sectional area (= the sum of the areas of all wires in parallel), and I is the total current flowing into cross-sectional area A . The temperature-dependent resistivity obeys the formula

$$\rho(T) = \rho_0 [1 + \alpha(T - T_0)] \quad (14.10)$$

over a wide range of temperatures, where ρ_0 is the resistivity at $T = T_0$ and α is the temperature coefficient of resistivity. For pure copper at $T_0 = 20^\circ\text{C}$, $\rho_0 = 1.72 \times 10^{-8} \Omega \cdot \text{m}$ and $\alpha = 0.0039$. For pure aluminum at $T_0 = 20^\circ\text{C}$, $\rho_0 = 2.83 \times 10^{-8} \Omega \cdot \text{m}$ and $\alpha = 0.0039$. Alloying these materials can change these resistivities considerably. The temperature dependence indicated in Equation 14.10 is significant for copper and aluminum. For example, both copper and aluminum resistivities and hence I^2R losses increase about 30% from 20 to 100°C .

14.3.2 Stray Losses

Stray losses are losses caused by stray or leakage flux. [Figure 14.6](#) shows the leakage flux pattern produced by the coil currents in the bottom half of a single phase or leg of a transformer, assuming cylindrical symmetry about the centerline. This was generated with a two-dimensional (2D) finite element program. The main components, core, coils, tank, and clamp, are shown. Shunts on the tank wall and clamp were given the material properties of transformer oil, so they are not active. [Figure 14.7](#) shows the same plot but with the tank and clamp shunts activated. These are made of the same laminated electrical steel as the core. The shunts divert the flux from getting into the tank or clamp walls so that the stray losses in [Figure 14.7](#) are much less than those in [Figure 14.6](#). Calculations show that the losses in the clamp were reduced by a factor of 8 with the shunts present relative to the losses without the shunts. For the tank wall, this reduction was about a factor of 40. The stray flux pattern depends on the details of the winding sizes and spacings, the tank size, the clamp position, and so forth. The losses generated by this flux depend on

whether shunts or shields are present, as well as geometric and material parameters.

In addition to the coils' stray flux, we also have flux produced by the leads. This flux can generate losses, particularly if the leads are close to the tank wall or clamps. Losses can also occur in the tank wall, depending on how the leads are taken out of the tank.

As Figures 14.6 and 14.7 indicate, there is also stray flux within the coils themselves. This flux is less sensitive to the details of the tank and clamp position or whether shunts or shields are present. Therefore, other methods besides the finite element method, such as Rabin's method, which uses a simplified geometry, can be used to accurately calculate this flux in the coils. The coil flux generates eddy currents in the wires or individual strands of cable conductors. The losses depend on the strand size and its orientation relative to the induction vector and the induction vector's magnitude. The localized losses are therefore different at different positions in the coil.

There are other types of stray loss that occur either in the case of an unusual design or when a manufacturing error occurs. In the latter category, extra losses are generated when a crossover or transposition is missed or misplaced in a coil made of two or more wires or cables in parallel.

We will examine many of these types of stray loss here, deriving analytic formulas or procedures for evaluating them where possible or relying on finite element studies or other numerical methods if necessary.

14.3.2.1 Eddy Current Losses in the Coils

To study the effect of stray flux on losses in the coils, we will examine an individual wire or strand that could be part of a transposed cable. We assume it has a rectangular cross section. The magnetic field at the site of this strand segment will point in a certain direction relative to the strand's orientation. This vector can be decomposed into components parallel to each side of the rectangular cross section as shown in Figure 14.8a. (In a transformer, there is little or no magnetic field directed along the length of the wire.) We will analyze the losses associated with each

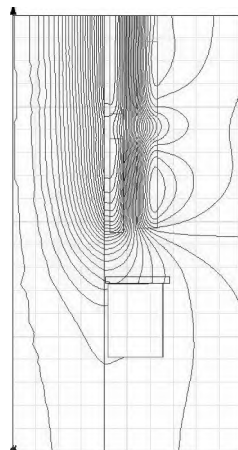


FIGURE 14.6

Stray flux in the lower half of a core leg with no shunts present. Although shown in the figure, they were given the properties of air (transformer oil).

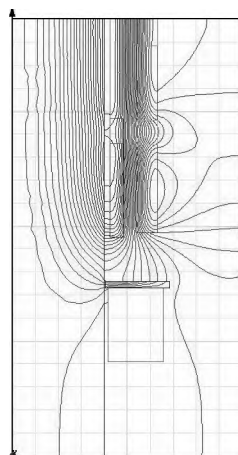
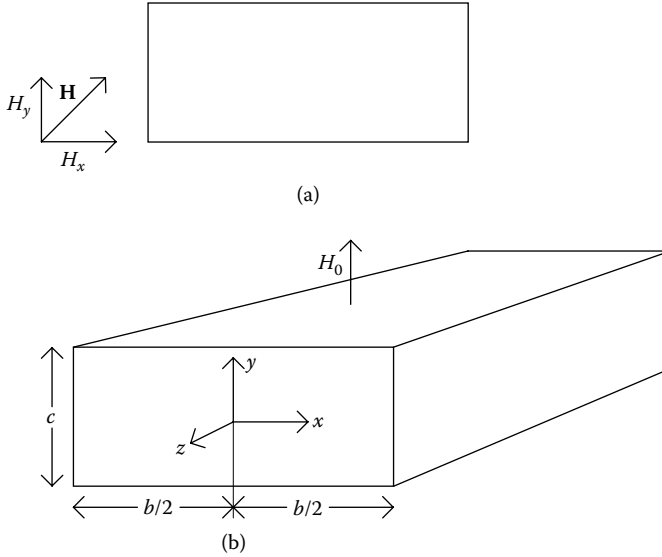


FIGURE 14.7

Stray flux in the lower half of a core leg with shunts present.

**FIGURE 14.8**

Geometry for calculating losses in a conducting strand due to an external magnetic field: (a) magnetic field at the location of a conducting material and (b) coordinate system for loss calculation.

component of the magnetic field separately and add the results. This is accurate to the extent that the eddy currents associated with the different field components do not overlap. We will see that the eddy currents tend to concentrate along the sides of the rectangular strand to which the field component is parallel. Thus, the eddy current patterns associated with the two field components do not overlap significantly, so our method of analysis is reasonably accurate.

Consider the losses associated with the y -component of an external magnetic field as shown in Figure 14.8b, in which the coordinate system and geometric parameters are indicated. We assume an idealized geometry where the strand is infinitely long in the z -direction. This implies that none of the electromagnetic fields have a z -dependence. We further assume that the magnetic field, both external and internal, has only a y -component. Applying Maxwell's equations in this coordinate system and with these assumptions, we obtain in the SI system,

$$\begin{aligned}
 \nabla \times \mathbf{E} &= -\frac{\partial \mathbf{B}}{\partial t} \Rightarrow \frac{\partial E_z}{\partial x} = \mu \frac{\partial H_y}{\partial t} \\
 \nabla \times \mathbf{H} &= \mathbf{J} \Rightarrow \frac{\partial H_y}{\partial x} = J_z \\
 \nabla \times \mathbf{B} &= 0 \Rightarrow \frac{\partial H_y}{\partial y} = 0
 \end{aligned} \tag{14.11}$$

where μ is the permeability, \mathbf{E} is the electric field, and \mathbf{H} is the magnetic field. We have ignored the displacement current term, which is only important at extremely high frequencies. In the metallic conductor, we have Ohm's law in the form

$$\mathbf{J} = \sigma \mathbf{E} \Rightarrow J_z = \sigma E_z \quad (14.12)$$

where σ is the electrical conductivity. There is only a z -component to \mathbf{J} and \mathbf{E} . Combining Equations 14.11 and 14.12, we obtain

$$\frac{\partial^2 H_y}{\partial x^2} = \mu \sigma \frac{\partial H_y}{\partial t} \quad (14.13)$$

where H_y is a function of x and t . Let H_y have a sinusoidal time dependence of the form

$$H_y(x, t) = H_y(x) e^{j\omega t} \quad (14.14)$$

Then, Equation 14.13 becomes

$$\frac{\partial^2 H_y}{\partial x^2} = j\omega \mu \sigma H_y = k^2 H_y, \quad k^2 = j\omega \mu \sigma \quad (14.15)$$

H_y is only a function of x in Equation 14.15. Solving Equation 14.15 with the boundary condition that $H_y = H_0$ at $x = \pm b/2$, where b is the strand width normal to the field direction and H_0 is the peak amplitude of the external field, we get

$$H_y(x) = H_0 \frac{\cosh(kx)}{\cosh(kb/2)} \quad (14.16)$$

and from Equation 14.11

$$J_z = -kH_0 \frac{\sinh(kx)}{\cosh(kb/2)} \quad (14.17)$$

The eddy current loss per unit length in the z -direction is

$$\frac{\text{Eddy current loss}}{\text{Unit length}} = \frac{c}{2\sigma} \int_{-b/2}^{b/2} |J_z|^2 dx = \frac{cH_0^2 |k|^2}{\sigma |\cosh(kb/2)|^2} \int_0^{b/2} |\sinh(kx)|^2 dx \quad (14.18)$$

where c is the strand dimension along the field direction. The factor of $1/2$ comes from taking a time average and using peak values of the field. The integration through only half the thickness is possible because of the symmetry of the integrand. The factor of 2 involved cancels the factor of 2 in the denominator. From Equation 14.15 we get

$$k = (1 + j)\sqrt{\frac{\omega\mu\sigma}{2}} = (1 + j)q, \quad q = \sqrt{\frac{\omega\mu\sigma}{2}} \quad (14.19)$$

Using this expression for k , we have the identities

$$\begin{aligned} |\sinh(kx)|^2 &= \frac{1}{2}[\cosh(2qx) - \cos(2qx)] \\ |\cosh(kx)|^2 &= \frac{1}{2}[\cosh(2qx) + \cos(2qx)] \end{aligned} \quad (14.20)$$

Substituting this into Equation 14.18, integrating, and dividing by the cross-sectional area, we get the specific eddy current loss (loss per unit volume), which is

$$P_{ec} = \frac{H_0^2 q}{\sigma b} \left[\frac{\sinh(qb) - \sin(qb)}{\cosh(qb) + \cos(qb)} \right] \quad (14.21)$$

in watts per cubic meter in the SI system. Simply divide this by the density in this system to get the loss per unit mass or weight.

This last equation applies to a broad frequency range up to where radiation effects start becoming important. At the low-frequency end, which applies to transformers at power frequencies (small qb), this reduces to

$$P_{ec} \xrightarrow{\text{small } qb} \frac{H_0^2 q^4 b^2}{6\sigma} = \left(\frac{\pi^2}{6} \right) f^2 \mu^2 b^2 \sigma H_0^2 = \left(\frac{\pi^2}{6} \right) \frac{f^2 b^2 B_0^2}{\rho} \quad (14.22)$$

where we have used $\sigma = 1/\rho$, where ρ is the resistivity, $\omega = 2\pi f$, where f is the frequency, and $B_0 = \mu H_0$.

As a numerical example, let $B_0 = 0.05$ T, a typical leakage induction value in the coil region, $\rho = 2 \times 10^{-8} \Omega \cdot \text{m}$ for copper at its operating temperature, $\sigma = 5 \times 10^7 (\Omega \cdot \text{m})^{-1}$, $\omega = 2\pi f = 2\pi (60)$ rads/s, $b = 6.35 \times 10^{-3}$ m, and $\mu = 4\pi \times 10^{-7}$ H/m. Then, $q = 108.8 \text{ m}^{-1}$ and $qb = 0.691$. This is small enough that the small qb limit should apply. Thus, we get from Equation 14.22, $P_{ec} = 2.985 \times 10^4 \text{ W/m}^3$. The exact Equation 14.21 yields $P_{ec} = 2.955 \times 10^4 \text{ W/m}^3$. Using the density of copper $d_{Cu} = 8933 \text{ kg/m}^3$, we obtain $P_{ec} = 3.35 \text{ W/kg}$ on a per-unit mass basis. The $I^2 R$ loss on a per-volume basis associated with an rms current of $3 \times 10^6 \text{ A/m}^2$ (a typical value) in a copper winding of the above resistivity is $1.8 \times 10^5 \text{ W/m}^3$ so that the eddy current loss amounts to about 17% of the $I^2 R$ losses in this case.

The losses given by Equation 14.21 or 14.22 must be combined with the losses given by a similar formula with H_0 or B_0 referring to the peak value of the x -component of the field and with b and c interchanged. This will give the total eddy current loss density at the location of the strand. We need a method to calculate the magnetic field or induction at various locations in the coils. From the axisymmetric field calculation (flux map) given in Figures 14.6 and 14.7, we obtain values of the radial and axial components of the field. These replace the x - and y -components in the loss formulas given in Equations 14.21 and 14.22. These loss densities will differ in different parts of the winding. To obtain the total eddy current loss, an average loss density can be obtained for the winding, and this is multiplied by the total weight or volume of the winding. However, in determining local winding temperatures and especially the hot spot temperature, we need to know how these losses are distributed.

From Equations 14.17, 14.19, and 14.20, we can obtain the eddy current loss density as a function of position in the strand:

$$\frac{|J_z|^2}{2\sigma} = \frac{H_0^2 q}{\sigma} \left[\frac{\cosh(2qx) - \cos(2qx)}{\cosh(qb) + \cos(qb)} \right] \quad (14.23)$$

This vanishes at the center of the strand ($x = 0$) and is a maximum at the surface ($x = \pm b/2$). The parameter q measures how fast this drops off from the surface. The falloff is more rapid, the larger the value of q . The reciprocal of q is called the skin depth δ and is given by

$$\delta = \frac{1}{q} = \sqrt{\frac{2}{\omega\mu\sigma}} \quad (14.24)$$

For copper at $\sim 60^\circ\text{C}$, $\sigma = 5 \times 10^7 (\Omega \cdot \text{m})^{-1}$ and $f = 60 \text{ Hz}$, we get $\delta = 9.2 \text{ mm}$. For aluminum at $\sim 60^\circ\text{C}$, $\sigma = 3 \times 10^7 (\Omega \cdot \text{m})^{-1}$ and $f = 60 \text{ Hz}$, we get $\delta = 11.9 \text{ mm}$. Thus, the skin depth is smaller for copper than aluminum, which means that the eddy currents concentrate more toward the surface of copper than aluminum.

The high-frequency limit of Equation 14.21 (large qb) is

$$P_{\text{ec}} \xrightarrow{\text{large } qb} \frac{H_0^2 q}{\sigma b} \quad (14.25)$$

This increases with the square root of the frequency.

14.3.2.2 Tieplate Losses

The tieplate (also called the flitch plate) is located just outside the core in the space between the core and the innermost winding. It is a structural plate that connects the upper and lower clamps. Tension in this plate provides the clamping force necessary to hold the transformer together should a short circuit occur. It is usually made of magnetic steel or stainless steel and can be

subdivided into several side-by-side vertical plates to help reduce the eddy current losses. Figure 14.9 shows a schematic diagram of one of the tieplates associated with one leg. There is another on the opposite side of the core leg. These generally have a rectangular cross section.

Since the flux plots in Figures 14.6 and 14.7 are for a 2D, axisymmetric geometry, the tieplate is not included. (This would have made it a solid cylinder around the core.) However, the flux pattern shown in Figures 14.6 and 14.7 should not be greatly altered by their presence because they occupy a fairly small fraction of the core’s circumference. As the flux pattern in the figures show, the flux is primarily radial at the location of the tieplate. However, when an actual tieplate is present, it will carry some axial flux. The amount will depend on the permeability of the tieplate relative to that of the core. We can estimate the axial tieplate flux by reference to Figure 14.10, where we see two side-by-side solids of permeabilities μ_1, μ_2 and cross-sectional areas A_1, A_2 carrying flux. We assume that the coils producing this flux create a

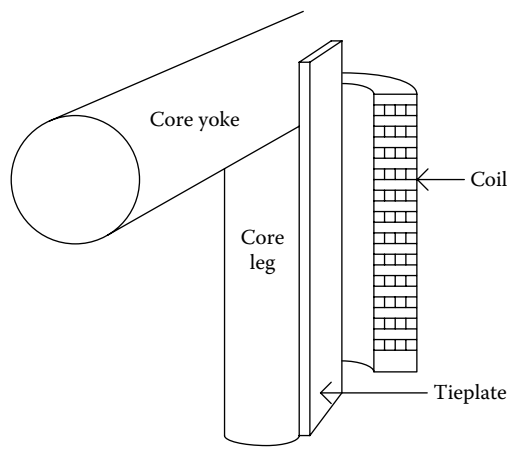


FIGURE 14.9
Tieplate location in a transformer.

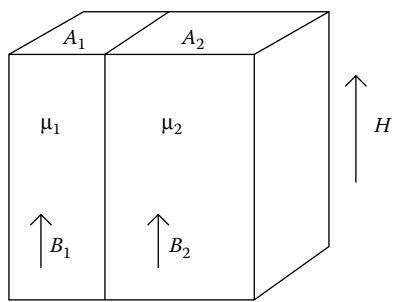


FIGURE 14.10
Dissimilar magnetic materials in a common magnetic field.

common magnetic field \mathbf{H} at the location of the solids. (The field inside an ideal solenoid is a constant axial field.)

The induction inside each solid is given by

$$B_1 = \mu_1 H, \quad B_2 = \mu_2 H \quad (14.26)$$

so that

$$\frac{B_1}{B_2} = \frac{\mu_1}{\mu_2} \quad (14.27)$$

Using Equation 14.27, we can estimate the induction in the tieplate. We can use the ratio of relative permeabilities from Equation 14.27. These are AC permeabilities, which we take to be ~ 5000 for the core and ~ 200 for a magnetic steel tieplate. With a typical core induction of 1.7 T, we find that $B_{\text{mag t.p.}} = 0.04$ and $B_{\text{core}} = 0.068$ T. For a stainless-steel tieplate of relative permeability = 1, we obtain $B_{\text{s.s. t.p.}} = 0.0002$ and $B_{\text{core}} = 0.00034$ T. Thus, the axial induction is not insignificant for a magnetic steel tieplate but ignorable for a stainless steel one.

We first look at the losses due to the radial induction because these are common to both magnetic and stainless steel tieplates. We have studied these losses using a 2D finite element analysis. Figure 14.11 shows a flux plot for a magnetic steel tieplate, assuming a uniform 60-Hz sinusoidal flux density of 1 T peak value far from the plate. The plate is assumed to be infinitely long in the dimension perpendicular to the page. Only half the geometry is modeled, taking advantage of symmetry about the left-hand axis. There is a space between the tieplate and the high-permeability core surface, which is the bottom boundary of Figure 14.11. This space allows for insulation and cooling duct. The loss density contours are shown in Figure 14.12. This indicates that the eddy currents are concentrated near the surface because of the skin effect. Figure 14.13 shows a similar flux plot for a stainless steel tieplate. Note that there is little eddy current screening so the flux penetrates the plate without much distortion. Figure 14.14 shows the loss density contours for the stainless steel tieplate. There is much less surface concentration of the eddy

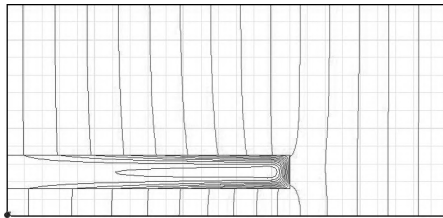


FIGURE 14.11

Flux lines for a magnetic steel tieplate in a uniform 60-Hz magnetic field of 1 T peak value normal to its surface. The tieplate is separated from the high-permeability core along the bottom by a space for insulation and cooling. Only half the geometry is modeled.

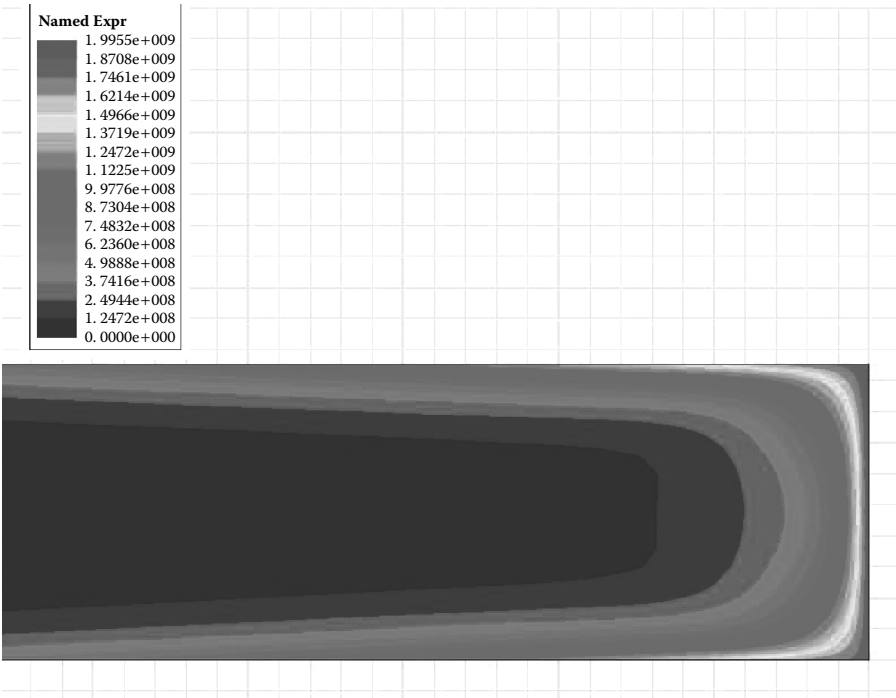


FIGURE 14.12
(See color insert following page 338.) Loss density contours for the magnetic steel tieplate shown in Figure 14.11. Only the right end of the tieplate is shown. The key is in watts per cubic meter.

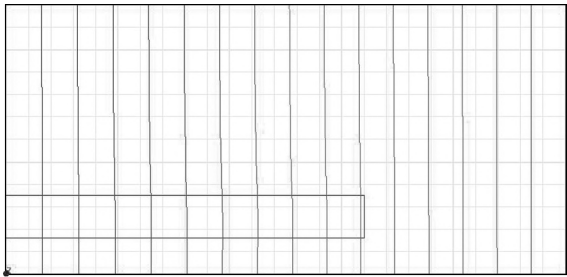


FIGURE 14.13
Flux lines for a stainless steel tieplate in a uniform 60-Hz field of 1 T peak value normal to its surface. The situation is otherwise the same as described in Figure 14.11.

currents. Although we only calculate eddy current losses with a finite element program, the hysteresis losses in a magnetic steel tieplate make up only a small fraction of the total losses for typical tieplate dimensions.

The finite element study was repeated for different tieplate widths (perpendicular to the flux direction) while keeping the thickness (along the flux

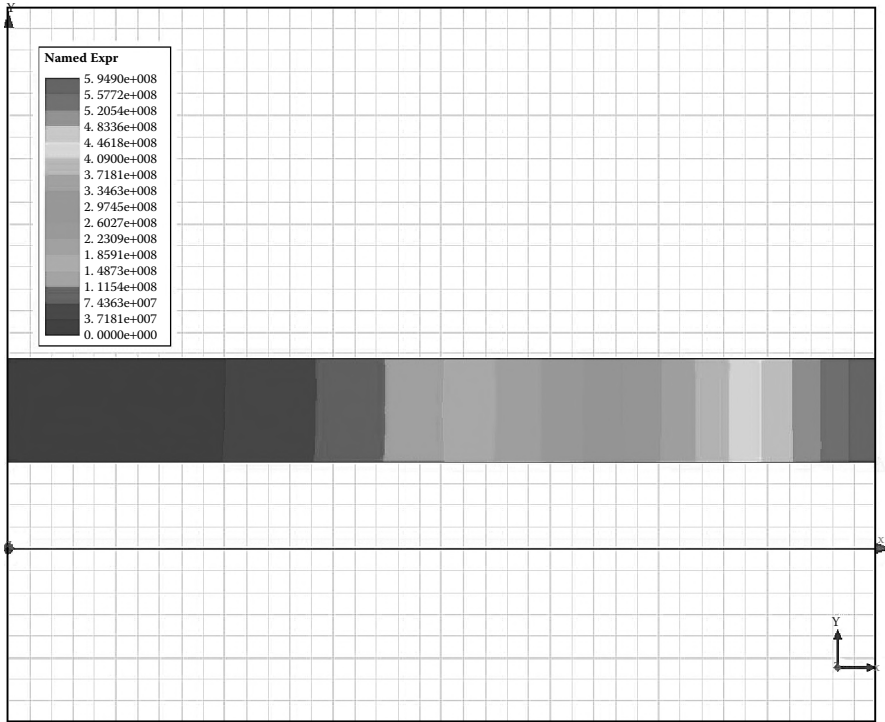


FIGURE 14.14

(See color insert following page 338.) Loss density contours for the stainless steel tieplate shown in Figure 14.13. The key is in watts per cubic meter.

direction) constant at 9.5 mm. The results are shown in Figure 14.15, where the losses per unit length in the infinitely long direction and per T^2 are plotted. To get the actual loss, we multiply the ordinate by the tieplate length or portion of the tieplate length affected by the losses and by the square of the peak radial induction in T^2 . Figure 14.16 shows the same information as plotted in Figure 14.15 but on a log–log plot. This allows us to extract the power dependence of the loss on the width of the tieplate. For magnetic steel, the material parameters assumed were resistivity = $25 \times 10^{-8} \Omega \cdot \text{m}$ and relative permeability = 200, and for stainless steel, the material parameters assumed were resistivity = $75 \times 10^{-8} \Omega \cdot \text{m}$ and relative permeability = 1. We obtain for the losses

$$\begin{aligned} \text{Loss}_{\text{mag steel}} (\text{W/mm}) &= 1.953 \times 10^{-3} w^{2.3} B_p^2, & w (\text{mm}), & B_p (\text{T}) \\ \text{Loss}_{\text{stainless}} (\text{W/mm}) &= 7.407 \times 10^{-5} w^3 B_p^2, & w (\text{mm}), & B_p (\text{T}) \end{aligned} \quad (14.28)$$

with the loss in watts per millimeter, the tieplate width w in millimeter, and the peak induction B_p in Tesla. These are losses per unit length in millimeters along the tieplate.

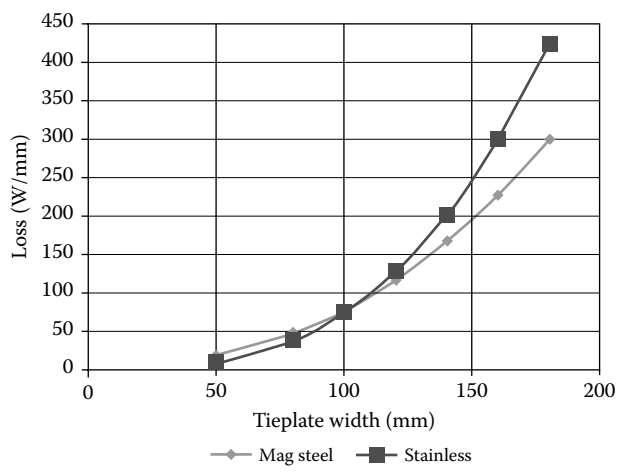


FIGURE 14.15 Losses for 9.5-mm thick tieplates made of magnetic and stainless steel versus the tieplate width. The tieplates are in a uniform 60-Hz magnetic field of 1 T peak value directed normal to the tieplate surface.

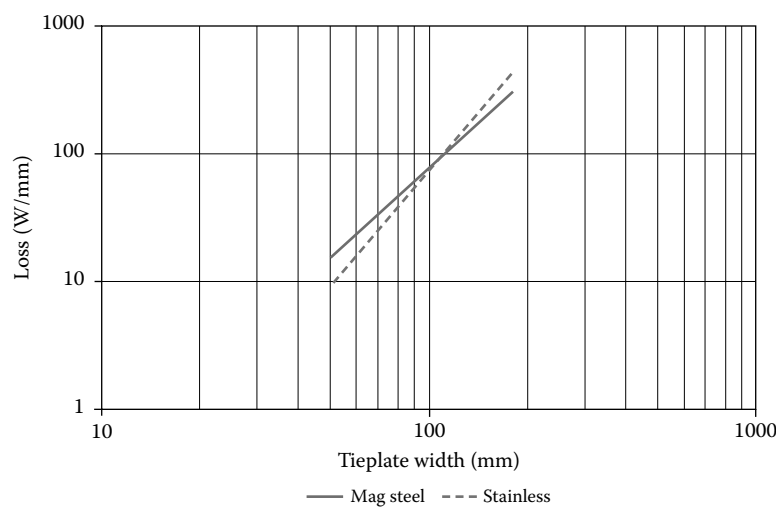


FIGURE 14.16 Same as Figure 10.15 but on a log–log scale.

Although this study was performed for a specific tieplate thickness of 9.5 mm, it is an example of the kind of study that can be done with a finite element code and that can be parameterized for future design use without the necessity of repeating it for each new case.

The stainless steel finite element study shows that the magnetic field and eddy currents inside the tieplate have nearly the same direction and

geometry dependence as we assumed for the eddy current loss in conducting strands. Therefore, if we multiply the loss density given in Equation 14.21 or 14.22 by the plate's cross-sectional area, we should get nearly the same result as given for stainless steel. Note that w should be substituted for b in the previous formulas. Using the small qb approximation in Equation 14.22, and putting in the stainless steel parameters, we obtain

$$\text{Loss (W/mm)} = 7.5 \times 10^{-5} w^3 B_p^2$$

which is close to the result given in Equation 14.28 in the same units (w in mm and B_p in Tesla). We do not expect exact agreement since qb ($=qw$) for stainless at $w = 127$ mm is ~ 2.26 , which is a little above the range of validity of the small qb formula.

In the case of magnetic steel, as Figures 14.11 and 14.12 show, the conditions under which the strand eddy current losses were developed do not hold. The field is not strictly y -directed (radially directed) and it does not depend only on x (the width direction). We should note that, according to Figure 14.15 the losses per unit length due to radial flux are higher in stainless steel tieplates for the larger widths than in magnetic steel plates. However, for magnetic steel tieplates, we need to add on the losses due to the axial flux they carry.

We can estimate the losses in the tieplate due to axial flux by resorting to an idealized geometry. We assume that the tieplate is infinitely long and the flux is driven by a uniform axial magnetic field parallel to the tieplate's surface. We also assume that the tieplate's width is much greater than its thickness; in fact, we assume an infinite width. Thus, as shown in Figure 14.17, the only relevant dimension is the y -dimension through the sheet's thickness. The eddy currents will flow primarily in the x -direction. We ignore their return paths in the y -direction, which are small compared to the x -directed paths.

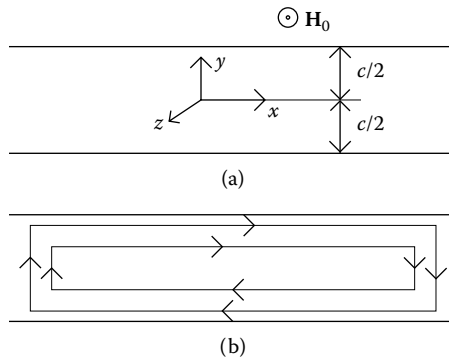


FIGURE 14.17

Geometry of an idealized plate or sheet driven by a uniform sinusoidal magnetic field parallel to its surface (perpendicular to page): (a) sheet geometry and (b) eddy current paths.

Applying Maxwell's equations and Ohm's law to this geometry, we obtain

$$\begin{aligned}\nabla \times \mathbf{E} &= -\frac{\partial \mathbf{B}}{\partial t} \Rightarrow \frac{\partial E_x}{\partial y} = \mu \frac{\partial H_z}{\partial t} \\ \nabla \times \mathbf{H} &= \mathbf{J} \Rightarrow \frac{\partial H_z}{\partial y} = J_x \\ \mathbf{J} &= \sigma \mathbf{E} \Rightarrow J_x = \sigma E_x\end{aligned}\tag{14.29}$$

in SI units. Combining these equations, we obtain

$$\frac{\partial^2 H_z}{\partial y^2} = \mu \sigma \frac{\partial H_z}{\partial t}\tag{14.30}$$

Equation 14.30 is identical in form to Equation 14.13. Thus, using the previous results but altering the notation to fit the present geometry, we get

$$H_z(y) = H_0 \frac{\cosh(ky)}{\cosh(kc/2)}, \quad J_x(y) = -kH_0 \frac{\sinh(ky)}{\cosh(kc/2)}\tag{14.31}$$

and

$$P_{\text{tp,axial}} = \frac{H_0^2 q}{\sigma c} \left[\frac{\sinh(qc) - \sin(qc)}{\cosh(qc) + \cos(qc)} \right], \quad k = (1+j)q, \quad q = \sqrt{\frac{\omega \mu \sigma}{2}}\tag{14.32}$$

This is a loss per unit volume (W/m^3) in the tieplate due to axial flux. Because the eddy currents generating this loss are at right angles to the eddy currents associated with the radial flux normal to the surface, there is no interference between them, and the two losses can be added to each other.

For magnetic steel at 60 Hz with $\mu_r = 200$, $\mu = \mu_r 4\pi \times 10^{-7} \text{ H/m}$, $\sigma = 4 \times 10^6 (\Omega \cdot \text{m})^{-1}$, and $c = 9.52 \times 10^{-3} \text{ m}$, we have $qc = 4.15$. This is large enough that Equation 14.32 must be used without taking its small qc limit. Substituting the parameters just given for magnetic steel and using $B_0 = 0.07 \text{ T}$ ($H_0 = B_0/\mu$), we obtain $P_{\text{tp,axial}} = 925 \text{ W/m}^3 = 0.12 \text{ W/kg}$, where we have used 7800 kg/m^3 for the density of magnetic steel. The radial flux loss formula for magnetic steel (Equation 14.28) must be divided by the cross-sectional area for comparison with the above loss. We find, using $B_p = 0.14 \text{ T}$, $w = 127 \text{ mm}$ and the previous value for c , that $P_{\text{tp,radial}} = 2.184 \times 10^6 \text{ W/m}^3 = 280 \text{ W/kg}$. Thus, it appears that for a magnetic steel tieplate, the loss associated with the axial flux is much less than the loss associated with the radial flux. In any event, these two losses must be added together to get the total loss.

Since the tieplate loss is due mainly to radial flux, and radial flux depends on the width to a power $\sim 2-3$, the losses can be reduced by reducing the width of an individual tieplate while keeping the total cross-sectional area

constant, since this area is necessary to provide the required mechanical strength. Thus, subdividing the tieplates either with axial slots or into separate plates can reduce the loss while maintaining the necessary axial tensile strength.

14.3.2.3 Tieplate and Core Losses Due to Unbalanced Currents

A rather specialized type of loss can occur in transformers with a large unbalanced net current flow. The net current is the algebraic sum of the currents flowing in all the windings. This can be unbalanced, in contrast with the net ampere (A)-turns, which are always nearly exactly balanced. To visualize the magnetic effect of a winding's current, consider a cylindrical (solenoidal) winding carrying a current that flows in at the bottom and out at the top. Outside the winding, the net upward current appears to be equally distributed around the cylinder. The magnetic field outside the cylinder associated with this current is the same as that produced by the current flowing along the centerline of the cylinder. In a core-form transformer, some of the windings carry current up and some down. The algebraic sum of all these currents can be considered to be carried by one cylinder of radius equal to a weighted average of the contributing windings, weighted by their current magnitudes. Outside this radius, the field is that of a straight wire along the centerline carrying the algebraic sum of the currents.

The field around a long straight wire carrying a current \mathbf{I} is directed along concentric circles about the wire and has the magnitude

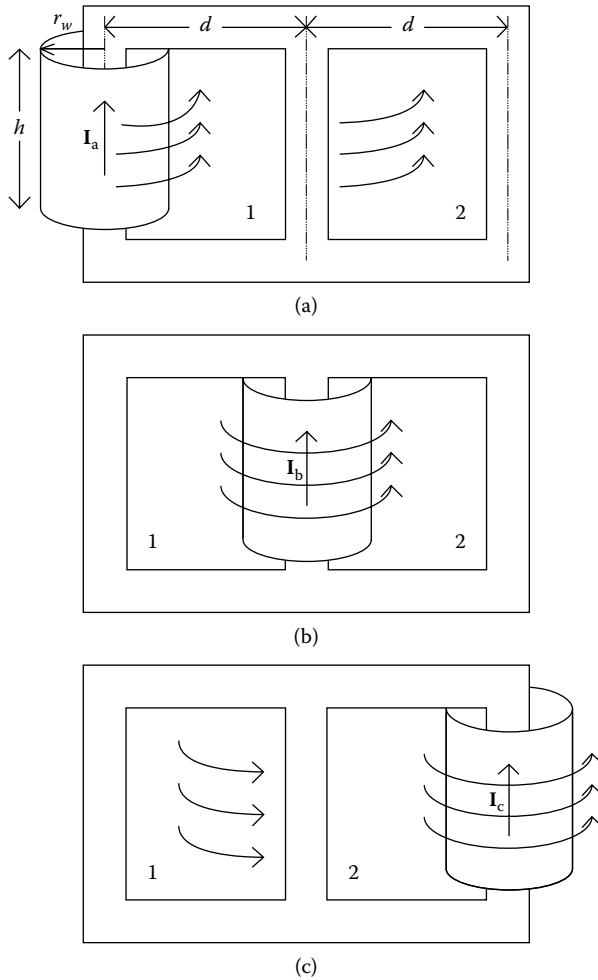
$$H_{\phi} = \frac{\mathbf{I}}{2\pi r} \quad (14.33)$$

in SI units, where r is the radial distance from the centerline and ϕ , the azimuthal angle, indicates that the field is azimuthally directed. We use bold-face type here to indicate that the current is a phasor quantity, since we are considering a three-phase transformer on a single three-phase core. This field cuts through the transformer core windows as shown in Figure 14.18. The alternating flux passing through the core window induces a voltage around the core structure that surrounds the window. The tieplates, including their connection to the upper and lower clamps, make a similar circuit around the core windows so that voltage is induced in them as well.

We can calculate the flux due to the coil in Figure 14.18a through the left-hand window, labeled 1, Φ_{a1} , using Equation 14.33:

$$\Phi_{a1} = \int B_{\phi} dA = \frac{\mu_o h \mathbf{I}_a}{2\pi} \int_{r_w}^d \frac{dr}{r} = \frac{\mu_o h \mathbf{I}_a}{2\pi} \ln \left(\frac{d}{r_w} \right) \quad (14.34)$$

where μ_o is the permeability of oil (air) = $4\pi \times 10^{-7}$ H/m, h is the effective winding height, d is the leg center-to-center distance, and r_w is the effective

**FIGURE 14.18**

Field around a cylindrical winding located on a transformer leg and carrying a net upward current: (a) phase a coil, (b) phase b coil, and (c) phase c coil.

winding radius. h can be obtained as a weighted average of the contributing windings as was done for r_w . We have integrated all the way to the centerline of the center leg. This is an approximation, as the flux lines will no doubt deviate from the ideal radial dependence given in Equation 14.33 near the center leg. Similarly, the flux through window 2 due to the phase a current Φ_{a2} , is

$$\Phi_{a2} = \int B_\phi dA = \frac{\mu_o h I_a}{2\pi} \int_d^{2d} \frac{dr}{r} = \frac{\mu_o h I_a}{2\pi} \ln 2 \quad (14.35)$$

Using the same procedure, we see the flux through the two windows due to phases b and c shown in [Figures 14.18b](#) and 14.18c:

$$\begin{aligned}\Phi_{b1} &= -\frac{\mu_o h \mathbf{I}_b}{2\pi} \ln\left(\frac{d}{r_w}\right), & \Phi_{b2} &= \frac{\mu_o h \mathbf{I}_b}{2\pi} \ln\left(\frac{d}{r_w}\right) \\ \Phi_{c1} &= -\frac{\mu_o h \mathbf{I}_c}{2\pi} \ln 2, & \Phi_{c2} &= -\frac{\mu_o h \mathbf{I}_c}{2\pi} \ln\left(\frac{d}{r_w}\right)\end{aligned}\quad (14.36)$$

Thus, the net fluxes through windows 1 and 2 are

$$\begin{aligned}\Phi_1 &= \Phi_{a1} + \Phi_{b1} + \Phi_{c1} = \frac{\mu_o h}{2\pi} \ln\left(\frac{d}{r_w}\right) \left[\mathbf{I}_a - \mathbf{I}_b - \frac{\ln 2}{\ln(d/r_w)} \mathbf{I}_c \right] \\ \Phi_2 &= \Phi_{a2} + \Phi_{b2} + \Phi_{c2} = \frac{\mu_o h}{2\pi} \ln\left(\frac{d}{r_w}\right) \left[\frac{\ln 2}{\ln(d/r_w)} \mathbf{I}_a + \mathbf{I}_b - \mathbf{I}_c \right]\end{aligned}\quad (14.37)$$

Considering \mathbf{I}_a , \mathbf{I}_b , and \mathbf{I}_c to be a positive-sequence set of currents and performing the phasor sums above, we get

$$\begin{aligned}\Phi_1 &= \frac{\mu_o h \mathbf{I}_a}{2\pi} \ln\left(\frac{d}{r_w}\right) \sqrt{3+g^2} e^{j\theta_1} & \theta_1 &= \tan^{-1} \left[\frac{\sqrt{3}(1-g)}{3+g} \right] \\ \Phi_2 &= \frac{\mu_o h \mathbf{I}_a}{2\pi} \ln\left(\frac{d}{r_w}\right) \sqrt{3+g^2} e^{j\theta_2} & \theta_2 &= -\tan^{-1} \left[\frac{\sqrt{3}}{g} \right]\end{aligned}\quad (14.38)$$

where

$$g = \frac{\ln 2}{\ln(d/r_w)}$$

From Faraday's law, we find that the voltages induced by the two fluxes are

$$\mathbf{V}_1 = -\frac{\mu_o h \omega \mathbf{I}_a}{2\pi} \ln\left(\frac{d}{r_w}\right) \sqrt{3+g^2} e^{j\theta_1}, \quad \mathbf{V}_2 = \mathbf{V}_1 e^{j\theta_2} \quad (14.39)$$

The direction of these voltages, or emfs, is given by Lenz's law, that is, they try to oppose the driving flux. We can assume that \mathbf{V}_1 is the reference phasor and thus drop the minus sign and phase factor from its expression. Then, \mathbf{V}_2 is given by Equation 14.39 with a phase of $\theta_2 - \theta_1$ relative to the reference phasor.

The induced voltages will attempt to drive currents through the tieplates and core in loops surrounding the two windows. This will be opposed by the resistances of the tieplates and core and by the self- and mutual inductances of the metallic window frames whether formed of core sections or of tieplate and clamp sections. We can treat these as lumped parameters, organized

into the circuits of Figure 14.19. Three circuits are involved because there are two tieplate circuits on either side of the core plus the core circuit. These are essentially isolated from each other except for coupling through the mutual inductances. Although the tieplate circuits share the top and bottom clamps in common, they are sufficiently symmetric that they can be regarded as separate circuits. We assume that magnetic coupling exists only between window 1 loops or window 2 loops but not between a window 1 loop and a window 2 loop. To make the circuit equations more symmetric, we have positioned V_2 in the circuit in such a way that we must take the negative of the expression in Equation 14.39.

Thus, for the voltage sources in the circuits of Figure 14.19, assuming V_1 is the reference phasor, we have

$$\begin{aligned} V_1 &= \mu_o h f I_a \ln\left(\frac{d}{r_w}\right) \sqrt{3+g^2}, \quad V_2 = -V_1 e^{j\theta} \\ \theta &= -\tan^{-1}\left(\frac{\sqrt{3}}{g}\right) - \tan^{-1}\left[\frac{\sqrt{3}(1-g)}{3+g}\right], \quad g = \frac{\ln 2}{\ln(d/r_w)} \end{aligned} \quad (14.40)$$

where f is the frequency in Hz.

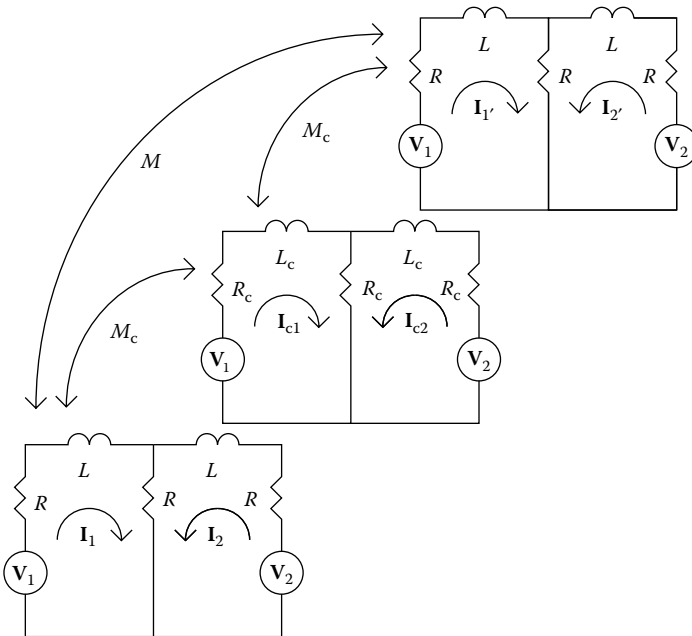


FIGURE 14.19

Equivalent circuits for tieplates and core driven by voltages induced through unbalanced currents. Here, 1 and 2 refer to the tieplate circuits on one side of the core, 1' and 2' refer to the tieplate circuits on the other side of the core, and c1 and c2 refer to the core circuits.

Using the notation of [Figure 14.19](#) and assuming sinusoidal conditions, we can write the circuit equations

$$\begin{pmatrix} \mathbf{V}_1 \\ \mathbf{V}_2 \\ \mathbf{V}_1 \\ \mathbf{V}_2 \\ \mathbf{V}_1 \\ \mathbf{V}_2 \end{pmatrix} = \begin{pmatrix} Z & R & j\omega M & 0 & j\omega M_c & 0 \\ R & Z & 0 & j\omega M & 0 & j\omega M_c \\ j\omega M & 0 & Z & R & j\omega M_c & 0 \\ 0 & j\omega M & R & Z & 0 & j\omega M_c \\ j\omega M_c & 0 & j\omega M_c & 0 & Z_c & R_c \\ 0 & j\omega M_c & 0 & j\omega M_c & R_c & Z_c \end{pmatrix} \begin{pmatrix} \mathbf{I}_1 \\ \mathbf{I}_2 \\ \mathbf{I}_1' \\ \mathbf{I}_2' \\ \mathbf{I}_{c1} \\ \mathbf{I}_{c2} \end{pmatrix} \quad (14.41)$$

where $Z = 2R + j\omega L$, $Z_c = 2R_c + j\omega L_c$

Note that R is the resistance of the tieplates associated with one leg side and R_c is the core resistance of one leg. The mutual and self-inductances refer to one window of the core. These can be solved for the currents using complex arithmetic. However, we can also solve them using real arithmetic by separating the vectors and matrix into real and imaginary parts. Thus, given a matrix equation:

$$\mathbf{V} = \mathbf{M}\mathbf{I} \quad (14.42)$$

Where \mathbf{V} and \mathbf{I} are complex column vectors and \mathbf{M} is a complex matrix, we write

$$\mathbf{V} = \mathbf{V}_{\text{Re}} + j\mathbf{V}_{\text{Im}}, \quad \mathbf{I} = \mathbf{I}_{\text{Re}} + j\mathbf{I}_{\text{Im}}, \quad \mathbf{M} = \mathbf{M}_{\text{Re}} + j\mathbf{M}_{\text{Im}} \quad (14.43)$$

Here, boldface type indicates both vector and phasor quantities. Substituting this separation into real and imaginary parts into Equation 14.42, we get

$$\begin{aligned} (\mathbf{V}_{\text{Re}} + j\mathbf{V}_{\text{Im}}) &= (\mathbf{M}_{\text{Re}} + j\mathbf{M}_{\text{Im}})(\mathbf{I}_{\text{Re}} + j\mathbf{I}_{\text{Im}}) \\ &= (\mathbf{M}_{\text{Re}} \mathbf{I}_{\text{Re}} - \mathbf{M}_{\text{Im}} \mathbf{I}_{\text{Im}}) + j(\mathbf{M}_{\text{Re}} \mathbf{I}_{\text{Im}} + \mathbf{M}_{\text{Im}} \mathbf{I}_{\text{Re}}) \end{aligned} \quad (14.44)$$

This reduces to two separate equations:

$$\mathbf{V}_{\text{Re}} = (\mathbf{M}_{\text{Re}} \mathbf{I}_{\text{Re}} - \mathbf{M}_{\text{Im}} \mathbf{I}_{\text{Im}}), \quad \mathbf{V}_{\text{Im}} = (\mathbf{M}_{\text{Re}} \mathbf{I}_{\text{Im}} + \mathbf{M}_{\text{Im}} \mathbf{I}_{\text{Re}}) \quad (14.45)$$

which can be organized into a larger matrix equation

$$\begin{pmatrix} \mathbf{V}_{\text{Re}} \\ \mathbf{V}_{\text{Im}} \end{pmatrix} = \begin{pmatrix} \mathbf{M}_{\text{Re}} & -\mathbf{M}_{\text{Im}} \\ \mathbf{M}_{\text{Im}} & \mathbf{M}_{\text{Re}} \end{pmatrix} \begin{pmatrix} \mathbf{I}_{\text{Re}} \\ \mathbf{I}_{\text{Im}} \end{pmatrix} \quad (14.46)$$

Here, the separate entries are real vectors and matrices. Thus, we have doubled the dimension of the original matrix Equation 14.41 from 6 to 12. This is still small considering the power of modern computers.

The remaining issues concern how to evaluate the resistances and the self- and mutual inductances in Equation 14.41. The resistance of a tieplate R can simply be taken as its DC resistance because it has a relatively small thickness. We can ignore the resistance of the clamps since these should have a much larger cross-sectional area than the tieplates. The core, with its fairly large radius and high permeability, will have an enhanced AC resistance relative to its DC value. The core resistance can be estimated from Figure 14.5, using an effective AC permeability and conductivity.

Since we do not expect total accuracy in this calculation in view of the approximations already made we can use approximate formulas for the self- and mutual inductances. For example, Grover [Gro73] gives a formula for the inductance of a rectangle of sides a and b made of wire with a circular cross section of radius r and relative permeability μ_r , which is (in SI units)

$$L = 4 \times 10^{-7} \left[a \ln \left(\frac{2a}{r} \right) + b \ln \left(\frac{2b}{r} \right) + 2\sqrt{a^2 + b^2} - a \sinh^{-1} \left(\frac{a}{b} \right) - b \sinh^{-1} \left(\frac{b}{a} \right) - 2(a+b) + \frac{\mu_r}{4}(a+b) \right] \quad (14.47)$$

where L is in henrys and lengths are in meters. Equation 14.47 can be applied directly to calculate the inductance of the core window. By defining an effective radius, it can be applied to the tieplate loop as well. In calculating the core inductance, remember that the core current generates magnetic field lines in the shape of concentric circles about the core centerline so that the appropriate relative permeability is roughly the effective permeability perpendicular to the laminations. For a stacking factor of 0.96 and infinitely permeable laminations, the effective perpendicular permeability is $\mu_r = 25$. Similarly, the effective tieplate relative permeability is close to 1.0 for both magnetic and stainless steel tieplates.

The mutual inductance terms are not as important, so an even cruder approximation may be used. Grover [Gro73] gives an expression for the mutual inductance between two equal coaxial squares of thin wire, which are close together. Letting s be the length of the side of the squares and d their separation, the mutual inductance (in SI units) is

$$M = 8 \times 10^{-7} s \left[\ln \left(\frac{s}{d} \right) - 0.7740 + \left(\frac{d}{s} \right) - 0.0429 \left(\frac{d}{s} \right)^2 - 0.109 \left(\frac{d}{s} \right)^4 \right] \quad (14.48)$$

where M is in henrys and lengths are in meters. With a little imagination, this can be applied to the present problem. Once Equation 14.41 or its equivalent Equation 14.46 is solved for the currents, the losses, which are I^2R type losses, can be calculated. As a numerical example, we found the core and

tieplate losses due to an unbalanced current of 20,000 A rms at 60 Hz in a transformer with the following geometric parameters:

Winding height (h)	0.813 m
Winding radius (r_w)	0.508 m
Leg center–center distance (d)	1.727 m
Core radius	0.483 m
Tieplate and core height	5.08 m
Tieplate width	0.229 m
Tieplate thickness	9.525×10^{-3} m

The tieplates were actually subdivided into three plates in the width direction, but this does not affect the calculation. For magnetic steel tieplates, the calculated core loss was 11 W and the total tieplate loss was 1182 W. For stainless steel tieplates, the calculated core loss was 28 W, and the total tieplate loss was 2293 W. For the magnetic steel case, the current in the core legs was about 200 A and in the tieplates about 600 A. For the stainless steel case, the current in the core legs was about 300 A and in the tieplates about 500 A. The stainless steel losses are higher mainly due to the higher resistivity of the material coupled with the fact that the impedances, which limit the currents, are mainly inductive and hence nearly the same for the two cases.

14.3.2.4 Tank and Clamp Losses

Tank and clamp losses are very difficult to calculate accurately. Here, we are referring to the tank and clamp losses produced by the leakage flux from the coils, examples of which were shown in Figures 14.6 and 14.7. The eddy current losses can be obtained from finite element calculations, especially 3D ones that can model the rectangular tank and leakage flux from all three phases simultaneously. These tend to be fairly time-consuming and not very routine. However, much can be done with a 2D approach. In [Pav93], several projection planes in the real 3D geometry were chosen for analysis with a 2D finite element program. The losses calculated with this approach agreed very favorably with the test results. As that study and ours show, 2D models allow quick assessment of the impact on losses of design changes such as the addition of tank and/or clamp shunts made of laminated electrical steel or the effect on losses of aluminum or copper shields at various locations. In fact, the losses in Figure 14.7 with tank and clamp shunts present were dramatically reduced when compared with those in Figure 14.6, where no shunts are present. While the real losses may not show as quantitative a reduction, the qualitative effect is real. Another study we performed very quickly using the parametric capability of the 2D modeling was to assess the impact of extending the clamp shunts beyond the top surface of the clamp. We found that some extension was useful in reducing the losses caused by stray flux hitting the vertical side of the clamp.

An example in which a 3D approach is crucial in understanding the effect of design options on losses is in the case of the laminated steel shunts on the clamps. The side clamps extend along all the three phases of a transformer, as shown in the top view of [Figure 14.20](#). Should the clamp shunts be made of laminations stacked flat on top of the clamps or should the laminations be on edge, that is, stacked perpendicularly to the top surface of the clamp? In addition, should the shunts extend uninterrupted along the full length of the clamps or can they be subdivided into sections that cover a region opposite each phase but with gaps in between? 2D models cannot really answer these questions. In fact, in a 2D model, the flux in the clamp shunts is forced to return to the core eventually, whereas in a 3D model the clamp shunt flux from the three phases can cancel within the shunts, assuming the shunts are continuous along the sides. Because of the laminated nature of the shunt material, the magnetic permeability and electrical conductivity are both anisotropic. This will affect both the flux and eddy current patterns in the shunts in a way that only a 3D model allowing for these anisotropies can capture. We will present some results obtained with a 3D finite element program later in this section that will examine this clamp shunt issue, as well as obtain tank and clamp losses that can be compared with test data. However, it is worthwhile first to consider analytic methods for obtaining these stray losses.

Analytic formulas for tank or clamp losses are useful. Once obtained, these enable a quick calculation of such losses at the design stage. By comparing these calculated losses with test data, we can assess their reliability. Often, simple correction factors can be applied to reach better agreement with the test data. Here, we present an analytic method for calculating tank losses based on solving Maxwell's equations in a simplified geometry [Lei99]. To appreciate the approximations that are made, consider the flux pattern near

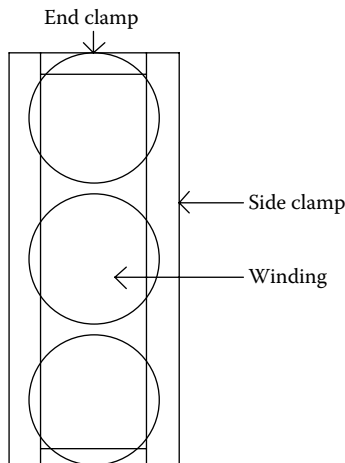


FIGURE 14.20

Geometry of clamp arrangement from a top view.

the tank wall produced by a generic two-winding transformer as shown in Figure 14.21a. The windings have no taps and uniform current density. Clamps are also absent.

Essentially, the flux enters the tank wall from the top of the windings and exits from the bottom of the windings. These directions can be reversed without changing the analysis. Figure 14.22 shows some details of the flux in the tank wall near the top of the windings. The flux enters the wall and is directed downward within the tank wall, increasing toward the winding center from the gradual accumulation of stray flux entering the tank wall. After passing through the vertical position corresponding to the windings' center, the flux begins to leave the tank wall and reenter the windings near their bottom. Thus, the vertical flux in the tank wall reaches a maximum at the windings' center. This is also the place where the losses in the tank wall are highest.

We will make the approximation that the flux (B-field) enters the tank wall perpendicularly and that this perpendicular flux has a sinusoidal distribution along the tank wall with the vertical center at a zero of the sine function. As Figure 14.21b shows, this is approximately true for the simple geometry shown. Further refinement can be achieved by Fourier analyzing the flux component perpendicular to the tank wall and applying the present analysis to each Fourier component. We will assume that the only other B-field

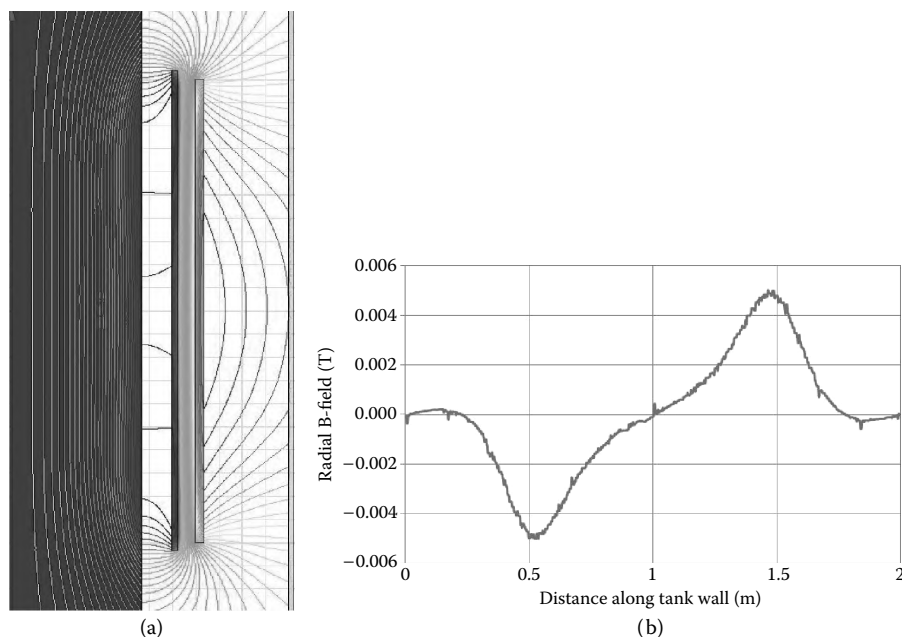
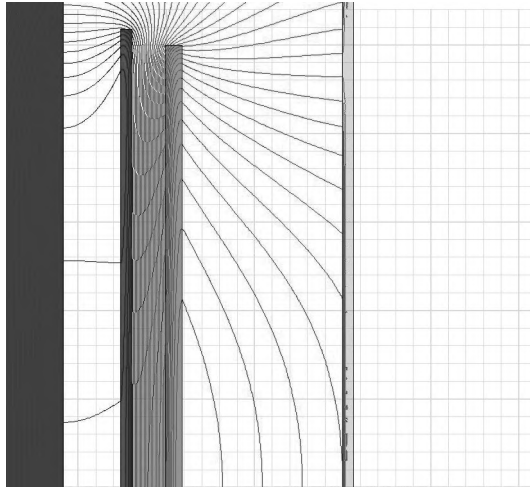
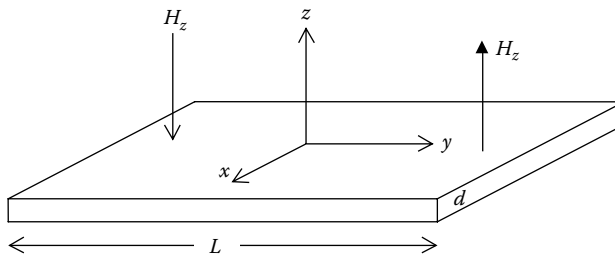


FIGURE 14.21

(See color insert following page 338.) (a) Flux pattern near the tank wall for a simple two-winding transformer with uniform current densities in the windings. (b) Radial B-field along a line next to the tank wall.

**FIGURE 14.22**

(See color insert following page 338.) Flux pattern in the tank wall from accumulation of stray flux from the top of the windings.

**FIGURE 14.23**

Geometry of tank wall with flux entering normal to its surface facing the windings. The wall is oriented horizontally. L is the effective height of the tank wall and will be taken as the wavelength of the sinusoidal B or H field normal to the tank wall.

component is vertically directed along and within the tank wall. The B -field is assumed to be independent of the tank wall dimension into the plane of the paper in [Figure 14.21a](#).

The geometry analyzed is shown in [Figure 14.23](#), which shows the tank wall in a horizontal position. The flux from the windings enters and leaves the tank wall in the z -direction. The flux within the wall is directed mainly in the y -direction with some in the z -direction. The wall is assumed to be infinite in the x -direction, that is the flux distribution is independent of this dimension. The losses calculated are per unit length in this direction so that the actual losses are obtained by multiplying the calculated losses by an effective length in the x -direction.

We assume that the tank is a homogeneous solid with permeability μ and conductivity σ . We assume that the fields are sinusoidal with angular frequency $\omega = 2\pi f$, with f the actual frequency in Hz. The relevant Maxwell's and Ohm's law equations to solve are

$$\begin{aligned}
 \nabla \times \mathbf{E} &= -\frac{\partial \mathbf{B}}{\partial t}, \quad \mathbf{B} = \mathbf{B}e^{j\omega t} \Rightarrow \nabla \times \mathbf{E} = -j\omega \mathbf{B} \\
 \mathbf{E} &= \frac{\mathbf{J}}{\sigma} \Rightarrow \nabla \times \mathbf{J} = -j\omega \sigma \mathbf{B} \\
 \nabla \times \mathbf{H} &= \mathbf{J} \Rightarrow \nabla \times (\nabla \times \mathbf{H}) = \nabla \times \mathbf{J} = -j\omega \sigma \mathbf{B} \\
 \nabla \times (\nabla \times \mathbf{H}) &= \nabla \times (\nabla \times \mathbf{H}) - \nabla^2 \mathbf{H} \\
 \mathbf{B} &= \mu \mathbf{H}, \quad \nabla \times \mathbf{B} = 0 \Rightarrow \nabla^2 \mathbf{H} = j\omega \sigma \mathbf{H}
 \end{aligned} \tag{14.49}$$

We assume that

$$\mathbf{H} = H_y(y, z)\mathbf{j} + H_z(y, z)\mathbf{k} \tag{14.50}$$

where \mathbf{j} and \mathbf{k} are unit vectors in the y - and z -directions, respectively. Using this, the last equation in Equation 14.49 becomes

$$\left(\frac{\partial^2 H_y}{\partial y^2} + \frac{\partial^2 H_y}{\partial z^2} \right) \mathbf{j} + \left(\frac{\partial^2 H_z}{\partial y^2} + \frac{\partial^2 H_z}{\partial z^2} \right) \mathbf{k} = j\omega \mu \sigma (H_y \mathbf{j} + H_z \mathbf{k}) \tag{14.51}$$

Let $k^2 = j\omega \mu \sigma$. The \mathbf{j} and \mathbf{k} component equations in Equation 14.51 can be solved separately. They both have the same form and differ only in the boundary conditions. Beginning with the \mathbf{k} equation, we have

$$\frac{\partial^2 H_z}{\partial y^2} + \frac{\partial^2 H_z}{\partial z^2} = k^2 H_z \tag{14.52}$$

With L the wavelength of the sinusoidal flux impinging normal to the tank wall, we assume a solution of Equation 14.52 in the form

$$H_z(y, z) = H_0 e^{\beta z} \sin\left(\frac{2\pi y}{L}\right) \tag{14.53}$$

Substituting Equation 14.53 into Equation 14.52, we obtain for β

$$\begin{aligned}
 \beta^2 &= k^2 + \left(\frac{2\pi}{L}\right)^2 = j\omega \mu \sigma + \left(\frac{2\pi}{L}\right)^2 = \sqrt{\left(\frac{2\pi}{L}\right)^4 + (\omega \mu \sigma)^2} e^{j \tan^{-1}\left(\frac{\omega \mu \sigma L^2}{4\pi^2}\right)} \\
 \beta &= \left[\left(\frac{2\pi}{L}\right)^4 + (\omega \mu \sigma)^2 \right]^{\frac{1}{4}} e^{\frac{j}{2} \tan^{-1}\left(\frac{\omega \mu \sigma L^2}{4\pi^2}\right)}
 \end{aligned} \tag{14.54}$$

Noting that the skin depth δ in the tank wall is given by Equation 14.24, we can express β in terms of this skin depth:

$$\beta = \frac{\sqrt{2}}{\delta} \left[1 + 4 \left(\frac{\pi\delta}{L} \right)^4 \right]^{\frac{1}{4}} e^{\frac{j}{2} \tan^{-1} \left(\frac{L}{\sqrt{2}\pi\delta} \right)^2} \quad (14.55)$$

For magnetic steel tank walls, the skin depth is very small, especially when compared with L , the length of the surface flux wave, so that $\pi\delta/L \approx 0$. Using this approximation, we have

$$\beta = \frac{\sqrt{2}}{\delta} e^{j\frac{\pi}{4}} = \frac{(1+j)}{\delta} \quad (14.56)$$

Thus, the exponential term in Equation 14.53 becomes

$$e^{\beta z} = e^{\frac{z}{\delta}} e^{j\frac{z}{\delta}} = e^{\frac{z}{\delta}} \left[\cos\left(\frac{z}{\delta}\right) + j \sin\left(\frac{z}{\delta}\right) \right] \quad (14.57)$$

Noting that z is negative into the tank wall, according to [Figure 14.23](#) where z is zero at the tank surface facing the windings and becomes negative into the tank wall, we see that the exponential term falls off rapidly with negative z .

According to Equation 14.49, we can obtain the solution for H_y by noting that

$$\nabla \cdot \mathbf{H} = 0 \Rightarrow \frac{\partial H_y}{\partial y} + \frac{\partial H_z}{\partial z} = 0 \Rightarrow \frac{\partial H_y}{\partial y} = -\beta H_0 \sin\left(\frac{2\pi y}{L}\right) e^{\beta z} \quad (14.58)$$

Integrating Equation 14.58, we get

$$H_y(y, z) = H_0 \left(\frac{\beta L}{2\pi} \right) e^{\beta z} \cos\left(\frac{2\pi y}{L}\right) \quad (14.59)$$

Thus, we get for \mathbf{H}

$$\mathbf{H} = H_0 e^{\beta z} \left[\left(\frac{\beta L}{2\pi} \right) \cos\left(\frac{2\pi y}{L}\right) \mathbf{j} + \sin\left(\frac{2\pi y}{L}\right) \mathbf{k} \right] \quad (14.60)$$

We see from this that the y -component of flux along the tank wall peaks at $y = 0$, whereas the z -component of flux is zero at this point. This is what we expect from the finite element [Figures 14.21](#) and [14.22](#).

We can obtain the current density \mathbf{J} by referring to Equation 14.49

$$\begin{aligned}
 \mathbf{J} &= \nabla \times \mathbf{H} = \left(\frac{\partial H_z}{\partial y} - \frac{\partial H_y}{\partial z} \right) \mathbf{i} \\
 &= H_0 e^{\beta z} \left[\left(\frac{2\pi}{L} \right) \cos \left(\frac{2\pi y}{L} \right) - \beta^2 \left(\frac{L}{2\pi} \right) \cos \left(\frac{2\pi y}{L} \right) \right] \mathbf{i} \\
 &= H_0 e^{\beta z} \left(\frac{2\pi}{L} \right) \cos \left(\frac{2\pi y}{L} \right) \left[1 - \left(\frac{\beta L}{2\pi} \right)^2 \right] \mathbf{i}
 \end{aligned} \tag{14.61}$$

Using the expression for β given in Equation 14.54 and the definition of skin depth, we get

$$\mathbf{J} = -j H_0 e^{\beta z} \left(\frac{L}{\pi \delta^2} \right) \cos \left(\frac{2\pi y}{L} \right) \mathbf{i} \tag{14.62}$$

The current density is directed along the unit vector \mathbf{i} , that is in the x -direction. From this, we can get the loss density per unit volume:

$$\begin{aligned}
 P_{\text{vol}} &= \frac{\mathbf{J} \cdot \mathbf{J}^*}{2\sigma} = \frac{1}{2\sigma} H_0^2 e^{(\beta+\beta^*)z} \left(\frac{L}{\pi \delta^2} \right)^2 \cos^2 \left(\frac{2\pi y}{L} \right) \\
 &= \frac{1}{2\sigma} H_0^2 e^{2z \text{Re}\beta} \left(\frac{L}{\pi \delta^2} \right)^2 \cos^2 \left(\frac{2\pi y}{L} \right)
 \end{aligned} \tag{14.63}$$

Note that the z -exponent is now real, indicating that the loss density drops off very rapidly with z with no oscillations. It is useful to integrate the z -dependence out so that the loss density will represent an effective surface loss density, P_{surf} . Because of the small skin depth and rapid exponential fall off, the z integral can be taken from $z = -\infty$ to $z = 0$. Thus, we get

$$P_{\text{surf}} = \frac{1}{\sigma \text{Re}\beta} H_0^2 \left(\frac{L}{2\pi \delta^2} \right)^2 \cos^2 \left(\frac{2\pi y}{L} \right) \tag{14.64}$$

We see that this loss density peaks at $y = 0$, that is at the winding center.

To get the total losses per unit length in the x -direction, we should integrate Equation 14.64 over the sine wave of flux from $y = -L/2$ to $L/2$. By doing this, the \cos^2 integral equals $L/2$ and we obtain

$$\frac{\text{Loss}}{\text{unit } x \text{ width}} = H_0^2 \left(\frac{L}{2\sigma \text{Re}\beta} \right) \left(\frac{L}{2\pi \delta^2} \right)^2 \tag{14.65}$$

Using the approximation for β given in Equation 14.56, which should be very accurate in this context, this last formula can be simplified to

$$\frac{\text{Loss}}{\text{unit } x \text{ width}} = H_0^2 \left(\frac{\pi}{\sigma} \right) \left(\frac{L}{2\pi\delta} \right)^3 = B_0^2 \left(\frac{\pi}{\mu^2\sigma} \right) \left(\frac{L}{2\pi\delta} \right)^3 \quad (14.66)$$

where the relationship between H and B has been used. Noting the definition of skin depth, we see that these losses increase with frequency to the 3/2 power, increase with conductivity to the 1/2 power (inversely with the resistivity to the 1/2 power), and increase inversely with the permeability to the 1/2 power. It has the expected dependence on the square of the amplitude of the B-field but a surprising dependence on the cube of the surface B-field wavelength, which is a little larger than the winding height.

As a numerical example, consider a magnetic steel tank wall with $\mu_r = 200$, $\mu = \mu_r 4\pi \times 10^{-7} \text{ H/m}$, $\sigma = 4 \times 10^6 (\Omega \cdot \text{m})^{-1}$, $\omega = 2\pi f = 2\pi(60 \text{ Hz})$, $L = 2 \text{ m}$, and $B_0 = 0.05 \text{ T}$. For these parameters, we get $\delta = 2.3 \times 10^{-3} \text{ m}$. We find the loss per meter in the x -direction = 82.4 kW/m. This should be multiplied by the effective length that these losses are present in the x -direction (which should be about equal to the diameter of the outer winding in meters) to get the total loss per leg at the tank wall. Of course for a three-phase unit, this should be multiplied by 3 to account for the losses on one tank side. For the other tank side and the tank ends, the B-field amplitude and wavelength need to be calculated and the same formula applied. Some additional effort must be applied to estimate the wavelength and amplitude of the approximate B-field wave at the tank surface, based on the Rabins' method of finding the B-field or on a finite element calculation. To reduce these losses, tank shunts are often used.

14.3.3 Stray Losses Obtained from 3D Finite Element Analyses

This section is based largely on [Ahu06]. Stray loss studies were performed for a three-phase, three-legged core. Because all three legs can be modeled and three-phase currents used, we will expect greater accuracy for these losses compared with analytical or 2D finite element analyses. Because anisotropic conductivity and permeability can be modeled in 3D, this presents the opportunity to study the relative effectiveness of shunts made of laminated core steel, which can be stacked flat or on edge. We also compare the 3D losses to losses obtained by analytic methods and test results for transformers of various ratings and types.

Transformer structural elements such as the clamps and tank, where much of the stray loss occurs, are generally made of magnetic steel, which has a small skin depth relative to the thickness of the material. To capture the eddy currents, a large number of finite elements will be required. In 2D this is not a problem, but in 3D the number of elements and solution times will be prohibitively large when modeling a large item such as a clamp or tank. A method

called the impedance boundary method has been developed to address this problem [Hol92], [Lam66]. This method only requires that the surface of the material be covered with finite elements. These are special elements called surface impedance elements. The properties of the material such as its relative permeability and conductivity are used in specifying these elements. Then, after running the 3D problem, the solution is processed to obtain the loss in watts, which is given by the formula

$$\text{Loss} = \sqrt{\frac{\omega \mu_r \mu_0}{8\sigma}} \int_{\text{Surface}} \mathbf{H}_t \cdot \mathbf{H}_t^* dS \quad (14.67)$$

where ω is the angular frequency $= 2\pi f$, f is the frequency in hertz, σ is the conductivity in $(\Omega\text{-m})^{-1}$, μ_r is the relative permeability, and μ_0 is the permeability of free space, which is $4\pi \times 10^{-7}$ H/m in SI units. \mathbf{H}_t is the tangential component of the magnetic field vector at the surface in amperes per meter and $*$ denotes complex conjugate. Note that if the currents in the windings are rms currents, the loss above must be multiplied by 2. We used Ansoft's software Maxwell 3D (Ansoft Corp., Pittsburg, PA) to perform the finite element calculations and obtain the losses.

Of course if materials having a relatively large skin depth such as aluminum, stainless steel, or copper are present, they are modeled with interior elements and the losses are calculated via the eddy currents generated inside them.

To get accurate and reproducible calculations, a reasonably large number of elements must be used, especially concentrated near the surfaces of interest. We found that ~100,000 3D elements were needed for most problems.

14.3.3.1 Shunts on the Clamps

To lower the stray losses in clamps with flat tops, shunts are typically placed on the top surface. These shunts extend continuously along the entire clamp, straddling all three phases. The idea is that the flux from the three balanced phases will cancel within the shunt. Thus, much of the leakage flux will be trapped within the shunt and therefore will not be available to induce losses in the conducting structural material.

An autotransformer with a maximum rating of 105 MVA (megavolt amperes) was modeled. The clamps were L-shaped and therefore had a large horizontal surface area, which was fairly close to the windings and their leakage flux. End clamps with a similar shape were also modeled. For the end clamps, the shunts cover only one phase so that the leakage flux must return to the core. A loss analysis with and without clamp shunts was performed. The three-phase model, excluding the tank, is shown in [Figure 14.24](#).

By giving the shunts the material properties of air or vacuum, the losses can be obtained in the clamps without the shunts. These are shown on the high voltage (HV) side bottom clamp in [Figure 14.25](#).

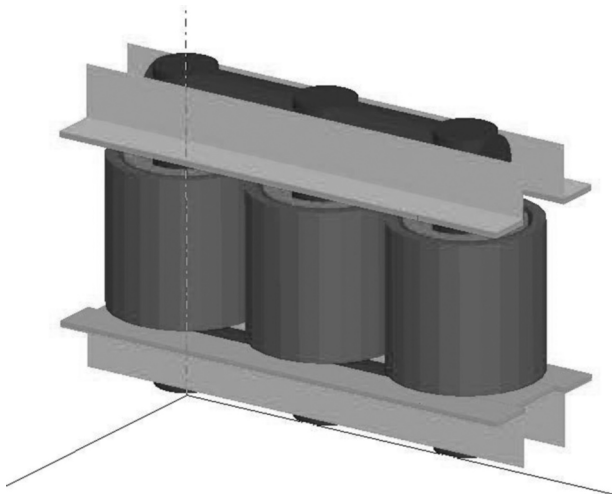


FIGURE 14.24
(See color insert following page 338.) Transformer geometry showing the three phases and the clamps. End clamps were modeled only on the bottom clamp structure for simplicity. There are two windings per leg shown in green and red. The clamp shunts are shown in coral.

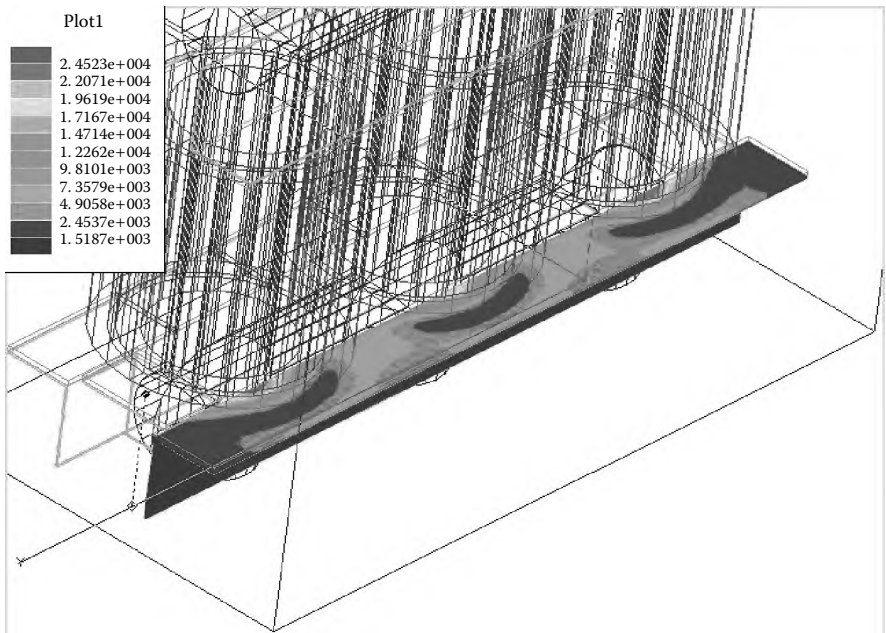


FIGURE 14.25
(See color insert following page 338.) Surface loss densities on the HV side bottom clamp without shunts. Note that the highest values are at the two end phases. There is more flux cancellation at the center phase than at the outer phases. The units are watts per square meter.

The shunts were 38 mm thick and made of high-permeability core laminations. The shunt material is assumed to be linear and therefore does not saturate. If an isolated spot in the material saturates, then we can assume that the flux density will redistribute itself within the material. However, if an entire cross section of the material saturates, this indicates that the flux will spill out of the material and create losses in the material that the shunts are supposed to protect. The flux densities in the shunts, having their core steel material properties, were obtained by looking at the shunt cross sections at various positions along the shunt. A contour plot of the flux density at the center leg position is shown in Figure 14.26.

The flux density is about 1.9 T at the leg centers, which is below the 2.1 T saturation limit. However, it averages about 2.1 T between legs, which is just at saturation. What is interesting is that the flux is fairly uniform along the side shunt. A vector diagram will show that it is directed along the shunts long direction, indicating that it remains within the shunt and does not leak out to any great extent. The surface loss densities on the side clamps are about 100 times lower than the loss densities without the shunts.

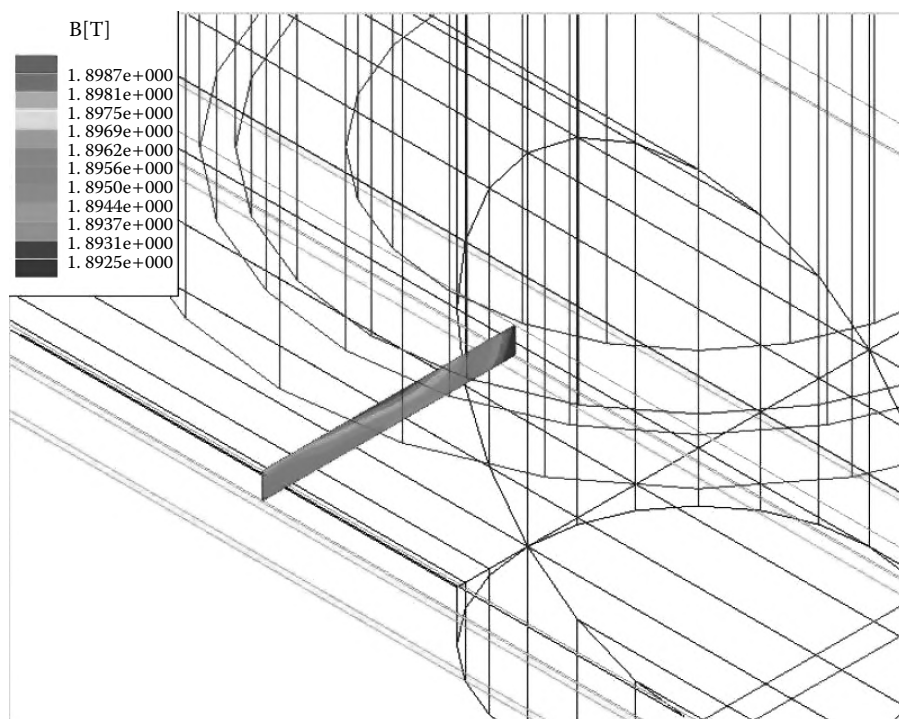


FIGURE 14.26

(See color insert following page 338.) Flux densities in the bottom LV side clamp shunt at the center of the center leg. The units are Teslas.

The flux density in the end clamp shunts is only about 0.2 T mainly because this flux is forced to return to the core through an air gap. They are therefore less effective at reducing the end clamp losses. This is another indication of how the flux from the three phases cancels within the side clamp shunts since it is not forced to return to the core.

14.3.3.2 Shunts on the Tank Wall

Shunts on the tank walls are frequently used to reduce losses or to eliminate hot spots. We will look at the effectiveness of these shunts when the laminations are placed flat on the tank wall or stacked on edge. Figure 14.27 shows a 160-MVA, two-winding power transformer with shunts on the low voltage (LV) side tank wall. The tank itself is not shown. The 25-mm thick shunts are centered on the three phases. In practice, if the shunts were stacked flat to the tank wall, they would be subdivided into several vertical sections to reduce the losses. Here, for simplicity, this has not been done. The shunts are made of core steel with the anisotropic properties shown in Table 14.1. The surface loss densities in the LV side tank wall without the shunts are

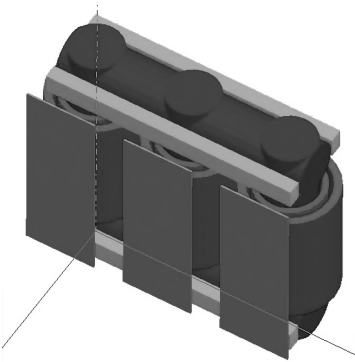
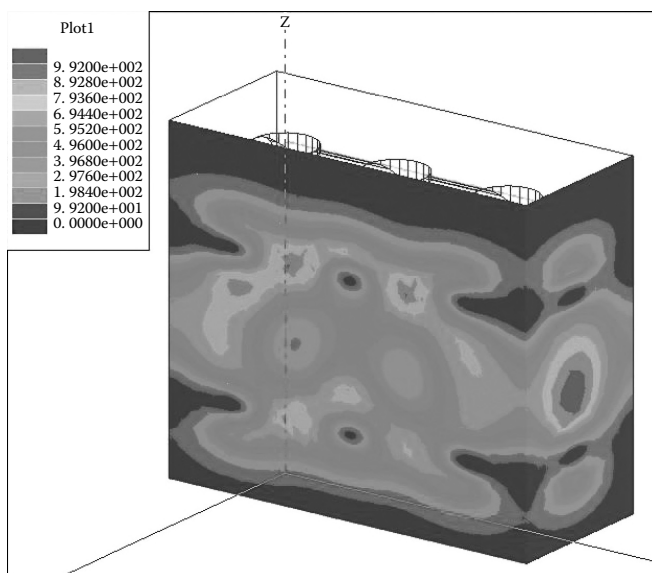


FIGURE 14.27
(See color insert following page 338.) Power transformer model with low-voltage side tank shunts.

TABLE 14.1
Characteristics of Stacked Core Laminations Used in the Finite Element Studies

Anisotropic Properties of Stacked Core Laminations		
	Relative AC Permeability	Resistivity ($\mu\Omega \cdot \text{cm}$)
Rolling direction	5000	50
Cross direction	2500	50
Stacking direction	25	50×10^4

**FIGURE 14.28**

(See color insert following page 338.) Surface loss densities in the LV side tank wall and end without shunts. The units are watts per square meter.

shown in Figure 14.28. Note that the losses are somewhat higher on the end phases than in the middle due to flux cancellation in the middle phase. Note also that on the end wall the losses are higher at the winding center than at the winding ends. This was a feature of the calculation performed in [Section 14.3.2.4](#).

The tank wall surface loss densities with the shunts present are shown in [Figure 14.29](#), which looks the same whether the shunts are placed flat or on edge. Tank wall and shunt losses are shown in [Table 14.2](#) for flat and on-edge shunts and compared with losses without the shunts. Since the shunts are on the LV side, they primarily lower the tank losses on this wall. The reduction in the LV side losses is about a factor of 10 for both shunt stackings. The flux densities in both types of shunt are well below saturation, and the losses in the shunts are negligible. It appears from this study that there is virtually no advantage to using shunts stacked on-edge as compared with flat shunts. Other considerations, such as convenience, economics, or possibly noise reduction should dictate the choice.

14.3.3.3 Effects of Three-Phase Currents on Losses

We have examined the effects of having three-phase currents in the windings. Because all three phases can be included, we might expect the losses to

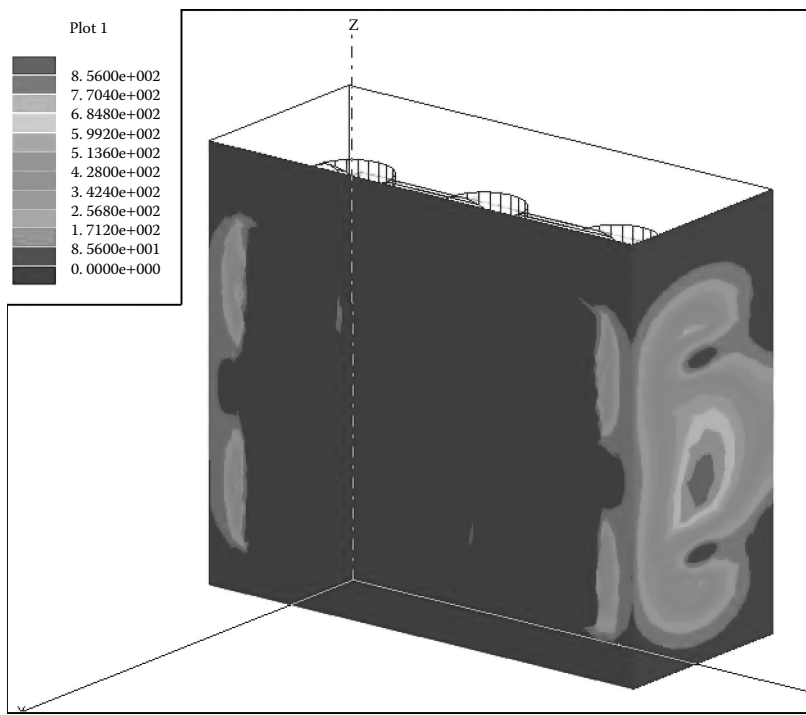


FIGURE 14.29
(See color insert following page 338.) Surface loss densities on the LV side and end tank walls when the shunts are present. There are no shunts on the end walls. The units are watts per square meter.

TABLE 14.2
Losses in the Tank Walls When the LV Side Shunts Are Stacked Flat or On-Edge to the Tank Wall

	Losses with and without 25-mm Shunts (kW)		
	No Shunts	Flat Shunts	On-Edge Shunts
Tank – LV side	13.57	1.14	1.14
Tank – HV side	5.97	5.87	5.87
Tank – left end	4.30	4.33	4.32
Tank – right end	4.85	4.30	4.29

be influenced by how the fluxes add (as phasors) in regions of flux overlap from the different phases. Losses were calculated with three-phase currents in the windings and with single-phase currents in each phase separately. The sum of the losses with the separate phases carrying current was then compared with the three-phase current losses. Transformers with several MVA

TABLE 14.3
Separate Phases versus Three-Phase Losses

	Tank + Clamp Losses (kW)			
	Three Phase	1 End Phase	Center Phase	Three Phase/ Separate
67 MVA	12.76	5.04	3.53	0.94
64 MVA	9.97	4.16	2.70	0.90
96 MVA	13.76	5.89	3.65	0.89

ratings were examined; this comparison is given in Table 14.3. The single end phase loss was multiplied by 2 and added to the center phase loss to get the separate phase loss. This is because the end phase geometry was identical for the two ends. As we can see, there is a loss reduction of about 10% when three-phase currents are used to compute the losses.

14.3.3.4 Stray Losses from the 3D Analysis versus Analytical and Test Losses

An important reason for using a 3D analysis is to improve the calculation of the losses. The rectangular shapes of tanks and shunts can be modeled in 3D, whereas they present a problem for 2D analyses, which generally model a single phase treated axisymmetrically. The increased model accuracy, along with the inclusion of three-phase effects, should improve the accuracy of the loss calculation. Since most of the stray losses, aside from eddy current losses in the windings, occur in materials that have a small skin depth, we must rely on the impedance boundary method to compute these losses.

One of the problems with evaluating the accuracy of the 3D loss calculation is that test stray losses are determined very indirectly. Only the total load losses are measured directly, and the calculated I^2R winding losses are subtracted from these. Then, the eddy current losses in the windings are estimated from a 2D flux plot together with analytical formulas that make use of the radial and axial field components throughout the windings. These winding eddy current losses are then subtracted and what remains are the stray losses. Sometimes, the eddy current losses in the windings are considered part of the stray losses, but not in this context. Since the I^2R + winding eddy losses comprise the major part of the total load losses, there can be considerable error in the result of subtracting two large numbers. Nevertheless, the losses were determined for several units using 3D finite element analysis and compared with losses extracted from the test data. Losses based on analytical formulas were also determined for a similar comparison. The losses were calculated separately for the clamps and tank. The miscellaneous losses include the tieplates and pressfeet (small structural supporting projections). [Table 14.4](#) shows the comparisons.

TABLE 14.4
Comparison of Stray Losses Determined by 3D FE and Analytical Methods with Losses Extracted from Test Data

MVA/Type	Analysis Type	Clamps	Tank	Misc	Total Calc	Test
60/	Analytic	8.22	5.26	1.0	14.48	21.7
Auto	3D	4.96	3.98	0.33	9.27	
64/	Analytic	10.25	4.29	1.54	16.08	22.6
Auto	3D	6.44	3.52	1.75	11.71	
96/	Analytic	13.81	6.29	1.71	21.81	21.6
Auto	3D	8.86	4.90	2.04	15.80	
60/	Analytic	5.17	2.72	1.17	9.06	9.30
Power	3D	3.62	0.63	0.57	4.82	
225/	Analytic	2.05	14.67	1.03	17.75	19.6
Auto	3D	1.32	3.29	1.83	6.44	

As we can see from Table 14.4, the analytical formulas better predict the test results. This is not unexpected, since these formulas were specifically adjusted to better agree with the measured losses for many units over a long period of time. The 3D losses are about 50% below the measured losses. The likely explanation can be found in [Kul04], which points out that the impedance boundary method is based on linear magnetic characteristics for the tank or clamp steel. In reality, because of the small skin depth, the material saturates magnetically within this depth. This requires a correction factor estimated to be in the range of 1.3–1.5 times the 3D losses. The inclusion of such a correction factor would cause a better agreement with the test losses in Table 14.4.

14.4 Tank and Shield Losses Due to Nearby Busbars

When busbars carrying relatively high current pass close to the tank wall, their magnetic field induces eddy currents in the wall, creating losses. The busbars are usually parallel to the tank wall over a certain length. Because of the magnetic field direction, laminated magnetic shunts positioned near the busbar are not as effective at reducing these losses as are metallic shields made of aluminum or copper. Since busbars are usually present from all three phases, the question arises as to how the grouping of two or three busbars from different phases would affect the losses. Intuitively, we expect a reduction in the losses due to some cancellation in the magnetic field from the different phases.

14.4.1 Losses Obtained with 2D Finite Element Study

These loss issues can be studied by means of a 2D finite element program if we assume that the busbars are infinitely long in the direction along their length. This geometry allows us to calculate losses per unit length, which can be multiplied by the total busbar length to get a reasonable approximation to the total loss. This can be made into a parametric study by varying the distance of the busbars from the tank wall. Other parameters, such as busbar dimensions, can be varied, but this will greatly complicate the study. We chose rather standard-sized busbars (76.2 mm \times 12.7 mm) with the long side perpendicular to the tank wall and separation distances of 82.6 mm when a grouping of busbars from different phases was studied. Of course, a particular geometry can always be studied if desired. Because eddy current losses are proportional to the square of the current when linear magnetic materials are involved, we need only calculate the losses at one current. These eddy current losses were studied with and without the presence of an aluminum shield, which was 12.7 mm thick and 230–300 mm wide placed flat on the tank wall. The losses in the busbars themselves were not considered in the study. We quote some of the qualitative results of this study here as an example of the useful insight that can be gained by such finite element analyses.

For a case of a single busbar, the losses in the tank wall without a shield drop off with the distance from the busbar to the tank wall, d , while the losses with shield are relatively constant with this distance. The losses with the shield include any losses in the tank as well. We found that shielding reduces the losses by about a factor of 5 at close distances (<150 mm) and a factor of 2–3 at further distances compared with the unshielded losses.

For a double busbar case, we found that the losses without a shield can be cut nearly in half by pairing two phases as compared to leaving them separate. We also found that shielding is very effective in reducing these losses.

For a group of three busbars, the losses are considerably reduced relative to the single or double busbar case. In this case, shielding does not provide much improvement. This is because the three-phase currents sum to zero at any instant in time, producing little net magnetic field at distances large relative to the conductor spacings.

It thus appears that loss reduction from busbars near bare tank walls can be achieved by pairing two or three phases together, with the latter being the most preferable. Shielding is very effective in reducing the losses associated with one or two busbars from different phases but not for three busbars, where the losses are small anyway.

14.4.2 Losses Obtained Analytically

This section is based on [Del03]. To further facilitate the calculation of the tank or shield losses due to the busbars, it will be useful to have an analytic

formula. Such a formula can be obtained if the tank or shield is allowed to be infinitely wide. Naturally, the losses will concentrate near the vicinity of the busbars so that the infinite approximation should have little influence on the real physical situation but makes the calculation feasible.

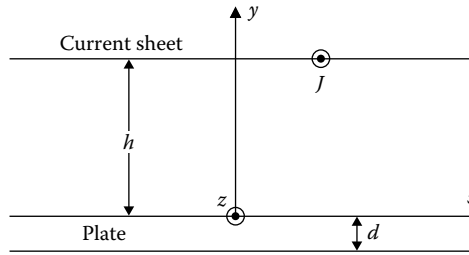
Previous work in this area focused on plate losses due to a current sheet [Jai70] and on plate losses due to a delta function current [Kul99]. These results can be extended by considering an arbitrary collection of busbars as approximated by a collection of delta function currents. The busbars can carry currents of differing magnitudes and phases, properties that are inherited by their associated delta function current approximations. Different busbar shapes can be approximated by strategically positioning the delta function currents (current filaments). For example, a rectangular shape can be approximated by a central current filament and one at each corner of the rectangle for a total of five filaments, each one carrying one-fifth of the total current. Other shapes, such as a circle, can be approximated using a central filament and others along the circumference. Additional filaments can be positioned for greater accuracy. Note that we consider the currents in the busbars to be uniformly distributed. Thus, we do not take into account the current redistribution in solid busbars that would result from the AC currents within the busbar or any of its neighbors.

14.4.2.1 Current Sheet

Jain and Ray [Jai70] solved the problem of a current sheet positioned at height h above a conducting plate of thickness d and carrying a current per unit width of

$$\mathbf{J} = J_0 \cos(ax) e^{j\omega t} \mathbf{k} \quad (14.68)$$

as shown in Figure 14.30. The current is directed along the positive z -axis as indicated by the unit vector \mathbf{k} in Equation 14.68. ω is the angular frequency, $\omega = 2\pi f$, where f is the frequency in hertz, and j is the unit imaginary. a is a parameter that plays the role of an inverse wavelength. J_0 has units of current per unit sheet width or amperes per meter in SI units, which are used here. The geometry in Figure 14.30 extends to infinity in all directions so that the plate and sheet are assumed to be infinitely long and wide. The plate and sheet are surrounded by air or any medium of relative permeability 1 and 0 conductivity. Because of the uniformity in the z -direction, the solution only depends on the x - and y -coordinates and will be given in SI units. It must be found throughout all space in order to satisfy all the boundary conditions.

**FIGURE 14.30**

Current sheet geometry. J indicates the direction of the current in the sheet, which is spread out over the entire sheet. (From Del Vecchio, R. M. 2003. *IEEE Trans Magn* 39(1):549–52. With permission.)

Here, we are only interested in the solution in the plate, in particular, the electric field E . Since it is z -directed like the current, we will drop the vector notation. The E -field in the plate due to the current sheet is given by

$$E_{\text{sheet}}(-d \leq y \leq 0) = -j\omega\mu_0 J_0 e^{j\omega t} e^{-ah} \cos(ax) \times \left[\frac{\left(a + \frac{\gamma}{\mu_r}\right) e^{\gamma(y+d)} - \left(a - \frac{\gamma}{\mu_r}\right) e^{-\gamma(y+d)}}{\left(a + \frac{\gamma}{\mu_r}\right)^2 e^{\gamma d} - \left(a - \frac{\gamma}{\mu_r}\right)^2 e^{-\gamma d}} \right] \quad (14.69)$$

$$\text{where } \gamma = \sqrt{a^2 + \frac{2j}{\delta^2}} \quad \text{and} \quad \delta = \sqrt{\frac{2}{\omega\mu_0\mu_r\sigma}}$$

where δ is the skin depth and j is the imaginary unit. In SI units, $\mu_0 = 4\pi \times 10^{-7}$ is the vacuum permeability, μ_r is the relative permeability, and σ is the conductivity of the plate. The plate thickness is d .

14.4.2.2 Delta Function Current

The dependence of E on x is that of a cosine function. This suggests that it can be a part of a Fourier expansion of a general function. In particular, the delta function of x , centered at the origin, has the expansion

$$\delta(0) = \frac{1}{\pi} \int_0^\infty \cos(ax) da \quad (14.70)$$

Thus, a current filament in the z -direction carrying a current I_0 can be written

$$\mathbf{I} = \frac{I_0}{\pi} \int_0^\infty \cos(ax) da \cdot \mathbf{e}^{j\omega t} \mathbf{k} \quad (14.71)$$

Basically, to get I , we sum over an infinite number of current sheets, each one contributing a current per unit width of

$$\frac{I_0}{\pi} \cos(ax) da \cdot \mathbf{e}^{j\omega t} \quad (14.72)$$

Since Maxwell's equations, including the constitutive relations as assumed here, are linear and since the E fields are unidirectional, the solution in the plate for the current in Equation 14.71 is given in terms of Equation 14.69 by

$$E_{\delta\text{-function}}(-d \leq y \leq 0) = \frac{I_0}{\pi J_0} \int_0^\infty E_{\text{sheet}}(-d \leq y \leq 0) da \quad (14.73)$$

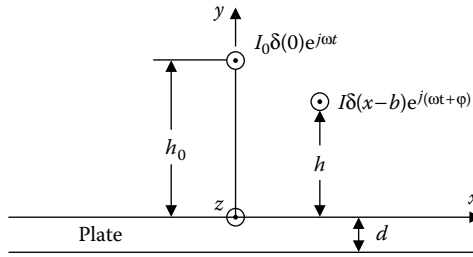
Now, consider a δ function offset from the origin by an amount b . This is given by the expansion

$$\delta(x - b) = \frac{1}{\pi} \int_0^\infty \cos[a(x - b)] da \quad (14.74)$$

If we assume that the sheet current in Equation 14.68 depends on $\cos[a(x - b)]$, the solution will go through unchanged except that $\cos[a(x - b)]$ will replace $\cos(ax)$ in Equation 14.69. Therefore, the corresponding δ function solution will be given by Equation 14.73, again with the cosine function replacement. More generally, if the current phase were different from zero so that the time dependence was given by $\exp[j(\omega t + \phi)]$, the same solution would have resulted with $\exp[j(\omega t + \phi)]$ replacing $\exp(j\omega t)$. The two types of delta function current filament are shown in [Figure 14.31](#).

The electric field in the plate from a general filament carrying current I , offset in space and time phase, is therefore given by

$$E_\delta = -j \frac{\omega \mu_0 I}{\pi} e^{j(\omega t + \phi)} \int_0^\infty da e^{-ah} \cos[a(x - b)] \times \left[\frac{\left(a + \frac{\gamma}{\mu_r} \right) e^{\gamma(y+d)} - \left(a - \frac{\gamma}{\mu_r} \right) e^{-\gamma(y+d)}}{\left(a + \frac{\gamma}{\mu_r} \right)^2 e^{\gamma d} - \left(a - \frac{\gamma}{\mu_r} \right)^2 e^{-\gamma d}} \right] \quad (14.75)$$

**FIGURE 14.31**

Delta function currents (filaments). (From Del Vecchio, R. M. 2003. *IEEE Trans Magn* 39(1):549–52. With permission.)

14.4.2.3 Collection of Delta Function Currents

Since we can approximate any shaped busbar or busbar collection with a number of current filaments, we will now consider the electric field in the plate due to such a collection. Again, because Maxwell's equations and the constitutive relations are linear, the net E -field in the plate, E_T , is simply the vector sum of all the individual E -fields. Since these vectors are colinear, we take the scalar sum $E_T = \sum_i E_i$, where E_i are the individual fields due to delta function currents. We label the individual current filaments and their parameters with i . Thus, h_i is the height of the filament above the plate, b_i is its offset from the origin, I_i is its current, and ϕ_i is its phase displacement in time.

The eddy current loss per unit length in the z -direction in the plate for such a collection of current filaments is given by

$$\text{Loss per unit length} = \sigma \int_{-d}^0 dy \int_{-\infty}^{\infty} dx E_T E_T^* \quad (14.76)$$

where $*$ denotes complex conjugation. The integral is over the cross-sectional area of the plate. We assume that the current and E -field magnitudes are rms quantities so that a factor of $1/2$ does not appear in Equation 14.76. Note that

$$E_T E_T^* = \left(\sum_i E_i \right) \left(\sum_k E_k^* \right) = \sum_i \sum_k E_i E_k^* \quad (14.77)$$

A typical term in the integrand is $E_i E_k^*$. The time exponential term in this product becomes $\exp[j(\phi_i - \phi_k)]$. However, the $E_k E_i^*$ term that also occurs in the sum will have $\exp[j(\phi_k - \phi_i)]$ as a time exponential term. Both of these terms are multiplied by the same factor and can therefore be added. Thus, in their sum, only the cosine part of this complex exponential survives because

the cos function is an even function and the sine function is an odd function of its argument. Thus,

$$\begin{aligned} e^{j(\varphi_i - \varphi_k)} + e^{j(\varphi_k - \varphi_i)} &= \cos(\varphi_i - \varphi_k) + j\sin(\varphi_i - \varphi_k) \\ &\quad + \cos(\varphi_k - \varphi_i) + j\sin(\varphi_k - \varphi_i) \\ &= 2\cos(\varphi_i - \varphi_k) \end{aligned} \quad (14.78)$$

Therefore, we should use a $\cos(\varphi_i - \varphi_k)$ term to multiply each term in the $E_i E_k^*$ product so that when the double sum is performed a factor of 2 will occur as required by Equation 14.78.

The remaining factor involves integrals over x , y , a , and a' . Both a and a' integrals are needed to express the two different E 's. An example of an E , expressed in terms of an a integral, is given in Equation 14.75. An E expressed in terms of an a' integral would have the a replaced by a' . The x integral in Equation 14.76 involves only the cos functions:

$$\int_{-\infty}^{\infty} \cos[a(x - b_i)] \cos[a'(x - b_k)] dx \quad (14.79)$$

Letting $\xi = x - b_i$, this can be rewritten

$$\int_{-\infty}^{\infty} \cos(a\xi) \cos[a'(\xi + b_i - b_k)] d\xi \quad (14.80)$$

Expanding the second cosine term, for the product in Equation 14.80 we get

$$\begin{aligned} \cos(a\xi) \cos[a'(\xi + b_i - b_k)] \\ &= \cos(a\xi) \times \{\cos(a'\xi) \cos[a'(b_i - b_k)] - \sin(a'\xi) \sin[a'(b_i - b_k)]\} \\ &= \cos(a\xi) \cos(a'\xi) \cos[a'(b_i - b_k)] - \cos(a\xi) \sin(a'\xi) \sin[a'(b_i - b_k)] \end{aligned} \quad (14.81)$$

Making use of

$$\begin{aligned} \int_{-\infty}^{\infty} \cos(a\xi) \cos(a'\xi) d\xi &= \pi \delta(a - a') \\ \int_{-\infty}^{\infty} \cos(a\xi) \sin(a'\xi) d\xi &= 0 \end{aligned} \quad (14.82)$$

we obtain for the integral in Equation 14.79

$$\int_{-\infty}^{\infty} \cos[a(x - b_i)] \cos[a'(x - b_k)] dx = \pi \delta(a - a') \cos[a'(b_i - b_k)] \quad (14.83)$$

Thus, the a' integral in Equation 14.76 can be performed immediately, removing the delta function, and we are left with

$$\begin{aligned} \text{Loss per unit length} = & \frac{\sigma(\omega\mu_0)^2}{\pi} \sum_i \sum_k \left\{ I_i I_k \cos(\phi_i - \phi_k) \int_0^a da e^{-a(h_i + h_k)} \cos[a(b_i - b_k)] \right. \\ & \times \int_{-d}^0 dy \left[\frac{\left(a + \frac{\gamma}{\mu_r} \right) e^{\gamma(y+d)} - \left(a - \frac{\gamma}{\mu_r} \right) e^{-\gamma(y+d)}}{\left(a + \frac{\gamma}{\mu_r} \right)^2 e^{\gamma d} - \left(a - \frac{\gamma}{\mu_r} \right)^2 e^{-\gamma d}} \right] \\ & \times \left. \left[\frac{\left(a + \frac{\gamma^*}{\mu_r} \right) e^{\gamma^*(y+d)} - \left(a - \frac{\gamma^*}{\mu_r} \right) e^{-\gamma^*(y+d)}}{\left(a + \frac{\gamma^*}{\mu_r} \right)^2 e^{\gamma^* d} - \left(a - \frac{\gamma^*}{\mu_r} \right)^2 e^{-\gamma^* d}} \right] \right\} \end{aligned} \quad (14.84)$$

Making use of

$$\begin{aligned} \gamma\gamma^* &= \eta^2 \\ \gamma + \gamma^* &= 2\eta \cos\theta \\ \gamma - \gamma^* &= j2\eta \sin\theta \end{aligned} \quad (14.85)$$

where

$$\begin{aligned} \eta &= \left[a^4 + \frac{4}{\delta^4} \right]^{1/4} \\ \theta &= \frac{1}{2} \tan^{-1} \left(\frac{2}{a^2 \delta^2} \right) \end{aligned} \quad (14.86)$$

after performing the y integral, we get for Equation 14.84

$$\begin{aligned} \text{Loss per unit length} = & \frac{\sigma(\omega\mu_0)^2}{\pi} \sum_i \sum_k \left\{ I_i I_k \cos(\phi_i - \phi_k) \right. \\ & \times \left. \int_0^a da e^{-a(h_i + h_k)} \cos[a(b_i - b_k)] \frac{\text{Numer}}{\text{Denom}} \right\} \end{aligned} \quad (14.87)$$

where

$$\begin{aligned}
 \text{Numer} = & \left(a^2 + \frac{2a\eta \cos \theta}{\mu_r} + \frac{\eta^2}{\mu_r^2} \right) \left(\frac{e^{2\eta d \cos \theta} - 1}{2\eta \cos \theta} \right) \\
 & + \left(a^2 - \frac{2a\eta \cos \theta}{\mu_r} + \frac{\eta^2}{\mu_r^2} \right) \left(\frac{1 - e^{-2\eta d \cos \theta}}{2\eta \cos \theta} \right) \\
 & - \left(a^2 - \frac{\eta^2}{\mu_r^2} \right) \frac{\sin(2\eta d \sin \theta)}{\eta \sin \theta} - \frac{2a}{\mu_r} [\cos(2\eta d \sin \theta) - 1]
 \end{aligned} \tag{14.88}$$

and

$$\begin{aligned}
 \text{Denom} = & \left(a^2 + \frac{2a\eta \cos \theta}{\mu_r} + \frac{\eta^2}{\mu_r^2} \right)^2 e^{2\eta d \cos \theta} \\
 & + \left(a^2 - \frac{2a\eta \cos \theta}{\mu_r} + \frac{\eta^2}{\mu_r^2} \right)^2 e^{-2\eta d \cos \theta} \\
 & - 2 \left[\left(a^2 - \frac{\eta^2}{\mu_r^2} \right)^2 - \left(\frac{2a\eta \sin \theta}{\mu_r} \right)^2 \right] \cos(2\eta d \sin \theta) \\
 & + \frac{8a\eta \sin \theta}{\mu_r} \left(a^2 - \frac{\eta^2}{\mu_r^2} \right) \sin(2\eta d \sin \theta)
 \end{aligned} \tag{14.89}$$

The a integral is left to perform numerically. The integral is well behaved at $a = 0$ and $\rightarrow 0$ as $a \rightarrow \infty$. Therefore, we need to evaluate to a large enough a so that the integrand becomes negligible. Also, since the i, k term in the double sum equals the k, i term for $i \neq k$, we need to evaluate only one of these terms and multiply the result by 2.

14.4.2.4 Model Studies

The methods outlined here were used to obtain the plate losses due to several configurations of rectangular busbars. Each of the busbars was modeled with a current filament in the center and one at each corner. Thus, the filament current associated with a busbar is 1/5 the busbar current. In the cases here, all the busbars carried the same current but with different phases. We used different plate materials with characteristics given in [Table 14.5](#).

The losses obtained from Equations 14.87 through 14.89 were compared with plate losses obtained with a 2D finite element program (Ansoft Corp.). We simulated the infinite geometry by choosing a plate width that was large

TABLE 14.5

Plate Characteristics

Plate Material	Relative Permeability	Conductivity ($\Omega \cdot \text{m}$) ⁻¹
Mag steel	200	4×10^6
Stainless	1	1.333×10^6
Aluminum	1	3.6×10^7
Copper	1	5×10^7

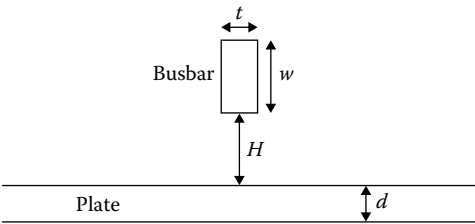


FIGURE 14.32

Single busbar geometry. (From Del Vecchio, R. M. 2003. *IEEE Trans Magn* 39(1):549–52. With permission.)

TABLE 14.6

Loss Comparisons for a Single Busbar

Plate Material	H (mm)	Analytic (W/m)	Finite Element (W/m)
Mag steel	127	1183	1197
Stainless	127	987	985
Aluminum	127	61.1	60.8
Copper	127	48.9	48.7
Mag steel	254	859	878
Stainless	254	664	670
Aluminum	254	34.3	34.6
Copper	254	27.4	27.7

The busbar current was 5000 A rms at 60 Hz.

compared with the busbar–plate separation and by using balloon boundary conditions.

The first configuration we studied was that of a single busbar positioned as shown in Figure 14.32. The busbar dimensions here and in all the subsequent configurations studied were $t = 12.7$ mm and $w = 76.2$ mm. The plate thickness was $d = 12.7$ mm and was kept the same in all the studies. The current details, separation distance H , and the loss comparisons are shown in Table 14.6, and they agree well.

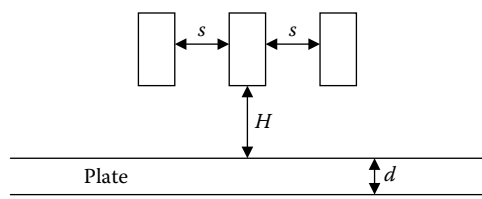


FIGURE 14.33 Three-phase busbar geometry. (From Del Vecchio, R. M. 2003. *IEEE Trans Magn* 39(1):549–52. With permission.)

TABLE 14.7
Loss Comparisons for a Three-Phase Busbar System

Plate Material	H (mm)	s (mm)	Analytic (W/m)	Finite Element (W/m)
Mag steel	127	101.6	214	213
Stainless	127	101.6	236	230
Aluminum	127	101.6	34.1	32.4
Copper	127	101.6	27.2	26.1

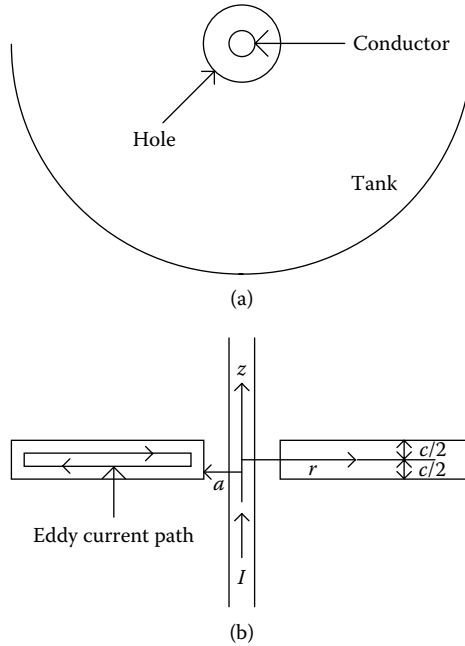
The currents in the busbars were 5000 A rms at 60 Hz with phases of 0°, 120°, and 240°.

The three-phase busbar configuration we studied is shown in Figure 14.33. An additional parameter, the separation distance between busbars, s , is shown in Figure 14.33. All the busbars are at a distance H from the plate and currents from a balanced three-phase system flow in them. For the parameters chosen, the analytic losses are compared with the finite element results in Table 14.7. Again the agreement is very good.

14.5 Tank Losses Associated with the Bushings

Current enters and leaves a transformer tank via the bushings. The bushings are designed to handle the voltage stresses associated with the voltage on the leads without breakdown and to dissipate heat due to the losses in the conductor that pass through the bushings. The conductor or lead, which must pass through the tank wall, creates a magnetic field that can generate eddy currents and accompanying losses in the tank wall near the lead. These losses must be calculated and appropriate steps taken to reduce them if necessary.

We can obtain a reasonable estimate of the tank losses due to a lead penetrating the tank wall by resorting to an idealized geometry as shown in Figure 14.34. Thus, we assume an infinitely long circular cross section lead

**FIGURE 14.34**

Idealized geometry and parameters used to calculate losses due to a lead passing through the tank: (a) top view and (b) side view.

passing perpendicularly through the center of a circular hole in the tank wall. We can assume that the tank wall itself is a circle of large radius centered on the hole. Since we expect the losses to concentrate near the hole, the actual radial extent of the tank will not matter much. Also, since most of the magnetic field that generates eddy currents in the tank comes from the portion of the lead near the tank, the infinite extent of the lead does not greatly affect the calculation.

The geometry in Figure 14.34 is axisymmetric. Thus, we need to work with Maxwell's equations in a cylindrical coordinate system. We assume that the tank wall has permeability μ and conductivity σ . Combining Maxwell's equations with Ohm's law inside the tank wall and assuming that \mathbf{H} varies harmonically in time as

$$\mathbf{H}(\mathbf{r}, t) = \mathbf{H}(\mathbf{r})e^{j\omega t} \quad (14.90)$$

we get

$$\nabla^2 \mathbf{H} = j\omega\mu\sigma\mathbf{H} \quad (14.91)$$

where \mathbf{H} in Equation 14.91 is only a function of position. Note that \mathbf{r} in bold-face type is a position vector in Equation 14.90.

Because the problem is axisymmetric, \mathbf{H} does not depend on ϕ , the azimuthal angle. We also assume that \mathbf{H} has only a ϕ component. This is all we need to produce the expected eddy current pattern indicated in [Figure 14.34b](#), where the eddy currents approach and leave the hole radially and the paths are completed along short sections in the z -direction. The approximate solution we develop here will neglect these z -directed eddy currents, which should not contribute much to the total loss. Thus, we have

$$\mathbf{H}(r) = H_\phi(r, z)\mathbf{a}_\phi \quad (14.92)$$

where \mathbf{a}_ϕ is the unit vector in the azimuthal direction. Expressing Equation 14.91 in cylindrical coordinates and using Equation 14.92, we get

$$\frac{1}{r} \frac{\partial}{\partial r} \left(r \frac{\partial H_\phi}{\partial r} \right) - \frac{H_\phi}{r^2} + \frac{\partial^2 H_\phi}{\partial z^2} = j\omega\mu\sigma H_\phi \quad (14.93)$$

We need to solve this equation subject to the following boundary conditions:

$$\begin{aligned} H_\phi &= \frac{I}{2\pi a} \quad \text{at } r = a \\ H_\phi &= 0 \quad \text{at } r = \infty \\ H_\phi &= \frac{I}{2\pi r} \quad \text{at } z = \pm \frac{c}{2} \end{aligned} \quad (14.94)$$

where a is the radius of the hole in the tank wall, c is the thickness of the tank wall, and I is the current in the lead. Once a solution is found, the current density \mathbf{J} is given by

$$\mathbf{J} = \nabla \times \mathbf{H} = -\frac{\partial H_\phi}{\partial z} \mathbf{r} + \frac{1}{r} \frac{\partial}{\partial r} (r H_\phi) \mathbf{k} \quad (14.95)$$

where \mathbf{r} and \mathbf{k} are unit vectors in the r - and z -directions, respectively.

To solve Equation 14.93, we use a separation of variables technique and write

$$H_\phi(r, z) = R(r)Z(z) \quad (14.96)$$

Substituting this into Equation 14.93 and dividing by RZ , we obtain

$$\frac{1}{R} \left[\frac{1}{r} \frac{\partial}{\partial r} \left(r \frac{\partial R}{\partial r} \right) - \frac{R}{r^2} \right] + \frac{1}{Z} \frac{\partial^2 Z}{\partial z^2} = j\omega\mu\sigma \quad (14.97)$$

Thus, we have two terms that are separately a function of r and z and whose sum is a constant. Hence, each term can be separately equated to a constant so long as their sum is $j\omega\mu\sigma$. We choose

$$\frac{1}{Z} \frac{\partial^2 Z}{\partial z^2} = j\omega\mu\sigma, \quad \frac{1}{R} \left[\frac{1}{r} \frac{\partial}{\partial r} \left(r \frac{\partial R}{\partial r} \right) - \frac{R}{r^2} \right] = 0 \quad (14.98)$$

Letting $k^2 = j\omega\mu\sigma$ so that

$$k = (1+j)q, \quad q = \sqrt{\frac{\omega\mu\sigma}{2}} \quad (14.99)$$

we can solve the first equation in Equation 14.98 up to an overall multiplicative constant, Z_0 :

$$Z(z) = Z_0 \cosh(kz) = Z_0 [\cosh(qz) \cos(qz) + j \sinh(qz) \sin(qz)] \quad (14.100)$$

This equation takes into account the symmetry about the $z = 0$ plane. The second equation in Equation 14.98 is solved up to an overall multiplicative constant, R_0 , by

$$R(r) = R_0 \frac{1}{r} \quad (14.101)$$

Thus, using the boundary conditions (Equation 14.94), the complete solution to Equation 14.97 is

$$H_\phi = \frac{I}{2\pi r} \left[\frac{\cosh(qz) \cos(qz) + j \sinh(qz) \sin(qz)}{\cosh(qc/2) \cos(qc/2) + j \sinh(qc/2) \sin(qc/2)} \right] \quad (14.102)$$

This does not exactly satisfy the first boundary condition in Equation 14.94 except in the limit of small $qc/2$.

Solving for the eddy currents (Equation 14.95) we see that the z -directed currents are zero when we substitute Equation 14.102. We expect that the losses contributed by these short paths will be small. Solving for the r -directed eddy currents, we obtain

$$J_r = \frac{Iq}{2\pi r} \left\{ \frac{\sinh(qz) \cos(qz) - \cosh(qz) \sin(qz) + j[\cosh(qz) \sin(qz) + \sinh(qz) \cos(qz)]}{\cosh(qc/2) \cos(qc/2) + j \sinh(qc/2) \sin(qc/2)} \right\} \quad (14.103)$$

and the loss density as a function of position, assuming I is an rms current, is

$$\frac{|J_r|^2}{\sigma} = \frac{2}{\sigma} \left(\frac{Iq}{2\pi r} \right)^2 \left[\frac{\cosh(2qz) - \cos(2qz)}{\cosh(qc) + \cos(qc)} \right] \quad (14.104)$$

This drops off with radius $1/r^2$ and so is highest near the opening. The total loss is given by

$$\text{Loss}_{\text{bush}} = 2\pi \int_{a-c/2}^b \int_{-c/2}^{c/2} \frac{|J_r|^2}{\sigma} r \, dr \, dz \quad (14.105)$$

We choose the upper limit of the r integration, b , to be a large enough radius that the tank area of interest is covered. The result will not be too sensitive to the exact value chosen. Performing the integrations, we obtain

$$\text{Loss}_{\text{bush}} = \frac{I^2 q}{\pi \sigma} \ln\left(\frac{b}{a}\right) \left[\frac{\sinh(qc) - \sin(qc)}{\cosh(qc) + \cos(qc)} \right] \quad (14.106)$$

For a magnetic steel tank wall, using $\mu_r = 200$, $\sigma = 4 \times 10^6 \, (\Omega \cdot \text{m})^{-1}$, $f = 60 \, \text{Hz}$, $c = 9.52 \times 10^{-3} \, \text{m}$, we get $qc = 4.15$. Thus, the small qc approximation to Equation 14.106 cannot be used. However, for a stainless steel tank wall of the same thickness and frequency, using $\mu_r = 1$, $\mu = 4\pi \times 10^{-7} \, \text{H/m}$, $\sigma = 1.33 \times 10^6 \, (\Omega \cdot \text{m})^{-1}$, we have $qc = 0.17$ so the low qc limit may be used. This is

$$\text{Loss}_{\text{bush}} \xrightarrow{\text{small } qc} \left(\frac{\pi}{6} \right) \frac{I^2 f^2 \mu^2 c^3}{\rho} \ln\left(\frac{b}{a}\right) \quad (14.107)$$

where $\omega = 2\pi f$ and $\sigma = 1/\rho$ have been substituted. Applying these last two equations to the case where $I = 1000 \, \text{A rms}$ (for normalization purposes), the hole radius $a = 165 \, \text{mm}$, the outer radius $b = 910 \, \text{mm}$, and using the above parameters for the two types of steel, we get $\text{Loss}_{\text{bush}}(\text{mag steel}) = 61.9 \, \text{W}/(\text{kA}_{\text{rms}})^2$ and $\text{Loss}_{\text{bush}}(\text{stainless}) = 5.87 \times 10^{-3} \, \text{W}/(\text{kA}_{\text{rms}})^2$. These losses are associated with each bushing. Applying this to a situation where the lead is carrying $10 \, \text{kA}_{\text{rms}}$, the loss in a magnetic steel tank wall would be $6190 \, \text{W}$ per bushing and in a stainless steel tank wall would be $0.587 \, \text{W}$ per bushing. These should be multiplied by the number of bushings carrying the given current to get the total tank loss associated with the bushings. Thus, when the leads carry heavy currents, it might be worthwhile to insert a stainless steel section of tank around the bushings, especially since these losses are concentrated in the part of the tank wall near the opening.

Another method for reducing these losses is to use a stainless steel insert only around part of the opening. This will reduce the effective permeability, as seen by the magnetic field that travels in concentric circles about the center of the opening. We can estimate the effective permeability using a magnetic circuit approach. This can then be substituted into the previous formulas to calculate the loss. A finite element 3D calculation, however, shows that this underestimates the loss. The flux is not confined to the tank wall, as it essentially is when the material is all magnetic steel, but can travel around the stainless insert in the surrounding air or oil.

14.5.1 Comparison with a 3D Finite Element Calculation

To check the above analytical result, a 3D finite element analysis was performed, using a large number of elements within the tank wall so that the eddy current distribution could be captured and used to obtain the losses. The losses were also calculated using the impedance boundary method, which requires far fewer elements. The geometry, shown in Figure 14.35, consists of a circular disk with a hole in it. The outer diameter of the disk is 305 mm, and the diameter of the hole is 132 mm. The disk is 9.5 mm thick and made of low carbon magnetic steel with a relative permeability of 200 and a conductivity of $4 \times 10^6 (\Omega \cdot \text{m})^{-1}$. The lead is 1270 mm long and has a diameter of 25.4 mm. The rms current in the lead is 5800 A at 60 Hz.

Figure 14.36 shows the surface loss densities on the plate obtained with the surface impedance boundary method. Figure 14.36 shows that the highest losses are near the center hole as expected. The total loss was 1095 W, calculated using the impedance boundary method. When the disk was internally subdivided into a large number of 3D finite elements and the losses were calculated by integrating the eddy current losses in the standard manner,

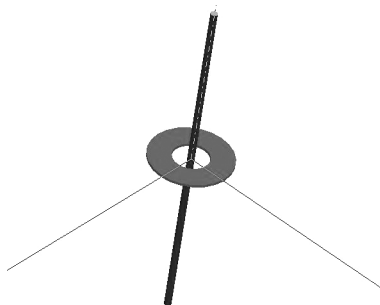


FIGURE 14.35

Geometry of lead passing through a plate with a hole in it to simulate a lead passing through a tank top.

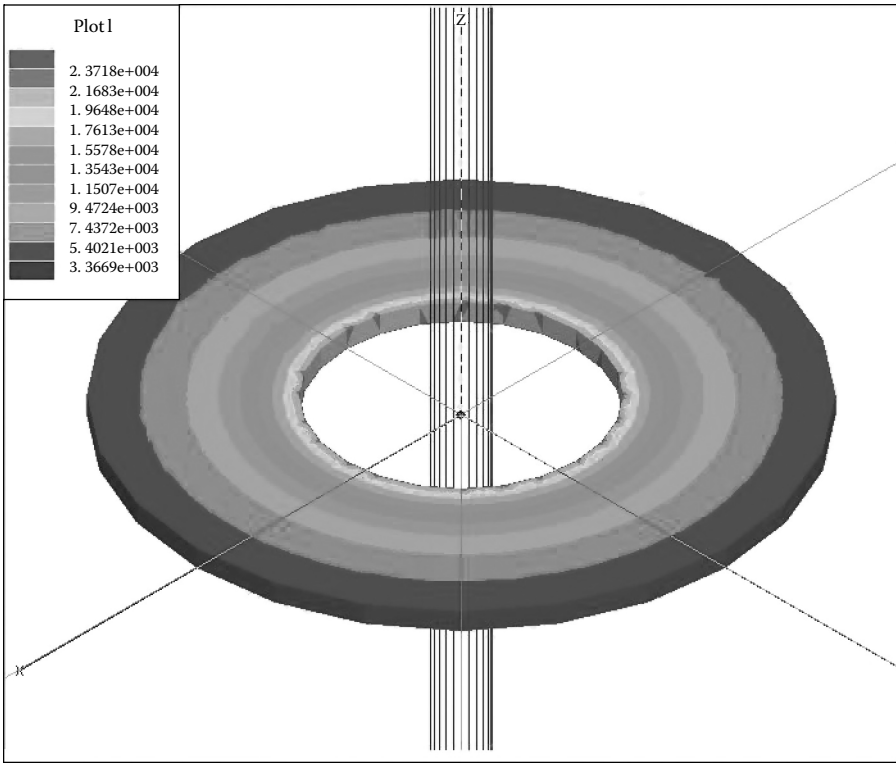


FIGURE 14.36
(See color insert following page 338.) Surface losses on the magnetic steel disk. The scale is in W/m^2 . Peak currents were used in generating this plot so the loss densities include the factor of 2, which will be necessary if rms currents were used.

a loss of 998 W was obtained. The two methods are in near agreement on this problem. Using the analytic formula developed in Equation 14.106 for the losses, the losses obtained were 1019 W. This agrees with both types of finite element analyses. Note however that all the methods used assume that the material is linear. This can require some correction for saturation effects.

15

Thermal Design

15.1 Introduction

In this chapter we will present a thermal model of an oil cooled power transformer, along with details of computer implementation and experimental verification. Any such model, particularly of such a complex system, is necessarily approximate and assumes that the oil flows in definite paths and ignores local circulation or eddy patterns that may arise. The most detailed model assumes that the oil flow through the disk coils is guided by oil-flow washers. We will also discuss oil flow through vertical ducts in less detail. Recent studies have shown that irregular eddy flow patterns may exist in nondirected oil-flow cooling in vertical ducts [Pie92]. Such patterns may also occur in the bulk tank oil. We assume these are small compared with the major or average convective cooling flow in the coil or in the tank. We further assume that the convective flow in the tank results in a linear temperature profile from the bottom of the radiators to the top of the coils in the tank oil external to the coils. The model ignores localized heating that may occur, due to high-current-carrying leads near the tank wall, for example. It accounts for these types of stray losses in an average way only. However, a localized distribution of eddy current losses in the coils is allowed for, along with the normal I^2R losses.

The radiators we model consist of a collection of radiator plates spaced equally along inlet and outlet pipes. The plates contain several parallel vertical ducts that have oblong-shaped, nearly rectangular, cross sections. Fans, vertically mounted, may or may not be present (or turned on). In addition to radiator cooling, cooling also occurs from the tank walls through both natural convection to the surrounding air and radiation. Although the oil can be pumped through the radiators, most of our designs are without pumps and we assume the oil flow in the radiators and coils to be laminar. This determines the expressions we will use for the heat transfer and friction coefficients along the oil-flow paths.

Our disk-winding model is similar to that of Oliver [Oli80]. However, since we will consider the whole transformer, we need to reconcile the

heat generated by individual coils and stray losses with heat dissipation or cooling in the radiator and tank in an overall iteration scheme to arrive at a steady-state condition. In transient heating, steady state is only reached gradually.

Previous thermal models of whole transformers have focused on developing analytic formulas with adjustable parameters to predict overall temperature rises in the oil and coils [IEE81], [Blu51], [Eas65], [Tay58], [Aub92], and [Pie92a]. Although these models produce acceptable results on average for a standard design, they are less reliable for a new design. The approach taken here is to develop a model to describe the basic physical processes occurring in the unit so that reliance on parameter fitting is minimized. Such an approach can accommodate future improvements in terms of a more detailed description of the basic processes or the addition of new features as a result of a design change.

15.2 Thermal Model of a Disk Coil with Directed Oil Flow

This section is essentially a reprint of our published paper [Del99]. We assume the disk coil to be subdivided into directed oil flow cooling paths as shown in [Figure 15.1](#). We number the disks, nodes, and paths, using the scheme shown. The geometry is really cylindrical and the inner radius R_{in} is indicated. Only one section (the region between two oil-flow washers) and part of a second is shown, but there can be as many sections as desired. Each section can contain different numbers of disks and the number of turns per disk, insulation thickness, and so on can vary from section to section. The duct sizes can vary within a section as well as from section to section.

[Figure 15.2](#) shows the cross-sectional areas, A , and hydraulic diameters, D , of the various paths. Normally the vertical duct geometric parameters, labeled 1 and 2, are the same throughout the coil, but the horizontal duct values can differ along the coil.

In [Figure 15.3](#) we have indicated the unknowns that must be solved for at each node and path. These include the nodal temperatures, T , the nodal pressures, P , the path oil velocities, v , the path oil temperature rises, ΔT , and the disk temperatures, T_c . These are labeled with their corresponding node, path, or disk number. Note that the surface heat transfer coefficients from the coil surfaces are associated with the oil path with which the surfaces are in contact. We do not allow for a temperature profile along a single disk but assume that each disk is at a uniform temperature. This is an approximation that can be refined if more detail is required.

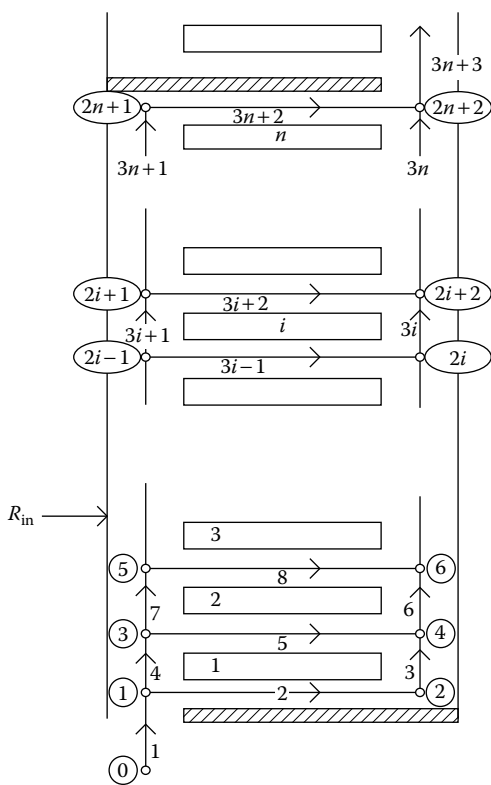


FIGURE 15.1 Disk, node, and path numbering scheme for a disk coil with directed oil flow. (From Del Vecchio, R. M., and P. Feghali. 1999. Thermal model of a disk coil with directed oil flow. IEEE Transmission and Distribution Conference, New Orleans, LA, 914–9. With permission.)

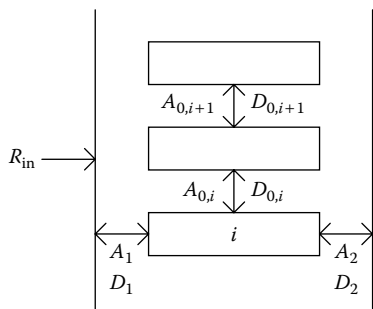


FIGURE 15.2 Cross-sectional areas and hydraulic diameters of different oil paths. The vertical ducts are assumed to be uniform along the coil. (From Del Vecchio, R. M., and P. Feghali. 1999. Thermal model of a disk coil with directed oil flow. IEEE Transmission and Distribution Conference, New Orleans, LA, 914–9. With permission.)

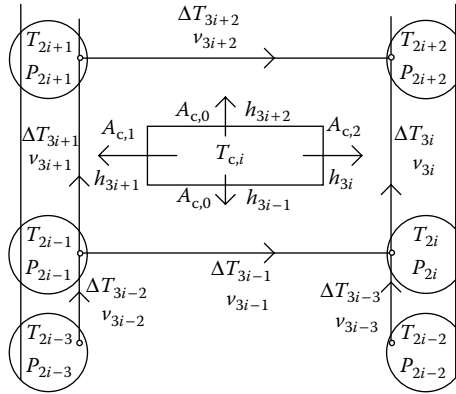


FIGURE 15.3

Numbering scheme for disk temperatures, node temperatures, node pressures, path velocities, and path temperature changes. Also indicated are the heat transfer surface areas, A_c , and the heat transfer coefficients, h , for these surfaces. (From Del Vecchio, R. M., and P. Feghali. 1999. Thermal model of a disk coil with directed oil flow. IEEE Transmission and Distribution Conference, New Orleans, LA, 914–9. With permission.)

15.2.1 Oil Pressures and Velocities

Along a given path, the oil velocities are uniform since the cross-sectional area is assumed to remain constant. Ignoring gravitational effects, which do not influence the oil flow, the pressure drop along a given path is only required to overcome friction. Treating a generic path, labeling the pressures at the beginning and end of the path P_1 and P_2 respectively, and using standard notation [Dai73], we can write

$$P_1 - P_2 = \frac{1}{2} \rho f \frac{L}{D} v^2 \quad (15.1)$$

where ρ is the fluid density, f is the friction coefficient, L is the path length, D is the hydraulic diameter, and v is the fluid velocity. We note that the hydraulic diameter is given by

$$D = 4 \times \text{cross-sectional area} / \text{wetted perimeter}$$

SI units are used throughout this chapter. For laminar flow in circular ducts, $f = 64 / \text{Re}_D$, where Re_D is the Reynolds number, given by

$$\text{Re}_D = \frac{\rho v D}{\mu} \quad (15.2)$$

where μ is the fluid viscosity. For laminar flow in noncircular ducts, the number 64 in the expression for f changes. In particular, for rectangular ducts with sides a and b with $a < b$, we can write

$$f = \frac{K(a/b)}{\text{Re}_D} \quad (15.3)$$

where $K(a/b)$ is given approximately by

$$K(a/b) = 56.91 + 40.31(e^{-3.5a/b} - 0.0302) \quad (15.4)$$

This expression is based on a fit to a table given in reference [Ols80].

Substituting Equations 15.2 and 15.3 into Equation 15.1, we obtain

$$P_1 - P_2 = \frac{1}{2} \frac{\mu K L}{D^2} v \quad (15.5)$$

where $K = K(a/b)$ is implied. This equation is linear in the pressures and velocities. However, the oil viscosity is temperature dependent, which will necessitate an iterative solution. Based on a table of transformer oil viscosities versus temperature given in [Kre80], we achieved a good fit to the table with the expression

$$\mu = \frac{6900}{(T + 50)^3} \quad (15.6)$$

with T in Celsius and μ in Newton second per square meter.

For nonlaminar flow ($Re_D > 2000$), the expression for f is more complicated and Equation 15.5 would no longer be linear in v . Note that we ignore the extra friction arising from flow branching and direction changing at the nodes. There is considerable uncertainty in the literature as to what the additional frictional effects are for laminar flow. Instead we have chosen to allow the friction coefficient in Equation 15.3 to be multiplied by a correction factor that is the same for all the branches. This correction factor is close to 1 in practice for disk coils.

We get an equation of the same type as Equation 15.5 for all the paths in Figure 15.1. Note that we need only to solve for the unknowns in one section at a time since the values at the topmost node and path can be taken as input to the next section. There are $3n + 2$ paths in the section, where n is the number of disks. However, the number of pressure unknowns is $2n + 2$, that is, the number of nodes. We do not include node 0, where the pressure must be input. This pressure will be given by the overall pressure drop through the coil as determined by buoyancy effects, as we will discuss below. The number of velocity unknowns is $3n + 2$, or the number of paths. Hence $2n + 2$ additional equations are required to solve for the pressures and oil velocities. We will treat the temperatures as fixed during the solution process. A separate set of equations will be derived for the temperatures and the two systems will ultimately be coupled through back and forth iteration.

The additional equations needed to solve for the pressures and velocity unknowns come from conservation of mass at the nodes. The mass of fluid of velocity v flowing through a duct of cross-sectional area A per unit time, dM/dt , is given by

$$\frac{dM}{dt} = \rho A v \quad (15.7)$$

Since the fluid is nearly incompressible, we can consider conservation of volume instead, where $Q = Av$ is the volume flow per unit time. Referring to [Figure 15.3](#) and using the areas indicated in [Figure 15.2](#), for a typical inner (smallest radii) node, $2i - 1$, we obtain

$$A_1 v_{3i-2} = A_1 v_{3i+1} + A_{0,i} V_{3i-1} \quad (15.8)$$

and for a typical outer node, $2i$, we obtain

$$A_0 v_{3i-1} + A_2 v_{3i-3} = A_2 v_{3i} \quad (15.9)$$

However, the nodes at the beginning and end require special treatment (see [Figure 15.1](#)). We want to calculate the velocity on path $3n + 3$, which is input to the next coil. We assume that the input velocity at the bottom of the section, v_1 on path 1, is known. It will be determined by an overall energy balance. This leaves $3n + 2$ unknown velocities to solve for, but v_{3n+3} will be re-labeled v_1 and v_1 will be called v_0 , a known input velocity, that is, $v_1 = v_0$. Thus, at the nodes requiring special treatment, we have at node 1

$$A_1 v_0 = A_1 v_4 + A_{0,1} v_2 \quad (15.10)$$

At node 2 we have

$$A_{0,1} v_2 = A_2 v_3 \quad (15.11)$$

At node $2n + 1$ we have

$$A_1 v_{3n+1} = A_{0,n+1} v_{3n+2} \quad (15.12)$$

And at node $2n + 2$ we have

$$A_{0,n+1} v_{3n+2} + A_2 v_{3n} = A_2 v_1 \quad (15.13)$$

We have $5n + 4$ equations to solve for the pressure and velocity unknowns, where n is the number of disks in the section. For $n = 30$, which is about as large a number of disks as would be used in one section, this yields 154 equations. Since the equations are quite sparse, we used a linear equation solver that employs sparsity techniques. Note that the cross-sectional areas must be calculated, taking into account the area lost due to key spacers or vertical spacer sticks. These also influence the hydraulic diameters.

The overall pressure drop through the coil is produced by the difference in buoyancy between the hot oil inside the coil's cooling ducts and the cooler tank oil outside the coil. Thus

$$\Delta P_{\text{coil}} = (\rho_{\text{ave,out}} - \rho_{\text{ave,in}}) g H \quad (15.14)$$

where $\rho_{\text{ave,in}}$ is the average oil density inside the coil, $\rho_{\text{ave,out}}$ the average density outside the coil, g is the acceleration of gravity, and H is the coil height. Letting β be the volume coefficient of thermal expansion, we have

$$\frac{1}{\rho} \frac{d\rho}{dT} = -\beta \quad (15.15)$$

Thus, since $\beta = 6.8 \times 10^{-4}/\text{K}$ for transformer oil, we have, to a good approximation over a reasonably large temperature range, $\Delta\rho = -\beta\rho\Delta T$ so that Equation 15.14 can be written

$$\Delta P_{\text{coil}} = \beta\rho g H (T_{\text{ave,in}} - T_{\text{ave,out}}) \quad (15.16)$$

Because we only consider pressures that produce oil flows, the pressure at the top of the coil when steady state is achieved should be zero. This means that $\Delta P_{\text{coil}} = P_0$, the pressure at node 0 in [Figure 15.1](#).

The oil velocity into the coil along path 1 is determined by the overall energy balance. The energy per unit time acquired by the oil must equal the energy per unit time lost by the coil. In steady state, the latter is simply the total resistive loss of the coil. Thus

$$\rho c v_0 A_1 \Delta T_{\text{oil}} = \sum_{i=1}^{\text{\#disks}} I^2 R_i \quad (15.17)$$

where c is the specific heat of the oil, ΔT_{oil} is the increase in temperature of the oil after passing through the coil, and R_i is the temperature dependent resistance of disk i , including eddy current effects. We use

$$R_i = \gamma_0 (1 + \alpha \Delta T_i) (1 + ecf_i) \frac{\ell_i}{A_{\text{turn}}} \quad (15.18)$$

where γ_0 is the resistivity at some standard temperature, T_0 , ΔT_i is the temperature rise of the disk above the standard temperature, α is the temperature coefficient of resistivity, ecf_i is the fraction of the normal losses due to eddy currents for disk i , ℓ_i is the length of the cable or wire in disk i , and A_{turn} is the cross-sectional current-carrying area of the cable or wire. Note that ecf_i can vary from disk to disk to account for the effects of nonuniform stray flux along the coil. For a given temperature distribution for the disks and for known input and output oil temperatures, we can solve Equation 15.17 for v_0 . These temperatures will be given by a subsequent analysis and a back and forth iteration is required to achieve consistency. Using these results, the path 1 equation can be written

$$P_0 - P_1 = \frac{1}{2} \frac{\mu K L}{D^2} v_0 \quad (15.19)$$

which contains only P_1 as an unknown.

After solving for the pressure and velocity unknowns for the first section of disks between oil flow washers, we proceed to the next section, taking $P_{0,\text{second}} = P_{2n+2}$ and $v_{0,\text{second}} = v_1 = v_0 (A_1/A_2)$. We proceed similarly from section to section. We must interchange A_1 and A_2 since the oil enters alternate vertical ducts in adjacent sections. This strategy keeps the equations looking the same from section to section. Some sort of relaxation technique must be used to keep the iteration process from becoming unstable. Thus P_0 and v_0 must vary gradually from iteration to iteration.

15.2.2 Oil Nodal Temperatures and Path Temperature Rises

For a given path, the temperature rise of the oil, ΔT , is determined from an energy balance. Thus, the energy rise of the oil per unit time is

$$c\Delta T \frac{dM}{dt} = cpAv\Delta T \quad (15.20)$$

where a constant oil specific heat c has been assumed. The energy lost per unit time through a surface of a conductor is given by

$$hA_c(T_c - T_b) \quad (15.21)$$

where h is the surface heat transfer coefficient, A_c is the surface area, T_c is the conductor temperature, and T_b is the average (bulk) oil temperature in the adjacent duct. h should include the effects of conductor insulation as well as convective heat transfer and can be expressed

$$h = \frac{h_{\text{conv}}}{1 + \frac{h_{\text{conv}}\tau_{\text{insul}}}{k_{\text{insul}}}} \quad (15.22)$$

where h_{conv} is the convection heat transfer coefficient, τ_{insul} is the insulation thickness, and k_{insul} is the thermal conductivity of the insulation. While k_{insul} is nearly constant over the temperature range of interest, h_{conv} varies with temperature and oil velocity. For laminar flow in ducts, we use [Kre80]:

$$h_{\text{conv}} = 1.86 \frac{k}{D} \left(\text{Re}_D \text{Pr} \frac{D}{L} \right)^{0.33} \left(\frac{\mu}{\mu_s} \right)^{0.14} \quad (15.23)$$

where k is the thermal conductivity of the oil, D is the hydraulic diameter, L is the duct length, Re_D is the Reynolds number (Equation 15.2), Pr is the Prandtl number ($\text{Pr} = \mu c/k$), μ is the viscosity of the bulk oil, and μ_s is the oil viscosity at the conductor surface. Equation 15.23 applies when $\text{Re}_D \text{Pr}(D/L) > 10$. A correction must be applied for smaller values. The major temperature variation comes from the viscosity (Equation 15.6) and the velocity dependence comes from the Reynolds number. The other parameters are nearly constant over the temperatures of interest. For transformer oil, we use $\rho = 867 \text{ kg/m}^3$, $c = 1880 \text{ J/kg} \cdot ^\circ\text{C}$, $k = 0.11 \text{ W/m} \cdot ^\circ\text{C}$ [Kre80].

Equating energy gains and losses per unit time (Equations 15.20 and 15.21), for a horizontal duct between two disks (path $3i - 1$ in Figure 15.3) we have

$$cpA_{0,i}v_{3i-1}\Delta T_{3i-1} = h_{3i-1}A_{c,0}[(T_{c,i} - T_{b,3i-1}) + (T_{c,i-1} - T_{b,3i-1})] \quad (15.24)$$

where losses occur through two conductor surfaces and the bulk duct oil temperature, $T_{b,3i-1}$, is approximately given by

$$T_{b,3i-1} = T_{2i-1} + \frac{\Delta T_{3i-1}}{2} \quad (15.25)$$

with T_{2i-1} the nodal oil temperature at the duct's entrance. For horizontal ducts at the beginning and end of a section, only one conductor surface contributes to the right side of Equation 15.24. For the vertical ducts, we have

$$\begin{aligned} cpA_1v_{3i+1}\Delta T_{3i+1} &= h_{3i+1}A_{c,1}(T_{c,i} - T_{b,3i+1}) \\ cpA_2v_{3i}\Delta T_{3i} &= h_{3i}A_{c,2}(T_{c,i} - T_{b,3i}) \end{aligned} \quad (15.26)$$

for the left and right ducts $3i + 1$ and $3i$ respectively. The T_b in these equations is calculated in the same manner as in Equation 15.25. We obtain $3n + 2$ equations in this manner. However, along the entrance and exit ducts (ducts 1 and $3n + 3$) we have $\Delta T = 0$ since no heat is going into the oil here. Hence Equation 15.26 can be eliminated for these entrance and exit ducts and the corresponding unknowns dropped.

We obtain further equations from the energy balance at the nodes. Thus the thermal energy the oil carries into a node must equal that which is leaving. The thermal energy per unit time carried by a mass of oil moving with velocity v normal to a surface of area A is given by

$$\rho c A v (T - T_{\text{ref}}) \quad (15.27)$$

assuming c remains constant from some reference temperature T_{ref} up to the temperature of interest T . Balancing these energy flows at node $2i - 1$ in Figure 15.3, we obtain

$$\rho c A_1 v_{3i-2} (T_{2i-3} + \Delta T_{3i-2} - T_{\text{ref}}) = \rho c A_1 v_{3i+1} (T_{2i-1} - T_{\text{ref}}) + \rho c A_{0,i} v_{3i-1} (T_{2i-1} - T_{\text{ref}})$$

Canceling ρc and using Equation 15.8, we get

$$T_{2i-3} + \Delta T_{3i-2} = T_{2i-1} \quad (15.28)$$

Similarly, at node $2i$ we obtain

$$A_{0,i} v_{3i-1} (T_{2i-1} + \Delta T_{3i-1}) + A_2 v_{3i-3} (T_{2i-2} + \Delta T_{3i-3}) = A_2 v_{3i} T_{2i} \quad (15.29)$$

Here we have used Equation 15.9 to cancel T_{ref} . These equations are slightly modified for a few nodes at the beginning and end of a section, as was also done for the mass conservation equations.

The temperature at node 0 or 1 will be taken as an input; it is the bottom tank oil temperature and will be obtained from an overall balance of heat generation and loss. The calculated temperature at the topmost node of the section, $2n + 2$, will be taken as input to the next section so that the calculation can proceed section by section up the coil, as was the case for the pressure-velocity equations. The temperature dependence of the heat transfer coefficients makes these equations nonlinear. In addition, the heat transfer coefficients depend on the oil velocity, which requires iteration between these equations and the pressure-velocity equations. Another set of unknowns that appears in these equations is the disk temperatures, T_c . These have not been dealt with yet. They are best solved for separately.

15.2.3 Disk Temperatures

The disk temperatures can be found by equating the I^2R losses to the heat passing through the disk surface in the steady state. Thus, for the generic disk shown in [Figure 15.3](#), using previously defined parameters we have

$$I^2R_i = h_{3i-1}A_{c,0}(T_{c,i} - T_{b,3i-1}) + h_{3i}A_{c,2}(T_{c,i} - T_{b,3i}) + h_{3i+1}A_{c,1}(T_{c,i} - T_{b,3i+1}) + h_{3i+2}A_{c,0}(T_{c,i} - T_{b,3i+2}) \quad (15.30)$$

Solving for $T_{c,i}$, we find

$$T_{c,i} = \frac{I^2R_i + h_{3i-1}A_{c,0}T_{b,3i-1} + h_{3i}A_{c,2}T_{b,3i} + h_{3i+1}A_{c,1}T_{b,3i+1} + h_{3i+2}A_{c,0}T_{b,3i+2}}{h_{3i-1}A_{c,0} + h_{3i}A_{c,2} + h_{3i+1}A_{c,1} + h_{3i+2}A_{c,0}} \quad (15.31)$$

We can use Equation 15.25 to express the T_b in terms of previously calculated quantities and Equation 15.18 for R_i . Thus, we can obtain the disk temperatures directly once we solve for the other unknowns. The equations must, however, all be iterated together until convergence to the steady state is achieved. This coil steady state depends on the average oil temperature of the tank oil outside the coil and the bottom tank oil that enters the coil. These temperatures are obtained from an overall energy balance involving heat generation from all the coils and heat lost through the radiators and tank surfaces. We therefore need an overall iteration strategy involving all the coils, the radiators, and the tank. Before discussing this, we need to model coils having vertical cooling ducts with nondirected flow and radiator and tank cooling.

15.3 Thermal Model for Coils without Directed Oil Flow

Our model for nondirected oil flow in coils is fairly simple. As shown in Figure 15.4, there are inner and outer vertical oil-flow channels with cross-sectional areas A_1 and A_2 and hydraulic diameters D_1 and D_2 . The oil velocities in the two channels can differ. They are labeled v_1 and v_2 in Figure 15.4. The oil temperature is assumed to vary linearly from T_o at the coil bottom to $T_o + \Delta T_1$ and $T_o + \Delta T_2$ at the top of the inner and outer channels, respectively. The conductor temperatures are also assumed to vary linearly with an average value of T_c .

The thermal pressure drops in the two channels are given by Equation 15.16, which, in terms of the variables defined above, becomes

$$\begin{aligned}\Delta P_1 &= \beta \rho g H \left(T_o + \frac{\Delta T_1}{2} - T_{\text{ave,out}} \right) \\ \Delta P_2 &= \beta \rho g H \left(T_o + \frac{\Delta T_2}{2} - T_{\text{ave,out}} \right)\end{aligned}\quad (15.32)$$

These pressure drops need only to overcome the fluid friction in the two channels, which is given by Equation 15.5 for laminar flow. In terms of the present parameters, this becomes

$$\Delta P_1 = \frac{1}{2} \frac{\mu_1 K_1 H}{D_1^2} v_1, \quad \Delta P_2 = \frac{1}{2} \frac{\mu_2 K_2 H}{D_2^2} v_2 \quad (15.33)$$

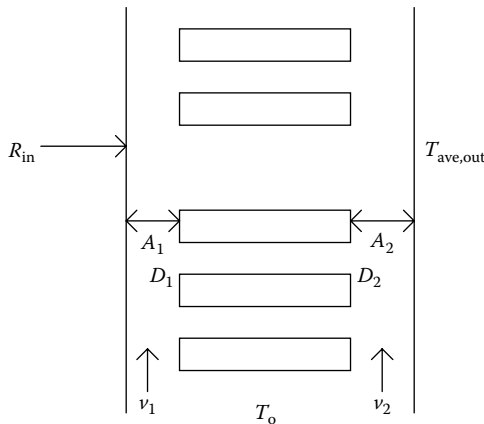


FIGURE 15.4

Thermal model of a nondirected oil-flow coil.

By equating Equations 15.32 and 15.33, we obtain

$$\begin{aligned}\frac{\mu_1 K_1}{\beta \rho g D_1^2} v_1 - \Delta T_1 &= 2(T_o - T_{\text{ave,out}}) \\ \frac{\mu_2 K_2}{\beta \rho g D_2^2} v_2 - \Delta T_2 &= 2(T_o - T_{\text{ave,out}})\end{aligned}\quad (15.34)$$

The overall energy balance equation, analogous to Equation 15.17, is

$$\rho c v_1 A_1 \Delta T_1 + \rho c v_2 A_2 \Delta T_2 = I^2 R \quad (15.35)$$

where R is the total resistance of the coil and is a function of T_c by a formula analogous to Equation 15.18. Further thermal equations come from the energy balance between the surface heat loss by the coil to the separate oil-flow paths. Thus, we have approximately

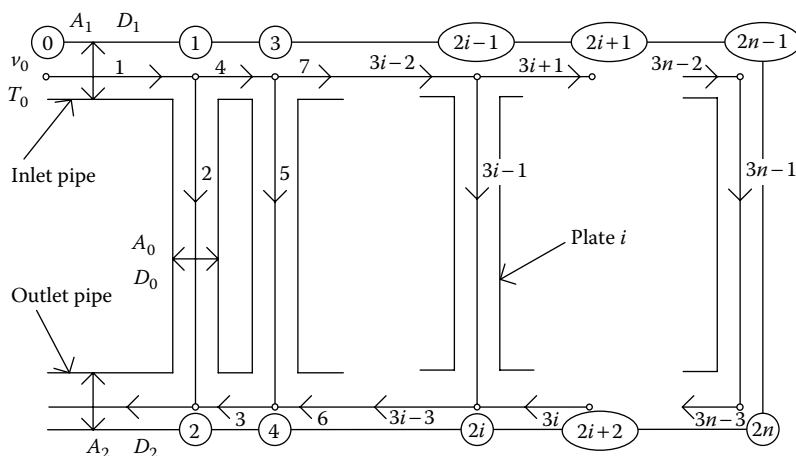
$$\begin{aligned}h_1 A_{c,1} \left[T_c - \left(T_o + \frac{\Delta T_1}{2} \right) \right] &= \rho c A_1 v_1 \Delta T_1 \\ h_2 A_{c,2} \left[T_c - \left(T_o + \frac{\Delta T_2}{2} \right) \right] &= \rho c A_2 v_2 \Delta T_2\end{aligned}\quad (15.36)$$

where h_1 and h_2 are the surface heat transfer coefficients as given by Equation 15.22 and $A_{c,1}$ and $A_{c,2}$ are the surface areas of the conductor across which heat flows into the two oil channels. We take these areas to be half the total surface area of the conductor. This approximation for the conductor cooling surface area assumes the oil makes its way partially into the horizontal spaces between the conductors on its way up the coil. We use Equation 15.23 for h_{conv} with a smaller effective value for L than the coil height.

Equations 15.34 through 15.36 are five equations with five unknowns v_1 , v_2 , ΔT_1 , ΔT_2 , and T_c . T_o and $T_{\text{ave,out}}$ will be determined from an overall energy balance for the transformer and are considered known values here. These equations are nonlinear because μ 's and h 's depend on temperature and velocity and also because products of unknowns such as $v\Delta T$ occur. We use the Newton–Raphson iteration scheme to solve these equations. If desired, we can obtain the pressure drop from Equation 15.33.

15.4 Radiator Thermal Model

The radiators modeled here are fairly typical in that they consist of a series of vertical plates containing narrow oil channels. The plates are uniformly spaced and are attached to inlet and outlet pipes at the top and bottom.

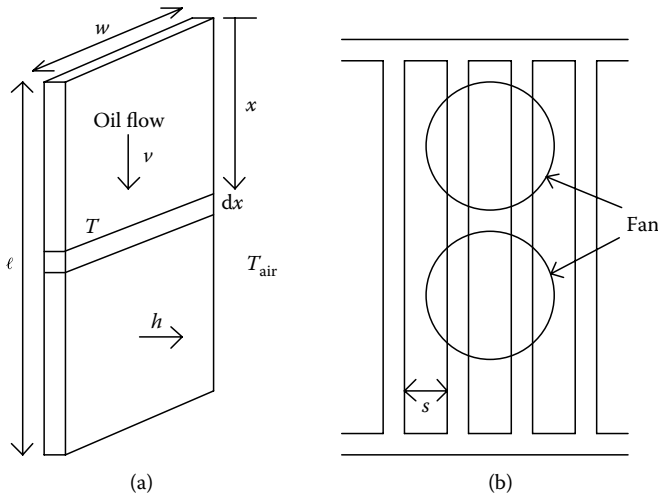
**FIGURE 15.5**

Node and path numbering scheme for a radiator containing n plates.

These pipes are attached to the transformer tank and must be below the top oil level. Fans may be present to blow air horizontally through one or more radiators stacked side by side. The oil-flow paths for a radiator are similar to those of a disk-winding section turned on its side as shown in Figure 15.5. In fact, the same node and path numbering scheme is used. In some paths, however, the positive flow direction is reversed. The analysis is very similar to that of disk coils with directed oil flow and therefore will only be sketched here.

Pressure differences along a path are balanced by the frictional resistance in the steady state so that, for laminar flow, Equation 15.5 holds along each path, where the unknown velocity and pressure will be labeled by the appropriate path and node numbers. For n plates along a radiator, there are $2n$ nodes and $3n - 1$ oil paths, as shown in Figure 15.5. Thus, we need $2n$ more equations. These are given by mass continuity at the nodes, similar to Equations 15.7 through 15.13. Some differences will occur because the positive flow direction is changed for some paths. Also, similar to what we did for the coils, we determine the overall pressure difference across the radiator from buoyancy considerations so that Equation 15.16 holds. However, $T_{\text{ave,out}}$ will differ from that used for the coils since the tank oil adjacent to the radiators will be hotter than that adjacent to the coils because the average radiator vertical position is above that of the coils. We need an overall energy balance to obtain the input oil velocity so that Equation 15.17 holds with the right-hand side replaced by the total heat lost by the radiators.

In the radiator cooling process, the oil temperature drops as it passes downward through a radiator plate, giving up its heat to the air through the radiator surface. Figure 15.6a shows a simplified drawing of a plate with some of the parameters labeled.

**FIGURE 15.6**

Parameters used in radiator cooling calculations: (a) a single radiator plate with parameters used in the calculations and (b) an end view of a stack of plates making up a radiator with cooling fans indicated.

We consider a thin, horizontal strip of a radiator's surface area $2w \, dx = 2w\ell \, (dx/\ell) = 2A_s \, (dx/\ell)$, where A_s is the area of one side of the plate and the factor of 2 accounts for both sides, ℓ is the plate height, and w is its width. The heat lost through this surface is $2hA_s (T - T_{air}) \cdot (dx/\ell)$, where h is the heat transfer coefficient, T is the oil temperature at position x , and T_{air} is the ambient air temperature. The heat lost by the oil in flowing past the distance dx is $-\rho cv A_R dT$, where v is the oil velocity and A_R is the cross-sectional area through which the oil flows through the plate. By equating these expressions and rearranging, we get

$$\frac{2hA_s}{\rho cv A_R \ell} dx = -\frac{dT}{T - T_{air}} \quad (15.37)$$

Assuming that h is constant here (it will be evaluated at the average temperature), we can integrate it to obtain the following:

$$\Delta T = (T_{top} - T_{air}) \left[1 - \exp\left(-\frac{2hA_s}{\rho cv A_R \ell}\right) \right] \quad (15.38)$$

where ΔT is the temperature drop across the plate and T_{top} is the top oil temperature.

We get an equation similar to Equation 15.38 for each plate so that for plate i , v should be labeled as v_{3i-1} , T_{top} as T_{2i-1} , h as h_i , and ΔT as ΔT_i . This gives n equations. The new unknowns are the $n \, \Delta T$'s and $2n$ nodal temperatures. However, the top nodal temperatures are all equal to the oil input temperature T_o since we

neglect any cooling along the input and output pipes. At the bottom nodes, using a method similar to that used to get Equation 15.29, for node $2i$ we obtain

$$A_R v_{3i-1} (T_o - \Delta T_i) + A_2 v_{3i} T_{2i+2} = A_2 v_{3i-3} T_{2i} \quad (15.39)$$

This equation needs to be slightly modified for node $2n$. Thus, we obtain sufficient equations to solve for all the unknowns. Iteration is required for the pressure–velocity equations and the $T - \Delta T$ equations because they are interdependent and because of the nonlinearities.

The expression for the surface heat transfer coefficient h depends on whether or not fans are used. For natural convection with no fans, we use an expression that applies to a row of vertical plates separated by a distance [Roh85]:

$$h = \frac{k_{\text{air}}}{s} \left[\left(\frac{24}{\text{Ra}} \right)^{1.9} + \left(\frac{1}{0.62 \text{Ra}^{1/4}} \right)^{1.9} \right]^{-\frac{1}{1.9}} \quad (15.40)$$

Ra is the Rayleigh number, given by the product of the Grashof and Prandtl numbers:

$$\text{Ra} = \text{GrPr} = \frac{g \beta_{\text{air}} c_{\text{air}} \rho_{\text{air}}^2 \Delta T}{k_{\text{air}} \mu_{\text{air}}} \left(\frac{s^4}{\ell} \right) \quad (15.41)$$

where the compressibility β , specific heat c , density ρ , thermal conductivity k , and viscosity μ all apply to air at the temperature $(T_s + T_{\text{air}})/2$, where T_s is the average surface temperature of the plate. Also, $\Delta T = T_s - T_{\text{air}}$. The quantities c , ρ , k , and μ for air vary with temperature [Kre80], and this must be taken into account in Equations 15.38, 15.40, and 15.41, since T_s can differ from plate to plate. However, we found in practice that a similar expression for tank cooling, Equation 15.44 with ℓ replacing L , works better for our radiators, so we will use it instead.

When fans are blowing, we use the heat transfer coefficient for turbulent flow of a fluid through a long, narrow channel of width s :

$$h = 0.023 \frac{k_{\text{air}}}{D} \text{Re}_D^{0.8} \text{Pr}^{0.33} \quad (15.42)$$

where the hydraulic diameter $D = 2s$. The Reynolds number is given by Equation 15.2 with ρ and μ for air, $D = 2s$, and v an average velocity determined by the characteristics of the fans and the number of radiators stacked together. The Prandtl number for air is nearly constant throughout the temperature range of interest and is 0.71.

A simple way of parameterizing the radiator air velocity with fans that works well in practice is

$$v_n = \left(\frac{1}{n} \right)^p v_1 \quad (15.43)$$

where n is the number of stacked radiators cooled by a given fan bank, v_n is the air velocity flowing past the radiator surfaces, p is an exponent to be determined by test results, and v_1 is the fan velocity when only one radiator is present. We find in our designs that $p = 0.58$ works well. In addition, we take v_1 to be the nominal fan velocity as specified by the manufacturer. (This can be determined from the flow capacity and the fan's area.) We assumed that the radiator surface cooled by fans was proportional to the fraction of the fan's area covering the radiator side (Figure 15.6b). We assume that the remaining surface was cooled by convective cooling.

15.5 Tank Cooling

Tank cooling occurs by means of natural convection and radiation. Of course, the radiators also cool to some extent by radiation; however, this is small compared with convective cooling, because the full radiator surface does not participate in radiative cooling. Because of the nearness of the plates to each other, much of a plate's radiant energy is reabsorbed by a neighboring plate. The effective cooling area for radiation is an outer surface envelope and as such is best lumped with the tank cooling. Thus, the effective tank area for radiative cooling is an outer envelope including the radiators. (A string pulled tautly around the tank and radiators would lie on the cooling surface.) However, in convective cooling the normal tank surface area is involved.

For natural convection in the air from the tank walls of height L , we use the heat transfer coefficient [Roh85]:

$$h_{\text{conv,tank}} = \frac{k_{\text{air}}}{L} \left\{ \left[\frac{2.8}{\ln \left(1 + \frac{5.44}{\text{Ra}_L^{1/4}} \right)} \right]^6 + 1.18 \times 10^{-6} \text{Ra}_L^2 \right\}^{1/6} \quad (15.44)$$

where Ra is the Rayleigh number which, in this context, is given by

$$\text{Ra}_L = \frac{g \beta_{\text{air}} c_{\text{air}} \rho_{\text{air}}^2 L^3 \Delta T}{k_{\text{air}} \mu_{\text{air}}} \quad (15.45)$$

where the temperature dependencies are evaluated at $(T_s + T_{\text{air}})/2$ and $\Delta T = T_s - T_{\text{air}}$ as before. The Rayleigh number in this formula should be restricted to the range $1 < \text{Ra}_L < 10^{12}$, which is satisfied for the temperatures and tank dimensions of interest. T_s is the average tank wall temperature and T_{air} is the

ambient air temperature. Thus, the heat lost from the tank walls per unit time due to convection, $W_{\text{conv,tank}}$ is given by

$$W_{\text{conv,tank}} = h_{\text{conv,tank}} A_{\text{conv,tank}} (T_s - T_{\text{air}}) \quad (15.46)$$

where $A_{\text{conv,tank}}$ is the lateral wall area of the tank.

The top surface contributes to the heat loss according to a formula similar to Equation 15.46 but with a heat transfer coefficient given by [Kre80]

$$h_{\text{conv,top}} = 0.15 \frac{k_{\text{air}}}{B} \text{Ra}_B^{0.333} \quad (15.47)$$

and with the tank top area in place of the side area. In Equation 15.47, B is the tank width which must also be used in the Rayleigh number (Equation 15.45) instead of L . In this formula, the Rayleigh number should be restricted to the range $8 \times 10^6 < \text{Ra}_B < 10^{11}$, which is also satisfied for typical tank widths in power transformers. On the bottom, we assume the ground acts as an insulator.

Radiant heat loss per unit time from the tank, $W_{\text{rad,tank}}$ is given by the Stephan–Boltzmann law.

$$W_{\text{rad,tank}} = \sigma E A_{\text{rad,tank}} (T_{K,s}^4 - T_{K,\text{air}}^4) \quad (15.48)$$

where $\sigma = 5.67 \times 10^{-8} \text{ W/m}^2 \cdot ^\circ\text{K}^4$ is the Stephan–Boltzmann constant, E is the surface emissivity ($E \approx 0.95$ for gray paint), $A_{\text{rad,tank}}$ is the effective tank area for radiation, $T_{K,s}$ is the average surface temperature of the tank in kelvin, and $T_{K,\text{air}}$ is the ambient air temperature in kelvin. Equation 15.48 can be written to resemble Equation 15.46 with a convection coefficient given by

$$h_{\text{rad,tank}} = \sigma E (T_{K,s} + T_{K,\text{air}}) (T_{K,s}^2 + T_{K,\text{air}}^2) \quad (15.49)$$

This is temperature dependent, but so is $h_{\text{conv,tank}}$.

The total tank power loss is given by the sum of Equation 15.46, together with the corresponding expression for the top heat loss and Equation 15.48. The total is then added to the radiator loss to get the total power loss from the transformer. The radiator loss is the sum of losses from all the radiators. Although we modeled only one radiator, the total radiator loss is just the number of radiators multiplied by the loss from each, assuming they are all identical. Otherwise, we must take into account the differences among the radiators. In equilibrium, the total power loss must match the total power dissipation of the coils, core, and stray losses in the tank walls, brackets, leads, and so on.

15.6 Oil Mixing in the Tank

Perhaps, the most complex part of the oil flow in transformers occurs in the tank. The lack of constraining channels or baffles means that the oil is free to take irregular paths, such as along localized circulations or eddies.

Nevertheless, there is undoubtedly some overall order in the temperature distribution and flow pattern. As with any attempt to model a complicated system, here we make some idealized assumptions in an effort to describe the average behavior of the tank oil.

As shown in Figure 15.7, we assume that the cold oil at the bottom of the tank has a uniform temperature, T_{bot} , from the bottom radiator discharge pipe to the tank bottom and that the top oil is at a uniform temperature, T_{top} , from the top of the coils to the top oil level. We further assume that the temperature variation between T_{bot} and T_{top} is linear. This allows us to calculate the average oil temperature along a column of oil adjacent to and of equal height as the coils and calculate likewise for the radiators, determining $T_{ave,out,coils}$ and $T_{ave,out,rads}$. These two temperatures will differ because the average radiator vertical position is above that of the coils. These average temperatures are used in determining the thermal pressure drop across the coils and radiators.

In Figure 15.7, we have labeled the volumetric oil flow Q with subscripts c for coils, r for radiators, s for stray loss oil flows, and n for net. Thus, we have

$$Q_n = Q_r - Q_c - Q_s \quad (15.50)$$

Q_s accounts for the oil flow necessary to cool the core, brackets, tank walls, and so on. Since there is no constraint, mechanical or otherwise, to force the radiator, coil, and stray loss flows to be identical, Q_n can differ from zero. The flow Q_c is the sum of the flows from all the coils and Q_r is the sum of the flows from all the radiators.

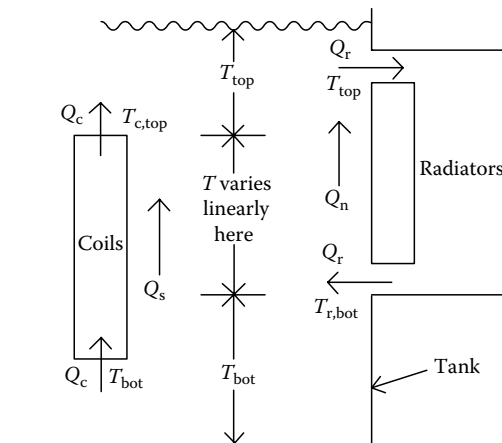


FIGURE 15.7

Assumed oil temperature distribution inside a tank. The oil flows, Q , as well as the flow-weighted temperatures are also indicated.

We have also indicated temperatures associated with some of the flows. The oil flowing into the bottom of the coils is at temperature T_{bot} , and the oil flowing into the top of the radiators is at temperature T_{top} . The temperature of the oil flowing out of the top of the coils, $T_{\text{c,top}}$, is a flow-weighted temperature of the oil from all the coils. Thus

$$Q_{\text{c}} T_{\text{c,top}} = \sum_{i=1}^{\text{\#coils}} Q_{\text{c},i} T_{\text{c,top},i} \quad (15.51)$$

where i labels the individual coil flows and top temperatures of the oil emerging from the coils. Since we assume that all radiators are identical, $T_{\text{r,bot}}$ is the bottom temperature of the oil exiting a radiator. If the radiators are not identical, we will use a flow-weighted average for this temperature also.

We assume for simplicity that the volumetric flow Q_{s} , associated with the stray power loss W_{s} , results in a temperature change of $\Delta T = T_{\text{top}} - T_{\text{bot}}$ for this oil flow. Thus, Q_{s} is given by

$$Q_{\text{s}} = \frac{W_{\text{s}}}{\rho c (T_{\text{top}} - T_{\text{bot}})} \quad (15.52)$$

This is inherently an upward flow and, like the coil flow, is fed by the radiators. We do not attribute any downward oil flow to the tank cooling, but assume that this simply affects the average oil temperature in the tank.

We assume that any net flow Q_{n} , if positive, results in the transport of cold radiator oil at temperature $T_{\text{r,bot}}$ to the top of the tank and, if negative, results in the transport of hot coil oil at temperature $T_{\text{c,top}}$ to the bottom of the tank. These assumptions imply that for $Q_{\text{n}} > 0$

$$T_{\text{top}} = \frac{T_{\text{c,top}} Q_{\text{c}} + T_{\text{r,bot}} Q_{\text{n}}}{Q_{\text{r}} - Q_{\text{s}}} \quad (15.53)$$

$$T_{\text{bot}} = T_{\text{r,bot}}$$

while for $Q_{\text{n}} < 0$

$$T_{\text{top}} = T_{\text{c,top}}$$

$$T_{\text{bot}} = \frac{T_{\text{r,bot}} Q_{\text{r}} - T_{\text{c,top}} Q_{\text{n}}}{Q_{\text{c}} + Q_{\text{s}}} \quad (15.54)$$

Another way of handling net flow Q_{n} is to assume that it raises the level of the bottom oil layer at temperature T_{bot} if positive and that it allows the top oil layer at temperature T_{top} to drop downward if negative. This will continue until $Q_{\text{n}} = 0$ at equilibrium.

After each calculation of the coil and radiator flows and temperatures, T_{top} , T_{bot} , $T_{\text{ave,out,coils}}$, $T_{\text{ave,out,rads}}$ and Q_{s} can be determined. Also, the losses in the coils and from the radiators can be obtained. Updated pressure drops across the coils and radiators as well as updated values of the oil velocities flowing

into the coils and radiators can be calculated from these. The iterations continue until the temperatures reach their steady-state values and the losses generated equal the losses dissipated to the atmosphere to within an acceptable tolerance. This requires several levels of iteration. The coil and radiator iterations assume that the tank oil temperature distribution is known and in turn influence the tank oil temperatures. A relaxation technique is required to keep the iteration process from becoming unstable. This means that the starting parameter values for the new iteration are a weighted average of the previous and newly calculated values.

15.7 Time Dependence

The basic assumption we make in dealing with time-dependent conditions is that at each instant in time the oil flow is in equilibrium with the heat (power) transferred by the conductors to the oil and with the power loss from the radiators at that instant. The velocities and oil temperatures will change with time, but in such a way that equilibrium is maintained at each time step. This is referred to as a quasistatic approximation. The conductor heating or cooling, on the other hand, is transient. We assume, however, that the temperature of a disk, which is part of a directed oil-flow coil, is uniform throughout the disk so that only the time dependence of the average disk temperature is treated. We make a similar assumption for nondirected oil-flow coils.

The heat generated in a conductor per unit time is I^2R , where R is its resistance (including eddy current effects) at the instantaneous temperature T_c and I its current. Here conductor refers to a single disk for a directed oil-flow coil and an entire coil for a nondirected oil-flow coil. The transient thermal equation for this conductor is

$$\rho_{\text{cond}} c_{\text{cond}} V \frac{dT_c}{dt} = I^2 R - \sum_i h_i A_{c,i} (T_c - T_{b,i}) \quad (15.55)$$

The left-hand side is the heat stored in the conductor of volume V per unit time. This equals the heat generated inside the conductor per unit time minus the heat lost through its surface per unit time. The sum is over all surfaces of the conductor. The other symbols have their usual meaning with the subscript “cond” indicating that they refer to the conductor properties. The usual temperature and velocity dependencies occur in some of the parameters in Equation 15.55. We solve these equations using the Runge–Kutta technique. These equations replace the steady-state disk coil equations for T_c (Equation 15.31) and, in a slightly modified form, one of the nondirected oil-flow coil equations.

Equation 15.55 accounts for heat (energy) storage in the current-carrying conductors as time progresses. Thermal energy is also stored in the rest of the transformer. We assume for simplicity that the rest of the transformer is at the average oil temperature. This includes the core, tank, radiators, brackets or braces, coils not carrying current, insulation, oil in the main tank, and so on. Thus, the conservation of energy (power) requires that

$$\left(\sum_i c_i m_i \right) \frac{dT_{\text{ave,oil}}}{dt} = \rho c Q_c (T_{\text{c,top}} - T_{\text{bot}}) + W_s - W_{\text{rads+tank}} \quad (15.56)$$

where c_i is the specific heat and m_i is the mass of the parts of the transformer, apart from the current-carrying coils, which store heat. Equation 15.56 states that the heat absorbed by the various parts of a transformer per unit time, except the current-carrying coils, at a particular instant equals the power flowing out of the coils in the form of heated oil plus the stray power losses, minus the power dissipated by the radiators and tank to the atmosphere. Here, the stray losses include core losses, tank losses, and any losses occurring outside the coils. Equation 15.56 is solved using a trapezoidal time-stepping method.

Thus, transient cooling can be handled by making relatively minor modifications to the steady-state treatment, using the quasistatic equilibrium approximation. So far, the computer program we have developed treats cases in which the megavolt ampere (MVA) of the transformer suddenly changes from one level to another. A steady-state calculation is performed at the first MVA level. Then, the transient calculation begins with currents and stray losses appropriate to the second MVA level. The fans also may be switched on or off for the transient calculation. As expected, the solution approaches the steady-state values appropriate to the second MVA level after a sufficient time. With some additional programming, we could input any desired transformer transient loading schedule and calculate the transient behavior.

15.8 Pumped Flow

The type of pumped flow considered here is one in which the radiator oil is pumped and a baffle arrangement is used to channel some or all of the pumped oil through the coils. Thus, the oil velocity in the entrance radiator pipes due to the pumps, v_o , is given by

$$v_o = \frac{Q_{\text{pump}}}{A_{\text{rad}} N_{\text{rad}}} \quad (15.57)$$

where Q_{pump} is the volume of oil per unit time which the pump can handle under the given conditions, A_{rad} is the area of the radiator entrance pipe, and N_{rad} is the number of radiators. In addition to the pressure drop across the radiators due to the pump, the thermal pressure drop is also present, contributing a little to the velocity in Equation 15.57.

We assume that a fraction f of the pumped oil through the radiators bypasses the coils and does not participate in cooling. This could be due to inefficient baffling or by design. We also assume that part of the oil flow from the radiators is used to cool the stray losses. This flow, Q_s , is given by

$$Q_s = \frac{W_s}{W_t}(1 - f)Q_{\text{pump}} \quad (15.58)$$

where W_s is the stray power loss, W_t is the total loss, and f is the fraction of the flow bypassing the coils. In addition to the thermal pressure drop across the coils, there is a pressure drop due to the pump. At equilibrium, this is determined by the requirement that

$$Q_c = (1 - f)Q_{\text{pump}} - Q_s \quad (15.59)$$

Thus, after each iteration, the flow from all the coils is determined and the pressure drop across the coils is adjusted until Equation 15.59 is satisfied at steady state.

For pumped flow, we should check for nonlaminar flow conditions and adjust the heat transfer and friction coefficients accordingly.

15.9 Comparison with Test Results

Computer codes were written to perform steady-state, transient, and pumped oil-flow calculations based on the analysis given in this chapter. Although we did not measure detailed temperature profiles along a coil, the codes calculate the temperatures of all the coil disks and the oil in all the ducts as well as duct oil velocities. Figures 15.8 through 15.10 show these profiles for one such coil with directed oil-flow washers. The oil ducts referred to in the figures are the horizontal ducts, and the conductor temperature is the average disk temperature. Thinning occurs in this coil, that is, the duct size increase at two locations, near disk numbers 35 and 105, and we can see this in the figures. The kinks in the profiles are an indication of the location of the oil-flow washers.

Some leeway was allowed for in the friction factors for the coils and radiators by including an overall multiplying factor. This accounts, in an average way, for nonideal conditions in real devices and must be determined

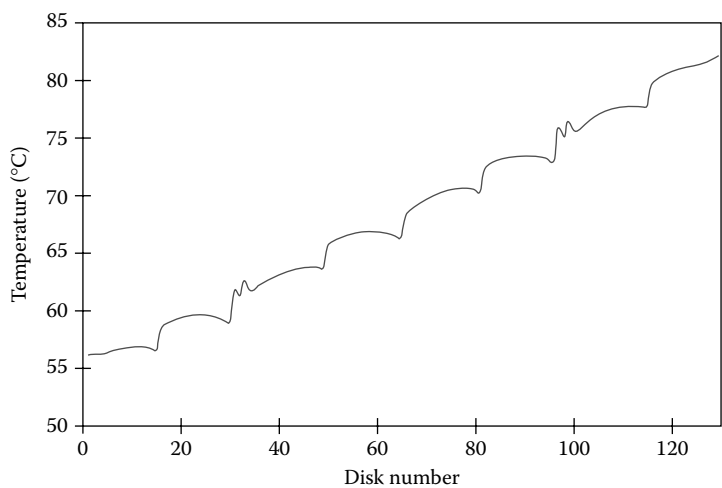


FIGURE 15.8
Calculated temperatures of the disks along a disk coil with directed oil flow washers. (From Del Vecchio, R. M., and P. Feghali. 1999. Thermal model of a disk coil with directed oil flow. IEEE Transmission and Distribution Conference, New Orleans, LA, 914–9. With permission.)

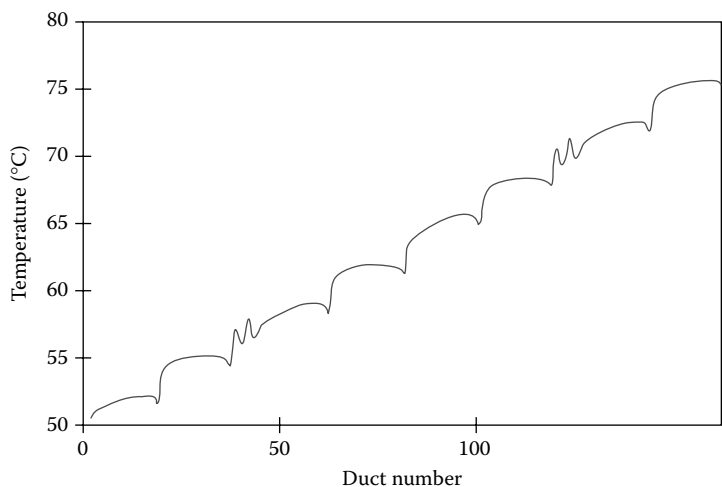
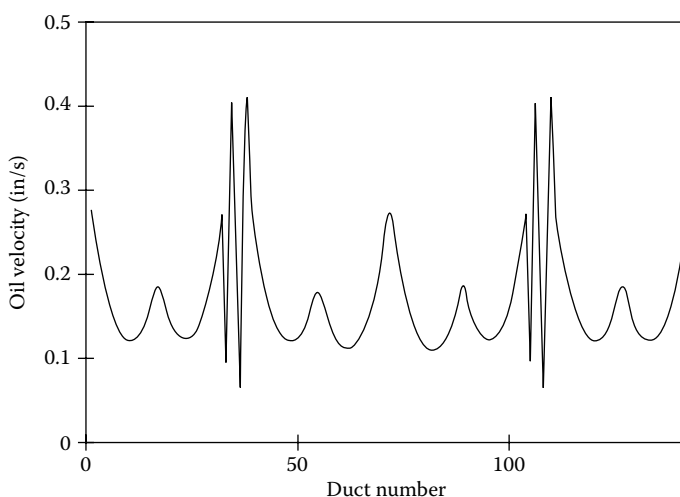


FIGURE 15.9
Calculated average oil temperatures in the horizontal ducts along a disk coil with directed oil-flow washers. The temperature is assumed to vary linearly in the ducts. (From Del Vecchio, R. M., and P. Feghali. 1999. Thermal model of a disk coil with directed oil flow. IEEE Transmission and Distribution Conference, New Orleans, LA, 914–9. With permission.)

**FIGURE 15.10**

Calculated velocities of the oil in the horizontal ducts along a disk coil with directed oil-flow washers. (From Del Vecchio, R. M., and P. Feghali. Thermal model of a disk coil with directed oil flow. IEEE Transmission and Distribution Conference, New Orleans, LA, 914–9. With permission.)

experimentally. The test data best agree with calculations when the multiplying factor is 1.0 for the coils and 2.0 for the radiators. Thus, the coil friction is close to the theoretical value, whereas that for the radiators is twice as high.

Temperature data normally recorded in our standard heat runs are (1) mean oil temperature rise, (2) top oil temperature rise, (3) temperature drop across the radiators, and (4) average temperature rise of the windings. These are usually measured under both natural convective cooling (OA) and fan cooling (FA) conditions. The rises are with respect to the ambient air temperature. A statistical analysis of such data, taken on a number of transformers with MVAs ranging from 12 to 320, was performed to determine how well the calculations and test results agreed. This is shown in [Table 15.1](#), where the mean and standard deviations refer to the differences between the calculated and measured quantities. Thus, a mean of zero and a standard deviation of zero would indicate a perfect fit. Nonzero results for these statistical measures reflect both the limitations of the model and some uncertainty in the measured quantities. Table 15.1 shows that the calculated and measured results generally agree. Essentially, only one parameter was adjusted to improve the agreement between the results: the overall friction factor multiplier for the radiators.

[Figures 15.11](#) and [15.12](#) graph representative output from the transient program. In this example, the transformer operates at steady state at $t = 0$ at

the first MVA value (93 MVA), and the loading corresponding to the second MVA (117 MVA) is suddenly applied. The time evolution of the oil temperature is shown in [Figure 15.11](#), while that of one of the coils is shown in [Figure 15.12](#). The program calculates time constants from this information. [Figure 15.13](#) shows a direct comparison of the calculated and measured hot-spot temperatures of a coil in which a fiber-optic temperature probe was embedded. Although the absolute temperatures are off by a few degrees, the shapes of the curves are very similar, indicating that the time constants are nearly the same.

TABLE 15.1
Comparison of Calculated and Measured Quantities

	OA		FA	
	Mean	Standard Deviation	Mean	Standard Deviation
Mean oil rise	0.86	2.58	0.19	5.11
Top oil rise	1.56	2.36	2.11	4.82
Drop across radiators	−2.23	4.51	−0.83	3.44
Average winding rise	−0.56	3.19	−0.14	2.38

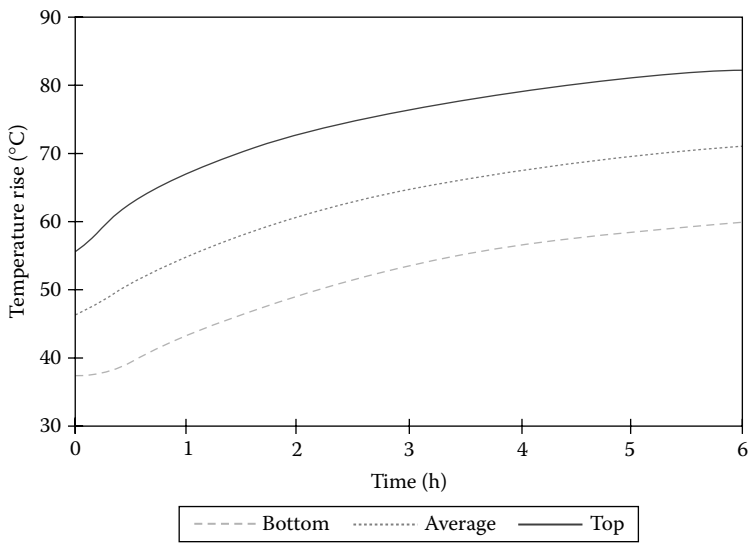


FIGURE 15.11
Time evolution of the bottom, average, and top tank oil temperatures starting from a steady-state loading of 93 MVA at $t = 0$, when a 117-MVA load is suddenly applied.

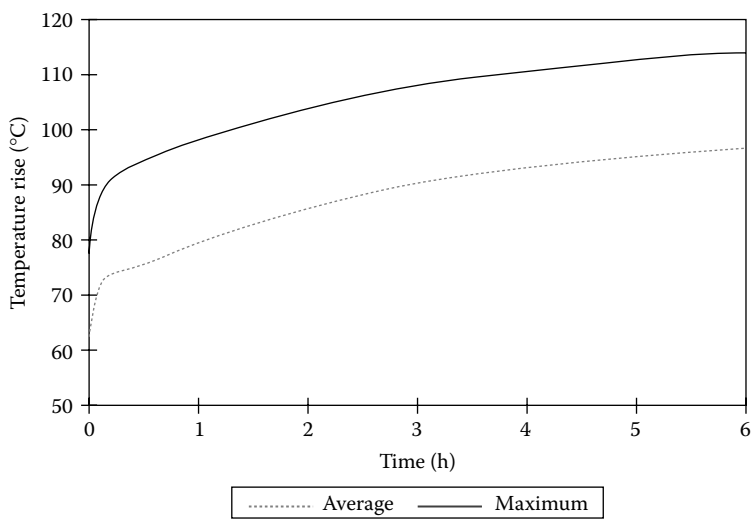


FIGURE 15.12 Time evolution of the average and maximum coil temperature starting from a steady-state loading of 93 MVA at $t = 0$, when a 117-MVA load is suddenly applied.

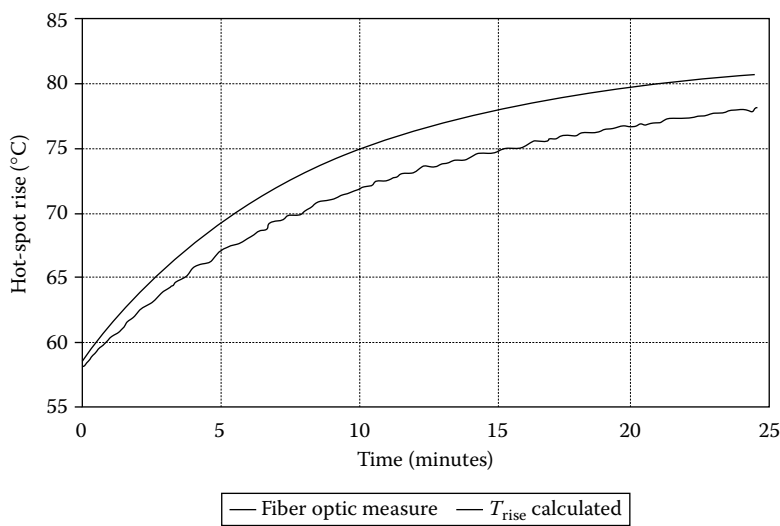


FIGURE 15.13 Comparison of calculated and measured temperatures of the coil's hot spot versus time. The coil is operating at steady state at $t = 0$ when a sudden additional loading is applied. The hot spot is measured by means of a fiber-optics probe. The top curve represents the calculated temperature and the bottom curve represents the temperature measured by the fiber optics probe.

15.10 Determining m and n Exponents

To estimate the temperature rises that occur under overload conditions, approximate empirical methods have been developed that use m and n exponents. Although for a detailed thermal model these approximations are unnecessary, these exponents are widely used to obtain quick estimates of the overload temperatures for transformers in service. Although they are frequently measured in heat run tests, we can also obtain them from either the steady-state or transient calculations.

The n exponent is used to estimate the top oil temperature rise above the ambient air temperature, ΔT_{top} , under overload conditions, based on the value of this quantity under rated conditions. For this estimation, we must know the transformer total losses under rated conditions as well as the losses at the overload condition, which we can estimate by knowing how the losses change with the increased loading, and will be estimated in Equation 15.61. The formula used to obtain the overload temperature rise above the ambient air temperature is

$$\frac{\Delta T_{\text{top},2}}{\Delta T_{\text{top},1}} = \left(\frac{\text{Total Loss}_2}{\text{Total Loss}_1} \right)^n \quad (15.60)$$

Thus, if 2 refers to the overload condition and 1 to the rated condition, the top oil rise, above air under overload conditions $\Delta T_{\text{top},2}$, can be obtained from a knowledge of the other quantities in Equation 15.60.

To estimate the losses under overload conditions, we must separate the losses into I^2R resistive losses in the coils and stray losses, which include the core, tank, clamp, and additional eddy current losses that occur in the coils due to the stray flux. The I^2R loss can be calculated accurately. By subtracting the I^2R loss from the total measured loss, the stray loss can be estimated. Alternatively, core loss, eddy current loss, tank loss, and clamp loss can be obtained from design formulas or other calculation methods. All of these losses depend on the square of the load current in either winding. (The stray losses depend on the square of the stray flux, which is proportional to the square of the current, assuming the materials operate in their linear range.) Since the load current is proportional to the MVA of the unit, these losses are proportional to the MVA squared. The I^2R losses are proportional to the resistivity of the winding conductor, which is temperature dependent, whereas the stray losses are inversely proportional to the resistivity of the material in which they occur. Thus, the total loss at higher loadings can be obtained from the rated loss by

$$\text{Total Loss}_2 = \left(\frac{\text{MVA}_2}{\text{MVA}_1} \right)^2 \left[I^2R \text{ Loss}_1 \left(\frac{\rho_2}{\rho_1} \right)_{\text{coil}} + \text{Stray Loss}_1 \left(\frac{\rho_1}{\rho_2} \right)_{\text{stray}} \right] \quad (15.61)$$

where ρ is the resistivity in this context. The resistivity ratios are temperature dependent so that some iteration with Equation 15.60 may be required to arrive at a self-consistent solution. The stray resistivity ratio is meant to be a weighted average over the materials involved in the stray loss. However, since the temperature dependence of the resistivity of the coil, tank, and clamp materials is nearly the same, this ratio will be nearly the same as that of the coils.

The n coefficient is generally measured or calculated under conditions in which the cooling is the same for the rated and overload conditions. Thus, if fans are on for the rated loading, they must also be on for the overload condition. Similarly, if pumps are on at one rating, they must also be on for the second rating. Although we could determine n from measurements or calculations performed at two ratings, we should determine it from three different loadings and do a best fit to Equation 15.60. The three ratings generally chosen are 70, 100, and 125%. The 70 and 100% or 100 and 125% combinations are chosen when only two ratings are used. Measurements and calculations show that n based on the 70 and 100% combination can be fairly different than n based on the 100 and 125% combination. This suggests that n is not strictly a constant for a given transformer and that it should be determined for loadings in the range where it is expected to be used. A typical value of n for large power transformers is 0.9.

The m exponent is defined for each winding and relates the winding gradient to the winding current. The winding gradient at a particular steady-state loading is the temperature difference between the mean winding temperature and the mean oil temperature in the tank:

$$\text{Gradient} = \text{Mean winding temperature} - \text{Mean tank oil temperature} \quad (15.62)$$

Letting 1 and 2 designate rated and overload conditions, the m coefficient for a particular winding relates the gradients to the winding currents by

$$\frac{\text{Gradient}_2}{\text{Gradient}_1} = \left(\frac{\text{Current}_2}{\text{Current}_1} \right)^{2m} \quad (15.63)$$

Since the currents are proportional to the MVAs, the MVA ratio could be substituted in Equation 15.63 for the current ratio. The m exponents can be determined from two or three MVA loadings and, like the n exponent, depend on the MVA range covered to some extent. They also can vary considerably for different windings. A typical value for large power transformers is about 0.8. The factor of 2 in the exponent in Equation 15.63 reflects the fact that the losses in the winding are proportional to the current squared and ideally the temperature would rise so that m takes into account deviations from this expectation.

The winding gradient is often used to estimate the winding's maximum temperature. A common procedure is to add a multiple of the gradient to the top oil temperature to find the maximum temperature of the winding:

$$\text{Max winding temp} = \text{Top oil temp} + 1.1 \times \text{Winding gradient} \quad (15.64)$$

The factor of 1.1 can differ among manufacturers or transformer types and should be determined experimentally. Formulas such as Equation 15.64 are unnecessary when detailed temperature calculations are available or maximum temperatures are measured directly by fiber optics or possibly other types of temperature probes, inserted into the winding at its most probable location. Detailed temperature calculations can provide some guidance as to where these probes should be inserted.

15.11 Loss of Life Calculation

Transformers can fail for a number of reasons such as from the application of excessive electrical or mechanical stress; however, even a highly protected unit will eventually fail due to the aging of its insulation. While the presence of moisture and oxygen affect the rate of insulation aging, these are usually limited to acceptable levels by appropriate maintenance practices. The main factor affecting insulation aging is temperature. The insulation's maximum temperature, called the hot-spot temperature, is the critical temperature governing aging. This is usually the highest of the maximum temperatures of the different windings, although it could also be located on the leads which connect the windings to the bushings or to each other.

Numerous experimental studies have shown that the rate of insulation aging as measured by various parameters such as tensile strength or degree of polymerization (DP) follows an Arrhenius relationship:

$$K = Ae^{-B/T} \quad (15.65)$$

where K is a reaction rate constant (fractional change in quantity per unit time), A and B are parameters, and T is the absolute temperature. For standard cellulose-based paper insulation, $B = 15,000$ K, which is an average value from different studies using different properties to determine aging [McN91]. If X is the property used to measure aging, for example, tensile strength or DP, then we have

$$\frac{dX}{X} = -Kdt \Rightarrow X(t) = X(t=0)e^{-Kt} \quad (15.66)$$

The time required for the property X to drop to some fraction f of its initial value if held at a constant temperature T , t_T is thus determined by

$$\frac{X(t = t_T)}{X(t = 0)} = f = e^{-Kt_T} \quad (15.67)$$

Using logarithms and Equation 15.65, we obtain

$$t_T = -\frac{\ln f}{K} = -\frac{\ln f}{A} e^{B/T} \quad (15.68)$$

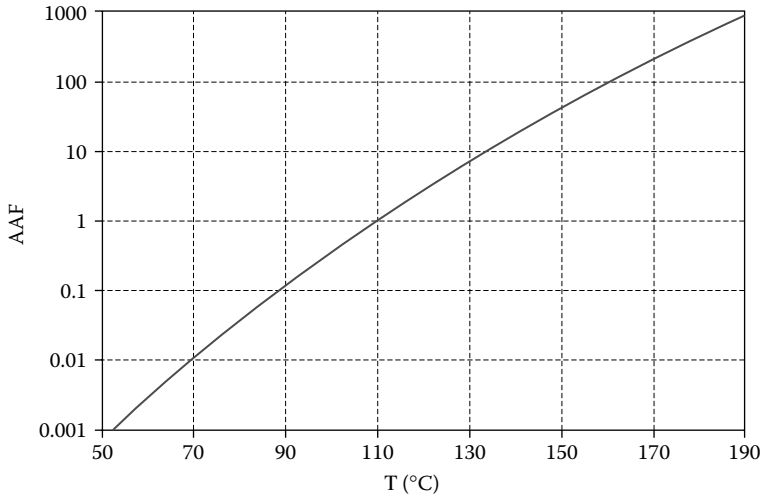
There are several acceptable standard or normal insulation lifetimes, in which the insulation is assumed to age at a constant temperature of 110°C and is well dried and oxygen free. Under these conditions, the time required for the insulation to retain 50% of its initial tensile strength is 7.42 years (65,000 hours), to retain 25% of its initial tensile strength is 15.41 years (1,35,000 hours), and to retain a DP level of 200 is 17.12 years (1,50,000 hours). Any of these criteria could be taken as a measure of a normal lifetime, depending on the experience or the degree of conservatism of the user. However, if the transformer is operated at a lower temperature continuously, the actual lifetime can be considerably longer than this. For example, if the maximum temperature is kept at 95°C continuously, the transformer insulation will take 36.6 years to lose 50% of its initial tensile strength. Conversely, if operated at higher temperatures, the actual lifetime will be shortened.

Depending on the loading, the hot-spot temperature will vary over the course of a single day; this must be taken into account in determining the lifetime. A revealing way of doing this is to compare the time required at a given temperature to produce a fractional loss of some material property, such as tensile strength, with the time required to produce the same loss of the property at the reference temperature of 110°C. The time required to produce the fractional loss f in the material property at temperature T is given by Equation 15.68, and the time to produce the same fractional loss at the reference temperature T_0 is given by the same formula, with T_0 replacing T . This latter time will be designated t_{T_0} . Hence, for the given fractional loss we have

$$\frac{t_{T_0}}{t_T} = e^{(B/T_0 - B/T)} = \text{AAF}(T) \quad (15.69)$$

We have defined the aging acceleration factor (AAF) in Equation 15.69. Thus, $\text{AAF}(T)$ times as much time is required at the reference temperature than at temperature T to produce the same fractional loss of life as determined by property X . Since T is in kelvin, converting to Celsius we have

$$\text{AAF}(T) = \exp \left\{ \frac{15,000}{T_0(^{\circ}\text{C}) + 273} - \frac{15,000}{T(^{\circ}\text{C}) + 273} \right\} \quad (15.70)$$

**FIGURE 15.14**

Aging acceleration factor relative to 110°C versus temperature.

The AAF is greater or lesser than 1 depending on whether $T(^{\circ}\text{C})$ is greater or lesser than $T_0(^{\circ}\text{C})$. This is plotted in Figure 15.14 for $T_0 = 110^{\circ}\text{C}$.

One method of using the daily variations of hot-spot temperature to compute aging is to subdivide a day into (not necessarily equal) time intervals over which the hot-spot temperature is reasonably constant. Let AAF_i be the aging acceleration factor for time interval Δt_i measured in hours. Then, for a full day

$$\text{AAF}_{\text{day ave}} = \frac{1}{24} \sum_{i=1}^N \text{AAF}_i \Delta t_i \quad (15.71)$$

where N is the total number of time intervals for that day.

The actual loss of lifetime will depend on the definition of lifetime. If the 50% retained tensile strength criterion is used, then in 1 day at a 110°C insulation hot-spot temperature, the transformer loses $24/65,000 = 3.69 \times 10^{-4}$ of its life. The fraction lost with variable hot-spot temperature is therefore $\text{AAF}_{\text{day ave}} \times 3.69 \times 10^{-4}$. For the 25% retained tensile strength criterion, the loss of life for 1 day is $\text{AAF}_{\text{day ave}} \times 1.78 \times 10^{-4}$.

A cautionary note must be sounded before too literal a use is made of this procedure. Gas bubbles can start to form in the oil next to the insulation when the insulation temperature reaches about 140°C. These bubbles can lead to dielectric breakdown, which can end the transformer's life, rendering the calculations inapplicable.

There is bound to be some uncertainty involved in determining the hot-spot temperature unless fiber optics or other probes are properly positioned and used. Short of this, the temperature should be estimated as best as

possible based on top oil temperature, winding gradients, and so on. A properly calibrated winding temperature indicator also can be used.

Since the AAF is independent of the choice made for the normal transformer lifetime, the fractional loss of life can be easily recalculated if a different choice of normal lifetime is made based on additional experience or knowledge.

15.12 Cable and Lead Temperature Calculation

Although the conductors in the coils are usually cooled sufficiently to meet the required hot-spot limits, we should also ensure that the lead and cable temperatures remain below these limits. Even though these are generally not in critical enough regions of electric stress to cause a breakdown, if gassing occurs the gassing itself can trigger alarms that could put the transformer out of service. Thus, the design engineer should ensure that the leads and cables are sized to meet the temperature requirements.

In general, no more insulation (paper) should be used on the leads and cables than is necessary for voltage standoff. Given the minimum paper thickness, the current-carrying area of the lead or cable should then be chosen so that the temperature limits are met when the rated current is flowing. A method for calculating the lead or cable temperature rise is given here that allows for the possibility that the lead is brazed to a cable and that some heat conduction can occur to the attached cable, acting as a heat sink. It also considers the case of a lead inside a duct or tube in addition to a lead in the bulk transformer oil.

We will consider a cylindrical geometry. If the lead is not cylindrical, an effective diameter should be calculated so that it may be approximated by a cylinder. The cylinder is assumed to be long so that end effects may be neglected. The geometric parameters are shown in Figure 15.15. The convective surface heat transfer coefficient of the oil is denoted by h . The thermal conductivities of the conductor and paper are denoted k_c and k_p , respectively, and the power generated per unit volume inside the conductor is denoted by q_v . This is given by the Joule loss density ρJ^2 , where ρ is the resistivity and J is the rms current density. To account for extra losses due to stray flux, we should multiply this by $(1 + f)$, where f is the stray flux loss contribution expressed as a fraction of the Joule losses.

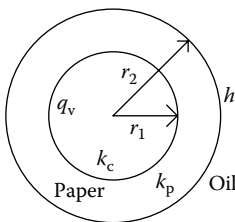


FIGURE 15.15
Cylindrical geometry of a paper-wrapped conductor surrounded by oil.

We will consider two cases for the convective heat transfer coefficient of the oil: (1) a horizontal cylinder in free tank oil and (2) a horizontal cylinder inside a channel. (The heat transfer coefficient for a vertical cylinder is higher, so the resulting temperature rises will be lower than for a horizontal cylinder.) These are given by [Kre80].

Natural convection from a horizontal cylinder of diameter D in bulk fluid is given by

$$\text{Nu}_D = \left[0.60 + 0.387 \left\{ \frac{\text{Gr}_D \text{Pr}}{[1 + (0.56/\text{Pr})^{9/16}]^{16/9}} \right\}^{1/6} \right]^2 \quad (15.72)$$

Mixed natural convection and laminar flow in horizontal ducts are given by

$$\text{Nu}_D = 1.75 \left[\text{Gz} + 0.012 (\text{Gz} \text{Gr}_D^{1/3})^{4/3} \right]^{1/3} \left(\frac{\mu_b}{\mu_s} \right)^{0.14} \quad (15.73)$$

where the symbols have the following meanings:

Nusselt number	$\text{Nu}_D = \frac{hD}{k}$
Reynolds number	$\text{Re}_D = \frac{\rho_m v D}{\mu}$
Prandtl number	$\text{Pr} = \frac{\mu c}{k}$
Grashof number	$\text{Gr} = \frac{g \beta \rho_m^2 D^3 (T_s - T_b)}{\mu^2}$
Graetz number	$\text{Gz} = \text{Re}_D \text{Pr} \left(\frac{D}{L} \right)$

v is fluid velocity, D is the hydraulic diameter for the flow inside ducts equal to $4 \times \text{flow area} / \text{wetted perimeter}$; D is equal to the outer cylinder diameter for external flow; L is the duct or cylinder length, g is acceleration of gravity (9.8 m/s^2), h is the surface convective heat transfer coefficient, k is thermal conductivity of transformer oil ($0.11 \text{ W/m} \cdot ^\circ\text{C}$), c is specific heat of transformer oil ($1880 \text{ J/kg} \cdot ^\circ\text{C}$), μ is oil viscosity ($6900.0/(T + 50)^3 \text{ N} \cdot \text{s/m}^2$), T is temperature in Celsius, ρ_m is oil mass density ($867 \exp[-0.00068 (T - 40)] \text{ kg/m}^3$), and β is the volume expansion coefficient of oil ($0.00068/^\circ\text{C}$). Subscripts s and b label the oil at the outside surface of the paper and the bulk oil.

In a steady state, the thermal equations governing this situation are as follows:

Inside the conductor:

$$\frac{1}{r} \frac{d}{dr} \left(r \frac{dT_c}{dr} \right) + \frac{q_v}{k_c} = 0 \quad (15.74)$$

Inside the paper:

$$\frac{1}{r} \frac{d}{dr} \left(r \frac{dT_p}{dr} \right) = 0 \quad (15.75)$$

The boundary conditions are

$$\text{At } r = 0, \quad \frac{dT_c}{dr} = 0$$

$$\text{At } r = r_1, \quad T_c = T_p \quad \text{and} \quad k_c \frac{dT_c}{dr} = k_p \frac{dT_p}{dr}$$

$$\text{At } r = r_2, \quad -k_p \frac{dT_p}{dr} = h(T_s - T_b)$$

where subscript c labels the temperature inside the conductor and subscript p labels the temperature inside the paper. The solution is given by

$$T_c(r) = \frac{q_v}{4k_c} (r_1^2 - r^2) + \frac{q_v r_1^2}{2k_p} \left[\ln \left(\frac{r_2}{r_1} \right) + \frac{k_p}{hr_2} \right] + T_b \quad (15.76)$$

$$T_p(r) = \frac{q_v r_1^2}{2k_p} \left[\ln \left(\frac{r_2}{r} \right) + \frac{k_p}{hr_2} \right] + T_b \quad (15.77)$$

The highest paper temperature occurs at $r = r_1$ at the conductor paper interface and is given in terms of temperature rise above the bulk oil by

$$T_c(r_1) - T_b = \frac{q_v r_1}{2} \left[\frac{r_1}{k_p} \ln \left(\frac{r_2}{r_1} \right) + \frac{r_1}{hr_2} \right] \quad (15.78)$$

The quantity $q_v r_1/2$ is the surface heat flux, q_s , since

$$q_s = \frac{q_v \pi r_1^2 L}{2\pi r_1 L} = \frac{q_v r_1}{2} \quad (15.79)$$

where L is the cylinder length, which is cancelled. Thus, Equation 15.78 can be expressed as

$$q_s = h_{\text{eff}} [T_c(r_1) - T_b] \quad (15.80)$$

in which

$$h_{\text{eff}} = \frac{h}{\frac{r_1}{r_2} + \frac{r_1 h}{k_p} \ln \left(\frac{r_2}{r_1} \right)} \quad (15.81)$$

is an effective heat transfer coefficient that takes into account conduction through the paper. In the case of a thin paper layer of thickness τ , where $\tau \ll r_1$ and $r_2 = r_1 + \tau$, Equation 15.81 reduces to

$$h_{\text{eff}} = \frac{h}{1 + \frac{\tau h}{k_p}} \quad (15.82)$$

Equation 15.82 also applies to a planar geometry. Note that the surface heat flux in Equation 15.79 is based on the surface area of a cylinder of radius r_1 , that is, the surface area of the metallic part of the cable.

We also need the temperature rise of the surface oil to compute the Grashof number. This is given by

$$T_p(r_2) - T_b = \frac{q_v r_1}{2} \left(\frac{r_1}{h r_2} \right) \quad (15.83)$$

Taking the ratio of Equation 15.83 to Equation 15.78, we get

$$\frac{T_p(r_2) - T_b}{T_c(r_1) - T_b} = \frac{1}{1 + \frac{h r_2}{k_p} \ln \left(\frac{r_2}{r_1} \right)} \quad (15.84)$$

so that the temperature rise of the surface paper can be found once the maximum temperature rise of the paper is calculated.

If another cable is brazed to the conductor, which may act as a heat sink, we must consider heat conduction along the conductor to the other cable. This situation is depicted in Figure 15.16.

Letting W equal the total power dissipated inside the conductor of length L , we have

$$\begin{aligned} W &= h_{\text{eff}} A_{\text{side}} (T_c - T_b) + h_{\text{cond}} A_{\text{cond}} (T_c - T_{\text{cable}}) \\ &= h_{\text{eff}} A_{\text{side}} (T_c - T_b) + h_{\text{cond}} A_{\text{cond}} (T_c - T_b) - h_{\text{cond}} A_{\text{cond}} (T_{\text{cable}} - T_b) \end{aligned} \quad (15.85)$$

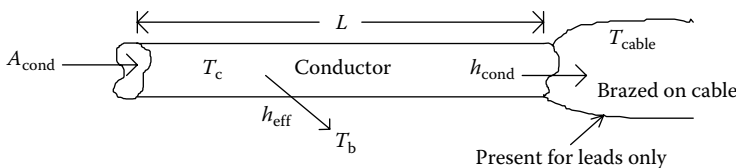


FIGURE 15.16

Geometry and thermal parameters for a cable or lead with another brazed to it.

where T_c is the temperature of the conductor's surface, T_b is the temperature of the bulk fluid, T_{cable} is the temperature of the brazed cable, p is the perimeter of the conductor's cooling surface, $A_{\text{side}} = pL$ is the conductor's side area through which heat flows to the cooling fluid, A_{cond} is the conductor's current-carrying area, $h_{\text{cond}} = k_{\text{cu}}/L$ is the heat transfer coefficient for heat to flow from the conductor to the brazed on cable. For copper, $k_{\text{cu}} = 400 \text{ W/m} \cdot ^\circ\text{C}$.

To use Equation 15.85 to obtain the temperature rise of the lead, the temperature rise of the cable must be calculated first. Since the cable is normally very long, its temperature rise can be obtained by neglecting its brazed connection.

Although we have indicated the numerical value of most of the material parameters in [Section 15.11](#), the missing ones are given as follows:

Thermal conductivity of paper $k_p = 0.16 \text{ W/m} \cdot ^\circ\text{C}$

Resistivity of copper $\rho = 1.72 \times 10^{-8} \{1 + 0.004 [T(^{\circ}\text{C}) - 20]\}$

v = oil velocity in duct = 2.54 mm/s (This is a conservative value. If a better value can be obtained, for example, from an oil flow calculated in the cooling program, then it should be used.)

In addition, note that many of these material parameters are temperature dependent so that we must specify a bulk oil temperature and iterate the calculations. The appropriate temperature to use for evaluating the oil parameters is $(T_s + T_b)/2$, that is, the average of the surface and bulk oil temperatures. The conductor's temperature is nearly uniform, so its maximum temperature can be used. The Grashof number depends on the temperature difference $T_s - T_b$, so this must be recalculated during the iteration process along with the other material parameters.

These formulas have been applied to some standard cable sizes to obtain the maximum continuous currents permissible for a hot-spot temperature rise of about 25°C. We assumed an oil temperature rise of 55°C above an ambient air temperature of 30°C resulting in a bulk oil temperature of 85°C. Thus, a rise of 25°C results in a hot-spot temperature of 110°C. The results are shown in [Table 15.2](#). Note that the conductor area does not fill 100% of the geometrical area of the cable since the conductor is stranded.

15.13 Tank Wall Temperature Calculation

Heating in the tank wall is due to eddy currents induced by the stray leakage flux from the main coils and flux from any nearby leads or busses. Generally, the presence of high-current-carrying leads near the tank wall is a chief cause for concern. We learned in Chapter 14 how these losses can be calculated. Here, we assume that these losses are known and that they are

TABLE 15.2
Maximum Continuous rms Currents for Standard Cable Sizes Producing a Temperature Rise above That of the Surrounding Oil (25°C)

Cable Size AWG/MCM	Conductor Area mm²	Conductor Diameter mm	Max Continuous Current (rms Amps)		
			2.4 mm Paper	6.35 mm Paper	12.7 mm Paper
6	13.30	4.72	125	100	85
4	21.15	5.97	170	135	114
2	33.63	7.52	230	180	152
1/0	53.48	9.50	320	245	205
2/0	67.42	10.67	375	285	235
3/0	85.03	13.54	465	345	285
4/0	107.23	15.22	545	405	330
300	152.00	18.14	700	515	415
350	177.35	19.63	780	570	460
400	202.71	20.96	860	625	505
500	253.35	23.44	1010	730	585
600	304.06	25.96	1155	830	660

uniformly distributed throughout the tank wall. We also assume that the tank wall surface dimensions involved are large compared with the tank wall thickness so that only one spatial dimension through the wall thickness is important. Figure 15.17 shows the geometric and other relevant parameters.

Here L is the wall thickness, q_v is the losses generated in the tank wall per unit volume, k is the thermal conductivity of the tank wall material, h_1 is the heat transfer coefficient from the inner tank wall to the oil, h_2 is the heat transfer coefficient from the outer tank wall to the air, and $T(x)$ is the temperature distribution in the tank wall.

The steady-state thermal equation for this situation is given by

$$\frac{d^2T}{dx^2} + \frac{q_v}{k} = 0$$

(15.86)

with the boundary conditions

$$k \frac{dT}{dx} \Big|_{x=0} = h_1 [T(x=0) - T_{oil}], \quad k \frac{dT}{dx} \Big|_{x=L} = -h_2 [T(x=L) - T_{air}]$$

(15.87)

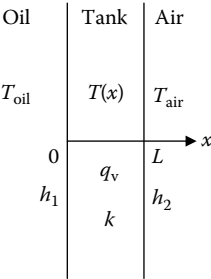


FIGURE 15.17
Tank wall geometry and thermal parameters.

The different signs in the two boundary conditions are necessary to properly account for the direction of heat flow. The solution can be expressed as

$$T(x) = T_{\text{oil}} - \frac{q_v L^2}{2k} \left(\frac{x}{L} \right)^2 + \left[\frac{\frac{q_v L^2}{2k} \left(1 + \frac{2k}{h_2 L} \right) - (T_{\text{oil}} - T_{\text{air}})}{1 + \frac{k}{h_1 L} \left(1 + \frac{h_1}{h_2} \right)} \right] \left(\frac{x}{L} + \frac{k}{h_1 L} \right) \quad (15.88)$$

Because the thermal transfer within the tank wall is much larger than that at the surface, that is k is much larger than $h_1 L$ or $h_2 L$, we ignore terms ≤ 1 relative to $k/h_1 L$ or $k/h_2 L$ and the $(x/L)^2$ term (which is also small), and thus, Equation 15.88 becomes

$$T(x) = T_{\text{tank}} = \frac{q_v L}{(h_1 + h_2)} + \frac{h_1 T_{\text{oil}} + h_2 T_{\text{air}}}{(h_1 + h_2)} \quad (15.89)$$

This equation is independent of x so that the tank wall temperature T_{tank} is essentially uniform throughout. The last term on the right is the weighted average of the oil and air temperatures, weighted by their respective heat transfer coefficients. The first term on the right accounts for the heat generated in the tank wall. We can use the heat transfer coefficients given in [Section 15.5](#). Another expression that could be used for heat transfer due to natural convection from one side of a vertical plate of height H immersed in a fluid (air or oil) is given by [Kre80]

$$h = 0.021 \frac{k}{H} (\text{Gr}_H \text{Pr})^{2/5} \quad (15.90)$$

The Grashof and Prandtl numbers have been defined in [Section 15.12](#). This expression holds for $10^9 < \text{Gr}_H \text{Pr} < 10^{13}$. To this, we would have to add the radiation term to the air heat transfer coefficient.

As a numeric example, let $h_1 = h_{\text{oil}} = 70 \text{ W}/(\text{m}^2 \cdot ^\circ\text{C})$, $h_2 = h_{\text{air}} + h_{\text{rad}} = 13 \text{ W}/(\text{m}^2 \cdot ^\circ\text{C})$, $k = k_{\text{steel}} = 40 \text{ W}/\text{m} \cdot ^\circ\text{C}$, $L = 9.525 \times 10^{-3} \text{ m}$. We then obtain $k/h_1 L = 60$ and $k/h_2 L = 323$. Both are much larger than 1. Let $q_v = 2 \times 10^5 \text{ W}/\text{m}^3$ and $q_v L^2/2k = 0.23$ so that the $(x/L)^2$ term is small and the approximate formula (Equation 15.89) may be used. At $T_{\text{oil}} = 85^\circ\text{C}$ and $T_{\text{air}} = 30^\circ\text{C}$, we obtain $T_{\text{tank}} = 99^\circ\text{C}$.

15.14 Tieplate Temperature

To calculate the tieplate's surface temperature, tieplate losses must be calculated using methods such as those discussed in Chapter 14. To make this temperature calculation tractable analytically, we make some idealized assumptions that appear to be reasonable. We assume the plate is infinite in two dimensions and that the losses decrease exponentially from the

surface facing the coils in the other dimension. The exponential drop-off is determined by the skin depth and has the form $e^{-x/\tau}$, where x is the distance from the free surface and τ is the skin depth. We assume that the surface facing the coils is cooled convectively by the oil with a heat transfer coefficient h . The boundary condition on the other surface facing the core will depend on the construction details, which may differ among manufacturers. We assume that there is a cooling gap here but that the heat transfer coefficient may be different from that at the other surface. To allow for an insulated-core facing surface, this heat transfer coefficient may simply be set to zero. This geometry and the cooling assumptions are identical to those we assumed for the tank wall temperature calculation. However, here we allow for an exponential drop-off of the loss density, which is more realistic in the case of magnetic steel tieplates. Thus, we use the geometric and thermal parameters given in Figure 15.17 except that air now refers to oil cooling on the surface at a distance $x = L$, where L is the tieplate thickness. Tieplates have a finite width, and we ignore the enhanced loss density at the corners, which is evident in the finite element study for magnetic steel in Chapter 14. However, there is also extra cooling at the corner from the side surface, which could mitigate the effect of this extra loss density. We can address this problem by means of a thermal finite element program. However, the analytic solution presented next should apply to temperatures away from the corner, and these may possibly be higher than or comparable to the corner temperature.

This is a one-dimensional steady-state heat transfer problem. The differential equation to solve is the same as Equation 15.86 in Section 15.13. However, here we have $q_v = q_{vo}e^{-x/\tau}$, where q_{vo} is the loss density at the surface ($x = 0$) and τ is the skin depth, rather than the constant assumption for q_v used for tank cooling. Thus, the side facing the coils is at $x = 0$. The boundary conditions are the same as Equation 15.87 with the air subscript replaced by oil. The solution is

$$T(x) - T_{oil} = \frac{q_{vo}\tau}{h_1} \left\{ 1 + \frac{h_1\tau}{k}(1 - e^{-x/\tau}) - \left(1 + \frac{h_1x}{k} \right) \left[\frac{e^{-L/\tau} \left(1 - \frac{h_2\tau}{k} \right) + \frac{h_2\tau}{k} + \frac{h_2}{h_1}}{1 + \frac{h_2L}{k} + \frac{h_2}{h_1}} \right] \right\} \quad (15.91)$$

We have expressed the solution in this form so that the case of an insulated back side ($h_2 = 0$) can be easily obtained. From Equation 15.91, we can obtain the surface temperature rise at $x = 0$:

$$T(x=0) - T_{oil} = \frac{q_{vo}\tau}{h_1} \left\{ 1 - \left[\frac{e^{-L/\tau} \left(1 - \frac{h_2\tau}{k} \right) + \frac{h_2\tau}{k} + \frac{h_2}{h_1}}{1 + \frac{h_2L}{k} + \frac{h_2}{h_1}} \right] \right\} \quad (15.92)$$

As a numerical example, let us consider the surface temperature rise above the surrounding oil for mag steel and stainless steel tieplates using the following parameters:

$$h_1 = 70 \text{ W/m}^2 \cdot ^\circ\text{C}$$

$$h_2 = 20 \text{ W/m}^2 \cdot ^\circ\text{C}$$

$$L = 9.525 \times 10^{-3} \text{ m}$$

$$k = 40 \text{ W/m} \cdot ^\circ\text{C} \text{ (mag steel)}$$

$$k = 15 \text{ W/m} \cdot ^\circ\text{C} \text{ (stainless steel)}$$

$$\tau = 2.297 \times 10^{-3} \text{ m} \text{ (mag steel)}$$

$$\tau = 5.627 \times 10^{-2} \text{ m} \text{ (stainless steel)}$$

We will compare these two materials when their total losses are the same. This means that the losses per unit surface area should be the same since we assume the geometry is unlimited in the plane of the surface. Letting q_A be the loss per unit area obtained by integrating q_v over the thickness of the tieplate L , we can obtain q_{vo} . We get

$$q_{vo} = \frac{q_A}{\tau(1 - e^{-L/\tau})} \quad (15.93)$$

Using Equations 15.92 and 15.93 and the numerical data given above, we obtain the surface temperature rise above the ambient oil for the two types of tieplates in terms of q_A :

$$T(x=0) - T_{oil} = 0.0111 q_A \text{ (mag steel)}$$

$$T(x=0) - T_{oil} = 0.0111 q_A \text{ (stainless steel)}$$

with q_A in watts per square meter (W/m^2) and temperatures in Celsius. Thus, we see that for the same total loss, which is simply q_A multiplied by the lateral dimensions of the tieplate, magnetic iron tieplates have the same surface temperature rise as stainless steel tieplates. Even though the losses are distributed quite differently in the two materials, with the mag steel having a higher concentration of losses near the surface, the higher thermal conductivity of the mag steel rapidly equalizes the temperature within the material so that extreme temperature differences cannot develop.

If the back surface were insulated ($h_2 = 0$), all the losses would have to leave the front surface in the steady state. In this case also, the surface temperatures of the mag steel and stainless steel tieplates would be nearly identical for the same total loss. As h_2 increases up to h_1 , the front surface temperatures gradually differ for the two cases but not significantly.

15.15 Core Steel Temperature Calculation

Because core steel is made up of thin stacked insulated laminations, it has an anisotropic thermal conductivity. The thermal conductivity in the plane of the laminations is much higher than the thermal conductivity perpendicular to this plane or in the stacking direction. The steady-state heat conduction equation in rectangular coordinates for this situation is

$$k_x \frac{\partial^2 T}{\partial x^2} + k_y \frac{\partial^2 T}{\partial y^2} + q_v = 0 \quad (15.94)$$

where the thermal conductivities k , which can differ in the x - and y -directions, are labeled accordingly. We assume the loss per unit volume q_v to be constant here. Again there are finite element programs that can solve this equation for complex geometries such as a stepped core. We will derive a simple but approximate analytical solution here for a rectangular geometry as shown in Figure 15.18.

This geometry could apply to one step of a core, say the central step, with cooling ducts on the long sides or to all or part of a core between two cooling ducts by suitably calculating the effective dimensions by approximating a rectangle from the steps involved.

We look for a solution of Equation 15.94 of the form

$$T(x, y) = A + Bx + Cx^2 + Dy + Ey^2 \quad (15.95)$$

that satisfies the boundary conditions at the center

$$\frac{\partial T}{\partial x} = \frac{\partial T}{\partial y} = 0 \quad \text{at} \quad x = y = 0 \quad (15.96)$$

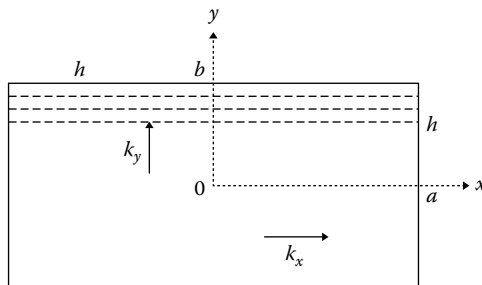


FIGURE 15.18

Rectangular geometry for anisotropic thermal calculation.

This is required by symmetry. At the outer surfaces, we only approximately satisfy the boundary conditions for convective cooling:

$$\begin{aligned} -k_x \frac{\partial T}{\partial x} &= h(T - T_{\text{oil}}) \quad \text{at } x = a, y = 0 \\ -k_y \frac{\partial T}{\partial y} &= h(T - T_{\text{oil}}) \quad \text{at } x = 0, y = b \end{aligned} \quad (15.97)$$

This means that we satisfy the convective boundary condition exactly only at the surface points on the two axes. However, this is where we will evaluate the surface temperature. Based on these assumptions, the solution is

$$T(x, y) - T_{\text{oil}} = \frac{q_v}{h} \left[\frac{1 - \left(\frac{\frac{ha}{2k_x}}{1 + \frac{ha}{2k_x}} \right) \left(\frac{x}{a} \right)^2 - \left(\frac{\frac{hb}{2k_y}}{1 + \frac{hb}{2k_y}} \right) \left(\frac{y}{b} \right)^2}{\frac{1}{a \left(1 + \frac{ha}{2k_x} \right)} + \frac{1}{b \left(1 + \frac{hb}{2k_y} \right)}} \right] \quad (15.98)$$

Note that a and b are half the rectangle dimensions. We can estimate the thermal conductivity in the direction perpendicular to the lamination plane (the y -direction here) by knowing the coating thickness or stacking factor and the thermal properties of the coating. For stacked silicon steel, we use $k_x = 30 \text{ W/m} \cdot ^\circ\text{C}$ and $k_y = 4 \text{ W/m} \cdot ^\circ\text{C}$. Letting $h = 70 \text{ W/m}^2 \cdot ^\circ\text{C}$ for convective oil cooling, assuming an effective stack or rectangle size of $0.762 \text{ m} \times 0.254 \text{ m}$, and using $q_v = 10^4 \text{ W/m}^3$ (1.3 W/kg), we find for the maximum internal temperature rise above the surrounding oil $T(x = 0, y = 0) - T_{\text{oil}} = 25.8^\circ\text{C}$. The surface temperature rise in the x or long dimension is $T(x = a, y = 0) - T_{\text{oil}} = 17.8^\circ\text{C}$, and the surface temperature rise at the surface at $y = b$ in the short direction perpendicular to the stack is $T(x = 0, y = b) - T_{\text{oil}} = 12.2^\circ\text{C}$. Note that the surface in the direction of lower thermal conductivity is actually cooler than the surface toward which heat is more easily conducted. This is because with the central temperature the same the thermal gradient is smaller in the high-conductivity direction relative to the lower one.

The temperatures calculated with Equation 15.98 were compared with temperatures obtained with a two-dimensional (2D) finite element thermal code, keeping the uniform loss density and thermal parameters the same for the two methods. The actual core step pattern and core ducts were used for the 2D model. The maximum internal core temperature and maximum surface temperature were compared for each step. They were the same within a few degrees for the two methods.

16

Load Tap Changers

16.1 Introduction

The flicker of the house lights while having dinner is a sign of a load tap changer (LTC) tap change. When most people get home from work, they start using electricity for cooking and lighting. This increases the electrical load on the distribution network, which causes the voltage to sag below its nominal value. This signals the LTC to change taps in order to adjust the voltage back to its nominal value with some tolerance.

There are many applications for transformers in modern electric power systems: generator step-up, system interconnection, distribution, arc furnace, and high-voltage direct current (HVDC) converters, to mention just a few. The role of a transformer is to convert electrical energy of one voltage level to another voltage level. As power systems become larger and more complex, power transformers play a major role in their efficiency and stability. For each transformer installed in a network, there is an ideal (optimal) voltage ratio for the optimal operation of the system. Unfortunately, this optimal voltage ratio varies depending on the operating conditions of the total network. Early in the history of electric power systems, it became evident that for power systems to operate satisfactorily, transformer voltage ratios needed to be adjustable without interrupting the flow of energy. This is the role of an LTC.

16.2 General Description of Load Tap Changers

An LTC is a device that connects different taps of the tapped windings of transformers without interrupting the load. It must be capable of switching from one tap position to another without interrupting the flow of the current to the load and without creating a short circuit between any two taps of the transformer winding. Tap-changing transformers are used to control the voltage or the phase angle—or both—in a regulated circuit.

An LTC is made up of four elements:

1. A selector switch that allows the selection of the active tap
2. A changeover switch, referred to as a “reversing switch” when it reverses the polarity of the tapped winding, used to double the number of positions available
3. A transition mechanism, including an arcing or diverter switch, which effects the transition from one tap to the other
4. A driving mechanism that includes a motor, gearbox, and controls to drive the system

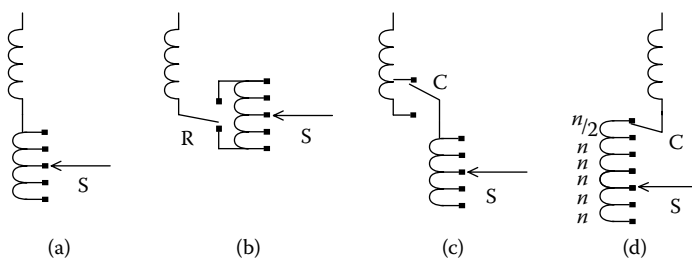
There are two generic types of tap changers:

1. In-tank: The cover-mounted, in-tank tap changer, known as the Jansen type, is seated in the main transformer oil with the core-and-coil assembly. Its selector and changeover switches are located at the bottom of the tap changer in the main oil. The arcing (diverter) switch is located in a separate compartment at the top, usually within a sealed cylinder made of fiberglass or other similar material. All arcing is confined to this compartment. They exist in single- or three-phase neutral end Wye (Y)-connected versions. For three-phase fully insulated applications, three single-phase tap changers must be used. This type of tap changer is used for higher levels of voltages or currents.
2. Separate compartment: The side-mounted, separate-compartment types have their own boxes and are assembled separately from the transformer. They are bolted to the side of the tank and connected to the transformer’s tapped windings through a connecting board. Their selector, changeover, and arcing switches are located in an oil compartment that is completely isolated from the main transformer oil. Some have two compartments—one for the arcing switch, and one for the selector and changeover switches. Others have all components within a single compartment. They are available in three-phase assemblies—either Y-connected for application at the neutral end of a three-phase transformer, or fully insulated for application at the line end.

16.3 Types of Regulation

The main types of regulation are illustrated in [Figure 16.1](#) and are discussed below.

Linear: In linear switching, tapped turns are added in series with the main winding, and their voltage adds to the voltage of the main

**FIGURE 16.1**

Main regulation types of LTCs. S = selector switch, C = changeover switch, R = reversing switch. (a) Linear, (b) reversing, (c) coarse-fine, and (d) bias winding.

winding. No changeover switch is needed for this type. The tapped winding is totally bypassed in the minimum-voltage position. The rated position can be any one of the tap positions.

Plus-minus (reversing): In a reversing-type regulation, the whole tapped winding can be connected in additive or reversed polarity with respect to the main winding, with the tapped turns adding or subtracting their voltages, respectively. The tapped winding is totally bypassed in the neutral (midrange)-voltage position. The rated position is normally the middle one. The total number of positions available is equal to twice the number of sections in the tapped winding, plus one.

Coarse-fine: The coarse-fine regulation is a two-stage linear regulation in which the first, or coarse, stage contains a large number of turns that can be totally bypassed by the changeover selector. These turns are shown as a single loop in the top coil of Figure 16.1. Fine regulation is achieved with the selector switch. Normally, the coarse section contains as many turns as the tapped winding plus one section. Thus, the total number of positions available is twice the number of sections in the tapped winding, plus one.

Bias winding: The bias-winding type is similar to the coarse-fine type, except that the number of turns in the bias winding is half the turns of one section of the tapped winding. It is used to provide half steps between the main tap steps. Thus, the total number of positions available is twice the number of sections in the tapped winding, plus one. The bias-winding technique can be combined with the reversing scheme to provide twice the number of positions (four times the number of sections in the tapped winding, plus one) at the expense of adding one more switch and increasing the complexity of the switching-and-driving mechanism.

Although not indicated in Figure 16.1, the tap-selector switch is often a circular type of switch that allows a smooth transition between the tap voltages when the changeover or reversing switch operates.

16.4 Principles of Operation

An LTC must be capable of switching from one tap position to another without interrupting the flow of current to the load at any time. It must, therefore, follow a “make-before-break” switching sequence. It also must not create a short circuit between any two taps of the transformer winding at any time. This means that during the make-before-break interval, some mechanism must prevent the shorting of the turns. This is accomplished primarily in two ways, discussed in [Sections 16.4.1](#) and [16.4.2](#).

16.4.1 Resistive Switching

Figure 16.2 shows an example of a six-step switching sequence. This particular type of tap changer has two selector switches and an arcing switch with four contacts.

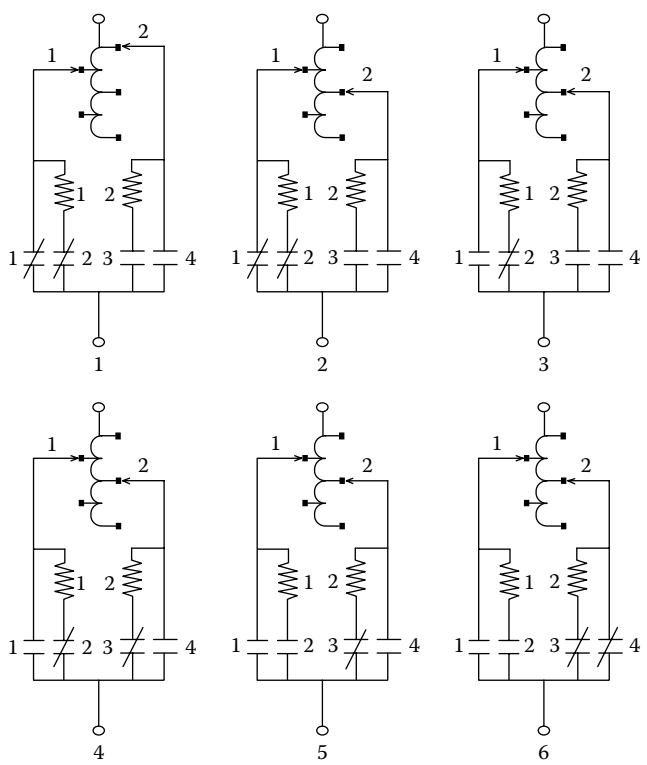


FIGURE 16.2 Sequence of operations involved in tap changers using resistive switching. The selector switches are the topmost switches. The arcing switch is closed when a diagonal (shorting) line is present and open in other cases.

1. Step 1 of [Figure 16.2](#) shows the steady state of the tap changer just before the switching operation. The load current is flowing through contact 1 and selector 1. We call that position tap 2.
2. At step 2, the nonconducting selector has moved two steps down, from position 1 to position 3. The current is still flowing in contact 1 and selector 1.
3. At step 3, contact 1 opens and the current flows through resistor 1 and selector 1.
4. At step 4, contact 3 closes and the current splits between the two resistors and the two selectors. There is also a circulating current flowing into the loop, limited by the two resistors and the reactance of the loop.
5. At step 5, contact 2 opens, breaking the current in the resistor and selector 1. Arcing occurs at that moment, and the arc remains on until the current crosses the zero line. At worst, the arc can last one half-cycle which, at 60 Hz, is 8 milliseconds. The average arcing time is around 5–6 milliseconds.
6. At step 6, contact 4 closes, and the load current bypasses resistor 2 and goes directly to selector 2. The tap changer has reached the steady state for tap position 3.

This type of transition requires that the resistors be capable of withstanding the full load current plus the circulating current during the transition (steps 3 to 5). To reduce the energy-absorption requirement for the resistors, the duration of the complete transition has to be minimized. These tap changers normally have very fast transitions.

16.4.2 Reactive Switching with Preventive Autotransformers

Another widely used method of handling the transition from one tap to another is to use reactors instead of resistors. These reactors do not have to dissipate as much energy as the resistors. They mainly use reactive energy, which does not produce any heat. Therefore, they can be designed to withstand the full load plus the circulating current for long periods, even continuously. Two reactors are needed per phase. They are normally wound on a common gapped core, making them mutually coupled. When they are connected in series, they act as an autotransformer, whereas in parallel, they act as a single reactor. Transformer designers take advantage of this feature, using the reactors not only to prevent the load current from being interrupted or sections of a tapped winding from being shorted, but also to act as a transformer and provide intermediate voltage steps between two consecutive tap sections of the main transformer. The total number of positions available using this scheme is twice the number of sections in the tapped winding plus one.

This method of operation is schematically represented in [Figure 16.3](#). The tap changer has two selectors, two reactors (actually, one reactor with two windings), two bypass switches (1 and 2), and an arcing switch (3).

1. In step 1 of Figure 16.3, the tap changer is in the steady-state mode in tap position 2. The load current flows through the two selectors, the two reactors, and the bypass switches. Although the arcing switch is closed, no current flows through it.
2. In step 2, the bypass switch opens. The current flows through switch 1 and splits up between the two reactors and the two selectors.
3. In step 3, the arcing switch opens. The entire current flows through reactor 1 and selector 1. Arcing occurs at this step because the current in the reactor is interrupted.
4. In step 4, the right selector moves a step to the right, but carries no current.
5. In step 5, the arcing switch closes, causing current to flow again in reactor 2 and selector 2. Note that the two selectors are on different taps. This causes a circulating current to flow into the loop.
6. In step 6, the bypass switch 2 closes and a steady-state condition is reached, in this case, tap position 1. Because the two ends of the

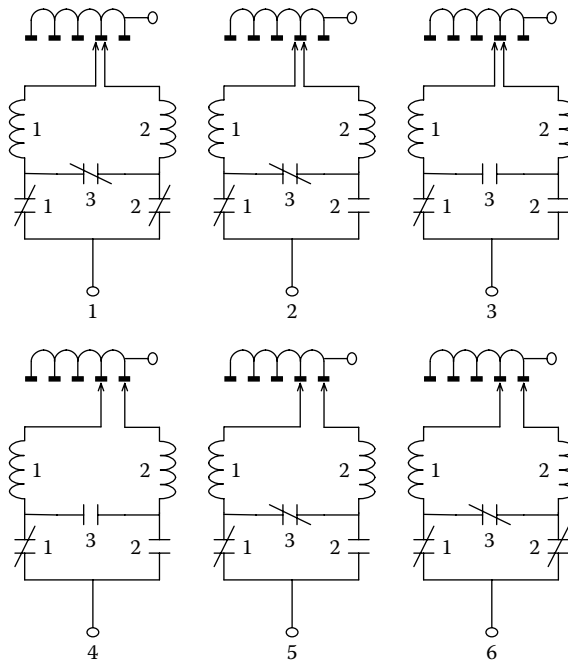


FIGURE 16.3

Sequence of operations involved in tap changers using reactive switching.

reactors are on two different taps, they are in series between the two taps. The voltage at their midpoint is half way between the two taps. This state is called the “bridging position,” where the reactors bridge the two taps.

When combined with a reversing switch, this scheme provides four times as many voltage positions as tapped sections in the winding plus one. The cost is that both the reactor and the tapped winding must be designed to continuously withstand the full load current plus the circulating current; moreover, the reactor introduces current losses and draws more magnetizing current from the source, especially at bridging positions. It might also add audible noise to the transformer.

16.5 Connection Schemes

16.5.1 Power Transformers

Normally, transformers’ primary winding is fed at a constant voltage and the role of the tap changer is to add or subtract turns to vary the voltage ratio of the transformer and maintain its output at a constant voltage despite fluctuations in the load current. In principle, this can be accomplished by changing the number of active turns either in the primary or secondary winding. There are subtle differences in the two ways of connecting the tap changer that transformer and system designers should be aware of.

Fixed volts per turn: The most natural way to add a tapped winding to a transformer is to connect it in series with the regulated side. As shown in Figure 16.4, the primary winding of the transformer (H1–H2) is fed at a constant voltage, and it has a fixed number of turns. Therefore, the value of volts per turn of the transformer is constant. The voltage across X1–X2 varies with the number of turns. If all the taps have an equal number of turns, then the voltage increase is equal for each step. If the X winding is Y-connected, then the tapped winding and the tap changer can be placed at the low-potential neutral end and do not require a high insulation level. The cost is that the tap changer must be capable of carrying the current of the X winding. For high-current windings, the cost of such a tap changer can become prohibitive. Another disadvantage is that low-voltage (LV) windings often have few turns. The design of the

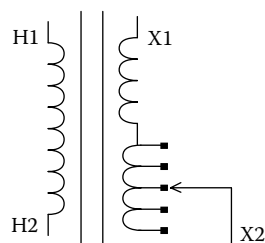


FIGURE 16.4
Fixed volts-per-turn tap-changer scheme.

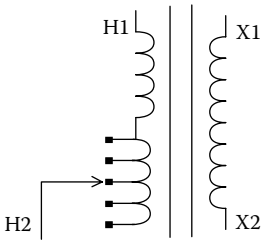


FIGURE 16.5
Variable volts-per-turn tap-
changing scheme.

tapped winding might become impractical—if not impossible—considering that fractional turns cannot be used.

Variable volts per turn: One way to solve the problem of high-current LV windings is to put the tapped winding on the high-voltage (HV) side. The LV side can still be regulated in this way. This is particularly applicable if the HV is Y-connected, since the tap changer could be placed at the neutral end and would not require a high insulation level while not carrying a high current. This scheme is illustrated in Figure 16.5.

Although this solution might look very attractive, it does have disadvantages:

1. If we consider that the voltage across H1–H2 is constant, varying the number of turns in that winding implies that the volts per turn, and thus the flux in the core, varies since the core flux is proportional to the volts per turn. This means that the core must be designed for the minimum-turn position because this position requires the core to carry its maximum flux. The core would be bigger than its fixed volt-per-turn counterpart and would really be used efficiently only at that minimum-turn position. At any other position, it operates at lower flux densities.
2. If the flux varies in the core, the no-load losses, exciting current, impedance, and sound level of the transformer will also vary. If a transformer is designed to meet certain guaranteed losses and sound level at the rated position, which is generally the middle position, it is likely that it will exceed these guaranteed values significantly at the minimum-turn position.
3. In a variable-flux transformer, the voltage variation per step is not constant, even if the number of turns per step is constant. This is because the volts per turn changes with the step position.
4. If a third winding in the transformer is used to feed a different circuit, its voltage will vary as the tap changer moves, which might not be desirable.

16.5.2 Autotransformers

Autotransformers with tap changers present special challenges for transformer designers. There are three ways of connecting a tap changer in an autotransformer without using an auxiliary transformer. These are illustrated in [Figures 16.6 through 16.8](#).

The connection shown in Figure 16.6 is used when the HV of the transformer will vary while the LV will be constant. In this case, we assume that the LV side is supplied by a fixed-voltage source. The voltage at the HV terminal varies linearly with the number of turns added to or subtracted from the series winding. The flux in the core is constant. In this type of connection, the tap changer and the tapped winding must be rated for the voltage level of the LV line terminal plus the voltage across the tapped section. The tapped winding is directly exposed to any voltage surge coming through the LV line; therefore, extra precautions have to be taken at the design stage itself.

Figure 16.7 shows the connection used when the HV side of the transformer will be kept constant while the LV varies. In this case, the HV side is fed from a constant-voltage source. The voltage at the LV terminal varies linearly with the number of turns added or subtracted in series with the LV line. As in the previous case, the flux in the core is constant; the tap changer and the tapped winding must be designed for the voltage level of the LV line terminal plus the voltage across the tapped section. The taps are directly exposed to any voltage surge coming through the LV line, so extra precautions must be taken at the design stage. Finally, the tap changer must be designed to carry the full load current of the LV terminal.

In the previous two cases, if a three-phase transformer is designed, the tap changer must have full insulation between the phases. If the voltage on the LV side is above 138 kV, then three single-phase, Jansen-type tap changers must be used.

The connection shown in Figure 16.8 can be used when the LV will vary while the HV will be kept constant. The advantages of this connection are

1. The level of insulation needed for the tapped winding and the tap changer is low.
2. A Y-connected three-phase tap changer can be used for a three-phase transformer.

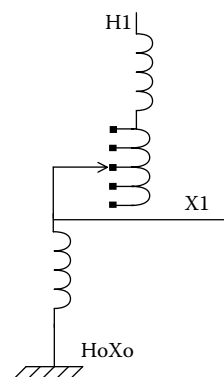


FIGURE 16.6
Taps in the series winding of an autotransformer.

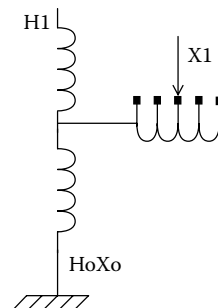


FIGURE 16.7
Taps in the LV line from the autotransformer connection.

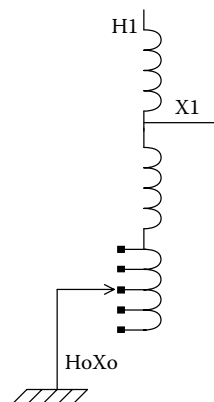


FIGURE 16.8
Taps at the neutral end in the common winding of an autotransformer.

3. The current in the common winding is lower than that in the LV line terminal, so a smaller tap changer can be selected.

As usual, there is a cost to obtaining these benefits. If we assume that the voltage between H1 and HoXo is constant, varying the number of turns implies varying the volts per turn, and therefore the flux in the core; this is a variable flux design. In a variable flux transformer, the losses, exciting current, impedance, and sound level vary with the tap position, and a bigger core must be selected for proper operation at the minimum-turn position. If there is a tertiary winding, its voltage will vary as the tap changer changes its position.

In an autotransformer connection, the turns in the common branch are part of both the HV and LV circuits. This means that if we add turns in the common branch, we add turns to both the HV and LV circuits. Because of this, the number of turns required to achieve a specified regulating range is higher than that needed for the other two cases.

We derive the tap-winding requirements for regulating the LV or common winding voltage by the positive and negative fractional voltages, respectively designated f_p and f_m . Let N_s , N_C , and N_T be the turns in the series, common, and tap windings, respectively. These turns are for the individual windings. Let V_H and V_X , respectively, be the high and low terminal-to-ground voltages, assuming a Y connection. For a delta connection, these would refer to the phase voltages. Although V_H is assumed to be fixed, V_X will change with tap position and will be labeled V_{Xp} , V_{X0} , and V_{Xm} for the positive, neutral, and negative tap positions, respectively.

Using the terms VPT_p , VPT_0 , and VPT_m to indicate the volts per turn for the positive, neutral, and negative tap settings, we have

$$\begin{aligned} VPT_p &= \frac{V_H}{N_s + N_C + N_T} \\ VPT_0 &= \frac{V_H}{N_s + N_C} \\ VPT_m &= \frac{V_H}{N_s + N_C - N_T} \end{aligned} \tag{16.1}$$

The LV voltages for the different tap positions are

$$\begin{aligned} V_{Xp} &= (N_C + N_T)VPT_p \\ V_{X0} &= (N_C)VPT_0 \\ V_{Xm} &= (N_C - N_T)VPT_m \end{aligned} \tag{16.2}$$

The fractional-voltage changes corresponding to the positive and negative tap settings are

$$\begin{aligned}
 f_p &= \frac{V_{xp} - V_{x0}}{V_{x0}} = \frac{V_{xp}}{V_{x0}} - 1 = \left(\frac{N_C + N_T}{N_C} \right) \frac{VPT_p}{VPT_0} - 1 \\
 &= \left(\frac{N_C + N_T}{N_C} \right) \left(\frac{N_S + N_C}{N_S + N_C + N_T} \right) - 1 = \left[\frac{1 + \frac{N_S}{N_C}}{1 + \frac{N_S}{N_C + N_T}} \right] - 1 \\
 f_m &= \frac{V_{x0} - V_{xm}}{V_{x0}} = 1 - \frac{V_{xm}}{V_{x0}} = 1 - \left(\frac{N_C - N_T}{N_C} \right) \frac{VPT_m}{VPT_0} \\
 &= 1 - \left(\frac{N_C - N_T}{N_C} \right) \left(\frac{N_S + N_C}{N_S + N_C - N_T} \right) = 1 - \left[\frac{1 + \frac{N_S}{N_C}}{1 + \frac{N_S}{N_C - N_T}} \right]
 \end{aligned} \tag{16.3}$$

Solving Equation 16.3 for N_T , we obtain two different values corresponding to f_p and f_m , which we will label N_{Tp} and N_{Tm} . They are

$$\begin{aligned}
 N_{Tp} &= \frac{N_C + N_S}{\frac{1}{f_p} \left(\frac{N_S}{N_C} \right) - 1} \\
 N_{Tm} &= \frac{N_C + N_S}{\frac{1}{f_m} \left(\frac{N_S}{N_C} \right) + 1}
 \end{aligned} \tag{16.4}$$

Here, we might want to take the largest N_T value to get the full regulation in one direction, at the expense of providing more than the required regulation in the other direction. If we take an average of the two values, calling it N_{Tave} , we get

$$N_{Tave} = \frac{1}{2} (N_C + N_S) \left(\frac{N_S}{N_C} \right) \left\{ \frac{\frac{1}{f_p} + \frac{1}{f_m}}{\left[\frac{1}{f_p} \left(\frac{N_S}{N_C} \right) - 1 \right] \left[\frac{1}{f_m} \left(\frac{N_S}{N_C} \right) + 1 \right]} \right\} \tag{16.5}$$

When we have $f_p = f_m = f$, this simplifies to

$$N_{\text{Tave}} = (N_C + N_S) \left\{ \frac{\frac{1}{f} \left(\frac{N_S}{N_C} \right)}{\left[\frac{1}{f} \left(\frac{N_S}{N_C} \right) \right]^2 - 1} \right\} \quad (16.6)$$

As an example, suppose that we want a $\pm 10\%$ voltage regulation on the LV winding and we have 100 turns each in the series and common windings. If the taps are X-line taps, $N_T = 10$ turns are required. For neutral taps, using Equation 16.4, we find that $N_{Tp} = 22.2$ turns and $N_{Tm} = 18.2$ turns. We might want to use 22 turns in the tap winding to get the full positive regulation and provide more than the required negative regulation. Taking an average of the positive and negative tap turns and using Equation 16.6, since $f_p = f_m$, we get $N_{\text{Tave}} = 20.2$ turns. This means we need about twice as many turns for the neutral taps compared with the X-line taps in order to achieve the $\pm 10\%$ voltage variation at the X terminal.

Another consideration is the core flux or, for a given-sized core, the flux density; this is proportional to the volts per turn. Because the negative tap setting has the highest value of volts per turn, the maximum core flux should not exceed this value. The maximum core flux is usually specified for rated conditions. This value would then have to be reduced to allow for the higher flux density at the negative tap setting. The reduction factor, F_R is given by

$$F_R = \frac{VPT_0}{VPT_m} = \frac{N_C + N_S - N_T}{N_C + N_S} = 1 - \frac{N_T}{N_C + N_S} \quad (16.7)$$

If we use the average value for N_T and assume that $f_p = f_m = f$, then we get, for F_R ,

$$F_R = 1 - \left\{ \frac{\frac{1}{f} \left(\frac{N_S}{N_C} \right)}{\left[\frac{1}{f} \left(\frac{N_S}{N_C} \right) \right]^2 - 1} \right\} \quad (16.8)$$

For the numerical example given after Equation 16.6, we get $F_R = 0.9$. Thus, the transformer would need to be designed for a flux density that is 10% below the rated value.

Another consideration is the million volt ampere (MVA) value of the tap winding. Since the full LV load current flows in the $\pm 10\%$ X-line taps, the

MVA rating is 10% of the terminal MVA. The neutral taps have 20% of the common winding turns and the current in them is the terminal current times the co-ratio. The neutral co-ratio is 0.5 and the positive- and negative-tap co-ratios are 0.455 and 0.556. Using the negative-tap co-ratio, the neutral tap rating is $0.2 \times 0.556 = 0.111$, or 11% of the terminal MVA; therefore, the rating is a bit higher than that for the X-line taps.

16.5.3 Use of Auxiliary Transformers

When a transformer with a relatively high-current LV winding is specified and regulation is desired on the LV side, using an auxiliary transformer to achieve regulation may be economical. It will give the designer greater flexibility in the design of the tapped winding, and the savings on the main transformer often outweigh the cost of the auxiliary transformer. There are two popular ways of using auxiliary transformers:

1. The series voltage regulator: The tapped winding is located on the auxiliary transformer, which is in turn inserted in series with the LV line terminal, adding or subtracting its voltage from the LV winding of the main transformer. The main transformer has only two windings and can be optimized independently from the series-voltage regulator. This is shown in Figure 16.9.

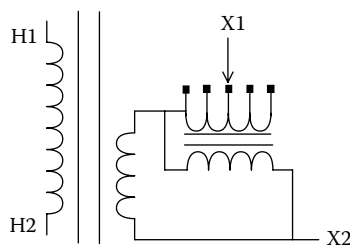


FIGURE 16.9
Tap-changing scheme using a series-voltage regulator.

2. The series (booster) transformer: The tapped winding is a separate winding on the main transformer. The advantage of this connection is that there is much more flexibility in the design of the tapped winding. The number of turns per step can be selected such that the tap changer carries a smaller current. The main savings in this case pertain to the tap changer itself and the greater flexibility available in the optimization of the main transformer. This is shown in Figure 16.10.

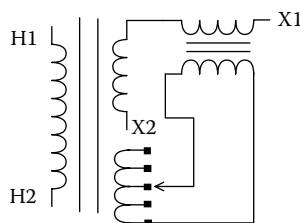


FIGURE 16.10
Tap-changing scheme using a series (booster) transformer.

Auxiliary transformers can be used with autotransformers in the same way. Numerous connections using auxiliary transformers are possible. The choice is limited only by the imagination of the designer.

16.5.4 Phase-Shifting Transformers

A phase-shifting transformer is ideally a transformer with a 1:1 voltage ratio that also has the ability to change the phase angle of its output voltage relative to its input. Electric power companies use this feature to help transfer power more efficiently within the electrical grid. In these transformers, the voltage from the tapped windings is added in quadrature with the input line terminals, producing an effective phase shift in the output. Many connection types are available to achieve this, some of which are discussed in Chapter 7. We will just mention here that the tap changer is a key element in a phase-shifting transformer and the sizes and ratings of the tapped windings are much higher than those for conventional transformers.

16.5.5 Reduced versus Full-Rated Taps

Because the current in the regulated winding and possibly in the tap winding and the tap changer is larger than the rated current at the negative tap setting, it is sometimes desirable to limit it to be the same as the rated current; effectively, this amounts to reducing the MVA of the transformer at the negative tap setting. In this case, the taps are referred to as having a reduced rating. In all other cases, the taps are referred to as having a full rating.

16.6 General Maintenance

Maintaining a tap changer ensures its reliability. Any device with moving parts, especially if some are used to interrupt currents and voltages, requires maintenance. It would be useless to repeat here what can be found in the manufacturers' instruction books. We will only mention the general principles. Factors affecting the reliability of tap changers include the following:

- Quality of the oil
- Contact pressure
- Contact resistance and temperature
- Timing of movements
- Load currents
- Number of operations

Maintenance of the controls and the drive mechanism is normally not a problem. The gears and other moving parts might wear out and require replacement, but in general they are designed to last a long time and do not need

frequent inspection. The main areas of concern are the switches and the connecting board, if present. The contacts have to be inspected and verified periodically. The frequency of these inspections depends mainly on the number of operations, the current flowing through the contacts, and the cleanliness of the oil.

The inspection and replacement of contacts requires that the transformer be taken out of service. Because it is always costly to take a transformer out of service, extending the period between inspections as much as possible is desirable. In addition to the recommendations that can be found in most instruction books for tap changers, some of the tactics used by utilities to reduce the maintenance costs and the failure rates of their tap changers are discussed next.

The process of changing the tap position includes arcing, which generates gases and carbon particles. The movement of contacts also promotes erosion of the metal and generates small metal particles. In the long run, these particles can affect the dielectric properties of the oil. Moreover, the carbon particles tend to aggregate on the surfaces of contacts and increase the contact resistance. They also accumulate on connecting boards and may lead to tracking on the surface of the board. For these reasons, the reliability of a tap changer and its overall performance can be improved by a simple filtering device that keeps the oil clean. This is especially important if the arcing switch is located in the same compartment as the selector and changeover switches. Some utilities have introduced oil filters for LTCs and have found that these filters can extend the interval between inspections. However, in some tap changers, arcing occurs in a separate vacuum chamber so that oil contamination is reduced or eliminated.

In a tap changer, contacts that operate frequently remain clean. The ones that do not move for long periods tend to oxidize, collect carbon, or both. With time, their contact resistance increases, which produces more heat, and the situation deteriorates. This is typical of changeover selectors. Some of these operate only twice a year. Many cases of damage to these switches have been reported. Several utilities now force their tap changers to ride over the midposition at least once a month, and they claim a much better performance of their tap changers since introduction of the procedure.

Instead of taking all transformers out of service for regular and frequent inspections of tap changers, some utilities have introduced monitoring procedures for tap changers without deenergizing their transformers. One of these procedures is dissolved-gas analysis. This involves regularly taking oil samples from tap changer compartments and monitoring the gases. After a while, the patterns of all the tap changers is observed. When a tap changer changes pattern, it is inspected. These utilities report that this procedure has helped them reduce the frequency of internal inspections while simultaneously alerting them to dangerous problems before they lead to a catastrophic failure.

Another trick is to have inspection windows in the tap changer box. When used in conjunction with an oil filter, utilities who do this can inspect their

contacts without opening the box and take the transformer out of service, if required.

Another possible procedure is to monitor the temperature on the tap changer compartment regularly with infrared measuring devices. It is very inexpensive and easy to do this. Utilities who do this claim that if anything goes wrong in a tap changer, it typically increases the temperature of the contacts to a point that you can detect it by checking the temperature on the outside of the wall of the box. The rule is that if the temperature on the surface of the tap changer compartment is higher than that on the surface of the tank of the transformer by more than 7–10°, something is wrong inside the tap changer. They then inspect the tap changer. Quite a few problems have been detected this way.

17

Miscellaneous Topics

17.1 Setting the Impulse Test Generator to Achieve Close to Ideal Waveshapes

This section is largely based on [Del02]. To simulate the effect of a lightning strike on the power lines connected to a transformer, standards organizations have arrived at a standard voltage waveform to be applied to the various transformer terminals undergoing impulse tests. Although these waveforms differ in peak value or basic insulation level (BIL) level, they have similar time characteristics. The general appearance of a full wave, which is the only type we consider in this chapter, is shown in Figure 17.1. The key parameters are the rise time to reach the peak value t_p and the fall time to decrease to 50% of the peak value t_f . A common parameterization for this waveform is given by

$$V = A(e^{-\alpha t} - e^{-\beta t}) \quad (17.1)$$

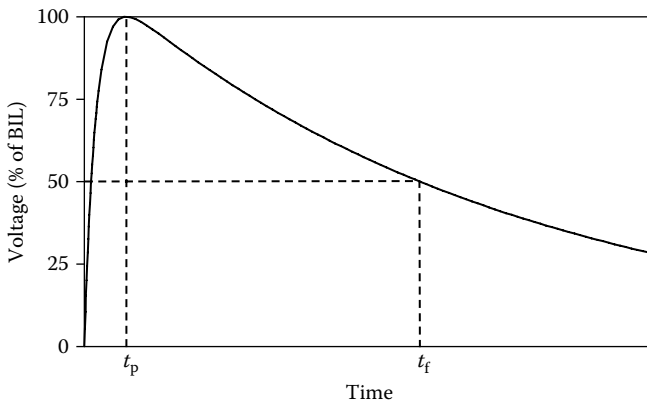
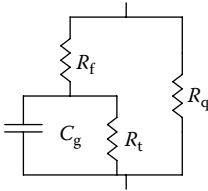


FIGURE 17.1

Standard full-wave impulse waveform. (From Del Vecchio, R. M., R. Ahuja, and R. D. Frenette. 2002. *IEEE Trans Power Deliv* 17(1):142–8. With permission.)

**FIGURE 17.2**

Circuit model of a generator stage: R_f is the front resistor, R_t is the tail resistor, R_q is the charging resistor, and C_g is the stage capacitance. (From Del Vecchio, R. M., R. Ahuja, and R. D. Frenette. 2002. *IEEE Trans Power Deliv* 17(1):142–8. With permission.)

where α , β , and A can be determined from t_p , t_f and the BIL level. More specifically, the standards often specify $t_p = 1.2$ microseconds and $t_f = 50$ microseconds, that is, a 1.2×50 waveform.

Impulse generators for large power transformers are generally of the Marx type [Kuf84]; that is, they use a number of capacitor stages that are charged in parallel at a lower voltage and discharged in series at a much higher voltage. We are concerned only with the discharge configuration and its equivalent circuit. Each stage generally has a front resistor in series with the capacitor and a tail resistor in parallel with the capacitor. There are also charging resistors in the circuit that are in parallel with the entire combination, although these are large and can be ignored. A circuit model of an individual stage is shown in Figure 17.2. In

addition, some inductance is associated with each stage, but it is unclear where this occurs. We will simply lump it into one inductor in the overall circuit model. These stages are not always connected in series, but some of them may be connected in parallel in order to obtain a more desirable overall capacitance value.

By suitably choosing the front and tail resistances and the series-parallel combination of stages, we can approximate the waveform of Figure 17.1. However, this usually requires a trial-and-error process or experience with previous impulse tests on similar transformers. In some cases we cannot achieve the desired waveform by varying the generator parameters because the tail resistance decreases too quickly, so that the 50% of peak voltage value is reached at times less than 50 microseconds. In such cases, we can add a grounding resistor to one of the nonimpulsed windings to help boost the tail. It also would be helpful to know in advance, before undue effort is spent on this process, that the proper waveform cannot be achieved by changing the generator parameters alone.

Here we will outline a method for obtaining a set of generator parameters, if they exist, which will produce an impulse waveform closely approximating the ideal. This method requires a suitable circuit model of the impulse generator as well as of the transformer. Such a combined model should come reasonably close to predicting the actual impulse waveform achieved when the generator parameters in the model are the same as those used for the test. Given such a combination, we can perform trial-and-error parameter variations on the computer rather than on the test floor in an attempt to achieve the desired waveform. However, this tedious process can be circumvented by relatively little additional effort as will be discussed in this section. First, we detail the generator circuit model and then briefly discuss the transformer circuit model before discussing the combination.

17.1.1 Impulse Generator Circuit Model

Although we discuss the Marx-type generator in this section, the impulse generator circuit model can be applied to any generator with the following provisos. The generator should be capable of producing the desired waveform with at least a simple load, for example, a capacitive load. Its overall circuit model description should also be available or reasonably possible to develop. To this end, we assume that each stage of the Marx generator is identical and that each series unit is made up of either one stage or the same number of stages in parallel. Thus, if we have n series units and each consists of m stages in parallel, there are altogether mn stages in the circuit.

Because the waveforms are not sinusoidal, we use Laplace transforms to analyze the circuit. Thus, the impedance of a single stage Z shown in Figure 17.2 is given by

$$Z = \frac{Z_1 R_q}{Z_1 + R_q} \quad (17.2)$$

where

$$Z_1 = R_f + \frac{R_t}{1 + sR_t C_g} \quad (17.3)$$

The impedance of the n series units, each consisting of m parallel stages, Z_{gen} , is given by

$$Z_{\text{gen}} = \left(\frac{n}{m}\right) Z = \frac{\left(\frac{n}{m}\right) Z_1 \left(\frac{n}{m}\right) R_q}{\left(\frac{n}{m}\right) Z_1 + \left(\frac{n}{m}\right) R_q} \quad (17.4)$$

Thus, we can define an equivalent impedance, $Z_{1,\text{eq}} = (n/m)Z_1$, and an equivalent charging resistor, $R_Q = (n/m)R_q$, so that

$$Z_{\text{gen}} = \frac{Z_{1,\text{eq}} R_Q}{Z_{1,\text{eq}} + R_Q} \quad (17.5)$$

We also have

$$Z_{1,\text{eq}} = \left(\frac{n}{m}\right) Z_1 = \left(\frac{n}{m}\right) R_f + \frac{\left(\frac{n}{m}\right) R_t}{1 + s \left(\frac{n}{m}\right) R_t \left(\frac{m}{n}\right) C_g} \quad (17.6)$$

We can therefore define an equivalent front resistor $R_F = (n/m)R_{\nu}$, an equivalent tail resistor $R_T = (n/m)R_{\nu}$, and an equivalent generator capacitance $C_G = (m/n)C_g$, so Equation 17.6 becomes

$$Z_{1,\text{eq}} = R_F + \frac{R_T}{1 + sR_TC_G} \quad (17.7)$$

Thus, we see that Equations 17.5 and 17.7 have the same form as Equations 17.2 and 17.3, but with different values for the circuit parameters. They therefore have the same circuit diagram. We have redrawn this for the overall generator in [Figure 17.3a](#).

The generator has some inductance, which we include as one lumped element as shown in [Figure 17.3b](#). From the manufacturer's data, this inductance seems to have a contribution from each stage, adding a term proportional to n/m , as well as a constant contribution, to the overall inductance. During the full-wave test, there is measuring equipment at the generator output as well as an inactive chopping gap circuit. The latter contributes something to the generator load. Both of these contributions can be adequately represented in the circuit model shown in [Figure 17.3c](#).

Because the transformer circuit model is solved with coupled differential equations, we develop a similar set of equations for the generator so that the circuits can be solved simultaneously. In addition, we can use these equations when the transformer is not attached to check the generator output at no-load conditions against test measurements and thus verify the accuracy of the generator model. We redraw the generator circuit, indicating the voltages and currents that must be solved for, in [Figure 17.4](#), in which I_L is the load current that enters the transformer and V is the impulse voltage. The initial condition is that the generator capacitor be initially charged to some voltage, V_0 , that is, $V_G = V_0$ at $t = 0$.

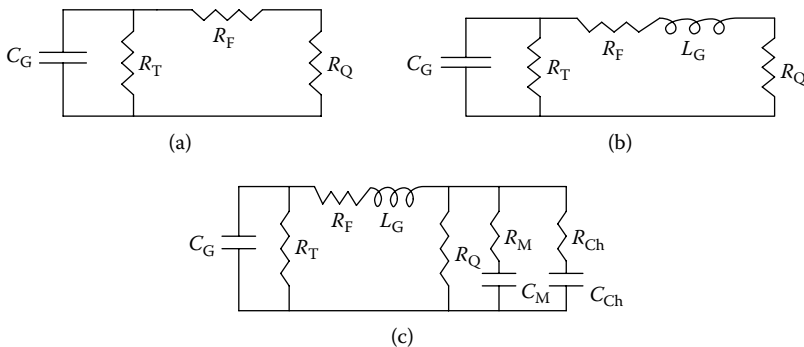
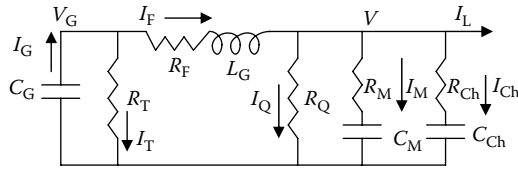


FIGURE 17.3

Circuit models of the impulse generator: (a) equivalent generator circuit built from the individual stages shown in [Figure 17.2](#), (b) generator circuit with inductance, and (c) generator circuit with the measuring equipment represented by R_M , C_M and the inactive chopping gap represented by R_{Ch} , C_{Ch} added. (From Del Vecchio, R. M., R. Ahuja, and R. D. Frenette. 2002. *IEEE Trans Power Deliv* 17(1):142–8. With permission.)

**FIGURE 17.4**

Generator circuit with unknown voltages and currents labeled. (From Del Vecchio, R. M., R. Ahuja, and R. D. Frenette. 2002. *IEEE Trans Power Deliv* 17(1):142–8. With permission.)

Using Kirchoff's laws, the circuit equations can be reduced to

$$\frac{dV_G}{dt} = -\frac{V_G}{R_T C_G} - \frac{I_F}{C_G} \quad (17.8)$$

$$\frac{dI_F}{dt} = \frac{(V_G - V - I_F R_F)}{L_G} \quad (17.9)$$

$$\frac{dV_M}{dt} = \frac{(V - V_M)}{R_M C_M} \quad (17.10)$$

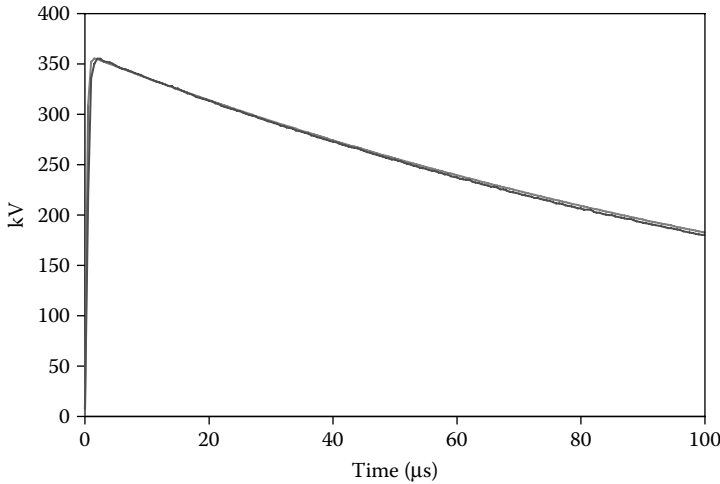
$$\frac{dV_{Ch}}{dt} = \frac{(V - V_{Ch})}{R_{Ch} C_{Ch}} \quad (17.11)$$

$$I_L = I_F - \frac{V}{R_Q} - \frac{(V - V_M)}{R_M} - \frac{(V - V_{Ch})}{R_{Ch}} \quad (17.12)$$

Equation 17.12 must be combined with another equation for V from the transformer circuit when the transformer is attached. When the transformer is not attached, setting $I_L = 0$ in Equation 17.12 allows us to solve for V in terms of the other unknowns. When we substitute V , obtained from Equation 17.12 with $I_L = 0$, into Equations 17.8 through 17.11, we obtain a coupled set of four differential equations in four unknowns that can be solved, starting from the initial condition. Once solved, we can use Equation 17.12 with $I_L = 0$ to find V , the output voltage without transformer. Figure 17.5 shows a comparison of the calculated and measured generator voltage output without transformer. A variety of generator settings also obtained similar agreement.

17.1.2 Transformer Circuit Model

The transformer circuit model discussed in Chapter 13 is very detailed. It includes the self-inductances of and mutual inductances between all the

**FIGURE 17.5**

Comparison of calculated and measured impulse generator output without a transformer load. The two curves practically coincide. (From Del Vecchio, R. M., R. Ahuja, and R. D. Frenette. 2002. *IEEE Trans Power Deliv* 17(1):142–8. With permission.)

winding sections, section resistances, section series capacitances, and section capacitances to the neighboring windings and/or core and tank. For our purposes, we will look at a typical nodal voltage equation for node i :

$$\left(C_j + C_{j+1} + \sum_p K_{ip} \right) \frac{dV_i}{dt} - C_j \frac{dV_{i-1}}{dt} - C_{j+1} \frac{dV_{i+1}}{dt} - \sum_p K_{ip} \frac{dV_p}{dt} = I_j - I_{j+1} \quad (17.13)$$

where the p sum is over all nodes connected to node i via shunt capacitances K_{ip} . C_j and C_{j+1} are series capacitances of neighboring sections attached to node i . C_j is set to 0 when node i is at the bottom of the coil and C_{j+1} to 0 when node i is at the top of the coil. These variables are shown in Figure 17.6.

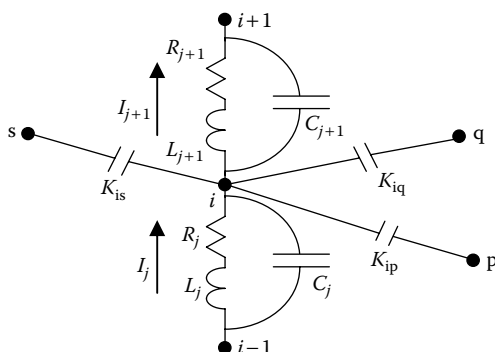
As discussed in Chapter 13, we combine these equations into a matrix equation for the nodal voltages V_i , where i ranges over all the nodes:

$$C \frac{d\mathbf{V}}{dt} = \mathbf{A} \mathbf{I} \quad (17.14)$$

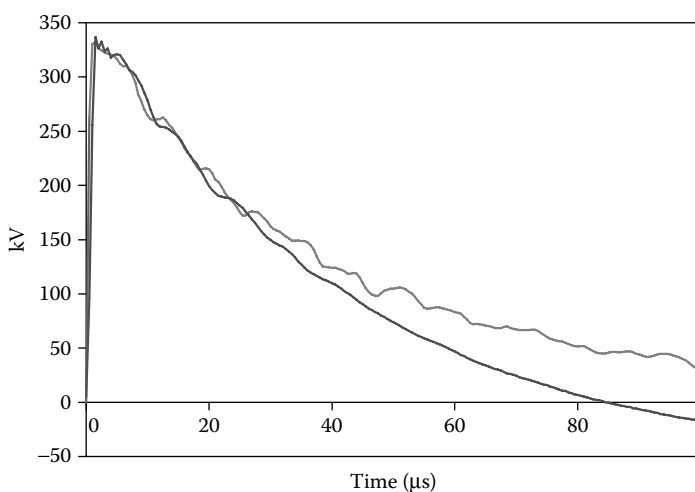
where C is a capacitance matrix and A is a matrix whose entries are ± 1 or 0. \mathbf{V} is a vector of nodal voltages and \mathbf{I} is a vector of branch currents. We can solve these, along with a set of differential equations for the currents obtained from the inductive–resistive branches.

In the normal solution method, if node k is the impulsed node, the k th equation in Equation 17.14, corresponding to V_k , is replaced by

$$\frac{dV_k}{dt} = \frac{d}{dt}(\text{Ideal Waveform}) \quad (17.15)$$

**FIGURE 17.6**

Typical winding section showing the labeling scheme. (From Del Vecchio, R. M., R. Ahuja, and R. D. Frenette. 2002. *IEEE Trans Power Deliv* 17(1):142–8. With permission.)

**FIGURE 17.7**

Comparison of a calculated waveform with a measured impulse waveform with transformer attached and without optimization. The smoother (faster drop off) curve is the measured waveform. (From Del Vecchio, R. M., R. Ahuja, and R. D. Frenette. 2002. *IEEE Trans Power Deliv* 17(1):142–8. With permission.)

When the impulse generator is attached to node k , instead of using Equation 17.15 we add I_L from Equation 17.12 to the right-hand side of Equation 17.13 and change V to V_k in Equations 17.8 through 17.12. We then solve all of these equations simultaneously, starting with $V_G = V_0$ on the generator capacitor. Figure 17.7 shows a comparison of a calculated versus measured impulse waveform for a particular choice of generator parameters when the transformer is attached. The calculated curve is obtained without any optimization.

From this comparison, we see that the method is capable of reproducing the test waveform fairly well, although it is far from the ideal waveform.

17.1.3 Determining the Generator Settings for Approximating the Ideal Waveform

When the transformer is attached, we redraw the circuit of Figure 17.3 to include the transformer, which we represent as lumped impedance Z_{Tr} in Figure 17.8. We now lump all the impedances in the dashed box in Figure 17.8 together into a load impedance Z_L . This impedance remains fixed as we vary the generator parameters R_F , R_T , and C_G . Note that we include the charging resistor as well as the measuring circuit and inactive chopping circuit in Z_L . These remain fixed for the given transformer and BIL level. At this point, we include the generator inductance in the circuit to the left of Z_L ; however, its effect on the impulse waveform is small provided R_F is large enough.

With Z_L as a load, we can analyze the remaining circuit using Thevenin's theorem as stated, for example, in [Des69]. For linear network elements, as is the case here, we can replace the network to the left of the terminals, labeled 1 and 1' in Figure 17.8, with an equivalent network consisting of a voltage source and an impedance in series with it. The voltage source is the open circuit voltage at terminals 1 and 1', and the series impedance is obtained by setting all independent sources to zero and all initial conditions to zero. There are no sources in our circuit but there is an initial condition on the capacitor. The open circuit voltage is that on a capacitor initially charged to a voltage V_0 in parallel with a resistor R_T . Thus, the open-circuit voltage, e_{oc} , is

$$e_{oc} = V_0 e^{-t/R_T C_G} \quad (17.16)$$

Its Laplace transform is

$$E_{oc} = \frac{V_0 R_T C_G}{1 + s R_T C_G} \quad (17.17)$$

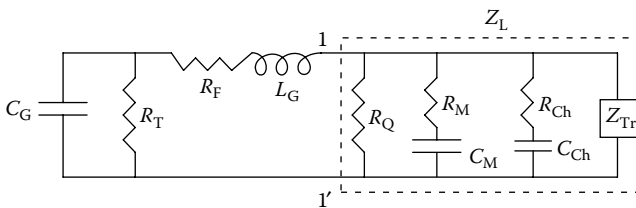


FIGURE 17.8

Circuit model of a generator with transformer attached, represented by the load Z_{Tr} . (From Del Vecchio, R. M., R. Ahuja, and R. D. Frenette. 2002. *IEEE Trans Power Deliv* 17(1):142–8. With permission.)

The Laplace transform of the equivalent impedance is

$$Z_{eq} = R_F + sL_G + \frac{R_T}{1 + sR_TC_G} \quad (17.18)$$

Substituting the Thevenin equivalent circuit, the circuit of [Figure 17.8](#) becomes similar to that of [Figure 17.9](#). The location of the impulse voltage V is indicated in [Figure 17.9](#).

The impulse voltage, V , in [Figure 17.9](#) is given by

$$V = E_{oc} \left(\frac{Z_L}{Z_{eq} + Z_L} \right) \quad (17.19)$$

Now we consider two cases. First, the generator parameters are set to some starting values based on a reasonable estimate of what might produce the desired waveform, and the resulting voltage V is recorded. Second, the ideal voltage V^I is produced by the unknown parameters of the generator, which we will label with a superscript I for ideal. Since E_{oc} and Z_{eq} depend on these unknown parameters, we also label them with the superscript I. However, Z_L remains the same since it does not depend on the variable parameters of the generator. Thus, we have

$$V^I = E_{oc}^I \left(\frac{Z_L}{Z_{eq}^I + Z_L} \right) \quad (17.20)$$

Solving Equation 17.19 for Z_L and substituting this value of Z_L into Equation 17.20, we find

$$\frac{Z_{eq}^I}{\left(\frac{E_{oc}^I}{V^I} - 1 \right)} = \frac{Z_{eq}}{\left(\frac{E_{oc}}{V} - 1 \right)} \quad (17.21)$$

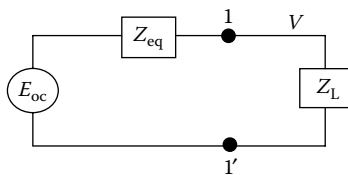


FIGURE 17.9

Thevenin equivalent circuit of [Figure 17.8](#). (From Del Vecchio, R. M., R. Ahuja, and R. D. Frenette. 2002. *IEEE Trans Power Deliv* 17(1):142–8. With permission.)

The ideal waveform is given in Equation 17.1. Its Laplace transform, using superscript I to label the parameters, is

$$V^I = \frac{A^I(\beta^I - \alpha^I)}{(s + \alpha^I)(s + \beta^I)} \quad (17.22)$$

Z_{eq}^I is given by Equation 17.18 with superscript I labeling the generator parameters. However, the presence of L_G makes it difficult to achieve the ideal waveform. This is clear from [Kuf84], in which the author shows that the ideal waveform is generated by the circuit to the left of the 1, 1' terminals in Figure 17.8 without L_G and with a capacitive load. We cannot eliminate L_G , but we can show that its effect on the waveform will be reduced if

$$\frac{L_G}{R_F} \ll t_p \quad (17.23)$$

that is, if the inductive time constant is much less than the time to reach the peak voltage. We assume this condition here and thus eliminate L_G from Equation 17.18.

We also eliminate L_G in generating the waveform V for the initial simulation, and we assume that it has the same form as given by Equation 17.1 and therefore the same Laplace transform as given in Equation 17.22, but without the I superscript labeling the parameters. Thus, Equations 17.8 through 17.12 must be modified for the initial simulation by eliminating L_G . With these approximations, both sides of Equation 17.21 will have the same form and differ only in the superscript labeling. Note that the waveform parameters A , α , and β for the initial simulation can be determined by a variety of curve fitting methods. After some algebraic manipulation, Equation 17.21 becomes

$$\begin{aligned} & \frac{A^I(\beta^I - \alpha^I)R_F^I}{V_0^I R_P^I C_G^I} \left\{ \frac{1 + sR_P^I C_G^I}{s^2 + \left[\alpha^I + \beta^I - \frac{A^I(\beta^I - \alpha^I)}{V_0^I} \right] s + \alpha^I \beta^I - \frac{A^I(\beta^I - \alpha^I)}{V_0^I R_T^I C_G^I}} \right\} \\ &= \frac{A(\beta - \alpha)R_F}{V_0 R_P C_G} \left\{ \frac{1 + sR_P C_G}{s^2 + \left[\alpha + \beta - \frac{A(\beta - \alpha)}{V_0} \right] s + \alpha \beta - \frac{A(\beta - \alpha)}{V_0 R_T C_G}} \right\} \end{aligned} \quad (17.24)$$

where

$$R_P = \frac{R_F R_T}{R_F + R_T}, \quad R_P^I = \frac{R_F^I R_T^I}{R_F^I + R_T^I} \quad (17.25)$$

To achieve equality in Equation 17.24, we require

$$\frac{A^I(\beta^I - \alpha^I)R_F^I}{V_0^I R_p^I C_G^I} = \frac{A(\beta - \alpha)R_F}{V_0 R_p C_G} \quad (17.26)$$

$$R_p^I C_G^I = R_p C_G \quad (17.27)$$

$$\alpha^I + \beta^I - \frac{A^I(\beta^I - \alpha^I)}{V_0^I} = \alpha + \beta - \frac{A(\beta - \alpha)}{V_0} \quad (17.28)$$

$$\alpha^I \beta^I - \frac{A^I(\beta^I - \alpha^I)}{V_0^I R_T^I C_G^I} = \alpha \beta - \frac{A(\beta - \alpha)}{V_0 R_T C_G} \quad (17.29)$$

Because the ideal waveform parameters are known, as well as the initial simulation parameters and the initial simulation waveform parameters obtained from curve fitting, the unknown parameters in Equations 17.26 through 17.29 are R_F^I , R_T^I , C_G^I , and V_0^I . Thus, we have four equations in which four unknowns can be solved uniquely. Letting

$$x = 1 + \frac{V_0}{A(\beta - \alpha)}[(\alpha^I + \beta^I) - (\alpha + \beta)] \quad (17.30)$$

$$y = 1 + \frac{V_p R_T C_G}{A(\beta - \alpha)}(\alpha^I \beta^I - \alpha \beta) \quad (17.31)$$

we find

$$R_F^I = \frac{R_F}{x} \quad (17.32)$$

$$C_G^I = \frac{C_G}{R_F^I \left[\frac{1}{R_p} - \left(\frac{y}{x} \right) \frac{1}{R_T} \right]} \quad (17.33)$$

$$R_T^I = \frac{R_T C_G}{C_G^I} \left(\frac{x}{y} \right) \quad (17.34)$$

$$V_0^I = V_0 \left(\frac{A^I}{A} \right) \left(\frac{\beta^I - \alpha^I}{\beta - \alpha} \right) \frac{1}{x} \quad (17.35)$$

17.1.4 Practical Implementation

To get a reasonable set of starting parameters for the generator, we adopt the simpler model of the generator and load discussed in [Kuf84]. The circuit diagram is given in Figure 17.10. Starting with an initial generator capacitor voltage V_0 , the voltage across the load C_L is given by

$$V = \frac{V_0}{R_F C_L (\beta - \alpha)} (e^{-\alpha t} - e^{-\beta t}) \quad (17.36)$$

α and β can be expressed in terms of the circuit parameters, but since we assume an ideal waveform, α and β are known and we want to express the circuit parameters in terms of these parameters. These are given by

$$R_F = \frac{1}{2C_L} \left(\frac{\alpha + \beta}{\alpha\beta} \right) \left[1 - \sqrt{1 - \frac{4\alpha\beta}{(\alpha + \beta)^2} \left(1 + \frac{C_L}{C_G} \right)} \right] \quad (17.37)$$

$$R_T = \frac{1}{2(C_G + C_L)} \left(\frac{\alpha + \beta}{\alpha\beta} \right) \left[1 + \sqrt{1 - \frac{4\alpha\beta}{(\alpha + \beta)^2} \left(1 + \frac{C_L}{C_G} \right)} \right] \quad (17.38)$$

From Equations 17.37 and 17.38, we see that we must assume some values for C_G and C_L . C_G can be selected based on BIL considerations or from experience. C_L can be calculated roughly from a simplified capacitive model of the transformer, but its selection is not critical.

Having calculated these initial parameters for the generator, we solve the generator–transformer circuit model to obtain the impulse voltage as a function of time. We do not include inductance in the generator model at this stage. We then analyze the waveform to obtain A , α , and β . To do this, we use a least-squares curve-fitting procedure. The output waveform is only considered out to times where it remains positive because Equation 17.1 is inherently positive provided $\beta > \alpha$, and this is always the case when the waveform begins with a positive slope. We then calculate the new generator parameters from Equations 17.30 through 17.35.

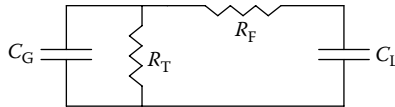


FIGURE 17.10

Simple generator load model to obtain starting generator parameters. (From Del Vecchio, R. M., R. Ahuja, and R. D. Frenette. 2002. *IEEE Trans Power Deliv* 17(1):142–8. With permission.)

The capacitance we calculate from Equation 17.33 usually is not obtainable exactly from the discrete possibilities that arise from grouping the stages into series-parallel combinations. We therefore use the series-parallel combination that comes closest to achieving the desired capacitance. The front and tail series-parallel equivalent resistances calculated from the above procedure also cannot be realized exactly in practice; their values must be approximated using the finite pool of available resistors.

We have found that for cases in which the tail of the waveform droops significantly, R_T^I can become negative. This is because y in Equation 17.31 becomes negative. In this case, we set y to a small value, say $y = 0.1$, and recalculate R_T^I . The calculation is then repeated with the new parameters and the resulting waveform is reanalyzed. If R_T^I is still negative, the process is repeated. After a few iterations, if the new R_T^I still remains negative, the process is stopped. A printout of the parameters before the last recalculation reveals that R_T^I has become extremely large and yet the waveform still has a drooping tail. This indicates that even if $R_T^I \rightarrow \infty$ (an open circuit) the ideal waveform cannot be achieved. One is then left with the possibility of adding grounding resistors to one or more windings in order to obtain the desired waveform.

When the new generator parameters obtained from Equations 17.30 through 17.35 are positive, or after the last iteration in cases in which the new R_T^I is persistently negative, the generator inductance is included in the circuit model. The transient calculation is then performed with these new parameters, including the inductance. Although the ideal waveform is usually well approximated when R_T^I does not become infinite, there is often a voltage spike near the peak of the waveform due to the generator inductance. Not only does this increase the peak voltage beyond the desired BIL level but it tends also to decrease the time to peak value t_p below the desired value. To counteract this, we can artificially increase the t_p value of the ideal waveform from say 1.2 to 2.0 microseconds to obtain a larger value of R_F^I , thus reducing the L_G/R_F time constant as discussed previously in the context of Equation 17.23. The inductance peak is thereby considerably reduced, and the rise time increases to a value closer to the optimum.

Figure 17.11 shows an example of a calculated impulse waveform obtained using the initially estimated values for the generator parameters: $C_G = 500$ nF, $R_F = 177 \Omega$, $R_T = 142 \Omega$. The top curve is the ideal waveform. The generator waveform has the time parameters of $t_p = 3.15$ microseconds, $t_f = 29.5$ microseconds. Figure 17.12 shows the waveform resulting from the recalculated parameters of $C_G^I = 596$ nF, $R_F^I = 90 \Omega$, $R_T^I = 249 \Omega$. The waveform comes very close to the ideal curve. Its time parameters are $t_p = 1.10$ microseconds, $t_f = 50.5$ microseconds. We should note that the recalculated generator parameters depend to a limited extent on the initial choice for these parameters.

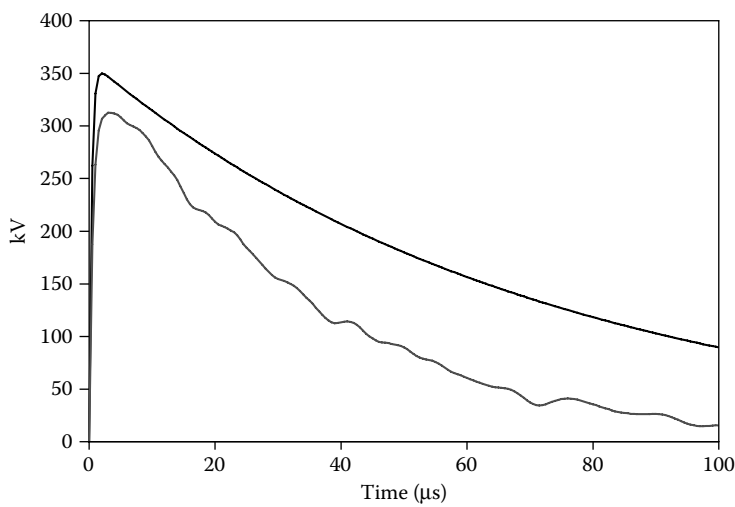


FIGURE 17.11 Waveform produced by the initial selection of generator parameters. The top curve is the ideal waveform. (From Del Vecchio, R. M., R. Ahuja, and R. D. Frenette. 2002. *IEEE Trans Power Deliv* 17(1):142–8. With permission.)

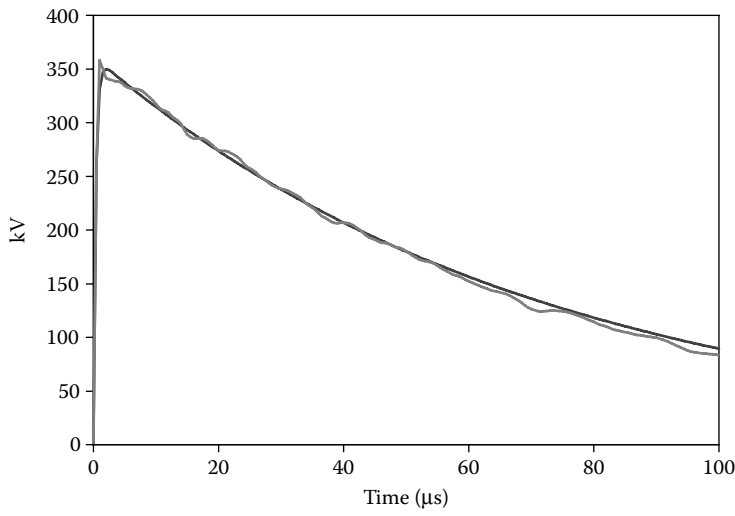


FIGURE 17.12 Waveform achieved with recalculated generator parameters. It nearly coincides with the ideal waveform. (From Del Vecchio, R. M., R. Ahuja, and R. D. Frenette. 2002. *IEEE Trans Power Deliv* 17(1):142–8. With permission.)

17.2 Impulse or Lightning Strike on a Transformer through a Length of Cable

For convenience we can sometimes place a surge arrester at some distance from a transformer to protect against an impulse or lightning strike. Thus, the impulse must travel through a length of cable before arriving at the transformer. Although the voltage is limited by the surge arrester, this voltage impulse can be enhanced by the time it reaches the transformer terminals due to an impedance mismatch. We will analyze this effect with a lumped parameter model and also check our analysis with equations from traveling wave theory.

17.2.1 Lumped Parameter Model

For the lumped parameter model, we model the transformer as a parallel combination of an inductor and a capacitor, ignoring the resistance. For the cable, we position the cable capacitance to ground at either end of the line, with each capacitor having half the total cable capacitance and the cable inductance between them. Although the cable resistance can also be included, its effect is small. Setting it to zero also provides a worst-case scenario. The diagram is shown in Figure 17.13.

In Figure 17.13, L_T and C_T are the transformer inductance and capacitance to the ground, respectively, and L and C refer to the cable series inductance and ground capacitances, respectively. V_{Imp} is the impulse waveform given in Equation 17.1, and V_T is the voltage at the transformer terminals.

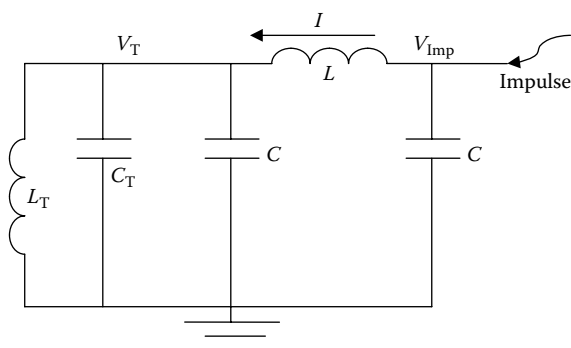


FIGURE 17.13

Lumped circuit model of a transformer impulsed through a cable. The subscript T refers to the transformer parameters, while the cable parameters have no subscripts.

Laplace transforms will be used to analyze this circuit. From [Figure 17.13](#), we see that

$$\begin{aligned} V_{\text{Imp}}(s) - V_T(s) &= sLI(s) \\ V_T(s) &= \left(\frac{sL_T}{1 + s^2L_T(C + C_T)} \right) I_C(s) \end{aligned} \quad (17.39)$$

Solving these equations for V_T in terms of V_{Imp} , we get

$$V_T(s) = \frac{V_{\text{Imp}}(s)}{L(C + C_T) \left[s^2 + \frac{(L + L_T)}{L_T L(C + C_T)} \right]} \quad (17.40)$$

The Laplace transform of the impulse waveform is given by

$$V_{\text{Imp}}(s) = A \left[\frac{1}{s + \alpha} - \frac{1}{s + \beta} \right] \quad (17.41)$$

Substituting this in Equation 17.40, we get

$$V_T(s) = \frac{A}{L(C + C_T)} \left[\frac{1}{s + \alpha} - \frac{1}{s + \beta} \right] \left(\frac{1}{s^2 + \gamma^2} \right)$$

where

$$\gamma^2 = \frac{(L + L_T)}{L_T L(C + C_T)} \quad (17.42)$$

Using

$$\begin{aligned} \frac{1}{(s + \alpha)(s^2 + \gamma^2)} &= \frac{1}{(\alpha^2 + \gamma^2)} \left[\frac{1}{s + \alpha} - \frac{s - \alpha}{s^2 + \gamma^2} \right] \\ \frac{1}{(s + \beta)(s^2 + \gamma^2)} &= \frac{1}{(\beta^2 + \gamma^2)} \left[\frac{1}{s + \beta} - \frac{s - \beta}{s^2 + \gamma^2} \right] \end{aligned} \quad (17.43)$$

and substituting this into Equation 17.42, after some algebraic manipulation we find

$$\begin{aligned} V_T(s) &= \frac{A}{L(C + C_T)(\alpha^2 + \gamma^2)(\beta^2 + \gamma^2)} \\ &\times \left[\frac{(\beta^2 + \gamma^2)}{s + \alpha} - \frac{(\alpha^2 + \gamma^2)}{s + \beta} + \frac{s(\alpha^2 - \beta^2)}{s^2 + \gamma^2} + \frac{(\beta - \alpha)(\alpha\beta - \gamma^2)}{s^2 + \gamma^2} \right] \end{aligned} \quad (17.44)$$

Taking the inverse transform of Equation 17.44, we get

$$V_T(t) = \frac{A}{L(C + C_T)(\alpha^2 + \gamma^2)(\beta^2 + \gamma^2)} \times \left[(\beta^2 + \gamma^2)e^{-\alpha t} - (\alpha^2 + \gamma^2)e^{-\beta t} + (\alpha^2 - \beta^2)\cos\gamma t + \frac{(\beta - \alpha)(\alpha\beta - \gamma^2)}{\gamma}\sin\gamma t \right] \quad (17.45)$$

17.2.1.1 Numerical Example

As a numerical example, we consider a cable with the per-unit length capacitance and inductance given by

$$c = 2.43 \times 10^{-4} \text{ } \mu\text{F/m}, \quad \ell = 0.348 \text{ } \mu\text{H/m}$$

Assuming a 300-meter-long cable, the total capacitance and inductance are given by

$$C_{\text{Tot}} = 0.0729 \text{ } \mu\text{F}, \quad L_{\text{Tot}} = 104.4 \text{ } \mu\text{H}$$

For use in our formulas, we need half the capacitance and the total inductance, thus

$$C = 0.03645 \text{ } \mu\text{F}, \quad L = 104.4 \text{ } \mu\text{H}$$

The transformer has a leakage reactance of $X_T = 12.3\%$ and a base impedance of $251.9 \text{ } \Omega$. For a frequency of 60 Hz, this gives a transformer inductance of $L_T = 82,200 \text{ } \mu\text{H}$. The transformer effective capacitance to ground is approximately $0.001 \text{ } \mu\text{F}$. Summarizing, we have

$$L_T = 82,200 \text{ } \mu\text{H}, \quad C_T = 0.001 \text{ } \mu\text{F}$$

The impulse waveform parameters are

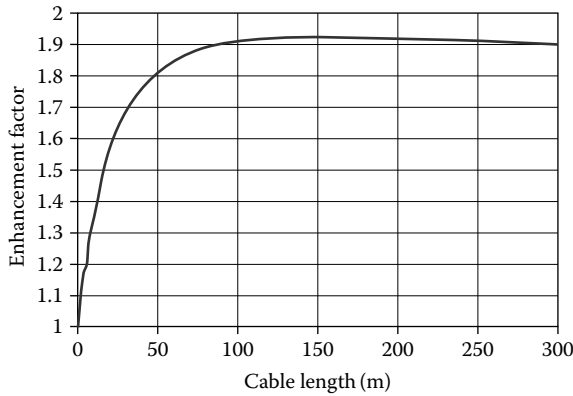
$$\alpha = 0.0143 \text{ } (\mu\text{s})^{-1}, \quad \beta = 4.88 \text{ } (\mu\text{s})^{-1}$$

Substituting these numerical values into Equation 17.42, we find

$$\gamma^2 = 0.2561 \text{ } (\mu\text{s})^{-2}, \quad \gamma = 0.50606 \text{ } (\mu\text{s})^{-1}$$

Substituting for the remaining parameters in Equation 17.45, we obtain

$$\frac{V_T(t)}{A} = \frac{(24.0705e^{-\alpha t} - 0.2563e^{-\beta t} - 23.8142\cos\gamma t - 1.7914\sin\gamma t)}{24.1203} \quad (17.46)$$

**FIGURE 17.14**

Voltage enhancement at the transformer terminals due to an impulse at a distance equal to the cable length.

Stepping Equation 17.46 in small time increments on a spreadsheet for up to 59 microseconds, for example, we find that it reaches a maximum of 1.901 at $t = 6.4$ microseconds. Thus, the impulse or lightning voltage level A at a cable position 300 m from the transformer will be enhanced by a factor of 1.901 at the transformer terminals. Figure 17.14 shows how this enhancement factor varies with cable length from the transformer terminals. It appears to peak at a cable length of approximately 150 m and then gradually to decline at longer cable lengths. To achieve an enhancement below 10% (factor equal to 1.1), the surge arrester should be placed at a cable length of less than 2 m from the transformer terminals.

17.2.2 Traveling Wave Theory

As a check on the above analysis, we use the results of traveling wave theory as given, for example, in [Gre71]. This uses the surge impedance Z of the cable, which is given by

$$Z = \sqrt{\frac{\ell}{c}} \quad (17.47)$$

where ℓ is the cable inductance per unit length and c is the cable capacitance per unit length. For the cable parameters given above

$$Z = 37.8 \, \Omega$$

There is some damping of the wave along the cable due to the cable resistance, but this is small in our case. This simplified version of the theory does not depend on the cable length, so it applies effectively to longer cables.

Using Laplace transforms, the voltage at the transformer terminal due to an impulse or lightning strike is given by

$$V_T(s) = \left[\frac{2Z_T(s)}{Z_T(s) + Z} \right] V_{\text{imp}}(s) \quad (17.48)$$

Here $V_T(s)$ is the Laplace transform of the transformer impedance which, ignoring its small capacitance, is given by sL_T . Substituting $V_{\text{imp}}(s)$ from Equation 17.41, we get

$$V_T(s) = A \left[\frac{2sL_T}{sL_T + Z} \right] \left[\frac{1}{s + \alpha} - \frac{1}{s + \beta} \right] \quad (17.49)$$

Noting that

$$\frac{sL_T}{sL_T + Z} = 1 - \frac{Z}{sL_T + Z}$$

and

$$\frac{1}{(sL_T + Z)(s + \alpha)} = \frac{1}{(Z - L_T\alpha)} \left[\frac{1}{s + \alpha} - \frac{L_T}{sL_T + Z} \right] \quad (17.50)$$

we can rewrite Equation 17.49 as

$$\begin{aligned} \frac{V_T(s)}{A} = 2 & \left[\frac{-L_T\alpha}{Z - L_T\alpha} \left(\frac{1}{s + \alpha} \right) + \frac{L_T\beta}{Z - L_T\beta} \left(\frac{1}{s + \beta} \right) \right. \\ & \left. + \frac{Z}{Z - L_T\alpha} \left(\frac{1}{s + Z/L_T} \right) - \frac{Z}{Z - L_T\beta} \left(\frac{1}{s + Z/L_T} \right) \right] \end{aligned} \quad (17.51)$$

Taking the inverse transform we get

$$\frac{V_T(t)}{A} = 2 \left[\frac{-L_T\alpha}{Z - L_T\alpha} e^{-\alpha t} + \frac{L_T\beta}{Z - L_T\beta} e^{-\beta t} + \left(\frac{Z}{Z - L_T\alpha} - \frac{Z}{Z - L_T\beta} \right) e^{-\frac{Z}{L_T}t} \right] \quad (17.52)$$

Using the surge impedance for this cable and the transformer and impulse parameters given earlier, for Equation 17.52 we get

$$\frac{V_T(t)}{A} = 2 \left[1.03323e^{-\alpha t} - 1.0001e^{-\beta t} - 0.03313e^{-\frac{Z}{L_T}t} \right]$$

This peaks at maximum enhancement of 1.959 at 1.2 microseconds. This value is close to the maximum enhancement obtained with the lumped parameter model. We see that over a long cable the impulse voltage is nearly double its original value when it reaches the transformer terminals.

17.3 Air Core Inductance

An air core inductor is used often in a transformer, sometimes to increase the LV to tertiary impedance for better short-circuit withstand capability. Air core inductors can have layered windings, made of one or more concentric coils. Here we consider the calculation of this inductance in a general case in which one or more coils of the same or different sizes are present. We assume that each coil has a uniform turn distribution over its cross section. We also assume that the coil's cross section is rectangular.

To obtain the inductance of a collection of coils, we must calculate the mutual inductance between the coils, because the self-inductance of a collection of N_c coils is given by

$$L = \sum_{i=1}^{N_c} L_i + 2 \sum_{i < j=1}^{N_c} M_{ij} \quad (17.53)$$

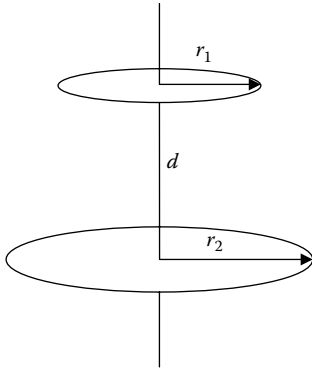


FIGURE 17.15
Coaxial thin circular wire geometry.

Here, L_i is the self-inductance of coil i and M_{ij} is the mutual inductance between coils i and j . The second sum is over all possible pairs of coils. The mutual inductances can be positive or negative depending on the winding directions of the coils. Equation 17.53 follows from the magnetic energy expression for a collection of coils in terms of their self- and mutual inductances given in Chapter 4 and the fact that all the coils in an inductor must carry the same current. Note that Equation 17.53 would apply if the L_i 's and M_{ij} 's referred to subdivisions of a single or multiple coils.

The method used here to obtain the self- and mutual inductances was briefly discussed in Chapter 12. The starting point is the mutual inductance between two circular coaxial thin wires of radii r_1 and r_2 , separated axially by a distance d as shown in Figure 17.15.

The mutual inductance M_{12} between these wires is given by [Smy68]

$$M_{12} = \frac{2\mu_0}{k} \sqrt{r_1 r_2} \left[\left(1 - \frac{k^2}{2} \right) K(k) - E(k) \right]$$

where

$$k^2 = \frac{4r_1 r_2}{(r_1 + r_2)^2 + d^2} \quad (17.54)$$

Here $K(k)$ and $E(k)$ are complete elliptic integrals of the first and second kinds, respectively. These are generally available in mathematical libraries. SI units are used and $\mu_0 = 4\pi \times 10^{-7}$ H/m in this system.

Lyle's method, described by Grover [Gro73], is used to obtain the mutual inductance between coils of rectangular cross section. In its simplest form, each coil is replaced by two thin wire coils that are strategically placed. The position of the thin wire coils depends on whether the coil's radial build b is larger or smaller than the coil's axial height h . If $h > b$, the two thin wire coils each have a radius r_1 given by

$$r_1 = r_{\text{ave}} \left[1 + \frac{1}{24} \left(\frac{b}{r_{\text{ave}}} \right)^2 \right] \quad (17.55)$$

where r_{ave} is the average radius of the rectangular cross-sectional coil. The two substitute coils are separated from the axial center line of the main coil by a distance β , where

$$\beta^2 = \frac{h^2 - b^2}{12} \quad (17.56)$$

The axial center line is a distance $h/2$ from the bottom of the main coil. Each substitute thin wire coil is assigned half the turns of the original coil.

If $h < b$, then the substitute thin wire coils are both positioned along the axial center line of the main coil at radial distances $r_2 + \delta$ and $r_2 - \delta$, where

$$r_2 = r_{\text{ave}} \left[1 + \frac{1}{24} \left(\frac{h}{r_{\text{ave}}} \right)^2 \right], \quad \delta^2 = \frac{b^2 - h^2}{12} \quad (17.57)$$

Also, each substitute thin wire coil is given half the turns of the main coil. Both of these cases are illustrated in [Figure 17.16](#).

Notice that if $b = h$, the two cases become identical, with $r_1 = r_2$ and $\beta = \delta$. In this case, the two thin circular wires coincide. This single wire would be given the full number of turns in the coil.

Because the two wires are now a proxy for the coil they represent, we can obtain the mutual inductance between this coil and another also represented by two wires by summing all possible pairs of one wire from one coil and one wire from the second coil. For one wire pair, because we assume the coils are coaxial, we use Equation 17.54 to obtain their mutual inductance. If the coils have N_1 and N_2 turns, respectively, each wire is assigned half the turns of its coil. Thus, if coil 1 is represented by wires 1 and 2 and coil 2 by wires 3 and 4, the mutual inductance M between these coils is given by

$$M = \frac{N_1 N_2}{4} (M_{13} + M_{14} + M_{23} + M_{24}) \quad (17.58)$$

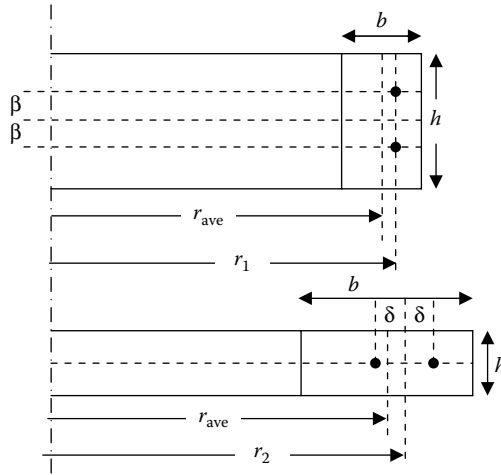


FIGURE 17.16
Geometry of Lyle's method.

We also need the self-inductance of each coil so we will use an expression given in [Gro73], which applies to circular coils having a square cross section. Letting c equal the length of the side of the square and r_{ave} equal the average coil radius as before, the self-inductance is given by

$$L = \mu_0 r_{\text{ave}} N^2 \times \left\{ \frac{1}{2} \left[1 + \frac{1}{6} \left(\frac{c}{2r_{\text{ave}}} \right)^2 \right] \ln \left[\frac{8}{(c/2r_{\text{ave}})^2} \right] + 0.2041 \left(\frac{c}{2r_{\text{ave}}} \right)^2 - 0.84834 \right\} \quad (17.59)$$

where the SI system is used with $\mu_0 = 4\pi \times 10^{-7}$ H/m and N is the number of turns in the square. This expression applies when $c/2r_{\text{ave}} \leq 0.2$. Because most of the coils of interest will not have a square cross section, we need to subdivide the coils into squares, which can be made small enough so that this criterion is met. At the same time, these squares can be used for Lyle's method to find mutual inductances. In this case, the two proxy wires coincide.

Thus, the strategy is to subdivide each coil into small-enough squares so that we can apply Equation 17.59 to calculate its self-inductance. This may not be exactly possible, depending on the coil dimensions, but can be approximated to any desired accuracy. Each square is also represented by two coincident wires, each carrying half the turns in the square. This is equivalent to a single wire with the full number of turns in the square. These wires are used to obtain the mutual inductances between this square and all the other square subdivisions in the system. The self-inductance of the system of coils is given by Equation 17.53, where N_c is now the total number of squares in the system. If one of the original coils has N_t turns and is subdivided into N_s squares, each square has N_t/N_s turns and each of the subcoils, used for calculating

mutual inductances, has $\frac{1}{2}(N_t/N_s)$ turns. Because the two mutual inductances between the two wires representing the squares are the same, only one needs to be calculated and the turns associated with it should be N_t/N_s . Also note that r_{ave} is the average radius of the square in the subdivision.

Because a lot of terms must be calculated, symmetry can be used to reduce the number of terms.

A computer can perform the sums without too much difficulty. This method has been checked by comparison with known formulas for the self-inductance of special coils and also through finite element calculations and is quite accurate.

The above method of subdividing into squares, which will be the same size for a given coil, and performing all the self- and mutual inductance calculations among the squares is useful to find the self-inductance of a single coil. When more than one coil is involved in the inductance calculation, the self-inductance of each coil can be calculated by the square subdivision method, with each coil having a different square size. However, the mutual inductance between a pair of coils in the group perhaps can be best obtained using Lyle's method based on a different type of subdivisions for each coil. These subdivisions would not necessarily be square and would be chosen so that they conform to one of the types shown in [Figure 17.16](#). They may be coarser than the square subdivisions used for the self-inductance of the coil, resulting in fewer terms to sum. These subdivisions, called Lyle subdivisions, can be chosen to more exactly fill the coil's cross section. For a given coil, they can be chosen to have or not have all the same dimensions. To obtain the mutual inductance between a pair of coils where each coil has its own set of Lyle subdivisions, the mutual inductances between all pairs (consisting of one wire from each coil) are summed. The number of proxy wires in each coil will be two times the number of Lyle subdivisions if these subdivisions are not square.

17.4 Electrical Contacts

Electrical connections are common throughout transformers, from winding cables crimped or brazed to leads, to leads bolted to bushings, to ground straps from the core or clamps, which are often bolted to the tank, and so on. A critical type of electrical contact occurs in tap changers. Because electrical contacts in tap changers must be free to move, they cannot be brazed or bolted and must maintain the contact by pressure. A loose or faulty contact can result in an element of the transformer floating relative to the ground. This can lead to charge build up and result in partial discharges and possible gassing in the oil. Needless to say, making good contact with a connection is important.

The science of electrical contacts has been well studied and the results are fairly surprising. We give a brief and simplified summary of some of these results, especially for copper contacts and bolted connections.

17.4.1 Contact Resistance

Under high magnification, even very smooth polished surfaces appear to be wavy and irregular. When two such surfaces come in contact to make an electrical connection, very few points on each surface actually touch. Yet it is only through these touching points, or asperities, that current can flow. The actual current-carrying area of such contacting surfaces is therefore a small fraction of the apparent surface area. This real contact area A is determined by the force F pressing the surfaces together and the hardness H of the material comprising the surfaces (both surfaces are assumed to be made of the same material) according to the formula

$$A = F/H \quad (17.60)$$

The hardness H must be expressed in units of pressure in order for this formula to be dimensionally correct. Thus, Knoop hardness values may be used but Rockwell hardnesses may not [Wil87].

For a circular contact spot of diameter D , the resistance (called the constriction resistance), R_c , is given by

$$R_c = \rho/D \quad (17.61)$$

where ρ is the resistivity of the material. For a number of such contact spots, the net resistance can be obtained by using an effective diameter in Equation 17.61 obtained from the total contact area [Wil87]. Thus

$$A = \frac{\pi}{4} D^2 = \frac{F}{H} \quad (17.62)$$

so that

$$D = 2 \sqrt{\frac{F}{\pi H}} \quad (17.63)$$

Combining this with Equation 17.61, we obtain

$$R_c = \frac{\rho}{2} \sqrt{\frac{\pi H}{F}} \quad (17.64)$$

where R_c now represents the total contact resistance.

A more complete treatment of a multicontact case is given by [Gre66]. The actual situation is more complicated than that implied by Equation 17.64. However, as mentioned at the end of [Gre66] and as supported by the data of [Wil55], Equation 17.64 works fairly well in practice. Note from this equation that the contact resistance does not depend on the apparent area of contact but, for a given material at a given temperature, depends only on the contact force. The higher the force, the lower the contact resistance, as expected. There is an analogy here with friction. The frictional force, due to static or sliding friction, is proportional to the normal force acting between the surfaces and is independent of the apparent contact area.

Hardness values for copper found in the literature vary from 40 to 160 kg/mm² on the Knoop scale. These possibly represent a range from soft to hard copper. We use a value of 100 kg/mm² = 980 N/mm² = 980 MPa.

17.4.2 Thermal Considerations

The temperature of the contact interface will rise as current passes through it. To avoid overheating and possibly thermal run away, the current must be limited. For an acceptable temperature rise, the maximum allowed current will be determined by the contact resistance, which in turn is determined by the applied force and the material properties of the contact. This theory has been developed in [Gre58], which shows that the current I can be related to the maximum interface temperature, T_m , through

$$IR_{20} = 2\rho_{20} \int_{T_0}^{T_m} \left(2 \int_T^{T_m} k\rho dT' \right)^{-1/2} k dT \quad (17.65)$$

where k is the thermal conductivity, ρ is the resistivity, ρ_{20} and R_{20} are the resistivity and contact resistance at 20°C, respectively, and T_0 is the temperature of the bulk material near the interface.

To integrate Equation 17.65, we need to know how k and ρ vary with temperature within the temperature range of interest and we should preferably have analytic formulas expressing this temperature dependence. For the resistivity, the standard formula is

$$\rho = \rho_{20}[1 + \alpha(T - 20)] \quad (17.66)$$

which expresses a linear variation and applies to most metals near room temperature. In Equation 17.66, T is in Celsius. Substituting in the constants for copper and measuring temperature in kelvin, this becomes

$$\rho_{Cu} = 1.72 \times 10^{-8} [1 + 0.004(T - 293)] \Omega \cdot m \quad (17.67)$$

The thermal conductivity data for copper can be fit reasonably well with

$$k_{\text{Cu}} = 350 \left(1 + \frac{40}{T} \right) \quad (17.68)$$

Here T is in kelvin and k is in watts per (meter kelvin).

Because the combination $k\rho$ appears in Equation 17.65, a simple expression for this product would facilitate the integration of Equation 17.65. Such an expression is given by the Wiedemann–Franz law, which holds approximately for many metals [Wil87]. This law states that

$$k\rho = LT \quad (17.69)$$

where $L = 2.4 \times 10^{-8} \text{ (V/K)}^2$ is the Lorentz constant, T is the absolute temperature in kelvin and k, ρ are in SI units. Figure 17.17 shows the applicability of this formula for copper, where the combination $k\rho/T$ is plotted using the fitted expressions for k and ρ .

Using these analytic formulas for copper and Equation 17.69, we can perform the integrals in Equation 17.65 and find

$$IR_{20} = \frac{2\rho_{20}(350)}{\sqrt{L}} \left[\frac{\pi}{2} - \sin^{-1} \left(\frac{T_0}{T_m} \right) + \frac{40}{T_m} \cosh^{-1} \left(\frac{T_m}{T_0} \right) \right] \quad (17.70)$$

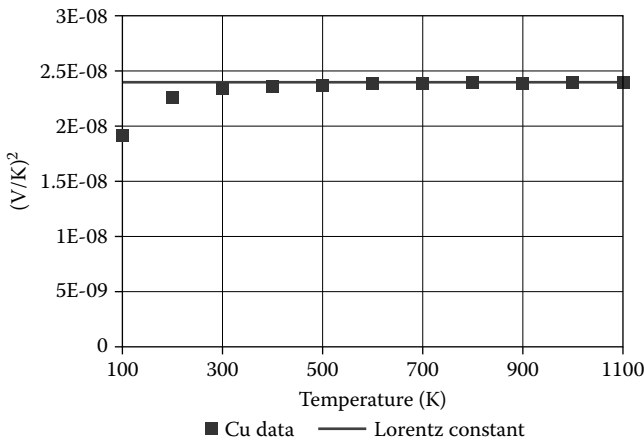


FIGURE 17.17

Copper $k\rho/T$ data compared with the Lorentz constant to check the Wiedemann–Franz law for copper.

with T_0 and T_m in kelvin. Using Equation 17.64 for the contact resistance at 20°C, we have

$$R_{20} = \frac{\rho_{20}}{2} \sqrt{\frac{\pi H}{F}} \quad (17.71)$$

and substituting this into Equation 17.70, we obtain

$$I = 4(350) \sqrt{\frac{F}{\pi H L}} \left[\frac{\pi}{2} - \sin^{-1} \left(\frac{T_0}{T_m} \right) + \frac{40}{T_m} \cosh^{-1} \left(\frac{T_m}{T_0} \right) \right] \quad (17.72)$$

Substituting in the values for H and L in appropriate units, this becomes

$$I = 162.9 \sqrt{F} \left[\frac{\pi}{2} - \sin^{-1} \left(\frac{T_0}{T_m} \right) + \frac{40}{T_m} \cosh^{-1} \left(\frac{T_m}{T_0} \right) \right] \quad (17.73)$$

with I in amperes, F in Newton (N), and temperatures in kelvin.

For connectors inside transformers, $T_0 = 90^\circ\text{C} = 363 \text{ K}$ is a reasonable temperature for copper near the interface. The maximum temperature can be taken as $T_m = 110^\circ\text{C} = 383 \text{ K}$ since the adjacent oil should not exceed this temperature. Using these values, Equation 17.73 becomes

$$I = 58.5 \sqrt{F} \quad (17.74)$$

Thus, a force of 4000 N will permit a current of 3700 A without exceeding the maximum temperature of 110°C at the interface. At this force, the interface resistance at 110°C, using Equation 17.64, is $1.026 \times 10^{-5} \Omega$, and the interface losses are $I^2 R_c = 140.5 \text{ W}$. For this 4000 N force, we find from Equation 17.63 that the effective diameter of the contact area at the interface is 2.28 mm. Thus, the effective contact area is usually a small fraction of the geometrical area over which the force is applied and is spread out over many small contact spots.

From Equation 17.72, we can define $G(T)$ as

$$G(T) = 4(350) \left[\frac{\pi}{2} - \sin^{-1} \left(\frac{T_0}{T_m} \right) + \frac{40}{T_m} \cosh^{-1} \left(\frac{T_m}{T_0} \right) \right] \quad (17.75)$$

so that

$$I = G(T) \sqrt{\frac{F}{\pi H L}} \quad (17.76)$$

Using Equations 17.76 and 17.64, we find

$$I^2 R_c = \frac{\rho G^2(T)}{2L} \sqrt{\frac{F}{\pi H}} \quad (17.77)$$

This shows that, since ρ and G are temperature dependent, for a given ratio of the interface temperature to the temperature of the bulk contact material, the interface losses are proportional to the square root of the contact force. Under these conditions, we see from Equation 17.76 that the current is also proportional to the square root of the contact force. Combining Equations 17.76 and 17.77, we get

$$I^2 R_c = \frac{\rho G(T)}{2\sqrt{L}} I \quad (17.78)$$

Thus, we see that, for the given ratio between the interface temperature and the temperature of the bulk contact material, the contact $I^2 R$ losses are directly proportional to the current. This is much different from conventional resistor behavior, however, note that in order to maintain a constant maximum interface temperature, both the current and resistance change with the applied force in such a way that the loss versus current relationship is linear. Even though the losses increase with current, the maximum interface temperature can remain constant because at higher currents (and forces) the actual contact area increases, so the losses are spread over a greater area.

17.4.3 Practical Considerations

In practice, bolted connections may use Belleville washers, which apply a given force when tightened to flatness. These washers come in different sizes and thicknesses corresponding to the different forces needed to tighten them to flatness. In addition, the applied force can be increased by stacking the washers. Thus, for a given current that the connection must carry, the required force can be obtained from Equation 17.74, and the appropriate size or number of washers is determined.

The apparent contact area is not critical. Our main concern should be to apply a sufficient force. However, in practice the washer or washers must cover the contact area in order to apply their force to the interface. Thus, a minimum area is necessary to accommodate the washers.

References

- [Abr72] Abramowitz, M., and I. A. Stegun, eds. 1972. *Handbook of Mathematical Functions*. New York: Dover Publications.
- [Aco89] Acosta, J., and K. J. Cornick. 1989. Computer models for complex plant based on terminal measurements. *IEEE Trans Power Deliv* 4(2):1393–400.
- [Ahu06] Ahuja, R., and R. M. Del Vecchio. 2006. Transformer stray loss and flux distribution studies using 3D finite element analysis. Seventh International Conference on Transformers, Mumbai, India, January 20–21. II-1–II-8.
- [Ame57] American Institute of Physics. 1957. *American Institute of Physics Handbook*. New York: McGraw-Hill.
- [Aub92] Aubin, J., and Y. Langhame. 1992. Effect of oil viscosity on transformer loading capability at low ambient temperatures. *IEEE Trans Power Deliv* 7(2):516–24.
- [Bel77] Bell, W. R. 1977. Influence of specimen size on the dielectric strength of transformer oil. *Trans Electr Insul* EI-12(4):281–92.
- [Blu51] Blume, L. F., A. Boyajian, G. Camilli, T. C. Lennox, S. Minneci, and V. M. Montsinger. 1951. *Transformer Engineering*, 2nd edition. New York: John Wiley & Sons.
- [Bos72] Bose, A. K. 1972. Dynamic response of windings under short circuit. CIGRE International Conference on Large High-Tension Electric Systems, August 28–September 6, 1972.
- [Bra82] Brandwajin, V., H. W. Dommel, and I. I. Dommel. 1982. Matrix representation of three-phase transformers for steady-state and transient studies. *IEEE Trans Power App Syst* PAS-101(6):1369–78.
- [Chu60] Churchill, R. V. 1960. *Complex Variables and Applications*, 2nd edition. New York: McGraw-Hill.
- [Cla62] Clark, F. M. 1962. *Insulating Materials for Design and Engineering Practice*. New York: John Wiley & Sons.
- [Cle39] Clem, J. E. 1939. Equivalent circuit impedance of regulating transformers. *AIEE Trans* 58:871–3.
- [Cyg87] Cygan, S., and J. R. Laghari. 1987. Dependence of the electric strength on thickness area and volume of polypropylene. *IEEE Trans Electr Insul* 22(6):835–7.
- [Dai73] Daily, J. W., and D. R. F. Harleman. 1973. *Fluid Dynamics*. Reading, MA: Addison-Wesley.
- [Dan90] Danikas, M. G. 1990. Breakdown of transformer oil. *IEEE Electr Insul Mag* 6(5):27–34.
- [deL92] de Leon, F., and A. Semlyen. 1992. Efficient calculation of elementary parameters of transformers. *IEEE Trans Power Deliv* 7(1):376–83.
- [deL92a] de Leon, F., and A. Semlyen. 1992. Reduced order model for transformer transients. *IEEE Trans Power Deliv* 7(1):361–9.
- [Del94] Del Vecchio, R. M. 1994. Magnetostatics. In *Encyclopedia of Applied Physics*, ed. G. L. Trigg, 9:207–27. Berlin: VCH Publishers.
- [Del98] Del Vecchio, R. M., B. Poulin, and R. Ahuja. 1998. Calculation and measurement of winding disk capacitances with wound-in-shields. *IEEE Trans Power Deliv* 13(2):503–9.

- [Del99] Del Vecchio, R. M., and P. Feghali. 1999. Thermal model of a disk coil with directed oil flow. *IEEE Transmission and Distribution Conference*, New Orleans, LA, April 11–16, 914–9.
- [Del01] Del Vecchio, R. M., B. Poulin, and R. Ahuja. 2001. Radial buckling strength calculation and test comparison for core-form transformers. In *Proceedings of the 2001 International Conference of Doble Clients*, Watertown, MA.
- [Del02] Del Vecchio, R. M., R. Ahuja, and R. D. Frenette. 2002. Determining ideal impulse generator settings from a generator-transformer circuit model. *IEEE Trans Power Deliv* 17(1):142–8.
- [Del03] Del Vecchio, R. M. 2003. Eddy-current losses in a conducting plate due to a collection of bus bars carrying currents of different magnitudes and phases. *IEEE Trans Magn* 39(1):549–52.
- [Del04] Del Vecchio, R. M. 2004. Geometric effects in the electrical breakdown of transformer oil. *IEEE Trans Power Deliv* 19(2):652–6.
- [Del06] Del Vecchio, R. M. 2006. Applications of a multiterminal transformer model using two winding leakage inductances. *IEEE Trans Power Deliv* 21(3):1300–8.
- [Del08] Del Vecchio, R. M. 2008. Multiterminal three phase transformer model with balanced or unbalanced loading. *IEEE Trans Power Deliv* 23(3):1439–47.
- [Des69] Desoer, C. A., and E. S. Kuh. 1969. *Basic Circuit Theory*. New York: McGraw-Hill.
- [Dwi61] Dwight, H. B. 1961. *Tables of Integrals and Other Mathematical Data*. 4th edition. New York: Macmillan.
- [Eas65] Eastgate, C. 1965. Simplified steady-state thermal calculations for naturally cooled transformers. *Proc IEE* 112(6):1127–34.
- [End57] Endicott, H. S., and K. H. Weber. 1957. Electrode area effect for the impulse breakdown of transformer oil. *Trans IEEE* 393–8.
- [For69] Forrest, J. A. C., and R. E. James. 1969. Improvements in or relating to windings for inductive apparatus. Patent no. 1,158,325, London, July 16.
- [Franc] Franchek, M. A., and T. A. Prevost. 1992. EHV Weidmann, private communication.
- [Gall75] Gallager, T. J. 1975. *Simple Dielectric Liquids*. Oxford, UK: Clarendon Press.
- [Gre58] Greenwood, J. A., and J. B. P. Williamson. 1958. Electrical conduction in solids, part II: Theory of temperature-dependent conductors. *Proc R Soc Lond A* 246:13–31.
- [Gre66] Greenwood, J. A. 1966. Constriction resistance and the real area of contact. *Br J Appl Phys* 17:1621–32.
- [Gre71] Greenwood, A. 1971. *Electrical Transients in Power Systems*. New York: Wiley-Interscience.
- [Gro73] Grover, F. W. 1973. *Inductance Calculations*, special edition prepared for the Instrument Society of America. New York: Dover Publications.
- [Gum58] Gumbel, E. J. 1958. *Statistics of Extremes*. New York: Columbia University Press.
- [Hig75] Higake, H., K. Endou, Y. Kamata, and M. Hoshi. 1975. Flashover characteristics of transformer oil in large cylinder–plane electrodes up to gap length of 200 mm, and their application to the insulation from outer winding to tank in UHV transformers. *IEEE PES Winter Meeting*, New York, January 26–31.
- [Hir71] Hiraishi, K., Y. Hore, and S. Shida. 1971. Mechanical strength of transformer windings under short-circuit conditions. Paper 71 TP 8-PWR, presented at the *IEEE Winter Power Meeting*, New York, January 31–February 5.
- [Hob39] Hobson, J. E., and W. A. Lewis. 1939. Regulating transformers in power-system analysis. *AIEE Trans* 58:874–86.

- [Hol92] Holland, S. A., G. P. O'Connell, and L. Haydock. 1992. Calculating stray loss in power transformers using surface impedance with finite elements. *IEEE Trans Magn* 28(2):1355–8.
- [Hue72] Huelsman, L. P. 1972. *Basic Circuit Theory with Digital Computations*. Englewood Cliffs, NJ: Prentice-Hall.
- [IEE81] ANSI/IEEE C57.92. 1981. Guide for loading mineral oil immersed transformers up to and including 100 MVA with 55°C or 65°C average winding rise.
- [IEE93] IEEE Std C57.12.00. 1993. IEEE standard general requirements for liquid-immersed distribution, power, and regulating transformers.
- [Jai70] Jain, M. P., and L. M. Ray. 1970. Field pattern and associated losses in aluminum sheet in presence of strip bus bars. *IEEE Trans Power App Syst* PAS-89(7):1525–39.
- [Jes96] Jeszenszky, S. 1996. History of transformers. *IEEE Power Eng Rev* 16(12):9–12.
- [Kau68] Kaufman, R. B., and J. R. Meador. 1968. Dielectric tests for EHV transformers. *IEEE Trans Power App Syst* PAS-87(1):135–45.
- [Kok61] Kok, J. A. 1961. *Electrical Breakdown of Insulating Liquids*. New York: Wiley-Interscience.
- [Kra88] Krause, R. F., and R. M. Del Vecchio. 1988. Low core loss rotating flux transformer. *J Appl Phys* 64(10):5376–8.
- [Kra98] Kramer, A., and J. Ruff. 1998. Transformers for phase angle regulation considering the selection of on-load tap-changers. *IEEE Trans Power Deliv* 13(2):518–25.
- [Kre80] Kreith, F., and W. Z. Black. 1980. *Basic Heat Transfer*. New York: Harper & Row Publishers.
- [Kuf84] Kuffel, E., and W. S. Zaengl. 1988. *High Voltage Engineering*. New York: Pergamon Press.
- [Kul99] Kulkarni, S. V. 1999. Stray loss in power transformers—Evaluation and experimental verification. PhD thesis, Indian Institute of Technology, Mumbai, India.
- [Kul04] Kulkarni, S. V., and S. A. Khaparde. 2004. *Transformer Engineering*. New York: Marcel Dekker.
- [Lam66] Lammeraner, J., and M. Stafl. 1966. *Eddy Currents*. London: Iliffe Books.
- [Lei99] Leites, L. 1999. Lecture notes from presentation at North American transformer plant, Milpitas, CA.
- [Les02] Lesaint, O., and T. V. Top. 2002. Streamer initiation in mineral oil, part I: Electrode surface effect under impulse voltage. *IEEE Trans Dielectr Electr Insul* 9(1):84–91.
- [Lyo37] Lyon, W. V. 1937. *Applications of the Method of Symmetrical Components*. New York: McGraw-Hill.
- [McN91] McNutt, W. J. 1991. Insulation thermal life considerations for transformer loading guides. Paper presented at the IEEE/PES Summer Meeting, San Diego, CA, July 28–August 1.
- [Meh97] Mehta, S. P., N. Aversa, and M. S. Walker. 1997. Transforming transformers. *IEEE Spectr* 34:43–9.
- [Mik78] Miki, A., T. Hosoya, and K. Okuyama. 1978. A calculation method for impulse-voltage distribution and transferred voltage in transformer windings. *IEEE Trans Power App Syst* PAS-97(3):930–9.
- [MIT43] Department of Electrical Engineering, Massachusetts Institute of Technology. 1943. *Magnetic Circuits and Transformers*. Cambridge, MA: MIT Press.
- [Mom02] Mombello, E. E. 2002. Impedances for the calculation of electromagnetic transients within transformers. *IEEE Trans Power Deliv* 17(2):479–88.

- [Mos79] Moser, H. P. 1979. Transformer boards. Special print of *Scientia Electrica*. Berlin: Springer Verlag.
- [Mos87] Moser, H. P., and V. Dahinden. 1987. *Transformer Boards II*. Rapperswil, Switzerland: H. Weidmann AG.
- [Nel89] Nelson, J. K. 1989. An assessment of the physical basis for the application of design criteria for dielectric structures. *IEEE Trans Elect Insul* 24(5):835–47.
- [Nor48] Norris, E. T. 1948. The lightening strength of power transformers. *J IEE* 95:389–406.
- [Nuy78] van Nuys, R. 1978. Interleaved high-voltage transformer windings. *IEEE Trans Power App Syst* PAS-97(5):1946–54.
- [Oli80] Oliver, A. J. 1980. Estimation of transformer winding temperatures and coolant flows using a general network method. *IEE Proc* 127(6):395–405.
- [Ols80] Olson, R. M. 1980. *Essentials of Engineering Fluid Mechanics*, 4th edition. New York: Harper & Row Publishers.
- [Pal69] Palmer, S., and W. A. Sharpley. 1969. Electric strength of transformer insulation. *Proc IEE* 116:1965–73.
- [Pat80] Patel, M. R. 1980. Dynamic stability of helical and barrel coils in transformers against axial short-circuit forces. *IEE Proc* 127(5):281–4.
- [Pav93] Pavlik, D., D. C. Johnson, and R. S. Girgis. 1993. Calculation and reduction of stray and eddy losses in core-form transformers using a highly accurate finite element technique. *IEEE Trans Power Deliv* 8(1):239–245.
- [Pee29] Peek, F. W., Jr. 1929. *Dielectric Phenomena in High Voltage Engineering*, 3rd edition. New York: McGraw-Hill.
- [Pie92] Pierce, L. W. 1992. An investigation of the thermal performance of an oil filled transformer winding. *IEEE Trans Power Deliv* 7(3):1347–58.
- [Pie92a] Pierce, L. W. 1992a. Predicting liquid filled transformer loading capability. IEEE/IAS Petroleum and Chemical Industry Technical Conference, San Antonio, TX, September 28–30.
- [Pry58] Pry, R. H., and C. P. Bean. 1958. Calculation of the energy loss in magnetic sheet materials using a domain model. *J Appl Phys* 29(3):532–3.
- [Pug62] Pugh, E. M., and E. W. Pugh. 1962. *Principles of Electricity and Magnetism*. Reading, MA: Addison-Wesley.
- [Rab56] Rabins, L. 1956. Transformer reactance calculations with digital computers. *AIEE Trans* 75(Pt. I):261–7.
- [Ree73] Rees, J. A., ed. 1973. *Electrical Breakdown in Gases*. New York: John Wiley & Sons.
- [Roh85] Rohsenow, W. M., J. P. Hartnett, and E. N. Ganic, eds. 1985. *Handbook of Heat Transfer Fundamentals*, 2nd edition. New York: McGraw-Hill.
- [Rud40] Rudenberg, R. 1940. Performance of traveling waves in coils and windings. *Trans AIEE* 59:1031–40.
- [Rud68] Rudenberg, R. 1968. *Electrical Shock Waves in Power Systems*. Cambridge, MA: Harvard University Press.
- [Sar00] Saravolac, M. P., P. A. Vertigen, C. A. Sumner, and W. H. Siew. 2000. Design verification criteria for evaluating the short circuit withstand capability of transformer inner windings. CIGRE Session 2000, 12-208.
- [Shi63] Shipley, R. B., D. Coleman, and C. F. Watts. 1963. Transformer circuits for digital studies. *AIEE Trans Part III* 81:1028–31.
- [Smy68] Smythe, W. R. 1968. *Static and Dynamic Electricity*, 3rd edition. New York: McGraw-Hill.

- [Ste62] Stenkvist, E., and L. Torseke. 1962. Short-circuit problems in large transformers. CIGRE, Report No. 142, Appendix II.
- [Ste62a] Stevenson, W. D., Jr. 1962. *Elements of Power System Analysis*. New York: McGraw-Hill.
- [Ste64] Stein, G. M. 1964. A study of the initial surge distribution in concentric transformer windings. *IEEE Trans Power App Syst* 83:877–93.
- [Ste72] Steel, R. B., W. M. Johnson, J. J. Narbus, M. R. Patel, and R. A. Nelson. 1972. Dynamic measurements in power transformers under short-circuit conditions. International Conference on Large High-Tension Electric Systems, August 28–September 6.
- [Tay58] Taylor, E. D., B. Berger, and B. E. Western. 1958. An experimental approach to the cooling of transformer coils by natural convection. *Proceedings of the IEE*, 105A:141–152.
- [Tho79] Thompson, H. A., F. Tillery, and D. U. von Rosenberg. 1979. The dynamic response of low voltage, high current, disk type transformer windings to through fault loads. *IEEE Trans Power App Syst* PAS-98(3):1091–8.
- [Tim55] Timoshenko, S. 1955. *Strength of Materials, Parts I and II*, 3rd edition. Princeton, NJ: D. Van Nostrand Co.
- [Tim70] Timoshenko, S. P., and J. N. Goodier. 1970. *Theory of Elasticity*, 3rd edition. New York: McGraw-Hill.
- [Top02] Top, T. V., G. Messala, and O. Lesaint. 2002. Streamer propagation in mineral oil in semi-uniform geometry. *IEEE Trans Dielectr Electr Insul* 9(1):76–83.
- [Top02a] Top, T. V., and O. Lesaint. 2002. Streamer initiation in mineral oil, part II: Influence of a metallic protrusion on a flat electrode. *IEEE Trans Dielectr Electr Insul* 9(1):92–6.
- [Tri82] Trinh, N. G., C. Vincent, and J. Regis. 1982. Statistical dielectric degradation of large-volume oil-insulation. *IEEE Trans Power App Syst* PAS-101(10):3712–21.
- [Wat66] Waters, M. 1966. *The Short-Circuit Strength of Power Transformers*. London: Macdonald & Co.
- [Web56] Weber, K. H., and H. S. Endicott. 1956. Area effect and its extremal basis for the electric breakdown of transformer oil. *AIEE Trans* 75(3):371–81.
- [Wes64] Central Station Engineers of the Westinghouse Electric Corp. 1964. *Electrical Transmission and Distribution Reference Book*. Pittsburgh, PA: Westinghouse Electric Corp.
- [Wil53] Wilson, W. R. 1953. A fundamental factor controlling the unit dielectric strength of oil. *AIEE Trans Power App Syst* 72:68–74.
- [Wil55] Wilson, R. W. 1955. The contact resistance and mechanical properties of surface films on metals. *Proc Phys Soc B* 68:625–41.
- [Wil87] Williamson, J. B. P. 1987. Intensive course on electrical contacts. Course notes, sponsored by the IEEE Holm Conference on Electrical Contacts, June 15–19, 1987, San Francisco, CA.
- [Wil88] Wilcox, D. J., M. Conlon, and W. G. Hurley. 1988. Calculation of self and mutual impedances for coils on ferromagnetic cores. *IEE Proc* 135(7):470–6.
- [Wil89] Wilcox, D. J., W. G. Hurley, and M. Conlon. 1989. Calculation of self and mutual impedances between sections of transformer windings. *IEE Proc* 136(5):308–14.